THE JOURNAL OF

PHYSICAL CHEMISTRY

Volume 74, Number 12 June 11, 1970

FUEL CELL SYSTEMS—II

ADVANCES IN CHEMISTRY SERIES NO. 90

Thirty-one papers from the fifth of the biennial Fuel Cell Symposia sponsored by the Division of Fuel Chemistry, chaired by Bernard S. Baker. Topics include:

- **fuel cell power systems**
- **electrode structure**
- **use of hydrocarbons**
- **electrode catalysis and mechanisms**
- **high temperature fuel cells**
- **fuel cell systems**

Fuel cells are still doing their job well in the space program. Total energy, stationary fuel cell power plants seem worth a commercial push, and some hybrid devices look promising.

456 pages with index Cloth bound (1969) $17.50

Free set of L. C. cards with library orders upon request

Other books in the ADVANCES IN CHEMISTRY SERIES in fuel chemistry include:

No. 80 Chemical Reactions in Electrical Discharges. A wide range of topics is covered in 37 papers by chemists, physicists, and engineers—treatments of decomposition and dissociation reactions, ion-molecule reactions, chemical syntheses, and chemical engineering aspects and physics of reactions in electrical discharges. 514 pages
Cloth (1969) $15.00

No. 78 Literature of Chemical Technology. Forty articles discuss the literature of many aspects of chemical technology; seven of these are related to fuel cells, including electrochemistry of non-metals, noble metals, ceramics, enamels and glass, refractories, resources for petroleum chemicals, rocket propulsion, and rocket construction materials. 732 pages
Cloth (1968) $17.50

No. 69 Fuel Gasification. Waning natural gas supplies and the threat of nuclear fuels are renewing interest in converting solid fuels to high B.t.u. gas. Sixteen studies survey current research in the U.S. and elsewhere from which commercial processes seem imminent. 276 pages
Cloth (1967) $10.50

No. 64 Regenerative EMF Cells. Seventeen papers survey current progress and research on regenerative systems for converting and storing electrical energy. Principal emphasis is on thermally regenerative systems, but chemical and photochemical systems are considered. 309 pages
Cloth (1967) $11.00

No. 55 Coal Science. Forty-seven papers include coal origins, coal metamorphosis, coal as an organic rock, physical and chemical structure of coals, reactivity and reactions of coal in relation to structure and rank. 743 pages
Cloth (1966) $17.50

No. 54 Advanced Propellant Chemistry. Primarily directed toward the search for new oxidizers. Topics include theoretical approaches to advanced oxidizers, surveys of oxygen- and fluorine-containing oxidizers, fuels and binders, liquid systems. 290 pages
Cloth (1966) $10.50

No. 47 Fuel Cell Systems. New systems for the energy converter proving itself in military and space uses. Topics include fuel cells for submarines and satellites, hydrogen-bromine fuel cells, molten carbonate fuel cells, and a coal burning fuel-cell power plant. 360 pages
Cloth (1965) $10.50

No. 20 Literature of the Combustion of Petroleum. Twenty-one papers about the chemistry and kinetics of combustion, petroleum products as the fuel for engines, and combustion studies in engines. 295 pages
Paper (1958) $8.00

No. 5 Progress in Petroleum Technology. Survey of 25 years of progress at the ACS Diamond Jubilee. Thirty-two papers on all aspects of petroleum processing and products. 392 pages
Paper (1951) $8.00

Postpaid in U.S. and Canada; plus 30 cents elsewhere.

Order from:

SPECIAL ISSUES SALES
AMERICAN CHEMICAL SOCIETY
1155 SIXTEENTH ST., N.W.
WASHINGTON, D.C. 20036

NOTES

COMMUNICATIONS TO THE EDITOR

AUTHOR INDEX

NOTICE TO AUTHORS

I. General Considerations

The Journal of Physical Chemistry is devoted to reporting both experimental and theoretical research dealing with fundamental aspects of physical chemistry. Space limitations necessitate giving preference to research articles dealing with previously unanswered basic questions in physical chemistry. Acceptable topics are those of general interest to physical chemists, especially work involving new concepts, techniques, and interpretations. Research that may lead to reexaminations of generally accepted views is, of course, welcome.

The Journal of Physical Chemistry publishes three types of manuscripts: *Articles*, *Notes*, and *Communications to the Editor*.

Authors reporting data should include, if possible, an interpretation of the data and its relevance to the theories of the properties of matter. However, the discussion should be concise and to the point and excessive speculation is to be discouraged. Papers reporting redeterminations of existing data will be acceptable only if there is reasonable justification for repetition: for example, if the more recent or more accurate data lead to new questions or to a reexamination of well known theories. Manuscripts that are essentially applications of chemical data or reviews of the literature are, in general, not suitable for publication in *The Journal of Physical Chemistry*. Detailed comparisons of methods of data analysis will be considered only if the paper also contains original data, or if such comparison leads to a genesis of new ideas.

Authors should include an introductory statement outlining the scientific rationale for the research. The statement should clearly specify the questions for which answers are sought and the connection of the present work with previous work in the field. All manuscripts are subject to critical review. It is to be understood that the final decision relating to a manuscript's suitability rests solely with the editorial staff.

Symposium papers are sometimes published as a group, but only after special arrangement with the editor.

Authors' attention is called to the "Handbook for Authors," available from the Special Issues Sales Department, American Chemical Society, 1155 Sixteenth St., N.W., Washington, D. C. 20036, in which pertinent material is to be found.

II. Types of Manuscripts

A. Articles should cover their subjects with thoroughness, clarity, and completeness. However, authors should also strive to make their *Articles* as concise as possible, avoiding unnecessary historical background. Abstracts to *Articles* should be brief—300 words is a maximum—and should serve to summarize the significant data and conclusions. The abstract should convey the essence of the *Article* to the reader.

B. Notes. Papers submitted in the category of *Notes* should report work that represents a complete and self-contained study of limited scope. *Notes* are a luxury in the present scientific literature; authors should not use a *Note* to report work that is part of a continuing study. *Notes* are not to be used for reporting preliminary results; reports of such work should be postponed until the work is completed or should be submitted as *Communications* if the results are of immediate or unusual interest to physical chemists. The same criteria of suitability for publication apply to *Notes* as to *Articles* (see General Considerations). The length of a *Note*, including tables, figures, and text, must not exceed 1.5 journal pages (1500 words or the equivalent). A *Note* should not be accompanied by an abstract.

C. Communications to the Editor are of two types, *Letters* and *Comments*. Both types are restricted to three-quarters of a page (750 words or the equivalent) including tables, figures, and text, and both types of *Communications* are subject to critical review, but special efforts will be made to expedite publication.

Letters should report preliminary results whose immediate availability to the scientific community is deemed important, and whose topic is timely enough to justify the double publication that usually results from the publication of a *Letter*.

Comments include significant remarks on the work of others. The editorial staff will generally permit the authors of the work being discussed to reply.

III. Introduction

All manuscripts submitted should contain brief introductory remarks describing the purpose of the work and giving sufficient background material to allow the reader to appreciate the state-of-knowledge at the time when the work was done. The introductory remarks in an *Article* should constitute the first section of the paper and should be labeled accordingly. In *Notes* and *Communications*, the introductory material should not be in such a separate section. To judge the appropriateness of the manuscript for *The Journal of Physical Chemistry*, the editorial staff will place considerable weight on the author's intentions as stated in the Introduction.

IV. Functions of Reviewers

The editorial staff requests the scientific advice of reviewers who are active in the area of research covered by the manuscript. The reviewers act only in an advisory capacity and the final decision concerning a manuscript is the responsibility of the editorial staff. The reviewers are asked to comment not only on the scientific content, but also on the manuscript's suitability for *The Journal of Physical Chemistry*. With respect to *Communications*, the reviewers are asked to comment specifically on the urgency of publication. All reviews are anonymous and the reviewing process is most effective

if reviewers do not reveal their identities to the authors. An exception arises in connection with a manuscript submitted for publication in the form of a comment on the work of another author. Under such circumstances the first author will, in general, be allowed to review the communication and to write a rebuttal, if he so chooses. The rebuttal and the original communication may be published together in the same issue of the journal. Revised manuscripts are generally sent back to the original reviewers, who are asked to comment on the revisions. If only minor revisions are involved, the editorial staff examines the revised manuscript in light of the recommendations of the reviewers and without seeking further opinions. For the convenience of reviewers, authors are advised to indicate clearly, either in the manuscript or in a covering letter, the specific revisions that have been made.

V. Submission of Manuscripts

All manuscripts must be submitted at least in duplicate and preferably in triplicate to expedite handling. Manuscripts must be typewritten, double-spaced copy, on $8^1/_2 \times 11$ in. paper. Legal sized paper is not acceptable. Authors should be certain that copies of the manuscript are clearly reproduced and readable. **Authors submitting figures must include the original drawings or photographs thereof, plus two xerographic copies for review purposes. These reproductions of the figures should be on $8^1/_2 \times 11$ in. paper.** Graphs must be in black ink on white or blue paper. Lettering at the sides of graphs may be penciled in and will be typeset. Figures and tables should be held to a minimum consistent with adequate presentation of information. All original data which the author deems pertinent must be submitted along with the manuscript. For example, a paper reporting a crystal structure should include structure factor tables for use by the reviewers.

Footnotes and references to the literature should be numbered consecutively within the paper; the number should also be placed in parentheses in the left margin opposite the line in which the reference first appears. A complete list of references should appear at the end of the paper. Initials of the authors referred to in the citations should be included in the complete reference at the back of the paper. Nomenclature should conform to that used in *Chemical Abstracts* and mathematical characters should be underlined for italics, Greek letters should be annotated, and subscripts and superscripts clearly marked.

Papers should not depend for their usefulness on unpublished material, and excessive reference to material in press is discouraged. References not readily available (*e.g.*, private technical reports, preprints, or articles in press) that are necessary for a complete review of the paper must be included with the manuscript for use by the reviewers.

VI. Revised Manuscripts

A manuscript sent back to an author for revision should be returned to the editor within 6 months; otherwise it will be considered withdrawn and treated as a new manuscript when and if it is returned. Revised manuscripts returned to the editor must be submitted in duplicate and all changes should be made by typewriter. **Unless the changes are very minor, all pages affected by revision must be retyped.** If revisions are so extensive that a new typescript of the manuscript is necessary, it is requested that a copy of the original manuscript be submitted along with the revised one.

VII. Supplementary Material

By arrangement with the National Auxiliary Publications Service (NAPS) of the American Society for Information Science (ASIS), supplementary material, such as extensive tables, graphs, spectra, and calculations, can be distributed in the form of microfiche copies or photoprints readable without optical aids. This material should accompany the manuscript for review by the editors and reviewers. Upon acceptance, it will be sent by the editor to NAPS where it is assigned a document number. A deposit fee of $12.50 (for 60 manuscript pages or less) is required and should be included with the material sent to the editor. The check must be made payable to CCMIC–NAPS. Further details may be obtained from NAPS c/o CCM Information Corp., 909 3rd Ave., New York, N. Y. 10022.

VIII. Proofs and Reprints

Galley proofs, original manuscript, cut copy, and reprint order form are sent by the printer directly to the author who submitted the manuscript. The attention of the authors is directed to the instructions which accompany the proof, especially the requirement that all corrections, revisions, and additions be entered on the proof and not on the manuscript. Proofs should be checked against the manuscript (in particular all tables, equations, and formulas, since this is not done by the editor) and returned as soon as possible. No paper is released for printing until the author's proof has been received. Alterations in an article after it has been set in type are made at the author's expense, and it is understood that by entering such alterations on proofs the author agrees to defray the cost thereof. The filled-out reprint form must be returned with the proof, and if a price quotation is required by the author's organization a request for it should accompany the proof. Since reprinting is generally done from the journal press forms, all orders must be filed before press time. None can be accepted later, unless a previous request has been made to hold the type. Reprint shipments are made a month or more after publication, and bills are issued by the printer subsequent to shipment. Neither the editors nor the Washington office keeps any supply of reprints. Therefore, only the authors can be expected to meet requests for single copies of papers.

A page charge is assessed to cover in part the cost of publication. Although payment is expected, it is not a condition for publication. Articles are accepted or rejected only on the basis of merit, and the editor's decision to publish the paper is made before the charge is assessed. The charge per journal page is $50.

THE JOURNAL OF
PHYSICAL CHEMISTRY
Registered in U. S. Patent Office © Copyright, 1970, by the American Chemical Society

VOLUME 74, NUMBER 12 JUNE 11, 1970

First-Order Perturbation Theory in the LCAO Approximation

by T. Vladimiroff[1]

Department of Chemistry, State University of New York at Stony Brook, Stony Brook, New York 11790
(Received March 24, 1969)

The Roothaan SCF LCAO method is extended to include the effects of a small, one-electron perturbation. The LCAO approximation is assumed to be valid for the perturbed problem but the method differs from that of McWeeny because an effort is made to find a new basis set which is more suitable for the expansion of the perturbed molecular orbitals than the one employed for the unperturbed problem. The proposed method differs from that of Cohen and Roothaan in that different orders in the perturbation parameter are separated.

Introduction

Advances in the capabilities of high-speed digital computers may soon make it possible to obtain reasonably accurate ab initio physical data for small molecules. With this end in mind, quantum chemists have shown considerable interest in all aspects of perturbation theory.[2a] In particular, two areas have been considered, one being the improvement of approximate wave functions,[2b] the other being the study of weak interactions.[3,4] The work reported in this paper will only be concerned with this second aspect and will be confined to one-electron perturbations.

The most common approach to the second-order energy in perturbation theory is to employ an infinite expansion using exact eigenstates of the Hamiltonian operator. Since for most molecular problems the exact eigenproblem has not been solved, approximations must be introduced. The expansion can be obtained in closed form if the "average energy" approximation is invoked; however, there is no rigorous method by which the average energy can be estimated so this does not constitute an ab initio method. Another approach is to truncate the series and to approximate the remaining terms. This is reasonable if the series converges rapidly and good approximations to the ground and exited states are available.[5] Usually neither of these conditions is satisfied in practice.

Hylleraas[6] proposed a variational method of solution whereby the second-order energy could be minimized with respect to certain adjustable parameters. Ishiguro and Koide[7] used this technique to perform calculations on the H_2 molecule. Tillieu and Guy[8] performed magnetic susceptibility calculations and Das and Bersohn[9] calculated the proton nmr shielding constant in a similar manner. Karplus and Kolker[10] succeeded in formulating a method which only utilized one-electron integrals; however, this resulted in a certain loss of accuracy.

More recently, McWeeny[11] and others[12,13] have developed the self-consistent field (SCF) perturbation

(1) Address communications to the Propellants Laboratory, Bldg. 162-N, Picatinny Arsenal, Dover, N. J. 07801.

(2) (a) J. O. Hirschfelder, W. Byers Brown, and S. T. Epstein, *Advan. Quantum. Chem.*, **1**, 255 (1964); (b) J. I. Musher, *Rev. Mod. Phys.*, **39**, 203 (1967).

(3) W. N. Lipscomb, *Advan. Magn. Resonance*, **2**, 137 (1966).

(4) A. Dalgarno, *Advan. Phys.*, **11**, 281 (1962).

(5) T. J. Dougherty, T. Vladimiroff, and S. T. Epstein, *J. Chem. Phys.*, **45**, 1803 (1966).

(6) E. A. Hylleraas, *Z. Phys.*, **65**, 209 (1930).

(7) E. Ishiguro and S. Koide, *Phys. Rev.*, **94**, 350 (1954).

(8) J. Tillieu and J. Guy, *C. R. Acad. Sci.*, **239**, 1203, 1283 (1954); **240**, 1402 (1955).

(9) T. P. Das and R. Bersohn, *Phys. Rev.*, **104**, 849 (1956).

(10) M. Karplus and H. J. Kolker, *J. Chem. Phys.*, **38**, 1263 (1963).

(11) R. McWeeny, *Phys. Rev.*, **126**, 1028 (1962).

method. This type of approach automatically incorporates an attractive feature: if μV is the correction for the "badness" of the approximate eigenfunction, then all properties determined by one-electron operators are necessarily accurate through the first order in μ. However, much of the inherent accuracy of this method may be lost because a poor basis set is used in the calculation. This formulation employs the same basis set to expand both the zero-order molecular orbitals (MO) and the higher-order corrections. Since the basis set chosen to "span"[14] the space of the zero-order molecular orbitals (MO's) cannot be expected to "span" the space of the perturbed MO's, additional basis functions must be used. However, the correct number and type of functions to be added is difficult to determine and recent calculations indicate that this is not always done successfully. For example, a calculation of the electrical polarizability of methyl fluoride produced only 65% of the experimental value.[15] This was attributed to the inadequacy of the basis set employed. Thus there is a real need of developing improved basis sets to be used in SCF perturbation calculations.

One such attempt has achieved a fair amount of acceptance. This is the use of gauge-invariant atomic orbitals (GIAO) in calculations involving a magnetic field. London[16] first suggested their use and subsequently they have been employed by Pople,[17] Aleksandrov,[18] and Hameka[19] for the calculation of magnetic susceptibilities and nmr chemical shifts.

The GIAO's have never been used in conjunction with the SCF perturbation theory in order to realize the full potential of this method. The approach may well be worth pursuing since the choice of a better basis set constitutes the only road to improvement within the linear combination of atomic orbitals (LCAO) approximation. However, the concept of gauge invariant orbitals cannot be easily generalized to other types of perturbations so that a somewhat different point of view will be adopted in this paper.

First-Order Wave Function in the LCAO Approximation

(*a*) *General Approach.* The wave function of a molecule is usually built up of molecular orbitals. Each molecular orbital is assumed to be a linear combination of atomic orbitals. For a molecular orbital, ψ_i^0 written as a linear combination of atomic orbitals ϕ_s^0, we have

$$\psi_i^0 = \sum c_{is}^0 \phi_s^0 \qquad (1)$$

If a perturbation of strength λ is applied, we shall still seek a solution of the form of eq 1 except that both the atomic orbitals and the coefficients will now depend on λ

$$\psi_i(\lambda) = \sum c_{is}(\lambda)\phi_s(\lambda) \qquad (2)$$

The general form of the solution is similar to eq 3 of Cohen and Roothaan[20] except that instead of adding new basis functions to eq 1 in order to expand the perturbed MO's we assume that there exists a basis set $\phi_s(\lambda)$ which is more suitable for the perturbed problem, and we would like to have the perturbation operator play a role in determining this basis set. If λ is small the expressions can be expanded and only the first-order terms kept

$$c_{is}(\lambda) = c_{is}^0 + \lambda c_{is}^1 + \ldots \qquad (3a)$$

$$\phi_s(\lambda) = \phi_s^0 + \lambda \phi_s^1 + \ldots \qquad (3b)$$

Expansion 3b is not true in general if the basis set is degenerate; however, one can always find a linear combination of the degenerate functions for which 3b is true, *i.e.*, the one with respect to which the perturbation is diagonal.[21] Equations 3a and 3b can be substituted into eq 2 to obtain

$$\psi_i(\lambda) = \sum c_{is}^0 \phi_s^0 + \lambda \sum (c_{is}^1 \phi_s^0 + c_{is}^0 \phi_s^1) + \ldots \qquad (4)$$

Thus in order to get the first-order correction to each molecular orbital, one must obtain the first-order corrections to the basis functions, ϕ_s^1 and the first-order corrections to the coefficients, c_{is}^1.

(*b*) *The Functions ϕ_s^1's.* Deciding what the $\phi_s(\lambda)$ should be is difficult because the original ϕ_s^0 basis set was never uniquely specified by Roothaan.[22] It is possible to "justify" the choice of $\phi_s(\lambda)$ about as well as the choice of ϕ_s^0 and this is done in the Appendix. From a physical point of view, it is possible to visualize that each of AO's is distorted by the perturbation in the same way that it would have been distorted if it actually was the eigenfunction of an appropriately defined Hamiltonian. If an electric field is applied, each of the AO's becomes polarized and it is these polarized AO's which should be used in the perturbed SCF calculation. In a more quantitative fashion the function ϕ_s^1 should be interpreted as the first-order distortion ϕ_s^0 undergoes as the perturbation is turned on. Since ϕ_s^0 is an atomic orbital, ϕ_s^1 can often be found exactly. ϕ_s^1 satisfies the usual inhomogeneous differential equation

(12) R. M. Stevens, R. M. Pitzer, and W. N. Lipscomb, *J. Chem. Phys.*, **38**, 550 (1963).

(13) A. T. Amos and G. G. Hall, *Theor. Chim. Acta*, **5**, 148 (1966).

(14) C. C. J. Roothaan and P. Bagus, "Methods in Computational Physics," Vol. 2, Academic Press, Inc., New York, N. Y., 1963, p 67.

(15) G. P. Arrighini, C. Guidotti, M. Maestro, R. Moccia, and O. Salvetti, *J. Chem. Phys.*, **51**, 480 (1969).

(16) F. London, *J. Phys. Radium*, **8**, 397 (1937).

(17) J. A. Pople, *Proc. Roy. Soc., Ser. A*, **239**, 541, 550 (1957).

(18) I. V. Aleksandrov, *Sov. Phys. Dokl.*, **3**, 325, 799 (1958).

(19) H. F. Hameka, *Mol. Phys.*, **1**, 203 (1958); *Rev. Mod. Phys.*, **34**, 87 (1962); *Physica*, **28**, 908 (1962).

(20) H. D. Cohen and C. C. J. Roothaan, *J. Chem. Phys.*, **43**, S34 (1965).

(21) In the usual GIAO method this condition is not met. To satisfy this requirement in the presence of a magnetic field the unperturbed basis set should be used in its complex form, *i.e.*, a radial part times a spherical harmonic.

(22) C. C. J. Roothaan, *Rev. Mod. Phys.*, **23**, 69 (1951).

$$(H_0^s - E_0^s)\phi_s^1 = (E_1^s - h_1)\phi_s^0 \quad (5a)$$

h_1 is the perturbation operator, $E_1^s = (\phi_s^0|h_1|\phi_s^0)$, and $H_0^s\phi_s^0 = E_0^s\phi_s^0$. Such an operator H_0^s can always be found[23] and is discussed further in the Appendix.

An alternate method suggested by Dalgarno and Lewis[24] and by Schwartz[25] is to solve the inhomogeneous equation (in atomic units)

$$\phi_s^0\nabla^2F_s + 2(\nabla F_s)\cdot(\nabla\phi_s^0) = 2(h_1 - E_1)\phi_s^0 \quad (5b)$$

where

$$\phi_s^1 = F_s\phi_s^0 - (\phi_s^0F_s\phi_s^0)\phi_s^0$$

Equation 5 has not had as much use as it merits. This is probably because there is more interest in molecular problems than in atomic problems and eq 5b is a lot easier to apply in the latter case than in the former case.

(*c*) *The Coefficients* c_{ts}'s. The new coefficients should be obtained in the same way as the original ones. This is possible since a variational principle exists at each step in perturbation theory just as it did for the unperturbed problem. The original coefficients were obtained by setting the secular determinant equal to zero

$$|(\phi_r, \mathcal{H}_{\text{eff}}\phi_s) - E(\phi_r, \phi_s)| = 0$$

To calculate the c_{ts}'s terms to order λ should be kept. Since $\mathcal{H}_{\text{eff}}$ usually involves all the other molecular orbitals, which now depend on the perturbation, the final solution should be obtained in a self-consistent way.[26]

(*d*) *The Self-Consistent Solution.* When the molecular orbitals are given by eq 1 the equations[22] determining the c_{is}'s and the orbital energies ϵ_i will be

$$\sum_s(F_{rs} - \epsilon_iS_{rs})c_{is} = 0 \quad (6a)$$

where

$$S_{rs} = \int \phi_r^*\phi_s \, d\tau \quad (6b)$$

$$F_{rs} = h_{rs} + \sum_{\text{ut}}\sum_{\substack{\text{occ}\\\text{orb}}}c_{iu}c_{it}^*\{2(tr|us) - (tr|su)\} \quad (6c)$$

and

$$(tu|rs) = \int\phi_t^*(1)\phi_u^*(2)r_{12}^{-1}\phi_r(1)\phi_s(2)d\tau_1d\tau_2 \quad (6d)$$

$$h_{rs} = \int\phi_r^*(-{}^1/_2\nabla^2 - \sum_\alpha z_\alpha/r_\alpha)\phi_s d\tau \quad (6e)$$

The application of a perturbation will not only affect F_{rs} directly by the addition of a term $\lambda H_{rs}^1 = \lambda(\phi_r^0h_1\phi_s^0)$ but indirectly as well since the basis functions and the molecular orbital coefficients will change so that

$$F_{rs} = F_{rs}^0 + \lambda F_{rs}^1 + \ldots \quad (7a)$$

$$\epsilon_i = \epsilon_i^0 + \lambda\epsilon_i^1 + \ldots \quad (7b)$$

$$S_{rs} = S_{rs}^0 + \lambda S_{rs}^1 + \ldots \quad (7c)$$

$$c_{is} = c_{is}^0 + \lambda c_{is}^1 + \ldots \quad (7d)$$

By substituting 4 into 6 one obtains by keeping only terms first-order in λ

$$F_{rs}^0 = h_{rs}^0 + \sum_{\text{ut}}\sum_{\substack{\text{occ}\\\text{orb}}}c_{iu}^0c_{it}^{0*} \times \{2(t^0r^0|u^0s^0) - (t^0r^0|s^0u^0)\} \quad (8a)$$

$$F_{rs}^1 = h_{rs}^1 + \sum_{\text{ut}}\sum_{\substack{\text{occ}\\\text{orb}}}[(c_{iu}^0c_{it}^{1*} + c_{iu}^1c_{it}^{0*}) \times (2(t^0r^0|u^0s^0) - (t^0r^0|s^0u^0)) + c_{iu}^0c_{it}^{0*}\{2(t^1r^0|u^0s^0) - (t^1r^0|s^0u^0) + 2(t^0r^1|u^0s^0) - (t^0r^1|s^0u^0) + 2(t^0r^0|u^1s^0) - (t^0r^0|s^0u^1) + 2(t^0r^0|u^0s^1) - (t^0r^0|s^1u^0)\} + H_{rs}^1 \quad (8b)$$

and $h_{rs}^1 = \int\phi_r^{1*}(-{}^1/_2\nabla^2 - \sum_\alpha z_\alpha/r_\alpha)\phi_s^0d\tau + \int\phi_r^0(-{}^1/_2\nabla^2 - \sum_\alpha z_\alpha/r_\alpha)\phi_s^1d\tau$. The s^0 indicates that ϕ_s^0 is to be used and s^1 indicates that ϕ_s^1 is to be used.

$$S_{rs}^0 = \int\phi_r^{0*}\phi_s^0d\tau \quad (9a)$$

$$S_{rs}^1 = \int\phi_r^{1*}\phi_s^0d\tau + \int\phi_r^{0*}\phi_s^1d\tau \quad (9b)$$

The equations to be solved become

$$\sum_s(F_{rs}^0 - \epsilon_i^0S_{rs}^0)c_{is}^0 = 0 \quad (10a)$$

$$\sum_s(F_{rs}^0 - \epsilon_i^0S_{rs}^0)c_{is}^1 = (\epsilon_i^0S_{rs}^1 + \epsilon_i^1S_{rs}^0 - F_{rs}^1)c_{is}^0 \quad (10b)$$

The zero-order equation should be solved in the usual way. The first-order equation can be written in matrix form

$$(\mathbf{F} - \epsilon_i\mathbf{S}^0)\mathbf{c}_i^1 = (\epsilon_i^0\mathbf{S}^1 + \epsilon_i^1\mathbf{S}^0 - \mathbf{F}^1)\mathbf{c}_i^0 \quad (11)$$

and the usual assumption made

$$\mathbf{c}_i^1 = \sum_j a_{ji}^1\mathbf{c}_j^0 \quad (12)$$

Restricting j to the unoccupied orbitals[11,12] one obtains, using the property that $\mathbf{c}_i^{0\dagger}\mathbf{S}^0\mathbf{c}_j^0 = \delta_{ij}$

$$a_{ji}^1 = \frac{\mathbf{c}_j^{0+}(\epsilon_i^0\mathbf{S}^1 - \mathbf{F}^1)\mathbf{c}_i^0}{\epsilon_j^0 - \epsilon_i^0} \quad (13)$$

i occupied, j unoccupied.

Since eq 8b for $\mathbf{F}^1$ involves the coefficient c_{is}^1, they can be found in an iterative manner. One can always assume they are zero initially, calculate a set using eq 12 and 13, calculate a new $\mathbf{F}^1$ etc., until self-consistency is achieved. Since much of the effect of the perturbation is already included in the functions ϕ_s^1, convergence should be rapid.

(23) R. M. Sternheimer, *Phys. Rev.*, **96**, 951 (1954).
(24) A. Dalgarno and J. T. Lewis, *Proc. Roy. Soc., Ser. A*, **233**, 70 (1955).
(25) C. Schwartz, *Ann. Phys.*, **6**, 156 (1959).
(26) A. Dalgarno, *Proc. Roy. Soc., Ser. A*, **251**, 282 (1959).

Discussion

In a sense, the present state of SCF calculations by the expansion method still remains somewhat unsatisfactory since the results are only as good as the guess of the basis set employed.[14] It is far more satisfying from both the theoretical and the practical points of view to allow the particular Hamiltonian of interest to play a role in determining the appropriate basis set. Perhaps the recently developed methods of exponent optimization[27,28] will help place more emphasis in this direction. This trend should likewise be encouraged for the perturbed problem.

Choosing an appropriate basis set for the perturbed problem is even more difficult in practice due to a lack of experience. Also, different perturbation operators require different basis sets making a trial and error procedure inefficient. An exception to this is the case of a magnetic field. In this case there is a close relationship between the solutions of eq 5a and the properties of gauge transformations from which it can be inferred[12,29] that $\phi_s^0(r)$ perturbed by a magnetic field should be $r\phi_s^0(r)$. The problem is not so straightforward if the perturbation operator is one of the electronic multipole moments[4] or the Fermi contact operator[30] used in the calculation of nmr spin–spin coupling constants. It is for these perturbations that the procedure described in this paper should be most helpful.

It should also be noted that the proposed technique handles the ϕ_s^1's more efficiently than the usual perturbed SCF method.[11-13] Including the ϕ_s^1's in the original unperturbed basis set primarily if not exclusively for the expansion of the first-order corrections requires the computation of extra coulomb and exchange integrals. The length of the calculation is to a large degree determined by the number of two-electron integrals which must be calculated. Doubling the basis set in the usual perturbed SCF calculation requires $2(2n)^4 = 32n^4$ such integrals to be evaluated. In the present method the original $2n^4$ integrals and the $8n^4$ integrals in eq 8b must be calculated, or a total of $10n^4$. If the zero-order basis set is essentially complete as far as the unperturbed problem is concerned, the accuracy for the two methods should be about the same since the ϕ_s^1 will not improve the zero-order wave function very much. But the proposed approach will be three times faster.

Acknowledgment. The author thanks Professors J. I. Musher and P. C. Lauterbur for helpful discussions and acknowledges the support of the National Science Foundation, Grant Number GP-5780.

Appendix

The LCAO approximation can always be considered to be an expansion of an unknown MO using a linear combination of known basis functions. As long as a complete set of basis functions is used, the particular choice is irrelevent. In practice a finite basis set is used and the particular choice of basis functions becomes very important. Let us now examine the process by which a reasonable basis set is obtained and by and analogy obtain the one which is suitable in the presence of a perturbation.

Following the development of Daudel, *et al.*,[31] we begin with the full Hamiltonian for the molecule using the Born–Oppenheimer approximation (in atomic units)

$$\mathcal{H} = -{}^1/_2 \sum_i \nabla^2(i) - \sum_{iN} \frac{z_N}{r_{iN}} + \sum_{i<j} 1/r_{ij} \quad \text{(A1)}$$

The eigenproblem for this Hamiltonian cannot be solved exactly. We proceed by simplifying the Hamiltonian to the point where it becomes possible to obtain solutions and then try to approximate the total solution by piecing together these partial solutions. The electron–electron interactions are neglected since they are the main source of our difficulties. Neglecting the $\sum_{i<j} {}^1/r_{ij}$ makes it possible to separate the total problem into smaller problems involving a single electron moving in the field of all the nuclei. In the vicinity of a particular nucleus N, electron 1 moves in a potential z_N/r_{1N} so that the solution in the vicinity of this nucleus is of the form of an atomic orbital which is the solution of

$$\left(-{}^1/_2\nabla^2(1) - \frac{z_N}{r_{1N}}\right)\phi_i(1) = E_i\phi_i(1) \quad \text{(A2)}$$

Exactly which of the ϕ_i's should be used depends on the energy of the electron as it approaches nucleus N. Part of the electron–electron interaction that was neglected previously can be taken into account by allowing the inner electrons to partially screen the nucleus. Thus a different effective nuclear charge z_N(eff) can be introduced for inner and outer atomic orbitals. As a first approximation of an MO which extends over all the nuclei, we choose a linear combination of atomic orbitals which are solutions in the vicinity of the individual nuclei, with the coefficients chosen in such a way as to minimize the total energy.

Calculations performed by Zener[32] revealed that the nodes of the hydrogen-like orbitals are not very important in other atomic calculations. Also the orthogonality requirement of SCF MO's automatically reintroduces nodes so that Slater[33] suggested the use of nodeless orbitals of the form $r^{n-1}e^{-rNz/n}Y_{lm}$. This is

(27) J. P. Olive, *J. Chem. Phys.*, **51**, 4340 (1969).

(28) T. Vladimiroff, *Int. J. Quantum Chem.*, **4**, 89 (1970).

(29) G. P. Arrighini, M. Maestro, and R. Moccia, *J. Chem. Phys.*, **49**, 882 (1968).

(30) E. Fermi, *Z. Phys.*, **60**, 320 (1930).

(31) R. Daudel, R. Lefebvre, and C. Moser, "Quantum Chemistry Methods and Applications," Interscience Publishers, New York, N. Y., 1959, p 48.

(32) C. Zener, *Phys. Rev.*, **36**, 51 (1930).

(33) J. C. Slater, *ibid.*, **36**, 57 (1930).

equivalent to adding $(n(n-1) - l(l+1))/2r^2$ to the Hamiltonian in eq A2. A more drastic approximation can be made by replacing the z_N/r_{1N} in eq A2 by $2\alpha^2r^2 - l(l+1)/2r^2$. The resulting Gaussian functions $e^{-\alpha r^2}Y_{lm}$ constitute an inferior basis set and are only used because the multicenter, two-electron integrals become easier to evaluate. In any case, the point of this discussion is that if a perturbation which is a sum of one-electron operators is included, in eq A1, we can proceed in the same way as before and no new approximations need to be introduced.

In the presence of a perturbation, eq A1 becomes

$$\mathcal{H}(\lambda) = -{}^1/_2 \sum_i \nabla^2(i) - \sum_{iN} z_N/r_{iN} + \sum_{i<j} \frac{1}{r_{ij}} + \lambda \sum_i h(i)$$

The one-electron perturbation introduces no new correlation effects so that we drop the $\sum_{i<j} {}^1/r_{ij}$ term as before. The total problem then separates into one-electron problems involving an electron moving in the field of all the nuclei plus the perturbation. In the vicinity of the nucleus N the Hamiltonian is approximately

$$H^N(\lambda) = -{}^1/_2\nabla^2(1) - \frac{z_N}{r_{1N}} + \lambda h(1) \qquad \text{(A3)}$$

Again a $z_N(\text{eff})$ can be introduced. It might be argued that $z_N(\text{eff})$ should depend on λ. This would be equivalent to optimizing exponents for the perturbed problem. Obviously this refinement would have little meaning unless exponents for the unperturbed problem were already optimized. Should this become desirable, optimization could be done in a manner similar to a method recently suggested for the unperturbed problem.[28] If we wish to use Slater orbitals we add $[n(n-1) - l(l+1)]/2r^2$ to eq A3. For Gaussian orbitals we replace z_N/r_{1N} by $2\alpha^2r^2 - l(l+1)/2r^2$ as before. This procedure can be used to define the perturbed, local Hamiltonians discussed earlier. Since we are only interested in the first-order solution, we proceed by conventional perturbation theory.

Geometric Programming and the Darwin–Fowler Method in Statistical Mechanics[1a]

by R. J. Duffin and C. Zener

Carnegie-Mellon University, Pittsburgh, Pennsylvania 15213 *(Received December 11, 1969)*

This paper concerns the classical problem of chemical equilibrium as formulated in the language of geometric programming. Thus the equilibrium state at constant temperature and volume is characterized by the duality principle, minimum F = maximum F^*. Here F is the Helmholtz function for free energy and F^* is a new function termed the anti-Helmholtz function. The minimization of F is constrained by the mass balance equations. However the maximization of F^* is unconstrained. Hence this gives a simplified practical procedure for calculating equilibrium concentration. The chemical equilibrium can also be analyzed by statistical mechanics. Comparing the two methods brings to light an intimate relationship between geometric programming and Darwin–Fowler[2] statistics.

Introduction

Geometric programming is a systematic analysis to aid engineers in designing for minimum cost.[3] The design problem so formulated is termed the *primal program.* The objective of the primal program is to minimize the cost function. Moreover, there is a related problem termed the *dual program.* The objective of the dual program is to maximize the "anticost function." These programs are termed dual because of the following basic theorem: minimum cost = maximum anticost. This dual formulation has proven to be a great aid both in understanding and solving optimum design problems.

The chemical equilibrium problem, as formulated by

(1) (a) Prepared under Research Grant DA-AROD-31-124-G680 Army Research Office, Durham, N. C.

(2) C. C. Darwin and R. H. Fowler, *Proc. Cambridge Phil. Soc.*, 21, 730 (1922).

(3) R. J. Duffin, E. Peterson, and C. Zener, "Geometric Programming," John Wiley and Sons, New York, N. Y., 1967.

Gibbs, is to minimize G, the free energy. The temperature and pressure are to be held constant. This program is feasible to carry out for reactions in which the reactants are gases obeying the laws of Boyle and Charles. For example, consider, the reaction

$$2H_2 + O_2 = 2H_2O \text{ (steam)}$$

Then the Gibbs free energy function G is given by a known formula $G = G(N_1, N_2, N_3)$ where N_1 is the number of moles of H_2, N_2 is the number of moles of O_2, and N_3 is the number of moles of steam.[4] It is a rather strange coincidence of science that such gaseous equilibrium problems can be expressed as geometric programs. The history of this coincidence can be found in Appendix C of ref 3.

The formulation of the chemical equilibrium problem by the geometric programming scheme leads to the dual relation, minimum $G(N)$ = maximum $G^*(\nu)$. The minimization problem posed on the left is the classical Gibbs approach. The maximization problem posed on the right is a new approach. We term the function $G^*(\nu)$ the *anti-Gibbs function.* Recently Passy and Wilde[5] have treated the hydrazine equilibrium problem by use of the anti-Gibbs function. They point out an advantage of this new approach in that ν has only three components while N has ten components in the hydrazine problem.

The initial purpose of this note is to give a further simplification of the chemical equilibrium problem by using the Helmholtz free energy function F instead of the Gibbs function G. F and G are related by $F = G - PV$ where P is the pressure and V is the volume. Thus the equilibrium state is characterized by minimizing the Helmholtz function, the volume being held constant. We first show that this Helmholtz problem leads to a geometric program of extended type and that the duality theorem applies. For example, in the steam equilibrium problem, min $F(N_1, N_2, N_3)$ = max F^*. (ν_H, ν_O). The minimization problem on the left is the classical Helmholtz approach. Of course the composition vector N is not arbitrary but must satisfy the mass balance equations

$$2N_1 + 2N_3 = E_H$$

$$2N_2 + N_3 = E_O$$

where E_H is the total number of moles of H atoms and E_O is the total number of moles of O atoms in the reaction chamber.

We term F^* the *anti-Helmholtz function.* Maximizing $F^*(\nu_H, \nu_O)$ gives a new approach to the chemical equilibrium problem. This approach is simpler for two reasons. (1) There is no constraint whatsoever on the dual variables ν_H and ν_O. (This is not true for the anti-Gibbs method.) (2) There are only two variables ν_H and ν_O even when other molecular species such as O_3 and H_2O_2 are considered.

The dual program applied to the chemical equilibrium problem was presented in Appendix C of ref 3 merely as a mathematical aid. Here we desire to give a physical interpretation of the functions and variables. Thus it results that ν_H may be interpreted as the chemical potential of atomic hydrogen. In other words, $\nu_H = \partial F/\partial E_H$. Then the anti-Helmholtz function may be defined as

$$F^*(\nu_H', \nu_O') = \nu_H' E_H + \nu_O' E_O - P'V$$

Here ν_H' and ν_O' are the chemical potentials and P' is the pressure when $E_H = E_H'$ and $E_O = E_O'$.

The chemical equilibrium problems just described have been interpreted in the light of classical thermodynamics. In this connection geometric programming is simply a rigorous mathematical structure which quantitatively corresponds to the phenomena of gaseous equilibrium.

However, there is another way of viewing chemical equilibrium. It may be interpreted in the light of statistical mechanics. In particular, Darwin and Fowler developed a beautiful statistical method based on complex function theory. Their method is especially suited to treat chemical equilibrium problems.

Of course properties derived by the thermodynamic approach must also be obtained by the statistical approach. Nevertheless this correspondence is remarkable because at heart the two approaches have no apparent similarity. With this thought in mind, we examined the treatment of the gaseous equilibrium problem given by Darwin and Fowler[2] to see if there was a correspondence with the geometric programming structure. Indeed, we found that their mathematical development does imply the existence of the anti-Helmholtz function. However, they did not bring this implication to the surface. Our analysis exposes a very interesting relationship between geometric programming and Darwin–Fowler statistics.

Gaseous Equilibrium Treated by Geometric Programming

The chemical potential for a perfect gas is

$$\mu = RT \log P + \mu^0 \qquad (1)$$

where R is the gas constant, T is the absolute tempera-

(4) The authors have been faced by two notational problems. Firstly, intrinsic to their analysis are two sets of mole numbers. One set refers to molecular species and is consequently dependent upon equilibrium conditions. The other set refers to atomic species and is dependent only on the overall composition. Associated with these two sets of mole numbers are the corresponding two sets of chemical potentials. Secondly, geometric programming developed outside the field of physical chemistry and has developed its own connotation for n, m, i, j. In order to help emphasize the applicability of geometric programming to physical chemistry, these symbols are here used in precisely the same way as in geometric programming. For mole numbers referred to molecular and to atomic species, we use $N_1, \ldots N_i, \ldots N_n$, and $E_1, \ldots E_l, \ldots E_i, \ldots E_m$, respectively, and for the corresponding chemical potentials we use $\mu_1, \ldots \mu_i, \ldots \mu_n$, and $\nu_1, \ldots \nu_j, \ldots \nu_m$.

(5) U. Passy and D. J. Wilde, *SIAM J. Appl. Math.*, 16, 363 (1968).

ture, P is the pressure, and μ^0 is the chemical potential at one atmosphere pressure. Then the Gibbs free energy for N moles of this gas is

$$G = NRT \log P + N\mu^0$$

The Hemholtz free energy is $F = G - PV$ where V is the volume. Thus

$$F = NRT \log P + N\mu^0 - PV$$

Using the perfect gas law $PV = NRT$ we eliminate P to obtain

$$F = NRT \log (N/eb)$$

where

$$b = (V/RT) \exp(-\mu^0/RT)$$

Next consider a homogeneous mixture of n perfect gases in a chamber of volume V. Each of these gases is to be composed of a single molecular species. If none of these n species are alike then the total free energy F is a sum

$$F = RT \sum_{i=1}^{n} N_i \log (N_i/eb_i) \qquad (2)$$

Here N_i denotes the number of moles of the molecular species i. We term $F(N)$ the *Helmholtz function.*

Suppose that there are m different chemical elements which compose the molecules of the n different gases. Then the following *mass balance equations* must hold

$$\sum_{i=1}^{n} N_i a_{ij} = E_j \qquad j = 1,2,\ldots,m$$

Here a_{ij} is the number of atoms of the jth chemical element in a molecule of the species i. Thus E_j is the total number of moles of the jth chemical element present in the chamber. (As is well known, it is often convenient to let E_j also denote stable groups of atoms.)

There are many different states N_i which satisfy the mass balance equation. However, the equilibrium state is the one that minimizes the Helmholtz function at constant temperature.

The chemical equilibrium problem just described may be put in the format of a geometric program as follows.

Equilibrium Program I. Seek the minimum of the Helmholtz function

$$F(N) = RT \log \left[\prod_{i=1}^{n} (N_i/eb_i)^{N_i} \right]$$

The variables N_i are subject to the linear constraints

$$N_1 > 0, N_2 > 0, \ldots, N_n > 0$$

$$\sum_{i=1}^{n} N_i a_{ij} = E_j \qquad j = 1, 2, \ldots, m$$

Program I comes under the category "extended geometric programming" and is discussed on page 100 and page 209 of ref 3. The analysis given there shows that program I has the following dual program.

Equilibrium Program II. Seek the maximum of the anti-Helmholtz function

$$F^*(\nu) = \sum_{j=1}^{m} \nu_j E_j - RT \sum_{i=1}^{n} b_i \exp\left(\sum_{j=1}^{m} a_{ij}\nu_j/RT \right)$$

The correspondence between program I and program II is indicated by the following theorem.

Theorem 1. Let N satisfy the constraints of program I and let ν be arbitrary; then

$$F(N) \geq F^*(\nu)$$

Moreover this inequality becomes an equality if and only if

$$N_i = b_i \exp\left(\sum_{j=1}^{m} a_{ij}\nu_j/RT \right) \qquad (3)$$

for $i = 1, \ldots, n$. *Proof.* It is clear that the elementary inequality $x \geq \log ex$ becomes an equality if and only if $x = 1$. Let $x = u_i/N_i$ where $u_i = b_i \exp(\Sigma_1^m \cdot a_{ij}\nu_j)$ so $u_i \geq N_i \log (eu_i/N_i)$. Summing gives

$$\sum_{1}^{n} u_i \geq \sum_{1}^{n} N_i \log (eu_i/N_i)$$

$$\sum_{1}^{n} u_i \geq \sum_{1}^{n} N_i \log (eb_i/N_i) + \sum_{1}^{n} N_i \sum_{1}^{m} a_{ij}\nu_j/RT$$

Using the mass balance equations gives

$$RT \sum_{1}^{n} N_i \log (N_i/eb_i) \geq \sum_{1}^{m} \nu_j E_j - RT \sum_{1}^{n} u_i \quad \text{(QED)}$$

It remains to show that conditions (3) can be satisfied.

Theorem 2. If N'' is a minimum point for program I then program II has a maximum point ν'' and $F(N'') = F^*(\nu'')$. *Proof.* Let $N_i = N_i'' + x_i s$ where s is a parameter. Then

$$\frac{dF}{ds} = \sum_{1}^{n} \frac{\partial F}{\partial N_i} x_i \qquad (4)$$

Also note that

$$\sum_{1}^{n} N_i a_{ij} = s \sum_{1}^{n} x_i a_{ij} + E_j$$

Therefore if x is chosen to satisfy

$$\sum_{1}^{n} x_i a_{ij} = 0 \qquad j = 1, \ldots, n \qquad (5)$$

then N satisfies the mass balance equation so when $s = 0$

$$\sum_{1}^{n} \frac{\partial F}{\partial N_i} x_i = 0 \qquad (6)$$

Thus relations 5 imply relation 6 so by the theory of linear dependence we know that there exist numbers $\nu_1'', \ldots, \nu_m''$ such that

$$\frac{\partial F}{\partial N_i} = \sum_{i=1}^{m} = a_{ij}\nu_j'' \qquad i = 1, \ldots, n \tag{7}$$

But differentiating 2 shows that

$$\frac{\partial F}{\partial N_i} = RT \log\left(\frac{N_i}{b_i}\right) \tag{8}$$

Then (7) and (8) give

$$N_i'' = b_i \exp(\sum a_{ij}\nu_j''/RT)$$

But this is relation 3 so it is a direct consequence of Theorem 1 that $F(N'') = F^*(\nu'')$. This completes the proof of Theorem 2. It is now desired to give the anti-Helmholtz function F^* and the variable ν a direct chemical interpretation.

Theorem 3. The anti-Helmholtz function may be written as

$$F^*(\nu') = \sum_{j=1}^{m} \nu_j' E_j - P'V \tag{9}$$

where P' is the pressure as a function of ν'. At equilibrium the following relations hold

$$\mu_i = \sum_{j=1}^{m} a_{ij}\nu_j \tag{10}$$

$$\sum_{i=1}^{n} \mu_i N_i = \sum_{j=1}^{m} \nu_j E_j \tag{11}$$

where $\mu_i = \partial F/\partial N_i$ is the chemical potential of molecular species i. *Proof.* Observe that relation 10 follows from relation 7. Multiply relation 10 by N_i and sum. Then on the right we obtain $\Sigma_1^n \Sigma_1^m N_i \cdot a_{ij}\nu_j$. Making use of the mass balance equations then proves relation 11. The function F^* may be written as

$$F^*(\nu') = \sum_{1}^{m} \nu_j' E_j - V \sum_{1}^{n} \exp\left(\frac{\sum_{1}^{m} a_{ij}\nu_j' - \mu_i^0}{RT}\right)$$

Making use of (10) gives

$$F^*(\nu') = \sum_{1}^{m} \nu_j' E_j - V \sum_{1}^{n} \exp\left(\frac{\mu_i' - \mu_i^0}{RT}\right)$$

But if P_i is the partial pressure of the molecular species i we know by relation 1 that $RT \log P_i' = \mu_i' - \mu_i s_0$

$$F^*(\nu') = \sum_{1}^{m} \nu_j' E_j - V \sum_{1}^{n} P_i'$$

But by Dalton's law the partial pressures add to the total pressure so $P' = \Sigma P_i'$ and this proves (9).

Theorem 4. If a_{ij} is of rank m then ν_j is the chemical potential of atomic type j. That is $\nu_j = \partial F/\partial E_j$. *Proof.* Since a_{ij} is of rank m it is possible to solve the equations

$$\sum_{1}^{n} x_i a_{ij} = 1 \qquad j = k$$

$$\sum_{1}^{n} x_i a_{ij} = 0 \qquad j \neq k$$

Then relations 4 and 10 give

$$dF/ds = \sum_{1}^{n} x_i \mu_i = \sum_{1}^{n} \sum_{1}^{m} x_i a_{ij} \nu_j = \nu_k$$

This is equivalent to the statement of the theorem so the proof is complete.

We are now able to give a complete thermodynamic interpretation of the anti-Gibbs program given in ref 3. In that program the variables are denoted by $t_1, t_2, \ldots, t_m$. The variable t_j is now seen to be the *activity* of atomic type j and is defined by the relation

$$t_j = e^{\nu_j/RT}$$

Then the objective of the program is to maximize the anti-Gibbs function

$$G^*(t) = \log\left(t_1^{E_1} t_2^{E_2} \ldots t_m^{E_m}\right)$$

This maximization is subject to as many constraints as there are phases. By virtue of the analysis just given it is seen that the constraint on the phase k is of the form $\Sigma_k P_i < P$. Here P is the ambient pressure and P_i is the partial pressure of molecular species i in phase k. If phase k does not vanish then this becomes an equality and expresses Dalton's law for phase k.

Darwin–Fowler Statistics

The partition function Z is defined in terms of the Helmholtz function by the formula

$$Z = e^{-F/RT}$$

Let us express the extremal property of the anti-Helmholtz function in terms of the partition function Z and activity variables t. This is seen to be

$$Z = \min \frac{\exp\left(\sum_{1}^{n} b_i \prod_{1}^{m} t_j^{a_{ij}}\right)}{\prod_{1}^{m} t_j^{E_j}} \tag{12}$$

To one familiar with the Darwin–Fowler approach to statistical mechanics relation 12 strikes a familiar chord. Our t_j is just the value along the real axis of their selector variable that ensures conservation of type j atoms. In fact (12) is embedded in their 1922 paper,[1] although not explicitly stated or employed. We give below a brief analysis of our problem by their method.

If A is Avogadro's number let $n_i = AN_i$, $e_j = AE_j$, and $R = Ak$. Then according to Darwin and Fowler

$$e^{-F/kT} = \Sigma \pi_i (z_i)^{n_i}/n_i!$$

the summation is over all values of the distribution numbers n_i satisfying

$$\sum_{1}^{n} n_i a_{ij} = e_j \tag{13}$$

Here z_i is the partition function for a molecule of type i. Following Darwin and Fowler we remove the con-

straint 13 by introducing complex selector variables, one for each atomic species

$$e^{-F/kT} = \left(\frac{1}{2\pi i}\right)^m \int \cdots \int \sum \pi_i \frac{(z_i \pi_j t_j^{a_{ij}})}{(n_i! \pi_j t_j^{e_j})} \pi_j \left(\frac{dt_j}{t_j}\right)$$

The path of integration is once around the origin of the complex plane. The summation is over all values of n_i so $\Sigma \pi_i = \pi_i \Sigma^{\infty}_{n_i=0}$. Also $\Sigma_0^{\infty} x^k/k! = e^x$ so (4) becomes

$$e^{-F/kT} = \left(\frac{1}{2\pi i}\right)^m \int \cdots \int \psi(t) \pi_j \frac{dt_j}{t_j}$$

$$\psi(t) = \exp\left(\sum_i z_i \pi_j t_j^{a_{ij}}\right) / \pi_j t_j^{e_j}$$

Since all the z_i are positive, it follows that for t confined to the positive real axis the function $\psi(t)$ has a minimum at a point $t'' = (t_1'', \ldots, t_m'')$. Choose contours of integration to be circles centered at the origin and of radii $t_1'', \ldots, t_m''$ and employ polar coordinates $t_1 = t_1'' e^{i\theta_1}$ etc. Thus

$$e^{-F/kT} = (2\pi)^{-m} \int_{-\pi}^{\pi} \cdots \int \psi(t) \pi_j d\theta_j$$

To estimate integrals of this form Darwin and Fowler use the saddle point method. It is easy to see that t'' is a saddle point for the real part of $\psi(t)$. Thus the integrand is small at all points of the circular contours except at t''. It results that

$$e^{-F/kT} = \psi(t'')/C$$

where C is a number whose order of magnitude is $A^{n/2}$. Taking the Ath root gives

$$e^{-F/RT} = \exp(\Sigma_i b_i \pi_j t_j^{a_{ij}}) / \pi_j t_j^{E_j}, \quad t = t''$$

where $b_i = z_i/A$. Also we take $C^{1/A} \cong 1$ without appreciable error. Thus we have derived the important relation 12 as a consequence of the Darwin–Fowler method in statistical mechanics.

Equilibrium of Sulfur Molecules

The following problem gives a simple example for the anti-Helmholtz approach.

Problem. Two moles of atomic sulfur are in a reaction chamber at temperature $T = 850°K$ and of volume $V = 1/RT$. Find the partial pressures of S, S_2, S_6, and S_8 molecules. *Solution.* Let N_1, N_2, N_6, and N_8 denote moles of S, S_2, S_6, and S_8 molecules. Then the mass balance equation is $N_1 + 2N_2 + 6N_6 + 8N_8 = 2$. Let $x = \nu_1/RT$; then F^* can be written as

$$F^*/RT = 2x - (e^{x-23.7} + e^{2x} + e^{6x+0.366} + e^{8x+1.65})$$

Here the numbers -23.7, 0, 0.366, and 1.65 are tabulated values of μ_i^0/RT for S, S_2, S_6, and S_8. It is readily found that F^* has a maximum at $x = -0.493$. At this value of x successive terms in the parentheses have the values 3.10^{-11}, 0.373, 0.0744, 0.1009. These are just the partial pressures, in atmospheres, of the S, S_2, S_6, and S_8 molecules. The free energy is here referred to S_2 as a standard state.

So far we have been supposing the reactants are perfect gases. However, the definition 9 for F^* could be extended to an arbitrary chemical system. This raised the question: is it true that the maximum of F^* is the equilibrium free energy? We answer this question in the affirmative by introducing a more basic function S^* termed the anti-entropy which applies to general thermodynamic systems. Then we find that maximum S = minimum S^*, where S is the entropy. In making this generalization we have been guided by Castigliano's principle in mechanics and by the general duality concepts given in ref 6. This analysis is developed in ref 7.

(6) R. J. Duffin, *SIAM J. Appl. Math.*, **10**, 119 (1962).
(7) R. J. Duffin and C. Zener, *Proc. Nat. Acad. Sci.*, **62**, 629 (1969).

Energy Parameters in Polypeptides. III. Semiempirical Molecular Orbital Calculations for Hydrogen-Bonded Model Peptides[1]

by F. A. Momany,[2] R. F. McGuire,[3] J. F. Yan, and H. A. Scheraga[4]

Department of Chemistry, Cornell University, Ithaca, New York 14850 *(Received January 14, 1970)*

The influence of hydrogen bonding (and other intermolecular interactions) in model peptides on charge distributions, dipole moments, and energies for internal rotation about the peptide bond has been determined by semiempirical molecular orbital calculations, primarily by the CNDO/2 method. The complexes treated are: the formamide linear dimer, the formamide planar cyclic dimer, the formamide parallel-plane dimer, the formamide planar linear trimer, the formamide planar forked trimer, the N-methyl acetamide linear dimer, and the N-methyl acetamide parallel-plane dimer. The stabilities of these complexes are discussed, and the redistribution of charges as the monomers approach each other (in various relative orientations) is examined. Also, comparisons are made between the calculated stable conformations and crystal structures.

Introduction

This is a continuation of the previous paper[5] of this series (referred to as paper II), and a related one,[6] in which semiempirical molecular orbital methods [the Complete Neglect of Differential Overlap theory (CNDO/2) of Pople and Segal[7] and the Extended Hückel Theory (EHT) of Hoffmann[8]] are used to improve and strengthen the physical basis of empirical methods[9] which are being applied to conformational energy calculations on polypeptides. It must be enphasized that, while the molecular orbital methods used here are approximations to the Hartee–Fock procedure, they provide valid information when a *group* of related compounds (rather than a few selected ones) is examined, as it is here and in previous[5,6] papers.

In this paper, we explore the influence of intermolecular complex formation (including hydrogen bonding and other intermolecular interactions) on the distribution of charge, the dipole moment, and the energies for internal rotation about the peptide bond in various conformations of some model peptides. Considerations of this kind will be used in a later paper[10] to develop an empirical energy function for the formation of a hydrogen bond.

The molecules treated here are binary and ternary complexes of formamide and N-methyl acetamide, as illustrated in Figure 1. The structural formulas and geometry are equivalent to those used previously,[5] except for small changes made in the geometry of formamide (in response to a reevaluation of the "best model for a peptide" in the literature); however, as will be shown here, the new geometry used for formamide in no way changes the results of the calculations reported in paper II.

Because of the expense involved in computer calculations, only a limited number of degrees of freedom were examined for the complexes of both formamide and N-methyl acetamide. These are shown in Figure 1 and defined as follows: (1) α is the angle between the axes of the C=O bond of molecule a and the H—N bond of molecule b, with the O, H, and N atoms being collinear, and both amides coplanar ($\alpha = 0°$ in Figures 1B and 1H); (2) δ is the angle between the axes of the C=O bond of molecule a and the H—N bond of molecule b, with the C, O, and H atoms being collinear, and both amides coplanar ($\delta = 0°$ in Figures 1B and 1H); (3) θ is the dihedral angle of rotation about the axis defined by the collinear atoms C_a, O_a, H_b, and N_b, with the positive direction being clockwise as one looks from a to b and rotates molecule b ($\theta = 0°$ in the planar conformations of Figures 1B and 1H; θ is not varied in the structures of Figures 1C to 1G); (4) ω is the dihedral angle of rotation about the peptide bond, defined by standard nomenclature;[11] it is not varied in the structures of Figure 1C to 1G; (5) R_{O-H} is

(1) This work was supported by research grants from the National Science Foundation (GB-7571X and GB-7160), from the National Institute of General Medical Science of the National Institutes of Health, U. S. Public Health Service (GM-14312), from the Eli Lilly, Hofmann-La Roche, and Smith Kline and French Grants Committees, and from Walter and George Todd.

(2) Special Fellow of the National Institute of General Medical Sciences, National Institutes of Health, 1968–1969.

(3) NIH postdoctoral trainee, 1968–1969; postdoctoral fellow of the National Institute of General Medical Sciences, National Institutes of Health, 1969–1970.

(4) To whom requests for reprints should be addressed.

(5) J. F. Yan, F. A. Momany, R. Hoffmann, and H. A. Scheraga, *J. Phys. Chem.*, **74**, 420 (1970).

(6) J. F. Yan, F. A. Momany, and H. A. Scheraga, *J. Amer. Chem. Soc.*, **92**, 1109 (1970).

(7) J. A. Pople and G. A. Segal, *J. Chem. Phys.*, **44**, 3289 (1966).

(8) R. Hoffmann, *ibid.*, **39**, 1397 (1963); **40**, 2474, 2480, 2745 (1964).

(9) See, *e.g.*, H. A. Scheraga, *Advan. Phys. Org. Chem.*, **6**, 103 (1968).

(10) R. F. McGuire, F. A. Momany, and H. A. Scheraga, in preparation.

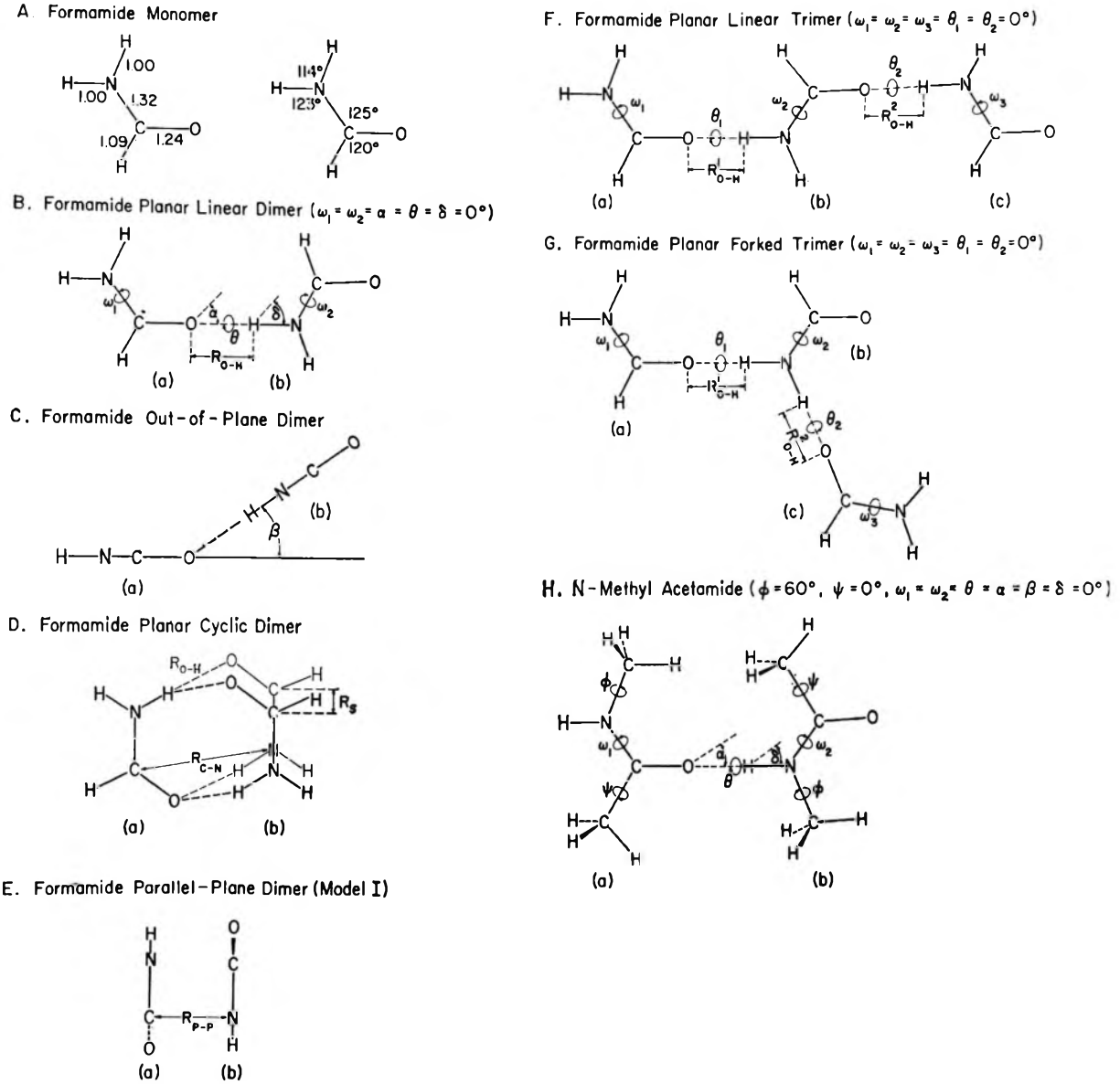

Figure 1. Geometry and conformations of molecules treated in this paper. See text for definitions of symbols.

the distance between the oxygen atom of molecule a and the H(N) atom of molecule b (Figures 1B and 1H); in the trimers of Figures 1F and 1G, the two R_{O-H} distances are distinguished as R^1_{O-H} and R^2_{O-H}; (6) β is the out-of-plane angle which the plane of molecule b makes with that of molecule a with the N_b—H_b bond directed toward the O_a atom (Figure 1C); (7) R_{C-N} is the distance between the C_a and N_b atoms in the planar cyclic dimer of Figure 1D, with both C—N bonds maintained parallel; movement of molecule b by an amount R_S, in the direction shown, is allowed; (8) R_{P-P} is the distance between the two *parallel* planes in the structure of Figure 1E; since the C—N bonds can be either parallel or antiparallel and the carbonyl groups either aligned or opposite, there are four possible combinations in this parallel-plane structure in which R_{P-P} is allowed to vary [(A) the C—N bonds antiparallel and the C=O bonds opposite (this is the conformation shown in Figure 1E), (B) the C—N bonds antiparallel and the C=O bonds aligned, (C) the C—N bonds parallel and the C=O bonds opposite, and (D) the C—N bonds parallel and the C=O bonds aligned].

Allowing for variation in only those degrees of freedom indicated above, calculations were carried out[12] to determine charge distributions and energies, as well as the most stable conformations, for the complexes shown in Figure 1.

Method

A brief description of the CNDO/2 and EHT methods

(11) J. T. Edsall, P. J. Flory, J. C. Kendrew, A. M. Liquori, G. Nemethy, G. N. Ramachandran, and H. A. Scheraga, *Biopolymers*, **4**, 121 (1966); *J. Biol. Chem.*, **241**, 1004 (1966); *J. Mol. Biol.*, **15**, 399 (1966).

(12) We are indebted to Professor R. Hoffmann for making the EHT and CNDO/2 computer programs available to us.

is given in paper II.[5] The same input parameters and geometry from the previous work[5] were used here in the computer programs,[12] except for the changes in the bond lengths and bond angles of formamide, which have already been mentioned. Because of limitations in computing time, bond lengths and bond angles are not varied, even though it is recognized that the formation of intermolecular hydrogen bonds could lead to changes in these quantities.

While we have carried out calculations with the EHT, along with the CNDO/2 method, essentially all of our interpretation is based on the latter procedure for several reasons, one being because of the way in which the EHT method treats polar molecules,[13] causing an overemphasis of charge separation.

Results and Discussion

The results are presented in the following order: (1) the formamide monomer, (2) the formamide linear dimer, (3) the formamide planar cyclic dimer, (4) the formamide parallel-plane dimer, (5) the formamide planar linear trimer, (6) the formamide planar forked trimer, (7) the N-methyl acetamide linear dimer, and (8) the N-methyl acetamide parallel-plane dimer. For each complex, we report: (a) the conformation, (b) the partial charges on the atoms, (c) the sum of the positive and negative partial charges, CS^+ and CS^-, respectively, (d) the charge transfer (CT), defined as the difference between CS^+ and CS^- for one molecule in the complex, (e) dipole moments (calculated from point charges[5]), and (f) energies for internal rotation about the peptide bond. Our primary focus is on the formation of stable complexes and their influence on the charge distribution. We will refer to such complex formation as hydrogen bonding only when the C=O···H—N grouping is in a reasonable geometric position; when such geometric criteria are not satisfied, *e.g.*, as in the structure of Figure 1E, the formation of the complex will be designated simply as an intermolecular one.

In some cases, the zero of the energy scale will be taken as that of the monomers at infinite separation; in others, the zero will be taken as that of the complex in a specified conformation. In this way, it is easy to see the changes in energy, ΔE, brought about either by bringing monomers together, or by changing the conformation of the complex. These choices of zero energy lead to negative values for a stabilization energy. While a rather extensive number of calculations were performed, with many numerical results, only selected values of charges and energies are reported here for illustrative purposes.

1. Formamide Monomer. The detailed calculations of the formamide monomer, reported in paper II, were repeated here with the geometry shown in Figure 1A. The results, shown in Table I, are in essential agreement with those of paper II, and provide a reference with respect to which the data for the formamide complexes can be compared.

Table I: Results for Formamide Monomer

ω, deg	CNDO/2 μ,[a] Debye units	CNDO/2 ΔE,[b] kcal/mol	EHT ΔE,[b] kcal/mol
0	4.00	0	0
30	3.80	4.64	5.33
60	3.33	14.62	17.70
90	3.04	20.06	25.12
Charges (ON)[c] for ω = 0 (in electronic units)		H(C′)	−0.038
		C′	0.449
		O	−0.365
		N	−0.409
		H (*cis*)[d]	0.189
		H (*trans*)[d]	0.174
		CS^+	0.812
		CS^-	−0.812

[a] Calculated to include a contribution arising from the displacement of atomic electron charge away from the center of the atom (see paper II). [b] ΔE = 0 for the planar conformation. [c] See paper II for definition of overlap-normalized charges. [d] *cis* and *trans* refer to the position of the amine protons with respect to the carbonyl oxygen.

2. Formamide Linear Dimer. One conformation of the linear dimer ($\omega_1 = \omega_2 = \alpha = \theta = \delta = \beta = 0°$) is shown in Figure 1B. This conformation is designated as the *trans* form since the H(N) atom of molecule b, *trans* to the carbonyl of the same molecule, is involved in the hydrogen bond with molecule a; if ω_2 were changed to 180°; the *cis* form would be obtained.

The dependence of ΔE on R_{O-H} for the linear dimer in the *trans* form is shown in Figure 2. It can be seen that the curve obtained by the EHT method does not show a minimum. Since a minimum would

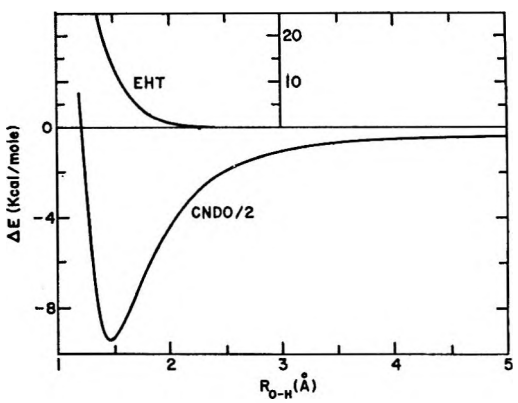

Figure 2. EHT and CNDO/2 results for the dependence of ΔE on R_{O-H} for the *trans* form of the formamide linear dimer ($\omega_1 = \omega_2 = \alpha = \theta = \delta = \beta = 0°$). ΔE = 0 for two monomers at infinite separation.

(13) W. Adam, A. Grimison, R. Hoffmann, and C. Z. de Ortiz, *J. Amer. Chem. Soc.*, 90, 1509 (1968).

Table II: Results for Formamide Linear Dimer for $\alpha = \delta = \beta = 0°$

					CNDO/2							EHT	
							Molecule a		Molecule b				
	R_{O-H}, Å	ω_1, deg	ω_2, deg	θ, deg	ΔE,[a] kcal/mol	ΔE,[b] kcal/mol	CS+	CS−	CS+	CS−	μ[c] Debye units	ΔE,[a] kcal/mol	ΔE,[b] kcal/mol
							in electronic units						
trans (N-H)	1.40	0	0	0	−8.975		0.853	−0.840	0.902	−0.915	8.75	20.864	
	1.50	0	0	0	−9.302		0.846	−0.836	0.883	−0.893	8.52	13.875	
	1.80	0	0	0	−6.109		0.832	−0.828	0.850	−0.854	8.10	3.693	
	3.00	0	0	0	−1.040		0.818	−0.818	0.822	−0.822	7.73	0.010	
	1.40	0	0	180	−8.871		0.851	−0.838	0.899	−0.912	9.16		
	1.50	0	0	180	−9.212		0.844	−0.834	0.879	−0.889	8.94		
	1.80	0	0	180	−6.039		0.827	−0.831	0.847	−0.851	8.51		
	3.00	0	0	180	−1.001		0.817	−0.817	0.820	−0.820	8.13		
cis (N-H)	1.30	0	180	0	−6.978		0.866	−0.848	0.929	−0.947	5.66		
	1.50	0	180	0	−9.577		0.849	−0.838	0.885	−0.896	5.22		
	1.80	0	180	0	−6.035		0.834	−0.830	0.851	−0.855	4.86		
	3.00	0	180	0	−0.803		0.818	−0.818	0.822	−0.822	4.55		
	1.30	0	180	180	−6.397		0.857	−0.839	0.926	−0.944	7.35		
	1.50	0	180	180	−9.092		0.841	−0.830	0.882	−0.893	6.93		
	1.80	0	180	180	−5.643		0.827	−0.823	0.849	−0.853	6.59		
	3.00	0	180	180	−0.586		0.814	−0.814	0.821	−0.821	6.31		
trans (N-H)	1.50	0	0	0		0							0
		0	0	30		0.002							0.0004
		0	0	60		0.023							0.0011
		0	0	90		0.049							0.0014
		0	0	120		0.062							0.0010
		0	0	150		0.076							0.0004
		0	0	180		0.088							0.0
	1.50	30	0	180		4.995[d]							5.329[d]
		60	0	180		15.842[d]							17.703[d]
		90	0	180		21.817[d]							25.127[d]
		0	30	180		4.697[d]							4.940[d]
		0	60	180		14.781[d]							16.255[d]
		0	90	180		20.249[d]							22.914[d]

[a] $\Delta E = 0$ for two planar monomers at infinite separation. [b] $\Delta E = 0$ for *trans* (N-H), $R_{O-H} = 1.50$ Å, $\omega_1 = \omega_2 = \theta = 0°$. [c] Calculated using Pople method (see paper II). [d] $\Delta E = 0$ for $\omega_1 = \omega_2 = 0°$ and $\theta = 180°$ at *trans* (N-H), $R_{O-H} = 1.50$ Å.

be expected for a stable dimer, the EHT results are not satisfactory for these complexes. On the other hand, the CNDO/2 method does give a minimum, not only for the conditions of Figure 2, but also for both the *trans* and *cis* forms at all values of θ. Therefore, most interpretations will be based on the CNDO/2 method. The energies for several conformations are shown in Table II. It can be seen that the most stable conformation is that of the *cis* form ($\omega_2 = 180°$) with R_{O-H} near 1.50 Å and $\omega_1 = \theta = 0°$; this conformation is about 0.5 kcal/mol more stable than the one in which $\theta = 180°$, and about 0.3 kcal/mol more stable than the lowest-energy *trans* form. In the *trans* form, at $\omega_1 = \omega_2 = \theta = 0°$ and $R_{O-H} = 1.50$ Å, the energy is only about 0.1 kcal/mol lower than for the conformation in which $\theta = 180°$. On the other hand, the EHT results indicate that ΔE is essentially independent of θ at all R_{O-H} values in the range of Figure 2.

The dependence of ΔE on α and δ is shown in Figure 3. The CNDO/2 results indicate a slight preference for $\alpha \sim -20°$. If the most stable conformation were in the direction of the oxygen lone-pair orbitals produced by pure sp^2 hybridization, the mimimum would occur near $\pm 60°$, depending on other nonbonded interactions. In fact, the electronic interactions distort the oxygen lone-pair orbitals in such a way that they appear to follow the H(N) atom, and a stable conformation (*i.e.*, value of α) is adopted which reflects the complete molecular electronic interaction, rather than being determined by the direction implied by pure sp^2 hybridization. On the other hand, the EHT results indicate a slight preference for α values approaching those implied by sp^2 hybridization; however, the variation in ΔE is only ± 0.1 kcal/mol at $R_{O-H} = 1.50$ Å for changes in α of up to $\pm 50°$. Figure 3B indicates that the conformation with $\delta = 0°$ is definitely preferred. The dependence of ΔE on β (not illustrated here) is very weak (within a few tenths of a kilocalorie), with a slight preference for the conformation for which $\beta = 0°$.

The partial charges, defined in paper II as overlap normalized, are shown as a function of R_{O-H} in Figure 4. It can be seen that, upon formation of a stable

Table III: Various CNDO/2 Charge Distributions, Charge Separations, and Charge Transfer for Formamide Linear Dimer ($\omega_1 = \omega_2 = \alpha = \delta = \beta = 0°$), in Electronic Units

	R_{O-H}, Å	θ, deg	Molecule	H(C')	C'	O	N	H (*cis*)	H (*trans*)	CS$^+$	CS$^-$	CT	μ, Debye units
trans (N-H)	1.50	0	a	−0.029	0.465	−0.400	−0.407	0.197	0.184	0.846	−0.836	+0.010	8.52
			b	−0.056	0.451	−0.387	−0.450	0.173	0.259	0.883	−0.893	−0.010	
	1.50	180	a	−0.027	0.464	−0.400	−0.407	0.196	0.184	0.844	−0.834	+0.010	8.94
			b	−0.053	0.450	−0.387	−0.449	0.171	0.258	0.879	−0.889	−0.010	
cis (N-H)	1.50	0	a	−0.032	0.466	−0.399	−0.407	0.201	0.182	0.849	−0.838	+0.011	5.22
			b	−0.058	0.453	−0.388	−0.450	0.274	0.158	0.885	−0.896	−0.011	
	1.50	180	a	−0.025	0.464	−0.398	−0.407	0.194	0.183	0.841	−0.830	+0.011	6.93
			b	−0.059	0.453	−0.385	−0.449	0.273	0.156	0.882	−0.893	−0.011	

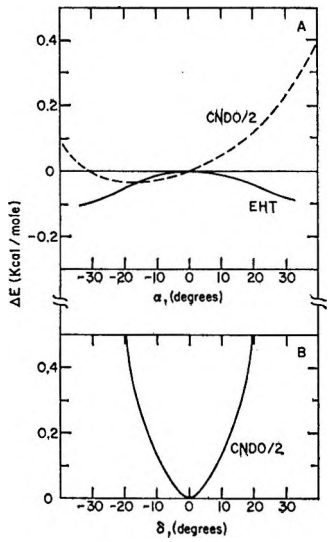

Figure 3. EHT and CNDO/2 results for the dependence of ΔE on α and δ, respectively, for the *trans* form of the formamide linear dimer with $R_{O-H} = 1.50$ Å and $\theta = 180°$. (A) $\omega = \delta = \beta = 0°$. (B) $\omega = \alpha = \beta = 0°$.

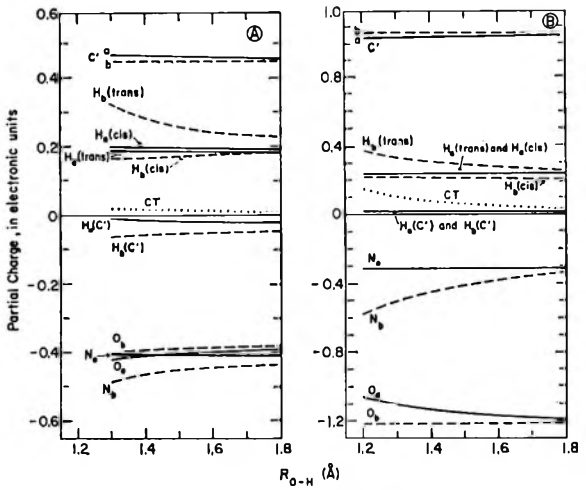

Figure 4. (A) CNDO/2 and (B) EHT results for the dependence of partial charge on R_{O-H} for the formamide linear dimer [*trans* (N-H)] with $\omega_1 = \omega_2 = \alpha = \delta = \beta = 0°$ and $\theta = 180°$. Solid and dashed lines refer to molecules a and b, respectively. The CT curves refer to a gain of positive charge (net loss of electrons) by molecule a.

hydrogen-bonded complex, the electron distribution has become polarized, compared to the monomer (see Tables I and III); *i.e.*, the partial charge on each atom has undergone some change. This change in distribution of electron density about the atoms is a result of the perturbation imposed by the presence of a second molecule, and is expressed in terms of the sum of the partial charges on each atom of a given molecule in the complex, *i.e.*, CS$^+$ and CS$^-$ (given in Tables II and III). It can be seen that the charge separations at the minimum-energy conformations differ from that found for the separate monomer. Further, the values for CS$^+$ and CS$^-$ in molecules a and b also differ from each other, *i.e.*, both molecules show increased charge separation, compared to the monomer, but to different extents. The charge transfer (CT) is defined as the net of CS$^+$ and CS$^-$ for each molecule; thus, only when these values are unequal for the two molecules in the complex is there a net transfer of electrons from one molecule to another through the hydrogen bond. This electron migration can be described as follows: concentrating primarily on the N_b–H_b (*trans*)$\cdots O_a$–C_a' group, we see the following from Figure 4A. The positive charge on H_b (*trans*) rises rapidly as the two molecules approach one another. Simultaneously, N_b and O_a both exhibit a *net gain of electrons* (CNDO/2).

In order to understand the changes in charge as R_{O-H} varies, we list the σ- and π-orbital contributions to the charge separately in Table IV. In the EHT theory, the largest variations in charge arise from the σ contributions (which include the lone-pair orbitals), and, in fact, the amount of charge transfer (CT curves of Figure 4) arises completely from σ contributions. However, in the CNDO/2 theory, both the σ and π contributions vary with R_{O-H} and in a complex way. Thus, as R_{O-H} decreases, N_b gains σ electrons with only a slight loss of π electrons, O_a gains π electrons with only a slight loss of σ electrons, while H_b (*trans*) loses considerable σ charge. Both carbonyl carbons

Table IV: σ and π Charges for Formamide Linear Dimer, $\omega_1 = \omega_2 = \alpha = \delta = \beta = 0°$, $\theta = 180°$ (*trans*), in Electronic Units

Molecule	Atom	R_{O-H} = 1.20 Å			R_{O-H} = 1.60 Å			R_{O-H} = 2.00 Å		
		π	σ	$\sigma + \pi$	π	σ	$\sigma + \pi$	π	σ	$\sigma + \pi$
					EHT					
a	H(C′)		0.01			0.01			0.01	
	C′	0.42	0.61	1.03	0.42	0.62	1.04	0.42	0.62	1.04
	O	−0.79	−0.28	−1.07	−0.79	−0.39	−1.18	−0.79	−0.43	−1.22
	N	0.37	−0.68	−0.31	0.37	−0.68	−0.31	0.37	−0.68	−0.31
	H (*cis*)		0.24			0.24			0.24	
	H (*trans*)		0.24			0.24			0.24	
b	H(C′)		0.02			0.02			0.02	
	C′	0.42	0.63	1.05	0.42	0.63	1.05	0.42	0.63	1.05
	O	−0.79	−0.43	−1.22	−0.79	−0.43	−1.22	−0.79	−0.43	−1.22
	N	0.37	−0.95	−0.58	0.37	−0.75	−0.38	0.37	−0.68	−0.31
	H (*cis*)		0.22			0.21			0.21	
	H (*trans*)		0.37			0.28			0.25	
					CNDO/2					
a	H(C′)		−0.02			−0.03			−0.03	
	C′	0.28	0.18	0.46	0.25	0.21	0.46	0.24	0.22	0.46
	O	−0.50	0.07	−0.43	−0.45	0.05	−0.40	−0.43	0.05	−0.38
	N	0.21	−0.61	−0.40	0.19	−0.60	−0.41	0.19	−0.60	−0.41
	H (*cis*)		0.21			0.20			0.19	
	H (*trans*)		0.19			0.18			0.18	
b	H(C′)		−0.07			−0.05			−0.04	
	C′	0.24	0.21	0.45	0.24	0.21	0.45	0.24	0.21	0.45
	O	−0.45	0.05	−0.40	−0.43	0.05	−0.38	−0.43	0.05	−0.38
	N	0.21	−0.71	−0.50	0.19	−0.65	−0.46	0.19	−0.61	−0.42
	H (*cis*)		0.16			0.18			0.18	
	H (*trans*)		0.35			0.24			0.20	

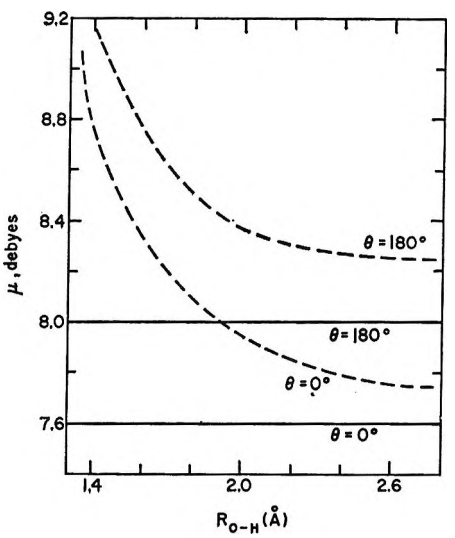

Figure 5. CNDO/2 results for dependence of dipole moment on R_{O-H} for the *trans* (N–H) form of the formamide linear dimer with $\omega_1 = \omega_2 = \alpha = \delta = \beta = 0°$. The solid lines (for which μ is almost independent of R_{O-H}) were computed from the vector sum of the dipole moments, using the charges for the *separate monomers*, at the values of θ indicated. The dashed lines were computed, taking into account the variation of the charges (of Figure 4) with R_{O-H}.

show comparatively little change in charge. In both theories, the direction of the transfer of negative charge is from the carbonyl group to the amide group (*i.e.*, molecule a shows a net loss of electrons—see CT curve in Figure 4). Both methods show that the CT curve increases slightly as R_{O-H} decreases; however, the CNDO/2 method gives a smaller magnitude than does the EHT method. Because of the difficulties already cited[13] with the EHT method, and as is seen from the unexpected result for O_a in Figure 4B, we will not discuss the EHT charges further in this paper.

Another observation, made from Table III, is that, at the position of minimum energy, it is the magnitudes of CS^+ and CS^- for each molecule in the complex, and *not* the magnitude of CT, which seems to correlate best with the binding energy (ΔE of Table II). For example, the *cis* (N—H) form with the lowest binding energy (−9.6 kcal/mol) has the largest absolute values of CS^+ and CS^-, when compared to the other minimum-energy conformations. We will return to this point after considering other types of complexes.

In light of the variation in charge, shown in Figure 4, we should expect a corresponding change in the dipole moment μ of the complexes (as calculated by the point-charge model with correction[5]) upon formation of a hydrogen bond. These are shown by the dashed curves of Figure 5 for $\theta = 0°$ and 180°, and compared (solid curves) to the values obtained by vector addition of the dipole moments computed with the charges for separate monomers. It can be seen that μ increases with decreasing R_{O-H}. Such changes

in charge and dipole moment will arise upon formation of the intramolecular hydrogen bond (as in the α helix) or of intermolecular hydrogen bonds to solvent molecules; hence, upon formation of intra- and intermolecular hydrogen bonds, changes in dipole moment can have a considerable influence on the behavior of a polar group.

Internal Rotation. In this section, we consider the effects of hydrogen bonding on the barrier to rotation about the peptide bond, U_ω. This subject has received considerable attention in the form of nmr studies of the effects of solvents on this rotational barrier.[14,15] We treat this problem by calculating the energy of the dimeric species, as rotation about one of the peptide bonds is allowed. For example, in the structure of Figure 1B, we vary ω_1 while holding ω_2 fixed at 0°, for $\theta = 180°$; then we vary ω_2 while holding ω_1 fixed at 0°, also for $\theta = 180°$. In this way, we obtain the effect of hydrogen bonding (on both the carbonyl and amine groups) on the rotational barrier.

The results of varying both ω angles individually are shown in Figure 6, in which the energies have been normalized to zero at $\omega = 0°$. The CNDO/2 results may be interpreted as follows: first, upon attack at the carbonyl group by a hydrogen-bonding agent, the barrier for variation of ω_1 rises significantly. At the position of the minimum of the hydrogen-bond energy (1.50 Å), the increase in U_{ω_1} is ~2 kcal/mol. Second, upon attack at the amine group, the barrier for variation of ω_2 also increases but only by ~0.2 kcal/mol at $R_{O-H} = 1.5$ Å.

The EHT results present a somewhat different picture of the effect of hydrogen bonding on the barrier

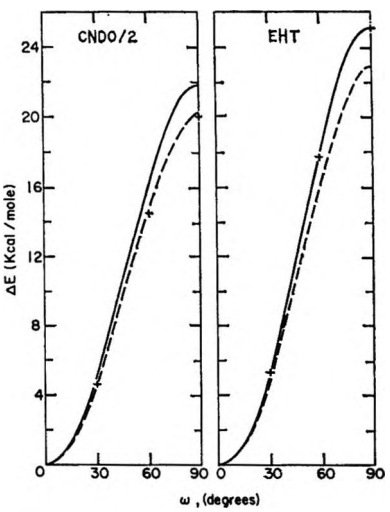

Figure 6. CNDO/2 and EHT results for the energy of internal rotation about the peptide bond in the *trans* (N–H) form of the formamide linear dimer with $\alpha = \delta = \beta = 0°$, $\theta = 180°$, and $R_{O-H} = 1.50$ Å. In varying ω_1, ω_2 is held fixed at 0° and vice versa. Solid and dashed lines correspond to variation of ω_1 and ω_2, respectively. The crosses correspond to the separated monomer.

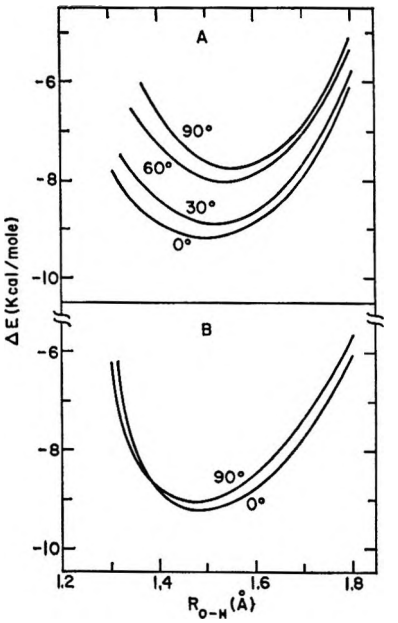

Figure 7. CNDO/2 results for the dependence of ΔE on R_{O-H} for (A) variable ω_1 and (B) variable ω_2 in the *trans* (N–H) form of the formamide linear dimer with $\alpha = \delta = \beta = 0°$ and $\theta = 180°$. The zero of the energy scale corresponds to the combination of a planar and a nonplanar monomer at infinite separation.

to rotation about the peptide bond. In this method, the effect is solely on the ω_2 barrier, with a considerable lowering of U_{ω_2} for attack at the amine group; attack at the carbonyl group has little or no effect on U_{ω_1}.

The CNDO/2 results seem to correlate with the nmr results of Kamei,[15] who obtained U_ω values for formamide of 18.9 kcal/mol (neat), 21.3 kcal/mol in water, 16.9 kcal/mol in acetone, and 16.8 kcal/mol in dioxane. Since acetone and dioxane can attack formamide only at the amine group, we expect the low values of 16.9 and 16.8 to correspond to U_{ω_2}. Hence, we may conclude that the high value (21.3) for water implies that the water molecule preferentially hydrogen bonds to the carbonyl group of monomeric formamide. The intermediate value (18.9) for neat formamide indicates the existence of some sort of complex, the nature of which is not clear at this point; however, several possible structures (planar cyclic dimer, parallel-plane dimer, and trimers) will be discussed later in this paper.

Another point of interest is the influence of a variation in ω on the strength of the hydrogen bond in the dimer. Plots of ΔE *vs.* R_{O-H} for various values of ω_1 and ω_2, respectively, are shown in Figure 7. From Figure 6, we see that the total energy is increased as ω_1 departs from 0°. However, when such a nonplanar molecule dimerizes with a planar one ($\omega_2 = 0°$), hy-

(14) R. C. Neuman, Jr., W. R. Woolfenden, and V. Jonas, *J. Phys. Chem.*, **73**, 3177 (1969).

(15) H. Kamei, *Bull. Chem. Soc. Jap.*, **41**, 2269 (1968).

drogen bond energies (at R_{O-H} = 1.50 Å) of −9.21, −8.85, −7.99, and −7.46, kcal/mol are obtained (Figure 7A) for ω_1 = 0°, 30°, 60°, and 90°, respectively. For ω_1 = 90°, the hydrogen bond energy of −7.46 kcal/mol is not low enough to offset rotational energy of +22 kcal/mol (Figure 6). However, for ω_1 = 30°, the hydrogen bond energy of −8.85 kcal/mol can offset the rotational energy of +5 kcal/mol (Figure 6). Hence, in a protein, some variation of ω (up to say 30°) can be tolerated if the resulting nonplanar amide can then form a hydrogen bond; of course, the total energy of the system will be lower if ω is closer to 0°. It is of interest to note that there is a slight shift of the position of minimum energy in Figure 7A upon variation of ω_1.

Similar results are shown in Figure 7B for variation of ω_2. Again we see a decrease in the strength of the hydrogen bond as ω_2 departs from 0°. Hydrogen bond energies of −9.21, −9.15, −9.05, and −9.02 kcal/mol are obtained for ω_2 = 0°, 30°, 60°, and 90°; hence, variation of ω_1 is more effective than variation of ω_2 in destabilizing the hydrogen bond.

Comparison with Other Results. Our CNDO/2 results for the formamide linear dimer are considerably different from those of Pullman and Berthod.[16] They found values of −4.9 and −4.6 kcal/mol for ΔE of the *trans* form, with θ = 0° and 180°, respectively, at a fixed value of R_{O-H}, whereas our minimum-energy values are −9.30 and −9.21 for similar values of θ. Since Pullman and Berthod[16] presented their results for only one value of R_{O-H} it is not clear that this value of R_{O-H} corresponded to the energy minimum. In fact, it is not clear what value of R_{O-H} was used by Pullman and Berthod[16] since, although they used experimental values of R_{O-H} found in glycylglycine,[17] these experimental values are found to vary between 1.7 and 1.9 Å. In order to try to resolve these apparent differences, we repeated the calculations for the formamide linear dimer, using geometry equivalent to that used by Pullman and Berthod; our results indicate that R_{O-H} is ∼1.45 Å at the energy minimum. While such a calculation produced a more stable hydrogen bond (∼−16 kcal instead of our value of −9.3 kcal), the total energy of the system was higher because the Pullman–Berthod geometry of the monomer is a higher-energy structure than the one shown in Figure 1A.

3. Formamide Planar Cyclic Dimer. In the study of the formation of the planar cyclic dimer, only two degrees of freedom (R_{C-N} and R_S) were considered for the structure of Figure 1D. The carbon and nitrogen atoms are in rectangular array only with R_S = 0.0 Å. A contour map for the dependence of the energy on these two variables is shown in Figure 8. The minimum in the energy occurs at R_{C-N} ∼ 3.22 Å and R_S ∼ +0.4 Å. Since the magnitude of the energy is ∼−11 kcal/mol per hydrogen bond formed, the planar

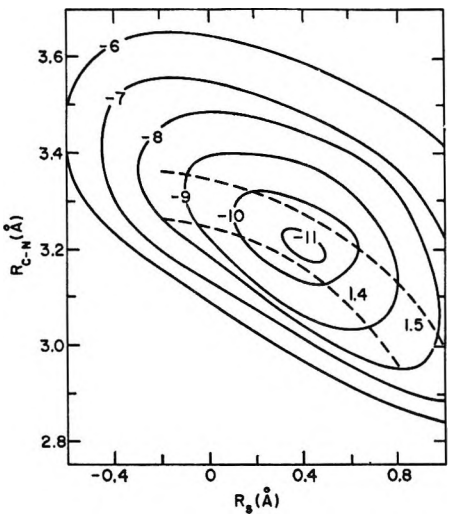

Figure 8. CNDO/2 results for energy contours (per hydrogen bond formed) for variation of R_{C-N} and R_S in the formamide planar cyclic dimer. The zero of the energy scale corresponds to the monomers at infinite separation. The dashed lines correspond to constant values of R_{O-H} of 1.4 and 1.5 Å, respectively.

cyclic dimer is about 1.5 kcal/mol per hydrogen bond more stable than the linear dimer. This result is consistent with the experimental observation of the cyclic dimer in the crystal structure of formamide found by Ladell and Post[18] by X-ray diffraction.

Lines of constant R_{O-H} (at 1.4 and 1.5 Å) are also shown in Figure 8. From these, we observe that the minimum energy occurs at about R_{O-H} ∼ 1.43 Å, and R_{N-O} ∼ 2.4 Å, which is somewhat short compared to the X-ray value[18] of ∼2.8 Å. This difference in R_{N-O} will be considered in section 6. In the minimum-energy conformation, the N—H···O and C=O···H angles are 170.6° and 121.5°, respectively, which are in agreement with many experimental values in the literature.[19] However, since the absence of an energy minimum at α = ±60° in the CNDO/2 calculations for the linear dimer led us to conclude that pure sp^2 hybrid orbitals are not of prime importance in the conformation of the hydrogen bond, we would thus expect that pure sp^2 hybridization does not determine the conformation of the cyclic dimer. Hence, although the *perturbed* sp^2 hybridized orbitals are directly involved in the formation of the hydrogen bond, the conformation is more directly determined by *all* interatomic interactions in the complex.

The variation of CNDO/2 charges of each atom with R_{O-H} is shown in Figure 9. It is clear that the

(16) A. Pullman and H. Berthod, *Theoret. Chim. Acta*, **10**, 461 (1968).

(17) A. B. Biswas, E. W. Hughes, B. C. Sharma, and J. N. Wilson, *Acta Crystallogr.*, **B24**, 40 (1968).

(18) J. Ladell and B. Post, *ibid.*, **7**, 559 (1954).

(19) W. C. Hamilton and J. A. Ibers, "Hydrogen Bonding in Solids," W. A. Benjamin, Inc., New York, N. Y., 1968.

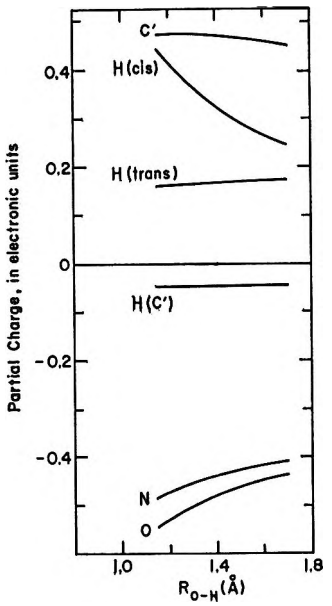

Figure 9. CNDO/2 results for the dependence of partial charge on R_{O-H} for the formamide planar cyclic dimer. R_{O-H} was computed from the values of R_{C-N}, with R_S fixed at +0.4 Å.

atom whose charge is most noticeably affected is H(*cis*), which is involved in hydrogen bonding; however, the N and O atoms also become more negative as R_{O-H} decreases toward the minimum-energy position. It is important to note that the charges on the atoms and the charge separation (CS^+ and CS^-) of *both* molecules in the complex are identical. Thus, since there is *no* charge transfer and yet stabilization occurs, we believe that charge transfer is not a requirement for hydrogen bonding. It should also be noted that the net charge separation of ±0.955 in the minimum-energy conformation is higher in absolute magnitude than in any complex with which we have previously dealt. This is in agreement with our previous statement relating the stability of the linear hydrogen bond to the magnitudes of CS^+ and CS^-.

4. Formamide Parallel-Plane Dimer. Another dimer conformation, which has received little attention in the literature, is that of the parallel planes, separated by a distance R_{P-P}, as shown in Figure 1E. Using the CNDO/2 method, we have studied the four forms (A, B, C, and D), and found considerable stability for three of them. The results are presented in Table V and in Figure 10. Considerable stabilization is predicted for both models A and B, about one-half of these energies for model C, and only slight stabilization for model D. An interesting behavior was observed for model D, for which ΔE became slightly negative at about 2.1 Å, with a minimum of −4.8 kcal/mol at about 2.5 Å, and rose to a maximum positive value of 0.9 kcal/mol at about 3.5 Å before approaching zero at large distances. A possible explanation would attribute this behavior to the resultant of a positive coulombic repulsion and a negative shorter-range $\pi-\pi$ stabilization.

Table V: CNDO/2 Results for Formamide Parallel-Plane Dimers

Model[a]	R_{P-P}, Å	R_{O-H}, Å	ΔE,[b] kcal/mol	CS^+ and CS^-, electronic units	μ, Debye units
A	1.40	1.42	+47.505	1.142	0
	1.60	1.62	−38.991	1.066	0
	1.80	1.81	−46.216	0.974	0
	2.00	2.01	−35.664	0.907	0
	3.00	3.01	−2.912	0.822	0
	5.00	5.01	−0.364	0.815	0
B	1.60		−38.191	1.071	6.37
	1.70		−45.877	1.022	6.06
	1.80		−45.197	0.977	5.76
	1.90		−40.716	0.939	5.51
C	1.90		−15.743	0.806	5.95
	2.00		−19.103	0.806	6.01
	2.50		−8.938	0.802	6.16
	3.00		−1.753	0.803	6.22
D	1.90		+13.651	0.815	7.73
	2.00		+1.863	0.813	7.73
	2.50		−4.780	0.805	7.74
	3.00		−0.184	0.803	7.78
	3.50		+0.927	0.806	7.85
	5.00		+0.549	0.809	7.93
	10.00		+0.104	0.811	7.99

[a] See text for description of conformations. [b] $\Delta E = 0$ for two monomers at infinite separation.

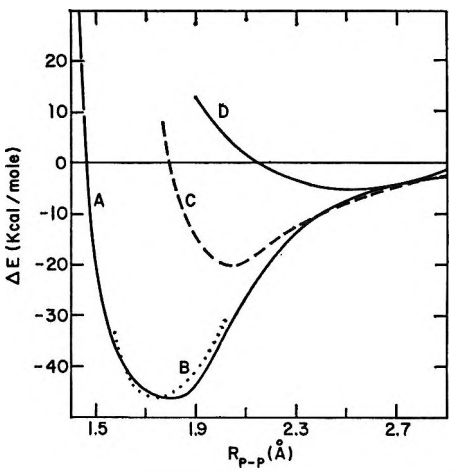

Figure 10. CNDO/2 results for the dependence of ΔE on R_{P-P} for the four models of the formamide parallel-plane dimer. $\Delta E = 0$ for infinite separation of the planar monomers.

The origin of the stabilization energies of models A, B, and C is not clear. They cannot be attributed to charge transfer, since none is found, as in the case of the cyclic dimer. However, CS^+ is very large for models A and B, whereas, in models C and D at the minimum-energy conformations, it is less than that found for the separate monomer. Figure 11 shows the variation of charge with R_{P-P} for models A and C.

Table VI: σ and π CNDO/2 Charges of the Formamide Parallel-Plane Dimer in the Minimum-Energy Conformation, in Electronic Units

Model	R_{C-N}, Å	$H_\sigma(C')$	C'_π	C'_σ	O_π	O_σ	N_π	N_σ	H_σ *cis*	H_σ *trans*
A	1.8	−0.066	0.362	0.168	−0.599	0.150	0.221	−0.680	0.207	0.237
B	1.8	−0.078	0.358	0.175	−0.595	0.156	0.221	−0.681	0.256	0.188
C	2.0	−0.013	0.280	0.175	−0.444	0.069	0.152	−0.571	0.180	0.171
D	2.5	−0.041	0.238	0.212	−0.411	0.061	0.172	−0.585	0.187	0.168
Monomer		−0.038	0.234	0.215	−0.416	0.051	0.182	−0.591	0.189	0.174

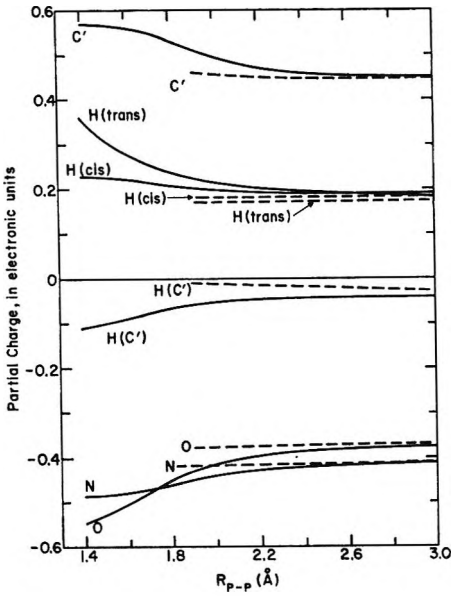

Figure 11. CNDO/2 results for the dependence of partial charge of R_{P-P} for models A (solid lines) and C (dashed lines) of the formamide parallel-plane dimer.

Model A shows considerable variation of charge, while model C shows practically no change from that of the infinitely separated (*i.e.*, monomer) molecules. Models B and D have nearly the same variations in charge as models A and C, respectively. These results for CS^+ and variation of charge do not provide an explanation for the stabilization energy, since model C still is stabilized to the extent of ~20 kcal/mol. We thus turn to an examination of the σ and π contributions in order to resolve the problem; these are given in Table VI for the minimum-energy conformations. Since the monomers approach each other in a direction perpendicular to the planes of the molecules, we might expect that the π electrons would be most strongly influenced. Indeed, we see that the carbon π electrons are redistributed to a considerable extent in models A and B, compared to models C and D, while the carbon σ electrons change slightly to values lower than that of the monomer. Also, oxygen π electrons and σ electrons are changed considerably. However, the nitrogen π electrons and σ electrons seem to hold the key to the problem, since their electron densities are higher than those of the monomer for models A and B and lower for models C and D. Thus, analysis of the resultant partial charges suggests that not only do π–π type interactions occur in all models but also that the favorable alignment of partial charges results in a total electrostatic attraction in models A and B, and that this alignment plays a prominent role in the stabilization. This analysis also explains the difference in energy between models C and D, in that the opposite alignment of the carbonyl groups in model C is sufficient to account for the observed energy.

Whatever the origin of the stabilization, these parallel planar complexes seem to be stable forms, and must be taken into consideration in interpreting experimental observation. In this regard, it is of interest to note that several authors[14,20,21] have postulated models of this nature to explain their nmr data. Certainly, we have shown by charge redistribution that the formation of these complexes would affect the magnetic anisotropy of the carbonyl bond, and this would in effect produce a very marked concentration-dependent chemical shift of the amine protons (or of the N-methyl protons considered in ref 14, 20, and 21) which would depend on the nature of the complex formed.

The crossover point in the variation of the charges of the two amine protons with R_{P-P} is of particular interest. Figure 11 shows that these charges become equivalent at about 2.8 Å for model A. Since the nmr spectrum shows a coalescence of the amine proton peaks as the temperature is raised,[15] it is of interest to speculate that this coalescence may possibly be due to expansion of the model A complex rather than the usual explanation in terms of rapid rotation about the peptide bond.

5. Formamide Linear Trimer. The conformation of the formamide planar linear trimer in the extended form ($\theta_1 = \theta_2 = 0°$) is shown in Figure 1F. A contour map for the dependence of the energy on R^1_{O-H} and R^2_{O-H} is shown in Figure 12. The diagram is very symmetric about the 45° diagonal, indicating that both hydrogen bonds are very close to the same length.

(20) M. Rabinovitz and A. Pines, *J. Amer. Chem. Soc.*, 91, 1585 (1969).

(21) A. G. Whittaker and S. Siegel, *J. Chem. Phys.*, 42, 3320 (1965).

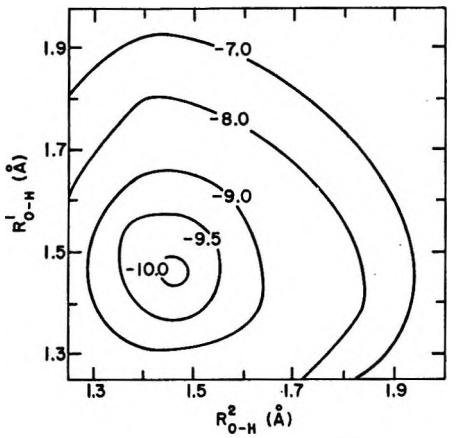

Figure 12. CNDO/2 results for energy contours (per hydrogen bond formed) for variation of R^1_{O-H} and R^2_{O-H} in the formamide planar linear trimer, for $\theta_1 = \theta_2 = 0°$. The zero of the energy scale corresponds to the monomers at infinite separation.

The energy minimum is about −10 kcal/mol per hydrogen bond, which is lower than that of the equivalent linear dimer by ∼0.7 kcal/mol per hydrogen bond,[22] but still not as low as that of the cyclic dimer. This implies that the formation of extended hydrogen-bonded structures in a polypeptide should be favored.[22]

As far as the charge distribution is concerned, we find that, at the minimum-energy conformation, molecule a (see Figure 1F) has a net positive charge of ∼0.016 electronic unit, molecule c a net negative charge of ∼0.016 electronic unit, while molecule b remains neutral. This implies that charge is transferred through the middle molecule to the same extent as we found in the linear dimer, and again in the direction from the carbonyl group to the amine group. The values of CS^+ and CS^- are +0.859 and −0.843, +0.944, and −0.944, and +0.907, and −0.923, for molecules a, b, and c, respectively, *i.e.*, smallest for molecule a, largest for molecule b, with that for molecule c being closer in magnitude to molecule b than molecule a. Figure 13 shows the variation of charge with R^1_{O-H} and R^2_{O-H}, respectively, and illustrates similar trends to those found previously for the linear dimer.

6. Formamide Planar Forked Trimer. The conformation of the formamide planar forked trimer, in which both amine hydrogens of molecule b are involved in hydrogen bonds, is shown in Figure 1G, for $\theta_1 = \theta_2 = 0°$. A contour map for the dependence of the energy on R^1_{O-H} and R^2_{O-H} is shown in Figure 14. Again, the diagram is nearly symmetric about the 45° diagonal, indicating that $R^1_{O-H} \approx R^2_{O-H}$.

We see from Figure 14 that, in this case, R_{O-H} for the minimum-energy conformation is larger (∼1.50 Å) than for the linear trimer (∼1.46 Å). However, the energy per hydrogen bond (∼−8.4 kcal/mol) is considerably less (*i.e.*, more positive) than that found for the other hydrogen-bonded complexes. For the planar forked trimer, values for CS^+ and CS^- of

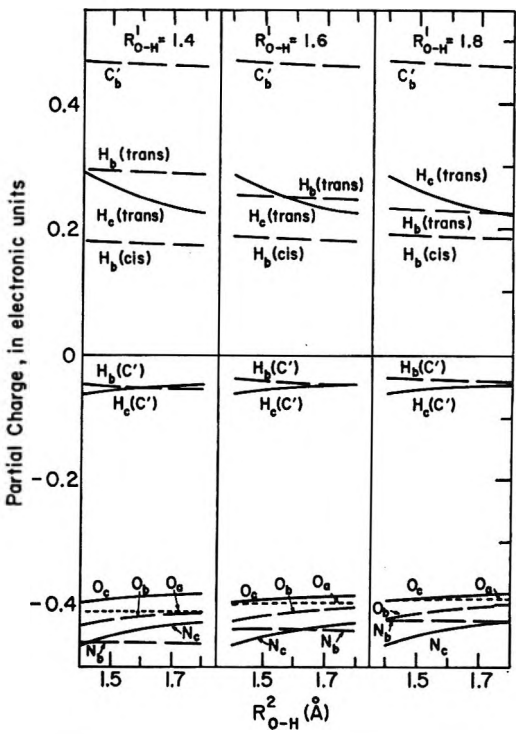

Figure 13. CNDO/2 results for dependence of partial charge on R^1_{O-H} and R^2_{O-H}, respectively, with one of these distances held fixed, for the formamide planar linear trimer with $\theta_1 = \theta_2 = 0°$.

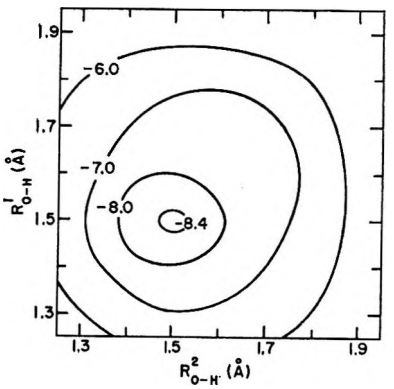

Figure 14. CNDO/2 results for energy contours (per hydrogen bond formed) for variation of R^1_{O-H} and R^2_{O-H} in the formamide planar forked trimer, for $\theta_1 = \theta_2 = 0°$. The zero of the energy scale corresponds to the monomers at infinite separation.

+0.837 and −0.831, +0.955 and −0.970, and +0.841 and −0.832, for molecules a, b, and c, respectively, are obtained. In this case, the net charge transfer

(22) This indicates that linear hydrogen bond formation is a cooperative process; *i.e.*, the formation of a linear trimer is more favorable than the formation of two linear dimers. It is of interest that qualitative arguments had been advanced by Frank and Wen[23] for the existence of such cooperativity in another hydrogen-bonded system, *viz.*, liquid H_2O. See also recent calculations on H_2O oligomers.[24]

(23) H. S. Frank and W. Y. Wen, *Discuss. Faraday Soc.*, **24**, 133 (1957).

(24) J. R. Hoyland and L. B. Kier, *Theoret. Chim. Acta*, **15**, 1 (1969).

is similar to that obtained for the other complexes; *i.e.*, the electron transfer is still from the carbonyl groups to the amine group. It is of interest that the total charge separation of the linear trimer is greater than that of the forked trimer, which again correlates with the magnitudes of the binding energies.

It is of interest at this point to compare our results for the various complexes with those deduced for the molecular environment in the crystal from X-ray analysis.[18] In the crystal, individual formamide molecules associate to form the cyclic dimer; however, these dimers are, in turn, linked to other molecules by hydrogen bonds of the same type, equivalent to our forked trimer conformation. Stacking interactions arise between puckered sheets of dimeric units, held together within the sheets by strong N—H···O hydrogen bonds. Thus, the plane-to-plane interactions are intermediate between our models A and D, *i.e.*, one member of the dimer lies above the hole in the cyclic dimer in the sheet below it. The experimental distances are: $N_1 \cdots O_2 = 2.94$ Å in the cyclic dimer, $N_1 \cdots O_3 = 2.88$ Å in the forked trimer, and the average distance between sheets is 3.1 Å. It should be noted that, in the trimers, all of our N···O distances are given for complexes in which the N—H···O atoms are collinear, whereas collinearity is not maintained in the crystal packing; this would tend to make the experimental hydrogen-bond lengths greater. We also suggest that the considerable amount of multiple bonding, which occurs in the crystal, is partially responsible for the large R_{O-H} values observed experimentally. Thus, the shorter R_{O-H}, R_{C-N}, and R_{P-P} distances computed for the *isolated* complexes in this work may be quite realistic, since the experimentally determined distances (and energies) are the resultant of multiple interactions, all of which would tend to increase these distances and weaken the bonds.

Table VII: Results for N-Methyl Acetamide Monomer ($\phi = 60°$, $\psi = 0°$)

		CNDO/2		EHT	
ω, deg		μ,[a] Debye units	ΔE,[b] kcal/mol	ΔE,[b] kcal/mol	
0		4.12	0	0	
30		3.95	4.504	5.077	
60		3.51	13.896	17.003	
90		3.18	18.789	24.166	
120		3.36	14.004	18.088	
150		3.78	5.590	10.103	
180		3.99	0.759	6.695	
Charges (ON)[c] for $\omega = 0°$ (in electronic units)	$H^{\alpha}(C')$	0.059	$C^{\alpha}(C')$	−0.174	
	$H^{\alpha}(C')$	0.049	C′	0.465	
	$H^{\alpha}(C')$	0.049	O	−0.387	
			N	−0.342	
	H(N)	0.156	$C^{\alpha}(N)$	0.041	
	$H^{\alpha}(N)$	0.050			
	$H^{\alpha}(N)$	0.017			
	$H^{\alpha}(N)$	0.017			
	CS^{+}	0.903			
	CS^{-}	−0.903			

[a] Calculated using Pople method (see paper II). [b] $\Delta E = 0$ for $\omega = 0°$. [c] See paper II for definition of overlap-normalized charges.

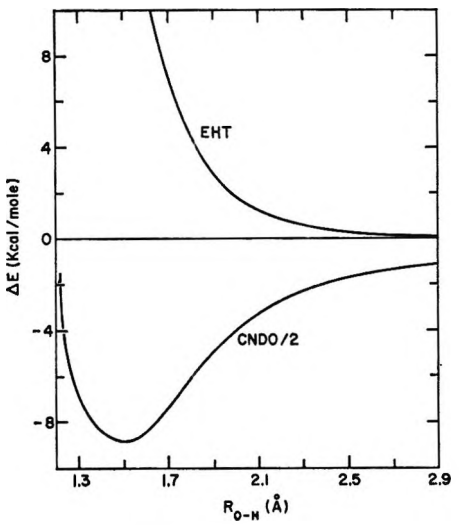

Figure 15. CNDO/2 and EHT results for the dependence of ΔE on R_{O-H} for the NMA linear dimer ($\phi = 60°$, $\psi = 0°$, $\omega_1 = \omega_2 = \alpha = \delta = \beta = \theta = 0°$). $\Delta E = 0$ for two monomers at infinite separation.

7. N-Methyl Acetamide Linear Dimer. The molecule N-methyl acetamide (NMA) is a considerably better model for a peptide than is formamide. However, more than twice the computer time is required to examine NMA as fully as formamide. For this reason, we have allowed only several of the possible conformational variables to change, selecting those (*viz.*, R_{O-H}, θ, and α) which show the most interesting conformational features (departure of δ from 0° leads to an increase in energy as found for formamide, and is not considered further here). The pertinent monomer data are given in Table VII.

The NMA linear dimer is shown in Figure 1H, for $\phi = 60°$, $\psi = 0°$, $\omega_1 = \omega_2 = \theta = \alpha = \beta = \delta = 0°$; ΔE is shown as a function of R_{O-H} for this conformation in Figure 15. As in the formamide calculations, the EHT method fails to give a minimum for the formation of a stable hydrogen bond. However, the CNDO/2 method does give a minimum at $R_{O-H} \sim 1.5$ Å, with an energy of about −9.4 kcal/mol for the usual *trans* conformation of the molecule.

The results for the NMA linear dimer are given in Table VIII. The effect of varying θ is particularly interesting in this complex. We see that the conformations with $\theta = 0°$ and $\theta = 180°$ have about the same hydrogen-bond strength. The CNDO/2 method indicates that the $\theta = 0°$ conformation is slightly more stable. The EHT method, on the other hand, indicates that the conformation with $\theta = 180°$ is more stable than the one with $\theta = 0°$, but not as

Table VIII: Results for N-Methyl Acetamide Linear Dimer ($\phi = 60°$, $\psi = 0°$, $\alpha = \delta = \beta = 0°$)

				CNDO/2							EHT	
				ΔE,[a]	ΔE,[b]	Molecule a		Molecule b		μ,[c]	ΔE,[a]	ΔE,[b]
R_{O-H}, Å	ω_1, deg	ω_2, deg	θ, deg	kcal/mol	kcal/mol	CS$^+$	CS$^-$	CS$^+$	CS$^-$	Debye units	kcal/mol	kcal/mol
1.3	0	0	0	−6.542		0.981	−0.962	0.983	−1.002	9.63		
1.5	0	0	0	−9.399		0.954	−0.943	0.952	−0.963	9.10	15.687	
1.8	0	0	0	−6.085		0.932	−0.929	0.930	−0.933	8.65		
2.0	0	0	0								1.719	
3.0	0	0	0	−0.999		0.912	−0.911	0.910	−0.911	8.25	0.012	
1.5	0	0	0		0							0
	30	0	0		4.870							4.118
	60	0	0		15.023							15.612
	90	0	0		20.377							22.745
	120	0	0		15.135							16.664
	150	0	0		5.945							8.676
	180	0	0		0.786							5.267
1.5	0	30	0									4.380
	0	60	0									14.320
	0	90	0									20.721
	0	120	0									15.287
	0	150	0									8.236
	0	180	0									5.238
1.5	0	0	30		0.014							−0.667
	0	0	60		0.025							−1.344
	0	0	90		0.039							−1.425
	0	0	120		0.028							−1.419
	0	0	150		0.025							−1.389
	0	0	180		0.037	0.952	−0.942	0.953	−0.963	9.26		−1.367
1.5	0	30	180		4.578[d]							
	0	60	180		13.861[d]							
	0	90	180		18.821[d]							
	0	120	180		14.221[d]							
	0	150	180		5.993[d]							
	0	180	180		1.241[d]	0.951	−0.939	0.947	−0.959	6.38		

[a] $\Delta E = 0$ for two monomers (with $\omega = 0°$) at infinite separation. [b] $\Delta E = 0$ for $\omega_1 = \omega_2 = \theta = 0°$, at $R_{O-H} = 1.5$ Å. [c] Calculated using Pople method (see paper II). [d] $\Delta E = 0$ for $\omega_1 = \omega_2 = 0°$, $\theta = 180°$, at $R_{O-H} = 1.5$ Å.

stable as those with θ in the range of 90–120°, which are lower in energy than the $\theta = 0°$ conformation by ~1.4 kcal/mol. Again, we place most credence in the CNDO/2 results.

The dependence of ΔE on α is shown in Figure 16. The CNDO/2 results for $\theta = 0°$ and $\theta = 180°$ are of particular interest. For $\theta = 0°$, α must lie in the range from 0° to −30°, with ΔE increasing sharply for positive values of α. For $\theta = 180°$, the minimum energy occurs at $\alpha = +30°$, and ΔE varies very little down to −20°. The rapid rise in ΔE at the extremes is probably due to interactions between the methyl groups, since this effect was much less noticeable in the formamide linear dimer. Again this conformational dependence on α seems to be dominated by the total molecular environment rather than by any strong directional orbital properties.

The EHT curve for $\theta = 0°$ is symmetric, with minima at $\alpha = \pm 10°$. Thus, even though both methods predict a departure from the linear conformation (*i.e.*, $\alpha = 0°$), there is no indication of a preference for the directions of $\alpha = \pm 60°$ as would be expected for pure sp^2 hybridized lone-pair orbitals.

The dependence of the partial charges on R_{O-H} is shown in Figure 17. The most obvious difference between NMA and formamide is the shifting of the relative positions of the nitrogens and oxygens (see Figure 4) the oxygens being more negative than the nitrogens in NMA. However, the basic features of redistribution of charges and charge transfer, occurring upon formation of a hydrogen bond, are very similar to those observed for formamide.

The energy for rotation about the peptide bonds is also given in Table VIII, and again the results are similar to those found for formamide; *i.e.*, the barrier to rotation increases in the order: U_ω for monomer, U_{ω_2}, and U_{ω_1}. These conclusions are also in excellent agreement with those of Neuman, *et al.*,[14] (based on nmr experiments) who observed an increase in the barrier of N,N-dimethyl acetamide in formamide as solvent; in this case, the solvent attacks the solute only at the carbonyl group, leading to an increase in the barrier.

In analyzing the preceding results for NMA, it is helpful to take note of the conformations found by X-ray diffraction analysis. Katz and Post[25]

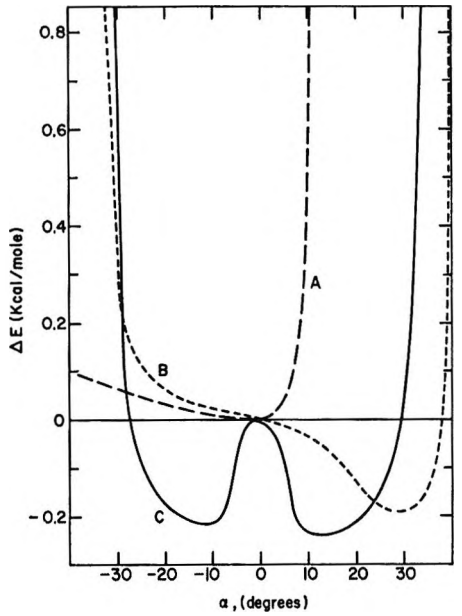

Figure 16. EHT (curve C, $\theta = 0°$) and CNDO/2 results for the dependence of ΔE on α for the NMA linear dimer with $R_{O-H} = 1.5$ Å, and $\theta = 0°$ and 180° (curves A and B, respectively—both CNDO/2), and $\phi = 60°$, $\psi = 0°$, $\omega_1 = \omega_2 = \delta = \beta = 0°$. $\Delta E = 0$ at $\alpha = 0°$.

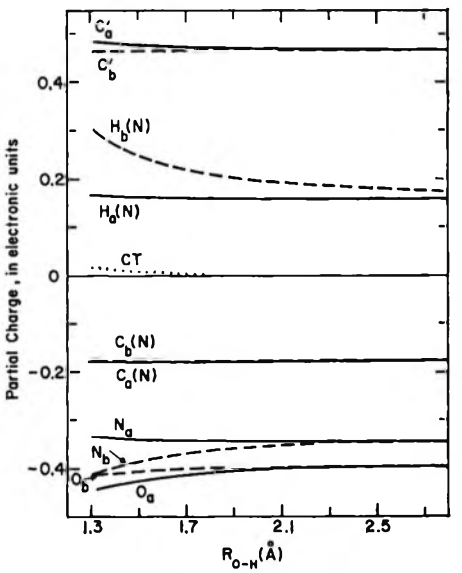

Figure 17. CNDO/2 results for the dependence of partial charges on R_{O-H} for the NMA linear dimer with $\phi = 60°$, $\psi = 0°$, $\omega_1 = \omega_2 = \alpha = \delta = \beta = \theta = 0°$. Solid and dashed lines refer to molecules a and b, respectively. The CT curve refers to a gain of positive charge (net loss of electrons) by molecule a.

found a solid phase transition at approximately 10° and, upon analyzing the diffraction data below and above this temperature, found planar *trans* molecules held together by extended hydrogen-bonded chains. Below the transition temperature, the conformation of the chain is similar to that of Figure 1H, with $\theta = 0°$ and α slightly negative. This conformation is, of course, similar to that found on adjacent peptide groups within the antiparallel pleated sheet conformation of the polypeptide chain. Above the transition temperature, a random rearrangement of the hydrogen-bonded molecules makes the structure determination difficult. This observation correlates well with our results since, because of the almost identical energies found for the $\theta = 0°$ and $\theta = 180°$ conformations, we could postulate a statistical mixture of both, under the experimental conditions, resulting in the observed random conformation. The observed[25] N···O hydrogen-bond distance of 2.8 Å is somewhat larger than our value 2.5 Å (see Table VIII). Again it is not clear that our calculations should lead to the larger hydrogen-bond lengths observed experimentally, since the NMA crystal data reflect the influence of very short methyl–methyl contacts from neighboring molecules which would tend to be repulsive and thereby increase the minimum-energy length of the hydrogen bond. It is also probable that the close contact of the methyl groups across the hydrogen bond would influence R_{O-H} considerably because of thermal and vibrational effects. We have also chosen the "best" methyl–methyl fit (*i.e.*, the hydrogen on the methyl group of molecule a positioned between two hydrogens on the adjacent methyl group of molecule b) in the computations; thus, rotation of the methyl groups would tend to expand the complex and weaken the hydrogen bond. This is the reason why our computed energies are larger in absolute magnitude than the usually observed ones.

8. N-Methyl Acetamide Parallel-Plane Dimer. The parallel-plane conformations considered for NMA are the same as models A and B for formamide, *i.e.*, with C—N bonds antiparallel and the C=O bonds either opposite or aligned. In both models, the methyl groups were rotated to $\phi = 30°$ and $\psi = 30°$ to obtain the closest packing for the complex; this is a similar criterion to that used for the choice of the ϕ, ψ values for the linear dimer of NMA. In model A, the methyl groups of molecule a interact with those of molecule b; hence, this model might be expected to be less stable than model B, in which the oxygen of molecule a interacts with the methyl group of molecule b. Figure 18 shows ΔE as a function of R_{P-P} for both models A and B. As expected, model B is more stable than model A by about 4.6 kcal/mol. It is of interest to note that the experimentally observed[25] interplanar stacking distance of 3.26 Å is larger than the minimum energy position of model B; however, it is less than that of model A. Since the magnitudes of the stabilization energies of models A and B are close to those found here for models A and B of formamide at the equivalent values of R_{P-P}, it would appear that the interplanar stacking is influenced primarily by amide–amide interactions; since the methyl–methyl

(25) J. L. Katz and B. Post, *Acta Crystallogr.*, 13, 624 (1960).

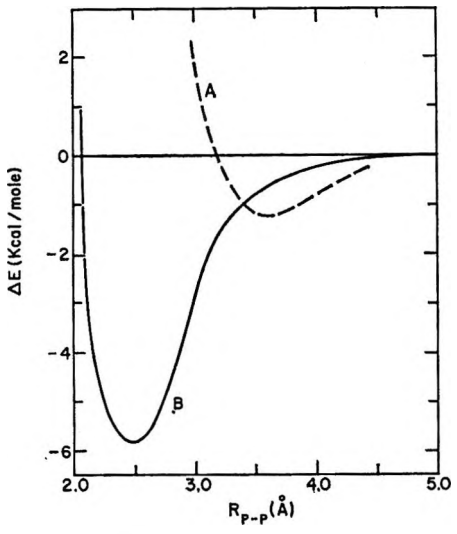

Figure 18. CNDO/2 results for the dependence of ΔE on R_{P-P} for models A and B of the NMA parallel-plane dimer ($\phi = \psi = 30°$, $\omega_1 = \omega_2 = \theta = \alpha = \delta = \beta = 0°$). $\Delta E = 0$ for infinite separation of the monomers of this conformation.

interactions are primarily repulsive, they tend to expand the contact distances between the planes. Another interesting result is that it is not necessary to invoke van der Waals interactions in order to obtain stabilized structures of the type studied here.

Considering the resulting charge separation for the two models, we find that the CS values of model B ($CS^{\pm} = 0.919$) are greater than those of model A ($CS^{\pm} = 0.908$), and both are lower than those found in the linear dimer. This result is in agreement with those reported earlier in this paper, which showed that, at the energy minimum, the more stable complex is the one with the higher degree of charge separation in the molecules of the complex.

On the basis of these results, we may now speculate about the formation of NMA complexes in solution. For example, Mizushima, *et al.*,[26] suggested that NMA is associated in solution, because of an observed increase in the dipole moment with increasing concentration. Since a model A complex would not lead to an increase in the dipole moment, it probably is not of importance in solution. However, both model B and the linear hydrogen-bond dimer would give rise to an increase in the total dipole moment upon formation of the complex. Thus, the observed dipole moment[26] of 5.4 D at low concentration could arise either from a model B complex (for which the calculated dipole moment is 5.5 D) or to a mixture of linear dimers and monomers, having dipole moments of 9.1 and 4.1 D, respectively. At higher concentrations, model B and linear dimers would be expected to form, consistent with the observed value[26] of 6.8 D.

Conclusions

Some of the conclusions derived from the calculations reported here are given below. (1) The EHT method was shown to be deficient in its inability to correctly predict certain physical properties of the polar model peptides studied in this work; *e.g.*, the absence of a binding energy for these hydrogen-bonded systems is particularly serious, especially when considering polypeptide interactions. The CNDO/2 method gives reasonable values for both the energies and conformations of the complexes studied here; hence, conclusions based only on this method will be presented. (2) Hydrogen-bond strength seems to correlate well with the magnitude of the resultant charge separation of the molecules making up the complex. (3) While charge transfer occurs upon formation of linear hydrogen-bonded complexes, it does not seem to be strongly correlated with the binding energy. (4) The formation of the linear trimer hydrogen-bonded complex appears to be a cooperative process; this has considerable implications for the stabilization of polypeptides and proteins. (5) The conformation around the carbonyl oxygen depends more on the total molecular interactions than on lone-pair hybridization. (6) Very stable complexes of the parallel-plane type were found; again, these have significance for the stabilization of protein structures, probably by π–π as well as by electrostatic interactions. (7) The variation of partial charges accompanying formation of all complexes studied must be taken into account in empirical conformational energy calculations on polypeptides. (8) The small change of partial charge on the C′ atom, accompanying formation of a hydrogen bond, implies that C^{13} nmr chemical shifts should not be influenced significantly by complex formation; thus our earlier statement,[5] that C^{13} nmr studies could provide information about the nonplanarity of the peptide group, is shown to be true here, even when hydrogen bonding occurs.

Acknowledgment. We wish to thank the Cornell Office of Computer Services for use of their facilities.

(26) S. Mizushima, T. Simanouti, S. Nagakura, K. Kuratani, M. Tsuboi, H. Baba, and O. Fujioka, *J. Amer. Chem. Soc.*, 72, 3490 (1950).

The Crystal and Molecular Structure of Di-μ-chlorotris(*trans*-cyclooctene)dicopper(I)

by P. Ganis[1]

Department of Chemistry, Polytechnic Institute of Brooklyn, Brooklyn, New York

U. Lepore

Istituto Chimico dell'Università di Napoli, Naples, Italy

and E. Martuscelli

Laboratorio di Ricerche su Tecnologia dei Polimeri e Reologisa, Naples, Italy *(Received October 31, 1969)*

A single crystal three-dimensional X-ray study of di-μ-chlorotris(*trans*-cyclooctene)dicopper(I) $[Cu_2Cl_2(C_8H_{14})_3]$ has been carried out. The unit cell data are: triclinic, $P\bar{1}$; $a = 14.95 \pm 0.03$ Å, $b = 11.50 \pm 0.02$ Å, $c = 11.20 \pm 0.12$ Å, $\alpha = 119.2 \pm 0.3°$, $\beta = 114.0 \pm 0.3°$, $\gamma = 101.5 \pm 0.3°$, $Z = 2$; $d_c = 1.32$ g cm^{-3}. The structure consists of units

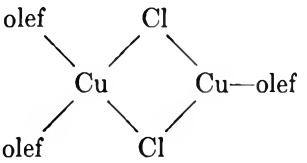

The coordination around one of the copper atoms is of trigonal-planar type, while that of the other copper atom may be described as a distorted pyramidal-trigonal arrangement. The bond distances and angles of the bridged system are Cu(1)–Cl(1) 2.361 ± 0.006 Å, Cu(1)–Cl(2) 2.928 ± 0.007 Å, Cu(2)–Cl(1) 2.291 ± 0.006 Å, Cu(2) 2.265 ± 0.006 Å; Cu(1)Cl(1)Cu(2) 87.2 ± 0.1°, Cl(1)Cu(2)Cl(2) 102.5 ± 0.1°, Cu(2)Cl(2)Cu(1) 75.1 ± 0.1°, Cl(2)Cu(1)Cl(1) 83.7 ± 0.1°. Relevant is the torsion angle around the double bond, *ca.* 135 ± 5°. Refinement has been based on visually measured intensities and has been accomplished by standard three-dimensional Fourier and least-squares methods to a final R value of 0.108.

No crystal structure of compounds containing the *trans*-cyclooctene ring has been reported in the literature so far.

From a study of molecular models it is possible to deduce that, basically, two different conformations can be assigned to this eight-term cycle;[2] either one characterized by a pseudo 2/m symmetry (a) or one with 2 symmetry (b) (Figure 1). On this basis conformation b has been proposed as the most probable one.[2] Besides, many experimental data based on dipole moment and infrared measurements[3] actually indicate that the angle of rotation around the double bond is considerably different from the ideal value of 180°.

It thus seemed useful to study the crystal structure of a compound containing molecules of *trans*-cyclooctene to substantiate these indications.

Owing to the difficulty of studying directly such a low-melting material as the free olefin, a complex with Cu(I) was chosen. The following considerations favored this choice. The presence of heavy atoms facilitates the solution of the structure; it was possible to gain new data on the stereochemistry of Cu(I) complexes which, in fact, have not received adequate attention up to the present time.

Experimental Section

Crystals of the complex were prepared according to previously described procedures;[4] two crystals were used in collecting the intensity data. Both were grown to a prism with near equal edges (0.3 × 0.3 × 0.3 mm) and approximately with the shape of the unit cell (see below). The crystals were enclosed in Lindemann capillaries in an atmosphere of olefin to retard decomposition. One crystal was used to record $h01$ to $h51$; the other was used to record $hk0$ to $hk3$. All data were collected using the multiple film equiinclination Weissenberg techniques (Cu Kα radiation). The intensities of 2605 nonzero observable reflections were

(1) Visiting professor.

(2) J. D. Dunitz, "Perspectives in Structural Chemistry," Vol II, John Wiley & Sons, Inc., New York, N. Y., 1968, p 49.

(3) N. L. Allinger, *J. Amer. Chem. Soc.*, **80**, 1953 (1958).

(4) H. L. Haight, J. R. Doyle, N. C. Baenziger, and G. F. Richards, *Inorg. Chem.*, **2**, 1301 (1963).

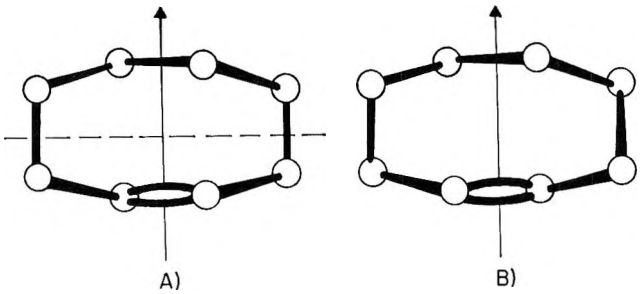

Figure 1. The most probable conformations of *trans*-cyclooctene are schematically represented: A, with a pseudo 2/m symmetry; B, with a 2 symmetry.

estimated visually by comparison with calibrated intensity strips.

The intensities were put on a common scale with a least-squares program using the reflections present in both sets. No correction was made for absorption (μ = 38.9 cm^{-1}); the maximum error in the intensities due to the absorption is not greater than ~12% if one assumes the crystal to be approximately cylindrical. The unit cell data are reported in Table I. The calculated density (1.32 g cm^{-3}) for two formula weights ($Cu_2Cl_2(C_8H_{14})_3$) per cell agrees with the experimental value (1.25–1.35 g cm^{-3}) measured by flotation.

Table I: Crystal Data of Di-μ-chlorotris(*trans*-cyclooctene)dicopper(I), $Cu_2Cl_2(C_8H_{14})_3$

Mol wt, 528.32
Triclinic, space group $P\bar{1}$ $F(000)$ = 556

a = 14.95	(3)	Å
b = 11.50	(2)	Å
c = 11.20	(2)	Å
α = 119.2°	(3)	
β = 114.0°	(3)	
γ = 101.5°	(3)	
d_x = 1.32 g cm^{-3}		
Z = 2		
μ = 38.9 cm^{-1} for λ 1.5418 Å		

Determination of the Structure

Copper and chlorine positions were determined from a three-dimensional Patterson map. These positions corresponded to a bridged system

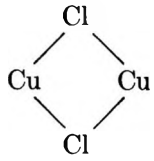

in which three Cu–Cl bond distances are nearly equal (2.3–2.4 Å); the fourth is considerably longer (~2.9 Å). The bridged system is not planar and is asymmetric.

A structure factors calculation using the coordinates of Cu and Cl atoms alone yielded an R value of ~0.48. A three-dimensional electron density map was evaluated using the amplitudes of 1150 of the 2605 nonzero observable reflections. From this map we were able to recognize the position of the carbon atoms of two cycloolefins. It was impossible to locate the third ring with certainty from the residual peaks. A second Fourier synthesis was calculated after a structure factors calculation including the C atoms of two olefins (R factors ~0.32). The third olefin was now clearly recognized.

At this stage the structure factors calculation using a thermal factor B = 5 Å^2 for all the atoms yielded an R factor of ~0.26. The structure was refined down to $R \cong 0.18$ with usual Fourier techniques. The programs used to compute the Patterson and the Fourier syntheses have been written by Immirzi.[5]

Refinement of the Structure

A block diagonal matrix least-square program written for an IBM computer was used.[5]

Variable isotropic thermal factors for each atom were applied, until the R factor dropped to 0.15. At this stage anisotropic thermal factors were introduced, also the contribution of the hydrogen atoms was included using geometrically calculated coordinates. The R factor dropped to 0.108. The weighting method of Cruickshank was employed: $w = 1/(A + BF_o + CF_o^2)$ with A = 0.11111, $B = 1/(18F_{o(min)})$, $C = 2/18F_{o(min)}F_{o(max)})$. The minimized function was

$$\frac{\sum w|\Delta F|}{\sum wF_o}$$

The atomic scattering factors of Hanson[6] were used. The final atomic coordinates and thermal factors, with their standard deviations, are given in Table II.[7]

Discussion of the Structure

The most important interatomic distances, bond angles, and torsional angles of the molecule, with their standard deviations, are given in Table III.

In Figure 2 is shown the bridged system

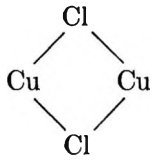

The most interesting conformational parameters are indicated. Both copper atoms present sp^2 hybridization.

(5) A. Immirzi, *Ric. Sci.*, **377**, 743 (1967).

(6) H. P. Hanson, J. D. Lea, and S. Skilmann, *Acta Cryst.*, **17**, 1040 (1967).

(7) A list of the observed and calculated structure factors has been deposited as Document No. 00899 with the ASIS, National Auxiliary Publication Science, c/o CCM Information Corp., 909 Third Ave., New York, N. Y. 10022. A copy may be secured by citing the document number and by remitting $1.00 for microfiche or $3.00 for photocopies; advanced payment is required. Make checks or money orders payable to CCMI–NAPS.

Table II: Positional and Thermal Parameters of Cu, Cl, and Carbon Atoms

	x	y	z	B_{11}	B_{22}	B_{33}	B_{12}	B_{13}	B_{23}
C(1)	0.181(1)	0.001(2)	−0.150(1)	4.7 (6)	3.8 (7)	4.4 (5)	2.8 (5)	2.5 (4)	2.5 (5)
C(2)	0.203(1)	−0.005(2)	−0.273(2)	4.4 (6)	8.8 (12)	5.3 (6)	3.2 (6)	3.2 (5)	3.9 (7)
C(3)	0.323(1)	0.007(2)	−0.214(2)	6.1 (8)	8.5 (12)	6.4 (8)	1.9 (7)	4.3 (7)	1.6 (7)
C(4)	0.417(1)	0.147(2)	−0.027(2)	3.4 (5)	9.0 (12)	6.5 (7)	1.7 (6)	2.5 (5)	4.3 (8)
C(5)	0.431(1)	0.134(2]	0.114(2)	3.8 (6)	10.3 (14)	6.5 (8)	3.7 (7)	2.4 (6)	4.1 (8)
C(6)	0.409(1)	0.241(2)	0.239(2)	5.1 (7)	9.0 (13)	4.6 (6)	3.1 (7)	1.7 (6)	3.3 (7)
C(7)	0.277(1)	0.177(2)	0.164(2)	5.1 (7)	7.8 (11)	5.3 (6)	3.7 (7)	2.7 (5)	4.6 (7)
C(8)	0.220(1)	0.144(2)	−0.003(2)	4.0 (6)	10.0 (12)	5.1 (6)	3.2 (6)	2.9 (5)	4.8 (7)
C(1′)	−0.067(1)	−0.218(1)	−0.434(1)	3.1 (4)	2.6 (6)	4.1 (5)	1.2 (4)	1.5 (4)	1.8 (4)
C(2′)	−0.052(1)	−0.345(2)	−0.466(2)	6.0 (8)	5.7 (9)	6.2 (7)	4.2 (7)	2.9 (6)	2.9 (7)
C(3′)	−0.150(1)	−0.496(2)	−0.657(2)	6.5 (8)	3.5 (7)	5.7 (7)	2.8 (6)	1.6 (6)	1.8 (6)
C(4′)	−0.271(1)	−0.524(2)	−0.711(2)	4.3 (6)	2.1 (6)	7.8 (8)	1.1 (5)	1.6 (6)	3.4 (7)
C(5′)	−0.310(1)	−0.426(2)	−0.760(2)	3.7 (6)	8.3 (12)	5.1 (6)	2.5 (6)	1.5 (5)	3.5 (7)
C(6′)	−0.331(1)	−0.309(2)	−0.640(2)	4.5 (6)	6.4 (9)	6.8 (7)	4.4 (6)	2.7 (6)	4.4 (7)
C(7′)	−0.224(1)	−0.152(2)	−0.473(2)	4.8 (6)	4.7 (7)	4.9 (5)	4.0 (5)	2.6 (5)	2.7 (5)
C(8′)	−0.136(1)	−0.186(2)	−0.383(2)	5.3 (6)	5.4 (8)	5.2 (5)	3.1 (6)	3.7 (5)	3.8 (6)
C(1″)	−0.189(1)	−0.289(2)	−0.146(2)	6.3 (7)	3.5 (6)	6.5 (7)	3.9 (6)	3.9 (6)	4.2 (6)
C(2″)	−0.285(2)	0.179(2)	−0.172(2)	8.7 (11)	10.2 (14)	8.7 (10)	6.5 (10)	6.2 (9)	6.7 (10)
C(3″)	−0.380(2)	0.221(2)	−0.206(2)	7.3 (10)	9.4 (14)	9.1 (10)	6.2 (9)	5.4 (9)	7.7 (11)
C(4″)	−0.411(1)	0.245(2)	−0.344(2)	5.9 (8)	6.7 (11)	9.5 (11)	4.0 (7)	4.4 (8)	4.7 (9)
C(5″)	−0.332(2)	0.404(2)	−0.285(2)	9.5 (11)	6.6 (10)	6.1 (7)	6.8 (9)	3.5 (8)	3.8 (8)
C(6″)	−0.269(2)	0.396(2)	−0.368(2)	8.7 (10)	6.3 (11)	7.6 (9)	4.2 (9)	3.8 (8)	6.3 (9)
C(7″)	−0.162(2)	0.395(2)	−0.291(2)	8.1 (10)	5.2 (10)	7.3 (9)	2.6 (8)	4.2 (8)	3.5 (8)
C(8″)	−0.190(1)	0.261(2)	−0.283(2)	3.7 (5)	5.5 (8)	4.9 (5)	2.8 (5)	2.1 (5)	2.9 (6)
Cu(1)	0.0342(2)	0.0099(3)	−0.1724(2)	4.42(8)	6.00(13)	5.01(8)	3.44(8)	2.74(7)	3.19(9)
Cu(2)	−0.0664(2)	0.2350(2)	−0.1522(2)	5.12(9)	5.05(12)	5.00(8)	3.32(8)	2.93(7)	3.50(9)
Cl(1)	−0.0067(3)	0.1627(4)	0.0100(4)	5.34(14)	5.50(21)	4.65(12)	3.82(14)	3.33(12)	3.94(15)
Cl(2)	0.0444(3)	0.2241(6)	−0.2432(5)	6.18(9)	9.00(32)	6.75(18)	5.14(19)	4.53(16)	5.73(21)

To Cu(1) are coordinated Cl(1) and two cycloolefins with a nearly undistorted trigonal geometry. The Cu double bond midpoint distances (ranging from 1.93 to 2.09 Å) agree, within the errors, with the values reported in the literature for similar compounds.[8]

The bond length Cu(1)–Cl(1), of 2.36 Å, is different from the known distances in Cl bridged systems of Cu(I) complexes (2.26–2.28 Å).

This lengthening is presumably due to the fact that Cu(1) is bonded to two rather strong electron donors—the two olefin ligands—which may induce some electron repulsion on the electron pair of Cl(1).

In the apical position of the system

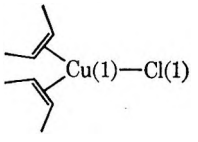

there can be found another chlorine atom, Cl(2), almost exactly in the direction of the p_z orbital of Cu(1), 2.93 Å apart. It can still be considered a weak bond distance.[8]

The coordination of Cu(1) may be considered as trigonal pyramidal. In the apical direction opposite to Cl(2) there is the Cl(1′) atom (3.35 Å apart) belonging to a centrosymmetrical molecule. A similar situation has been observed in other Cu(I) compounds and in the case of some Cu(II) compounds although in these cases different geometric factors are involved.

The coordination around Cu(2) is trigonal, but the apical positions are completely free. The Cu–Cl bond distances range between 2.26 and 2.29 Å and are comparable with those of the compounds quoted in ref 8.

The bridged system is strongly distorted; the four bridged atoms do not lie on the same plane as shown by the torsional angles on the Cu–Cl bonds of the four-member ring, all of the order of $|\sim 25°|$.

The two cycloolefins bonded to Cu(1) have the same configuration. The contact distances C(1)----C(1′) and C(1)----C(2′), though very short (3.0 and 3.3 Å, respectively), are comparable to those found in other organic compounds, and the involved repulsion energy is less than 1–2 kcal/mol.[9] The third cycloolefin bonded to Cu(2) in the same molecule has the opposite configuration.

For all three cycloolefins, the double bond is orthogonal within 2–3° to the line joining the copper atom with the center of the double bond. The direction of the double bond makes an angle not greater than 15–

(8) N. C. Baenziger, G. F. Richards, and J. R. Doyle, *Inorg. Chem.*, **3**, 1529 (1964); N. C. Baenziger, H. L. Haight, and J. R. Doyle, *ibid.*, **3**, 1535 (1964).

(9) P. Ganis, A. Panunzi, and C. Pedone, *Ric. Sci.*, **38**, 801 (1968); G. Avitabile, P. Ganis, and E. Martuscelli, *Acta Cryst.*, in press; G. Allegra, E. Benedetti, and C. Pedone, *ibid.*, **A25**, S3, S136 (1969).

Table III: Molecular Parameters[a]

Bond lengths, Å		Bond angles, deg		
C(1)–C(2)	1.51 (3)	C(5′)C(6′)C(7′)	116	(1)
C(2)–C(3)	1.59 (3)	C(6′)C(7′)C(8′)	107	(1)
C(3)–C(4)	1.53 (4)	C(7′)C(8′)C(1′)	118	(1)
C(4)–C(5)	1.59 (4)	C(8′)C(1′)C(2′)	120	(1)
C(5)–C(6)	1.56 (3)	C(1″)C(2″)C(3″)	108	(1)
C(6)–C(7)	1.61 (3)	C(2″)C(3″)C(4″)	113	(1)
C(7)–C(8)	1.49 (3)	C(3″)C(4″)C(5″)	118	(1)
C(8)–C(1)	1.40 (3)	C(4″)C(5″)C(6″)	116	(1)
C(1′)–C(2′)	1.42 (3)	C(5″)C(6″)C(7″)	117	(1)
C(2′)–C(3′)	1.59 (4)	C(6″)C(7″)C(8″)	106	(1)
C(3′)–C(4′)	1.56 (3)	C(7″)C(8″)C(1″)	119	(1)
C(4′)–C(5′)	1.60 (3)	C(8″)C(1″)C(2″)	121	(1)
C(5′)–C(6′)	1.56 (3)	Cu(1)Cl(1)Cu(2)	87.2	(1)
C(6′)–C(7′)	1.56 (3)	Cl(1)Cu(2)Cl(2)	102.5	(1)
C(7′)–C(8′)	1.56 (3)	Cu(2)Cl(2)Cu(1)	75.1	(1)
C(8′)–C(1′)	1.39 (2)	Cl(2)Cu(1)Cl(1)	83.7	(1)
C(1″)–C(2″)	1.52 (3)	A Cu(1)B	123	(1)
C(2″)–C(3″)	1.55 (4)	A Cu(1)Cl(1)	118	(1)
C(3″)–C(4″)	1.60 (4)	A Cu(1)Cl(2)	92	(1)
C(4″)–C(5″)	1.58 (4)	B Cu(1)Cl(1)	118	(1)
C(5″)–C(6″)	1.56 (4)	B Cu(1)Cl(2)	103	(1)
C(6″)–C(7″)	1.49 (4)	C Cu(2)Cl(1)	128	(1)
C(7″)–C(8″)	1.58 (3)	C Cu(2)Cl(2)	129	(1)
C(8″)–C(1″)	1.40 (3)			
Cu(1)–C(1)	2.14 (2)	**Internal-rotation angles, deg**		
Cu(1)–C(8)	2.19 (2)	C(1)C(2)C(3)C(4)	−53	
Cu(1)–C(1′)	2.24 (2)	C(2)C(3)C(4)C(5)	+82	
Cu(1)–C(8′)	2.17 (2)	C(3)C(4)C(5)C(6)	−115	
Cu(2)–C(1″)	2.08 (2)	C(4)C(5)C(6)C(7)	+82	
Cu(2)–C(8″)	2.03 (2)	C(5)C(6)C(7)C(8)	−52	
Cu(1)–Cl(1)	2.361(6)	C(6)C(7)C(8)C(1)	+87	
Cu(1)–Cl(2)	2.928(7)	C(7)C(8)C(1)C(2)	−136	
Cu(2)–Cl(1)	2.291(6)	C(8)C(1)C(2)C(3)	+88	
Cu(2)–Cl(2)	2.265(6)	C(1′)C(2′)C(3′)C(4′)	−50	
Cl(1)–Cl(2)	3.553(8)	C(2′)C(3′)C(4′)C(5′)	+80	
Cu(1)–Cu(2)	3.208(4)	C(3′)C(4′)C(5′)C(′6)	−115	
Cu(1)–A	2.04 (2)[b]	C(4′)C(5′)C(6′)C(7′)	+83	
Cu(1)–B	2.09 (2)	C(5′)C(6′)C(7′)C(8′)	−53	
Cu(2)–C	1.93 (2)	C(6′)C(7′)C(8′)C(1′)	+83	
		C(7′)C(8′)C(1′)C(2′)	−133	
Bond angles, deg		C(8′)C(1′)C(2′)C(3′)	+87	
C(1)C(2)C(3)	107 (1)	C(1″)C(2″)C(3″)C(4″)	+47	
C(2)C(3)C(4)	113 (1)	C(2″)C(3″)C(4″)C(5″)	−80	
C(3)C(4)C(5)	119 (1)	C(3″)C(4″)C(5″)C(6″)	+116	
C(4)C(5)C(6)	117 (1)	C(4″)C(5″)C(6″)C(7″)	−83	
C(5)C(6)C(7)	114 (1)	C(5″)C(6″)C(7″)C(8″)	+53	
C(6)C(7)C(8)	105 (1)	C(6″)C(7″)C(8″)C(1″)	−84	
C(7)C(8)C(1)	120 (1)	C(7″)C(8″)C(1″)C(2″)	+133	
C(8)C(1)C(2)	119 (1)	C(8″)C(1″)C(2″)C(3″)	−86	
C(1′)C(2′)C(3′)	110 (1)	Cu(1)Cl(1)Cu(2)Cl(2)	+31	
C(2′)C(3′)C(4′)	113 (1)	Cl(1)Cu(2)Cl(2)Cu(1)	−25	
C(3′)C(4′)C(5′)	116 (1)	Cu(2)Cl(2)Cu(1)Cl(1)	+24	
C(4′)C(5′)C(6′)	115 (1)	Cl(2)Cu(1)Cl(1)Cu(2)	−23	

[a] Standard deviations are given in parentheses. [b] A, B, and C are the middle points of the bonds between the atoms C(1)–C(8), C(1′)–C(8′), C(1″)–C(8″).

20° with the plane of the sp^2 hybrid of the copper atoms. In this way a good overlap between the hybrid orbitals of Cu and the molecular π orbitals of the olefin is achieved.[8]

The corresponding conformational parameters of the three cycloolefinic rings of the structural unit do not differ from each other by values greater than the standard deviations (these being, however, rather high

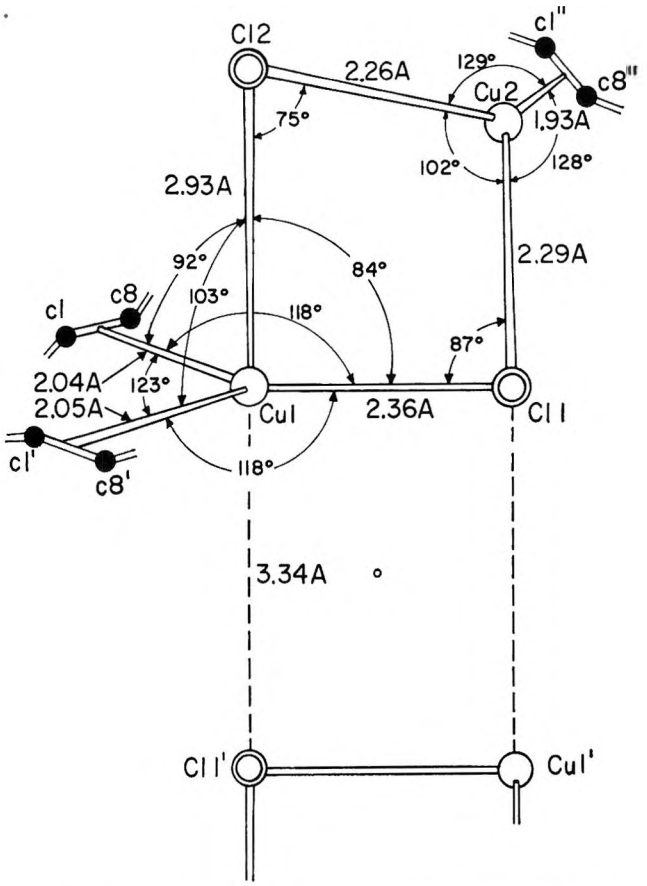

Figure 2. The most relevant conformational parameters of the bridged systems Cl / Cu Cu \ Cl are shown. The geometrical arrangement of the ligands around the copper atoms is evident; the Cl(1′) atom belongs to a centrosymmetrical molecule.

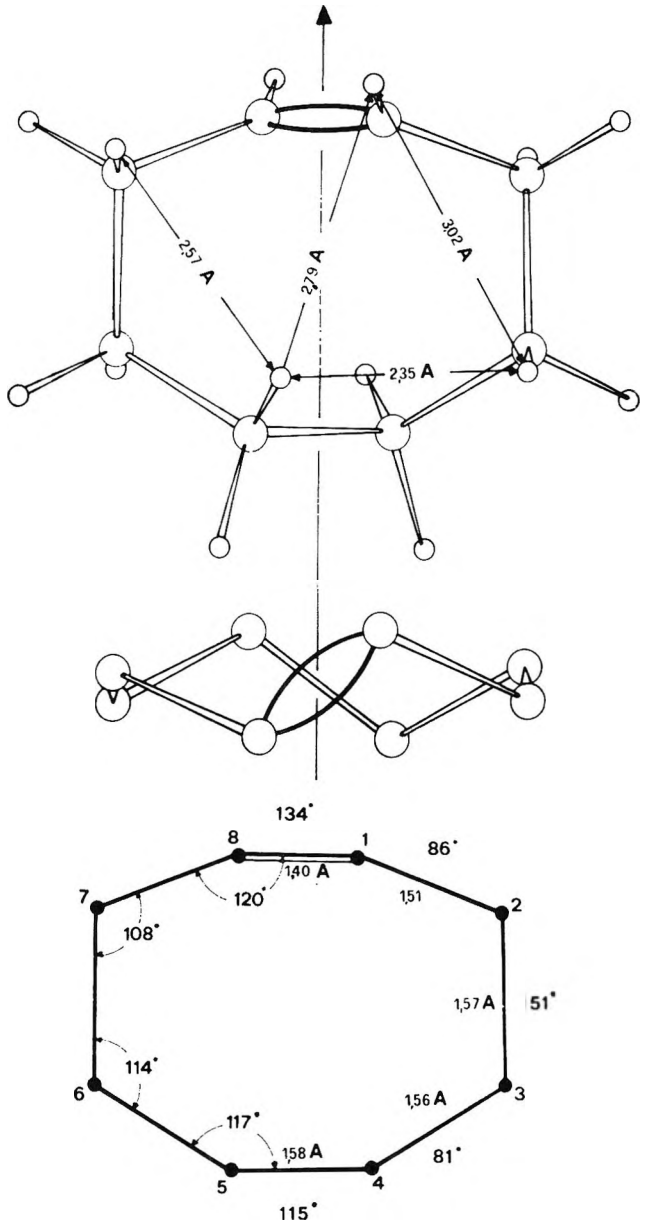

Figure 3. The averaged conformational parameters of the three molecules of cyclooctene are reported.

for the carbon atoms: see Table III). Each olefin shows a C_2 pseudo-symmetry.

The deviations from the exact twofold symmetry are again less than the standard deviations. Therefore we shall assume for the following discussion conformational parameters averaged over the three rings and the two pseudo-symmetrical moieties of each.

The averaged conformation is shown in Figure 3. The local twofold axis passes through the midpoints of the double bond and of the single bond opposite to it. The C–C bond lengths are normal; the C=C length is 1.40 ± 0.06 Å.

Owing to the error connected with this parameter it is difficult to tell whether it has lost part of the double bond character.

The torsional angles about the C(1)–C(2) and C(2)–C(3) bonds correspond to a nearly staggered conformation, the torsional angle about the C(4)–C(5) bond is nearly eclipsed and that one about C(3)–C(4) is intermediate between eclipsed and staggered conformation. Also, the internal rotation angle around the double bond deviates considerably (40 to 45° from *trans* conformation, at any rate much more than in the case of *trans*-cyclodecene[10] as foreseen by the mentioned dipolar moment and ir measurements.

The contact distances between Cu and the methylenic groups adjacent to the double bond are rather long (Cu–C > 3.10 Å and Cu–H > 3.16 Å).

Therefore the deviation from the *trans*-planar conformation of the double bond does not seem due to steric interactions with the metal, but to intraannular tensions.

The conformation of *trans*-cyclooctene, as a whole, appears rather strained, as a consequence mainly of

(10) P. Ganis and J. D. Dunitz, *Helv. Chim. Acta*, **50**, 2379 (1967).

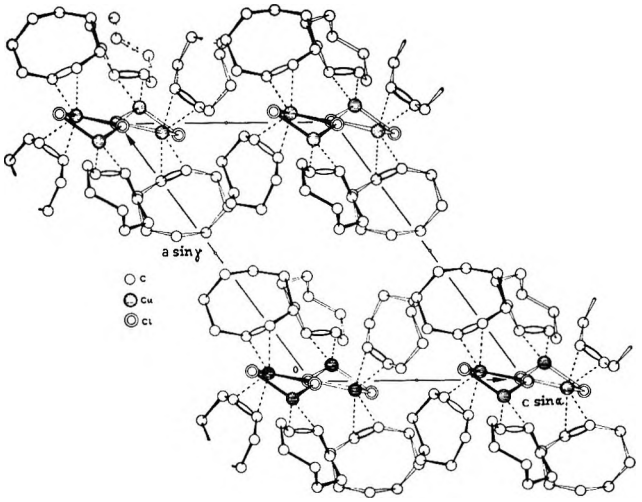

Figure 4. Projection of the structure of $Cu_2Cl_2(C_8H_{14})_3$ on 010. The intermolecular contact distances are omitted; they are given in Table IV.

torsional strains, since intramolecular van der Waals H–C and H–H interactions and angle strains are negligible.

In Figure 4, the projection of the structure along (010) is shown. The molecules of the complex appear to be associated in dimers around symmetry centers, through weak Cu---Cl bonds as previously mentioned. These dimers constitute units of almost spherical encumbrance which pack according to a pseudo-hexagonal symmetry as can be seen in Figure 4. The packing is closest in the 100 planes as indicated by the greater number of short contact distances (Table IV) among adjacent molecules in these planes.

Table IV: Shortest Intermolecular Distances between Atoms (a) of the Molecule in *xyz* and Atoms (b) of the Molecule in the Positions (c)

a	b	c	
C(2)	Cl(2)	$(\bar{x},\bar{y},\bar{z}-1)$	4.0 Å
C(1′)	Cl(2)	$(\bar{x},\bar{y},\bar{z}-1)$	3.7 Å
C(3′)	C(2′)	$(\bar{x},\bar{y}-1,\bar{z}-1)$	4.0 Å
C(2′)	C(2′)	$(\bar{x},\bar{y}-1,\bar{z}-1)$	4.0 Å
C(4″)	C(6′)	$(\bar{x}-1,\bar{y},\bar{z}-1)$	4.0 Å
C(7)	C(7′)	$(\bar{x},\bar{y},\bar{z})$	4.0 Å
C(7)	C(8′)	$(\bar{x},\bar{y},\bar{z})$	3.8 Å
C(8′)	Cl(1)	$(\bar{x},\bar{y},\bar{z})$	3.7 Å
Cu(1)	Cl(1)	$(\bar{x},\bar{y},\bar{z})$	3.34 Å
C(8)	C(5″)	$(\bar{x},\bar{y}+1,\bar{z})$	4.0 Å
C(7″)	Cu(2)	$(\bar{x},\bar{y}+1,\bar{z})$	3.7 Å
C(7″)	Cl(1)	$(\bar{x},\bar{y}+1,\bar{z})$	3.8 Å

The C–C intermolecular distances are nevertheless all larger than 3.8 Å; the Cl---C and Cu–C distances are both not less than 3.7 Å.

Vibrational Energy Transfer in Thermal Methyl Isocyanide Isomerization. Relative Cross Sections in Complex Molecular Systems[1]

by L. D. Spicer and B. S. Rabinovitch

University of Washington, Seattle, Washington 98105 *(Received January 28, 1970)*

Relative energy transfer collision cross sections for several complex hydrocarbon and substituted hydrocarbon molecules have been determined in the methyl isocyanide thermal isomerization system. Particular interest was placed in the incremental cross sectional changes due to geometric isomerization in C_6 hydrocarbons. Three generalizations are illustrated by the data. (1) Substitution for hydrogen in alkane molecules tends to increase their size. (2) Progressive branching of alkanes having constant carbon number causes a progressive decrease of the collision diameter. (3) Cyclization of the alkane chain decreases the effective size of the molecule. The energy transfer data are compared with viscosity-derived collision diameters where possible. A simple spherical model based on end-to-end carbon distances is proposed for systematizing the relative collision diameters of related complex molecules.

Introduction

The study of molecular collision processes is a very active area of chemical kinetics. Most of the existing experimental determinations of collision cross sections for complicated molecular systems have been derived from the study of transport phenomena and of gas imperfection. However, the vibrational activation–deactivation collisions which are of importance in the thermal activation of reacting molecules involve highly excited states. There is no rigorous justification for applying the cross sections determined from distantly related processes to these interactions.

In this work, we have experimentally determined a consistent set of relative cross sections for energy transfer between a number of complex organic molecules and methyl isocyanide, at 280.5°. The collision cross sections reported are pertinent to the transfer of significant amounts of vibrational energy: more than 5 kcal mol^{-1} per collision. Of particular interest here is the variation of cross section with structural isomerization as demonstrated by the 11 C_6 hydrocarbons studied. Also measured are the incremental cross sectional changes due to such substituents as chlorine and methyl groups. When possible, we have attempted to compare the cross sections obtained with viscosity-derived values.

Rationale of the Method

The experimental probe used to determine the cross sections is the unimolecular isomerization reaction of methyl isocyanide to acetonitrile which follows the critical energy-transfer collision. Details of this process have been reported earlier.[2]

The isomerization was studied at 280.5° in the second-order region of pressure and at infinite dilution with added inert bath gas. From the rate constant data for the isomerization at various pressures of added inert gas, it is possible to calculate the efficiency for activation of methyl isocyanide by the inert gas relative to that for self-activation by the parent isocyanide molecule. The procedure consists of relating the observed change in isomerization rate constant, Δk, for a constant pressure change, Δp, *via* the slopes of the plots of rate constant *vs.* pressure for both the inert gas, M, and the parent isocyanide, A. Then

$$\beta_p = \Delta k^M/\Delta k^A; \qquad \Delta p^M = \Delta p^A \tag{1}$$

The efficiency, β_p, is converted from a pressure basis to the more fundamental collision-per-collision basis, $\beta_0(\infty)$[3]

$$\beta_0(\infty) = \beta_\mu(s_{AA}/s_{AM})^2 = \beta_p(\mu_{AM}/\mu_{AA})^{1/2}(s_{AA}/s_{AM})^2 \tag{2}$$

where the subscript 0 refers to the low-pressure region and ∞ refers to infinite dilution; s_{AA} and s_{AM} are the collision diameters for the parent–parent and parent–inert interactions, respectively; and μ_{AA} and μ_{AM} are the corresponding reduced masses of the systems. Thus $\beta_0(\infty)$ is the relative intrinsic efficiency *per collision* of the inert gas in activating the isocyanide independent of the collision cross sections. It is not expected to exceed the value unity since the parent gas, being identical in structure with its collision partner, should be at least as good an energy transfer agent as any nonidentical molecule. This surmise appears to be borne out by the existing literature.

β_μ, defined in eq 2, depends on the relative cross section ratio as well as on the intrinsic efficiency of the inert gas. It has been shown that for sufficiently complex molecules the intrinsic efficiency is constant and

(1) This work was supported by the National Science Foundation.

(2) F. J. Fletcher, B. S. Rabinovitch, K. W. Watkins, and D. J. Locker, *J. Phys. Chem.*, **70**, 2823 (1966).

(3) D. C. Tardy and B. S. Rabinovitch, *J. Chem. Phys.*, **45**, 3720 (1966); **48**, 1282 (1968).

thus any changes in β_μ are due to cross sectional changes.[4] From eq 2, this is expressed as

$$\beta_{\mu 1}/\beta_{\mu 2} = \frac{(s_{1A}/s_{AA})^2\beta_{01}(\infty)}{(s_{2A}/s_{AA})^2\beta_{02}(\infty)} = (s_{1A}/s_{2A})^2 \qquad (3)$$

for inert gas molecules 1 and 2. It has been shown that hydrocarbon molecules reach a constant intrinsic efficiency at C_4 (the critical member) in normal alkanes and alkenes and at C_4 or C_5 in alkynes.[4] Here we have examined only molecules of equal or greater complexity than *n*-butane. Thus all of the molecules studied may be assumed to have the same intrinsic efficiency, $\beta_0(\infty)$; *i.e.*, a sufficient number of inelastic channels are operative.

Experimental Section

Much of the experimental detail has been described previously,[2,4] including the preparation and purification of the methyl isocyanide. Other chemicals used were the best quality available. Any impurities were removed by distillation. Final chromatographic analysis showed no detectable impurities. After degassing by repeated freeze-pump-melt cycles under vacuum, the inert gases were vacuum distilled into a glass storage bulb from which they were withdrawn for experimental use. Standard vacuum line techniques were employed.

The reactor was a 12-l. Pyrex bulb with a Teflon stopcock attached through which gases were admitted. The entire reactor was submerged in a salt bath at 280.5°. Temperature control was monitored at various positions. During an experiment the reactor temperature did not vary by more than 0.2° and was controlled to within 0.5° from experiment to experiment.

Accurately known quantities of both reactant and inert gas were measured with a gas buret, frozen into a small connecting arm to the reactor, and then admitted to the reactor by expansion. Dead space corrections were less than 1%.

The isomerization reaction was carried to between 10% and 20% completion (~600–1500 sec) and the reaction components were withdrawn by freezing at liquid nitrogen temperature.

Analysis of the isomerization product was by gas chromatography. Sensitivity calibrations with measured amounts of acetonitrile were performed regularly to compensate for any drift in the thermal conductivity detector. Chromatography columns used for analysis were as follows: (1) 10 ft of 1% tetraglyme on a Fluoropak 80 base for butane and pentane, and (2) 25 ft of 1% squalane on a fluoropak-80 base for all other inert gases. Unreacted isocyanide was removed from the reaction products before analysis by passing them through a short length of solid silver cyanide granules packed in a glass tube.

Data Processing and Results

First-order rate constants for collisional activation of the isocyanide in the second-order pressure region were calculated. These were plotted against the pressure of added inert gas, and the least squares slope of the resulting straight line was evaluated along with the percentage deviation in that slope. From these data, and the value of 0.96 for the slope of the parent curve,[2] the β_p's were obtained and were then converted to the β_μ values which are listed in Table I.

Table I: Relative Energy Transfer Efficiencies and Collision Diameters

Inert	$\beta_{\mu 1}$	s_{1A}, Å	Δs_{1A},[a] Å
n-Butane	0.890 ± 0.035[b]	5.53 ± 0.11[b]	−0.57
n-Pentane	0.992 ± 0.020	5.83 ± 0.06	−0.25
n-Hexane	1.08 ± 0.040	6.08 ± 0.11	(0.00)
3-Methylpentane	1.08 ± 0.045	6.08 ± 0.13	−0.00
2-Methylpentane	1.06 ± 0.055	6.03 ± 0.16	−0.05
2,3-Dimethylbutane	0.977 ± 0.051	5.78 ± 0.15	−0.30
2,2-Dimethylbutane	0.934 ± 0.035	5.65 ± 0.10	−0.43
Cyclohexane	0.962 ± 0.017	5.74 ± 0.05	−0.34
trans-1-Methyl-2-ethylcyclopropane	1.04 ± 0.013	5.98 ± 0.04	−0.10
1,1,2-Trimethylcyclopropane	0.992 ± 0.065	5.83 ± 0.19	−0.25
Methylcyclopentane	0.897 ± 0.051	5.54 ± 0.16	−0.54
2-Methylpentene-2	1.06 ± 0.020	6.03 ± 0.06	−0.05
Benzene	0.836 ± 0.024	5.35 ± 0.08	−0.73
Chlorobenzene	0.897 ± 0.041	5.54 ± 0.12	−0.54
Toluene	0.937 ± 0.010	5.66 ± 0.03	−0.42
Pentanol	2.02 ± 0.079	8.32 ± 0.16[c]	+2.24[c]

[a] Relative to *n*-hexane. [b] Standard deviation. [c] See text.

To arrive at a consistent set of collision cross sections for individual inert gases by use of eq 3, a standard for comparison must be chosen. The substrate was selected; new data (see Table I) indicate that *n*-butane has unit efficiency, $\beta_0(\infty) = 1.02$,[5,6] when $\sigma = 5.20$ Å, $\epsilon/k = 325$°K are adopted. The usual combining rules were applied: $\sigma_{xy} = (\sigma_x + \sigma_y)/2$; $(\epsilon/k)_{xy} = [(\epsilon/k)_x \times (\epsilon/k)_y]^{1/2}$; the approximation $s_{xy} = \sigma_{xy}[\Omega^{(2,2)*}(T^*)]^{1/2}$, where the $\Omega^{(2,2)*}$ integrals are tabulated[6b] for the Lennard–Jones potential as a function of the reduced temperature, $T^* = (kT/\epsilon)_{xy}$. Listed in Table I are the relative energy transfer collision diameters for inert gas–isocyanide collisions at 280.5° calculated using

(4) (a) B. S. Rabinovitch, Y. N. Lin, S. C. Chan, and K. W. Watkins, *J. Phys. Chem.*, **71**, 3715 (1967); (b) Y. N. Lin, S. C. Chan, and B. S. Rabinovitch, *ibid.*, **73**, 1932 (1968); (c) S. C. Chan, B. S. Rabinovitch, L. D. Spicer, and J. T. Bryant, *ibid.*, **73**, 2464 (1969).

(5) This value of $\beta_0(\infty)$ is higher than the value obtained in the earlier work[4a,b] which had a systematic error of about 18%.

(6) (a) R. A. Svehla, NASA Technical Report R-132, Lewis Research Center, Cleveland, Ohio, 1962; (b) J. O. Hirschfelder, C. F. Curtiss, and R. B. Bird, "Molecular Theory of Gases and Liquids," John Wiley and Sons, New York, N. Y., 1954; (c) for methyl isocyanide, $\sigma = 4.47$ Å and $\epsilon/k = 380$°K were used, consistent with ref 3; $s_{AA} = 5.9$ Å, as calculated by S. C. Chan (to be published) with the use of the tables of L. Monchick and E. A. Mason, *J. Chem. Phys.*, **35**, 1676 (1961); for *n*-butane, $\sigma = 4.69$ Å, $\epsilon/k = 531$°K, $s_{AM} = 5.51$ Å. If $\beta_\mu = 0.89$ for *n*-butane, $\beta_0(\infty) = 0.89(s_{AA}/s_{AM})^2 = 1.02$.

eq 3 with *n*-butane as a secondary standard, s_{2A} = 5.53 Å.

Also tabulated is the value $\Delta s_{1A} = s_{n\text{-hex, A}} - s_{1A}$, which is the difference between the collision diameters with isocyanide of *n*-hexane and the various inert gases. This is an indication of the changes in collision radii with structure for the various inert molecules. Although the collision radius of methyl isocyanide is not necessarily the same for all inert–isocyanide interactions at 280.5°, it will be expected to vary little for the various C_6 isomers.

Discussion

From the data in Table I, a few generalizations can be drawn. The increase in collision diameter with CH_2 group in alkanes is about 0.25–0.30 Å for the series *n*-butane, *n*-pentane, and *n*-hexane in agreement with previous work.[4b] The effect on the collision diameter due to structural isomerization or cyclization, however, can be equal to or greater than that due to a CH_2 addition.

The doubly branched six-carbon members, 2,2- and 2,3-dimethylbutane, are considerably smaller than *n*-hexane, showing a size intermediate between *n*-butane and *n*-pentane. It is expected of course that a C_4 chain with two branching methyl groups should be larger than an *n*-butane molecule which has only a C_4 carbon skeleton.

The singly branched C_6 isomers, 2- and 3-methyl pentane, show at most only a slight decrease in cross section from *n*-hexane, being larger than *n*-pentane. This is probably due to the fact that at 280.5° the *n*-hexane molecule has appreciable probability of existing in a constricted conformation because of *gauche* contributions, rather than the energetically favored totally extended *trans* configuration.[7]

Cyclization has a dramatic effect in diminishing the cross section by the equivalent of between one and two carbons. Thus cyclohexane is smaller than *n*-hexane and between *n*-butane and *n*-pentane in diameter; the collision diameter of cyclohexane is about equal to that of the two dimethylbutanes. These molecules are similar in that they are all rather compact structurally. Benzene is even more compact and thus might be expected to be the smallest six-carbon compound. Indeed benzene appears to be smaller even than *n*-butane.

Other six carbon compounds containing three- and five-membered rings were investigated to determine how the geometry of the rings affected the molecular size. Methyl cyclopentane is seen to be smaller than cyclohexane and comparable to *n*-butane, *i.e.*, a contraction of almost two carbons. The trimethyl cyclopropane and the methyl ethyl cyclopropane molecules are larger than cyclohexane; the three-membered ring obviously corresponds to a diminution in diameter of something less than one carbon. *trans*-1-Methyl-2-ethylcyclopropane is an interesting molecule; it may be comparable to 2-methyl pentene-2 if the constriction caused by the ring between the second and third carbon atoms has an effect similar to a double bond. Both shorten the C–C bond length while ensuring the *trans* configuration around this bond, giving a similar end-to-end distance for the longest available carbon skeleton, C_5. The data indicate that the two molecules show very similar cross sections, both of which are larger than the *n*-pentane or an unbranched C_5 chain.

In addition to measuring the relative collision diameters for hydrocarbon isomers, the effective size of certain functional groups was found by using substituted benzenes. It is seen (Table I) that a CH_3 group is larger than a Cl group when bonded to a benzene ring; the C–Cl bond distance in this case may be shortened relative to a normal C–Cl bond because of the neighboring aromatic ring, and thus the cross sectional increase reported due to Cl may be smaller than a typical chlorine substituted on an alkane. Also apparent is the fact that the CH_3 substituent in toluene is about equal to or slightly larger than the CH_2 incremental size in the normal alkanes.

An attempt was also made to find the incremental cross sectional increase for the hydroxyl group. The efficiency and corresponding collision diameter found for *n*-pentanol was unreasonably high, however. Together with a similar unusual efficiency for ethanol, this suggests that the isomerization proceeds by a mechanism different from simple energy transfer and thus cannot be used to measure the cross section.

Three qualitative generalizations are demonstrated by the data, the first of which is the most intuitively obvious. (1) Both increase of chain length and substitution for hydrogen in alkane molecules tend to increase their size. (2) Progressive branching of alkanes with the same carbon number causes a progressive decrease of the collision diameter. (3) Cyclization of the alkane chain decreases the effective size of the molecule. The quantitative magnitudes to be associated with each of these effects are revealed by the data of Table I.

It is of interest to compare the energy-transfer collision diameters found here with collision diameters derived from viscosity data on the basis of the Lennard–Jones potential. Viscosity data are available for several of the molecules in Table I[6]; values were calculated at 280.5°. The resulting collision diameters, $s_{AM}{}^{v}$, are listed in Table II together with $\Delta s_{AM}{}^{v}$ values relative to *n*-hexane. Also listed are the appropriate energy transfer values, s_{AM} and Δs_{AM}, determined in this work. The values of s_{AM} and $s_{AM}{}^{v}$ for *n*-butane are identical since the viscosity data were used to calculate the s_{AM} for *n*-butane which was then used as the standard s_{2A} in eq 3. It is apparent that the viscosity-derived

(7) L. S. Bartell and D. A. Kohl, *J. Chem. Phys.*, **39**, 3097 (1963).

values for the *n*-alkanes are virtually identical with the relative energy transfer values. The ring compounds, however, exhibit smaller s_{AM} quantities than are predicted from viscosity data. Nevertheless, the incremental changes in diameters from cyclohexane to benzene to toluene are consistent on both bases. The reason for the deviation in ring compounds relative to straight chain compounds is unclear.

Table II: Comparison of Collision Diameters at 280.5°

Inert gas	σ,[a] Å	ϵ/k, °K	$s_{AM}{}^{v}$,[b] Å	$\Delta s_{AM}{}^{v}$, Å	s_{AM},[c] Å	Δs_{AM}, Å
n-Butane	4.69	531	5.53	−0.54	5.53	−0.55
n-Pentane	5.78	341	5.84	−0.21	5.83	−0.25
n-Hexane	5.95	399	6.05	(0.00)	6.08	(0.00)
Cyclohexane	6.09	324	6.00	−0.05	5.75	−0.34
Benzene	5.35	412	5.70	−0.35	5.35	−0.73
Toluene	5.93	377	6.00	−0.05	5.66	−0.42
Pentene-2	6.48	204	5.96	−0.09	6.03[d]	−0.05

[a] Lennard–Jones viscosity-derived values for inert gases.[6] [b] Temperature–corrected collision diameters for inert gas plus methyl isocyanide collisions. [c] Calculated energy-transfer collision diameters for the inert gas plus methyl isocyanide collisions. [d] s_{AM} for energy transfer from 2-methylpentene-2.

Since viscosity data are not always available (and when available are not necessarily reliable in giving a consistent set of values for energy transfer cross sections pertinent to reaction kinetics), it is desirable to correlate the data presented in Table I with a simple model which could be extended to other molecule systems. The above results suggest that we may treat molecules as spheres whose diameters are simply proportional to their end-to-end molecular geometric lengths. This is particularly appealing since geometric factors can be intuitively invoked to explain most of the trends outlined above and because the viscosity diameters which are calculated on the basis of assuming spherical potentials tend to give reasonable values for each independent series of molecules considered here.

Qualitative rationale for the model comes from the fact that molecules with the same number of carbons in the longest end-to-end chain tend to group together. Thus compounds whose longest chain is four, *n*-butane, 2,2-dimethylbutane, 2,3-dimethylbutane, cyclohexane, methylcyclopentane, 1,1,2-trimethylcyclopropane, and benzene tend to be smaller than groups with five carbon atoms in the longest chain, *e.g.*, *n*-pentane, 2-methylpentane, 3-methylpentane, *trans*-1-methyl-2-ethylcyclopropane, and 2-methylpentene-2. *n*-Hexane with its six-membered skeleton is larger in general than the five-membered groups. For unbranched chains there appears to be some shortening due to *gauche* contributions to the configurations: *n*-pentane is the smallest of the five-carbon chain examples. In cases where chains are branched, these *gauche* contributions are less favored because of additional repulsion due to the methyl substituents. Thus branched skeletons of a given chain length might be expected to show similar collision diameters. For such a model to be a good representation of reality requires that the colliding species tumble in three dimensions on a time scale comparable with the duration of the interaction. This further requires that at 280.5° any directed contribution to the interaction potential (such as dipole–dipole interactions) is small compared with the energy of rotation of the molecules. For the hydrocarbon molecules studied here, this is a valid requirement since the dipole moments are small.

Acknowledgment. We thank Mr. S. C. Chan for his interest in the problem and helpfulness in the experimental work.

Kinetics of the Thermal Decomposition of 1,1-Difluoroethane in Shock Waves. A Consecutive First-Order Reaction[1a]

by E. Tschuikow-Roux, W. J. Quiring,[1b] and J. M. Simmie[1c]

Department of Chemistry, University of Calgary, Calgary, Alberta, Canada *(Received January 5, 1970)*

The kinetics of the thermal decomposition of 1,1-difluoroethane diluted with argon has been studied in a single-pulse shock tube in the temperature range 1040–1320°K at total reflected shock pressures of about 2300–4000 Torr. It is shown that 1,1-difluoroethane decomposes to vinyl fluoride by molecular elimination of hydrogen fluoride, $CH_3CHF_2 \xrightarrow{k_1} CH_2CHF + HF$, with a first-order rate constant given by, $\log (k_1, \text{sec}^{-1}) = 13.9 \pm 0.3 - (61.9 \pm 1.8 \text{ kcal})/2.303RT$, in reasonable agreement with a previous study in a conventional flow system. At temperatures above 1200°K a consecutive first-order reaction involving the decomposition of vinyl fluoride to acetylene plus hydrogen fluoride becomes important and must be taken into account. The observed activation energy, E_{exp}, for the initial HF-elimination process is compared with activation energies derived previously from *chemical activation* studies using the RRK and RRKM theories of unimolecular reactions, and the predicted theoretical values based on (a) the intimate ion-pair transition state model and (b) the electrostatic semiion pair model for four-center elimination reactions. Satisfactory agreement is found only in the case of the RRKM treatment of chemical activation systems.

Introduction

The dehydrohalogenation reactions of simple alkyl halides have been of considerable practical and theoretical interest. In the case of alkyl fluorides, however, the studies have been confined largely to chemical activation systems in which the alkyl fluoride is formed in a vibrationally excited state. The simplest such chemical activation systems involve excited fluoroethanes[2-5] which may be produced in a number of ways, such as radical combination,[2-5] by reaction (insertion–abstraction) of a methylene diradical with a partially fluorinated methane molecule,[2,4c] or by reaction of suitable ethyl radicals with elemental fluorine.[2a,2b] Interest has centered on the determination and interpretation of the HF elimination:stabilization ratio of the "hot" fluoroethane molecule as a function of pressure, nature of the deactivating gas, temperature, and energy content of the excited molecule.[2,6] Such information can yield considerable insight into the problem of intermolecular energy transfer and energy distribution in chemical reactions. The alkyl fluorides appear to be particularly suited for such investigations because of noncomplicated kinetics derived principally from the strength of the carbon–fluorine bond which is not attacked by radicals and which is not involved in isomerizations.

In contrast to the numerous chemical activation studies the thermal decomposition of some fluoroethanes has only recently been reported.[7,8] Previous unsuccessful attempts may be traced, in part, to the heterogeneous nature of many of the dehydrohalogenation reactions.[8] Sianesi, *et al.*,[7] have studied the thermolysis of C_2H_5F, CH_3CHF_2, and CH_3CF_3 in the neighborhood of 600° in a conventional flow system using a platinum-coated reactor. Most recently, Day and Trotman-Dickenson[8] have reported the pyrolysis of ethyl fluoride at 410–465° in a static system in which the Pyrex reaction vessel was seasoned with ethyl fluoride.

An examination of the activation or critical energies derived from chemical activation data[2a,2b,5,6,9] with those obtained from thermal studies[7,8] shows a considerable degree of disparity both in magnitude as well as in the trend of the activation energy with the degree of fluorination. The RRKM theory calculations of Kirk and Trotman-Dickenson[6] have shown that increased fluorination of ethane results in an *increased* activation energy for the elimination of hydrogen

(1) (a) Work supported by the National Research Council of Canada; (b) Graduate predoctoral Fellow; (c) Postdoctorate Fellow 1968–1970.

(2) (a) A. W. Kirk, A. F. Trotman-Dickenson, and B. L. Trus, *J. Chem. Soc., A*, 3058 (1968); (b) J. A. Kerr, A. W. Kirk, B. V. O'Grady, D. C. Phillips, and A. F. Trotman-Dickenson, *Discuss. Faraday Soc.*, 263 (1967); (c) J. A. Kerr, B. V. O'Grady, and A. F. Trotman-Dickenson, *J. Chem. Soc., A*, 275 (1969).

(3) (a) W. G. Alcock and E. Whittle, *Trans. Faraday Soc.*, **61**, 244 (1965); (b) R. D. Giles and E. Whittle, *ibid.*, **61**, 1425 (1965); (c) R. D. Giles, L. M. Quick and E. Whittle, *ibid.*, **63**, 662 (1967).

(4) (a) G. O. Pritchard, M. Venugopalan, and T. F. Graham, *J. Phys. Chem.*, **68**, 1786 (1964); (b) G. O. Pritchard and J. T. Bryant, *ibid.*, **69**, 1085 (1965); (c) G. O. Pritchard, J. T. Bryant, and R. L. Thommarson, *ibid.*, **69**, 2804 (1965); (d) G. O. Pritchard and R. L. Thommarson, *ibid.*, **71**, 1674 (1967); (e) J. T. Bryant, B. Kirtman, and G. O. Pritchard, *ibid.*, **71**, 1960 (1967).

(5) (a) J. T. Bryant and G. O. Pritchard, *ibid.*, **71**, 3439 (1967); (b) G. O. Pritchard and J. T. Bryant, *ibid.*, **72**, 1603 (1968); (c) M. J. Perona, J. T. Bryant, and G. O. Pritchard, *J. Amer. Chem. Soc.*, **90**, 4782 (1968).

(6) A. W. Kirk, private communication.

(7) D. Sianesi, G. Nelli, and R. Fontanelli, *Chim. Ind. (Milan)*, **50**, 619 (1968).

(8) M. Day and A. F. Trotman-Dickenson, *J. Chem. Soc., A*, 233 (1969).

fluoride for the series $CH_3CH_{3-n}F_n$ (n = 1, 2, 3). These results do not corroborate earlier, less appropriate, calculations based on classical RRK theory.[2b,5,9] The experimental results of Sianesi, *et al.*,[7] indicate a small decrease in the activation energy with additional α-fluoro substitution. However, such decrease as has been observed lies well within the experimental error and may not be significant. They also find that the preexponential factors decrease correspondingly by a factor of 13 to 14 for each additional F-substitution. The latter is contrary to what one would expect from theoretical considerations.[10] For ethyl fluoride, the only thermal study for which two independent results are available, the Arrhenius expression for the rate constant reported by Sianesi, *et al.*,[7] differs from that of Day and Trotman-Dickenson[8] by a factor of 13.3 in the A factor and 4.4 kcal in the activation energy.

In view of the above discrepancies it was deemed desirable to reinvestigate the thermal decomposition of the fluoroethanes in a systematic manner under assured homogeneous reaction conditions. The present paper reports the first study in this series, the thermal decomposition of 1,1-difluoroethane as carried out in a modified single-pulse shock tube (SPST).

Experimental Section

The single-pulse shock tube was of the ball-valve type design,[11] and together with the associated apparatus and mode of operation has been described previously.[12] The isolated ball-valve section was filled with a dilute mixture of CH_3CHF_2 in argon, while the rest of the channel was filled with pure argon to the same pressure (~150 Torr). Helium at pressures of 2.7 to 4.1 kTorr was used as the driver gas and the scribed aluminum diaphragms were burst under load pressure.

Incident and reflected shock velocities were determined by recording the transit times of the incident and reflected shocks across two high-frequency pressure transducers (located 10 and 20 cm from the end plate) using two universal counters of 0.1-μsec-resolution. The pressure history just before and after shock reflection and the arrival of the quenching rarefaction wave were also recorded, photographically. Details of these measurements have been described earlier.[12]

The dilute reaction mixture (0.60% CH_3CHF_2 in Ar) was prepared from commercially available 1,1-difluoroethane (Matheson Co.) and stored in a separate stainless steel tank. The purity of the 1,1-difluoroethane was determined by vpc analysis to be better than 99.1%, the principal impurities being some unidentified higher molecular weight compounds, which, however, were unlikely to interfere with the product analysis. Immediately after a run, the ball valve was closed and the reactant and products of decomposition were isolated in the end section of the shock tube. A sample of the shocked and fully mixed gases was then withdrawn for gas chromatographic analysis (Varian, Model 1740). A quantitative identification of the reaction products was obtained by comparison with standard mixtures of 1,1-difluoroethane, vinyl fluoride, and acetylene prepared for this purpose. The analysis was carried out using flame ionization detection with temperature programming in the range 75–155° on a 12-ft silica gel column with helium carrier gas at a flow rate of ~30 ml/min. Temperature programming was necessary because the retention time of 1,1-difluoroethane on silica gel at 75° is very long and acetylene–vinyl fluoride mixtures cannot be separated successfully at higher temperatures. An estimate of the amount of three additional trace products, C_2H_6, C_2H_4, and CH_2CF_2, was made by assuming equal sensitivities for these compounds with that for 1,1-difluoroethane. In the case of the hydrocarbons this represents an upper limit. The per cent conversion of 1,1-difluoroethane ranged from 0.4 at 1041°K to about 87% at 1318°K.

Computations and Results

The thermal decomposition of 1,1-difluoroethane at reflected shock temperatures below 1200°K yields predominantly vinyl fluoride, which suggests molecular elimination of hydrogen fluoride. This is in accord with the study by Sianesi, *et al.*,[7] and the generally accepted dehydrohalogenation reactions of alkyl halides.[8,13] Above 1200°K the product vinyl fluoride itself undergoes an HF elimination to yield acetylene.[14] Trace quantities of ethane and somewhat larger quantities of ethylene and 1,1-difluoroethylene were also detected over the entire temperature range and their amount increased with temperature. Their presence suggests the occurrence of complicated side or parallel reactions. However, at all temperatures the amount of 1,1-difluoroethylene, the principal side product, did not exceed 7% of the vinyl fluoride and acetylene yields. It was therefore deemed permissible to neglect these side reactions in the reduction of data. Accordingly, the principal reactions over the entire temperature range may be represented by the mechanism of two consecutive first-order reactions involving the sequential elimination of hydrogen fluoride

$$CH_3CHF_2 \xrightarrow{k_1} CH_2{=}CHF + HF \qquad (I)$$

$$CH_2{=}CHF \xrightarrow{k_2} CH{\equiv}CH + HF \qquad (II)$$

or simply

(9) S. W. Benson and G. Haugen, *J. Phys. Chem.*, **69**, 3898 (1965).

(10) E. Tschuikow-Roux, *J. Chem. Phys.*, **43**, 2251 (1965); **49**, 3115 (1968).

(11) E. Tschuikow-Roux, *Phys. Fluids*, **8**, 821 (1965).

(12) J. M. Simmie, W. J. Quiring, and E. Tschuikow-Roux, *J. Phys. Chem.*, **73**, 3830 (1969).

(13) H. E. O'Neal and S. W. Benson, *ibid.*, **71**, 2903 (1967).

(14) J. M. Simmie, W. J. Quiring, and E. Tschuikow-Roux, *ibid.*, **74**, 992 (1970).

Table I: Experimental Results

Mach no. W_{11}	Mach no. W_{21}	P_2, Torr	T_2, °K	P_5, Torr	T_5, °K	t, μsec	Product ratios[a] R_1	R_2	R_3	R_4	R_5	Rate const k_1, sec^{-1}	k_2, sec^{-1} I	k_2, sec^{-1} II
2.050	1.210	751	638	2293	1041	488	0.0039	...	...	...	...	7.93	...	...
2.067	1.226	764	652	2372	1072	477	0.010	...	...	0.0002	0.0005	20.3	...	...
2.112	1.241	799	662	2533	1100	505	0.017	...	...	0.0002	0.0005	33.9	...	...
2.123	1.240	808	666	2563	1108	483	0.013	...	...	0.0001	0.0005	27.6	...	...
2.115	1.249	802	665	2561	1109	505	0.022	...	...	0.0003	0.0016	43.4	...	...
2.131	1.236	814	669	2576	1112	460	0.036	...	...	0.0008	0.0019	76.3	...	...
2.124	1.248	809	667	2585	1114	542	0.039	...	...	0.0004	0.0019	70.1	...	...
2.145	1.238	826	674	2623	1122	379	0.039	...	...	0.0005	0.0021	101	...	...
2.163	1.251	840	682	2704	1142	507	0.050	...	...	0.0006	0.0036	95.9	...	...
2.178	1.265	858	689	2798	1163	542	0.115	...	...	0.0026	...	204	...	...
2.197	1.270	868	701	2849	1186	552	0.219	0.0033	0.0023	...	0.015	363	54.6	53.3
2.207	1.266	876	703	2873	1190	509	0.156	0.0020	0.0045	...	...	288	49.8	42.8
2.207	1.273	887	703	2924	1193	557	0.293	0.0066	0.0042	...	0.020	471[b]	c	76.6
2.289	1.270	894	710	2946	1204	671	0.349	0.0081	0.0034	...	0.022	455	62.9	65.1
2.253	1.265	914	724	3009	1228	660	1.21	0.092	0.037	...	0.089	1260	198	197
2.251	1.297	913	724	3082	1243	600	0.639	0.022	0.0045	...	0.043	958	119	88.8
2.270	1.287	929	729	3115	1248	738	0.924	0.064	...	0.017	0.046	932	167	165
2.304	1.261	958	745	3155	1263	714	2.27	0.235	0.0010	0.0072	0.020	1760	218	232
2.307	1.304	961	746	3277	1289	622	2.18	0.302	0.0048	0.034	0.094	2000	352	353
2.310	1.300	963	748	3275	1290	604	2.84	0.678	0.0049	0.036	0.127	2500	583	582
2.305	1.298	959	753	3256	1298	643	4.04	2.49	0.0098	0.018	0.124	3140[b]	c	1180
2.324	1.298	975	755	3312	1302	712	3.79	1.36	0.0083	0.040	0.122	2550	690	690
2.340	1.309	989	761	3393	1318	636	4.59	2.31	0.0077	0.023	0.114	3250[b]	1000	1000

[a] $R_i = [X_i]/[CH_3CHF_2]$ where X_i = C_2H_3F, C_2H_2, C_2H_6, C_2H_4, and CH_2CF_2 for i = 1, 2, 3, 4, 5, respectively. [b] Runs with added nitric oxide. [c] No real root found (see text).

$$A \xrightarrow{k_1} B \xrightarrow{k_2} C \qquad \text{(III)}$$

where A, B, and C denote, respectively, 1,1-difluoroethane, vinyl fluoride, and acetylene, and are given by the standard integrated expressions

$$A = A_0 \exp(-k_1 t) \qquad (1)$$

$$B = A_0 k_1 [\exp(-k_1 t) - \exp(-k_2 t)]/(k_2 - k_1) \qquad (2)$$

$$C = A_0\{1 - [k_2 \exp(-k_1 t) - k_1 \exp(-k_2 t)]/(k_2 - k_1)\} \qquad (3)$$

Subject to the neglect of the side or parallel reactions mass balance requires that $A_0 = A + B + C$ and hence k_1 is conveniently evaluated from the relation

$$k_1 = (1/t) \ln (1 + R_1 + R_2) \qquad (4)$$

where R_1 = (B)/(A) and R_2 = (C)/(A) are the experimentally determined product to reactant ratios after time t, where t is the calculated reaction time.[11] The latter could be made to correspond closely to the measured "transducer dwell time," t_d', through a suitable choice of shock tube geometry.[11,12]

The experimental results are summarized in Table I, where W_{11} and W_{21} are incident and reflected shock Mach numbers, and subscript 2 and 5 refer to incident and reflected shock conditions, respectively. An attempt was also made to evaluate k_2 and to compare the latter with an independent direct determination.[14]

Here two methods are available since both R_1 and R_2 were determined. Thus, from eq 1 and 2 we obtain, method I

$$e^{-k_2 t} + \alpha k_2 - \beta = 0 \qquad (5)$$

where

$$\alpha = (R_1/k_1) \exp(-k_1 t) \qquad (6)$$

$$\beta = (1 + R_1) \exp(-k_1 t) \qquad (7)$$

Similarly, from eq 1 and 3 we obtain, method II

$$e^{-k_2 t} + \gamma k_2 - \phi = 0 \qquad (8)$$

with

$$\gamma = [1 - (1 + R_2) \exp(-k_1 t)]/k_1 \qquad (9)$$

$$\phi = 1 - R_2 \exp(-k_1 t) \qquad (10)$$

Equations 5 and 8 may formally be written as $f(k_2) = 0$ and $g(k_2) = 0$, respectively. Since they have no exact analytical solution, approximate solutions were found by an iterative technique using an IBM 360 computer. Here, Newton's method has been employed. If x_1 is the first approximation chosen to solve the equation $f(x) = 0$, then x_2 is a better approximation and is given by

$$x_2 = x_1 - f(x_1)/f'(x_1)$$

Computations were carried out until two successive roots x_n, x_{n+1} satisfied the condition

$$|x_n - x_{n+1}| \leqslant 0.001$$

Since the smallest k_2 found was $k_2 = 0.179$ sec^{-1} this is equivalent to a precision in locating the root to better than 99%. It may be noted that eq 5 and 8 contain the trivial solution: $k_2 = k_1$. These equations, true for all values of k_1, t, and R_1 or R_2 were ignored. Since experimentally it is known that $k_2 < k_3$, searches for k_2 were made in the region $k_1 > k_2 > 0$. Some runs were found to have no real root in the region of interest, which undoubtedly is due to experimental errors in the values of the input data. The values of k_2 so obtained are given in Table I.

Discussion

The four-center hydrogen halide eliminations from *alkyl halides* in the gas phase form a well-known group of unimolecular reactions,[13] and 1,1-difluoroethane is no exception. The unimolecular character of this reaction has also been demonstrated by Sianesi, *et al.*[7] The kinetic aspects of the dehydrohalogenation reactions of *alkenyl halides* are much less known. Recently, however, we have reported the shock tube decomposition of vinyl fluoride to acetylene plus HF under conditions similar to those employed in the present study.[14] In the light of this work the present results clearly indicate the occurrence of two consecutive first-order processes, reactions I and II, as the principal reaction mechanism. The observed small amounts of side products CH_2CF_2 and CH_2CH_2 are more difficult to explain. 1,1-Difluoroethylene may be formed by the molecular elimination of hydrogen from 1,1-difluoroethane

$$CH_3CHF_2 \longrightarrow CH_2CF_2 + H_2$$

$\Delta H = +36.5$ kcal mol^{-1}. Since this reaction is at least 10 kcal more endothermic than the corresponding HF elimination ($CH_3CHF_2 \rightarrow CH_2{=}CHF + HF$) the activation energy may also be some 10 kcal higher, *i.e.*, *ca.* 70 kcal mol^{-1}. If this is the case, then the ratio $[CH_2CF_2]/[CH_2CHF]$ has a calculated value of ~0.02 at 1300°K. From Table I we obtain values for $R_5/(R_1 + R_2)$, between 0.019 and 0.024 under these conditions. However, inspection of the variation of $[CH_2CF_2]/[CH_2CHF]_{total}$ with temperature, particularly in the range 1180–1320°K where the results are most precise, shows that the ratio *decreases* with increasing temperature, *e.g.*, 0.065 at 1200°K as opposed to 0.022 at 1300°K. This is the opposite to what would be expected were H_2 elimination from CH_3CHF_2 the major route to the formation of CH_2CF_2. There is some evidence that H_2 elimination competes with HF elimination from vibrationally excited 1,1-difluoroethane[5c] but further work is required before this matter can be regarded as settled. 1,1-Difluoroethylene is also found as a major product in the mercury-photosensitized decomposition of CH_3CHF_2.[15] Similar difficulties are encountered in explaining its occurrence although it is suggested that it is formed from disproportionation reactions of the type

$$CH_3CF_2\cdot + CH_3CF_2\cdot \longrightarrow CH_2{=}CF_2 + CH_3CHF_2$$

However, in our system, thermochemical considerations show that homolytic initiation is energetically unlikely to occur. Furthermore, the addition of nitric oxide in amounts equal to the reactant in the CH_3CHF_2–Ar mixture had no discernible suppressive effect. Thus for the present, the formation of these side products remains unexplained.

The rate constants, k_1, reported in Table I are high-pressure limiting values. In support of this view we offer the following observations: over the relatively narrow range of total reflected shock pressures (2300–4000 Torr) no detectable trend of the first-order rate constant with pressure was observed. In the case of ethyl fluoride pyrolysis over a wide range of initial pressures (0.7–115 Torr) Day and Trotman-Dickenson[8] have found that above 5 Torr and 452° the rate becomes independent of pressure. The higher temperatures in the present study would shift the fall-off region somewhat toward higher pressures but not nearly enough to compensate for the ~500-fold higher total pressures used in our work. Furthermore, because of the lower frequency pattern in 1,1-difluoroethane due to the additional C–F bond, the latter would be expected to enter the fall-off region at lower pressures than ethyl fluoride for any given temperature.

The temperature dependence of k_1 is shown in Figure 1. A least-squares analysis of the data yields the Arrhenius equation

$$k_1 = 10^{13.9 \pm 0.3} \exp[-(61{,}900 \pm 1800)/RT] \text{ sec}^{-1}$$

where the error limits shown are standard deviations. Figure 1 also shows the extrapolated rate constant of Sianesi, *et al.*[7] The two results agree within experimental error in the activation energy but differ by a factor of ~4 in the preexponential factor. The activation energy obtained for HF elimination from CH_3CHF_2 is further compared with reported values in Table II. Also listed in Table II are calculated values based on the intimate ion pair transition state model of Maccoll[16] and the electrostatic semiion pair model for four-center hydrogen halide addition to olefins developed by Benson and coworkers.[17,18]

According to the ion-pair hypothesis by Maccoll,[16] the activation energy for dehydrohalogenation reac-

(15) P. M. Scott and K. R. Jennings, *J. Phys. Chem.*, **73**, 1513 (1969).

(16) A. Maccoll, *Discuss. Faraday Soc.*, **44**, 288 (1967).

(17) S. W. Benson and G. R. Haugen, *J. Amer. Chem. Soc.*, **87**, 4036 (1965).

(18) S. W. Benson and A. N. Bose, *J. Chem. Phys.*, **39**, 3463 (1963).

Table II: Activation Energies for HF Elimination from CH_3CHF_2

E_a, kcal mol^{-1}	Method-system	Ref
45, 47–48	Chemical activation RRK treatment (CH_2 + CH_2F_2 abstraction + combination)	*a*
53[b]	Chemical activation RRK treatment (CF_2H + CH_3 combination)	*c*
58.5[b]	Chemical activation RRKM treatment (radical combination)	*d*
61.9 ± 1.8	Pyrolysis, SPST	This work
61.9 ± 2	Pyrolysis, flow system	*e*
75	Theoretical calculation for reverse reaction; electrostatic semiion pair model	*f*
76	Calculated from heterolytic bond strength	*g*

[a] Reference 2b and J. A. Kerr, D. C. Phillips, and A. F. Trotman-Dickenson, *J. Chem. Soc., A*, 1806 (1968). [b] Critical energy. [c] See ref 5a. [d] See ref 6. [e] See ref 7. [f] See ref 17. [g] See ref 16.

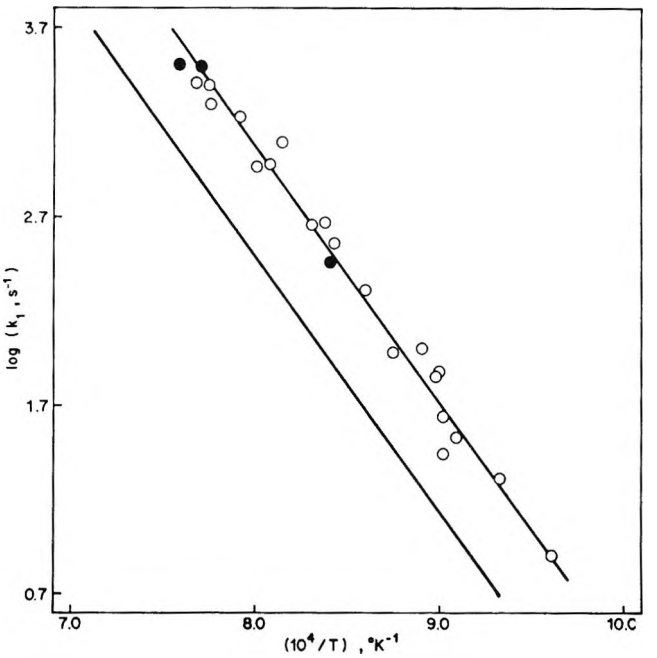

Figure 1. Temperature dependence of the rate constant k_1 for HF elimination from CH_3CHF_2; filled circles, runs with added NO; lower line, extrapolated rate constant from ref 7.

tions, E(HX), is directly proportional to the heterolytic bond dissociation energy $D(R^+–X^-)$, the empirical relationship being given by

$$E(HX) = 0.29\, D(R^+–X^-)$$

The value of $D(R^+–X^-)$ may be calculated from the relationship

$$D(R^+–X^-) = D(R–X) + I(R) - E(X) = AP(R^+,X) - E(X)$$

where D(R–X) is the homolytic bond dissociation energy; I(R) is the ionization potential of the radical R; E(X) is the electron affinity of the halogen atom, and $AP(R^+,X)$ is the appearance potential in the process

$$RX + e^- \longrightarrow R^+ + X + 2e^-$$

Using literature values for $AP(CH_3CHF^+,F)$ = 14.9 eV[19] and E(F) = 3.56 eV,[20] we obtain E(HF) = 76 kcal mol^{-1}. This value is in serious disagreement with our experimental energy of activation and indicates that the intimate ion-pair model for HF elimination is invalid in the case of 1,1-difluoroethane. However, it should be pointed out that Maccoll's numerical coefficient of 0.29 was proposed strictly for α-methyl-substituted monohalides, *i. e.*, ethyl-, isopropyl-, and *t*-butyl halides.

The activation energy, $E_f = E$(HF), may also be estimated from the activation energy for the reverse addition reaction, E_r

$$HF + CH_2{=}CHF \longrightarrow CH_3CHF_2$$

and the enthalpy change for the forward reaction' ΔH_I. E_r was calculated by the method of Benson and Haugen[17,21] using the parameters given in ref 17 with the exception of the dipole moment,[22] $\mu^0_{CH_2CHF}$ = 1.43 D, and the longitudinal molar polarizability of vinyl fluoride, $\alpha^0_{l(CH_2CHF)} \simeq 5.7$ Å^3. This latter quantity was calculated from the known[23] longitudinal, b_l, and transverse, b_t, bond polarizabilities of the C=C and C—H bonds and from estimated b_l and b_t values for the C—F bond. The calculated activation energy is thus E_r = 51 ± 3 kcal mol^{-1} at 298°K. For comparison, the calculated activation energies for HF addition are: to ethylene[17] 54 ± 2 kcal mol^{-1}, fluoroacetylene 51 ± 3 kcal mol^{-1}, and acetylene[21] 52 ± 2 kcal mol^{-1}.

The enthalpy of reaction at 298°K is calculated from the known standard heats of formation of hydrogen fluoride (−64.8 kcal mol^{-1}),[24] vinyl fluoride (−28 kcal mol^{-1}),[25] and 1,1-difluoroethane. Estimates of the enthalpy of formation of 1,1-difluoroethane range from −100 to −121 kcal mol^{-1} and are summarized in Table III. We have selected a recent experimental value,[26]

(19) J. L. Franklin, J. G. Dillard, H. M. Rosenstock, J. T. Herron, K. Draxl, and F. H. Field, NSRDS-NBS-26, 1969.

(20) T. L. Bailey, *J. Chem. Phys.*, **28**, 792 (1958).

(21) S. W. Benson and G. R. Haugen, *J. Phys. Chem.*, **70**, 3336 (1966).

(22) R. D. Nelson, Jr., D. R. Lide, Jr., and A. A. Maryott, NSRDS-NBS-10, 1967.

(23) K. G. Denbigh, *Trans. Faraday Soc.*, **36**, 936 (1940).

(24) National Bureau of Standards Technical Note 270-3, 1968.

(25) P. G. Maslov and Yu. P. Maslov, *Tekhnol. Topliv i Masel*, **3**, 50 (1958).

(26) V. P. Kolesov, S. N. Shtekher, A. M. Martynov, and S. M. Skuratov, *Zh. Fiz. Khim.*, **42**, 3033 (1968).

$\Delta H_f°_{298}(CH_3CHF_2) = -117.3 \pm 2$ kcal mol^{-1}, which was determined by combustion calorimetry. Using these values we obtain $\Delta H_I = 24$ kcal mol^{-1} and hence, $E_f = E_r + \Delta H_I = 75$ kcal mol^{-1}. This value does not agree well with our experimental result, $E_{exp} = 61.9 \pm 1.8$ kcal mol^{-1}. A similar disagreement may be present in the system $CH_2{=}CF_2 \rightarrow CH{\equiv}CF + HF$ for which we calculate $E_f = 74$ kcal mol^{-1} by estimating E_r and ΔH_r as in the case of 1,1-difluoroethane. Preliminary results[27] show that the activation energy for HF elimination from 1,1-difluoroethylene considerably exceeds 74 kcal mol^{-1}. This indicates that the method of Benson, Bose, and Haugen[17,18,21] cannot be applied directly to calculate activation energies for the addition of HF to fluoro-substituted ethylenes and acetylenes. A similar observation has recently been made by Carlton, *et al.*,[28] who have found that the point–dipole model of Benson, *et al.*,[17,18,21] predicts the incorrect activation energies for the addition of HI to 1,1-difluoroethylene even when account was taken of the polar carbon–fluorine bonds in the alkene. It would therefore appear that the point–dipole model cannot be successfully applied to unsaturated systems with *polar* ground states. However, the point–dipole model is only valid for α,β elimination. There is some evidence[5c] that for fluoroethanes with two geminal F atoms α,α elimination may be a significant component of the total. Our present experiments cannot distinguish between these alternatives. Work in progress on isotopically labeled compounds should resolve this question. It may also be noted that the empirical method of estimating activation energies for four-center elimination reactions, as proposed by Szabo and Bercés,[29] does not lend itself to calculations in the case of polyfluorinated hydrocarbons.

Table III: Standard Heat of Formation of CH_3CHF_2

$\Delta H_f°_{298}$ (CH_3CHF_2, g)	Method	Ref	$\Delta H_f°_{298}$ (CH_3CHF_2, g)	Method	Ref
			−113.6	*a*	*f*
−120.9 ± 3	*a*	*b*	−108	*a*	*g*
−119.4	*a*	*c*	−101	*a*	*h*
−117.3 ± 2	Calorimetry	*d*	−100	*a*	*i*
−114.3	*a*	*e*			

[a] Estimated by various methods in references cited. [b] A. S. Rodgers, *J. Phys. Chem.*, **71**, 1996 (1967). [c] S. W. Benson, F. R. Cruikshank, D. M. Golden, G. R. Haugen, H. E. O'Neal, A. S. Rodgers, R. Shaw, and R. Walsh, *Chem. Rev.*, **69**, 279 (1969). [d] See ref 26. [e] See ref 24. [f] Quoted in ref 26. [g] Estimated by Bryant's modification of the method of Anderson, Beyer, and Watson as given in: G. J. Janz "Thermodynamic Properties of Organic Compounds," Academic Press, New York, N. Y., 1967, p 79–81, 280. [h] Estimated from group equivalent values listed in ref 19. [i] Estimated by method of Anderson, Beyer, and Watson as given in ref *g*.

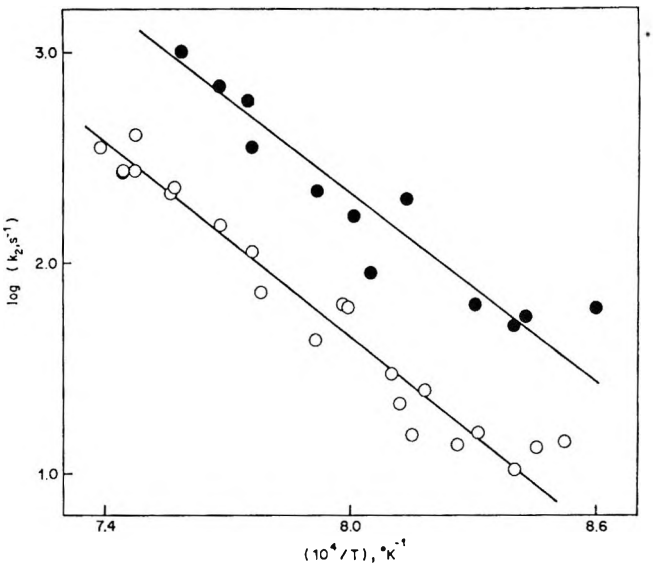

Figure 2. Temperature dependence of the rate constant k_2 for HF elimination from CH_2CHF; filled circles, this study (consecutive reaction); open circles, data from ref 14.

For the purpose of further comparison we have evaluated the preexponential factor in terms of $\Delta S^\dagger$, the entropy of activation at 1200°K (the mean temperature of this study). Because of its simplicity the approximate method of O'Neal and Benson[13] was employed. Rather than using the actual fundamental frequencies for the ground-state molecule[30] and *assumed* frequencies for the activated complex, we have employed the tabulated group frequencies of ref 13 for self-consistency. In any case, for four-center elimination reactions the largest contribution to $\Delta S^\dagger$ is derived from symmetry changes and the entropy loss of the CH_3 group in going from the hindered internal rotation of the ground state to the torsional mode of the complex. Using the known value for the potential barrier to internal rotation in CH_3CHF_2,[31,32] $V = 3.2$ kcal mol^{-1}, we obtain $\Delta S^\dagger_{su} = -1.68$ cal deg^{-1} mol^{-1} as the intrinsic (symmetry-uncorrected) entropy of activation at 1200°K. After correction for the reaction path degeneracy of six, the total entropy of activation is given by $\Delta S^\dagger = \Delta S^\dagger_{su} + R \ln 6 = 1.88$ cal deg^{-1} mol^{-1}. The preexponential factor is then obtained from the transition state theory expression $A = (ekT/h) \exp(\Delta S^\dagger/R)$ which yields the value log (A, sec^{-1}) = 14.2. In view of the approximate nature

(27) J. M. Simmie and E. Tschuikow-Roux, unpublished data.

(28) T. S. Carlton, A. B. Harker, W. K. Natale, R. E. Needham, R. L. Christensen, and J. L. Ellenson, *J. Amer. Chem. Soc.*, **91**, 555 (1969).

(29) Z. G. Szabo and T. Bercés, *Z. Phys. Chem.*, **57**, 113 (1968).

(30) D. C. Smith, R. A. Saunders, J. R. Nielsen, and E. E. Ferguson, *J. Chem. Phys.*, **20**, 847 (1952).

(31) W. G. Fateley and F. A. Miller, *Spectrochim. Acta*, **17**, 857 (1961).

(32) D. R. Herschbach, *J. Chem. Phys.*, **25**, 358 (1956).

of this calculation this value of 14.2 is judged to be in reasonable agreement with our experimental value of 13.9 ± 0.3 and supports the value of 61.9 kcal mol^{-1} obtained for the activation energy.

The temperature dependence of the first-order rate constant, k_2, for the elimination of HF from vinyl fluoride is shown in Figure 2 and the Arrhenius equation is given by

$$k_2 = 10^{14.6\pm1.4} \exp[-(70{,}000 \pm 8200)/RT] \text{ sec}^{-1}$$

The activation energy is in moderate agreement with the considerably more accurate datum obtained by us in an independent direct study[14] [log (A, sec^{-1}) = 14.0 ± 0.7, E_a = 70.8 ± 3.6 kcal mol^{-1}], although the absolute values of the rate constants differ by a factor of 4 to 5. We can offer no explanation for this discrepancy at this time.

A Microchemical Study of Gas-Phase Kinetics for Three Irreversible Reactions

by D. G. Retzloff, B. M. Coull, and J. Coull

Department of Chemical and Petroleum Engineering, University of Pittsburgh, Pittsburgh, Pennsylvania 15213
(Received February 20, 1969)

In this work a comparison is made between reliable macroscopic measurements of the homogeneous reaction kinetics for the systems vinylcyclopropane and di-*t*-butyl peroxide and the microreaction measurements for these two systems over a higher temperature range, as a test for the reliability of the latter technique. Extension to the measurement of kinetic parameters for the system 2,3-dihydropyran is also considered.

Introduction

In this work a study was made of the reactions involving the homogenous gas-phase thermal unimolecular isomerization of vinylcyclopropane to cyclopentene, the pyrolysis kinetics of di-*t*-butyl peroxide and of 2,3-dihydropyran. The first two reactions have received extensive treatment in the literature.[1-6]

The main purpose of the present study was to establish reliability of a simple experimental procedure, in comparison with other more complex methods for which data are available. It was decided in testing our method for the first two systems to study kinetics over a higher temperature range than for those previously published. In addition it was also apparent that extrapolation between widely separated data points, as between other investigators and ourselves, would provide an excellent test for the reliability of our technique.

Having established reliability, our next purpose was to investigate the kinetics for the 2,3-dihydropyran system.

Previous Experimental Studies

A brief description of the methods used by other investigators for the first two mentioned reactions will now be presented.

In their study of the isomerization of alkene and alkyl cyclopropanes, Flowers and Frey[1,2,4] used conventional glass-blown equipment. The reaction involving vinylcyclopropane

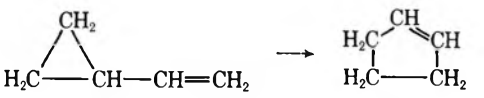

was conducted batchwise in a 200-cm^3 Pyrex cylinder placed horizontally in an electric furnace controlled to within 0.1°. At the end of each time interval the contents of the reactor was discharged into an evacuated bulb immersed in liquid oxygen. Analysis of the reaction mixture for each run was made by gas chromatography, using tc as the detector, with area quantitation by electronic integration. The temperature range covered was from 339 to 391°. It is evident from a

(1) M. C. Flowers and H. M. Frey, *J. Chem. Soc.*, 3547 (1961).
(2) M. C. Flowers and H. M. Frey, *ibid.*, 3953 (1959).
(3) J. P. Chesick, *J. Amer. Chem. Soc.*, **82**, 3277 (1960).
(4) M. C. Flowers and H. M. Frey, *Proc. Roy. Soc., Sec. A*, **257**, 122 (1960).
(5) N. A. Milas and D. M. Surganor, *J. Amer. Chem. Soc.*, **68**, 206 (1944).
(6) J. H. Raley, F. P. Rust, and W. E. Vaughan, *ibid.*, **70**, 88 (1948).

study of the data obtained that the measurements made were highly reproducible.

The mechanism for the second reaction, the decomposition of di-*t*-butyl peroxide, was reported almost simultaneously by Milas and Surgenor[5] and by George and Walsh[7] to be as follows

$$(CH_3)_3COOC(CH_3)_3 \longrightarrow 2(CH_3)_3CO$$

$$(CH_3)_3CO \longrightarrow (CH_3)_2CO + \dot{C}H_3$$

$$\dot{C}H_3 + CH_3 \longrightarrow C_2H_6$$

The foregoing mechanism was acceptable to Raley, Rust, and Vaughan,[6] who conducted kinetic studies on this system. The reactor used was a 500-cm^3 Pyrex bulb connected to a quartz spiral pressure gauge, the pressure increase being followed by using the gauge as a null point instrument. The oil bath temperature was controlled to within 0.04°, the range covered being 140–160°. "The reaction was halted by freezing the vapors into a bulb and pumping the residual gases into a sample bulb for analysis with a mass spectrometer." Ketone was determined by the standard hydroxylamine hydrochloride method.

Experimental Equipment Used in This Work. The simple essential of our technique involves the use of a "microreactor" in series with a chromatographic column. This technique is by no means new[8-12] and for an excellent coverage of experimental methods involving reaction kinetics, prior to and within the gc column, one should consult the recent article by Langer, *et al.*,[13] containing also 110 literature references.

In our study the reactor unit was attached at the injection port, ahead of the flash vaporizer in series with the gc column. The flash vaporizer in our case was used to quench the reaction. The reactor tube was machined from Inconel-X, mp 1400°, was resistance heated, and had a spot-welded chromel–alumel thermocouple attached for temperature measurement. Power input to the reactor was controlled by a variable transformer. Temperature controls for the flash vaporizer, predetector, detector, and column were present as in all standard chromatographic equipment.

Volumetric flow rates were obtained for the carrier and reference gases using a bubble flow meter calibrated in units of 1 ml, for each vernier setting of the valve orifice. It was thus possible to measure input–output rates for the reactor and gc column. Allowing for pressure drop in the gc column, it was possible, by measuring the gas flow rate from the column, to account for residence times in the reactor and gc column. The instrument was equipped with a flame ionization detector and areas on the recorder printout were measured by a disk integrator.

Chromatograph Calibration. In this investigation it was not possible to use an internal standard because of the nature of the reaction products formed. One can, however, operate on the principle that for any fixed weight ratio of components B and C, the ratio of the number of ions will remain essentially constant, within the accuracy of the settings used. For details of instrument calibration see Retzloff[14] and Coull.[15]

Flow Pattern in the Reactor. Langer, *et al.*,[13] in their rigorous analysis of flow where the gc column is used as the reactor have laid great stress on the comparison of what is defined as the ideal reactor and departures from same.

Our concern is with flow within the reactor and to the possibility of axial diffusion which might affect the residence time distribution. For this reason it is important that the dimensions of the reactor be known. In our case the ratio of length to diameter was 5.94 to 0.598 cm, well below the accepted value for laminar flow to develop.

If ϵ is the length of the injected slug, one may readily obtain the equation[13]

$$C = \sum_{n=1}^{\infty}\{2C_0[1 - (-1)^n]/n\pi\} \times \sin(n\pi/\epsilon)Z \exp[-k^\infty + n^2\pi^2D/\epsilon^2)t] \quad (1)$$

where C is the concentration of reactant at some point along the reactor and C_0 the initial concentration, D being the diffusion coefficient. Only diffusion in the Z direction is considered.

If diffusion in the Z direction along the reactor becomes important $D > 0$, and one obtains the following equation for k^∞

$$k^\infty = \frac{1}{t}\ln\left(\frac{N_{C_0}}{N_C}\right) + \frac{1}{t}\ln\left(\frac{8}{\pi^2}\right) + \frac{1}{t}\ln M(D, t) = (\pi^2D/\epsilon^2) \quad (2)$$

where

$$M(D, t) = 1 + \frac{1}{9}\exp[-(8\pi^2D/\epsilon^2)t] + \frac{1}{25}\exp[-(24\pi^2D/\epsilon^2)t] + \ldots \quad (3)$$

N_C and N_{C_0} are, respectively, the moles of reactant and the initial moles of reactant.

(7) George and Walsh, *Trans. Faraday Soc.*, **42**, 94 (1946).

(8) P. H. Emmett, R. J. Kokes, and H. H. Tobin, U. S. Patent 2,905,539 (1959).

(9) R. J. Kokes, H. H. Tobin, and P. H. Emmett, *J. Amer. Chem. Soc.*, **77**, 5860 (1955).

(10) P. H. Emmett, *Advan. Catal.*, **9**, 645 (1957).

(11) W. K. Hall and P. H. Emmett, *J. Amer. Chem. Soc.*, **79**, 2091 (1957).

(12) W. K. Hall and P. H. Emmett, *J. Phys. Chem.*, **63**, 1102 (1959).

(13) S. H. Langer, J. Y. Yurchak, and J. E. Patton, *Ind. Eng. Chem.*, **61**, 11 (1969).

(14) D. G. Retzloff, Thesis, University of Pittsburgh.

(15) B. M. Coull, Thesis, University of Pittsburgh.

If the entrance mixing effect predominates, the flow conditions will be essentially plug flow, where $D = 0$. Equation 1 then reduces to

$$C = C_0 \exp(-k^\infty t) \quad (4)$$

Solving for k^∞ in terms of N_C and N_{C_0}

$$k^\infty = \frac{1}{t} \ln\left(\frac{N_{C_0}}{N_C}\right) \quad (5)$$

2,3-Dihydropyran Reaction Kinetics. In this study it was found that dihydropyran pyrolyzed to form exclusively ethylene and acrolein in the temperature range 450–510° in the absence of a catalyst. The reaction may be written as

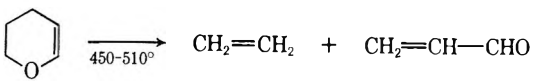

Above 510° it was found that additional reactions occurred, but these reactions were not investigated. However, dihydropyran is reported to condense with acrolein to produce a product assigned the following structure[16,17]

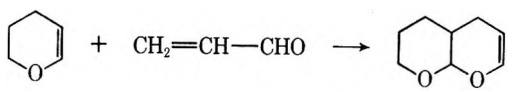

This may account for the additional reactions observed. However, for this work the temperature bounds were held between 450 and 510° and the latter reaction was not found to occur under the experimental conditions used although it is well known that, in the presence of certain catalysts, acrolein readily polymerizes.

Experimental Data. All compounds used in the present study were of spectroanalyzed purity as purchased and were further examined by nmr, mass spectrography, and glpc column separation.

Calibration curves for the three systems, based on disk integration measurements of the areas under the peaks, were found to be linear.[14,15]

Calculation of Results. In order to ascertain the importance of axial diffusion in our system, values of k^∞ were calculated using both eq 2 and 5. The diffusion coefficient used in eq 2 was estimated by the methods of Hirschfelder, Curtiss, and Bird.[18] It was found that where diffusion effects were considered, negative k^∞ values resulted for many of the data points, thus indicating that $D = 0$. Equation 5 was found to give values of k^∞ which are in keeping with unimolecular kinetics and, therefore, was used to calculate the values of k^∞ presented in this paper.

Complete results for all three reactions are given in Table I. The Arrhenius form of the rate constant is calculated in the usual way from a plot of log k^∞ *vs.* $1/T$ (see Figure 1).

Table I: Di-*t*-butyl Peroxide Reaction

Temp, °K	k^∞
Di-*t*-butyl Peroxide Reaction	
503.6	0.296
513.8	0.645
513.2	0.617
514.3	0.670
524.2	1.379
526.9	1.677
532.6	2.495
527.1	1.701
Vinylcyclopropane Reaction	
780.9	0.370
777.4	0.320
791.95	0.579
785.1	0.440
799.7	0.785
787.2	0.478
692.1	0.006
679.2	0.003
695.1	0.007
737.3	0.056
745.1	0.079
726.1	0.033
752.3	0.109
754.1	0.119
708.6	0.014
2,3-Dihydropyran Reaction	
722.9	0.037
736.1	0.083
745.6	0.110
756.4	0.176
768.1	0.275
781.1	0.456

Results

For the peroxide reaction, the experimentally determined value of k^∞ for the temperature range 230–255° is

$$k^\infty = 10^{16.48\pm0.02} \exp(-39{,}040 \pm 80/RT) \quad (6)$$

The value reported by Raley, Rust, and Vaughan[6] for the temperature range 140–160° is

$$k^\infty = 10^{16.51} \exp(-39{,}100 \pm 50/RT) \quad (7)$$

For the vinylcyclopropane reaction, the experimental value of k^∞ in the temperature range 400–560° is

$$k^\infty = 10^{13.50\pm0.02} \exp(-49{,}602 \pm 70/RT) \quad (8)$$

and the value reported by Flowers and Frey[1] for the temperature range 339–391° is

(16) Technical Bulletin No. 137, The Quaker Oats Co., Chemicals Division, Chicago, Ill.

(17) R. Paul and S. Tchelitcheff, *Bull. Soc. Chim. Fr.*, 672 (1954).

(18) J. O. Hirschfelder, C. F. Curtiss, and R. R. Bird, "Molecular Theory of Gases and Liquids," John Wiley and Sons, New York, N. Y., 1964.

$$k^{\infty} = 10^{13.50} \exp(-49{,}600/RT) \quad (9)$$

For the dihydropyran reaction the experimental results for the temperature range 450–510° gives

$$k^{\infty} = 10^{12.81 \pm 0.02} \exp(-46{,}974 \pm 80/RT) \quad (10)$$

Comparison could not be made with the results published in the literature for this reaction because they pertain to heterogeneous catalytic studies.[19,20]

Conclusions

The results reported here extend the temperature range for both the molecular rearrangement of vinylcyclopropane and the pyrolysis reaction of di-*t*-butyl peroxide. Using the methods of Hirschfelder, Curtiss, and Bird[18] to estimate the diffusion coefficient, it was found that negative values for k^{∞} were obtained when diffusion in the axial direction was considered. Therefore, diffusion effects were considered negligible and eq 5, describing the nondiffusion (plug flow) case, was used to calculate k^{∞}. The values of k^{∞} reported here for the above mentioned reactions are in excellent agreement with those published in the literature when extrapolated to the temperature ranges reported in the literature (see Figure 2). This close agreement between the results presented here for k^{∞} and those previously published further support the conclusion that diffusion phenomena were negligible. This is not surprising because the reactor is not of sufficient length to allow laminar flow to develop and the entrance mixing

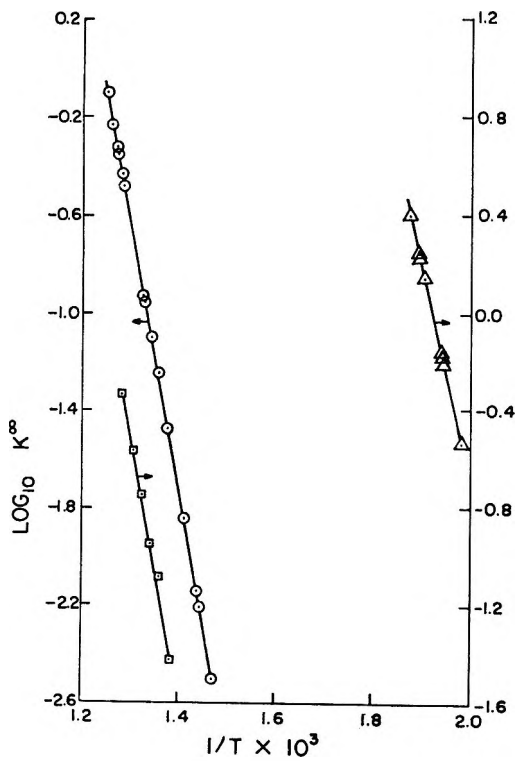

Figure 1. Di-*t*-butyl peroxide reaction, △; vinylcyclopropane reaction, ⊙; 2,3-dihydropyran reaction, ⊡.

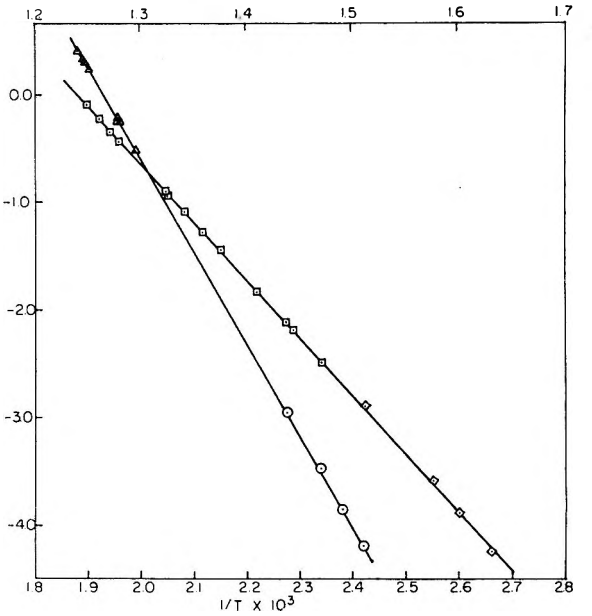

Figure 2. Di-*t*-butyl peroxide reaction; ⊙, data of Raley, Rust, and Vaughan, *J. Amer. Chem. Soc.*, **70**, 89 (1948); △, data of Retzloff, Coull, and Coull, vinylcyclopropane reaction; ⋄, data of Flowers and Frey, *J. Chem. Soc.*, 3547 (1961); ⊡, data of Retzloff, Coull, and Coull.

effect is strong enough to maintain a well mixed plug flow system.[14]

The data for the dihydropyran reaction fit the form of the Arrhenius equation extremely well when the nondiffusion equation was used to calculate the rate constant and negative results are obtained when the diffusion equation is used, being consistent with the neglect of diffusion phenomena. The values of the frequency factor and activation energy obtained for this reaction fit within the range for unimolecular reactions and well above those reported for bimolecular reactions by Maccoll.[21] Thus it is concluded that the uncatalyzed pyrolysis of dihydropyran in the temperature range 450–510° is a true unimolecular reaction.

The uncatalyzed unimolecular pyrolysis of 2,3-dihydropyran, which has not been previously reported in the literature, was found to form exclusively ethylene and acrolein between 450 and 510° as follows

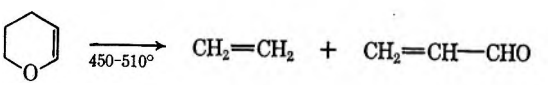

However, above 510° additional reactions were observed and are presently under investigation.

Acknowledgments. The first mentioned author re-

(19) C. L. Wilson, *J. Amer. Chem. Soc.*, **69**, 3004 (1947).

(20) N. J. Shukin, R. A. Karashanov, and S. N. Khar'kov, *Akad. Nauk SSSR, Ser. Khim.* (1966).

(21) A. Maccoll, "Investigations of Rates and Mechanisms of Reaction," Part 1, 2nd ed, Interscience Publishers, New York, N. Y., 1961, p 427.

ceived fellowship support from the Shell Companies Foundation, Inc. The authors extend thanks to the following: Dr. C. C. Sweeley, now of Michigan State University, for mass spectral determinations; Dr. Eleanor J. Fendler, Chemistry Department, for nmr studies; The University of Pittsburgh computer center.

Radical Intermediates in the Vacuum Ultraviolet Photolysis of Cyclohexane and Cyclohexene Vapors[1]

by M. D. Sevilla

Atomics International, A Division of North American Rockwell Corporation, Canoga Park, California 91304

and R. A. Holroyd

Chemistry Department of Brookhaven National Laboratory, Upton, New York 11973
(Received December 8, 1969)

The radical intermediates in the vacuum uv photolysis of cyclohexane and cyclohexene vapor have been identified. Two methods were used for radical detection: the $^{14}CH_3$-radical sampling method and esr identification of the radicals trapped on a cold finger at 77°K. Results of the radical sampling technique show that at 1470 Å the principal radical intermediates in cyclohexane at 10 Torr are methyl, allyl, and cyclohexyl. Similar results were obtained for cyclohexane-d_{12}. Increasing the photon energy results in an increase in the yields of methyl, allyl, and other fragment radicals. Although the spectrum of the allyl radical predominates, the esr data are shown to be consistent with the radical sampling data. In cyclohexene the main radical intermediates at 1470 Å are methyl, allyl, cyclohexyl, and 3-cyclohexenyl. The mechanism of formation of radicals in these hydrocarbons is discussed.

Introduction

Studies of the vacuum uv photolysis of hydrocarbons have shown that the most important primary processes involve the molecular elimination of smaller molecules.[2,3] However, there is also evidence for radical formation processes.[4] Studies of the yields and nature of radical intermediates are useful in elucidating the process by which these radicals are formed.

This report deals with the detection of radical intermediates in vacuum uv photolysis by two methods: esr spectroscopy and $^{14}CH_3$-radical sampling.[5,6] Yields of radical intermediates in the vapor phase photolysis of cyclohexane and cyclohexene are reported. The present results show that allyl radicals are more important than indicated by an earlier study of cyclohexane[4] in which H_2S was used as a radical scavenger.

Experimental Section

The photolysis arcs were prepared in the manner prescribed by McNesby and Okabe.[2] The arcs were baked under vacuum and gettered prior to filling with inert gas. A sapphire window was joined by a graded seal to the xenon arc and a MgF_2 window was sealed with epoxy to the krypton arc. Both arcs were equipped with 29/42 joints for attachment to the photolysis vessels. The arcs were powered by a microwave diathermy unit (Raytheon).

For detection of radicals by esr spectroscopy a flow system similar to that of Smith and Tole[7] was used. Hydrocarbon vapors (Phillips Research Grade) passed by the window of the photolysis arc and were subsequently collected on a cold finger, cooled to 77°K, located 4 cm from the window. After several minutes of photolysis, the system was pressurized with nitrogen and the cold finger was quickly immersed in liquid nitrogen and transferred to the variable temperature

(1) This work was supported by the Research Division of the U. S. Atomic Energy Commission.

(2) J. R. McNesby and H. Okabe, *Advan. Photochem.*, **3**, 157 (1964).

(3) L. W. Sieck in "Fundamental Processes in Radiation Chemistry," P. Ausloos, Ed., John Wiley & Sons, New York, N. Y., 1968, p 136 ff.

(4) P. Ausloos, R. E. Rebbert, and S. G. Lias, *J. Phys. Chem.*, **72**, 3904 (1968).

(5) R. A. Holroyd and G. W. Klein, *Int. J. Appl. Radiat. Isotop.*, **15**, 633 (1964).

(6) R. A. Holroyd, *J. Amer. Chem. Soc.*, **91**, 2208 (1969).

(7) D. R. Smith and J. C. Tole, *Can. J. Chem.*, **45**, 779 (1967).

Table I: Radical Yields in the 1470-Å Photolysis of Cyclohexane

	C_6H_{12}					C_6D_{12}	
P, Cyclohexane	3.4	10	20	69	79	7.7[a]	20
P, $^{14}CH_3I$	0.03	0.03	0.03	0.1	0.03	...	0.03
ϕ(Methyl)	0.040	0.044	0.045	0.054	0.044	0.039	0.069
ϕ(Ethyl)	0.012	0.012	0.012	0.010	0.010	0.016	0.010
ϕ(Allyl)	0.031	0.034	0.034	0.041	0.034	<0.013[b]	0.042
ϕ(*n*-Propyl)	0.004	0.003	0.005	0.008	0.008	~0.002	0.005
ϕ(Cyclohexyl)	0.016	0.022	0.028	0.040	0.049	nd	0.032
ϕ(Methyl-^{14}C)	0.045	0.035	0.023	0.030	0.038	...	0.016

[a] Results obtained with H_2S scavenger (ref 5). [b] This is an upper limit since the yield of C_3D_5H was not specifically determined.

control (Varian) dewar in the esr (Varian 4500-10A) cavity; care was taken to avoid oxygen contact during transfer. Esr spectra were recorded at various temperatures.

Application of the $^{14}CH_3$-radical sampling technique to radical detection in vacuum uv photolysis studies has been described elsewhere.[6] Light intensity measurements were based on the yield of cyclohexene, for which quantum yield measurements have been made.[8]

Results

Cyclohexane. The major radioactive products formed at 1470 Å in the presence of $^{14}CH_3I$ were ethane, propane, 1-butene, and methylcyclohexane. Smaller amounts of labeled butane and pentenes[9] were also observed. It is inferred on the basis of these labeled products that the major radical intermediates are methyl, ethyl, allyl, and cyclohexyl, and that minor amounts of propyl and butenyl radicals are present.

The relative yields of radicals were calculated from the relative yields of labeled hydrocarbons by the method described in previous studies.[6,10,11] Calculation of the relative yield of methyl radicals is a special case. The methyl radical yield can be obtained from the yield of labeled ethane, however, if the ratio $[CH_3]/[^{14}CH_3]$ is known.[5,6] This ratio was obtained independently from measurements of the specific activity of the propane in each experiment. An earlier study with added NO showed that propane is formed by radicals,[12] most likely by reactions 1a and 1b. Thus

$$CH_3 + C_2H_5 \longrightarrow C_3H_8 \qquad (1a)$$

$$^{14}CH_3 + C_2H_5 \longrightarrow {}^{14}C_3H_8 \qquad (1b)$$

the ratio of the yield of unlabeled to labeled propane is equal to $[CH_3]/[^{14}CH_3]$.

Quantum yields of radicals as a function of pressure for the 1470-Å photolysis are given in Table I. The results show that the yields of all radicals except cyclohexyl are independent of pressure. In addition to the radicals listed there is also a small yield ($\phi = 0.005$) of 3-butenyl radicals. For photolysis at 1236 Å the yields of all radicals except cyclohexyl are a factor of 2 higher than the yields observed at 1470 Å. Photolysis experiments were also performed on perdeuteriocyclohexane. The results (Table I) show that deuteration has little effect on the fragmentation process (compare columns 4 and 8). Columns 7 and 8 are the radical yields observed for C_6D_{12} by the H_2S[4] and $^{14}CH_3$-radical sampling techniques, respectively.

The esr spectra found for the photolysis of cyclohexane at 1470 Å (−190°) and 1236 Å (−112°) are shown in Figures 1 and 2. The spectra observed at −190° for photolysis at both 1470 and 1236 Å show hyperfine structure from several radical species. Warming the sample obtained from photolysis at either wavelength greatly improves the resolution for one of the species. This was most pronounced for the sample which was photolyzed at 1236 Å. In this case, the spectrum at −112° is dominated by one radical with splittings of 14.6 G (4 protons) and 4.0 G (1 proton). The splittings and number of protons found here are consistent with those found previously for the allyl radical.[13−16] The spectrum is, therefore, assigned to the allyl radical. The allyl radical has been generated by various other methods in both the solid and liquid phase. The spectrum observed here at −112° is much better resolved than that found previously in

(8) R. R. Hentz and S. J. Rzad, *J. Phys. Chem.*, 71, 4096 (1967).

(9) Only 1-pentene was identified but several other small peaks were observed with similar retention times which could be isomeric pentenes.

(10) The ratio D_i/C_i for $^{14}CH_3 + C_2H_5 \rightarrow$ is taken as 0.06 and D_i/C_i for $^{14}CH_3 + i\text{-}C_3H_7 \rightarrow$ is 0.22 (J. A. Kerr and A. F. Trotman-Dickenson, *Progr. React. Kinet.*, 1, 107 (1961)).

(11) The value of D_i/C_i for reaction of $^{14}CH_3$ with normal type alkyl radicals is assumed to be 0.1; D_i/C_i for $^{14}CH_3$ + cyclohexyl is 0.22 (W. G. Burns, R. A. Holroyd, and G. W. Klein, *J. Phys. Chem.*, 70, 910 (1966)); methyl and allyl radicals are assumed not to disproportionate on reaction with $^{14}CH_3$.

(12) R. D. Doepker and P. Ausloos, *J. Chem. Phys.*, 42, 3746 (1965).

(13) E. L. Cochran, F. J. Adrian, and V. A. Bowers, *ibid.*, 34, 1161 (1961).

(14) K. A. Maas and D. H. Volman, *Trans. Faraday Soc.*, 60, 1202 (1964).

(15) J. E. Bennet and A. Thomas, *Proc. Roy. Soc., Ser. A*, 280, 123 (1964).

(16) R. W. Fessenden and R. H. Schuler, *J. Chem. Phys.*, 39, 2147 (1963).

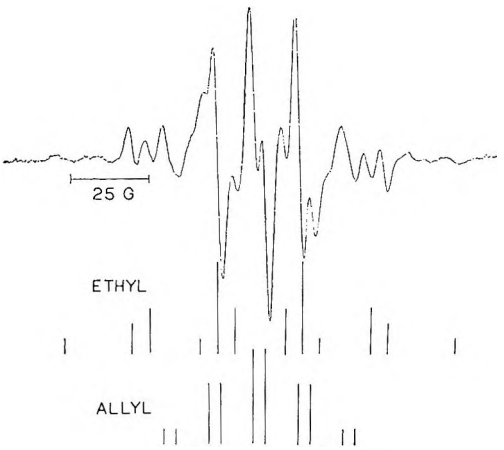

Figure 1. Top: the esr spectrum of radicals formed by the photolysis of cyclohexane at 1470 Å in the gas phase and trapped on a cold finger at 77°K. (Observed at −180°.) Bottom: stick diagrams of the ethyl (three protons at 26.9 G and two protons at 22.4 G) and the allyl (four protons at 14.6 G and one proton at 4.0 G) radicals. The remaining components not accounted for by the ethyl and allyl diagrams are at positions consistent with the end components of the cyclohexyl radical. The other cyclohexyl components are obscurred by the more intense ethyl and allyl spectra.

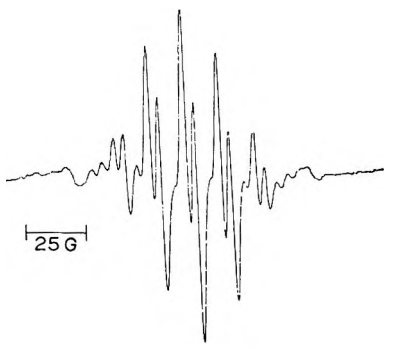

Figure 2. The esr spectrum of radicals formed by the photolysis of cyclohexane at 1236 Å in the gas phase and trapped on a cold finger at 77°K. (Observed at −112°.) The most intense components are due to the allyl radical. (See the stick diagram in Figure 1). The broad end components are at positions consistent with the cyclohexyl radical. The remaining components arise from the ethyl radical which has decreased in intensity during the warming process.

the solid state[13−15] and suggests reorientation is taking place at this temperature.

In addition to the allyl radical the spectra show at least two other species are present. The end lines in Figure 1 are separated by 125 G. The ethyl radical is consistent with this separation and other line components in the spectrum. Stick diagrams for ethyl and allyl radicals, as shown in Figure 1, account for all but two of the lines in the spectrum. These two remaining components, which are more clearly seen in Figure 2, are separated by 100 G. The total width of the cyclohexyl radical is known to be approximately 100 G.[15] Thus the observed components are consistent with that expected for the cyclohexyl radical.[17]

The relative yields of radicals found by esr are difficult to determine due to anisotropies, varying line widths, and overlapping spectra. In addition there may be differences in efficiencies of trapping which cannot be accounted for. An estimate of the relative yield of allyl to ethyl of 2.5:1 at 1470 Å was calculated from line intensities.[18] This is in good agreement with the radical sampling technique which gave 3.3:1. The esr spectra indicated that photolysis at 1236 Å led to an increase in the ratio [allyl]/[ethyl] relative to that observed at 1470 Å. The small yield of cyclohexyl radicals detected by esr is consistent with the sampling results since the yield of cyclohexyl radicals decreases with decreasing pressure. The pressure in the vessel in which the esr samples were collected was less than the lowest pressure used in the sampling study, and less than 10% of the radicals should be cyclohexyl at this pressure.

Cyclohexene. The $^{14}CH_3$-radical sampling technique and the gas-phase radical trapping technique were also employed to investigate the photolysis of cyclohexene. Analysis of the results found by the radical sampling technique showed that the major radical products in cyclohexene are 3-cyclohexenyl, cyclohexyl, methyl, and allyl (Table II). The yields reported in Table II are relative yields. The quantum yield of radicals is 0.35 times the yield of butadiene. For a constant ratio of $[^{14}CH_3I]$ to $[C_6H_{10}]$ the ratio of $\phi(C_6H_9)/\phi(C_6H_{11})$ increases with increasing pressure. Increasing the $^{14}CH_3I$ concentration at any particular cyclohexene pressures results in a lower yield of C_6H_{11} radicals. The yields of the other two major radicals, methyl and allyl, are independent of pressure. The main stable products of the photolysis are ethylene and butadiene which are formed in comparable yields.

Analysis of the esr spectra observed for photolyzed cyclohexene yields results which are interesting but less informative than those found by the $^{14}CH_3$-radical sampling technique. At −190° only a broad nearly unresolved spectrum is observed. However, warming the sample to −115° results in the well resolved spectrum shown in Figure 3. Comparison of this spectrum with that observed previously[19] for the 3-cyclohexenyl radical confirms that this species predominates. The fact that only this radical is observed at the higher temperature is attributed to the occurrence of reaction 2. Some C_6H_9 radicals are formed in the photolysis

(17) It should be noted that the *n*-propyl radical spectrum extends 110 G and therefore could interfere in this region.

(18) The ratio of allyl to cyclohexyl could not be estimated at −190°. At −112° where the line width of the cyclohexyl radical is less, the ratio is approximately 2:1, which is in reasonable agreement with the radical sampling technique; however, at this temperature radical decay is occurring and the ratio may not be representative of that found at −190°.

(19) S. I. Ohnishi and I. Nitta, *J. Chem. Phys.*, **39**, 2848 (1963).

$$R + C_6H_{10} \longrightarrow C_6H_9 + RH \qquad (2)$$

but the other radicals which are present at the lower temperature abstract from the matrix molecules when the sample is warmed, to form more of the allylic species, C_6H_9.

Table II: Relative Radical Yields in the 1470-Å Photolysis of Cyclohexene

	P, Torr					
	5	5	10	10	20	40
$^{14}CH_3I$(%)	2	1	2	1	1	1
Methyl	42[a]	16	40[a]	11	34[a]	30[a]
Methyl-^{14}C		16		19		
Ethyl	4	3	4	3	2	2
Propyl	3	2	3	2	1	1
Allyl	11	10	9.4	10	10	10
Cyclohexyl	18	31	22	28	26	25
3-Cyclohexenyl	22	23	24	26	27	31

[a] Includes both methyl and methyl-^{14}C.

Discussion

The $^{14}CH_3$-radical sampling results indicate that the most important radicals in the 1470-Å photolysis of cyclohexane at low pressures are methyl and allyl. Cyclohexyl becomes a major intermediate as the pressure is increased. Of lesser importance are ethyl, *n*-propyl, and 3-butenyl radicals.

The esr spectra (Figures 1 and 2) indicate that allyl radicals predominate in the frozen-out sample. Methyl radicals were not observed because, even if trapped on the cold finger, they are known to decay rapidly in hydrocarbon matrices at 77°K.[16,20] Ethyl radicals were detected (they do not decay at 77°K) and the ratio of (ethyl)/(allyl) found with the esr method is comparable to that found with radical sampling. Thus the esr results are consistent with the $^{14}CH_3$-radical sampling results.

From the radicals observed one would expect the products: ethane, propane, 1-butene, methylcyclohexane, 1,5-hexadiene, and dicyclohexyl to be formed in the photolysis from combination of radicals. The first four of these have been identified as products and further the formation of ethane, propane, and 1-butene is completely inhibited by radical scavengers.[4] The yields of these products are consistent with the yields of radicals as given in Table I. Thus, for example, from the yield of allyl relative to the yield of methyl one would expect that the yield of 1-butene should exceed that of ethane, as is actually observed.[4]

An earlier study in which H_2S was used as a radical scavenger[4] indicated the major radical in cyclohexane to be methyl, with lesser amounts of ethyl, vinyl, and allyl, and a trace of *n*-propyl. Cyclohexyl radicals were not reported. The yields of radicals obtained by

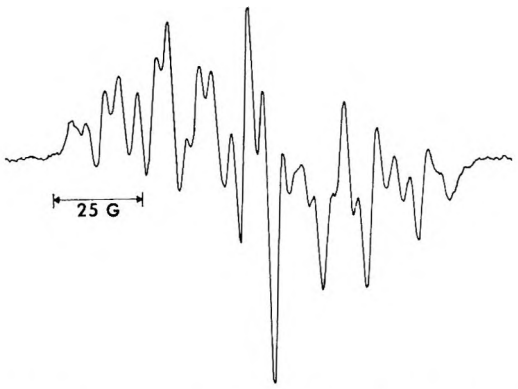

Figure 3. The esr spectrum of radicals formed by the gas phase photolysis of cyclohexene at 1470 Å and trapped at 77°K observed at −115°. The spectrum is essentially identical with that found for the cyclohexenyl radical (ref 19).

the H_2S method (Table I, column 7) are comparable to the $^{14}CH_3$-radical sampling results except that a much lower yield of allyl radicals is obtained with H_2S as scavenger. The reason for this discrepancy may be the slow rate of reaction 3. This reaction is endother-

$$\text{allyl} + H_2S \longrightarrow C_3H_6 + HS \qquad (3)$$

mic[21,22] and could have an activation energy of several kcal/mol. The reaction of alkyl radicals with H_2S on the other hand is characterized by low (~2 kcal/mol) activation energies.[22] Since reaction 3 is slower than the reaction of other radicals with H_2S, it is possible that H_2S does not quantitatively titrate allyl radicals.

To identify the precursor of fragment radicals is difficult because of the many secondary decompositions which can occur in vacuum uv photolysis. In cyclohexane the most likely precursors are C_6H_{12}*, C_6H_{11}*, and possibly C_6H_{10}*. The latter is formed as a result of the main primary process which is H_2 elimination. This intermediate decomposes to ethylene and butadiene and is stabilized by collisions to cyclohexene. The yields of these products vary with pressure[4,8] over the pressure range investigated here, whereas the yields of fragment radicals are independent of pressure. Thus C_6H_{10}* must not be the major source of radicals. Whatever the precursor of fragment radicals, it must be short-lived, always decomposing in the pressure range investigated; but at some higher pressure this primary species will be stabilized.

The mechanism that has been proposed[4] to account for the formation of fragment radicals in the photolysis of cyclohexane involves the isomerization of an electronically excited C_6H_{12}* molecule first to an excited hexamethylene diradical and then to a linear vibra-

(20) J. E. Willard, *Mol. Cryst. Liq. Crystal.*, **9**, 135 (1969).
(21) J. B. Homer and F. P. Lossing, *Can. J. Chem.*, **44**, 2211 (1966).
(22) W. A. Pryor and U. Tonellato, *J. Phys. Chem.*, **73**, 850 (1969).

tionally excited hexene molecule which subsequently decomposes. The overall reactions are (4) and (5). It

$$C_6H_{12}^* \longrightarrow CH_3 + C_5H_9^* \quad (4)$$

$$\longrightarrow C_2H_5 + C_4H_7 \quad (5)$$

was originally suggested[4] that allyl radicals result from a secondary decomposition of the $C_5H_9^*$ species formed in reaction 4. However, in view of the fact that allyl is one of the major radicals in the photolysis and is formed in a constant ratio to the other fragment radicals, it may be formed directly[23] from $C_6H_{12}^*$, reaction 6. This reaction would be followed by secondary decomposition of the $C_3H_7^*$ radical at low pressures which would ac-

$$C_6H_{12}^* \longrightarrow C_3H_5 + C_3H_7^* \quad (6)$$

count for the fact that the yield of allyl radicals exceeds the yield of propyl radicals.

An alternate scheme can be conceived to account for the formation of fragment radicals. Excited cyclohexyl radicals are formed in the primary process[9] and could dissociate in parallel paths as in reactions 7 through 10. Cyclohexyl radicals are known to decom-

$$C_6H_{11}^* \longrightarrow C_3H_5 + C_3H_6 \quad (7)$$

$$\longrightarrow CH_3 + \text{1,4-pentadiene} \quad (8)$$

$$\longrightarrow C_2H_5 + \text{1,3-butadiene} \quad (9)$$

$$\longrightarrow C_4H_7 + C_2H_4 \quad (10)$$

pose thermally[24,25] and these four reactions have been proposed[24] to account for the products observed in the pyrolysis at temperatures around 400°. Allyl is a major radical in the pyrolysis as it is in the photolysis. One drawback of this mechanism is that it requires the propylene yield to be comparable to the allyl yield, whereas it is reported to be much less; further 1,4-pentadiene has not been reported as a product.[23] An advantage of this scheme over the former is that it readily accounts for the fact that the only radical formed in the liquid-phase photolysis is cyclohexyl.[26] In the liquid the excited $C_6H_{11}^*$ species would be stabilized to cyclohexyl radicals precluding the formation of fragment radicals. The first mechanism suggests that hexenes will be products at high pressures and in the liquid.[27]

The cyclohexyl radicals that are detected at the pressures studied are probably not primary species formed from $C_6H_{11}^*$ but are secondary species formed by hydrogen atom abstraction. The observed increase in yield of cyclohexyl radicals with pressure is a result of the increased importance of abstraction relative to other reactions of hydrogen atoms. For example, the number of hydrogen atoms which react with methyl iodide, reaction 11, decreases with increasing pressure

$$H + {}^{14}CH_3I \longrightarrow {}^{14}CH_3 + HI \quad (11)$$

since the methyl iodide concentration remained constant at 0.03 Torr for most of the runs.

In the photolysis of cyclohexene a majority of the radicals are cyclic. The 3-cyclohexenyl radicals can be accounted for by process 12 which results in cleavage of an allylic carbon–hydrogen bond. Hydrogen atoms would be expected to add to cyclohexene, reac-

$$C_6H_{10} + h\nu \longrightarrow H + C_6H_9^* \quad (12)$$

$$H + C_6H_{10} \longrightarrow C_6H_{11} \quad (13)$$

tion 13, to form the observed cyclohexyl radicals and also to react with $^{14}CH_3I$, reaction 11. This competition accounts for the decrease in yield of cyclohexyl radicals with increasing methyl iodide pressure at any particular cyclohexene pressure.

The ratio $\phi(C_6H_9)/\phi(C_6H_{11})$ increases slightly with increasing pressure at 1% $^{14}CH_3I$. This can be accounted for if the $C_6H_9^*$ species formed in reaction 12 fragments at low pressure, reaction 14, and is sta-

$$C_6H_9^* \longrightarrow H + C_6H_8 \quad (14)$$

bilized by collisions at higher pressures.

Fragment radicals are less important in the photolysis of cyclohexene than in cyclohexane. The species $C_6H_{10}^*$, $C_6H_{11}^*$, and $C_6H_9^*$ are expected to be present and should be considered as a source of these radicals. The $C_6H_{10}^*$ species might conceivably split into two C_3H_5 radicals, for example, but this possibility is considered unlikely since excited $C_6H_{10}^*$ is known to decompose to ethylene and butadiene, and this process accounts for the main products of the photolysis of cyclohexene.

Another possibility is fragmentation of $C_6H_9^*$ in reactions parallel to 14 such as reactions 15 and 16.

$$C_6H_9^* \longrightarrow C_3H_5 + C_3H_4 \quad (15)$$

$$\longrightarrow CH_3 + C_5H_6 \quad (16)$$

This mechanism would require the yields of fragment radicals to decrease with increasing pressure. Since the yields of fragments relative to the yield of C_6H_9 radicals does decrease at higher pressures this mechanism cannot be ruled out.

The fragment radicals are the same as those observed in the photolysis of cyclohexane which suggests that a common intermediate such as $C_6H_{11}^*$ may be involved. Excited cyclohexyl radicals are formed in reaction 13, and it is known that alkyl radicals formed in this way do decompose into olefins and fragment radicals.[28] However, consideration of the excitation

(23) We are indebted to one of the referees for pointing this out.

(24) S. Arai, S. Sato, and S. Shida, *J. Chem. Phys.*, **33**, 1277 (1960).

(25) A. S. Gordon, *Pure Appl. Chem.*, **5**, 441 (1962).

(26) J. A. Yang, F. M. Servedio, and R. A. Holroyd, *J. Chem. Phys.*, **48**, 1331 (1968).

(27) Hexene-1 is a product of the photolysis of the solid at 77°K, private communication, P. Ausloos.

energy gained by hydrogen atom addition and the minimum energy required for reactions 7–10 would suggest the rate of decomposition to be too slow and stabilization to cyclohexyl radicals by collision predominate at the pressures involved. If the hydrogen atom were translationally excited, however, the C_6H_{11}* might be sufficiently activated to decompose.

To summarize, radical intermediates have been detected in the photolysis of cyclohexene and cyclohexane by esr spectroscopy and $^{14}CH_3$-radical sampling. The results for cyclohexane agree with those obtained with H_2S as a scavenger except that a higher yield of allyl radicals is observed here. This is clearly illustrated by the esr results. Allyl radicals are a major radical in the photolysis of cyclohexane and may be formed in other hydrocarbons as well.[29]

(28) B. S. Rabinovitch and D. W. Setser, *Advan. Photochem.*, **3**, 1 (1964).

(29) The formation of allyl radicals in cyclohexane is not a unique case; allyl radicals are also of major importance in the photolysis of neopentane (M. D. Sevilla and R. A. Holroyd, unpublished results).

Electronic Transitions in Phenylboronic Acids. I. Substituent and Solvent Effects

by Brian G. Ramsey

Departments of Chemistry, The University of Akron, Akron, Ohio, and San Francisco State College, San Francisco, California *(Received May 22, 1969)*

On the basis of substituent effects, it is concluded that the first intense transition in the spectra of substituted phenylboronic acids is not charge transfer but is ^1L_a. These ^1L_a transitions of phenylboronic acids exhibit an anomalous solvent effect in that the transition moves to higher energy with a change to more polar solvent. This may be accounted for by substantial, but less than 50%, charge-transfer character in the ^1L_a transition. The Goodman criteria for vacant "d" orbitals was applied to aryl boranes and found correct. Simple Hückel molecular orbital calculations are in agreement with experimental results.

Introduction

Studies of the effect of simple substituents on the electronic transitions of benzene are, for theoretical reasons, intrinsically interesting, but there has been no published systematic study of the effect of substituent or solvent on the spectra of arylboronic acids $ArB(OH)_2$. The few spectra reported[1] in the literature for phenylboronic acids possess a strong absorption maximum in the range 220–250 nm depending on the substituent. Armstrong and Perkins,[2] on the basis of Pariser–Parr–Pople self-consistent field calculations, concluded that the first four absorption maxima reported for phenylboronic acid corresponded to $^1B_{2u}$, $^1B_{1u}$, and $^1E_{1u}$ benzene states.

An alternative interpretation of the second tansition is possible since the triarylboranes, such as $(C_6H_5)_3B$, exhibit an intense intramolecular charge-transfer (CT) transition near 300 nm.[3,4] By analogy, it was possible that the first intense transitions of $RC_6H_4B(OH)_2$ might also be best characterized as intramolecular charge transfer, since molecular orbital calculations by Armstrong and Perkins[4b] on $(C_6H_5)_3B$ fail to predict observed transition energies and charge-transfer character in the spectrum of $(C_6H_5)_3B$.

The *para*-substituted phenylboronic acids belong to the C_{2v} point group, and if we consider an approximation of completely localized group orbitals with zero overlap, the highest filled benzene orbitals transform as A_1 and B_2 where the vacant $-BO_2$ orbital transforms as A_1. The possible CT transitions are therefore $^1A_1 \rightarrow {}^1A_1$ and $^1A_1 \rightarrow {}^1B_2$, and allowed. The localized benzene transitions possess the symmetry ^1L_a ($^1A_1 \rightarrow {}^1A_1$) and ^1L_b ($^1A_1 \rightarrow {}^1B_2$) and mixing be-

(1) (a) A. N. Nikitina, V. A. Vaver, N. S. Fedotov, and B. M. Mikhailov, *Opt. Spectrom.*, **7**, 389 (1959); (b) A. N. Nikitina, V. A. Petukhov, A. F. Galkin, N. S. Fedotov, Yu. N. Bubnov, and P. M. Aronovich, *ibid.*, **16**, 528 (1964).

(2) D. R. Armstrong and P. G. Perkins, *J. Chem. Soc., A*, 123 (1967).

(3) B. G. Ramsey, *J. Phys. Chem.*, **70**, 611 (1966).

(4) (a) T. J. Weismann, 155th Meeting American Chemical Society, San Francisco, 1968, 150th Meeting American Chemical Society, Atlantic City, N. J., 1965; (b) *Theoret. Chim. Acta*, **8**, 138 (1967).

tween these states and CT states of the same symmetry would be expected.

It seemed reasonable that a distinction between these two possibilities could be made on the basis of substituent and solvent effects on the transition in question. Charge-transfer transitions, both intra- and intermolecular, exhibit a linear correlation between the observed transition energy and the ionization potential of the donor portion of the molecule or complex.[5] This is not true for ^1L_a transitions. The ^1L_a transitions of benzene and substituted benzenes are well known to undergo shifts to lower energy when the change is made from nonpolar to polar solvents. The opposite solvent effect on transition energy has been observed for the charge-transfer transitions of triarylboranes.[3,6]

The spectra of $R-C_6H_4B(OH)_2$ also offer a unique possibility of testing the Goodman substituent interference effect criteria[7] for the presence of low-lying vacant orbitals. On a theoretical basis Goodman and coworkers[7] predicted that if RC_6H_5 were substituted in the *para* position by a metal atom functional group (M) possessing a vacant orbital slightly higher in energy than the lowest vacant benzene orbitals, the ^1L_b transition intensity of RC_6H_4M would be less than that of the most intense ^1L_b transition of the pair C_6H_5M or RC_6H_5. This criterion has been widely applied[8] to the controversy surrounding "d" orbitals, as proof of the importance of "d" orbital interaction in the excited states of phenyl derivatives of groups IVA, VA, VIA. The criterion has not, however, been tested in any case where it is generally accepted that vacant atomic orbital in question is low enough energy to be significantly involved. The importance of p–p π bonding in boranes is well established and would provide the needed test.

Experimental Section

The phenylboronic acids whose spectra are reported below were synthesized by reaction of the appropriate Grignard reagent with $(CH_3O)_3B$ according to the method of Bean and Johnson,[9] with the exception of *p*-bromo- and *m*-nitrophenylboronic acids which were purchased from Aldrich Chemical. The boronic acids were recrystallized twice from benzene and once from water. Where the anhydride was desired a third recrystallization from benzene after azeotropic removal of the water was carried out.

Solvents used were Matheson Coleman and Bell Spectro-quality hexane and acetonitrile, and distilled water.

Spectra were taken in 1.0-cm and 0.1-nm path length quartz cells using Perkin-Elmer Model 450 recording or Cary Model 14 spectrophotometers.

Where extinction coefficients could be compared with the literature,[10] agreement was satisfactory. Because of poor solubility publishable extinction coefficients were sometimes not obtained in hexane. The results are reported as in Table I.

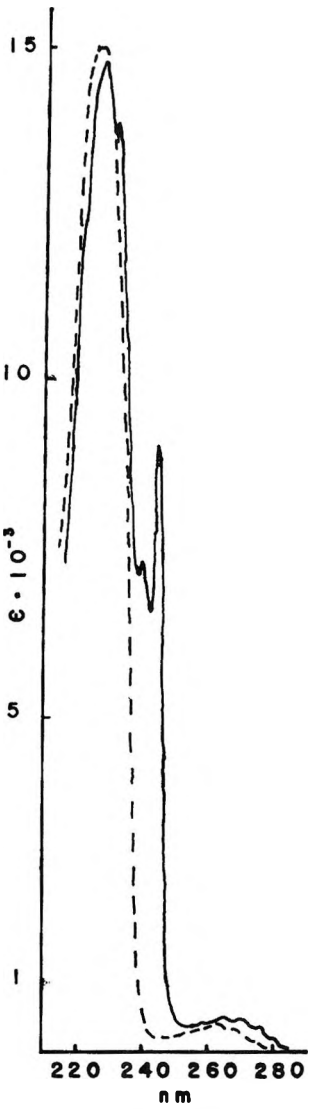

Figure 1. The spectrum of p-$CH_3C_6H_4B(OH)_2$ in hexane (——) and water (– – – –).

Intrigued by the absence in the literature of any comments on a difference in ultraviolet spectra between phenylboronic acids and their anhydrides, we compared the spectra of the anhydrides of p-$BrC_6H_5B(OH)_2$ and p-$CH_3OC_6H_4B(OH)_2$ in hexane and acetonitrile

(5) (a) J. N. Murrell, "The Theory of Electronic Spectra of Organic Molecules," John Wiley and Sons, New York, N. Y., 1963; (b) J. N. Murrell, *Quart. Rev.*, **2**, 191 (1961).

(6) J. L. R. Williams, P. J. Grisdale, and J. C. Doty, *J. Amer. Chem. Soc.*, **89**, 4538 (1967).

(7) L. Goodman, A. Konstam, and L. H. Sommer, *ibid.*, **87**, 1013 (1965).

(8) (a) L. Goodman and R. W. Taft, *ibid.*, **87**, 4385 (1965); (b) J. E. Bisssy, and H. Goldwhite, *Tetrahedron Lett.*, 3247 (1966); (c) W. K. Musker and G. B. Savitsky, *J. Phys. Chem.*, 71, 431 (1967).

(9) F. R. Bean and J. R. Johnson, *J. Amer. Chem. Soc.*, **54**, 4415 (1932).

(10) K. V. Nahabedian and H. G. Kuivila, *ibid.*, **83**, 2167 (1961); (λ_{max} were not reported).

Table I

$RC_6H_4B(OH)_2$ R	λ max, nm (molar extinction coefficients × 10^{-3}) ^1B	^1L_a	^1L_b	Solvent
m-NO_2	212	255		Hexane
m-NO_2	210 (19.5)	264 (7.35)		CH_3CN
m-NO_2	208 (13.5)	269 (6.6)		H_2O
m-CH_3	197	217.0, 222.5, 238.8	272.7, 280.0, 286 sh	Hexane
m-CH_3	195 (50)	216.5 (9.0)	271 (0.83), 277 sh	H_2O
m-CH_3O	202 (34)	224.5 (6.8), 243 sh	283 (2.0), 292 sh	Hexane
m-CH_3O	198.5 (39)	221.2 (7.4)	282.2 (2.1)	H_2O
H		216 (7.1)	265 (0.401)	H_2O
H	194[a]	220 (9.52), 235 (1.49)	262 (0.11), 267 (0.45), 274 (0.37)	Hexane
p-CH_3	196.8 (20)	226.8 (15.0), 231.8 sh, 238.6 (7.3), 244.1 (9.2)	262 (0.40)	Hexane
p-CH_3	195 (32)	225.2 (15.2)	263 (0.354)	H_2O
p-CH_3O	200, 205 sh 211 sh	239.5, 252.4, 256.5	270, 280	Hexane
p-CH_3O	199 (30)	236.5 (12)	264 sh, 272 (1.0), 280 (0.83)	CH_3CN
p-CH_3O		235.5 (11)	261.9, 269.2 (0.88), 278.1	H_2O
p-Br	198 (40)	234.2 (15), 238.8 (15), 252.6 (6.3)	267 (0.6)	Hexane
p-Br	198 (9.5)	232 (3.6)	266 (0.5)	CH_3CN
p-Br	197 (32)	231 (13)	265 (0.6)	H_2O
p-F	197 (48)	230 sh, 232.5 (22), 237 (24)	256, 262.5 (0.8), 269.5	Hexane
o-CH_3		217 (9.18), 242 (2.53)	273 (0.93), 277 (0.80)	Hexane
o-CH_3		210 sh (8.41)	267 (0.54), 270 (0.54)	H_2O
2,4,6-$(CH_3)_3$	203 (55)	218 sh (8.72)	270 (0.27)	Hexane
2,4,6-$(CH_3)_3$	201 (48.2)	217 sh (8.32)	267 (0.29)	H_2O
p-$(CH_3)_2N$ (anhydride)[b]	198 (25)	221.6 (13), 285 (22)	302 (30)[c]	Hexane
p-$(CH_3)_2N$ anhydride	198 (21.9)	222.2 (10.2), 304 (30.6)		CH_3CN

[a] Taken from ref 1. [b] Molar extinction coefficient of anhydride based on mol wt of 147. [c] Apparent ε of ^1L_b transition superimposed on dimethylaniline type CT transition.

with the spectra of the corresponding acids in the same solvents and found no discernible difference in spectra. Infrared spectra of boronic acids in acetonitrile did not indicate loss of water by the acid to form anhydride.

Results and Discussion

General. With the exception of *m*-nitro- and *p*-dimethylaminophenylboronic acid, the ultraviolet spectra of the substituted phenylboronic acids are all similar in their general appearance and the spectrum of *p*-tolylboronic acid is given in Figure 1 as an example.

In all of the boronic acids $RC_6H_4B(OH)_2$ (except R equals NO_2 or $N(CH_3)_2$) the first observed transition may be readily identified by virtue of its typical vibrational structure and intensity as the usual ^1L_b benzenoid transition. A second rather evident conclusion is that all of the maxima at 226.8, 231.8, 238.6, and 244.1 nm in the spectra *p*-$CH_3C_6H_4B(OH)_2$ and similar maxima in the spectra of other phenylboronic acids in hexane, are vibrational structure of the same electronic transition. Armstrong and Perkins[2] have therefore mistakenly assigned the 235-nm and 220-nm maximum to separate transitions ^1L_a and ^1B, respectively, an error which is clearly the consequence of Armstrong and Perkins not having the experimental spectra available. Agreement between calculated and observed transition energies is much better than realized by Armstrong and Perkins.

Substituent Effects. Ideally one would like to examine the effect of substituent on the zero–zero transition. However, for a large nonvolatile molecule whose spectrum must be taken in solution and where an emission spectrum cannot be obtained, it is usually impossible to unambiguously assign the zero–zero transition. We therefore make the common assumption that the substituent effect on the absorption maximum of the envelope will parallel the effect on the zero–zero transition energy.

The energy of a charge-transfer transition is to a good approximation[5] given by eq 1.

$$E_{CT} = I_p - E_a - C \quad (1)$$

in which I_p represents the donor group ionization potential, E_a is the acceptor group electron affinity, and C is an electrostatic work term (e^2/r). In the case of the phenylboronic acids, $RC_6H_4B(OH)_2$, donor group is RC_6H_4 and the acceptor would be the lowest vacant orbital of $-B(OH)_2$. If a linear correlation between the transition energy of the 220–250-nm absorption band of p-$RC_6H_4B(OH)_2$ and the ionization potential of RC_6H_5 as required by eq 1 were observed, we could properly term the transition, charge transfer. In fact, such a correlation is extremely poor even when limited to mono *para*-substituted phenylboronic acids.

A second substituent effect criterion which has been used to assign intramolecular charge-transfer transitions between aryl rings and p-π donor or acceptor substituents is a decrease in transition intensity with increasing steric hindrance at *ortho* positions which forces the donor or acceptor group orbitals out of the plane of the aromatic ring. For example, the large decrease in intensity of the N,N-dimethylaniline 250-nm transition with increasing alkyl substitution and steric hindrance at the *ortho* positions has been used to assign this transition to an intramolecular charge-transfer transition and to calculate the twist angle between the aryl ring and the dimethylamino group.[11] A similar decrease but of smaller magnitude in the charge-transfer transition intensity of triarylboranes is observed between triphenyl- and trimesitylboron.[3]

By contrast, the molar extinction coefficients of the first intense transitions of $C_6H_5B(OH)_2$ (H_2O 8,700; hexane 9,523) and p-$C_6H_4B(OH)_2$ (H_2O 8,300; hexane 9,177) are not significantly different from those of o-$CH_3C_6H_4B(OH)_2$ (H_2O 8,410; hexane 9,177) or 2,4,6-$(CH_3)_3C_6H_2B(OH)_2$ (H_2O 8,320; hexane 8,720). We therefore conclude that the 210 to 240-nm transition of the phenylboronic acids is ^1L_a and not charge transfer in spite of an unusual solvent effect on the transition energy discussed below.

The spectrum of p-N,N-dimethylaminophenylboronic acid anhydride (Figure 2) is quite different from, and a first sight may appear unrelated to, the spectra of the other *para*-substituted phenylboronic acids or anhydrides. However, as the following arguments are intended to show, the absorption maxima of the *para* dimethylamino derivative can be related in simple qualitative fashion to the transitions of both N,N-dimethylaniline and phenylboronic acid. Murrell and coworkers[5,12] have shown that good agreement between calculated and observed ultraviolet transition energies of aniline and similar molecules can be obtained from a perturbation calculation on a localized transition model beginning with localized benzene excited states and charge-transfer states followed by mixing under a perturbation

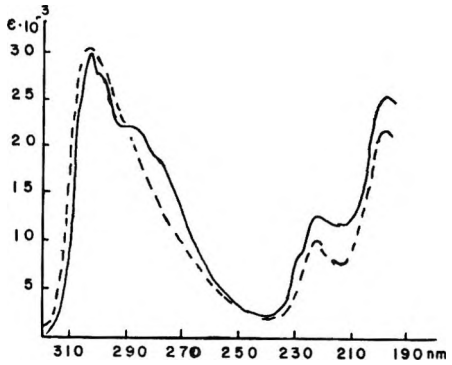

Figure 2. The spectrum of p-$(CH_3)_2NC_6H_4B{=}O$ in hexane (——) and acetonitrile (– – – –).

interaction between states of the same symmetry. The same method has been used to describe the transitions of phenylarsines.[13] Presumably then a similar approach can be applied to the ^1L_a and $^1A_1$ CT electronic transitions of N,N-dimethylaminophenylboronic acid or anhydride. To do this, however, it is necessary to have some estimate of the ^1L_a and $^1A_1$ charge-state transition energies in the absence of mixing between them. Equation 1 could be used to calculate a zero-order charge-transfer $^1A_1$ transition energy, provided a value for the electron affinity of N,N-dimethylamino phenylboronic acid were available. For the qualitative arguments here, however, it should be sufficient to take the zero-order approximation to the $^1A_1$ charge-transfer transition of p-dimethylaminophenylboronic acid as equal to that observed experimentally for N,N-dimethylaniline at (λ_{max} 251 nm) or about 40,000 cm^{-1}. Next, it is necessary to have a transition energy for the ^1L_a boronic acid transition in the absence of mixing with the charge-transfer state. Schubert[14] and coworkers, and Buraway and Thompson[15] concluded that *para*-substituent effects in electronic transition energies of p-halonitrobenzenes, p-haloanisoles, p-haloacetophenones, and p-alkylnitrobenzenes depended primarily on the polarizability of the substituents. Assignment of the 254-nm transitioe of thioanisole to ^1L_a also becomes reasonable relativn to the ^1L_a transition of anisole on the basis of the greater polarizability of CH_3S compared to CH_3O.

(11) (a) E. G. McRae and L. Goodman, *J. Mol. Spectrosc.*, **2**, 464 (1958); (b) J. N. Murrell, *J. Chem. Soc.*, 3779 (1956); (c) B. M. Wepster, *Rec. Trav. Chim.*, **73**, 661 (1953); *ibid.*, **76**, 335, 357 (1957); (d) H. B. Klevens and J. R. Platt, *J. Amer. Chem. Soc.*, **71**, 1714 (1949).

(12) M. Godfrey and J. N. Murrell, *Proc. Roy. Soc., Ser. A*, **278**, 57, 64 (1964).

(13) (a) W. R. Cullen, B. R. Green, and R. M. Hochstrasser, *J. Inorg. Nucl. Chem.*, **27**, 641 (1965); (b) W. R. Cullen and R. M. Hochstrasser, *J. Mol. Spectrosc.*, **5**, 118 (1960); (c) B. C. Ramsey, "Electronic Transitions in Organometalloids," Academic Press, New York, N. Y., 1969, p 172.

(14) (a) W. M. Schubert, J. M. Craven, and H. Steadly, *J. Amer. Chem. Soc.*, **81**, 2695 (1959); (b) W. M. Schubert and J. Robins, *ibid.*, **80**, 559 (1958).

(15) A. Buraway and A. R. Thompson, *J. Chem. Soc.*, 4314 (1956).

Taft and Lampe[16] found an unprecedented order of substituent effects in the ability of a substituent R to stabilize the methyl cation RCH_2^+ in the gas phase. For instance, $CH_3SCH_2^+$ was more stable than $CH_3OCH_2^+$ and $BrCH_2^+$ was more stable than FCH_2^+. In the absence of solvent capable of stabilizing positive charge, the polarizability of R appears to play the major role in stabilization of the cation RCH_2^+. We have noted[17] that although the ^1L_a transition energies of nine[18] *p*-RC_6H_4CHO and the above *p*-R-$C_6H_4B(OH)_2$ or anhydride ($R \neq N(CH_3)_2$) in hydrocarbon solvent show only a very poor correlation with substituent parameters such as Hammett σ^+ or $(\sigma_p - \sigma_m)$, a very good correlation of these ^1L_a transition energies is obtained with the relative gas-phase mass spectroscopic stabilization energies[16] of RCH_2^+. This correlation of ^1L_a transition energies with RCH_2^+ stabilization energies predicts a ^1L_a transition energy for *p*-dimethylaminophenylboronic acid anhydride of 250 nm(40,000 cm^{-1}) *in the absence of formal interaction between the* ^1L_a *state and the CT state involving the* $(CH_3)_2$ *N group*. In a Murrell type calculation based on the above localized initial ^1L_a and $^1A_1$ CT state energies which are very nearly degenerate, the final states, which would be neither pure ^1L_a or charge transfer but approximately an equal mixture of both, would be found at equal energies split above and below 250 nm (40,000 cm^{-1}). On this basis the strong absorption maxima at 285 nm (35,000 cm^{-1}) and at 222 nm (45,000 cm^{-1}) in the spectrum of N,N-dimethylaminophenylboronic acid anhydride can at least in a formal sense, be related to the first N,N-dimethylaniline charge-transfer transition and to the ^1L_a phenylboronic acid transitions, respectively. As may be seen (Figure 2), a solvent change from hexane to acetonitrile shifts the 285-nm transition to the red, whereas a very slight blue shift is observed on the 222-nm transition. The absorption maximum at 302 nm is probably the ^1L_b transition emerging from the long wavelength side of the more intense 285-nm transition. The ^1L_b transition of N,N-dimethylaniline is found at 296 nm by way of comparison.

Solvent Effects. J. N. Murrell,[5] among others, has suggested that a further characteristic of charge-transfer bands should be their wavelength sensitivity to solvent polarity because of a highly polar excited state relative to the ground state, but our own results indicate this may not be the most reliable criterion.

The use of solvent effects on electronic transition energy to assign transitions is certainly common; it is standard textbook knowledge that $n \rightarrow \pi^*$ transitions blue shift and $\pi \rightarrow \pi^*$ transitions red shift when the solvent is charged from hexane to a more polar solvent, such as water. The nitro group is π electron withdrawing, as is the $-B(OR)_2$ group, and the ^1L_a transition of nitrobenzene[19] is *red shifted* by 14 nm on changing solvent from hexane to water. Contrasting sharply with this is a 5–8-nm *blue* shift in the 220–240-nm absorption maxima of $RC_6H_4B(OH)_2$ ($R \neq NO_2$) with a solvent change from hexane to acetonitrile or water. The 236 nm maximum of *p*-$CH_3OC_6H_4B(OH)_2$ in aqueous KOH disappears entirely, or at any rate, is shifted below 210 nm. These results are similar in direction and magnitude to the solvent effects found on the charge-transfer transition energy of the triarylboranes[3,6] and clearly support the presence of significant charge-transfer character in the ^1L_a transition due to configuration interaction.

If we regard the excited state of the observed transition as the result of configuration interaction between a ^1L_a excited state and a slightly higher energy CT state, an increase in the energy of the the CT state due to change in solvent would also result in a higher energy excited state in the nominally ^1L_a transition by reducing the amount of interaction between the CT and ^1L_a configurations because of poorer energy matching between the ^1L_a and CT states. The solvent effect on the charge-transfer transition, and in turn the ^1L_a transition, can be easily understood in terms of weak bonding by the $B(OH)_2$ group to solvent lone pair electrons which reduces the $B(OH)_2$ electron affinity and thereby increases the charge-transfer transition energy. The absence of any significant solvent effect on the ^1L_a transition of the highly sterically hindered mesitylboronic acid is in accord with this interpretation, since the two *ortho* methyl groups effectively shield the boron vacant 2p orbital from the solvent molecules.

The band widths of the ^1L_a transitions in hexane are greater than in water, and the possibility that two transitions existed between 210 and 250 nm was considered. However, semiempirical molecular orbital calculations including configuration interaction on phenylboronic acids[20] do not predict two electronic transitions in this range, a fact which can be qualitatively predicted by the observation that both the ^1L_a and first CT states are of the same symmetry and are kept apart energetically by configuration interaction. The possibility of an $n \rightarrow \pi^*$ transition originating from the oxygen nonbonding lone pair of electrons seems ruled out by the absence of a similar transition in alkyl[21] or vinyl boronic acids.[22]

Intensities. The ^1L_b transition intensities in the

(16) R. W. Taft, R. H. Martin, and F. W. Lampe, *J. Amer. Chem. Soc.*, **87**, 2490 (1965).

(17) B. G. Ramsey, unpublished results.

(18) J. C. Rearden and W. F. Forbes, *Can. J. Chem.*, **36**, 1362 (1958).

(19) H. E. Ungenade, *J. Amer. Chem. Soc.*, **75**, 432 (1953).

(20) B. G. Ramsey and H. Ito, *Theor. Chim. Acta*, in press.

(21) T. D. Coyle, S. L. Stafford, and F. G. A. Stone, *J. Chem. Soc.*, 3103 (1961).

(22) D. S. Matteson and G. D. Schaumberg, *J. Amer. Chem. Soc.*, **82**, 4231 (1960).

spectra of *para*-substituted phenylboronic acids are also of interest. Goodman, Konstam, and Sommer[7] have derived a first-order approximation for the intensity of a slightly perturbed benzene ^1L_b transition which predicts that for p-X-C_6H_4-Y if X is π electron donating and Y is net π electron withdrawing by virtue of a lowest vacant π orbital higher in energy than the degenerate lowest vacant benzene orbitals, then the p-X-C_6H_4-Y $^1L^b$ transition intensity will be *less than* that of the *most intense* monosubstituted, C_6H_5Y or C_6H_5X, benzene ^1L_b transition. This criterion has been widely[8] used to test the importance of a d–p π bonding in the excited state of phenyl derivatives of groups IV, V, VI, and VIIA. For example,[8a] the measured oscillator strengths $CH_3OC_6H_5$ (20.0×10^{-3}), $C_6H_5SiH_3$ (3.56×10^{-3}), and p-CH_3-$OC_6H_4SiH_3$ (17.75×10^{-3}) are said to demonstrate that in the excited state the SiH_3 group withdraws electrons into the Si 3d orbitals. The theoretically derived Goodman "substituent interference" criterion for d orbital π participation has not, however, to our knowledge been previously tested with a substituent where the availability of a low-lying vacant orbital, such as, the vacant boron 2p, is generally agreed upon and uncontested. It is important, therefore, to find that the ^1L_b molar extinction coefficients in water for anisole (1,500), phenylboronic acid (401) and p-$CH_3OC_6H_4B(OH)_2$ (800), or toluene (225) and p-$CH_3C_6H_4B(OH)_2$ (354) are in agreement with the prediction of Goodman and coworkers.[19] Although Goodman and coworkers did not point it out, if the substituent vacant orbital, in this case the $B(OH)_2$ group orbital, is lower in energy than the vacant degenerate benzene orbitals, the ^1L_b transition intensities would be predicted to be greater for the *para* methyl and methoxyl substituted phenylboronic acids than either monosubstituted benzene.

Molecular Orbital Calculations. We wished to establish whether the assignment of 220–240 nm transition of phenylboronic acids and anhydrides to a ^1L_a transition while at the same time assigning the first observed transition in the triarylboranes to charge transfer, could be made consistent with the predictions of simple molecular orbital theory. Although the most widely used value for the Coulomb integral, α, for boron is that recommended by Streitwieser[18] $\alpha_B = \alpha^0 - 1.0\beta^0$ *or greater*, we have already pointed out[3] that the observation of a charge-transfer transition in the spectrum of triphenylboron required in simple LCAO MO calculations a Coulomb integral for boron *less than* that of the lowest degenerate benzene orbitals of benzene and suggested a value of $\alpha_B = \alpha^0 - 0.9\beta^0$.

Figure 3 is a correlation diagram which summarizes the results of a simple Hückel molecular orbital calculation on $C_6H_5B(OH)_2$ and $-B(OH)_2$. Numbers to the left indicate energies in units of the C–C resonance integral β^0; numbers to the right and in parentheses are

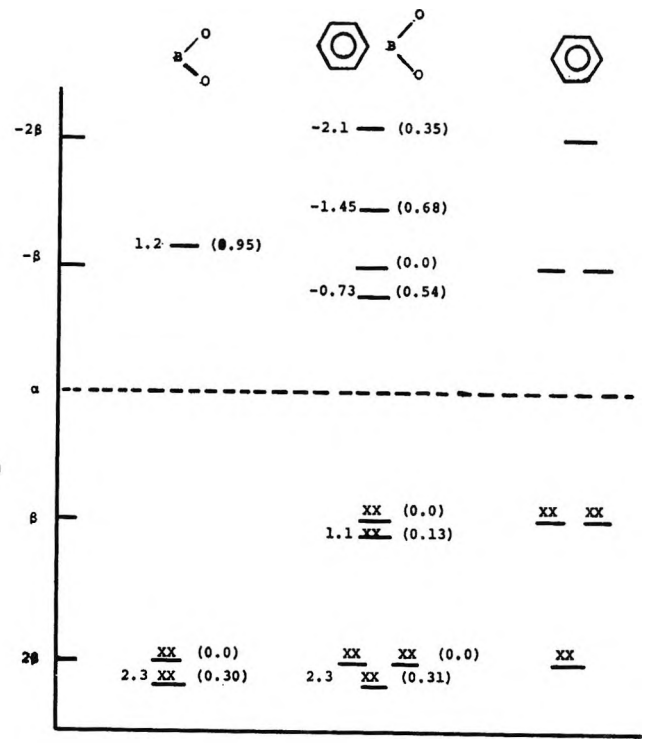

Figure 3. The Hückel molecular-orbital energies in units of β, and boron 2p atomic orbital mixing coefficients (in parenthesis) of BO_2, $C_6H_5BO_2$, and C_6H_6.

the boron atomic orbital mixing coefficients in the molecular orbital. The parameters chosen with the exception of boron were those recommended by Streitwieser:[18] $\alpha_B = \alpha^0 - 0.9\beta^0$, $\alpha_O = \alpha^0 + 2.0\beta^0$, $k_{BO} = 0.7$.

The conclusion reached is that although "perturbation" of the vacant degenerate benzene orbitals by a vacant boron orbital gives rise to a lowest vacant molecular orbital with a large boron mixing coefficient and the observation of a charge-transfer transition, the lowest vacant BO_2 *group* orbital is *higher* in energy than the vacant benzene orbitals with the net result that the two lowest vacant $C_6H_5B(OH)_2$ orbitals have relatively small boron mixing coefficients. On the basis of the simple Hückel approach we would predict that electronic transitions to the lowest vacant molecular orbital of phenylboronic acid would have 25% charge-transfer character. Thus, it may be seen that the simple molecular orbital calculations simultaneously support the proposed CT and ^1L_a assignments in the spectra of triarylboranes and phenylboronic acids, respectively. It is certainly not unreasonable that 25% CT character in the ^1L_a transition would result in the observed solvent effect on the transition.

Acknowledgments. We wish to thank Mr. Thomas H. Connors and Mrs. N. K. Das for preparing some of the boronic acids. This research was supported by the Office of Naval Research.

Kinetic Studies with Photogenerated Hydrated Electrons in Aqueous Systems Containing Nitrous Oxide, Hydrogen Peroxide, Methanol, or Ethanol[1]

by Bernard Hickel and Klaus H. Schmidt

Argonne National Laboratory, Argonne, Illinois 60439 *(Received December 23, 1969)*

With a recently developed, compact photoflash apparatus,[2] we studied the e_{aq}^-—OH—H—e_{aq}^- chain reaction in H_2-saturated solutions of NaOH into which submicromolar quantities of N_2O or H_2O_2 had been injected. The rate of disappearance of e_{aq}^- varied linearly with the injected amounts. The unexpectedly short chain lengths observed could be accounted for by the carbonate contamination of the NaOH. The chain lengths also varied with pH in the manner predicted from the proposed mechanism. No significant difference was found between the chain lengths obtained with N_2O and with H_2O_2 in comparable solutions. The large decrease in e_{aq}^- half-life which one observes when adding molar quantities of methanol or ethanol to NaOH–H_2 solutions can be considerably reduced by irradiating the mixture with a mercury lamp or a ^{60}Co source, thereby destroying impurities present in the alcohol. Using this procedure, we determined $k_{e_{aq}^-+MeOH} \leq 400\ M^{-1}\ sec^{-1}$ and $k_{e_{aq}^-+EtOH} \leq 400\ M^{-1}\ sec^{-1}$, values much lower than those previously reported.[3]

Introduction

If hydrated electrons are generated by a photoflash in a hydrogen-saturated solution of NaOH containing H_2O_2 or N_2O, one expects the following chain reaction: initiation

$$OH^- \xrightarrow[185\text{–}220\ m\mu]{h\nu} OH + e_{aq}^-\ ^4 \quad (1)$$

propagation

$$OH + H_2 \longrightarrow H + H_2O \qquad k_2 = 4.5 \times 10^7\ M^{-1}\ sec^{-1}\ ^3 \quad (2)$$

$$H + OH^- \longrightarrow e_{aq}^- \qquad k_3 = 2 \times 10^7\ M^{-1}\ sec^{-1}\ ^3 \quad (3)$$

$$e_{aq}^- + N_2O \longrightarrow N_2 + OH + OH^- \qquad k_{4a} = 9.1 \times 10^9\ M^{-1}\ sec^{-1}\ ^5 \quad (4a)$$

$$e_{aq}^- + H_2O_2 \longrightarrow OH + OH^- \qquad k_{4b} = 1.23 \times 10^{10}\ M^{-1}\ sec^{-1}\ ^6 \quad (4b)$$

termination[7]

$$e_{aq}^- + e_{aq}^- \longrightarrow H_2 + 2OH^- \qquad k_5 = 5.5 \times 10^9\ M^{-1}\ sec^{-1}\ ^8 \quad (5)$$

$$e_{aq}^- + OH \longrightarrow OH^- \qquad k_6 = 3 \times 10^{10}\ M^{-1}\ sec^{-1}\ ^3 \quad (6)$$

In previous experiments[2] a nonlinear relationship was observed between the amount of H_2O_2 injected and the pseudo-first-order decay constant of e_{aq}^-, which could not be explained by the above mechanism. We now regard this result as an artifact caused by the destruction of part of the injected H_2O_2 by the photoflashes.

During transient conductivity studies[8] on pulse-irradiated alkaline solutions containing H_2O_2, the formation of a negatively charged species with a half-life of about 0.3 sec, presumably from the reaction of e_{aq}^- with H_2O_2, was observed. Experiments with N_2O showed no evidence of such a species. Our present investigation, therefore, was to study the above-mentioned chain reactions involving H_2O_2 or N_2O, and to look for possible differences which might indicate a deviation from the assumed mechanism in the case of H_2O_2. Included in this study was a redetermination of the rate constants for the reaction of e_{aq}^- with methanol and ethanol, as we used these substances as scavengers of H and OH.

Experimental Section

Apparatus. For our experiments, we used the

(1) Based on work performed under the auspices of the U. S. Atomic Energy Commission. B. H. gratefully acknowledges the support of the Centre d'Etudes Nucléaires de Saclay, France, during his stay at Argonne.

(2) K. Schmidt and E. J. Hart, Advances in Chemistry Series, No. 81, American Chemical Society, Washington, D. C., 1968, p 267.

(3) M. Anbar and P. Neta, *Int. J. Appl. Radiat. Isotop.*, 18, 493 (1967).

(4) M. S. Matheson, W. A. Mulac, and J. Rabani, *J. Phys. Chem.*, 67, 2613 (1963).

(5) Our measurement at 27°.

(6) For 20–22°.[3] In our subsequent calculations, we shall use the value $1.35 \times 10^{10}\ M^{-1}\ sec^{-1}$ for 27°.

(7) The reactions of H with e_{aq}^- and OH are negligible because of the prevalence of reaction 3.

(8) K. H. Schmidt and S. M. Ander, *J. Phys. Chem.*, 73, 2846 (1969).

photoflash apparatus described in ref 3, with the following improvements: (1) The three-dimensional multiple-reflection optics were modified to avoid the reflection losses on the quartz–air interfaces. Figure 1s hows the new arrangement schematically. Two plano-convex lenses, silvered on the convex surface except for a 90° sector, now take the place of the concave mirrors described in ref 3. Their flat surfaces are in optical contact with the cell windows through a thin layer of immersion oil. The new arrangement transmits about 70% more light than the old one. (2) Flash irradiation and uv preirradiation of the cell are now independent of each other so that they can be carried out simultaneously if so desired.

Preparation of Solutions. The NaOH–H_2 matrix solutions and the H_2O_2 stock solutions used for injection were prepared as before.[2] N_2O stock solutions of about equivalent concentration were prepared in the following way. Triply distilled water was saturated with 98% pure N_2O (Matheson). This solution (0.5–5 ml) was then transferred with an all-glass syringe into a gas wash bottle[9] filled with about 250 ml of NaOH–H_2 matrix solution. H_2 bubbling was stopped immediately before injecting the concentrated N_2O solution. After injection, the bottle was shaken to ensure equilibrium between the N_2O in solution and in the gas phase. The N_2O concentration calculated under this assumption agreed sufficiently well with that determined by gas chromatography.

Irradiation Procedure and Evaluation. In both the H_2O_2 and N_2O experiments, the absorption cell was filled with the NaOH–H_2 matrix and preirradiated with the mercury lamp. At regular intervals, an e_{aq}^- concentration of *ca.* 10 n*M* was produced by a xenon flash and the e_{aq}^- half-life was determined. It usually reached a constant value of $t_{1/2}^0$ = 6–10 msec after 1–3 min of preirradiation. The shutter of the Hg lamp was then closed, the desired amount of H_2O_2 or N_2O stock solution injected into the cell, and, after stirring, the new half-life $t_{1/2}$ measured. From the two half-lives, we calculated the change $\Delta\lambda$ of the pseudo-first-order decay constant of e_{aq}^-

$$\Delta\lambda = k_{app}[X] = \ln 2(1/t_{1/2} - 1/t_{1/2}^0)^{10} \quad (7)$$

[X] is the concentration of H_2O_2 or N_2O in the cell and k_{app}, the apparent second-order rate constant of the observed reaction. Equation 7 is only an approximation, but a calculation shows that, even if $t_{1/2}^0$ is predominantly determined by a second-order reaction, the error is less than 2%. There was, therefore, no need for the more detailed analysis of the decay curves described elsewhere.[2,11]

After each[12] injection, we cleaned the solution by irradiation with the Hg lamp. If the new $t_{1/2}^0$ did not closely approach the previous value, we filled the cell with fresh matrix solution.

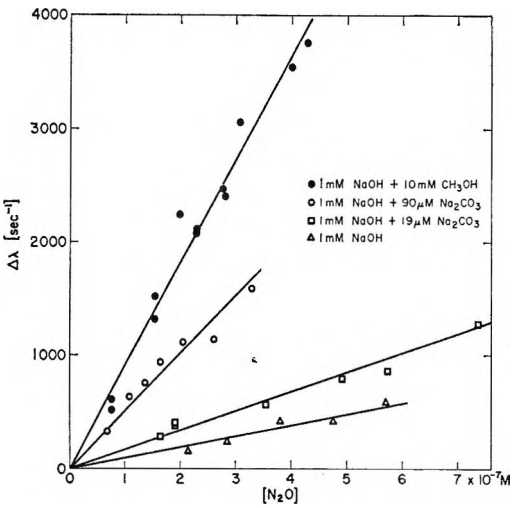

Figure 1. Effect of N_2O concentration on the pseudo-first-order decay of e_{aq}^- in different matrix solutions. All solutions are H_2 saturated. Ordinate: $\Delta\lambda = \ln 2(1/t_{1/2} - 1/t_{1/2}^0)$.

Alcohol Experiments. For the alcohol experiments, we used "absolute, pure" ethanol (U.S.I.) and methanol from different sources (see below). The alcohols were purged with H_2 and subsequently injected into the cell containing the NaOH–H_2 matrix solution. During injection, the contents of the cell was stirred so that the alcohol concentration in the overflow liquid could be taken into account. In a few cases, the alcohol was added to the matrix solution before filling the cell.

Results and Discussion

N_2O and H_2O_2 Experiments. In Figure 1, the increase $\Delta\lambda$ of the pseudo-first-order decay constant of e_{aq}^- is plotted *vs.* the injected amount of N_2O for different matrix solutions. $\Delta\lambda$ is proportional to [N_2O] in all cases. We obtained analogous results with H_2O_2, but for reasons of economy we shall omit the corresponding figure for H_2O_2. From the slopes, we calculated the apparent rate constant $k_{app} = \Delta\lambda/[X]$, X standing for N_2O or H_2O_2. k_{app}, is, in most cases, smaller than k_{4a} or k_{4b}, respectively, which indicates a chain reaction presumably consisting of reactions 4, 2, and 3. The chain length is defined as k_4/k_{app}, k_4 being identical with k_{4a} in the case of N_2O and with k_{4b}' in the case of H_2O_2. k_{4b}' is a linear combination of k_{4b} and k_8 determined by the pH. In our calculations we used $pK(H_2O_2)$ = 11.75.[13]

(9) Of the same kind as described in ref 2, except for an additional taper joint just below the neck, which was used for injecting the concentrated N_2O solution.

(10) E. J. Hart and E. M. Fielden, Advances in Chemistry Series, No. 50, American Chemical Society, Washington, D. C., 1965, p 253.

(11) K. H. Schmidt, Report ANL 7400, Argonne National Laboratory, Argonne, Ill., 1967.

(12) Contrary to the procedure described in ref 2.

(13) M. G. Evans and N. Uri, *Trans. Faraday Soc.*, **45**, 224 (1949).

Table I: Length of the e_{aq}^-—OH—H—e_{aq}^- Reaction Chain in Various Matrix Solutions Containing N_2O and H_2O_2

Matrix soln, μM			e_{aq}^- scavenger injected		$k_{apparent} \times 10^{-9}$,	Chain length		Carbonate contamination,
[NaOH]	[CH_3OH]	[Na_2CO_3]	N_2O	H_2O_2	M^{-1} sec^{-1}	Exptl[a]	Theoret[b]	calcd,[c] %
1	10	...	X	...	9.1	1.0[d]	1.0	...
1	1	...	...	X	12.0	1.02[e]	1.05	...
1	...	100	...	X	7.45	1.65[e]	2.15	...
1	...	90	X	...	5.1	1.8	2.3	...
1	...	19	X	...	1.7	5.35	7.0	...
1	...	...	X	...	0.96	9.5	...	2.8
1	...	...	...	X	1.35	9.0[e]	...	3.0
8	...	...	X	...	2.68	3.4	...	3.3
100	...	...	X	...	1.44	6.3	...	1.0
0.2	...	...	...	X	0.57	23.4[f]	...	6.3

[a] Defined as $k_{app}/k_{e_{aq}^- + N_2O}$ or k_{app}/k_{4b}', respectively. k_{4b}' is the effective rate constant calculated for the given pH, based on $pK(H_2O_2) = 11.75$, $k_{e_{aq}^- + H_2O_2} = 1.35 \times 10^{10}\ M^{-1}$ sec^{-1}, $k_{e_{aq}^- + HO_2^-} = 3.5 \times 10^9\ M^{-1}$ sec^{-1}. [b] Calculated disregarding involuntary contamination. [c] Given as $2[Na_2CO_3]/[NaOH]$, calculated from the observed chain lengths disregarding other impurities. [d] By definition, assuming $k_{app} = k_{e_{aq}^- + N_2O}$. [e] $k_{4b}' = 1.22 \times 10^{10}\ M^{-1}$ sec^{-1}. [f] $k_{4b}' = 1.32 \times 10^{10}\ M^{-1}$ sec^{-1}.

$$e_{aq}^- + HO_2^- \longrightarrow O^- + OH^- \qquad k_8 = 3.5 \times 10^9\ M^{-1}\ \text{sec}^{-1}\ [3] \quad (8)$$

As the literature values for k_{4a} vary between 5.6×10^9 M^{-1} sec^{-1} [3] and 9.4×10^9 M^{-1} sec^{-1}, [14] we used our own value of $k_{4a} = 9.1 \times 10^9\ M^{-1}$ sec^{-1} at 27° (see below).

All results are compiled in Table I. One observes that, in comparable matrix solutions, there is no significant difference between the respective chain lengths measured with N_2O and with H_2O_2. In our further discussion we shall therefore not distinguish between results obtained with either of the two solutes.

In the experiment listed in the first row of Table I, 10^{-2} M CH_3OH was added to the matrix to scavenge OH

$$OH + CH_3OH \longrightarrow CH_2OH + H_2O \qquad k_9 = 5 \times 10^8\ M^{-1}\ \text{sec}^{-1}\ [3] \quad (9)$$

In this case, more than 99% of the OH reacts with methanol, so that the chain reaction is completely suppressed, and $k_{app} = k_{4a} = 9.1 \times 10^9\ M^{-1}$ sec^{-1}. If Na_2CO_3 is added, the chain lengths decrease. This supports our assumption that the relative short chain length of 9–9.5 observed in 10^{-3} M NaOH solution (rows 6 and 7) is due to carbonate contamination of the NaOH.

pH Dependence. For a quantitative discussion of the effect of carbonate, one has to take into account the two equilibria

$$H^+ + CO_3^{2-} \rightleftharpoons HCO_3^- \qquad pK_{10} = 10.25 \quad (10)$$

$$OH + OH^- \rightleftharpoons H_2O + O^- \qquad pK_{11} = 11.9\ [15] \quad (11)$$

At low pH values (<8), we have essentially a competition between reaction 12 and reaction 2, $r = k_{12}/k_2$ determining the effect of carbonate on the chain length.

$$OH + HCO_3^- \longrightarrow H_2O + CO_3^- \qquad k_{12} = 1.5 \times 10^7\ [3] \quad (12)$$

$$OH + CO_3^{2-} \longrightarrow OH^- + CO_3^- \qquad k_{13} = 4.2 \times 10^8\ [3] \quad (13)$$

$$O^- + H_2 \longrightarrow OH^- + H \qquad k_{14} = 1.6 \times 10^8\ [3] \quad (14)$$

$$O^- + CO_3^{2-} \longrightarrow \text{products} \qquad k_{15} < 10^7\ [16] \quad (15)$$

As the pH is raised, there is increasing competition by reaction 13, and later by reactions 14 and 15. One obtains

$$r = \frac{k_{12}'}{k_2'} = \frac{k_{12} + q_1 k_{13} + q_2(1 + q_1)k_{15}}{k_2 + q_1 k_2 + q_2(1 + q_1)k_{14}}$$

where k_2' is the weighted means of k_2 and k_{14}, k_{12}' that of k_{12}, k_{13}, and k_{15}, $q_1 = [CO_3^{2-}]/[HCO_3^-]$, and $q_2 = [O^-]/[OH]$.

The relation between the chain length, L, and the carbonate concentration [Carb] = $[CO_3^{2-}] + [HCO_3^-]$ is

$$L = 1 + \frac{[H_2]}{r[\text{Carb}]} \quad (16)$$

For [NaOH] = 0.2, 1, 8, and 100 mM, one obtains r = 4.67, 5.51, 2.03, and 0.26, respectively. Using these values in eq 16, we calculated the theoretical chain lengths in rows 3–5 of Table I and the values for the carbonate contamination in rows 6–10 of the same table. The theoretical chain lengths agree sufficiently well with the experimental ones, if one considers the

(14) K. D. Asmus and J. H. Fendler, *J. Phys. Chem.*, **72**, 4285 (1968).

(15) J. Rabani and M. S. Matheson, *J. Amer. Chem. Soc.*, **86**, 317 (1964).

(16) J. L. Weeks and J. Rabani, *J. Phys. Chem.*, **70**, 2100 (1966).

additional involuntary carbonate contamination which is probably present. The calculated carbonate values are also reasonable: according to the manufacturer the NaOH pellets may contain up to 1% carbonate. Additional CO_2 from the air may be absorbed by the 20 M NaOH stock solutions as the solubility of Na_2CO_3 in this solution is *ca.* 0.4 M, *i.e.*, $2[CO_3^{2-}]/[Na^+] \leq 4\%$. At the lowest NaOH concentration (0.2 mM) the calculated $[HCO_3^-]$ is 6.3 μM. Carbonate determinations by conductometric titration or gas chromatography on duplicate solutions yielded similar values. Experiments with low-carbonate NaOH or $Ba(OH)_2$ solutions are in preparation.

The relatively small effect of carbonate on the chain length in 0.1 M NaOH agrees with the observations by Cheek and Swinnerton.[17]

Experiments with Methanol and Ethanol

General Observations. When, in preliminary experiments, we injected small amounts of methanol or ethanol into the cell containing the alkaline matrix solution, we observed a large reduction in e_{aq}^- half-life with poor reproducibility. If we then irradiated the cell with the mercury lamp, the e_{aq}^- half-life increased steadily, finally reaching a plateau after up to 2 hr of irradiation. The same plateau was obtained by irradiating the cell with 10–100 krads from a ^{60}Co source and subsequently with uv for a few minutes. Further uv irradiation for several hours did not alter the plateau in either case.

A conservative estimate, based on the rate of oxygen removal from the matrix solution, shows that irradiation with the Hg lamp produces less than 10^{-4} M of e_{aq}^- in 2 hr. Thus, the possible destruction of alcohol by this process is entirely negligible, and consequently the observed increase in e_{aq}^- half-life is solely due to the removal of impurities introduced with the alcohol. The quantitative results reported below will, therefore, be based on the above-mentioned plateau values.

Quantitative Results. Methanol. In solutions containing methanol, the first-order decay constant for e_{aq}^- is

$$\lambda = k_{17}[H_2O] + k_{18}[CH_3OH] + k_{19}[Imp] + k_{19}'[Imp']$$

$$e_{aq}^- + H_2O \longrightarrow H + OH^- \qquad k_{17} = 16\ M^{-1}\ sec^{-1}\ ^{13} \quad (17)$$

$$e_{aq}^- + CH_3OH \longrightarrow CH_3O^- + H \quad (18)$$

$$e_{aq}^- + Imp \longrightarrow products \quad (19a)$$

$$e_{aq}^- + Imp' \longrightarrow products \quad (19b)$$

Imp represents impurities in the matrix and Imp′ impurities introduced with the alcohol which are not destroyed by uv irradiation. The term $k_{17}[H_2O]$ is necessary because the reverse reaction 3 is prevented by reaction 20. In the alcohol-free matrix solution

$$H + CH_3OH \longrightarrow H_2 + CH_2OH \qquad k_{20} = 1.65 \times 10^6\ M^{-1}\ sec^{-1}\ ^{3} \quad (20)$$

(pH 11) the equilibrium (3) $\rightleftharpoons$ (17) with its pH of 9.7 favors e_{aq}^- so that the term $k_{17}[H_2O]$ must be omitted and the decay constant is $\lambda_m = k_{19}[Imp]$. Thus

$$\Delta\lambda = \lambda - \lambda_m = k_{17}[H_2O] + k_{19}'[Imp'] + k_{18}[CH_3OH] \quad (21a)$$

In Figure 2 (lower curve), $\Delta\lambda - k_{17}[H_2O] = k_{18}[CH_3OH] + k_{19}'[Imp']$ is plotted against $[CH_3OH]$, using $k_{17} = 16\ M^{-1}\ sec^{-1}$. The points were obtained with methanol from two different manufacturers, and in some cases the methanol was preirradiated with ^{60}Co γ rays. As the source of methanol had no significant effect on the result, all points were used for the least-squares fit

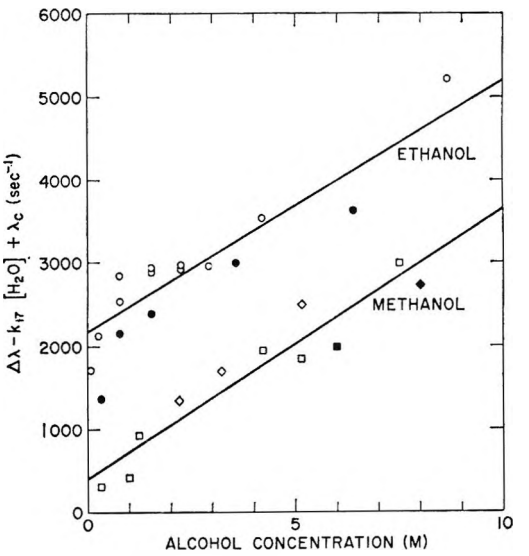

Figure 2. Effect of methanol and ethanol concentration on the pseudo-first-order decay of e_{aq}^-. $\Delta\lambda = \ln 2(1/t_{1/2} - 1/t_{1/2}^0)$. The term $k_{17}[H_2O]$ accounts for the reaction of e_{aq}^- with H_2O. λ_c is a correction term for the reverse reaction $H + OH^- \rightarrow e_{aq}^-$ (only necessary for [NaOH] = 0.08 M). Methanol: [NaOH] = 0.001 M; □, Fluka; ■, Fluka, ^{60}Co irradiated; ◊, Malinckrodt; ◆, Malinckrodt, ^{60}Co irradiated. Ethanol: ○, [NaOH] = 0.001 M; ●, [NaOH] = 0.08 M.

represented by the straight line. The latter has a small positive intercept which would disappear if $k_{17} = 23\ M^{-1}\ sec^{-1}$ were used. As the intercept could also be caused by a mechanism similar to the one discussed below for ethanol, we shall continue to use the literature value of $k_{17} = 16\ M^{-1}\ sec^{-1}$ for our further calculations.

The slope of the straight line corresponds to $k_{18} = 325\ M^{-1}\ sec^{-1}$. Taking into account the scattering of the points, the uncertainty of k_{17},[18] and possible im-

(17) C. H. Cheek and J. W. Swinnerton, *J. Phys. Chem.*, **68**, 1429 (1964).

(18) For $k_{17} = 23\ M^{-1}\ sec^{-1}$, the value would be 340 $M^{-1}\ sec^{-1}$.

purities in the methanol, we conclude $k_{18} \leq 400\ M^{-1}$ sec^{-1}.

Ethanol. The measurements on ethanol were carried out with two different initial NaOH concentrations: 0.001 and 0.08 M. At the higher concentration, reaction 3 competes with reaction 22, and eq 21 has to be modified

$$\Delta\lambda = k_{17}[H_2O] + k_{19}'[Imp'] + k_{23}[C_2H_5OH] - \lambda_c \quad (21b)$$

$$H + C_2H_5OH \longrightarrow H_2 + CH_3CHOH \quad k_{22} = 1.6 \times 10^7\ M^{-1}\ sec^{-1}\ ^3 \quad (22)$$

$$e_{aq}^- + C_2H_5OH \longrightarrow C_2H_5O^- + H \quad (23)$$

with the correction term

$$\lambda_c = \frac{k_3[OH^-]}{k_{22}[C_2H_5OH] + k_3[OH^-]} \times (k_{17}[H_2O] + k_{23}[C_2H_5OH])$$

In Figure 2 (upper curve), the values $\Delta\lambda - k_{17}[H_2O] + \lambda_c = k_{23}[C_2H_5OH] + k_{19}'[Imp']$ are plotted *vs.* $[C_2H_5OH]$. The correction term λ_c is only significant at the three lowest ethanol concentrations. Its maximum value (for $[C_2H_5OH] = 0.32\ M$) is $\lambda_c = 232\ sec^{-1}$ or *ca.* 15%. For $[NaOH] = 10^{-3}\ M$, no correction is required.[19] The upper straight line in Figure 2 is the product of a least-squares fit using all points with $[C_2H_5OH] \geq 1\ M$. We assume that the large positive intercept of 2160 sec^{-1} is caused by the formation of a limited quantity of acetaldehyde during preirradiation and the flash according to the following mechanism

$$OH + C_2H_5OH \longrightarrow CH_3CHOH + H_2O \quad k_{24} = 1.1 \times 10^9\ M^{-1}\ sec^{-1}\ ^3 \quad (24)$$

$$2CH_3CHOH \longrightarrow CH_3\text{–}CHOH \quad (25)$$
$$\qquad\qquad\qquad\qquad\quad |$$
$$\qquad\qquad\qquad\qquad CH_3\text{–}CHOH$$

$$2CH_3CHOH \longrightarrow CH_3CH_2OH + CH_3CHO \quad (26)$$

$$CH_3CHO + e_{aq}^- \longrightarrow \text{products} \quad k_{27} = 3.5 \times 10^9\ M^{-1}\ sec^{-1}\ ^3 \quad (27)$$

with $k_{26}/k_{25} = 0.25$.[20] As reaction 24 is complete even with small ethanol concentrations, the acetaldehyde concentration must be independent of ethanol concentration. From the intercept, one calculates $[CH_3CHO] = 2160/k_{27} \approx 6 \times 10^{-7}\ M$.

The analogous product in the case of methanol is formaldehyde. However, formaldehyde forms a hydrate[21] which reacts with e_{aq}^- at a rate so low ($k < 10^7\ M^{-1}\ sec^{-1}$)[3] that this could not account for the intercept of the methanol curve.

The slope of the ethanol curve is 305 M^{-1} sec^{-1}. Considering the same uncertainty factors as in the case of methanol, we conclude $k_{23} \leq 400\ M^{-1}\ sec^{-1}$.

Comparison with Literature Values. The new upper limits of the rate constants for the reaction of e_{aq}^- with methanol and ethanol, namely, k_{18}, $k_{23} \leq 400\ M^{-1}\ sec^{-1}$ are much smaller than the values previously reported in the literature: $k_{18} < 10^4\ M^{-1}\ sec^{-1}$ and $k_{23} < 10^5\ M^{-1}$ sec^{-1}.[3] These high estimates are probably due to impurities in the alcohols and, in the case of ethanol, to the formation of acetaldehyde.

(19) This is also true in the case of methanol in spite of the small value of k_{20}.

(20) I. A. Taub and L. M. Dorfman, *J. Amer. Chem. Soc.*, **84**, 4053 (1962).

(21) Acetaldehyde also partly hydrates, but here the ratio of hydrated to unhydrated aldehyde is 1.27,[22] whereas it is 10^4 for formaldehyde.

(22) R. P. Bell and J. C. Clunie, *Trans. Faraday Soc.*, **48**, 439 (1952).

Kinetics of the Oxidation of Cerium(III) by Peroxysulfuric Acids Induced by Cobalt-60 γ Radiation[1]

by R. W. Matthews,[2] H. A. Mahlman, and T. J. Sworski

Chemistry Division, Oak Ridge National Laboratory, Oak Ridge, Tennessee 37830 *(Received January 26, 1970)*

$G(Ce^{III})$ decreases with increase in ammonium persulfate concentration for cerium(IV)–cerium(III) mixtures in air-saturated 4.0 *M* sulfuric acid solutions. At any particular ammonium persulfate concentration, $G(Ce^{III})$ decreases also with increase in age of solution owing to hydrolytic formation of peroxymonosulfuric acid. Oxidation of cerium(III) by peroxysulfuric acids is induced by reaction of H atom with peroxysulfuric acids to yield the HSO_4 radical which oxidizes cerium(III). The dependence of $G(Ce^{III})$ on the concentration of peroxysulfuric acids is explicable by a competition between peroxysulfuric acids and oxygen for reaction with H atom. Kinetic analysis yielded $G_H + G_{e_{aq}^-} = 3.38 \pm 0.12$, $k_{H,H_2S_2O_8}/k_{H,O_2} = 0.0012 \pm 0.0001$, and $k_{H,H_2SO_5}/k_{H,O_2} = 0.0106 \pm 0.0006$.

Introduction

Interest in the radiation chemistry of peroxysulfuric acids was stimulated by the report[3] of their formation in the radiolysis of aqueous sulfuric acid solutions, presumed to be direct evidence for reaction of OH radical with sulfuric acid to yield the HSO_4 radical as a secondary intermediate. On the other hand, Boyle[4] proposed that both OH and HSO_4 were primary intermediates with G_{OH} and G_{HSO_4} dependent on electron fraction of water and sulfuric acid, respectively. He presented convincing evidence for formation of peroxysulfuric acids in the spur by combination reactions of these primary OH and HSO_4 intermediates. We have recently confirmed Boyle's model by determinations of $G_{OH} = 1.70 \pm 0.02$ and $G_{HSO_4} = 0.97 \pm 0.03$ in 4.0 *M* sulfuric acid for ^{60}Co γ radiation.[5]

Our interest in the reactions of H atom with peroxysulfuric acids resulted from a study of cerium(III) oxidation in 4.0 *M* sulfuric acid induced by ^{60}Co γ radiation.[6] Although neither absolute rate constants nor rate constant ratios have been reported, there is evidence for reactions of H atom with both peroxymonosulfuric acid[7] and peroxydisulfuric acid.[8,9]

In this paper we report the dependence of $G(Ce^{III})$ on the concentration of peroxysulfuric acids for cerium(IV)–cerium(III) mixtures in air-saturated sulfuric acid solutions for ^{60}Co γ radiation. A kinetic analysis yielded rate constant ratios for reactions of H atom with oxygen, peroxymonosulfuric acid, and peroxydisulfuric acid, in 4.0 *M* sulfuric acid.

Experimental Section

Materials. Baker Analyzed ammonium persulfate and arsenious acid, Baker and Adamson ferrous ammonium sulfate, Du Pont reagent sulfuric acid, Lehigh Valley Chemical Co. unstabilized reagent 30% hydrogen peroxide, and Fisher purified ceric ammonium sulfate were used without further purification. All solutions were prepared with water, from a Barnstead still, which was further purified by successive distillations from an acid dichromate solution, from an alkaline permanganate solution, and finally from an all-silica system into silica storage vessels.

The G. Frederick Smith Co. reagent cerous sulfate hydrated required further purification. A saturated solution was prepared in pure water and filtered. Sulfuric acid was slowly added until the sulfuric acid concentration became about 4.0 *M* and much of the cerous sulfate had precipitated. The solution was allowed to stand overnight. White crystalline cerous sulfate was separated from solution by filtration.

Irradiations. Solutions in 2.0-cm Pyrocell cylindrical absorption cells were irradiated in a kilocurie ^{60}Co source of the Ghormley–Hochanadel design.[10] The cells had S18-260 silica windows which did not become colored enough during irradiation to interfere with spectrophotometric analyses of the solutions with a Cary Model 11 recording spectrophotometer. Dose rates were determined with the ferrous sulfate dosimeter using $G(Fe^{III}) = 15.6$[11] and a molar extinction co-

(1) Research sponsored by the U. S. Atomic Energy Commission under contract with Union Carbide Corp.

(2) Guest scientist from the Australian Atomic Energy Research Establishment, Sydney, Australia.

(3) M. Daniels, J. Lyon, and J. Weiss, *J. Chem. Soc.*, 4388 (1957).

(4) J. W. Boyle, *Radiat. Res.*, 17, 427 (1962).

(5) R. W. Matthews, H. A. Mahlman, and T. J. Sworski, *ibid.*, 39, 534 (1969).

(6) R. W. Matthews, H. A. Mahlman, and T. J. Sworski, *J. Phys. Chem.*, 72, 3704 (1968).

(7) J. W. Boyle, ORNL-3679, 42 (1964); ORNL-3832, 55 (1965).

(8) A. Buu and J. Pucheault, *J. Chim. Phys.*, 63, 1037 (1966).

(9) W. K. Wilmarth and A. Haim, *Peroxide React. Mech., Pap. Conf.*, 175 (1962).

(10) J. A. Ghormley and C. J. Hochanadel, *Rev. Sci. Instrum.*, 22, 473 (1951).

(11) C. J. Hochanadel and J. A. Ghormley, *J. Chem. Phys.*, 21, 880 (1953).

efficient for iron(III) of 2210 at 305 mμ and 25° in 0.4 *M* sulfuric acid.[12] Energy absorption in 4.0 *M* sulfuric acid solutions relative to the ferrous sulfate dosimeter was assumed to be in the ratio of electron densities. A molar extinction coefficient for cerium(IV) of 6590 at 320 mμ in 4.0 *M* sulfuric acid was determined relative to the previously reported[11] value of 5580 at 320 mμ in 0.4 *M* sulfuric acid.

Procedure: 4.0 M Sulfuric Acid. Stock solutions of peroxysulfuric acids were prepared by dissolution of ammonium persulfate in 4.0 *M* sulfuric acid. Ammonium persulfate is unstable in 4.0 *M* sulfuric acid owing to hydrolysis which yields a mixture of peroxydisulfuric acid, peroxymonosulfuric acid, and hydrogen peroxide.[13] Three stock solutions were allowed to hydrolyze for 2.5, 6.0, and 16.0 hr before preparation of solutions for irradiation. Table I shows their compositions, determined by the method of Mariano.[14]

Table I: Composition of Ammonium Persulfate Stock Solutions

Time, hr	% $H_2S_2O_8$	% H_2SO_5	% H_2O_2
2.5	79.0	21.0	0
6.0	47.5	52.5	0
16.0	12.8	85.5	1.7

All solutions prepared for irradiation contained 3×10^{-3} *M* cerium(III), about 10^{-4} *M* cerium(IV), and desired amounts of peroxysulfuric acids by addition of aliquots from the three stock solutions. After solutions were prepared, they were cooled immediately in Dry Ice to inhibit further hydrolysis. Just before irradiation, each solution was warmed quickly to room temperature and shaken vigorously for air saturation. Intermittent irradiations and spectrophotometric analyses for cerium(IV) concentration were made as quickly as possible. All solutions were reequilibrated with air between irradiations.

For each solution, the observed rate of reaction had to be corrected for a thermal rate of cerium(IV) reduction to obtain the radiation-induced rate of reaction. The thermal rate of cerium(IV) reduction, attributed to hydrolytic formation of hydrogen peroxide, was determined for each solution after irradiations were completed and was found to be sensibly constant for each solution, independent of changes in cerium(IV) concentration. The corrections were not negligible when the concentration of peroxysulfuric acids was 5×10^{-3} *M* or more and amounted to as much as 10% for 5×10^{-2} *M*.

Procedure: 0.4 M Sulfuric Acid. Solutions of ammonium persulfate in 0.4 *M* sulfuric acid containing 3×10^{-3} *M* cerium(III) and about 10^{-4} *M* cerium(IV) were prepared using a stock solution of ammonium persulfate in pure water. There was no indication of significant hydrolysis of ammonium persulfate in 0.4 *M* sulfuric acid during the time required for solution preparation, irradiations, and spectrophotometric analyses. This apparent stability is consistent with the reported decreases[13,14] in rate of hydrolysis of peroxydisulfuric acid with decrease in sulfuric acid concentration. For concentrations of ammonium persulfate of 0.1 *M* and more, the observed rate of reaction had to be corrected for thermal oxidation of cerium(III) by peroxydisulfuric acid to obtain the radiation-induced rate of reaction.

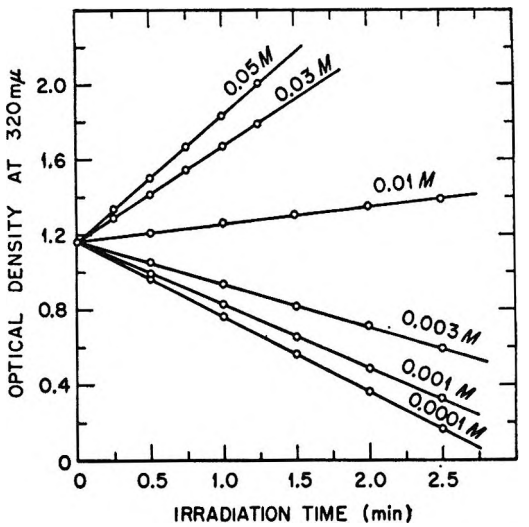

Figure 1. Effect of concentration of peroxysulfuric acids on the radiolysis of cerium(IV)–cerium(III) mixtures in air-saturated 4.0 *M* sulfuric acid. Solutions prepared with the ammonium persulfate stock solution which had hydrolyzed for 6.0 hr. Optical densities of solutions in a 2.0-cm cell were adjusted for a common initial ordinate. Dose rate = 1.86×10^{19} eV $l.^{-1}$ sec^{-1}.

Results

Typical experimental data are shown in Figure 1 for solutions containing ammonium persulfate which had hydrolyzed for 6.0 hr. The cerium(IV) concentration, proportional to the solution optical density at 320 mμ, is to a very good approximation a linear function of irradiation time for all solutions. The data in Figure 1 are not corrected for thermal reduction of cerium(IV) induced by hydrolytic formation of hydrogen peroxide but the correction is also to a good approximation a linear function of time.

The dependence of $G(Ce^{III})$ on the total concentration of peroxysulfuric acids is shown in Figure 2 for solutions which had hydrolyzed for either 2.0, 6.0, or 16.0 hr. $G(Ce^{III})$ decreases markedly with increase in total concentration of peroxysulfuric acids until,

(12) T. J. Sworski, *Radiat. Res.*, **4**, 483 (1956).
(13) H. Palme, *Z. Anorg. Allog. Chem.*, **112**, 97 (1920).
(14) M. H. Mariano, *Anal. Chem.*, **40**, 1662 (1968).

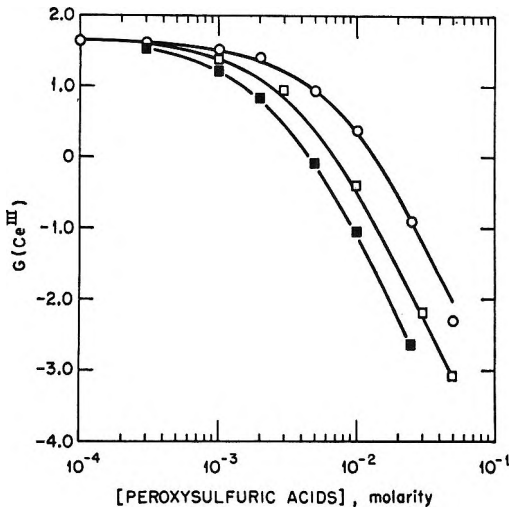

Figure 2. Dependence of $G(Ce^{III})$ on concentration of peroxysulfuric acids in air-saturated 4.0 M sulfuric acid. Hydrolysis time of ammonium persulfate stock solutions: ○, 2.5 hr; □, 6.0 hr; ■, 16.0 hr.

instead of cerium(IV) reduction, cerium(III) oxidation is observed. At any particular total concentration of peroxysulfuric acids, $G(Ce^{III})$ decreases with increase in concentration of peroxymonosulfuric acid.

An attempt was made to determine the dependence of $G(Ce^{III})$ on ammonium persulfate concentration in 4.0 M sulfuric acid solutions for which the hydrolysis time was a minimum, being only the time for solution preparation, irradiations, and spectrophotometric analyses. For ammonium persulfate concentrations which significantly decreased $G(Ce^{III})$, the cerium(IV) concentration was not a linear function of irradiation time. $G(Ce^{III})$ decreased with increase in irradiation time. Estimations of initial $G(Ce^{III})$ were too difficult to obtain reliable values. Effective concentrations of peroxymonosulfuric acid were apparently present and significant changes in the ratio of peroxymonosulfuric acid to peroxydisulfuric acid occurred even during the few minutes required for each irradiation and analysis.

An attempt was made to determine the dependence of $G(Ce^{III})$ on peroxymonosulfuric acid concentration in 0.4 M sulfuric acid. Solutions were prepared using the stock solution of ammonium persulfate in 4.0 M sulfuric acid which had been allowed to hydrolyze for 16.0 hr. However, at the concentrations of peroxysulfuric acids required to decrease $G(Ce^{III})$ significantly, thermal reduction of cerium(IV) was too rapid to obtain reliable values of $G(Ce^{III})$. The thermal rate of cerium(IV) reduction decreased with decrease in cerium(IV) concentration, indicating reduction of cerium(IV) by peroxymonosulfuric acid as reported by Mariano.[14]

The dependence of $G(Ce^{III})$ on ammonium persulfate concentration in air-saturated 0.4 M sulfuric acid is shown in Figure 3.

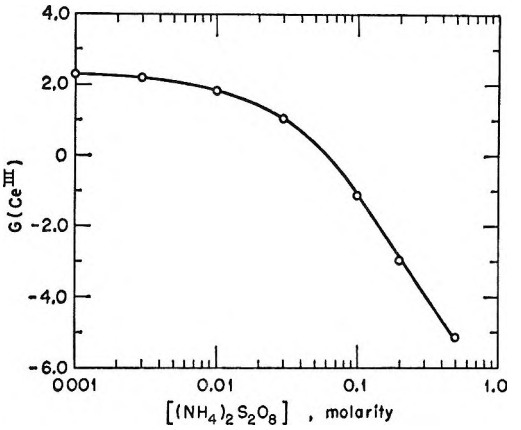

Figure 3. Dependence of $G(Ce^{III})$ on $(NH_4)_2S_2O_8$ concentration in air-saturated 0.4 M sulfuric acid.

Discussion

4.0 M Sulfuric Acid Solutions. The formation of earliest detectable intermediates by ^{60}Co γ radiation is denoted by the reactions

$$H_2O \rightsquigarrow H_2, H_2O_2, H, OH, e_{aq}^-, H_3O^+ \quad (1)$$

$$H_2SO_4 \rightsquigarrow H_2S_2O_8, H_2SO_5, HSO_4 \quad (2)$$

Reaction 2 denotes those additional products which diffuse from the spur owing to the high concentration of sulfuric acid.[4] The formulas used in reactions 1 and 2, and throughout this paper, denote the chemical compounds in solution regardless of their state of ionization or complexation.

We define $G(Ce^{III})^0$ as the G value for cerium(IV) reduction in air-saturated sulfuric acid solutions

$$G(Ce^{III})^0 = 2G_{H_2O_2} + G_H + G_{e_{aq}^-} - G_{OH} - G_{HSO_4} \quad (I)$$

Equation I is based on the reaction mechanism

$$e_{aq}^- + H^+ \longrightarrow H \quad (3)^{15,16}$$

$$H + Ce^{IV} \longrightarrow H^+ + Ce^{III} \quad (4)^{17}$$

$$H + O_2 \longrightarrow HO_2 \quad (5)^{17}$$

$$HO_2 + Ce^{IV} \longrightarrow H^+ + O_2 + Ce^{III} \quad (6)^{17}$$

$$H_2O_2 + Ce^{IV} \rightleftharpoons H^+ + HO_2 + Ce^{III} \quad (7)^{18,19}$$

$$OH + Ce^{III} \longrightarrow OH^- + Ce^{IV} \quad (8)^{20,21}$$

$$OH + H_2SO_4 \longrightarrow H_2O + HSO_4 \quad (9)^{22}$$

$$HSO_4 + Ce^{III} \longrightarrow HSO_4^- + Ce^{IV} \quad (10)^{22}$$

(15) N. F. Barr and A. O. Allen, *J. Phys. Chem.*, **63**, 928 (1959).
(16) G. Czapski and H. A. Schwarz, *ibid.*, **66**, 471 (1962).
(17) T. J. Hardwick, *Can. J. Chem.*, **30**, 23 (1952).
(18) P. B. Sigler and B. J. Masters, *J. Amer. Chem. Soc.*, **79**, 6353 (1957).
(19) G. Czapski, B. H. J. Bielski, and N. Sutin, *J. Phys. Chem.*, **67**, 201 (1963).
(20) J. Weiss and D. Porret, *Nature*, **139**, 1019 (1937).

Reactions of the hydrated electron with solutes other than the hydrogen ion are assumed to be negligible owing to the absolute rate constant of 2.36×10^{10} M^{-1} sec^{-1} reported[23] for reaction 3. Reduction of cerium(IV) by the peroxysulfuric acids formed in reaction 2 has been shown by Boyle[4] to be negligible in 4.0 M sulfuric acid.

Mariano[14] reported reduction of cerium(IV) by both peroxysulfuric acids in 0.4 M sulfuric acid. The rate of reduction of cerium(IV) by peroxymonosulfuric acid was markedly decreased[14] by either increasing the concentration of sulfuric acid to 5.0 M or addition of 4×10^{-4} M cerium(III). We have observed no evidence for a thermal reaction between cerium(IV) and peroxysulfuric acids in 4.0 M sulfuric acid solutions containing 3×10^{-3} M cerium(III), 10^{-4} M cerium(IV), and peroxysulfuric concentrations as high as 5×10^{-2} M. The solution instability at high concentrations of peroxysulfuric acids is attributed to hydrogen peroxide formation from hydrolysis of peroxymonosulfuric acid.

The following reactions of HO_2 radical with peroxysulfuric acids have been postulated

$$HO_2 + S_2O_8^{2-} \longrightarrow HSO_4^- + SO_4^- + O_2 \quad (11)^8$$

$$HO_2 + HSO_5^- \longrightarrow HSO_4^- + OH + O_2 \quad (12)^{14}$$

The occurrence of either reaction 11 or 12 in competition with reaction 6 would cause $G(Ce^{III})$ to decrease with increase in $([H_2S_2O_8] + [H_2SO_5])/[Ce^{IV}]$ at constant $[H_2S_2O_8]/[H_2SO_5]$. However, since $G(Ce^{III})$ is independent of variations in Ce^{IV} concentration during irradiation, reactions 11 and 12 do not compete significantly with reaction 6 under our experimental conditions. We obtained evidence to support this conclusion; 3×10^{-3} M peroxysulfuric acids had no sensible effect on the stoichiometry of the thermal reduction of cerium(IV) by hydrogen peroxide. Significant occurrence of reaction 11 or 12 followed by reaction 8 or 10, in competition with reaction 6, would alter the stoichiometry.

The dependence of $G(Ce^{III})$ on the concentration of peroxysulfuric acids is explicable by a competition between peroxysulfuric acids and oxygen for reaction with H atom

$$H + S_2O_8^{2-} \longrightarrow HSO_4 + SO_4^{2-} \quad (13)^{8,9}$$

$$H + H_2SO_5 \longrightarrow H_2O + HSO_4 \quad (14)^7$$

The independence of $G(Ce^{III})$ on cerium(IV) concentration indicates that cerium(IV) does not compete significantly with either oxygen or peroxysulfuric acids for reaction with H atom in agreement with $k_5 > k_4$ as reported by Boyle.[7] The dependence of $G(Ce^{III})$ on the concentration of peroxysulfuric acids is given by eq II.

$$G(Ce^{III}) = G(Ce^{III})^0 - \frac{2(G_H + G_{e_{aq}^-})}{1 + k_5[O_2]/(k_{13}[H_2S_2O_8] + k_{14}[H_2SO_5])} \quad (II)$$

A generalized least-squares computer program[24] was used to fit the data to eq II. The oxygen concentration was assumed to be 1.33×10^{-4} M as reported by Boyle.[25] The data were weighed with the assumption that all G values had the same percentage error. The least-squares analysis yielded $G(Ce^{III})^0 = 1.66 \pm 0.03$, $G_H + G_{e_{aq}^-} = 3.38 \pm 0.12$, $k_{13}/k_5 = 0.0012 \pm 0.0001$, and $k_{14}/k_5 = 0.0106 \pm 0.0006$. The data adhere well to eq II as indicated by the low standard errors and shown by the agreement between the experimental points and computed curves of Figure 2.

The values for k_{13}/k_5 and k_{14}/k_5 are in agreement with the relative reactivities of oxygen and peroxysulfuric acids reported by Boyle:[7] $k_5 > k_{14} > k_{13}$. The reactivity of hydrogen peroxide with H atom has

$$H + H_2O_2 \longrightarrow H_2O + OH \quad (15)$$

also been reported relative to oxygen. The values for k_{15}/k_5 of 0.0022,[26] 0.0033,[27] and 0.0062[28] are all between our values for k_{13}/k_5 and k_{14}/k_5. If it can be assumed that k_{15}/k_5 is the same for 4.0 M sulfuric acid as for the media in which these values of k_{15}/k_5 were determined, then the order of rate constants for the reaction of H atom with the homologous series of peroxides is $k_{14} > k_{15} > k_{13}$.

The value for $G_H + G_{e_{aq}^-}$ of 3.38 ± 0.12 is slightly lower than the value of 3.66 determined by Boyle.[25] This may be due to eq II being admittedly only a good approximation. An implicit assumption in eq II is that all G values for earliest detectable intermediates are independent of the concentration of peroxysulfuric acids. However, it is well established that the G values for earliest detectable intermediates are dependent on solute concentration. For example, $G(Ce^{III})^0$ decreases[12] with increase in cerium(III) concentration owing to a concomitant decrease in $G_{H_2O_2}$ and $G(Ce^{III})^0$ increases[29] with increase in cerium(IV) concentration owing to a concomitant decrease[30] in G_{H_2}.

0.4 M Sulfuric Acid Solutions. Figures 2 and 3

(21) T. J. Sworski, *J. Amer. Chem. Soc.*, **79**, 3655 (1957).

(22) T. J. Sworski, *ibid.*, **78**, 1768 (1956); *Radiat. Res.*, **6**, 645 (1957).

(23) S. Gordon, E. J. Hart, M. S. Matheson, J. Rabani, and J. K. Thomas, *J. Amer. Chem. Soc.*, **85**, 1375 (1963).

(24) M. H. Lietzke, ORNL-3259 (March 21, 1962).

(25) J. W. Boyle, *Radiat. Res.*, **17**, 450 (1962).

(26) C. J. Hochanadel, *ibid.*, **17**, 286 (1962).

(27) J. K. Thomas, *J. Phys. Chem.*, **67**, 2593 (1963).

(28) H. Fricke and J. K. Thomas, *Radiat. Res. Suppl.*, **4**, 35 (1964).

(29) J. T. Harlan and E. J. Hart, *Nucleonics*, **17**, 286 (1959).

(30) H. A. Mahlman, *J. Amer. Chem. Soc.*, **81**, 3203 (1959).

show that higher concentrations of ammonium persulfate were required to obtain comparable decreases for $G(Ce^{III})$ in 0.4 M sulfuric acid. This is consistent with negligible hydrolysis of ammonium persulfate in 0.4 M sulfuric and $k_{14}/k_{13} = 9 \pm 1$ determined in 4.0 M sulfuric acid.

The hydrated electron reacts with the $S_2O_8^{2-}$ anion according to reaction 16 with an absolute rate constant[31,32] of 1.06×10^{10} M^{-1} sec^{-1}. Since the highest

$$e_{aq}^- + S_2O_8^{2-} \longrightarrow SO_4^{2-} + SO_4^- \qquad (16)$$

ammonium persulfate concentration of 0.5 M is approximately equal to the hydrogen ion concentration in 0.4 M sulfuric acid, reaction 16 should compete significantly with reaction 3. The dependence of $G(Ce^{III})$ on ammonium persulfate concentration would then be given by the equation

$$G(Ce^{III}) = G(Ce^{III})^0 - 2G_H - 2G_{e_{aq}^-} + \frac{2G_H + 2G_{e_{aq}^-}/(1 + k_{16}[H_2S_2O_8]/(k_3[H^+]))}{1 + k_{13}[H_2S_2O_8]/(k_5[O_2])} \qquad (III)$$

There are too many unknowns in eq III to obtain a unique solution by the method of least squares from the limited data shown in Figure 3. Assuming $G_H = 0.6$,[33] values for $G(Ce^{III})^0$, $G_{e_{aq}^-}$, and $k_{16}/(k_3[H^+])$ were obtained as a function of $k_{13}/(k_5[O_2])$. The best fit was obtained for $k_{13}/(k_5[O_2]) = 2.8$ with $G(Ce^{III})^0 = 2.33 \pm 0.02$, $G_{e_{aq}^-} = 4.16 \pm 0.08$, and $k_{16}/(k_3[H^+]) = 2.6 \pm 0.2$.

Although the data adhere well to eq II, the good fit is only fortuitous since the value of $G_H + G_{e_{aq}^-}$ is much higher than the "standard value"[34] of 3.65 for 0.4 M sulfuric acid solutions. We have not established why eq III is not valid, but assume that it is due to an effect of the high ammonium persulfate concentrations on G values of earliest detectable intermediates.

(31) J. K. Thomas, S. Gordon, and E. J. Hart, *J. Phys. Chem.*, **68**, 1524 (1964).

(32) W. Roebke, M. Renz, and A. Henglein, *Int. J. Radiat. Phys. Chem.*, **1**, 39 (1969).

(33) J. T. Allan and G. Scholes, *Nature*, **187**, 218 (1960).

(34) A. O. Allen, "The Radiation Chemistry of Water and Aqueous Solutions," D. Van Nostrand Company, Inc., Princeton, N. J., 1961.

The Kinetics of the Tungsten-Oxygen-Bromine Reaction

by E. G. Zubler

Lamp Research Laboratory, General Electric Company, Nela Park, Cleveland, Ohio 44112 *(Received January 26, 1970)*

A microbalance-flow system technique has been used to investigate the kinetics of the reaction of tungsten with 10^{-4} to 10^{-2} Torr oxygen and 0.3–2.7 Torr bromine in the range 600–950°. The reaction was zero order with respect to bromine and first order with respect to oxygen. The function of the bromine was to remove the oxidation product by the formation of volatile WO_2Br_2 which permitted the oxidation to proceed as it would at higher temperatures where the oxide is volatile. An empirical rate equation with an apparent activation energy of 31.0 kcal/mol was obtained and compared with similar equations for tungsten oxidation at higher temperatures.

Introduction

The use of iodine and bromine transport cycles in incandescent lamps[1-3] has contributed to the current interest in high-temperature tungsten–oxygen–halogen chemistry. Recent work on the W–O–I[4-8] system has provided important thermochemical data and an insight into the transport mechanism.[9] A more complete understanding of the transport chemistry requires kinetic data which are not available for either system. Extensive kinetic data are available for the tungsten–oxygen reaction[10-20] but lacking for the tungsten–halogen reactions. Even with these data, addi-

(1) E. G. Zubler and F. A. Mosby, *Ill. Eng.*, **54**, 734 (1959).

(2) G. R. T'Jampens and M. H. A. van de Weijer, *Philips Tech. Rev.*, **27**, 165 (1966).

(3) F. A. Mosby, L. J. Schupp, G. G. Steiner, and E. G. Zubler, *Ill. Eng.*, **62**, 198 (1967).

(4) J. Tillack, P. Eckerlin, and J. H. Dettingmeijer, *Angew. Chem.* **78**, 451 (1966).

(5) J. H. Dettingmeijer and B. Meinders, *Z. Anorg. Allg. Chem.*, **357**, 1 (1968).

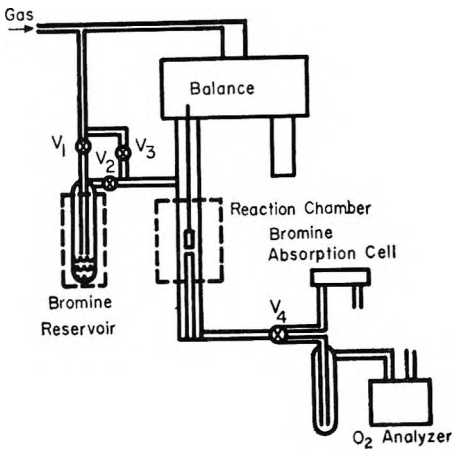

Figure 1. Microbalance–flow system: V_1, V_2, O-ring stopcocks; V_3, metal needle valve; V_4, high-vacuum stopcock.

tivity procedures for predicting tungsten removal rates can be grossly inaccurate as shown by Rosner and Allendorf for the tungsten–oxygen–chlorine system.[21]

The present investigation was undertaken to elucidate the kinetics of the reaction of tungsten with 10^{-4} to 10^{-2} Torr oxygen and 10^{-1} to 10^{1} Torr bromine in the range 600–1000°. This was based on some preliminary work by Dr. L. J. Schupp of this laboratory which suggested that the reaction of tungsten with oxygen and excess bromine was kinetically similar to the tungsten–oxygen reaction at temperatures above 1000° where the oxides are volatile.

Experimental Section

The apparatus, shown schematically in Figure 1, was based on a Cahn RH microbalance with a Pyrex–quartz–stainless steel flow system at atmospheric pres sure. Hoke needle valves, high-vacuum stopcocks and glass flow meters were used to regulate and direct the gas flow.

Metal diaphragm regulators were used on the cylinders containing the N_2 (99.9985% purity) carrier gas and the N_2 + 56 ppm O_2 which were mixed to attain the desired O_2 level measured by a solid electrolyte sensor.[22] In addition, a small amount (5–10%) of high-purity He could be added to prevent condensation of the N_2 if the gas were passed through a liquid N_2 trap. With the pure N_2 or N_2 + He, the minimum O_2 level after appropriate flushing was 0.5 ppm (4×10^{-4} Torr) and was unaffected by passing the gas over Cu filings at 600°. Normally, the gas flow was 224 cm³/min through the balance and 110 cm³/min through the Br_2 reservoir. This minimized back diffusion of Br_2(g) into the balance.

The reagent grade Br_2 was distilled through magnesium perchlorate into a glass-vacuum system. After several condensing (−196°)–pumping–thawing cycles, it was distilled into a temporary reservoir on a manifold. The flow system reservoir was attached to this manifold by Viton O-ring connectors and baked out. The Br_2 was then distilled into the reservoir which was filled with an atmosphere of N_2 and returned to the flow system. When the flow of N_2 (+He) through the Br_2 reservoir was passed through a liquid N_2 trap and into the O_2 sensor, there was no increase in the residual O_2 level. The Br_2 pressure was determined spectrophotometrically[23] to 0.1 Torr in a 10-cm absorption cell. The pressure was variable from 0.3 to 2.7 Torr by a combination of the reservoir bath temperature (−20 to 20°) and the by-pass valve. In some preliminary runs, bromine corrosion of the balance mechanism was encountered and precluded runs at higher bromine pressures. The Br_2 pressure was insensitive to flow but was a function of the liquid Br_2 level.

The pure tungsten was a 1.02 × 1.93 cm strip cut from 1-mil stock (General Electric—a typical analysis is available[24]). A small hole was punched at one end for the quartz fiber suspension of the microbalance. Initially the weight of the sample was 99.216 mg and the geometric surface area was 3.93 cm². After chemical cleaning, the tungsten was suspended in the reaction chamber and heated to 1000° for several hours in N_2 containing 0.5 ppm O_2. No attempt was made to reduce the carbon[13] and oxygen levels by high-temperature (>2000°) treatment.

In a typical run, the gas flow and O_2 level were adjusted and allowed to stabilize. The reaction chamber was rapidly brought to temperature and Br_2 was admitted to the gas stream which passed through the absorption cell. An immediate, sharp decrease in

(6) J. Tillack, *Z. Anorg. Allg. Chem.*, **357**, 11 (1968).
(7) H. Schafer, D. Giegling, and K. Rinke, *ibid.*, **357**, 25 (1968).
(8) S. K. Gupta, *J. Phys. Chem.*, **73**, 4086 (1969).
(9) A. Rabenau, *Angew. Chem.*, **79**, 43 (1967).
(10) I. Langmuir, *J. Amer. Chem. Soc.*, **35**, 105 (1913).
(11) R. A. Perkins, W. L. Price, and D. D. Crooks, Proceedings of the Joint AIME–Air Force Materials Laboratory Symposium, Technical Document Report No. ML-TDR-64-162, 1962, p 125.
(12) R. W. Bartlett, *Trans. AIME*, **230**, 1097 (1964).
(13) J. A. Becker, E. J. Becker, and R. G. Brandes, *J. Appl. Phys.*, **32**, 411 (1961).
(14) R. J. Ackermann and E. G. Rauh, *J. Phys. Chem.*, **67**, 2596 (1963).
(15) J. B. Beckowitz-Mattuck, A. Büchler, J. L. Engelke, and S. N. Goldstein, *J. Chem. Phys.*, **39**, 2722 (1963).
(16) Yu. G. Ptushinskii and B. A. Chuikov, *Surface Sci.*, **6**, 42 (1967).
(17) P. O. Schissel and O. C. Trulson, *J. Chem. Phys.*, **43**, 737 (1965).
(18) B. McCarroll, *ibid.*, **46**, 863 (1967).
(19) J. H. Singleton, *ibid.*, **45**, 2819 (1966); **47**, 73 (1967).
(20) D. E. Rosner and H. D. Allendorf, *J. Electrochem. Soc.*, **114**, 305 (1967).
(21) D. E. Rosner and H. D. Allendorf, *AIAA J.*, **5**, 1489 (1967).
(22) S. S. Lawrence, H. S. Spacil, and D. Schroeder, *Automatika* (Sept 1969).
(23) A. A. Passchier, J. D. Christian, and N. W. Gregory, *J. Phys. Chem.*, **71**, 937 (1967).
(24) E. C. Sutherland and W. D. Klopp, NASA TN D-1310, Feb 1963.

weight was observed. This was more pronounced at the higher temperatures and O_2 levels and was due to the removal of the oxide layer formed in bringing the sample to temperature. This was followed by a linear decrease in weight with time. The output signal from the Cahn microbalance was displayed on a 1-mV strip chart recorder with a chart speed of 6 min/hr. The balance controls were generally adjusted to give 1 mg full scale on the recorder. Under these conditions, the noise level was about 0.015 mg. For high-reaction rates, 2 or 4 mg full scale settings were used. Generally, the weight loss was observed for 1 hr. Thirty minutes was adequate for the higher rates, and 2 hr was necessary for the lowest rates. Near the end of the run, the partial pressure of Br_2 was determined spectrophotometrically. Finally, the tungsten weight loss was converted to mol/(cm² sec).

Results and Discussion

Rate measurements above $\sim 10^{-11}$ mol/(cm² sec) were made at 50° intervals from 600 to 950° with O_2 at 4.7×10^{-4} to 4.3×10^{-2} Torr and Br_2 at 0.3 to 2.7 Torr. The weight loss of tungsten was linear with time at all temperatures and gas compositions investigated with one exception which will be discussed. The geometric surface area of the tungsten was used in the rate calculations.

During the principal series of runs, the tungsten sample weight decreased from about 96 to 65 mg. Microscopic examination showed a slightly roughened surface containing a number of etch pits and holes about 0.04 mm in diameter. Some were at a 45° angle to the surface.

The reaction rate was independent of total gas flow in the range 250–500 cm³/min at all partial pressures of O_2. Below about 250 cm³/min, the residual O_2 pressure increased with decreasing flow and produced a corresponding increase in reaction rate. All runs reported here were made at 334 cm³/min or higher where the rate was independent of flow at all O_2 pressures.

A reddish brown wall deposit of WO_2Br_2 (by X-ray diffraction) was observed downstream of the reaction zone. At the highest temperatures and O_2 pressures, a less volatile yellow deposit assumed to be WO_3 was observed nearer the reaction zone. The quantities collected were insufficient for chemical analysis. There was no evidence for the purple-black $WOBr_4$ which has been obtained with excess bromine below 400°.[25] Recently, an absorption and emission band at 998 cm^{-1} has been attributed to gaseous $WOBr_4$ over a WO_3–LiBr mixture above 500°.[26] The appearance of the band coincided with a pale brown sublimate in a cold zone.

The reaction rate was independent of Br_2 pressure in the range 0.3–2.7 Torr at different temperatures and O_2 pressures as shown in Figure 2. Most runs were made with a Br_2 pressure of about 1 Torr. During a series of runs, the $Br_2(l)$ level in the reservoir gradually decreased with a corresponding decrease in the Br_2 pressure from about 1.2 to 0.8 Torr with no indication of change in the reaction rate at a given oxygen pressure. The fraction of Br_2 dissociated as calculated from JANAF data[27] varied from 0.008 to 0.03 at 600° and 0.3 to 0.7 at 900°.

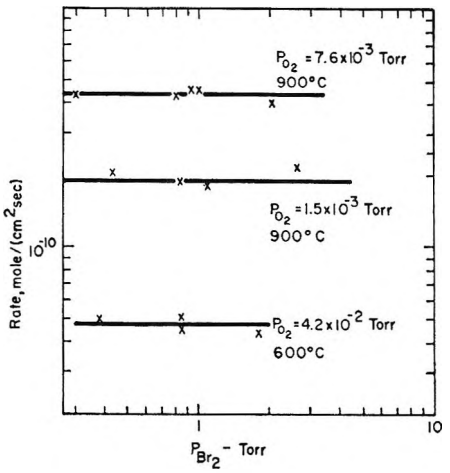

Figure 2. Reaction rate dependence on bromine pressure.

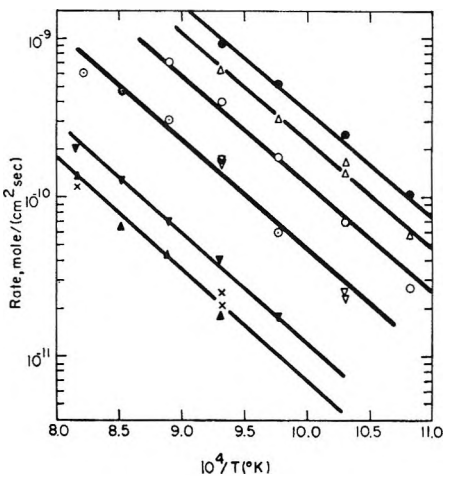

Figure 3. Temperature dependence of reaction rate at various oxygen pressures (Torr): ●, 4.3×10^{-2}; ⊙, 6.8×10^{-3}; △, 2.3×10^{-2}; ▼, 1.8×10^{-3}; ○, 1.5×10^{-2}; ▲, 7.0×10^{-4}; ▽, 6.8×10^{-3}; ×, 4.7×10^{-4}.

While the reaction rate was independent of Br_2 pressure, it was dependent on the O_2 pressure as shown in the Arrhenius plot in Figure 3. The rate measurements at a given O_2 pressure were normally obtained in 1 day. The data at $P_{O_2} = 6.8 \times 10^{-3}$ Torr, however, were obtained on different days (indicated by ▽ and ⊙) and are indicative of the reproducibility of the system.

(25) R. Colton and I. B. Tomkins, *Aust. J. Chem.*, **21**, 1975 (1968).

(26) B. G. Ward and F. E. Stafford, *Inorg. Chem.*, **7**, 2569 (1968).

(27) "JANAF Thermochemical Tables," Dow Chemical Co., Midland, Mich., 1967.

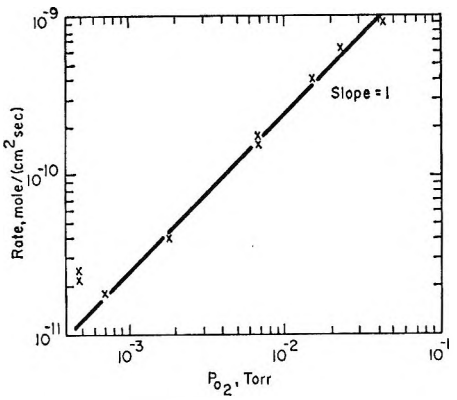

Figure 4. Reaction rate dependence on oxygen pressure at 800°.

At each O_2 pressure the data are reasonably well represented by a straight line although a slight curvature is apparent and expected. Under these experimental conditions where the tungsten and reactive gas are at the same temperature, the O_2 impingement rate which is a function of temperature should be considered. Impingement rates calculated from the Hertz–Knudsen equation introduce a $T^{-1/2}$ term which accounts for the apparent curvature. Over the limited temperature range investigated, this correction is less than 20% which is within the accuracy of the final rate equation. For convenience in comparing the final rate equation with those in the literature, this minor refinement was not introduced.

A plot of the rate data at 800° against O_2 pressure in Figure 4 indicates a linear O_2 pressure dependence. The data at the lowest (residual) O_2 pressures are less reliable but included. In view of the experimental technique of measuring the O_2 pressure at room temperature, the residual O_2 pressure during a run may well be slightly above that indicated due to the evolution of gases from the system at the elevated temperature. This complication should be restricted, however, to the residual O_2 pressures.

For the determination of the activation energy, the ratio ϵ of the rate of tungsten removal, mol/(cm² sec), to the rate of O_2 arrival, mol/(cm² sec), was used as shown in Figure 5. This convenient reactivity parameter brings all the data except that at the residual O_2 pressures onto a straight line. A least-squares treatment gives an activation energy, E_a, of 31.0 ± 2.2 kcal/mol. Combining this activation energy with the O_2 pressure dependence in Figure 4, the following empirical rate equation was obtained

$$R(\text{mol}/(\text{cm}^2\ \text{sec})) = 4.05 \times 10^{-2} P_{O_2} e^{-31{,}000/RT}$$

The experimental data indicate that the tungsten removal rate at 600–950° by 10^{-4} to 10^{-2} Torr O_2 and 0.3–2.7 Torr Br_2 is a linear function of the O_2 and independent of the Br_2. From the Arrhenius plots, the apparent activation energy which may contain the

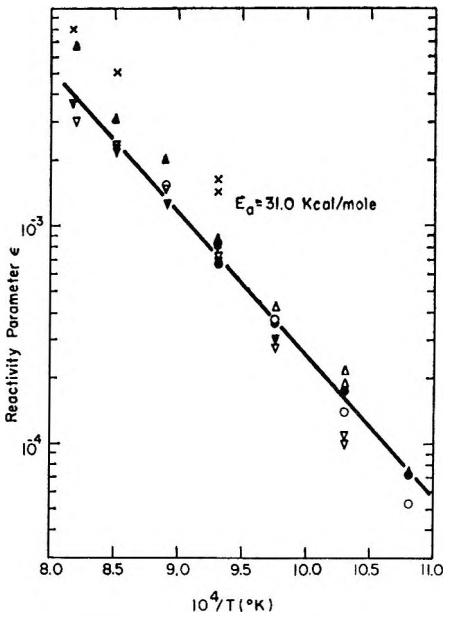

Figure 5. Temperature dependence of the reactivity parameter ϵ (reaction rate/O_2 impingement rate), for various oxygen pressures (Torr): ●, 4.3×10^{-2}; ⊙, 6.8×10^{-3}; △, 2.3×10^{-2}; ▼, 1.8×10^{-3}; ○, 1.5×10^{-2}; ▲, 7.0×10^{-4}; ▽, 6.8×10^{-3}; ×, 4.7×10^{-4}.

heat of adsorption of O_2 is 31.0 kcal/mol. The role of the Br_2 is to remove the surface oxidation product by the formation of volatile WO_2Br_2 which condenses on the cold walls outside the reaction zone. This relatively fast reaction prevents the formation of an oxide surface layer and permits the reaction to proceed as it would at slightly higher temperatures (>1000°) where the oxide is volatile. In this temperature range, 1000–1500°, and with comparable or lower O_2 pressures, there is substantial evidence[14-17] for the formation of a tungsten oxide on the surface. In addition, Schissel[17] has identified $(WO_3)_3$ and $(WO_3)_2$ as the major gaseous species under these conditions. $WO_3(g)$ and $WO_2(g)$ become dominant above about 1500 and 1700°, respectively.

If the W + O_2 + Br_2 reaction at 600–950° is kinetically the same as the W + O_2 reaction at 1000–1500°, a comparison of the extrapolated rate data should be revealing. Several investigators have determined similar rate equations for the pressure and temperature ranges of interest. After converting to the same units, mol/(cm² sec), these rate equations with the oxygen pressure in Torr are compared in Table I. In the Arrhenius plot based on these rate equations in Figure 6, the current work compares favorably with the extrapolated data of the previous investigations at lower total pressures. This agreement suggests that the N_2 carrier gas in these experiments does not influence the reaction kinetics.

During this investigation, the reaction rate was independent of bromine with $(Br_2)/(O_2)$ ratios in the range 25–2500. At slightly lower $(Br_2)/(O_2)$ ratios,

Table I: Comparison of Empirical Rate Equations for Tungsten Oxidation

Worker	Ref	Rate, mol/cm² sec (P_{O_2}, Torr)	Temp range, °C	P_{O_2} range, Torr
Langmuir	10	$2.32 \times 10^{-2} P_{O_2} e^{-27,000/RT}$	927–1500	10^{-4}–10^{-2}
Becker, *et al.*	13	$2.32 \times 10^{-2} P_{O_2} e^{-25,400/RT}$	927–1327	10^{-7}–10^{-5}
Perkins, *et al.*	11	$0.216 P_{O_2}^{0.59} e^{-43,900/RT}$	1300–1760	10^{-6}–3
Bartlett	12	$0.191 P_{O_2}^{0.55} e^{-42,000/RT}$	1320–1600	10^{-3}–1
Singleton	19	$2.4 \times 10^{-2} P_{O_2}^{0.7} e^{-32,800/RT}$	1000–1200	10^{-7}
Zubler		$4.05 \times 10^{-2} P_{O_2} e^{-31,000/RT}$	600–950	10^{-4}–10^{-2}

e.g., 10, there was some indication that the rate of formation of WO_2Br_2 was insufficient to prevent the formation of an oxide surface layer. While Br_2 will react with WO_2 forming volatile WO_2Br_2, there is evidence[28] that it will not react with WO_3. During a run at 600° with $P_{O_2} = 4.3 \times 10^{-2}$ Torr and $(Br_2)/(O_2) = 10$, the initial tungsten removal rate was normal but then slowly decreased. Subsequent runs with $(Br_2)/(O_2) = 25$ gave abnormally low but linear weight losses. When the tungsten was then taken to 1000° in pure N_2, a weight loss was observed with the simultaneous appearance of a yellow wall deposit assumed to be WO_3.

This suggests that the initial oxide product on the surface was WO_2 (or WO_{3-z}) which in the presence of a sufficient excess of Br_2 (or Br) was removed by the rapid formation of WO_2Br_2. Below some critical Br_2 level, there was competition from the reaction $WO_2 + {}^1/_2O_2 \rightarrow WO_3$. As the WO_3 was formed and remained on the surface, the rate of tungsten removal decreased. After a short time at 1000° where the WO_3 was volatile, the tungsten removal as WO_2Br_2 was again predictable.

Previous mechanistic work[13–18] on tungsten oxidation has established two distinct binding states or layers of oxygen. Schissel and Trulsen[17] have proposed a two-layer oxygen atom model while McCarroll[18] has evidence that the first layer is atomic oxygen. In addition, the reaction of tungsten with chlorine and oxygen at 10^{-6}–10^{-4} Torr has been investigated at 1200–2400°K.[21,29] McKinley[29] has identified WO_2Cl_2, WO_2, and WO_3 as the dominant gaseous species desorbing at the lower temperatures. With chlorine:oxygen ratios in the range 1–10, the desorption of WO_2Cl_2 was first order in chlorine and oxygen. Assuming a two-layer model and that the first layer was atomic oxygen, the presence of simple oxides and absence of simple chlorides suggest that the second layer contains both chlorine and oxygen with the oxygen more extensively adsorbed.

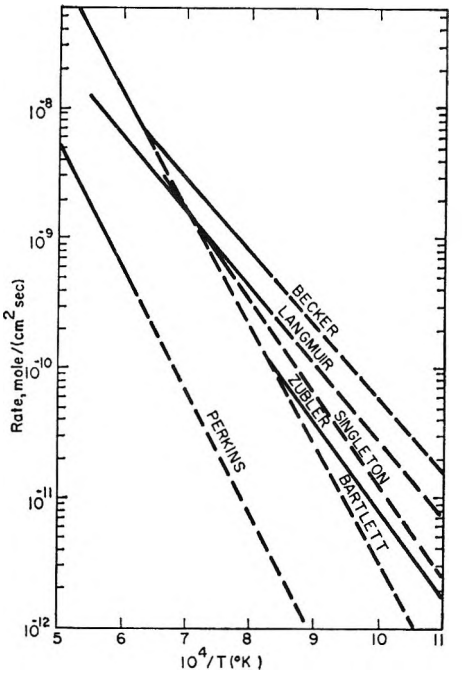

Figure 6. Comparison of rate data at 10^{-3} Torr oxygen.

The present work supplies no evidence for the two-layer model. The zero-order dependence on the excess bromine and first-order dependence on oxygen do indicate that while the surface was saturated with respect to bromine, there was no interference with the adsorption of oxygen. Either the oxygen and bromine were adsorbed on different kinds of sites or the oxygen successfully competed with the excess bromine for the same sites. McKinley[29] found that oxygen was more strongly adsorbed than chlorine on tungsten. He also observed a rapid decrease from first- to zero-order dependence above some total chlorine + oxygen pressure ($\sim 5 \times 10^{-4}$ Torr). This transition was temperature dependent, and as the temperature was increased, the first-order dependence was followed to higher total pressures.

While the reaction product was not monitored here, the condensate outside the reaction zone was predominantly WO_2Br_2 with no evidence for $WOBr_4$. The simplest possible mechanism, therefore, would involve the direct combination of WO_2 and Br_2 on the surface. A similar proposal was offered by McKinley[29] because no oxychlorides other than WO_2Cl_2 were observed.

Conclusion

The reaction rate of tungsten at 600–950° with 10^{-4}–10^{-2} Torr oxygen and 0.3–2.7 Torr bromine was zero order in bromine and first order in oxygen. The bromine removed the oxidation product by the formation of volatile WO_2Br_2 at a sufficient rate to permit the oxidation to proceed as it would at higher

(28) L. J. Schupp, unpublished results.

(29) J. D. McKinley, *Reactiv. Solids, Proc. Int. Symp.*, 345 (1969).

temperatures where the oxide itself is volatile. An empirical rate equation compares favorably with similar rate equations in the literature for tungsten oxidation at comparable pressures but higher temperatures. The correlation with the oxidation data at very low total pressures indicates that the N_2 carrier gas at atmospheric pressures does not affect the reaction kinetics. The oxygen either successfully competes with the excess bromine for adsorption sites or is adsorbed on different kinds of sites than the bromine. The reaction mechanism, which is independent of the dissociative state of the gaseous bromine, may simply involve the direct combination of WO_2 and Br_2 on the surface.

Acknowledgements. Drs. L. V. McCarty, S. K. Gupta, and R. J. Campbell participated in many helpful discussions and critically reviewed the manuscript.

The Kinetics of Interaction of Oxygen with Evaporated Iron Films

by Seihun Chang and William H. Wade

Department of Chemistry, The University of Texas at Austin, Austin, Texas 78712 *(Received May 19, 1970)*

The fast interaction of oxygen with iron films has been investigated with a quartz crystal microbalance in the pressure range 2×10^{-7} to 5×10^{-5} Torr at 24°. A relatively rapid formation of the equivalent of 4 oxide (FeO) layers was observed which, subsequently, was followed by a much slower growth up to 10 layers. The process kinetically approaches first order with respect to oxygen pressure in the initial stages and decreases to fractional orders as incorporation proceeds. This can be interpreted in terms of a surface regeneration by incorporation of adatoms into the interior at rates comparable to the adsorption process. The Elovich direct logarithmic rate law does not hold for the rapid chemisorption since it is observed to be autocatalytic.

Introduction

There have been several reports on the kinetics of oxygen chemisorption on iron films.[1-3] They show several inconsistencies but there appears to be general agreement that an initial fast process is followed by a slow one. The fast process takes place so rapidly that, to the present time, it has not been followable using conventional gravimetric or volumetric methods, and all the extant rate data for oxygen chemisorption on iron pertain to the slow process. Recently Pignocco and Pellissier[4,5] reported LEED data for the first stages of the interaction of oxygen with oriented iron crystal faces. Their study was mainly concerned with structural changes during oxygen adsorption coupled with rather qualitative studies of adsorption kinetics.

The quartz crystal microbalance (QCM) introduced by Sauerbrey[6] is a new tool for investigating surface processes. This instrument has several advantages over conventional gravimetric measuring devices: (1) The sensitivity of the QCM is sufficient to permit measurement of changes in surface mass of 10^{-10} g/cm^2. (2) The response time of a QCM to changes in mass of the active surface is on the order of microseconds, enabling one to follow fast adsorption processes. (3) The frequency shift of the crystal due to factors other than mass change can be minimized or corrected. (4) Buoyancy and wall effects can be completely eliminated. Previously a quartz crystal microbalance was used successfully by Slutsky and Wade[7] for measuring adsorption isotherms of hexane on a quartz single-crystal face. Later, using the same technique Wade and Allen[8] followed fast adsorption kinetics for oxygen on evaporated aluminum films.

Experimental Section

The vacuum system and circuits used in this work have been described in a previous paper.[8] The quartz crystals used in this study were 10-mHz, AT plates furnished by Scientific Electronic Products Corp. of Loveland, Colo. The quartz crystal was mounted in the vacuum system and covered by an aluminum hous-

(1) J. Bagg and F. C. Tompkins, *Trans. Faraday Soc.*, **51**, 1071 (1955).

(2) M. A. H. Lanyon and B. M. W. Trapnell, *Proc. Roy. Soc., Ser. A.*, **227**, 387 (1955).

(3) M. W. Roberts, *Trans. Faraday Soc.*, **57**, 99 (1961).

(4) A. J. Pignocco and G. E. Pellissier, *J. Electrochem. Soc.*, **112**, 1188 (1965).

(5) A. J. Pignocco and G. E. Pellissier, *Surface Sci.*, **7**, 261 (1967).

(6) G. Sauerbrey, *Z. Phys.*, **155**, 206 (1959).

(7) L. J. Slutsky and W. H. Wade, *J. Chem. Phys.*, **36**, 2688 (1962).

(8) W. H. Wade and R. C. Allen, *J. Coll. Interface Sci.*, **27**, 722 (1968).

ing. The housing contained two 0.25-in. diameter collimation holes allowing the films to be deposited on both sides of the active area of the crystal.

Mass loading of the active area of the quartz crystal is calculated by the equation[6]

$$\frac{\Delta f}{f^\circ} = -\frac{\Delta m}{\delta F d} \quad (1)$$

f° is the unperturbed (initial) frequency of the crystal, Δf is the change in frequency due to deposited mass on active area, Δm is the mass change of the active area of the quartz crystal, δ is the density of the crystal, F is the active area of the crystal, and d is the thickness of the crystal. Since the change of thickness of the crystal due to film deposition on the electrodes is negligible, eq 1 can be reduced to the form

$$\Delta m = -\frac{m^\circ \Delta f}{f^\circ} \quad (2)$$

where m° is the mass of the active area of the crystal. The crystal thickness and film area are such that the sensitivity of this microbalance is 1.44×10^{-9} g/Hz.

A grease-free high-vacuum system was used. By baking the system for 24 hr at 150°, the base pressure of the system reached 5×10^{-9} Torr.

Direct evaporation of iron was made from a helical iron filament of 99.99% purity, which was supplied by Material Research Corp. Before evaporation, the iron filament was well outgassed and transformed to the γ phase at pressures of $\sim 10^{-8}$ Torr. The pressures of the system during evaporation were generally less than 3×10^{-8} Torr. The evaporators were mounted perpendicular to the plane of the crystal and radiation shields made of stainless steel plates were provided to protect the walls from unnecessary heating and metal deposition. Oxygen of 99.95 mol %, furnished by Airco (Matheson), was used.

For BET surface area determinations of both unreacted and oxidized films, tetramethylsilane was used as an adsorbate. The tetramethylsilane, of 99% purity (Matheson Coleman and Bell), was degassed by repeated freezing and thawing in vacuum and dehydrated with 4A molecular sieve before obtaining the adsorption isotherms. The pressure of tetramethylsilane was measured with a mercury manometer using an MKS Baratron pressure transducer as a null detector.

For all kinetics measurements, the oxygen pressure was controlled manually. The pressure rise was monitored by recording the output from the ionization gauge. At pressures greater than 10^{-4} Torr, the pressure rise time was no faster than the observed chemisorption kinetics. This obviously set an upper limit to meaningfully measurable rates which could be followed.

Results and Discussion

Film Area Measurements. It was demonstrated in a previous study[8] that tetramethylsilane as a room-temperature adsorbate can be a good replacement for N_2 which is traditionally used in BET area determinations. The value of 46.3 Å^2 (relative to 16.2 Å^2 for N_2 as measured on a nonporous, low-area alumina) was taken as the molecular cross-sectional area for tetramethylsilane (TMS).

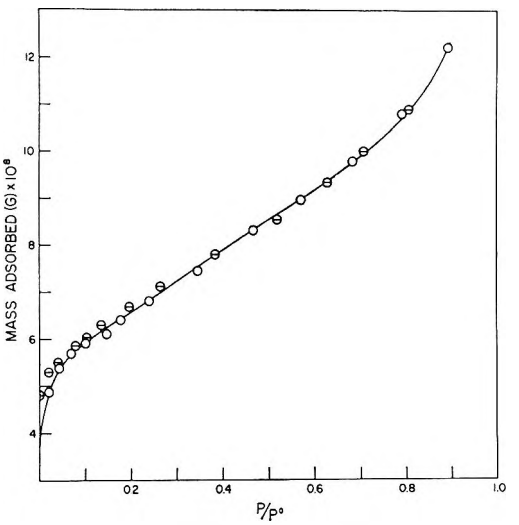

Figure 1. TMS isotherm (grams of TMS *vs.* relative pressure) on an iron film at 23.3°: O, adsorption; ⊖, desorption.

TMS adsorption isotherms were obtained over the relative pressure range, $0.01 < P/P^\circ < 0.90$, at 25.0°. Desorption branches were also obtained for several representative substrates.

One of the isotherms is displayed in Figure 1, and several representative BET plots are displayed in Figure 2. Calculated BET areas for substrates given a variety of pretreatments are listed in Table I.

Table I

Film wt, g/cm² × 10⁶	Film thickness, Å	Film area, cm²	Roughness factor	Remarks
4.7	60	1.85	2.9	Unoxidized
4.2	54	1.76	2.8	Unoxidized
5.5	70	0.77	1.2	O_2, 4.5 hr at 8×10^{-8} Torr
4.9	63	0.63	1.0	O_2, 1 hr at $\sim 5 \times 10^{-7}$ Torr
4.2	53	0.82	1.3	O_2, 10 min at $\sim 7 \times 10^{-6}$ Torr
5.3	67	0.61	0.95	O_2, 5 min at 4×10^{-4} Torr

Geometric area, 0.64 cm²

As can be seen in Table I, there is marked diminution in film area concomitant with oxidation. Experimental uncertainties coupled with the usual reservations associated with the BET model dictate a roughness factor of 2.9 ± 0.4 for virgin films and 1.1 ± 0.2 for oxidized

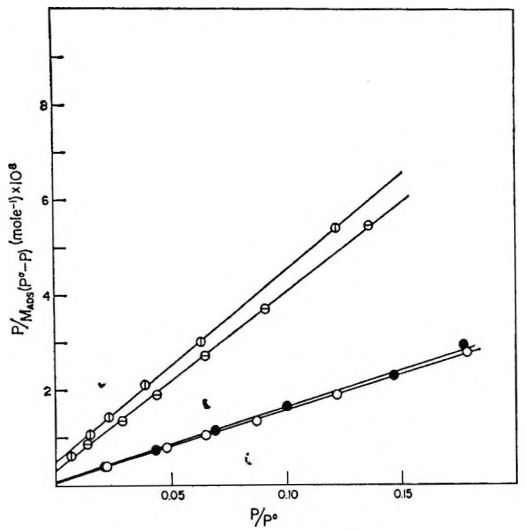

Figure 2. TMS BET plots for iron (O and ●) and oxide (⊕ and ⊖) films.

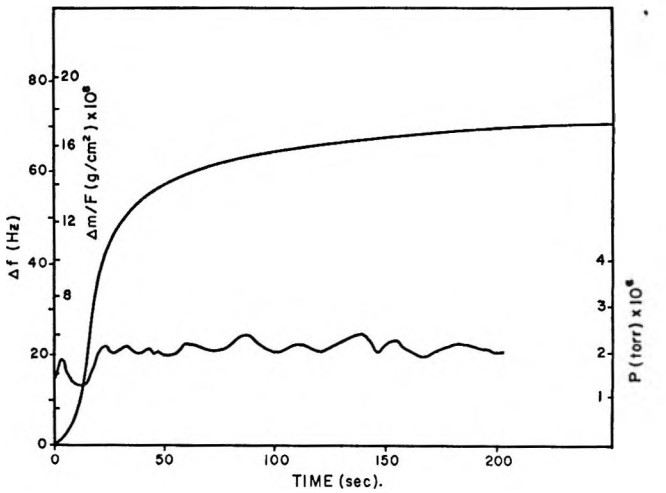

Figure 3. Typical frequency (cycles)–time, mass–unit area (g/cm²)–time, and pressure–time plots for oxygen–iron at 24°.

films. This diminution in film area is in agreement with the work of Brennan, Hayward, and Trapnell,[9] who found a 57% reduction in film area.

Little is known about the microtopology and pore structure of evaporated films. This provided the motivation for obtaining both the adsorption and desorption branches of the TMS isotherms. Hysteresis in these branches would be an indication of pore volumes with restricted pore necks. As would be expected no hysteresis was observed for oxidized films with roughness factors near unity, but neither was any hysteresis observed for the pure iron films. This latter finding obviates any extensive porosity and the identical roughness factors found here with TMS and elsewhere with N_2[9]—two molecules with quite different dimensions—negates an appreciable concentration of fissures in the size range of 3 Å (N_2) to 6 Å (TMS). Rather the findings are consistent with an exposed "hill and valley" profile for the pure iron substrate with characteristic dimensions on the order of the film thickness.

No dependence of film area on film mass could be detected although wide variations in film mass were not attempted. Porter and Tompkins[10] reported a linear variation between the area and mass for evaporated iron. They followed Beeck's[11] method in comparing areas by using the amount of hydrogen adsorbed at 273°K and 0.1 Torr. There are two obvious possible explanations for their discrepancies with the present data: either hydrogen is adsorbed in addition to being adsorbed or there are pores accessible to H_2 but not to N_2 or TMS.

Oxygen Interaction Kinetics. Uptake rate measurements were performed in the pressure interval 2×10^{-7} to 5×10^{-5} Torr at 24°. The lower limit was established as 100-fold greater than the background partial pressure of O_2 and CO by residual gas analysis. The upper limit does not reflect a time constant limitation on the quartz crystal microbalance but is realistically set by a limiting dexterity in manually controlling the dosing valve.

A representative trace of frequency change (which can be transformed into mass uptake *via* eq 2) *vs.* time is shown in Figure 3. When the abscissa is depressed to accommodate longer uptake times, there is a knee bend at $\Delta f \cong 60$–70 cycles and an asymptotic approach of Δf to 140–170 cycles at which time O_2 uptake rates were on the order of a monlayer per year. Both the knee bend point and asymptotic limit varied randomly (but tandemly) from run to run between the above limits and appeared to be consistent with the observed variations in BET surface areas. For analysis of rate behavior which would be consistent from run to run, it was necessary to refer to coverages relative to the knee bend which were assigned a value $\theta = 4.00$ corresponding to the number of layers of FeO (see below). Below the knee bend point uptake is referred to as the "fast" process and, above the knee bend, the "slow" process.

If the growth product is assumed to be FeO, $\Delta f = 60$ Hz corresponds to 4.0 layers based on the average roughness factor of 1.1. The limiting asymptote either reached slowly or induced rapidly by raising the O_2 pressure to $\sim 10^{-2}$ Torr, corresponds to 10 layers of oxide based on a roughness factor of 1.1, in good agreement with other studies.[2,3,12] Of course, the chemical stoichiometry of thin oxides in their initial growth stages is questionable. For thicker growths Vernon, *et al.*,[13]

(9) D. Brennan, D. O. Hayward, and B. M. W. Trapnell, *Proc. Roy. Soc., Ser. A*, **256**, 81 (1960).

(10) A. S. Porter and F. C. Tompkins, *ibid., Ser. A*, **217**, 544 (1953).

(11) O. Beeck, *Advan. Catal.*, **2**, 151 (1950).

(12) J. Kruger and H. T. Yolken, *Corrosion*, **20**, 29t (1964).

(13) W. H. J. Vernon, E. A. Coleman, C. J. B. Clews, and T. J. Nurse, *Proc. Roy. Soc., Ser. A*, **216**, 375 (1953).

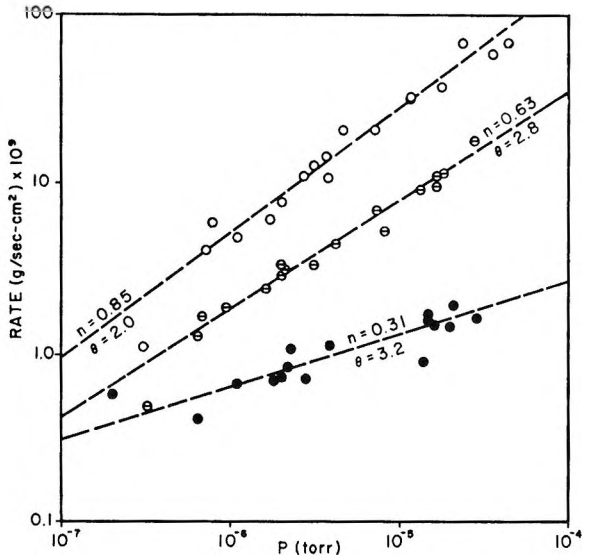

Figure 4. Oxygen uptake rate *vs.* pressure at θ = 2.0, 2.8, and 3.2 with apparent reaction orders shown.

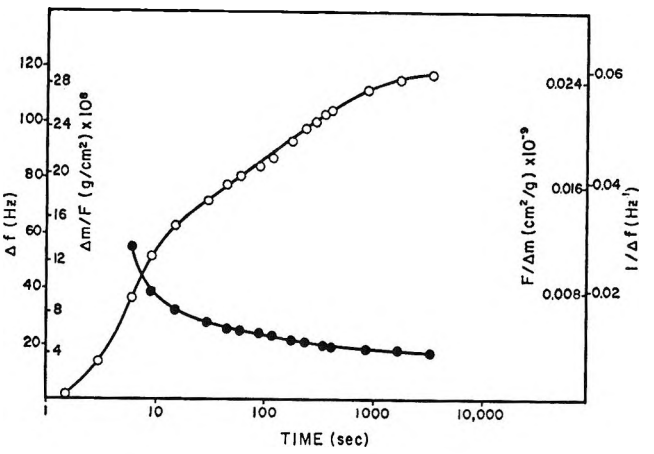

Figure 5. Diagnostic rate plots: O, Cabrera–Mott (mass change *vs.* log time); ●, Elovich (reciprocal mass uptake *vs.* log time).

using electron diffraction identified Fe_2O_3 formed on polycrystalline Fe at 200°. Davies and Evans[14] also observed the formation of Fe_2O_3 at temperatures up to 200°. On the other hand, in the thin-film region Pignocco and Pellissier[4,5] preferred to consider that FeO is formed on (011) and (001) faces of iron exposed to O_2 at very low pressures. These results could be compatible if the initial growth corresponds closely to a 1:1 stoichiometry which with increased thickness converges to a 2:3 limiting ratio. In any event the limiting growth is multilayer in character and is much larger than found in a previous study on Al.[8] Interestingly, the residual oxidation rate for iron in the asymptotic limit is no greater than that for Al.

If the kinetics obey the rate equation

$$\frac{\mathrm{d(mass)}}{\mathrm{d}t} = A p_{O_2}{}^{n}(1 - \theta b) m e^{-E(\theta)/RT} \qquad (3)$$

where $E(\theta)$ is an activation energy at a coverage θ and A and b are constants, then the slope, n, of a log rate *vs.* log p plot at constant θ is the reaction order with respect to O_2. Such plots are constructed in Figure 4 corresponding to θ = 2.0, 2.8, and 3.5, respectively. The rms slopes are 0.85, 0.63, and 0.31, respectively, clearly indicating that as $\theta \rightarrow 0$, $n \rightarrow 1$ and as $\theta \rightarrow 4$ or greater, $n \rightarrow 0$. Such variations in reaction order are always indicative of multistage mechanisms with one or more transitions in rate-limiting steps.

In the initial stages of surface oxidation processes there should, in principle, be at least two regimes: the first corresponds to chemisorption and the second to lattice penetration by oxygen. Simple chemisorption processes are commonly first order at constant coverage whereas oxidation in the limit of thick, coherent oxides is zero order. Obviously the "fast" process cannot be identified solely or even largely with chemisorption, for the uptake corresponds to 4 layers of FeO. The detailed overall mechanism for the "slow" process is just as complicated. However in the oxidation regime one can possibly evoke the Cabrera–Mott inverse-log rate law and avoid a more detailed mechanistic description. In Figure 5 such a plot is reconstructed for the slow process at a pressure of $5 \pm 1 \times 10^{-6}$ Torr. The lack of linearity is discouraging but is hardly surprising in the light of the thinness of the oxide layer.

A detailed examination of Figure 3 reveals that at low coverages the oxygen uptake has an induction period. Such processes are usually referred to as autocatalytic. To demonstrate this behavior more graphically, sticking probabilities $\left(\uparrow\atop\downarrow\right)$(S), which are essentially derivatives of the uptake–time curves, were calculated for the data in Figure 3 and are plotted in Figure 6. The exact character of either of the two plots below θ = 1 is subject to considerable experimental uncertainty because of the difficulty of rapidly attaining a steady-state system pressure. This is demonstrated by a plot of the corresponding pressure–time behavior in Figure 3. In the first 5 sec of exposure the pressure is constant to no better than ±30%. However such large uncertainties still do not eliminate the maximum in Figure 6. For exposures at the lowest pressure (2×10^{-7} Torr) initial pressure fluctuations were similar but the initial uptake rate was approximately tenfold lower with nominal monolayer completion taking approximately 150 sec. Under these conditions the same induction effect was noted. The maximum sticking probability (reaction rate) was always found to occur at $\theta = 1 \pm 0.2$ regardless of O_2 pressure. Since the reaction order is still near unity up to θ = 2, the incorporation rate clearly must be

(14) D. E. Davies and U. R. Evans, *J. Chem. Soc.*, 4373 (1956).

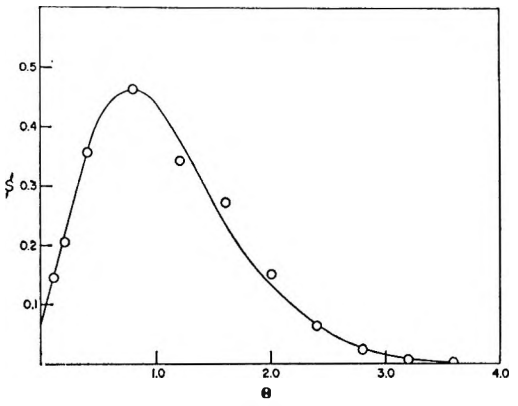

Figure 6. Sticking probability ($\overset{\uparrow}{S}$) *vs.* coverage (Θ).

greater than the chemisorption rate up to these coverages over the pressure range studied. At a nominal $\theta = 1$ the external surface must consist almost entirely of iron atoms with the oxygen incorporated in the lattice and the sticking probability of O_2 on the initially regenerated iron surface is considerably enhanced over the pure iron substrate if one is to observe an induction period. Although it is obvious that rate data exhibiting maxima cannot exhibit Elovich behavior, the corresponding direct-log plot is also exhibited in Figure 5. At intermediate uptake times there is a very restricted linear region.

As oxidation proceeds at a given pressure, a steady-state concentration of surface regenerated iron sites will be reached. The onset of the steady state with regard to the extent of oxidation is dependent on the O_2 pressure—the higher the pressure, the less extensive the oxidation prior to the steady state. For instance, at 10^{-4} Torr the oxidation of iron has been predicted to be zero order[15] for $\theta > 1$. Likewise the above argument explains previous observed[2,3] fractional orders varying between (0.20 and 0.29) wherein experimental techniques did not permit a study of the "fast" process.

In partial conflict with the present data is an ellipsometric study by Kruger and Yolken.[12] They reported abnormally low sticking coefficients of $\sim 5 \times 10^{-3}$—two orders of magnitude lower than reported here. They cleaned their iron surface by an 800° reduction in a hydrogen atmosphere. Chemisorbed hydrogen may have diminished $\overset{\uparrow}{S}$ for O_2 as Ponec and Knor[16] reported for nitrogen on iron films with preadsorbed hydrogen.

The pertinent conclusions may be summarized as follows: (1) The chemisorption of O_2 on iron is a first-order process. (2) There is a rapid incorporation of oxygen to give the equivalence of 4 layers of FeO followed by a slow incorporation to give an asymptotic approach to 10 layers of FeO. (3) The incorporation of O_2 is rapid compared to the rate of chemisorption at a pressure of 2×10^{-6} Torr for the first several layers of FeO formed but at 4 layers and greater the incorporation process has become rate limiting and is zero order in O_2. (4) The sticking coefficient on iron is ~ 0.5 when one layer of FeO is formed and subsequently diminishes to ~ 0 at 4 layers. (5) The process may be schematically pictorialized as

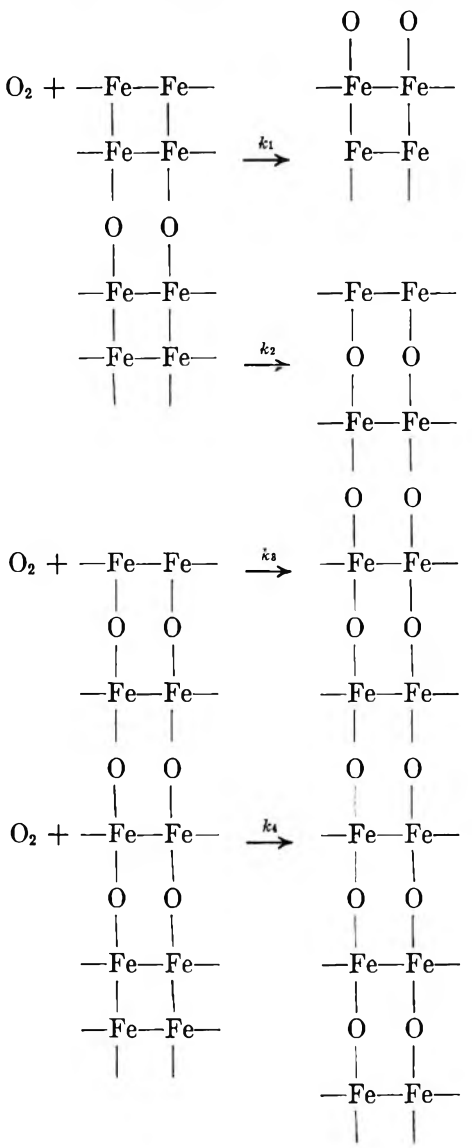

The results dictate that $k_3 > k_1$ and that initially step 2 is faster than 1 or 3. Transiently a steady state such as step 4 is attained and subsequently further incorporation becomes limited by migration velocity. Whether the oxygen incorporation into the lattice is a concerted process or not is open to question. (6) Such studies on evaporated films are complicated by a diminution of the surface roughness during the oxidation process.

Acknowledgment. The authors wish to express their appreciation to the United States Army Research Office, Durham, N. C., and to The Robert A. Welch Foundation for their support.

(15) N. Cabrera, *Phil. Mag.*, **40**, 175 (1949).
(16) V. Ponec and Z. Knor, *J. Catal.*, **10**, 73 (1968).

Composition and Surface Structure of the (0001) Face of α-Alumina by Low-Energy Electron Diffraction

by T. M. French and G. A. Somorjai

Inorganic Materials Research Division of the Lawrence Radiation Laboratory and the Department of Chemistry of the University of California, Berkeley, California 94720 *(Received December 29, 1969)*

The (0001) crystal face of α-alumina undergoes a change of surface structure upon heat treatment under vacuum above 1250°. This order–order phase transformation [$(Al_2O_3(0001)(1 \times 1) \rightarrow$ rotated $(\sqrt{31} \times \sqrt{31})$] is accompanied by a change in the chemical composition of the surface, *i.e.*, by the loss of oxygen. The structural change is reversible and either surface structure can be obtained alternately by heat treatment of the samples in oxygen ($>10^{-4}$ Torr) or in the presence of excess aluminum on the surface. The large unit cell which characterizes the high-temperature oxygen-deficient surface structure is indicative of a marked mismatch between the surface layer and the underlying layers. Evidence is presented to show that the aluminum cation in the high-temperature surface structure is in a reduced valence state and that the structure could be composed of a cubic overlayer on the hexagonal α-alumina substrate. It appears that compounds with unusual oxidation states which would not be stable in the solid state may be stabilized in the surface environment.

Introduction

Low-energy electron diffraction (LEED) studies have revealed that the structure of single-crystal surfaces can be correlated with the chemical-bonding properties which characterize the solid. Semiconductors (Si, Ge, GaAs, InSb, diamond, etc.) have surface structures which are mainly characterized by unit meshes which are larger than the bulk unit cell.[1] The surface structures have well-defined temperature ranges of stability and can undergo order–order phase transformations as a function of temperature. It has been suggested[2] that the surface structures are due to small, periodic displacements of atoms out of the surface plane (surface buckling) to optimize the overlap of localized electron orbitals of the covalently bonded atoms. Metal surfaces with some notable exceptions (Au,[3] Pt,[4] Bi,[5] and Sb[5]), largely appear to have the same periodicity at the surface which also characterized the bulk structure. If there is only scanty experimental information available on the structure of a few semiconductor and metal surfaces, large band gap insulators have been investigated to even a lesser extent. Among large band gap insulators α-alumina, Al_2O_3,[6,7] and some of the alkali halides[8,9] have been the subject of extensive low-energy electron diffraction studies. It has been reported that different crystal faces of α-alumina assume surface structures after heating to high temperatures which are different from that predicted by the bulk unit cell.[6,7,10] Alkali halides, on the other hand, maintain their bulk structure up to the surface although the freshly cleaved surface may be stabilized by halogen evolution (excess anion vacancies) or precipitation of the alkali metal (excess cation vacancies).[11]

We have studied the (0001) surface of α-alumina under a variety of experimental conditions in the temperature range of 25–1700°. It is the purpose of this paper to show that changes of the surface structure are accompanied by changes in the chemical composition of the surface. The ordered alumina surface transforms into a new surface structure upon heating the solid, with simultaneous evolution of oxygen. The transition between this oxygen-deficient, high-temperature surface structure and the simple, low-temperature, bulk-like surface is reversible and depends on the partial pressure of oxygen over the surface. Arguments will be presented to show that the aluminum cation in the high-temperature surface structure is in a reduced, lower oxidation state. Such a change in the chemical surface composition as a function of temperature may not be restricted to alumina alone but could well be detectable for many compounds with similar bonding characteristics as well.

(1) J. J. Lander, *Progr. Solid State Chem.*, **2**, 26 (1965); and J. W. May, *Ind. Eng. Chem.*, **57**, 19 (1965).

(2) D. Haneman and D. L. Heron, "Proceedings of the Conference on the Structure and Chemistry of Solid Surfaces," G. A. Somorjai, Ed., John Wiley and Sons, New York, N. Y., 1969, p 24; J. J. Burton and G. Jura, *ibid.*, p 21.

(3) P. W. Palmberg and T. N. Rhodin, *Phys. Rev.*, **161**, 586 (1967).

(4) A. E. Morgan and G. A. Somorjai, *Surface Sci.*, **12**, 405 (1968).

(5) F. Jona, *ibid.*, **8**, 57 (1967).

(6) J. M. Charig, *Appl. Phys. Lett.*, **10**, 139 (1967).

(7) C. C. Chang, *J. Appl. Phys.*, **39**, 5570 (1968).

(8) I. Marklund and S. Andersson, *Surface Sci.*, **5**, 197 (1966).

(9) H. Tokutaka and M. Prutton, *ibid.*, **11**, 216 (1968).

(10) J. M. Charig and D. K. Skinner, "Proceedings of the Conference on the Structure and Chemistry of Solid Surfaces," G. A. Somorjai, Ed., John Wiley and Sons, New York, N. Y., 1969, p 34.

(11) M. Prutton, private communication.

Experimental Section

The crystals were the best grade available from the Union Carbide Corp. A spectroscopic analysis by the supplier of typical boules showed the impurity levels (in ppm): Mg < 2, Si < 4, Fe < 2, Ca < 2, Ga < 2, Cu < 0.5. The samples which were cut to size 5 × 7 × 1 mm were supplied already oriented to the (0001) face and polished. The crystals were chemically etched using potassium persulfate and boric acid mixed in equal parts by volume. The crystals were heated in the etching mixture to approximately 750° in a gold-covered combustion boat for about 30 min. Weak diffraction beams were often observed without further treatment. Varian LEED apparatus was used for all these experiments.

The crystal was mounted in a star-shaped piece of 1-mil tungsten foil. The points of the star were bent around the sample to hold it securely. There was minimum contact of the points with the front surface. The tungsten foil was spot welded to tantalum supports which were attached to the crystal holder and manipulator.

The crystal was heated by radiation from the resistively heated tungsten foil. The temperature was measured by an optical pyrometer focused on the tungsten which had been vacuum evaporated on the back of the sample. The error in measuring the sample temperature is difficult to estimate but should be less than ±100°.

Vacuum evaporation by heating the crystal to high temperatures (>1200°) was used most frequently to clean the surface. Ion bombardment could also be used for surface cleaning. Ion bombardment using 1–2-keV argon ions disordered the alumina surface and eliminated the diffraction features. Heating, above about 900° after ion bombardment, would restore the surface order. The minimum conditions of ion bombardment to disorder the diffraction pattern were 10^{-5} Torr argon, 2 keV accelerating potential, and 4 mA ionizing electron flux (~4×10^{-6} A ion current) for 10 min.

Bulk aluminum oxide has a hexagonal structure. The hexagonal unit cell has 6 layers of close-packed oxygen as shown in Figure 1a. In between these layers in the octahedral holes are placed the aluminum atoms.[12] In each aluminum layer there are as many octahedral sites as there are oxygen atoms. In order to maintain the stoichiometry characteristic of Al_2O_3, only two-thirds of these sites are filled. The sites that contain aluminum atoms are of two kinds as shown in Figure 1b. The octahedral holes are large enough so that the aluminum ions can occupy different positions. An octahedral site can either have an aluminum in A′ position or in B′ position or the site can be empty. If only the aluminum sites are considered in the successive layers, there is a progression of A′, B′, empty site, A′, B′, empty site, etc. Since the oxygen ions are hexagonally close packed,

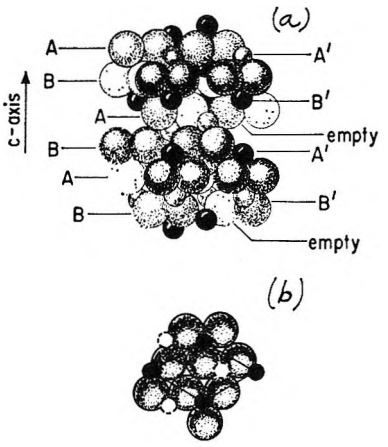

Figure 1. (a) Bulk structure of α-Al_2O_3. Large balls are oxygen ions and the small balls show the position of the aluminum ions. (b) View of the α-Al_2O_3 structure from the direction normal to the (0001) face. The dotted balls are underneath the oxygen layer.

the oxygen atoms in successive layers occupy alternating positions which may be labeled A, B, A, B. Therefore the successive layers of the crystal could be labeled A, A′, B, B′, A, empty, B, A′, A, B′, B, empty, A, A′, etc. Hence we have six oxygen layers in the bulk unit cell.

The vapor pressure over α-alumina has been measured as a function of temperature. The vapor of aluminum oxides contains both AlO and Al_2O molecules in addition to aluminum and oxygen species.[13,14] Figure 2 shows the vapor pressure curves as reported by Searcy and Brewer.[13] The melting point of aluminum oxide is 2050°.

Elimination of Surface Charge at Insulator Surfaces during LEED Studies

When electrons in the energy range 5–100 eV strike the aluminum oxide surface, a surface charge builds up rapidly such as to repel the incident electron flux before it can penetrate the crystal or be scattered by the periodic atomic potential at the surface. Thus, under usual operating conditions which are employed in LEED studies of metal surfaces, no diffraction pattern can be obtained from an Al_2O_3 surface below a certain voltage, usually 100 eV. This negative surface charge build-up poses serious limitation to structural studies of insulator surfaces since most of the experimental information about the surface structure is obtained in the electron energy range 30–120 eV. Above these energies a larger fraction of the electrons penetrate below the surface and the back-scattered beam contains more information about the bulk than about the top-

(12) R. W. G. Wyckoff, "Crystal Structure," Vol. II, Interscience Publishers, New York, N. Y., p 8.

(13) L. Brewer and A. W. Searcy, *J. Amer. Chem. Soc.*, **73**, 5315 (1951).

(14) R. P. Burns, *J. Chem. Phys.*, **44**, 3307 (1966).

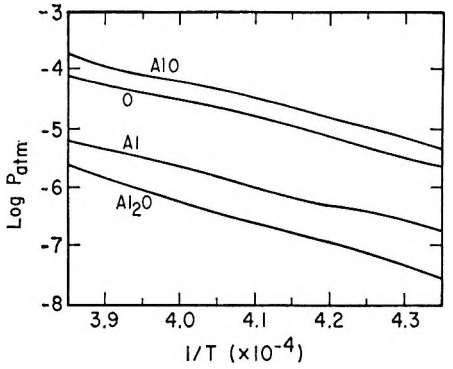

Figure 2. The vapor composition over aluminum oxide.

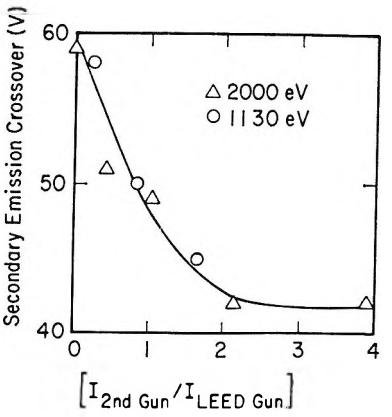

Figure 3. The secondary emission crossover as a function of the gun current ratio, I_2/I_{LEED} scaled by an arbitrary factor, for two different electron energies of the second gun.

most atomic layer. Therefore, in LEED studies of insulator surfaces it is imperative that this negative surface charge layer be removed from the studied surface.

We have been successful in removing the negative surface charge layer from the (0001) face of alumina by the simultaneous application of two electron guns; one, operating at 1–2 kV at grazing angle of incidence (15°), was continuously discharging the surface while the usual LEED gun, operating in the range 10–350 eV, was used to obtain the diffraction pattern.

This technique should be applicable for the elimination of negative surface charge from all those insulator surfaces which (a) have a secondary electron emission flux above a given incident electron energy which is larger than the incident electron flux and which (b) do not decompose or otherwise interact chemically with the high-energy electron beam. It is well known that for many insulators the yield of secondary electrons which leave the solid during electron bombardment is greater than the incident electron flux, above a certain threshold energy of the incident electron beam.[15] The incident electron energy at which the ratio of the secondary electron emission current and the incident electron beam current becomes larger than unity is often called the "secondary emission crossover." By continuously spraying the insulator surface with electrons with energies above the secondary crossover the surface can be discharged or a small positive surface charge may be established. Since this positive surface charge attracts electrons toward the crystal, it does not affect the diffraction process although it may change the energy of the incident electrons to a small extent.

The secondary emission crossover for the clean (0001) face of alumina which exhibits a (1 × 1) surface structure appears to be in the range 80–100 eV. The crossover energy varied within this range from sample to sample and was found to be dependent on the purity of the surface. Slight contamination (found by X-ray fluorescence) of the sample by tantalum which was often used at first as a crystal holder could increase the crossover to over 200 eV.

The secondary emission crossover may also depend on the chemical surface composition. When the surface structure was changed to an ordered, oxygen-deficient surface structure (to be discussed later), the crossover energy decreased to approximately 50 eV. Since heat treatments were necessary to produce this new structure and the accompanying changes in surface composition, the possibility of unwanted impurities diffusing to the surface and aiding reduction of the crossover cannot be eliminated. It is likely, however, that the lowering of the secondary emission crossover is caused by the change in the surface composition of the (0001) face of alumina.

Since the electrons from the high-energy electron gun which is used to eliminate the negative surface charge are energetic enough to pass through the grid system of the electron optics and reach the fluorescent screen, the background intensity is increased. This, however, does not prevent the detection of diffraction spots from a fairly ordered alumina surface to as low as 25-eV incident electron beam energy from the LEED electron gun. The high-energy electron flux which is used to discharge the surface was cut back to a minimum in order to minimize the background intensity on the fluorescent screen. Figure 3 gives the secondary electron emission crossover for the α-alumina with a (1 × 1) surface structure as a function of the ratio of the current from the high-energy gun (I_2) and the LEED electron gun (I_{LEED}) for two different electron energies of the discharging gun. The crossover decreases with increasing I_2/I_{LEED} ratio at first, but above I_2/I_{LEED} = 2, the ratio remains constant. The crossover appears to be independent of the discharging gun energy in the range 1000–2000 eV. No studies have been made with the discharging gun below this energy range.

Although our technique, *i.e.*, the simultaneous use of two electron guns, was successful in removing the space

(15) A. J. Decker, *Solid State Phys.*, **6**, 251 (1958).

charge, other techniques might also be employed in studies of insulator surfaces. For alkali halide crystals which are known to interact with the electron beam LEED surface studies may be carried out at elevated temperatures using thin samples in order to increase the ionic conductivity sufficiently. For crystals which exhibit photoconductivity, illumination by light of suitable wavelength might be employed to increase the surface conductivity and thereby eliminate the surface charge. Pulsing the grazing angle electron gun and the grids at a well-chosen frequency and energies could also be considered. This would minimize the high-background intensity common in experiments with the continuous application of a discharging electron gun.

Surface Structures of Alumina

It is well known that the structure of alumina surfaces is different from that which is expected by projection of the bulk unit cell to the various crystal surfaces.[7,10] The (0001) crystal face exhibits its (1 × 1) bulk-like structure up to ~1250° under vacuum. It rearranges above this temperature to give a weak ($\sqrt{3} \times \sqrt{3}$) (rotated 30°) surface structure and upon further heating to the final rotated ($\sqrt{31} \times \sqrt{31}$) surface structure which is stable to the highest studied temperature of 1700°. Schematic representations of the resultant diffraction patterns are shown in Figure 4.

It is customary to designate the complex surface structures by the coefficients of its transformation matrix which generate the structures with the two unit cell vectors of the bulk-like substrate, vectors of equal length 4.76 Å and 60° apart.[3] This is given, for the rotated ($\sqrt{31} \times \sqrt{31}$) pattern by

$$A = \begin{pmatrix} 11/2 & \sqrt{3/2} \\ -\sqrt{3/2} & 11/2 \end{pmatrix} \qquad B = \begin{pmatrix} 11/2 & -\sqrt{3/2} \\ \sqrt{3/2} & 11/2 \end{pmatrix}$$

These matrices generate the basic vectors for two domains (A and B) which must be present on the surface simultaneously in order to generate the observed diffraction pattern. These domains are formed from the original unit mesh by expanding the unit vectors by a factor of $\sqrt{31}$ and by rotating them either +9 or −9°. We shall show evidence that the alumina surface which exhibits the rotated ($\sqrt{31} \times \sqrt{31}$) surface structure is oxygen deficient.

The other two crystal faces, the ($\bar{1}012$) and ($11\bar{2}3$) orientations which have been studied, give (2 × 1) and (4 × 5) surface structures, respectively, at high temperatures (>900°).[16]

We have been able to confirm the presence of the surface structures on the (0001) face of α-alumina which have also been reported by Charig[6,10] and Chang.[7,16] Due to the reproducibility of these surface characteristics there can be little doubt that these structures are the property of the clean alumina. We have not employed electron bombardment heating of the samples in our experiments to avoid difficulties in interpreting our results which are due to the well-documented interaction of the high-energy electron beam with the crystal surface.[6,7,10]

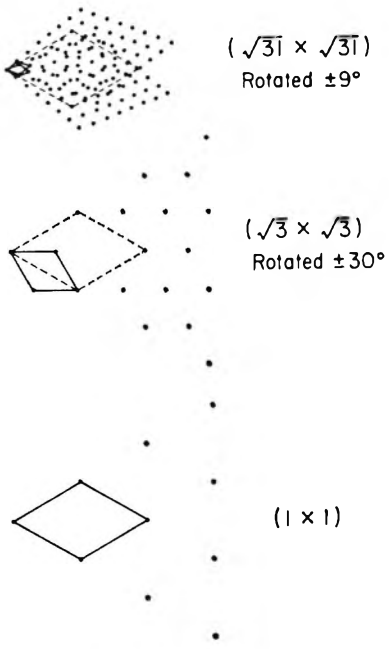

Figure 4. Schematic representation of three aluminum oxide diffraction patterns which are due to the appearance of different surface structures on the (0001) crystal face.

Properties of the Rotated ($\sqrt{31} \times \sqrt{31}$) Surface Structure

Heating, by radiation, the freshly etched (0001) alumina surface which exhibits the (1 × 1) surface structure under vacuum, above 1250°, readily produces the rotated ($\sqrt{31} \times \sqrt{31}$) surfaces structure (Figure 5). During its formation oxygen evolution is detectable by mass spectrometer. Oxygen evolution was also detected by Charig during the formation of the rotated ($\sqrt{31} \times \sqrt{31}$) surface structure by electron bombardment heating above 900°.[10] Ion bombardment using high-energy (2 keV) argon ions disorders the surface structure. The ($\sqrt{31} \times \sqrt{31}$) structure is readily regenerated, however, by annealing the surface at approximately 800°. Ion bombardment appears to disorder the surface without changing the ratio of Al to O in the topmost layers. Thus, once it forms upon heat treatment at high temperatures this surface structure is extremely stable and reproducible under various experimental conditions.

Its stability temperature range is clearly shown by the silicon deposition studies which have been made to investigate the epitaxy of silicon on the (0001) alumina surface. Silicon is known to etch the alumina surface

(16) C. C. Chang, "Proceedings of the Conference on the Structure and Chemistry of Solid Surfaces," G. A. Somorjai, Ed., John Wiley and Sons, New York, N. Y., 1969, p 77.

Scheme I

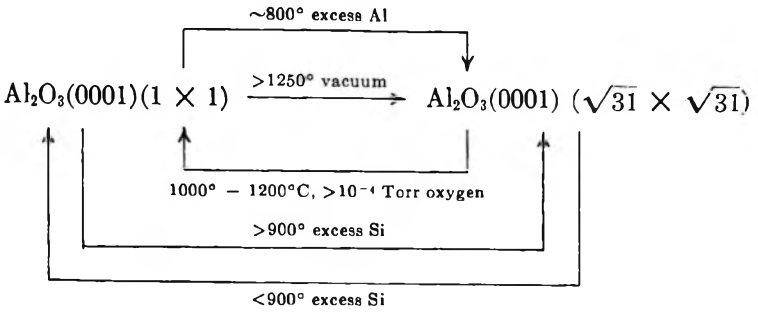

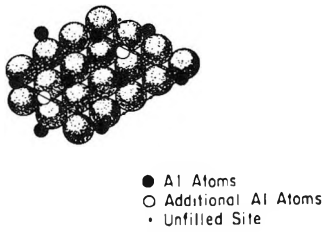

Figure 5. One of the possible unit cells to generate the rotated ($\sqrt{3} \times \sqrt{3}$) aluminum oxide surface structure.

by removing both aluminum and oxygen according to the overall reaction

$$3Si(g) + Al_2O_3 = 3SiO(g) + 2Al(g)$$

Chang has detected all of the gaseous species in their proper atomic ratios by mass spectrometer.[16] Charig by heating the alumina surface above 900°, after deposition of silicon at lower temperatures either on the (1 × 1) or rotated ($\sqrt{31} \times \sqrt{31}$) surface of alumina, has regenerated the rotated ($\sqrt{31} \times \sqrt{31}$) surface structure. Heating the (0001) face below 900° after silicon deposition yields the (1 × 1) bulk-like surface structure.[10]

In order to establish that the stable high-temperature rotated ($\sqrt{31} \times \sqrt{31}$) surface structure has a chemical composition which is different from that of the low-temperature (1 × 1) surface structure and to establish its stoichiometry we have heated the (0001) face in excess oxygen and aluminum vapor.

When the rotated ($\sqrt{31} \times \sqrt{31}$) surface structure is heated in oxygen at pressures $>10^{-4}$ Torr (these pressures considered to be high in ultrahigh-vacuum LEED studies) at 1200° the (1 × 1) surface structure was obtained. Removal of the oxygen and heating to a slightly higher temperature (1250° or higher) under vacuum caused the reappearance of the rotated ($\sqrt{31} \times \sqrt{31}$) surface structure. This reversible phase transformation could be induced at will, upon introduction or removal of oxygen. The reproducible reversible behavior of the transformation makes contamination (for example by WO) unlikely as a mechanism for the transformation.

Pressures lower than 10^{-4} Torr of O_2 did not induce detectable changes in the high-temperature surface structure during the usual heat treatment times (15 min).

When aluminum metal was condensed on the (0001) alumina surface which exhibits the (1 × 1) surface structure, the rotated ($\sqrt{31} \times \sqrt{31}$) surface structure is formed with heating to about 800°. In the absence of excess aluminum on the surface, the (1 × 1) surface structure would have formed at this temperature. Thus, the structural changes which occur under vacuum (mass spectrometric detection of oxygen while the rotated ($\sqrt{31} \times \sqrt{31}$) structure forms), in oxygen (the (1 × 1) surface structure is regenerated in a temperature range, ~1200°, where the rotated ($\sqrt{31} \times \sqrt{31}$) structure is stable), and with aluminum (the rotated ($\sqrt{31} \times \sqrt{31}$) structure is formed in a temperature range, ~800°, where the (1 × 1) surface structure is stable) indicate that the (0001) face of alumina undergoes a surface phase transformation from a (1 × 1) surface structure to an oxygen-deficient rotated ($\sqrt{31} \times \sqrt{31}$) surface structure which is stable at high temperatures. This phase transformation can be made reversible by variation of the chemical surface composition using excess oxygen or aluminum. The transformations which have been found to occur under the various experimental conditions may be summarized by Scheme I.

Discussion

The following statements summarize those results of our experiments which can be used to interpret the surface structures of the (0001) face of α-alumina.

(1) Upon heating the (0001) face of alumina, which exhibits a (1 × 1) surface structure, *in vacuo* (>800°) new ordered surface structure which can be characterized as ($\sqrt{3} \times \sqrt{3}$) (rotated 30°) appears. Subsequent heating to even higher temperatures produces the ordered rotated ($\sqrt{31} \times \sqrt{31}$) surface structure. Simultaneously, there is oxygen evolution from the surface. This surface structure, once formed, is extremely stable under a variety of experimental conditions.

(2) Heating the high-temperature rotated ($\sqrt{31} \times \sqrt{31}$) surface structure in oxygen at pressures greater than 10^{-4} Torr at 1000–1200°, restores the low-temperature (1 × 1) surface structure [($\sqrt{31} \times \sqrt{31}$) $\xrightarrow{O_2}$ (1

$\times$ 1)]. Excess aluminum on the (0001) face, on the other hand, catalyzes the reverse [$(1 \times 1) \xrightarrow{Al} (\sqrt{31} \times \sqrt{31})$] order–order transformation at ~800°.

These results would indicate that the ordered surface structures which appear at high temperature are oxygen deficient with respect to the bulk structure of alumina. The transient $(\sqrt{3} \times \sqrt{3})$ surface structure can be explained to form by the removal of oxygen atoms or by the addition of aluminum atoms to the (0001) surface. A possible model of the rearranged surface which would give rise to the observed diffraction pattern is shown in Figure 5. Other explanations are also possible: in all of the proposed models, however, the substrate serves as a template for the arrangement of the surface atoms.

Many of the diffraction patterns which exhibit fractional order diffraction beams can be rationalized in a straightforward manner. The extra spots appear at positions which are some fraction of the distance between the integral order diffraction beams and they indicate the appearance of a new surface periodicity which is an integral multiple of and is parallel to the bulk unit cell. Such a surface structure can be generated by periodic buckling of the surface or by the result of partial occupation of the available surface sites. The surface structure thus formed retains the symmetry of the underlying substrate and there is little reason to postulate any marked change in the chemical bonding of surface atoms with respect to the atoms in the bulk.

It is however, difficult to explain the appearance of large surface unit cells which are also rotated with respect to the bulk unit cell without invoking significant chemical rearrangements in the surface layer. The rotated $(\sqrt{31} \times \sqrt{31})$ unit mesh signifies mismatch between the newly formed surface structure and the underlying hexagonal substrate. The surface atoms which are built into the new structure can no longer adjust to the symmetry of the substrate, and the observed diffraction pattern is likely to be due to the coincidence of lattice sites between the rearranged surface layer and the hexagonal substrate.

Let us assume that, along with the change of chemical composition, the aluminum cation, Al^{3+}, is reduced in the oxygen-deficient surface layer to the Al^{+} (or Al^{2+}) oxidation state. The ionic radius would be expected to increase as the valency is decreased. Let us estimate the ionic radius of Al^{+} ion. This ion may be more stable than the Al^{2+} ion because it has a pair of s electrons in the outer shell. It can be assumed that the radii of isoelectronic atoms and ions are inversely proportional to the effective nuclear charges.[17] Using this rule and using the interatomic distance of Mg and Na in the solid, we have ~0.8 Å for the radius of Al^{+}, and ~0.7 Å for the Al^{2+} radius. It is clear that ions of this size will be unable to pack the same way as the small (0.5 Å) Al^{3+} ions pack in the α-alumina. It seems unlikely that the larger ions will be able to fit in the "holes" in a close-packed oxygen lattice at all. If the valency of the aluminum cation is reduced in the aluminum-rich surface layer whose chemical composition should be closer to Al_2O or AlO than to Al_2O_3, what kind of surface structure would be expected to form? It is instructive to compare several oxides of the M_2O_3 type which have the same structure as Al_2O_3 such as V_2O_3, α-Fe_2O_3, and Ti_2O_3.[12] These cations form stable oxides in their 2+ oxidation states as well (VO, FeO, and TiO).[18] The oxides of the MO type, however, have face-centered cubic structure. The ratios of the ionic radii M^{3+}/O^{2-} and M^{2+}/O^{2-} are very similar for all these compounds to that which is found for Al_2O_3 and is expected for AlO.

Both Al_2O(vapor) and AlO(vapor) are stable and were detected in the vapor composition over α-alumina in equilibrium and also during vaporization into vacuum. The other group III elements are also known to form stable oxides in their higher (3+) oxidation states (Ga_2O_3, In_2O_3, Tl_2O_3) while their vapors contain the monovalent oxides (Ga_2O, In_2O, and Tl_2O_2) in large concentrations.[14,19] The monovalent oxides in group III of the periodic table, M_2O, appear to be much more stable (Tl_2O is a stable solid whose thermodynamic properties have been measured although only an X-ray powder pattern is reported)[20] than the divalent oxides of the MO type. Other stable monovalent oxides such as Li_2O and Na_2O which should have similar ion ratios as in Al_2O form cubic structures of the fluorite (CaF_2) type.

Thus, it appears that if the high-temperature oxygen-deficient rotated $(\sqrt{31} \times \sqrt{31})$ surface structure has a composition which corresponds to Al_2O (or AlO), it would be likely to form a cubic overlayer in which the cation is appreciably larger than in the underlying hexagonal (0001) substrate. Strong mismatch due to the differences in structure and ion sizes in the two layers should be expected.

We have been able to generate the rotated $(\sqrt{31} \times \sqrt{31})$ surface structure by placing a cubic overlayer in which the interatomic distance was increased to adjust for the increased cation radius on top of the (0001) substrate. There are several cubic structures which can generate the rotated $(\sqrt{31} \times \sqrt{31})$ unit mesh by coincidence with the (0001) substrate. One of these surface structures is given in Figure 6.

Additional evidence that the $(\sqrt{31} \times \sqrt{31})$ structure is due to a reduced aluminum oxide overlayer comes

(17) L. Pauling, "The Nature of the Chemical Bond," Cornell University Press, Ithaca, N. Y., 1960, p 512.

(18) R. W. G. Wyckoff, "Crystal Structure," Vol. I, Interscience Publishers, New York, N. Y., 1963, pp 86–91.

(19) National Bureau of Standards Circular 500, U. S. Government Printing Office, Washington, D. C., 1961, pp 166–175.

(20) F. Halla, H. Tompa, and L. Zimmerman, *Z. Kristallogr., Kristallgeometrie, Kristallphys., Kristallchem.*, **86**, 304 (1933).

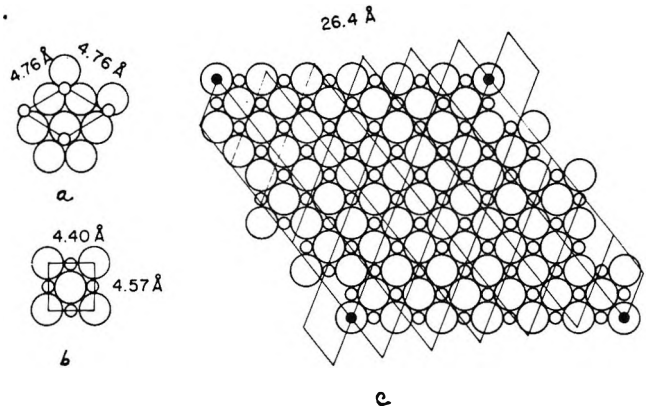

Figure 6. (a) The hexagonal unit cell of the (0001) substrate and the (b) square unit cell of the oxygen-deficient overlayer which together generate the (c) unit cell corresponding to the rotated ($\sqrt{31} \times \sqrt{31}$) by coincidence.

from studies of the epitaxial deposition of silicon on the (0001) face. Silicon was found to etch the α-alumina surfaces efficiently. Silicon however, is also a reducing agent which could remove oxygen from the surface by the postulated reaction $Al_2O_3 + 2Si(vapor) \rightarrow Al_2O + SiO(vapor)$ in addition to the reaction proposed by Chang.[16] It should be noted that the reduced oxides Al_2O, AlO, and O and Al are all among the products of the disassociative vaporization of α-alumina.[14] It was found that silicon causes the formation of the rotated ($\sqrt{31} \times \sqrt{31}$) surface structure above 900°, a temperature too low for this phase transformation under vacuum.[10]

Additional evidence that the rotated ($\sqrt{31} \times \sqrt{31}$) surface structure is composed of a cubic overlayer on the hexagonal (0001) substrate comes from studies of aluminum oxide structures which are formed on the aluminum metal surface. The oxide has a cubic structure in this aluminum-rich environment.[21]

So far we have considered the rotated ($\sqrt{31} \times \sqrt{31}$) structure (Figure 7) as a two-dimensional surface structure which forms due to the composition change in the topmost atomic layers at the (0001) face of α-alumina. The possibility that these structural changes are not restricted to the surface layer but are propagated into the bulk of the solid cannot be overlooked. It is unlikely, however, that the oxygen-deficient structure could be present in more than a few atomic layers in the bulk. Since oxygen has to be removed to affect the surface rearrangement, this would make the rate of

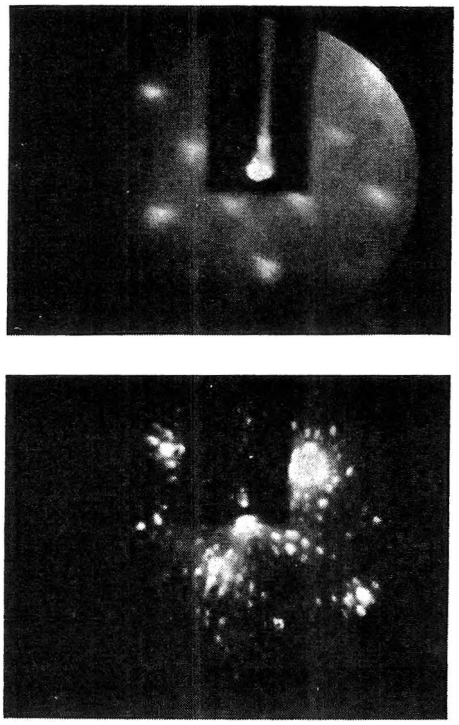

Figure 7. The diffraction patterns which correspond to the (1 × 1) (top) and to the high-temperature rotated ($\sqrt{31} \times \sqrt{31}$) (bottom) surface structures.

bulk rearrangements oxygen diffusion limited. Thus, this process would be markedly decelerated as the thickness of the oxygen-deficient layer increases.

If the reduced oxides of aluminum, Al_2O or AlO, are stable in the α-alumina surface at elevated temperatures, it is likely that the other group III oxides of the M_2O type might also be stable in the surface environment. Investigation of the surface structures of Ga_2O_3 and In_2O_3 would be of interest. It is also likely that oxides of other metals (MgO, BaO, for example) may have unusual oxidation states which are stabilized in the surface environment. It should be noted that vanadium pentoxide, V_2O_5, has been reported recently[22] to undergo a change of surface composition (accompanied by loss of oxygen) upon heating *in vacuo* with a corresponding order–order transformation of its surface structure.

Acknowledgment. This work was supported by the U. S. Atomic Energy Commission.

(21) F. A. Cotton and G. Wilkinson, "Advances in Inorganic Chemistry," Interscience, New York, N. Y., 1966, p 439.

(22) L. Fiermans and J. Vennik, *Surface Sci.*, 9, 187 (1968).

Thermal Degradation of an Anhydride-Cured Epoxy Resin by Laser Heating[1a]

by A. S. Vlastaras[1b]

Advanced Materials Technology Laboratory, General Electric Company, Philadelphia, Pennsylvania 19142
(Received October 27, 1969)

A 100-W CO_2 continuous laser beam has been used to heat a cycloaliphatic epoxy polymer sample, through a platinum crucible suspended in the glass reaction tube of a Cahn RG electrobalance. The beam was transmitted through an IRTRAN-4 entrance window into the system. Calibration of the laser was made with respect to temperatures attained by the platinum crucible and measured with a chromel–alumel thermocouple and a recorder. The electrobalance, which was in an all-glass conventional vacuum system, was used to record the changes of weight with time and obtain the rates of degradation. Chemical analysis, by ir and mass spectrometry, showed that the major gaseous products formed during degradation were water and carbon dioxide. Other products, such as toluene, pyridine, acetone, methyl formate, hexatriene, methylacetylene, and butadiene, were found to be present in smaller amounts. The activation energy associated with the weight loss process was 18 ± 3 kcal/mol. An attempt is made to explain the thermal degradation of the epoxy polymer, by postulating a mechanism based on the degradation products and the prevailing conditions in the system.

Introduction

Lasers have provided a powerful new tool for the study of the interaction of matter with radiation and the development of new techniques for the investigation of material properties and processes. One of those techniques, which is used in the present investigation, is the utilization of laser irradiation as a convenient method of heating polymeric materials for thermal degradation studies. There are a limited number of publications in the literature dealing with this method. In all of them the laser used was a ruby (pulsed) laser and the sample was exposed directly to the laser radiation. Direct laser heating of polymeric materials and organic compounds in the ionization chamber of a T.O.F. mass spectrometer revealed that ions as well as neutral species were produced during the pyrolysis reaction.[2,3] The principal gaseous decomposition products formed from aromatic compounds in a focused laser beam experiment were methane and acetylene.[4] Finally, the pyrolysis of coal and graphite has been studied using lasers.[5–7]

In the present study a continuous laser (CW) was used to heat a platinum crucible containing the polymeric material. The continuous laser was selected since it provides faster heating rates than heating techniques used by other workers[8–10] for studying thermal degradation of polymers and facilitates kinetic studies at relatively high temperatures.

The object of this paper is to describe some of the thermogravimetric experiments carried out under almost isothermal conditions using the Cahn RG electrobalance. Rates, activation energy, degradation products, and degradation mechanism of Union Carbide ERL-4221 epoxy resin cured with hexahydrophthalic anhydride will be discussed.

Experimental Section

Materials. The polymer was a cycloaliphatic epoxy, cross-linked through hexahydrophthalic anhydride. Epoxy ERL-4221 was obtained from Union Carbide, and HHPA from the Allied Chemical Co. The polymer consisted of 100 parts by weight of ERL-4221 and 89 parts by weight of HHPA. It was cured for 3.5 hr at 125° and then for another 4 hr at 160°.

Apparatus and Procedures. The experiments were carried out with the apparatus shown in Figure 1. The laser used was an adjustable 0–100-W CO_2 gas laser (Coherent Radiation Laboratories, Model 40). The beam was transmitted through an IRTRAN-4 entrance window into the system. The window was attached to

(1) (a) Paper presented at the Eighth Conference on Vacuum Microbalance Techniques, Wakefield, Mass., June 12–13, 1969. (b) Address communications to Bell Telephone Laboratories, Inc., Whippany, N. J. 07981.

(2) (a) F. J. Vastola and A. J. Pirone, *Amer. Chem. Soc., Div. Fuel Chem., Preprints*, **10**, C-53 (1966); (b) F. J. Vastola, A. J. Pirone, and B. E. Knox, Proceedings of the 14th Annual Conference on Mass Spectrometry and Allied Topics, 1966, p 78.

(3) F. J. Vastola and A. J. Pirone, International Mass Spectrometry Conference, Berlin, Germany, Sept 1967.

(4) R. H. Wiley and P. Veeravagu, *J. Phys. Chem.*, **72**, 2417 (1968).

(5) F. S. Karn and J. M. Singer, *Fuel*, **47**, 235 (1968).

(6) F. S. Karn and A. G. Sharkey, Jr., *ibid.*, **47**, 193 (1968).

(7) W. K. Joy, W. R. Ladner, and E. Pritchard, *Nature (London)*, **217**, 640 (1968).

(8) H. H. G. Jellinek, *J. Polym. Sci.*, **4**, 13 (1949).

(9) N. Grassie and W. W. Kerr, *Trans. Faraday Soc.*, **55**, 1050 (1959).

(10) S. L. Madorsky, *J. Res. Nat. Bur. Stand.*, **62**, 219 (1959).

the hangdown tube of the electrobalance with GE RTV-156 adhesive. A small copper cylinder, with a hole punched to match the IRTRAN-4 window, was inserted in the hangdown tube. This helped to prevent back-reflection of the laser beam from the platinum crucible and provided more uniform heating of the crucible from the multiple reflection of the laser beam on the copper.

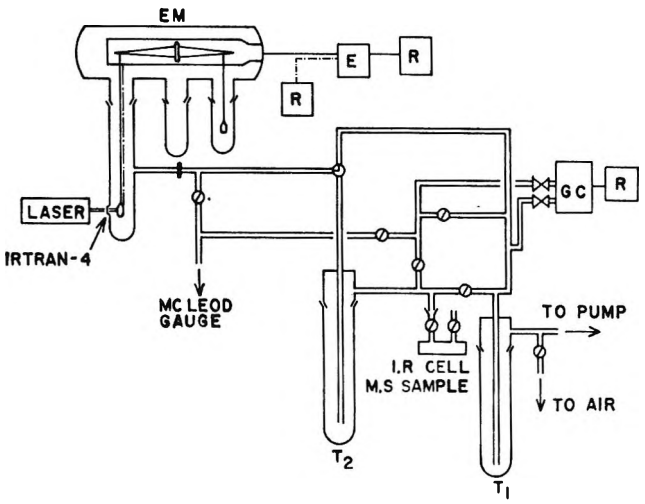

Figure 1. Diagram of the apparatus.

In a typical experiment the sample (8–10 mg) was first evacuated to approximately 0.35 Torr and then thermally degraded by using the laser. The temperature of the sample was the one corresponding to the laser calibration curve, for certain laser parameters, as will be discussed later. The loss of weight was recorded with time and the degradation products were trapped at liquid nitrogen temperature. After the experiment was terminated, the products could be transferred to and analyzed by a Beckman GC-5 gas chromatograph, coupled to the vacuum system, or by infrared and mass spectrometric analyses. Ir analyses were performed on a Perkin-Elmer 457 spectrophotometer. A Consolidated Electrodynamics Corp. Model 21-620A mass spectrometer was used for mass spectrometric analysis.

Laser Calibration. The power output of a continuous laser is a function of the premixed gas pressure in the discharge tube and the laser current. By changing either parameter, the power output changes. The power output of the laser was calibrated with respect to temperatures attained by a platinum crucible containing the same amount of sample as in a typical experiment. The temperature of the crucible was measured with a chromel–alumel thermocouple and a recorder. The recorded temperature was the one within the platinum crucible. The pressure of the premixed gas in the laser system was 16 Torr. The temperature was determined for various laser currents from 10 to 110 mA, as shown in Figure 2.

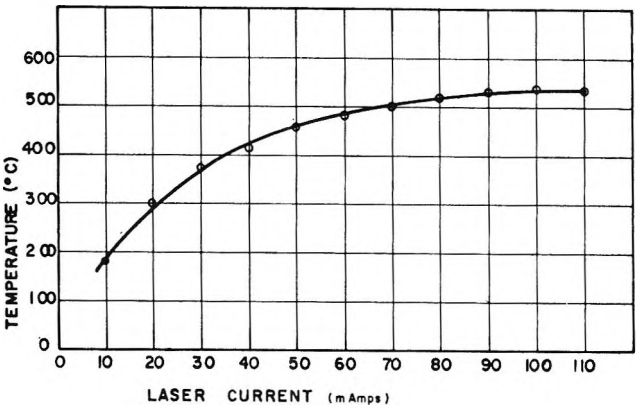

Figure 2. Laser calibration curve.

Discussion of Results

Rates and Activation Energy. Some of the experimental difficulties in thermogravimetry include weight loss due to spattering of the sample, delay in the vaporization of volatile products due to diffusion, the effect of aerodynamic forces, and thermomolecular flow. It should be pointed out that this investigation was conducted with a goal of obtaining, if possible, thermogravimetric data commensurate with our research objectives regarding the use of the laser and not the detailed study of these difficulties. Nevertheless, weight losses due to spattering, for example, were eliminated by the use of small samples (8–10 mg).

The experiments were carried out as described in the Experimental Section. The volatilization of the polymer as a function of time at various temperatures is shown in Figure 3. As indicated, complete volatilization takes place in the temperature range 373–455° after 2–7 min of heating. The polymer degradation was complete and no residue was left at the end of any experiment.

In Figure 4, the rates of volatilization are plotted against per cent volatilization. These rates were calculated from the slopes of the volatilization–time curves with the aid of an electronic computer. The data in Figure 4 indicate that distinct maxima were reached at approximately 70% volatilization.

During the above thermal degradation studies, a white deposit appeared in the hangdown reaction tube at a place immediately next to the hot zone. The nature of the deposit can best be discussed later, following the presentation of these results.

The activation energy for the degradation of polymers can be obtained from either extrapolated apparent initial rates or from maximum rates,[10] unless the degradation follows simple kinetics from which the order and rate constants of the reaction can be obtained. The activation energy was calculated from the Arrhenius relationship $k = Ae^{-E/RT}$, by plotting the maximum rates against $1/T$ as shown in Figure 5. The straight line shown is the best fit through the three points, and

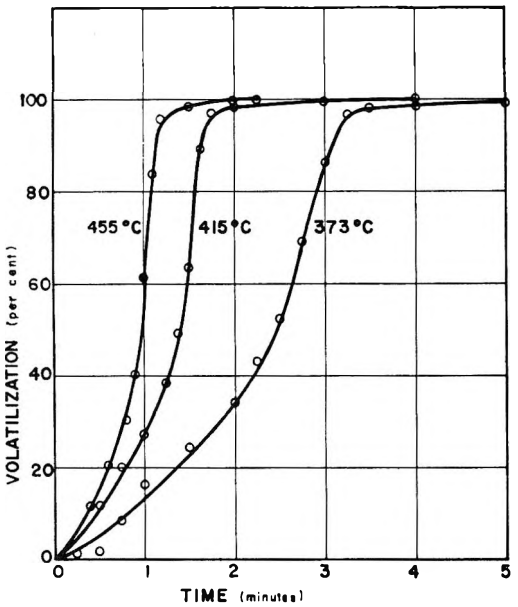

Figure 3. Thermal degradation curves.

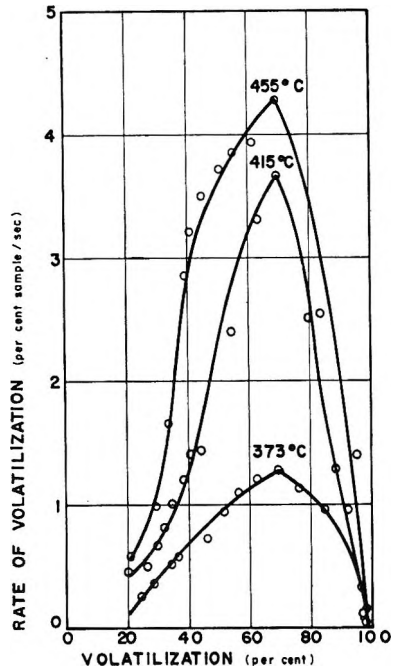

Figure 4. Rates of thermal degradation.

its slope corresponds to an activation energy of 18 ± 3 kcal/mol.

Degradation Products. A preliminary and incomplete analysis of the degradation products was performed on the gas chromatograph coupled to the system. The gas-sampling valve (1-cm³ loop) was evacuated and the sample admitted to it. Then, the sample was passed through a stainless steel column (6 ft long, $^1/_8$ in. o.d., packed with 3% SE30 on 42–60 mesh Chromosorb G) and subsequently through a thermal conductivity detector. A typical chromatogram

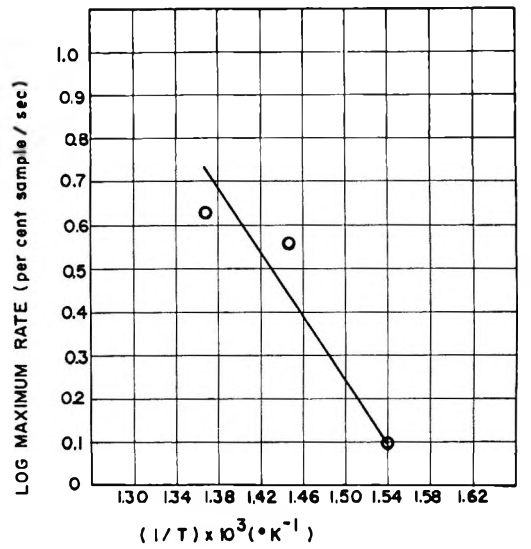

Figure 5. Arrhenius plot for the thermal degradation.

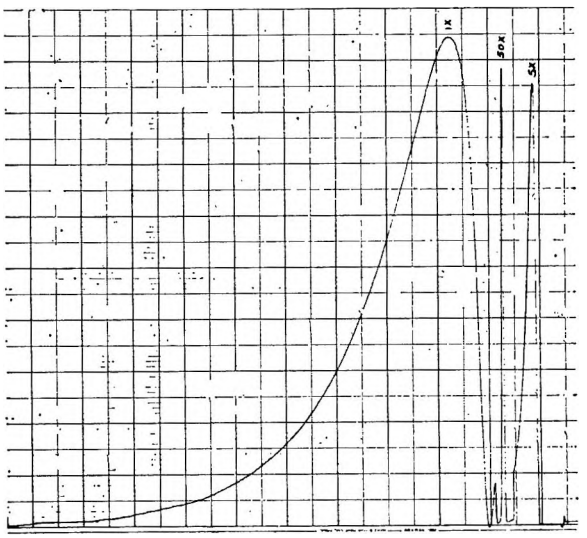

Figure 6. Typical chromatogram.

Table I: Mass Spectrometric Analysis of the Gaseous Degradation Products Collected at Liquid Nitrogen Temperature[a]

Component	Temp, °C 373	415	455
Water	87.0	89.0	83.0
Carbon dioxide	9.7	8.2	12.7
Toluene	0.70	0.71	1.2
Pyridine	0.65	0.64	0.89
Acetone	0.33	0.045	0.45
Methyl formate	0.28	0.068	0.60
Hexatriene	0.23	0.23	0.30
Methylacetylene, Butadiene	0.51	0.57	0.78

[a] Composition in % v/v.

is shown in Figure 6. The first peak (right to left) is due to the pressure differential between detector (high

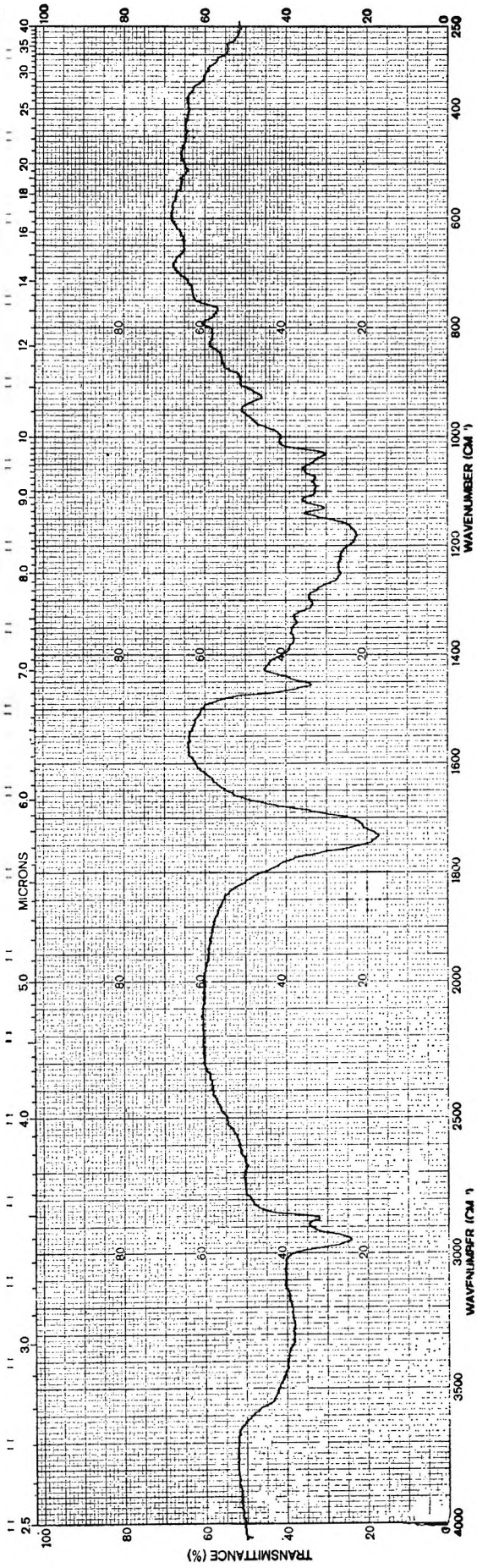

Figure 7. Infrared spectrum of undegraded polymer (KBr pellet).

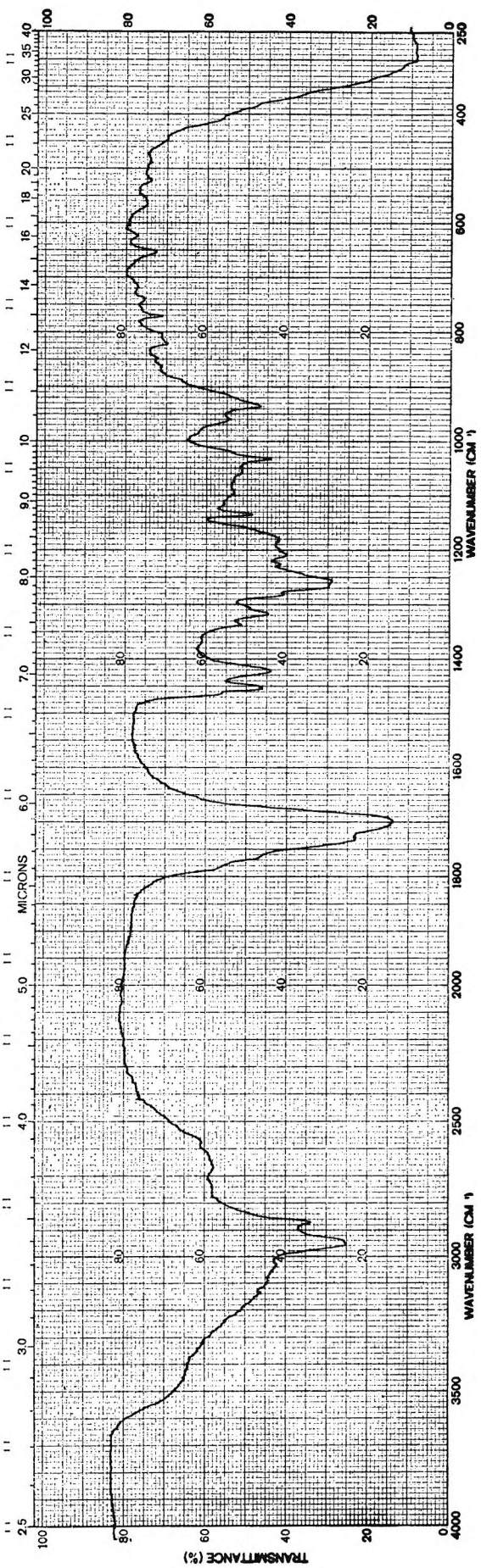

Figure 8. Infrared spectrum of reaction tube deposit (thin film between KBr plates).

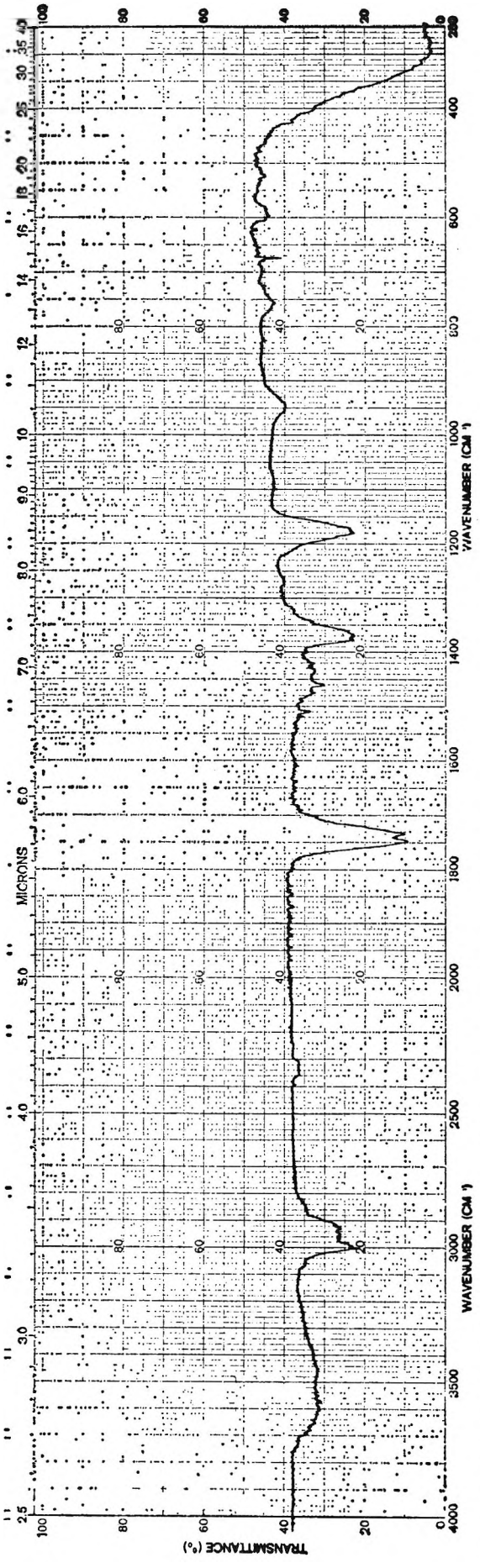

Figure 9. Typical infrared spectrum of degradation products (gas cell, 10 cm cell path).

pressure) and sampling valve (low pressure) during sample injection. The second peak represents carbon dioxide and the third one water. This method can be developed further for quantitative analysis, by selecting the proper column, or columns in series, capable of separating all of the degradation products.

The infrared spectra of undegraded polymer, white deposit in the reaction tube, and thermal degradation products are shown in Figures 7–9. A comparison between the spectra of undegraded polymer and the white deposit indicates that no major differences exist between the two, except the enhancement of the bands at 1420, 1180, and 930 cm^{-1} for the latter. The significant bands for the degradation products (Figure 9) are the water bands between 3450 and 3650 cm^{-1}, the carbon dioxide bands at 2350, 1340, and 670 cm^{-1}, the methyl formate bands at 1745 and possibly 1190 cm^{-1}, and the acetone bands at 1730 and 1175 cm^{-1}.

Further evidence as to the nature of the degradation products arises from the mass spectrometric analysis of these products collected at liquid nitrogen temperature. Table I summarizes the results for the various degradation temperatures. No explanation can be given for the small amounts of acetone and methyl formate at 415°.

It should be emphasized that the mass spectrometric data do not include decomposition products such as carbon monoxide and hydrogen since these will condense below the temperature of liquid nitrogen. However, it is expected that the degradation of the polymer would give rise to both of them, as will be discussed later.

Thermal Degradation Mechanism. One of the initial reactions is most likely dehydration of the polymer. Lee[11,12] has presented considerable evidence that water is a reaction product in the thermal degradation of epoxy polymers.

Based on analytical results, it appears that the initial decomposition reaction can be expressed as shown in eq 1. The residue from the initial stage of decomposition proceeds further to another solid, carbon dioxide, and carbon monoxide as shown in eq 2 until in eq 3 acetylene is produced.

The cleavage of the main epoxy structure, eq 4, gives rise to carbon dioxide, hexatriene, and a radical. Dehydrogenation of this radical leads to the formation of toluene and hydrogen. There is evidence from esr that resonance-stabilized free radicals occur in the thermal degradation of epoxies.

The presence of pyridine among the degradation products is rather unusual, since no nitrogen-containing compounds were used in preparing the polymer, including the minor impurities in the epoxy resin and HHPA, and it is difficult to postulate a mechanism.

(11) L. H. Lee, *J. Polym. Sci., Part A*, **3**, 859 (1965).
(12) L. H. Lee, *J. Appl. Polym. Sci.*, **9**, 1981 (1965).

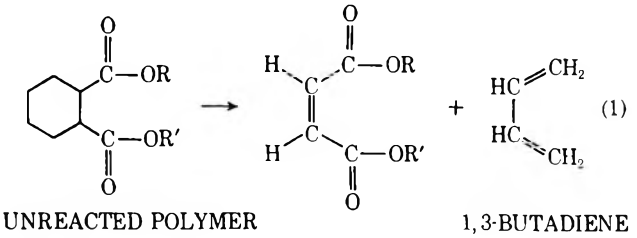

UNREACTED POLYMER 1,3-BUTADIENE (1)

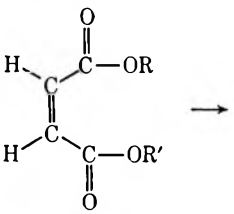

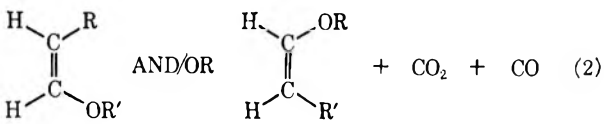

AND/OR (2)

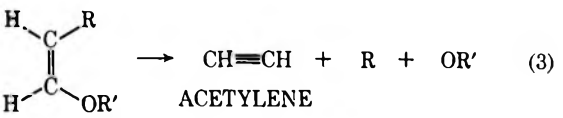

ACETYLENE (3)

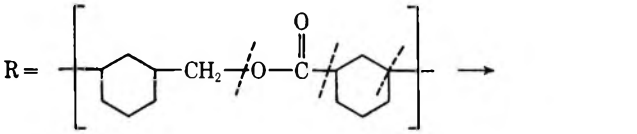

1,3,5-HEXATRIENE (4)

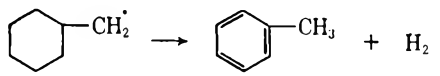

TOLUENE

However, a literature survey revealed that laser radiation can induce dissociation of gases.[13-15] About 10^8 W/cm^2 is necessary to induce field ionization of a gas, and this is about five orders of magnitude greater than that available from an unfocused CO_2 laser (recommendation of reviewer). Thus any dissociation of gas would have to be thermal. Here, it is clearly indicated that atomic nitrogen (thermal dissociation) or an excited nitrogen species (electronic or vibrational excitation of nitrogen molecule) can be formed in the neighborhood of the platinum crucible through laser excitation of the molecular nitrogen present in the system at approximately 0.35 Torr pressure. It has been established that active nitrogen reacts with unsaturated hydrocarbons by insertion to the double bond.[16] Consequently, hexatriene is attacked by active nitrogen and through an intermediate activated complex forms pyridine and a methyl radical as shown in eq 5.

Acetylene formed in eq 3 reacts with a methyl radical to give methylacetylene. Subsequently, a water molecule adds on the triple bond of methylacetylene, in accordance with Markovnikov's rule, and rearranges into acetone (eq 5).

Finally, as an alternative to the cleavage of the main epoxy structure proposed in the first step of eq 4, another cleavage pattern is postulated in eq 6 to account for the presence of methyl formate among the degradation products.

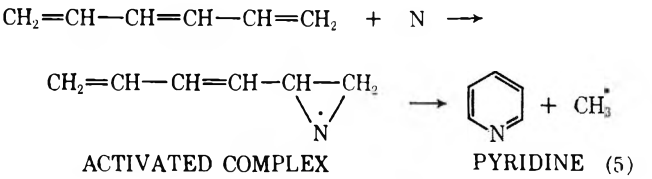

ACTIVATED COMPLEX PYRIDINE (5)

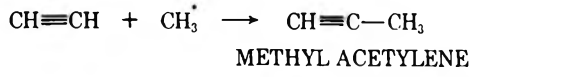

METHYL ACETYLENE

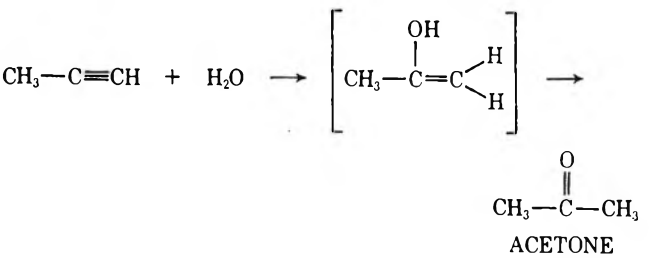

ACETONE

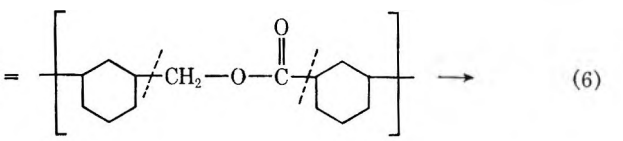

(6)

METHYL FORMATE

(13) M. Young and M. Hercher, *J. Appl. Phys.*, **38**, 4393 (1967).

(14) R. G. Meyerand, Jr., *AIAA J.*, **5**, 1730 (1967).

(15) J. F. Verdieck and A. W. H. Mau, *Chem. Commun.*, 226 (1969).

(16) H. G. V. Evans, G. R. Freeman, and C. A. Winkler, *Can. J. Chem.*, **34**, 1271 (1956).

Thermal Decomposition of Hydrated Cadmium Oxide

by R. B. Fahim

Department of Chemistry, Faculty of Science, University of Assiut, Assiut, United Arab Republic

and G. A. Kolta

National Research Centre, Dokki, Cairo, United Arab Republic *(Received August 25, 1969)*

The work comprises a comparative study of the thermal decomposition of hydrated cadmium oxide and that of precipitated cadmium hydroxide. In both cases, four processes are involved: (a) dehydration, *i.e.*, removal of excess (combined) water, (b) crystallization of the dehydration product, (c) decomposition to the oxide, and (d) deoxygenation of the formed oxide. The energy of activation of decomposition for both materials is the same, while that for dehydration process is higher in case of the hydroxide. On hydration of oxygenated cadmium oxide (*i.e.*, prepared at 300° in an oxygen atmosphere of 760 Torr), no combined water is taken up by the formed hydroxide. This fact is confirmed by thermogravimetry and infrared analysis.

Introduction

In an earlier work,[1] it was shown that cadmium oxide takes up water from the vapor phase almost stoichiometrically to give the hydroxide. This phenomenon was noticed primarily by the color change of the oxide, attending hydration, from dark brown to pale yellow, and it was confirmed by X-ray investigation. A mechanism was suggested for the hydration process.

Similar behavior was noticed with magnesium oxide.[2] Studying the isothermal decomposition, it was found that the rate of decomposition of the hydrated magnesium oxide is much higher than that of the original hydroxide. This result was attributed to the fact that water is bound much less strongly to the oxide as indicated from the low energy of the decomposition process. A similar conclusion was recorded for the decomposition of calcite and carbonated calcium oxide.[3]

In general very limited work has been devoted to the study of the isobaric dehydration of cadmium hydroxide.[4,5] Low and Kamel[6] studied the thermal decomposition of cadmium hydroxide and they showed that dehydration is not, in reality, continuous but occurs in steps accompanied by considerable textural changes of the solid.

The present investigation deals with a comparative study of the thermal decomposition of hydrated cadmium oxide and that of the corresponding hydroxide. This was investigated by thermogravimetry, differential thermal analysis, X-ray diffraction techniques, and infrared spectroscopy. Furthermore, experiments were extended for the study of the isothermal decomposition of the parent materials.

Experimental Section

Apparatus and Techniques. Thermogravimetry was performed with an automatically recording thermobalance (Gebruder Hetzsch-Selb, West Germany) as described by Gordon and Campbell.[7] The weight change was recorded on a 6-in. chart over a range of 240 mg, simultaneously with temperatures up to 600° at a rate of 5°/min. The isothermal decomposition was also followed with the thermobalance incorporating a device to keep the temperature constant arbitrarily throughout the experiment. The temperature of the furnace was first raised to the required temperature and the specimen was then shock-heated by lowering the furnace to surround it. Differential thermal analysis was carried out using an automatically recording Linseis apparatus, Type L 160 KS (West Germany); the rate of heating was 5°/min. For tga and dta, the technique adopted was according to the recommendations of McAdie.[8] X-Ray diffraction patterns were obtained with the aid of a Philips unit, Type PW 1010, applying a copper tube, and using a 114.83-mm Debye–Scherrer powder camera, Type PW 1024. The diffraction patterns were matched with ASTM cards.[9] Infrared absorption spectra were obtained with the aid of a Perkin-Elmer grating infrared spectrophotometer, Model 337, and adopting the KBr technique.

Materials. The preparation of cadmium hydroxide was described earlier.[1] Cadmium oxide was prepared by the thermal decomposition of the corresponding hydroxide at 200, 250, or 300° for 5 hr *in vacuo*. Hydration was effected by directly exposing this oxide

(1) R. B. Fahim and K. M. Abd El-Salaam, *J. Catal.*, 9, 63 (1967).

(2) R. I. Razouk and R. Sh. Mikhail, *J. Phys. Chem.*, 62, 920 (1958).

(3) H. S. Britton, S. J. Gregg, and G. M. Windsor, *Trans. Faraday Soc.*, 48, 63 (1952).

(4) G. F. Hüttig and R. Mytyzek, *Z. Anorg. Allg. Chem.*, 190, 353 (1930).

(5) G. F. Hüttig, "Hydroxide und Oxyhydrate," R. Fricke and G. F. Hüttig, Ed., Akademische Verlagsgesellschaft m.b.H., Leipzig, 1937, p 413 ff.

(6) M. J. D. Low and A. M. Kamel, *J. Phys. Chem.*, 69, 450 (1965).

(7) S. Gordon and C. Campbell, *Anal. Chem. Annu. Rev.*, 32, 287R (1960).

(8) H. G. McAdie, *Anal. Chem.*, 37, 543 (1967).

(9) J. V. Smith, Ed., "X-Ray Powder Data File," American Society for Testing Materials, Philadelphia, Pa., 1960.

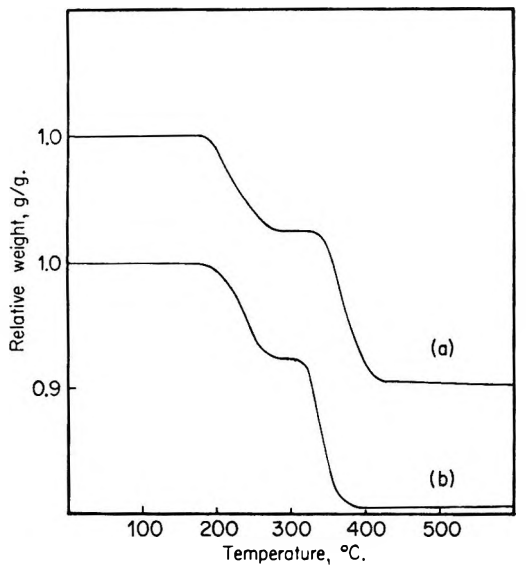

Figure 1. Tga curves for (a) precipitated cadmium hydroxide and (b) hydrated cadmium oxide (rate of heating 5°/min).

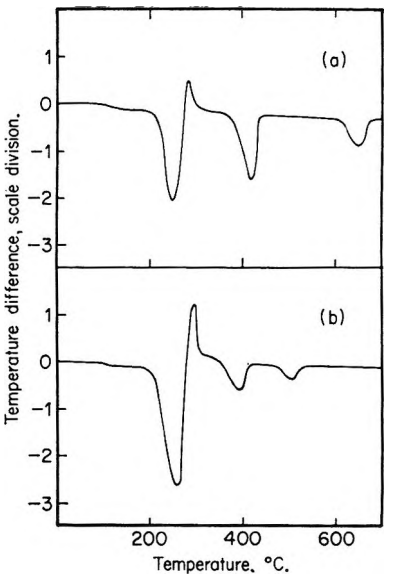

Figure 2. Dta curves for (a) precipitated cadmium hydroxide and (b) hydrated cadmium oxide (rate of heating 5°/min).

to saturated water vapor at 35° for enough time. The sample was then degassed thoroughly. Details of the hydration process are described elsewhere.[1]

Results

(*A*) *Thermogravimetry.* The results of thermogravimetric experiments on the dehydration of cadmium hydroxide and the hydration product of cadmium oxide which had been prepared at 300° are shown in Figure 1. It is evident that the behaviors of the two samples are essentially the same, despite the slight difference in the characteristic temperature range. It is clear that dehydration takes place in two stages. The first stage, which can be ascribed to the removal of excess (combined) water, starts in the two materials at about 200°, showing a similar loss in weight (7–8%); it can be noticed that the rate of removal of combined water in the hydroxide is slower than that in the hydrated oxide. The second decomposition stage, which is preceded by a well-defined plateau, starts in the two samples at 300° and shows a great similarity in behavior both in the amount and in the shape of the curve.

(*B*) *Differential Thermal Analysis.* The dta curves for the precipitated cadmium hydroxide and the hydration product of oxide which had been prepared at 300° are shown in Figure 2. The endothermic peak noticed at 250° in both materials corresponds to the region of decrease in weight in tga curves that starts at about 200°. However, this peak is followed by an exothermic peak at about 290°, that can be attributed to a crystallization or rearrangement type process such as from amorphous to crystalline. It is probable that removal of excess water leaves the material in a finely divided poorly crystallized or amorphous state. The decomposition of the hydroxide to the oxide takes place at 410 and 350° in case of the hydroxide and the hydrated oxide, respectively; the same trend is also noticed in tga curves, where the decomposition of the former material starts at a higher temperature. An endothermic peak is finally noticed at about 650° for the hydroxide sample, corresponding to the deoxygenation of the oxide.[10,11] A similar peak but a smaller one is also noticed at about 510° in case of the hydrated oxide which may be considered to be already partially deoxygenated having been subjected, before hydration, to thermal treatment at 300° under vacuum.

(*C*) *Isothermal Dehydration.* This series of experiments was performed on the hydroxide and the hydration product of oxide which had been prepared at 300°. Two ranges of temperatures were used, *viz.*, 160–240° for dehydration and 300–370° for decomposition to the oxide. The set of results on the rate of dehydration of the hydroxide is shown, as an example, in Figure 3.

The mechanism of dehydration may be explained in terms of general hypothesis that the reaction consists of the formation of nuclei at certain localized spots in the reactant, followed by relative rapid growth of these nuclei. The present results are in good agreement with Mampel's theory.[12,13] By plotting $(\omega/\omega_0)^{1/3}$ against t, where ω_0 is the initial mass of reactant and ω is the mass at time t, a straight line is obtained from which k the velocity constant is obtained at various temperatures for both materials. A plot of log k against the reciprocal of the absolute temperature (T) gives a satis-

(10) E. F. Lamb and F. C. Tompkins, *Trans. Faraday Soc.*, 58, 1424 (1962).

(11) S. A. Abd El-Hadl, I. F. Hewaidy, F. A. Khadra, and M. S. Farag, *J. Phys. UAR*, in press.

(12) K. L. Mampel, *Z. Phys. Chem., Abt. A*, 187, 43, 257 (1940).

(13) S. J. Gregg and R. I. Razouk, *J. Chem. Soc.*, 36 (1949).

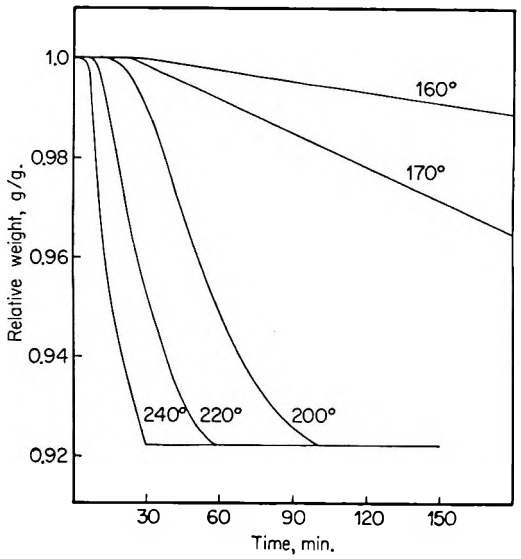

Figure 3. Weight changes accompanying the dehydration of precipitated cadmium hydroxide.

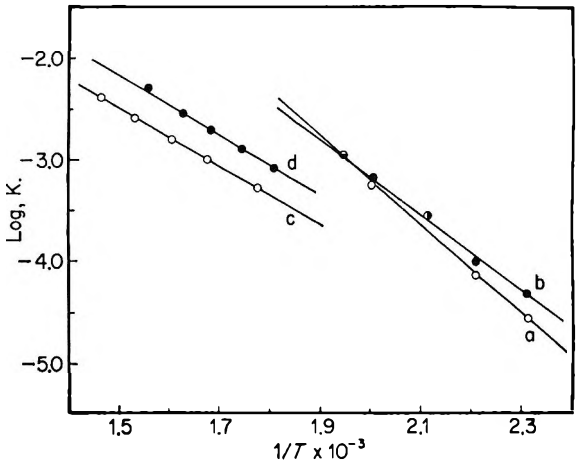

Figure 4. Plot of log k against $1/T$ for: (a) dehydration of precipitated cadmium hydroxide, (b) dehydration of hydrated cadmium oxide prepared at 300°, (c) decomposition of the hydroxide, and (d) decomposition of the hydrated oxide.

factory straight line from which it is possible to evaluate the energy of activation from the Arrhenius equation

$$\mathrm{d} \ln k/\mathrm{d}(1/T) = -E/R$$

The energy of activation for the dehydration of the hydroxide and the hydrated oxide is then determined. The same mechanism is considered also to apply for the decomposition of both materials, after removal of excess water, to the corresponding oxide. The activation energies of the two processes, dehydration and decomposition, that can be evaluated from Figure 4, are shown below

	Activation energy, kcal mol^{-1}	
	Hydroxide	Hydrated oxide
Dehydration (−excess water)	21.90	17.52
Decomposition to the oxide	13.77	13.24

It can be noticed that while the energy of activation of decomposition for both materials is almost the same, that for the dehydration process is higher in the case of the hydroxide.

(*D*) *X-Ray Analysis.* X-Ray diffraction patterns of the hydroxide, the hydrated oxide, and the products of dehydration of both materials are illustrated in Figure 5. Although the results of X-ray are only qualitative, they can throw much light on the mechanism of hydration of the oxide as well as dehydration process. The diagrams of the hydroxide and the hydrated oxide do not give the characteristic d spacings and relative intensities of the hydroxide given in the ASTM cards. However, the partial dehydration of both compounds, to expell the excess water, can give products having the original pattern of the hydroxide given in the ASTM cards. The main d spacings of the products of partial dehydration of both materials are slightly shifted. It is not possible, however, to detect the presence of the principal lines of the oxide in the products of partial dehydration, *i.e.*, $Cd(OH)_2$. Finally, the products of complete dehydration, formed at 300°, showed only the pattern of cadmium oxide. Despite of the fact that there is a difference in the color of the hydroxide (white) and the hydrated oxide (pale yellow), the X-ray analysis of both materials is the same.

(*E*) *Ir Analysis.* The ir spectra of four original samples and some of their products were investigated and the results are shown in Figures 6 and 7, the curves being displaced to prevent overlapping. The spectrum of the hydroxide (Figure 6a) shows characteristic bands: a sharp one at 3600 cm^{-1} which is probably due to the O–H stretching[14-16] of the hydroxides, two distinct bands at 3400 and 1700 cm^{-1} that can be referred to the water molecules adsorbed by the solid[17] and three other sharp bands at 1450, 860, and 720 cm^{-1}. The latter three bands may be related to the water molecules combined with the hydroxide. Similar bands are noticed in some inorganic compounds containing combined water.[18] To confirm this view, the ir spectrum of a hydroxide specimen which had been freshly dehydrated at 200° was determined and found to have a diminished band at 1400 cm^{-1} (Figure 7a). This indicates the presence of traces of combined water. The other two bands at 860 and 720 cm^{-1} have completely disappeared. The bands corresponding to the adsorbed water have also disappeared.

(14) B. A. Philips and W. A. Busing, *J. Phys. Chem.*, **61**, 502 (1957).
(15) R. T. Mara and G. B. B. M. Sutherland, *J. Opt. Soc. Amer.*, **46**, 464 (1956).
(16) R. M. Hexter, *ibid.*, **48**, 770 (1958).
(17) R. S. McDonald, *J. Amer. Chem. Soc.*, **79**, 850 (1957).
(18) M. Y. Karmarrec, *C. R. Acad. Sci.*, **258**, 5836 (1964).

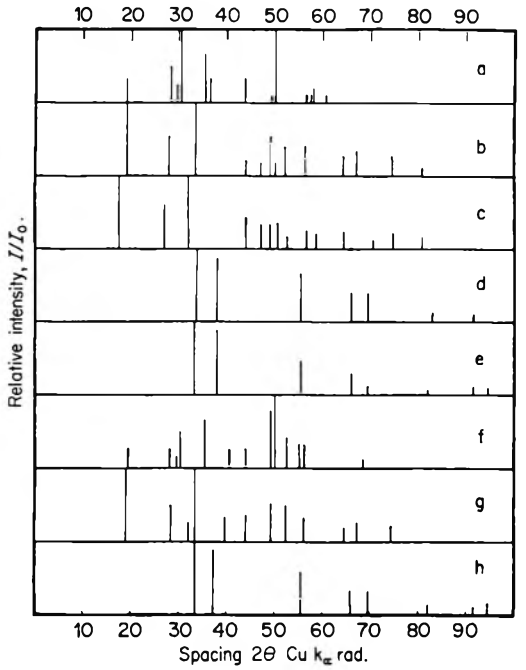

Figure 5. X-Ray diffraction patterns of: (a) precipitated cadmium hydroxide, (b) dehydrated cadmium hydroxide, (c) ASTM pattern for $Cd(OH)_2$, (d) cadmium oxide prepared from (a), (e) ASTM pattern for CdO, (f) hydrated cadmium oxide prepared at 300°, (g) dehydrated sample of (f), and (h) cadmium oxide prepared from (f).

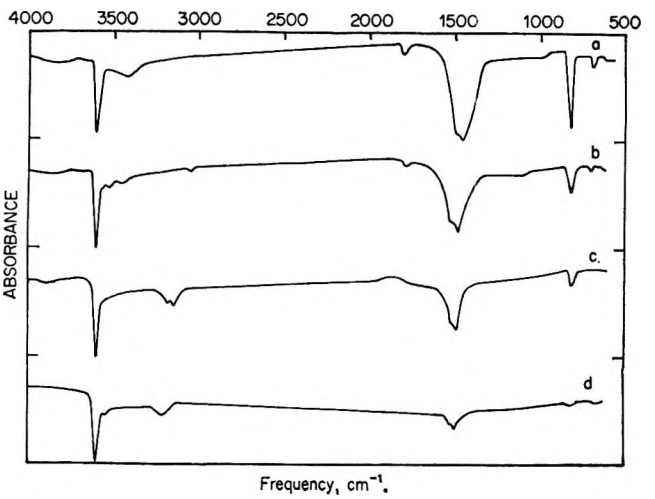

Figure 6. Infrared absorption spectra of: (a) precipitated cadmium hydroxide, (b) hydrated cadmium oxide prepared at 200°, (c) hydrated oxide prepared at 250°, and (d) hydrated oxide prepared at 300°.

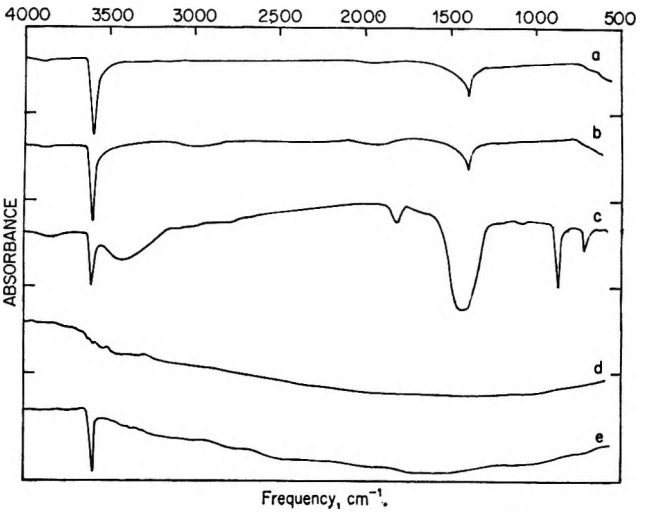

Figure 7. Infrared absorption spectra of: (a) dehydrated precipitated cadmium hydroxide, (b) dehydrated sample of hydrated cadmium oxide prepared at 300°, (c) moistened cadmium oxide, (d) cadmium oxide, and (e) hydrated oxygenated cadmium oxide.

On the other hand, it is noticed from Figure 6 that the three bands related to the combined water show decreased absorbance in the hydrated oxides, which had been prepared at 200 and 250°, compared to that of the hydroxide. The lower the temperature of treatment of the oxide before hydration, the bigger the relative absorbance of the three bands. Hence, the ir spectrum of the hydrated oxide, previously prepared at 300°, does not show the latter two bands but a broad band is given at 1400 cm^{-1}, with small absorbance value (Figure 6d). Furthermore the hydrated oxide, which had been prepared at 300°, gives a spectrum (Figure 7b) which is similar to Figure 7a of the hydroxide when both materials are treated at 200° in air thus removing the combined water.

The spectrum of the oxide (Figure 7d) does not show any characteristic band in accord with the observation of Miller and Wilkins[19] that metal oxides generally have no sharply defined infrared absorption between 2 and 16 μ.

Figure 7c which is similar to Figure 6a of the original hydroxide is the ir spectrum for the sample prepared by heating the hydroxide in air at 300° and then exposing it to moisture for 24 hr during which time it turned white.

Cadmium oxide, particularly when prepared *in vacuo*, is known to be nonstoichiometric with deficient oxygen in the lattice.[10] In order to find out whether or not this nonstoichiometry of the oxide has an effect on the processes of hydration and dehydration, an ir spectrum (Figure 7e) was investigated for an oxide prepared at 300° in an oxygen atmosphere of 760 Torr thus preventing deoxygenation; then the oxide was subjected after cooling and careful evacuation to saturated water vapor at 35°. From Figure 7e, it is clear that the three bands of the hydroxide (Figure 6a) at 1450, 860, and 720 cm^{-1} have completely disappeared indicating the absence of combined water. This fact was confirmed by a tga experiment for this sample. The results show that only one weight loss is recorded in the temperature range 300–370°, corresponding to the decomposition of the hydrated oxide (hydroxide) to the oxide, while the

(19) F. A. Miller and C. H. Wilkins, *Anal. Chem.*, **59**, 638 (1952).

Table I: Composition of Starting Materials and Their Decomposition Products

Process	Temp, °C	Precipitated hydroxide: % Cd	Precipitated hydroxide: Empirical formula	Hydrated oxide: % Cd	Hydrated oxide: Empirical formula
(Starting material)	35	70.91	$CdO \cdot 1.67H_2O$	71.19	$CdO \cdot 1.64H_2O$
Dehydration	200	76.89	$CdO \cdot 0.99H_2O$	77.13	$CdO \cdot 0.96H_2O$
Crystallization	290	77.01	$CdO \cdot 0.98H_2O$	77.61	$CdO \cdot 0.92H_2O$
Decomposition	360	88.02	CdO	88.38	$CdO_{0.92}$
Deoxygenation	600	88.71	$CdO_{0.89}$	88.68	$CdO_{0.89}$

weight loss representing the removal of excess water from the sample is not detected.

(*F*) *Product Compositions.* In order to support the interpretations already given for the processes involved in the thermal decomposition of the starting materials, the composition of the various products was determined by chemical analysis. Cadmium was estimated by ethylenediaminetetraacetic acid (EDTA) according to Welcher.[20] The results of analysis (% Cd) and the empirical formulas of the analyzed samples are cited in Table I. The empirical formulas were calculated[6] on the assumption that the samples consisted only of cadmium and oxygen and that the difference between them lies in the loss of water and oxygen.

Discussion

It was shown[1] that cadmium oxide, prepared by the thermal decomposition of the corresponding hydroxide *in vacuo*, retains water when exposed to saturation water vapor pressure at 35°. The plot of water retained against percentage decomposition of the hydroxide is a straight line which on extrapolation gives a value of 0.154 g of H_2O/g of hydrated material at 100% decomposition as compared to 0.123 g of H_2O/g of $Cd(OH)_2$. This fact shows that the oxide prepared at 300° on hydration gives the corresponding hydrous hydroxide. However, in case of magnesium oxide,[21] the water uptake by samples prepared at temperatures below 650° is stoichiometric giving an anhydrous hydroxide.

From tga experiments on cadmium hydroxide and the hydrated oxide, it became clear that both materials behave similarly and that water is removed in two stages, *viz.*, dehydration and decomposition. The mechanism of dehydration in both materials is the same, where the initial stages of the dehydration spreads from sites on the external surface across the external faces and simultaneously down the subgrain boundary network. This mechanism reflects a process leading the establishment of the reactant–product (hydrous–anhydrous) interface which penetrates the crystal at a constant rate. This is preferred to a true contracting envelope which is suggested by Mampel.[12]

The fact that the energy of activation for dehydration process is, on the whole, high indicates that excess water attached to both materials, hydroxide and hydrated oxide, is not only adsorbed but mainly diffused in the crystal lattice. That dehydration is slower in case of the precipitated hydroxide may be attributed to the difference in chemical bonding between excess water and the hydroxide materials, as indicated by ir spectra. Hence, when hydration of the oxide is effected by moistening, we get an ir spectrum very similar to that of the precipitated hydroxide. While in case of hydration of oxides under reduced pressure, ir absorption indicated that combined water decreased the higher the temperature of the oxide preparation showing a gradual reduction in the bond strength of excess water compared to that of the formed hydroxide. Moreover, we can assume that the hydrated oxide, which was subjected to thermal treatment before hydration, already contains channels for diffusion of water which permit dehydration to proceed faster.

In dta, the endothermic peak at about 250° corresponding to the dehydration process is followed by an exothermic peak at about 290° which may be attributed to a crystallization process. It is probable that removal of excess water causes disruption of the crystal structure and leaves the anhydrous material in a very fine or amorphous state. Then at slightly higher temperatures the material crystallizes releasing some heat of crystallization.

The contracting envelope suggested by Mampel as a mechanism for dehydration seems to be applicable also to the decomposition process. The isothermal decomposition of the anhydrous hydroxide and hydrated oxide is found to be of the same order of magnitude, with almost similar energy of activation, indicating the presence of similar bonds attaching the hydroxyl groups to the metal in both materials. However, the hydroxide shows a delayed decomposition. Hence, while the reaction is complete in case of the hydroxide at 380° after 15 min, in case of the hydrated oxide it is achieved at only 360° after 7 min. This fact may be interpreted in terms of the absence of the intermolecular OH coordination bond in the hydrated oxide as indicated from its relatively decreased absorbance in the ir spectra at 3600 cm^{-1}, when compared with that of the hydroxide.[17]

(20) F. J. Welcher, "The Analytical Uses of Ethylenediamine Tetraacetic Acid," D. Van Nostrand Co., Inc., Princeton, N. J. 1958, p 161.

(21) R. I. Razouk and R. Sh. Mikhail, *J. Phys. Chem.*, **59**, 638 (1955).

This interpretation may also explain the contradicting results obtained for the decomposition process in tga and dta, where the same weight loss is recorded in this process for both the hydroxide and the hydrated oxide, while the endothermic peak in case of the hydroxide is longer and broader than that of the hydrated oxide. Despite this difference in structure, the anhydrous hydroxide and hydrated oxide (being heated at 200°) give the same X-ray pattern as that of $Cd(OH)_2$.

Deoxygenation takes place at about 650 and 510° for the hydroxide and the hydrated oxide, respectively. This process takes place earlier with the hydrated oxide because this material had already suffered partial deoxygenation while being previously heated at 300° under vacuum before rehydration.

An interesting experimental fact has revealed that when nonstoichiometric cadmium oxide, being deficient in oxygen, is oxygenated and rehydrated, no combined water is taken up by formed hydroxide. This fact is confirmed by thermogravimetry and infrared analysis. A similar observation was made by Glemser, *et al.*,[22] in studying the crystal lattice of some MnO_2 varieties. They came to the conclusion that in the nonstoichiometric MnO_2, water replaces the oxygen deficiency in the lattice; hence, the stoichiometric oxide does not contain water. The behavior of hydrated oxygenated cadmium oxide can be explained on the same basis.

Acknowledgments. Thanks are due to Mr. K. M. Abd El-Salaam for preparing the starting materials and also to Dr. F. El-Milligy for his help in discussing the results of ir analysis.

(22) V. O. Glemser and E. Hartert, *Z. Anorg. Allg. Chem.*, **283**, 111 (1956).

Transport Processes in Molten Binary Acetate Systems

by Roger F. Bartholomew

Research and Development Laboratories, Corning Glass Works, Corning, New York 14830 *(Received January 16, 1970)*

Equivalent conductance and glass-transition temperature measurements were made on two melts in the binary system sodium acetate–lithium acetate. The conductance exhibited non-Arrhenius behavior but could be described by a three-parameter equation of the form $\Lambda = \Lambda_0 T^{-1/2} \exp[-k_\Lambda/(T - T_0)]$. The ideal glass-transition temperature T_0, determined by a computer best fit of the data to the above equation, was found to increase with an increase in the mean cationic potential term, $\Sigma N_i Z_i / r_i$. Experimental glass-transition temperatures T_g, obtained from dta data, showed similar behavior. The ratio T_g/T_0 was found to be approximately unity for acetate glass-forming melts.

Introduction

The theory of Adam and Gibbs[1] for relaxation rates at low temperatures has been applied in the past few years to the transport properties of low-melting glass-forming ionic liquids. A recent review by Angell and Moynihan[2] covers the work in this field up to the end of 1968. Considerable effort has been directed toward the study of the known nitrate glass-forming melts as well as $ZnCl_2$. However, glass formation from molten acetate mixtures has recently been reported in the literature.[3-5] These systems are very extensive in their glass-forming nature, for example, quenching molten lithium acetate results in glass formation. Because of this ease of glass formation and the similarity between the nitrate anion and the acetate anion, transport properties of two glass-forming acetate melts in the binary system CH_3COONa–CH_3COOLi were determined.

The purpose of the present paper is to show that the equivalent conductance of these glass-forming melts can be described by the low-temperature approximation to the Adam–Gibbs theory. This theory relates the equivalent conductance Λ to the absolute temperature T by the three-parameter equation

$$\Lambda = \Lambda_0 T^{-1/2} \exp\left(\frac{-k_\Lambda}{T - T_0}\right) \quad (1)$$

(1) G. Adam and J. H. Gibbs, *J. Chem. Phys.*, **43**, 139 (1965).

(2) C. A. Angell and C. T. Moynihan in "Molten Salts. Characterization and Analysis," G. Mamantov, Ed., Marcel Dekker Inc., New York, N. Y., 1969, pp 315–376.

(3) J. A. Duffy and M. D. Ingram, *J. Amer. Ceram. Soc.*, **52**, 224 (1969).

(4) R. F. Bartholomew and H. J. Holland, *ibid.*, **52**, 402 (1969).

(5) R. F. Bartholomew and S. S. Lewek, *ibid.*, in press.

This semiempirical equation is usually known as the Vogel–Tammann–Fulcher (VTF) equation. The low-temperature region has been arbitrarily defined as the region $T_0 \leqslant T \leqslant 2T_0$.[6] The parameter T_0 is interpreted as the zero mobility temperature, or the temperature at which the configurational entropy tends to zero. The k_A term is analogous to an activation energy in the Arrhenius sense, and Λ_0 is the preexponential term.

Values of T_0 obtained by applying the VTF equation can be compared with the experimental glass-transition temperature T_g, which is determined by dta methods. Exact agreement between T_0 and T_g is not expected. The former term is in the strictest sense a thermodynamic quantity; the latter term is time dependent. Angell[7] has proposed that the closer the value of the ratio T_g/T_0 is to unity, the more "ideal" a glass the material is. Recently Weiler, *et al.*,[8] have shown that for transport properties determined close to the glass-transition temperature the value of T_0 becomes dependent on the range over which the data are taken. The closer the property is measured to T_0, the lower the value of T_0.

Experimental Section

Chemicals. The $CH_3COOLi \cdot 2H_2O$ was reagent grade supplied by the G. Frederick Smith Chemical Co. Anhydrous CH_3COONa was Baker Analyzed reagent grade. Both chemicals were used without further purification.

Melts of composition 50 mol % CH_3COONa–50 mol % CH_3COOLi (melt A) and 43 mol % CH_3COONa–57 mol % CH_3COOLi (melt B) were made up by fusing the weighed materials in a dry-nitrogen atmosphere in a Kewanee drybox. After cessation of bubbling, indicating no further loss of water, the melt was quenched, broken into small pieces, and kept in the drybox until needed.

Electrical Conductivity. A dip-type conductivity cell was supplied by Industrial Instruments and was calibrated with KCl solutions in the standard fashion[9] in the resistance range over which the melt data were obtained (9–80 ohms). The cell constant was 1.040 ± 0.005 at 25.00°.

The resistance of the melt was measured using a General Radio Co. impedance bridge, Type 1650A. It was necessary to balance out the capacitance of the solution using a variable capacitance connected in parallel to the impedance bridge. A bank of Cornell-Dubilier Electronics Division Decade Capacitors with a range of 0–10 μF was used for this purpose. The maximum capacitance required for balancing was 4×10^{-3} μF.

A Cenco audio oscillator was used to generate the ac signal. The frequency of the ac signal was found to have negligible effect on the value of the resistance of the melt above 10 kHz.

The melt was contained in a Pyrex brand glass test tube which rested on sand in a larger similar glass tube. This precaution was needed to prevent possible explosion if molten acetate came into contact with a nitrate–nitrite melt.[10] Both tubes were placed in a molten salt bath ($NaNO_2$:$NaNO_3$:KNO_3 = 40:7:53 by weight; freezing point 157°) whose temperature was controlled to ± 0.2°. The temperature of the melt was measured by a chromel–alumel thermocouple. At all times a dry-nitrogen atmosphere was maintained over the melt.

Because the resistance measurements required a fairly lengthy span of time, it was necessary to keep the melt fluid overnight. It seems that, provided the melt had a blanket of nitrogen over it, the data were not affected by thermal decomposition. The resistance change in either melt when left overnight was less than 0.2%, well within experimental error. The resistance measurements were continued until a brown discoloration was noticed in the melt. After this appeared, the runs were discontinued and the melts checked by chemical analysis for lithium content. Calculations showed that the composition was correct in mole per cent to the first decimal place, indicating that any decomposition which may have taken place at the end of the run was very small. The final point was discarded for both runs.

Density of Molten Acetates. A manometric densitometer was used to measure the densities of the molten acetates.[11]

Differential Thermal Analysis. A Du Pont 900 thermal analyzer was used for dta measurements. At all times the samples were contained in a nitrogen atmosphere. Heating rates of 10° min^{-1} were used.

Results

Dta. A typical dta trace, for lithium acetate glass, is shown in Figure 1. The glass-transition temperature T_g occurs at 121° for this sample. Reproducibility of ±2° was obtained for T_g for samples of the same glass composition run several times. The exothermic peak following the glass transition is due to crystallization of the sample. The large endothermic feature with a peak at 289° represents the melting point of the sample. This is in good agreement with the value of 291° reported by Diogenov.[12] The dta trace obtained for the so-called eutectic composition in the lithium acetate–sodium acetate binary system gave a melting point of 225°. This composition has been reported to have a melting point as low as 160°.[12] It would appear that a

(6) C. A. Angell, *J. Phys. Chem.*, **70**, 2793 (1966).

(7) C. A. Angell, *J. Amer. Ceram. Soc.*, **51**, 117 (1968).

(8) R. Weiler, S. Blaser, and P. B. Macedo, *J. Phys. Chem.*, **73**, 4147 (1969).

(9) G. Jones and B. C. Bradshaw, *J. Amer. Chem. Soc.*, **55**, 1780 (1933).

(10) T. R. Kozlowski and R. F. Bartholomew, *Inorg. Chem.*, **7**, 2247 (1968).

(11) L. J. B. Husband, *J. Sci. Instrum.*, **35**, 300 (1958).

(12) G. G. Diogenov, *Russ. J. Inorg. Chem.*, **1**, 199 (1956).

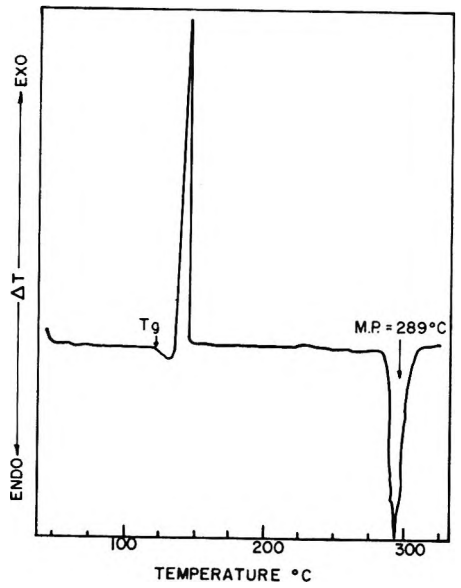

Figure 1. Dta trace of pure CH_3COOLi glass; heating rate 10° min^{-1}; nitrogen atmosphere.

reinvestigation of the sodium acetate–lithium acetate binary-phase diagram is necessary.

The effect on T_g of changing the ratio of potassium acetate to sodium acetate in a ternary glass system of composition sodium acetate–potassium acetate–calcium acetate was also determined in this study and is shown in Table I, along with data on other acetate glasses.

Table I: Glass-Transition Temperatures of Acetate Glasses

Compn, mol %				T_g,
$(CH_3COO)_2Ca$	CH_3COOK	CH_3COONa	CH_3COOLi	°K
33.3	...	66.7	...	383
50	20	30	...	388
50	30	20	...	373
50	40	10	...	373
33.3	66.7	...	...	360
...	...	50	50 (melt A)	333
...	...	43	57 (melt B)	335
...	...	...	100	394

Density. The complete temperature range used for the electrical measurements was not covered by the density measurements. However, because the densities of the melts can be obtained very accurately, extrapolating to higher or lower temperatures would result in negligible error in the equivalent conductance. The density data were fitted to the linear equation

$$\rho = a - bT \qquad (2)$$

where T is the temperature in degrees centigrade. These parameters are shown in Table II.

Table II: Values of the Constants "a" and "b" in Eq 2

Compn	a	10^4b	Temp range, °C
A	1.3606	4.40	220–260
B	1.4046	6.40	243–258

Equivalent Conductance. Equivalent conductances Λ were calculated from the specific resistivities χ and densities of the melts, using the relationship

$$\Lambda = \frac{\chi E}{\rho} \qquad (3)$$

where E is the mass of the melt containing 1 equiv of salt, and ρ is the density.

These data are given in Table III. The precision of measurement of resistance was better than ±0.5%. All values reported were taken using a 10-kHz ac sine wave signal.

Table III: Equivalent Conductance for 50 Mol % CH_3COONa–50 Mol % CH_3COOLi (Melt A) and 43 Mol % CH_3COONa–57 Mol % CH_3COOLi (Melt B) as a Function of Temperature

Melt A		Melt B	
Temp, °C	Λ, ohm^{-1} cm^2 mol^{-1}	Temp, °C	Λ, ohm^{-1} cm^2 mol^{-1}
219.5	0.725	224.5	0.652
226	0.860	232	0.850
230	0.994	233	0.869
239	1.333	237	0.979
246	1.518	241.5	1.113
252.5	1.773	248	1.323
258.5	2.041	253	1.510
265.5	2.398	260	1.790
272	2.798	274	2.372
282	3.276	284.5	2.899
290	3.715	289.5	3.206
298	4.160	295.5	3.486
		303.5	4.093
		308	4.359

Discussion

The data in Table III could not be fitted to a simple Arrehenius-type plot. However, a computer best fit of these data was made to the VTF equation. The results of this fit are given in Table IV and shown in Figure 2.

Table IV: Adjustable Parameters in Eq 1 for Melts A and B

Melt	A_0, ohm^{-1} cm^2 mol^{-1}	k_A, °K	T_0, °K
A	4717	935	328
B	6010	1041	324

The errors in the three parameters of the VTF equation were determined (using a 95% confidence level), assuming that two of the three parameters have no error in them. The error associated with T_0 for melt A was ±25°K, and for melt B ±19°K. Similarly the

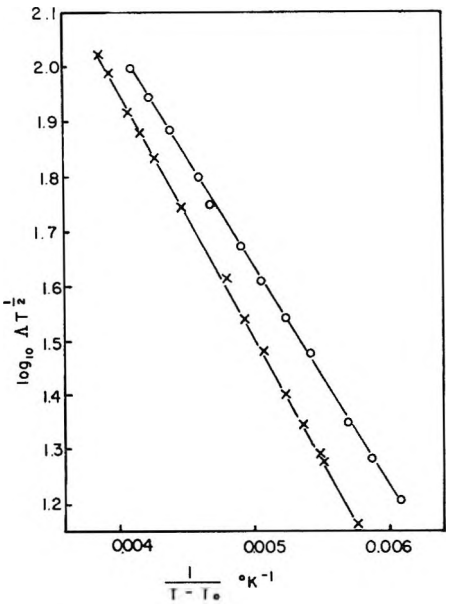

Figure 2. Equivalent conductance as a function of $1/(T - T_0)$: O, melt A; ×, melt B.

errors for k_Λ were computed to be ±230 and 190°K, for melt A and melt B, respectively. The errors associated with the preexperimental terms are much greater. The upper limit and lower limit of the Λ_0 values were 8450 and 2630 for melt A and 9419 and 3837 for melt B. Another way of expressing the goodness of the fit is the fact that in both plots the standard deviation of the data was 0.5%.

The problems of fitting such data to eq 1 have been discussed by Robbins and Braunstein[13] and by Moynihan, *et al.*[14] In their work on the conductance of molten KNO_3 Robbins and Braunstein obtained a value of T_0 of 153.9°K by a computer fit when all three parameters were allowed to vary. However, constraining a two-parameter least-squares fit of the data by putting k_Λ equal to 690°K resulted in a value of T_0 = 300°K. That is twice the value detained by the three-parameter fit. For their work on hydrate melts, Moynihan, *et al.*, showed that they obtained more meaningful data by making the constant k_Λ independent of composition changes (that is, independent of the ratio of $Ca(NO_3)\cdot 4H_2O$ to $Cd(NO_3)_2\cdot 4H_2O$). They used a three-parameter equation to determine k_Λ for pure $Ca(NO_3)_2\cdot 4\cdot 09\text{-}H_2O$ and then used this value in subsequent calculations, thereby reducing eq 1 to a two-parameter equation.

Because the compositions of melt A and melt B are not too far apart, one would expect that for the data to be meaningful the parameters Λ_0, k_Λ, and T_0 would be not too different for either melt. The fact that Table IV substantiates this postulate is evidence that the values of the parameters obtained by the computer are meaningful.

According to Angell,[6] a precise determination of T_0 for a liquid requires measurement of the transport properties of the liquid over at least 1.5 orders of magnitude, bearing in mind these measurements must be carried out in the temperature range between T_0 and $2T_0$. The values of T_0 shown in Table IV show that for melt A this range lies between 328 and 656°K, and for melt B 324 and 648°K. The upper temperature limit for melt A was 583°K, and melt B 581°K. Therefore, the equivalent conductance for both melts was determined such that they were both inside the upper limit of $2T_0$. Because of this limit, as well as the problem of thermal decomposition, it was impossible to determine the equivalent conductance of these melts over 1.5 orders of magnitude required. However, approximately one order of magnitude was covered, which appears to be more than adequate for the determination of T_0.

The temperature coefficient E_Λ for conductance can be obtained by taking the derivative of eq 1 with respect to temperature. That is

$$E_\Lambda = -R\frac{\partial \ln \Lambda}{\partial(1/T)} = -\tfrac{1}{2}RT + k_\Lambda R\left(\frac{T}{T - T_0}\right)^2 \quad (4)$$

As can be seen from eq 4, E_Λ is a function of temperature. The values for both melts of E_Λ as a function of T°K indicate an increase in E_Λ as T decreases. Viscosity measurements over a range of 10^9 P on the melt 60% KNO_3–40% $Ca(NO_3)_2$ (mol %) showed departures from the Fulcher equation, $\ln \eta = A + B/(T - T_0)$ as the temperature approached T_0.[8] The low-temperature region tended to show Arrhenius behavior (*i.e.*, T_0 = 0°K). However, for temperatures 76° or greater above T_0 the Fulcher equation was followed, although T_0 depended on the range over which the data were obtained, but the conductance data reported here do not approach close enough to the T_0 region to see if the same type of behavior is observed in these melts.

The "ideality" of acetate glasses can be determined from the data in Table I and Table IV. The ratio of T_g/T_0 from these data gave a value of 1.02 for melt A, while melt B resulted in a value of 1.03. These values are similar to those computed for nitrate glasses but lower than those found for silica or B_2O_3.[7] Because of the closeness of these values to unity, it appears that acetate glasses can be considered as "ideal" glasses from a thermodynamic standpoint.

(13) G. D. Robbins and J. Braunstein, *J. Electrochem. Soc.*, 116, 1218 (1969).

(14) C. T. Moynihan, C. R. Smalley, C. A. Angell, and E. J. Sare, *J. Phys. Chem.*, 73, 2287 (1969).

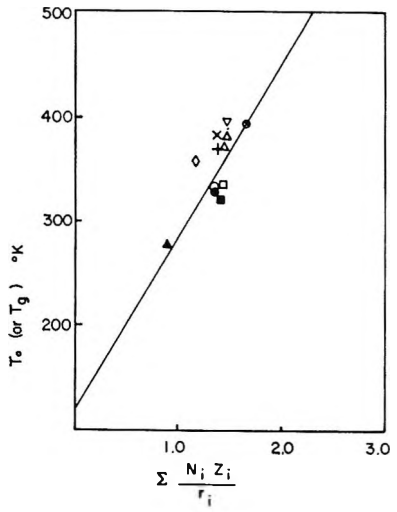

Figure 3. Ideal glass-transition temperature (T_0) and experimental glass-transition temperature (T_g) as a function of $\Sigma N_i Z_i / r_i$ (solid line from ref 15): T_0, ■, 57 mol % CH_3COOLi, 43 mol % CH_3COONa; T_0, ●, 50 mol % CH_3COOLi, 50 mol % CH_3COONa; T_0, ▲, 53.7 mol % CH_3COOK, 46.3 mol % CH_3COONa; T_g, ⊡, 57 mol % CH_3COOLi, 43 mol % CH_3COONa; T_g, ⊙, 50 mol % CH_3COOLi, 50 mol % CH_3COONa; T_g, ×, 33.3 mol % $(CH_3COO)_2Ca$, 66.7 mol % CH_3COOK; T_g, ◇, 33 mol % $(CH_3COO)_2Ca$, 66.7 mol % CH_3COOK; T_g, +, 50 mol % $(CH_3COO)_2Ca$, 10 mol % CH_3COO Na, 40 mol % CH_3COOK; T_g, △, 50 mol % $(CH_3COO)_2Ca$, 20 mol % CH_3COONa, 30 mol % CH_3COOK; T_g, ▽, 50 mol % $(CH_3COO)_2Ca$, 30 mol % CH_3COONa, 20 mol % CH_3COOK; T_g, ⊕, pure CH_3COOLi.

Angell[15] showed that a plot of T_0 against $\Sigma N_i Z_i / r_i$, the mean "cationic potential" of the melt, for binary nitrate glass-forming melts was linear (where Z_i is the charge on the cation, and r_i the radius of the ith cation). This means that a higher value of T_0 would be expected for a cation of high charge and low radius. Figure 3 shows how the T_0 values obtained in this study compare with those obtained in nitrate glasses. The line drawn by Angell to represent his data is shown as a solid line in the figure. In addition, values of T_g taken from Table I for the ternary system calcium acetate–potassium acetate–sodium acetate as well as the lithium-containing glasses are also indicated. The data shown in Figure 3 for acetate glasses do show a trend indicating that T_0 does increase with increasing valence or decreasing radius as was found with nitrate glasses. The value of T_g of 478°K obtained by Onodera, *et al.*,[16] for magnesium acetate ($(N_i Z_i / r_i) = 3.28$) in the amorphous state is well below the value of about 660°K predicted by extrapolation of the solid line.

There is only one other paper in the literature in which the equivalent conductance of a binary molten acetate system has been reported. Hazlewood, *et al.*,[17] determined both the equivalent conductance and viscosity for the eutectic composition in the binary system CH_3COONa–CH_3COOK. They give this composition as 53.7 mol % CH_3COOK–46.3 mol % CH_3COONa. A second-order polynomial was fitted by a computer to the data, giving the equations

$$\log \Lambda = 0.742 + 1.717(10^3/T) - 0.894(10^3/T)^2 \quad (5)$$

and

$$\log \eta \text{ (mP)} = 2.005 - 1.903(10^3/T) + 1.056(10^3/T)^2 \quad (6)$$

In the case of equivalent conductance the data showed a standard deviation of ±0.3% for the temperature range 232–360°, while for the viscosity the fit was estimated to be ±1% over the range 232–340°. We took these data and determined the quantities at 10° intervals over the temperature ranges shown in parentheses in eq 5 and 6. These calculated values were then fitted by a computer to eq 1, in the case of the equivalent conductance, and to

$$\eta = \eta_0 T^{1/2} \exp\left(\frac{k_\eta}{T - T_0}\right) \quad (7)$$

in the case of the viscosity. For the same melt T_0 should be the same for both conductance and viscosity, because the same transport process is taking place in determining both quantities. The computer gave T_0 values of 279°K from the equivalent conductance data, and 265°K from the viscosity data. Values of k_Λ equal to 401°K and Λ_0 equal to 5670 ohm^{-1} cm^2 mol^{-1} were computed for the conductance, with k_η of 548°K and η_0 of 5.503×10^{-2} mP for the viscosity. It should be noted that only up to $1/(T - T_0)$ equal to 0.00365 for the equivalent conductance and 0.00373 for the viscosity data, is the temperature below $2T_0$. However, these data do not extend far above the region $2T_0$ in temperature, so this would not constitute an argument regarding the applicability of eq 1 and 7. In addition, because of the thermal decomposition occurring in the melt at high temperatures, neither quantity was determined over even one order of magnitude change in value. It is interesting to note that the T_0 value obtained for conductance when plotted against the mean "cationic potential" term falls below the values of T_0 obtained for the two lithium acetate–sodium acetate glass-forming melts (see Figure 3). This linear relationship between the ideal glass-transition temperature T_0 and the term $\Sigma N_i Z_i / r_i$ may be fortuitous. However, the acetate glass-forming systems do appear to follow such a relationship in the same way as the nitrate glass-forming melts.

The glass-transition temperature T_g may be taken as the point at which the viscosity attains the value of 10^{13} P. By substituting the computed values of η_0, k_η, and

(15) C. A. Angell, *J. Phys. Chem.*, 68, 1917 (1964).

(16) N. Onodera, H. Suga, and S. Seki, *Bull. Chem. Soc. Jap.*, 41, 2222 (1968).

(17) F. J. Hazlewood, E. Rhodes, and A. R. Ubbelohde, *Trans. Faraday Soc.*, 62, 3101 (1966).

T_0 into eq 6, a value of T_g of 281°K was obtained for the eutectic sodium acetate–potassium acetate melt. This is a reasonable value, especially in view of the fact that the ratio T_g/T_0 comes out to be 1.06. Such a value falls in the same range as calculated for melt A and melt B.

Despite the fact that the value of T_0 for the CH_3COONa–CH_3COOK eutectic melt is just below room temperature a glass cannot be made by quenching such a liquid. However, the closeness of T_0 for this melt to room temperature could explain the ease of glass formation observed in the equimolar CH_3COONa–CH_3COOK system to which less than 5 mol % alkaline earth acetate had been added.[5] Such melts readily formed glasses using normal quenching methods.

These data reported here, as well as those reported by Hazlewood, *et al.*,[17] have shown that low-melting binary acetate systems can be described by the VTF equation in the conductance range investigated. The values of T_0, the zero mobility temperature, as well as the experimental glass-transition temperature T_g, show similar behavior to these parameters determined for nitrate glass-forming melts.

One of the major problems encountered with the acetate melts is the short temperature range available before decomposition of the melt becomes important. The extensive glass-forming nature of acetate melts suggests that they could be useful for the study of many transport problems where change in composition is of interest. The variation of k_A and the preexponential term with composition in not only the CH_3COOLi–CH_3COONa system but other systems based on CH_3COOLi would be of interest. An attempt was made to determine the equivalent conductance of pure lithium acetate in this study. Unfortunately, decomposition of the melt took place before enough data points were obtained.

Acknowledgments. I wish to thank Dr. William A. Plummer for making the dta measurements and Dr. Walter M. Buehl for his assistance in running the computer solutions.

New Aromatic Anions. VIII. Acidity Constants of Rhodizonic Acid[1]

by Elizabeth Patton and Robert West

Department of Chemistry, The University of Wisconsin, Madison, Wisconsin 53706 *(Received November 25, 1969)*

The apparent dissociation constants of rhodizonic acid (IIIa) in aqueous solution have been determined spectrophotometrically. The values found are $pK_1 = 4.25 \pm 0.05$ and $pK_2 = 4.72 \pm 0.07$. Evidence is presented that hydration takes place concurrently with protonation; rhodizonate dianion is unhydrated, the monoanion is in equilibrium between the hydrated and unhydrated forms, and rhodizonic acid exists as the dihydrated structure (V). The measured constants are actually combinations of the acidity constants of the hydrated and unhydrated structures, and the equilibrium constant for the two forms of monoanion. The simple dissociation constants of anhydrous rhodizonic acid cannot be measured, but an upper limit of about 2 for pK_1' and 4.72 for pK_2' is indicated.

The cyclic oxocarbon dianions, $C_nO_n^{2-}$, have been recognized as a family of unusually stable species with electron delocalization around the ring, *i.e.*, an "aromatic" series.[2,3] Single crystal X-ray studies[4-6] and normal coordinate analyses[7] of the anion salts indicate symmetric, planar structures for squarate (I), croconate (II), and rhodizonate (III) anions. Hückel molecular orbital calculations predict them to be resonance stabilized with delocalization energies per π electron of 0.332β, 0.300β, and 0.285β for I, II, and III respectively.[5,5a] Because of the stability of the oxocarbon

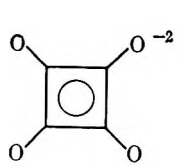

I

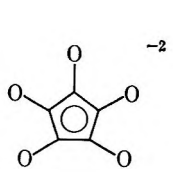

II

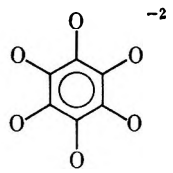

III

(1) Previous paper in this series: R. West and H. Y. Niu, *J. Amer. Chem. Soc.*, **85**, 2589 (1963).

(2) R. West and J. Niu in "Nonbenzenoid Aromatic Compounds," J. Snyder, Ed., Vol. I, Academic Press, Inc., New York, N. Y., 1969, p 312.

(3) R. West and D. L. Powell, *J. Amer. Chem. Soc.*, **85**, 2577 (1963).

(4) W. M. MacIntyre and M. S. Werkema, *J. Chem. Phys.*, **40**, 3563 (1964).

(5) (a) N. C. Baenziger and J. J. Hegenbarth, *J. Amer. Chem. Soc.*, **86**, 3250 (1964); (b) E. Patton and R. West, calculations using parameters of Baenziger and Hegenbarth.[5]

(6) M. A. Neuman, Thesis, University of Wisconsin, 1966; *Diss. Abstr.*, **26**, 6394 (1966).

(7) M. Ito and R. West, *J. Amer. Chem. Soc.*, **85**, 2580 (1963).

dianions, the strengths of the parent acids are of particular interest. The acids have structures Ia, IIa, and IIIa, as indicated by infrared spectra and dipole moment measurements.[8] The monoanions should be partially delocalized, *i.e.*, IV. The increased stabilization of the dianions compared to the undissociated compounds should make Ia–IIIa very strong acids.

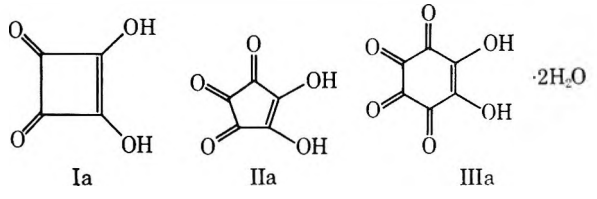

Ia IIa IIIa

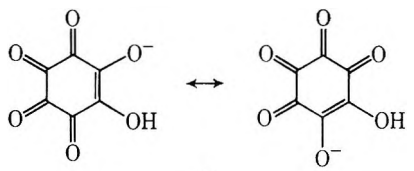

IV

Table I: Reported Dissociation Constants of the Oxocarbon Acids

Acid	pK_1	pK_2	Method	Ref
$H_2C_4O_4$	1.7 ± 0.3	3.21 ± 0.03	p[a]	9
	1.2 ± 0.2	3.48 ± 0.02	p	10
$H_2C_5O_5$	0.32	1.51	s[b]	11
$H_2C_6O_6$	3.15	4.9	p	12
	3.15	4.9	s	13
	4.1	4.5	p	14
	3.15	4.9	p	15
	4.20	4.65	s	16

[a] p is potentiometric. [b] s is spectrophotometric.

Accurate dissociation constants for squaric and croconic acids have recently been determined and are listed in Table I.[9–16] There is some discrepancy in the results listed for squaric acid, but its low solubility in water makes potentiometric measurements difficult. The uv maxima for the acid and anion forms overlap, so a spectrophotometric determination is not possible. Croconic acid is apparently the strongest of the three, in spite of the fact that molecular orbital calculations predict that squarate anion will have the greatest resonance stabilization.[17]

All of the previously determined pK values for rhodizonic acid are questionable. Carpeni's[12] potentiometric values of 3.15 and 4.9 have been generally accepted, but results are doubtful because in the same experiments the constants 2.93 and 4.05 were reported for croconic acid, and these have been proved incorrect.[11] Schwarzenbach studied the acidity of IIIa spectrophotometrically, selecting several wavelengths of the uv-visible spectrum which showed maxima when $\log \epsilon$ was plotted as a function of pH. He equated the pH's at the half-heights of these curves with the pK's of the acid and found that his results were consistent with Carpeni's. However, the method employed is not valid since the concentration of species in solution is proportional to the optical density, not its logarithm. Also, the fact that the spectrum changes due to further protonation beyond the neutral acid was not taken into consideration. Preisler originally reported $pK_1 = 4.1$ and $pK_2 = 4.5$ from oxidation–reduction studies,[14] but later noted that the values of Schwarzenbach and Carpeni were just as consistent with his results.[15]

Takahashi and coworkers[16] reported pK values of 4.20 and 4.65 for IIIa, found by setting pK_1 equal to the pH at which the wavelength characteristic of $H_2C_6O_6$ was 50% of its maximum absorption, and pK_2 equal to the pH for which the $C_6O_6^{2-}$ ion peak reached 50% of its maximum. This method is valid only if the two constants are sufficiently separated that the equilibria are independent. It must be simultaneously true that

$$pK_1 = pH - \log \frac{[HC_6O_6^-]}{[H_2C_6O_6]} \quad (1)$$

and that

$$pK_2 = pH - \log \frac{[C_6O_6^{2-}]}{[HC_6O_6^-]} \quad (2)$$

In order for only 1% of $HC_6O_6^-$ to be converted to $C_6O_6^{2-}$ when $pH = pK_1$, it is necessary that $pK_2 - pK_1$ equal 2. Takahashi's constants are only 0.45 unit apart, so that in a solution of pH 4.20, it follows from eq 2 that

$$\frac{[C_6O_6^{2-}]}{[HC_6O_6^-]} = 0.35$$

and $[H_2C_6O_6]$ does not equal $[HC_6O_6^-]$. Therefore the log term in eq 1 is not 0, and pK_1 is not equal to the pH of the solution.

This paper reports a determination of the strength of rhodizonic acid in aqueous solution using a spectrophotometric method developed by Thamer and Voigt[18]

(8) M. Washino, K. Yamada, and Y. Kurita, *Bull. Chem. Soc. Jap.*, **31**, 552 (1958).

(9) D. T. Ireland and H. F. Walton, *J. Phys. Chem.*, **71**, 751 (1967).

(10) D. J. MacDonald, *J. Org. Chem.*, **33**, 4559 (1958).

(11) B. Carlqvist and D. Dyrssen, *Acta Chem. Scand.*, **16**, 94 (1962).

(12) G. Carpeni, *J. Chim. Phys.*, **35**, 193 (1938).

(13) G. Schwarzenbach and J. Suter, *Helv. Chim. Acta*, **24**, 617 (1941).

(14) P. W. Preisler, L. Berger, and E. S. Hill, *J. Amer. Chem. Soc.*, **69**, 326 (1947).

(15) P. W. Preisler, L. Berger, and E. S. Hill, *ibid.*, **70**, 871 (1948).

(16) H. Takahashi, A. Kotaki, and K. Yagi, *Seikagaku*, **37**, 413 (1965).

(17) Possible reasons for the lower acid strength of Ia from IIa include destabilizing ring strain or 1,3 electron repulsion in I.[2]

(18) B. J. Thamer and A. F. Voigt, *J. Phys. Chem.*, **56**, 225 (1952).

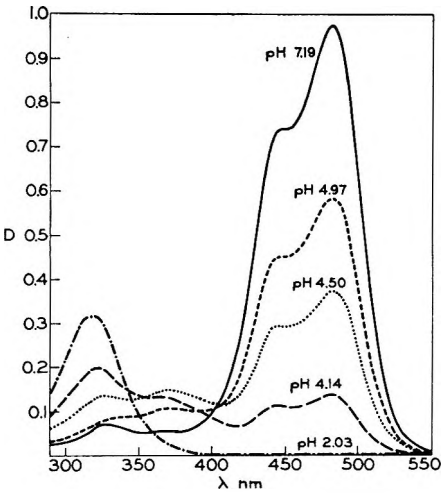

Figure 1. Spectra of rhodizonic acid in buffer solutions (concentration 3.00×10^{-5} M, path length 1 cm). Curve at pH 7.19 is characteristic of rhodizonate dianion (λ_{max} 483 nm, ϵ 3.3×10^4), and that at pH 2.03 characteristic of the hydrated acid (λ_{max} 320, ϵ 1.1×10^4). The intermediate spectra were taken after the system had reached equilibrium.

specifically for cases in which the equilibria may not be treated independently. The method requires that there be a portion of the spectrum which has a maximum or minimum occurring in the pH region in which monoanion has its highest concentration. The wavelength λ 370 nm satisfies this for rhodizonic acid (see Figure 1). An additional reaction which takes place concurrently with the dissociation, and the effect of this reaction on the reported constants, is also discussed.

Experimental Section

Sodium rhodizonate (Eastern Chemical Co.) was dried in an oven to constant weight before use. Water used to make up solutions was passed through a strong acid–strong base ion-exchange column, boiled, and then cooled to room temperature with a stream of nitrogen bubbling through it. It was necessary to deoxygenate the water in this way to prevent the oxidative decarboxylation of the rhodizonate anion.[19] Solutions were made up immediately before use and experiments were terminated within 4 hr to minimize the effects of this reaction. The rhodizonate salt was dissolved and diluted to volume in a volumetric flask which was then flushed with nitrogen and capped with a septum. Buffer solutions were made up with deoxygenated water and the buffer mixtures of Clark and Lubs[20] plus sufficient potassium chloride to make a total ionic strength of 0.1 M. One milliliter of stock solution was removed by syringe and added to 100 ml of buffer. The concentration of sample in the final solution was 4.90×10^{-5} M.

The pH of the final solution was measured using a Beckman Model G pH meter and a Sargent miniature combination glass electrode. Each measurement was standardized with two Sargent Standard Buffers. The optical density *vs.* time was measured with a Cary 14 recording spectrophotometer at λ 370 nm with the scan turned off. Two 5-cm matched quartz cells were used with water in the reference cell. The absorbance of each buffer solution was checked and was generally zero. Small deviations were subtracted from D.

In the pH region in which a period of several minutes was required before equilibrium was reached, the asymptotic value of the absorbance was used. If there was a small decrease with time due to oxidative decarboxylation, a correction factor of the rate of decrease times the time elapsed since mixing was added. This was never greater than 4% of the final value.

Method of Calculation. The optical density of a dibasic acid at a given wavelength may be expressed

$$\frac{D}{L} = \epsilon_2[H_2A] + \epsilon_1[HA^-] + \epsilon_0[A^{2-}] \qquad (3)$$

in which L is the path length of cell, D is the optical density, ϵ_2 is the absorptivity of H_2A at that wavelength, ϵ_1 is the absorptivity of HA^- at that wavelength, ϵ_0 is the absorptivity of A^{2-} at that wavelength.

The equilibrium constants K_1 and K_2 are defined as

$$K_1 = \frac{[HA^-][H^+]}{[H_2A]}; \qquad K_2 = \frac{[A^{2-}][H^+]}{[HA^-]} \qquad (4)$$

and (3) may be written as

$$D = \frac{Lc\left[\epsilon_2 + \frac{K_1}{[H^+]}\epsilon_1 + \frac{K_1K_2}{[H^+]^2}\epsilon_0\right]}{1 + \frac{K_1}{[H^+]} + \frac{K_1K_2}{[H^+]^2}} \qquad (5)$$

where $c = [H_2A] + [HA^-] + [A^{2-}]$, the total concentration of chromophore.

If the optical density of buffered solutions with the same path length and total concentration is plotted as a function of pH, ϵ_2 and ϵ_0 are found at the limits of the resulting curve since (5) reduces to

$$D_2 = Lc\epsilon_2 \qquad (6)$$

when $[H^+]$ is very large and only H_2A is present.

$$D_0 = Lc\epsilon_0 \qquad (7)$$

when $[H^+]$ is very small and only A^{2-} is present. ϵ_1 is not experimentally measurable because it is the extinction coefficient of a substance which never exists alone in solution.

By using a wavelength which has a maximum optical density between the limits of (6) and (7), the derivative

(19) A. J. Fatiadi, H. S. Isbell, and W. F. Sager, *J. Res. Nat. Bur. Stand. Sect. A*, 67, 153 (1963).

(20) I. M. Kolthoff and H. A. Laitinen, "pH and Electrotitrations," 2nd ed, John Wiley and Sons, New York, N. Y., 1941, p 34.

of eq 5 can be set equal to zero at the maximum to give the expression

$$\epsilon_2 = \frac{2K_2\epsilon_2}{[H^+]_m} - \epsilon_1 + \frac{K_1K_2\epsilon_1}{[H^+]_m^2} - \frac{2K_2\epsilon_0}{[H^+]_m} - \frac{K_1K_2\epsilon_0}{[H^+]_m^2} = 0 \quad (8)$$

where $[H^+]_m = [H^+]$ at the maximum.

The optical density at $[H^+]_m$ is

$$D_m = \frac{Lc\left[\epsilon_2 + \frac{K_1}{[H^+]_m}\epsilon_1 + \frac{K_1K_2}{[H^+]_m^2}\epsilon_0\right]}{1 + \frac{K_1}{[H^+]_m} + \frac{K_1K_2}{[H^+]_m^2}} \quad (9)$$

Equations 8 and 9 are combined to eliminate ϵ_1, leading to a quadratic expression in K_1K_2

$$(K_1K_2)^2 + [H^+]_m\left\{K_1 + [H^+]_m\left[1 - \left(\frac{D_m - D_2}{D_m - D_0}\right)\right]\right\} \times (K_1K_2) - [H^+]_m^3\left(\frac{D_m - D_2}{D_m - D_0}\right)(K_1 + [H^+]_m) = 0 \quad (10)$$

whose only positive root is

$$K_1K_2 = [H^+]_m^2\left(\frac{D_m - D_2}{D_m - D_0}\right) \quad (11)$$

Substituting

$$[H^+] = 10^{-pH} \quad (12)$$

into eq 5 and combining it with (9) and (11), the following equation for D as a function of pH is obtained

$$D = D_2 + (D_m - D_2) \times \frac{\frac{K_1}{[H^+]_m} + 2 + [H^+]_m\left(\frac{D_0 - D_2}{D_m - D_0}\right)10^{pH}}{\frac{K_1}{[H^+]_m} + \frac{10^{-pH}}{[H^+]_m} + [H^+]_m\left(\frac{D_m - D_2}{D_m - D_0}\right)10^{pH}} \quad (13)$$

The constant K_1 may be calculated directly using the rearranged form of (13)

$$K_1 = \frac{(D_m - D_0)(D - D_2)10^{-pH} + [H^+]_m^2(D_m - D_2) \times (D - D_0)10^{pH} - 2[H^+]_m(D_m - D_2)(D_m - D_0)}{(D_m - D_0)(D_m - D)} \quad (14)$$

This plus eq 11 leads directly to the constants K_1 and K_2.

Results

When 1 ml of a solution 5×10^{-4} M in rhodizonate ion is added to 100 ml of buffer solution the reaction is instantaneous except in the pH range between 3 and 6. In stronger acids the orange anion becomes colorless immediately, but in this intermediate range it slowly becomes lighter yellow. Observing the reaction spectrophotometrically, it is slowest around pH 4.5 where it takes about 8 min for the optical density *vs.* time curve to become level. The reverse process, equilibration of rhodizonic acid in buffer to pH 3–6, is also slow.

This slow step has been observed previously.[13,21] It was thought to be due to the rearrangement of the acid from the ene-diol to the keto form, but no proof that this rearrangement takes place was ever found. The most probable cause is the addition of water to the molecule. Rhodizonic acid as crystallized from water contains two molecules of water, in addition to the regular oxocarbon acid structure. In order to obtain the anhydrous acid it is necessary to sublime $H_2C_6O_6 \cdot 2H_2O$ at 14 Torr and 155°; at any higher pressure, CO_2 is given off rather than water.[22] The anhydrous compound picks up water from the air instantaneously after it is exposed. Skujins[23] found a parent peak at m/e 206 ($H_2C_6O_6 \cdot 2H_2O$) in a low-temperature mass spectrum of rhodizonic acid, indicating that these are not simply waters of hydration but are chemically bonded to the molecule. The most likely structure is V.

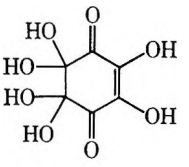

V

The total equilibrium, with all species present, may be written

$$\begin{array}{ccccc} H_2C_6O_4(OH)_4 & \overset{K_1''}{\rightleftharpoons} & HC_6O_4(OH)_4^- & \overset{K_2''}{\rightleftharpoons} & [C_6O_4(OH)_4^{2-}] \\ k_3\uparrow\downarrow k_{-3} & & k_4\uparrow\downarrow k_{-4} & & k_5\uparrow\downarrow k_{-5} \\ [H_2C_6O_6] & \overset{K_1'}{\rightleftharpoons} & HC_6O_6^- & \overset{K_2'}{\rightleftharpoons} & C_6O_6^{2-} \end{array}$$

However, the bracketed compounds are not likely to exist in significant concentrations. Anhydrous rhodizonic acid is unstable to hydration as discussed above. A visible spectrum of the solid compound immediately after sublimation contains a strong peak at λ 470 nm, which disappears rapidly when the compound is exposed to air leaving a spectrum of the hydrated acid. This peak is not observed in aqueous solution. Rhodizonate dianion in solution, which has the same maximum in its visible spectrum as the solid anhydrous salt, would be unlikely to destroy its symmetric, resonance-stabilized structure by reacting with water. Therefore, it may be assumed that the system at equilibrium is made up of the remaining four species.

During the slow reaction of the dianion to the equilibrium mixture, the peak at 483 nm characteristic of

(21) P. Souchay and F. Tatibouet, *J. Chim. Phys.*, **49**, 108 (1952).

(22) B. Eistert and G. Bock, *Angew. Chem.*, **70**, 595 (1958).

(23) S. Skujins, J. Delderfield, and G. A. Webb, *Tetrahedron*, **24**, 4805 (1968).

dianion decreases, that at 320 nm characteristic of the acid increases, and the absorption at 370 nm increases. These observations are readily explained if the absorbance at 370 nm is due primarily to the hydrated monoanion. When rhodizonate dianion is added to the buffer it immediately comes to equilibrium with anhydrous monoanion and then slowly reacts with water to form the hydrate, which quickly comes to equilibrium with the hydrated acid. Hence, the acid hydrate peak (320 nm) and the monoanion absorbance (370 nm) increase simultaneously. As the acid form goes to equilibrium the opposite changes occur at each wavelength, and the final spectrum is the same.

Using the above reaction scheme it is possible to derive the significance of the constants which are measured in aqueous solution. Considering the concentration of water to be constant

$$K_4 = \frac{[HC_6O_4(OH)_4^-]}{[HC_6O_6^-]} \text{ (at equilibrium)} \quad (15)$$

$$K_1' = \frac{[H^+][HC_6O_6^-]}{[H_2C_6O_6]}; \quad K_2' = \frac{[H^+][C_6O_6^{2-}]}{[HC_6O_6^-]} \quad (16)$$

$$K_1'' = \frac{[H^+][HC_6O_4(OH)_4^-]}{[H_2C_6O_4(OH)_4]};$$

$$K_2'' = \frac{[H^+][C_6O_4(OH)_4^{2-}]}{[HC_6O_4(OH)_4^-]} \quad (17)$$

Using the same derivation as above, the following is true at equilibrium

$$c = [H_2C_6O_4(OH)_4] + [HC_6O_4(OH)_4^-] + [HC_6O_6^-] + [C_6O_6^{2-}]$$

$$c = [H_2C_6O_4(OH)_4] + (1 + K_4)[HC_6O_6] + [C_6O_6^{2-}]$$

$$\frac{D}{L} = \epsilon_2''[H_2C_6O_4(OH)_4] + \epsilon_1''[HC_6O_4(OH)_4^-] + \epsilon_1'[HC_6O_6] + \epsilon_0'[C_6O_6^{2-}]$$

$$\frac{D}{L} = \epsilon_2''[H_2C_6O_4(OH)_4] + (\epsilon_1''K_4 + \epsilon_1')[HC_6O_6^-] + \epsilon_0'[C_6O_6^{2-}]$$

Define

$$\epsilon_1 = \frac{\epsilon_1''K_4 + \epsilon_1'}{K_4 + 1} \quad (18)$$

Combining these, an equation analogous to eq 5 may be derived.

$$D = \frac{Lc\left[\epsilon_2'' + \frac{K_1''(K_4+1)}{K_4}\frac{\epsilon_1}{[H^+]} + \frac{K_1''K_2'}{K_4}\frac{\epsilon_0'}{[H^+]^2}\right]}{1 + \frac{K_1''(K_4+1)}{K_4}\frac{1}{[H^+]} + \frac{K_1''K_2'}{K_4}\frac{1}{[H^+]^2}} \quad (19)$$

Comparing eq 19 with eq 5, it is apparent that the constants measured in aqueous solution will be

$$K_1(\text{measured}) = K_1''\frac{K_4 + 1}{K_4} \quad (20)$$

$$K_2(\text{measured}) = K_2'\frac{1}{K_4 + 1} \quad (21)$$

where K_1'' is the first dissociation constant for $H_2C_6O_4(OH)_4$, and K_2' is the second dissociation constant for the anhydrous acid.

The measured constants represent the strength that rhodizonic acid will show in water—they are valid physical quantities in that they indicate how the system will interact with other acids and bases under experimental conditions, but they do not have the theoretical significance of simple dissociation constants.

Results of Calculations

Use of the method of Thamer and Voigt[18] for determination of acidity constants requires precise values for D_m, the maximum optical density, and for D_2 and D_0. The experimental curve, D *vs.* pH, does reach a limit at high pH, so D_0 may be found by measurement. However, the change in D at very low pH indicates that further protonation beyond the neutral acid is taking place, and D_2 may not be found directly. Although D_m may be measured, it cannot be determined as precisely as necessary because it is in the pH region in which the correction factor for loss of absorbance due to oxidative carboxylation is used (see Experimental Section). It was therefore decided to treat the constants D_2 and D_m along with K_1 and K_2, as dependent parameters of eq 11 and 13. Initial estimates of K_1 and K_2 were made using several data points and eq 11 and 14, with likely values for D_2 and D_m. These were entered as initial values into a computer program[24] which fit them to eq 13, a nonlinear mathematical model. D_0 was entered as an independent constant, and the data points D *vs.* pH as independent variables. The program uses an iterative technique, varying the dependent parameters until a least-squares fit between the data points and the ideal curve is found. The following results were obtained: $pK_1 = 4.15 \pm 0.04$, $pK_2 = 4.42 \pm 0.03$.

Table II lists the initial and final values for the parameters. The confidence limits given are based on a linear approximation in the region of the constant. The final values of D make up the theoretical curve in Figure 2. The experimental points included in this figure illustrate the change in D due to the third protonation. Those values taken below a pH of 2.40 were not included in the calculations since they contained this systematic error.

(24) Gaushaus, available as a subroutine at the University of Wisconsin Computing Center.

Table II: Data Used in Calculating K_1 and K_2[a]

Variables

pH	D, initial	D, final	pH	D, initial	D, final
6.04	0.535	0.530	4.57	1.16	1.151
5.93	0.545	0.542	4.51	1.17	1.179
5.87	0.55	0.551	4.18	1.205	1.192
5.66	0.60	0.589	4.08	1.15	1.145
5.42	0.65	0.658	3.97	1.09	1.072
5.30	0.706	0.706	3.87	0.974	0.994
5.24	0.74	0.734	3.79	0.903	0.928
5.19	0.759	0.759	3.70	0.873	0.854
5.10	0.080	0.808	3.63	0.794	0.798
5.02	0.856	0.857	3.50	0.702	0.703
4.91	0.929	0.929	3.40	0.630	0.639
4.91	0.95	0.929	3.18	0.534	0.528
4.81	0.998	0.999	3.03	0.492	0.474
4.80	0.99	1.006	2.70	0.400	0.398
4.72	1.106	1.061	2.40	0.351	0.363
4.66	1.105	1.100			

Dependent Parameters

	Initial	Final
K_1	9.0×10^{-5}	$(7.1 \pm 0.6) \times 10^{-5}$
K_2	3.7×10^{-5}	$(3.8 \pm 0.3) \times 10^{-5}$
D_2	0.25	0.33 ± 0.01
D_{max}	1.227	1.22 ± 0.01

Independent Parameter

D_0	0.485

[a] Total concentration 4.90×10^{-5} M, path length 5 cm.

In Appendix A the corrections for activity are calculated. Assuming an error of 10% in these corrections, the thermodynamic dissociation constants are $pK_1 = 4.25 \pm 0.05$ and $pK_2 = 4.72 \pm 0.07$.

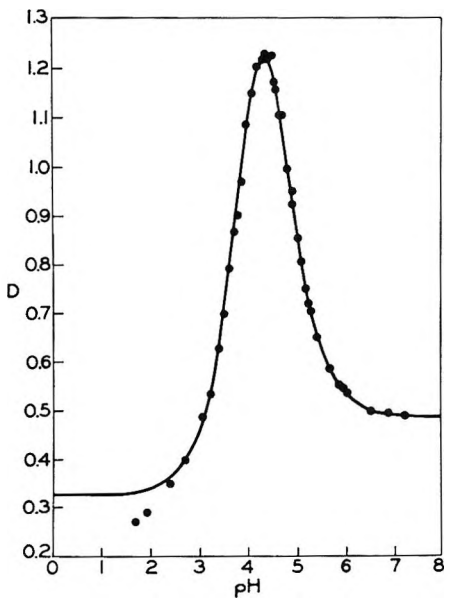

Figure 2. D *vs.* pH for λ 370 nm (concentration 4.90×10^{-5} M, path length 5 cm). The points are experimental values, and the solid line is the theoretical curve, eq 13, based on the final constants.

Discussion

The experimental constants which we have determined are similar to those reported by Takahashi, *et al.*,[16] whose method should give reasonably good approximate values. The results of both of these experiments indicate that the pK's reported by Carpeni[12] and Schwarzenbach[13] are erroneous. The largest difference is in pK_1, the earlier values being one unit lower than ours. It is probable that they have measured a combination of pK_1 and the dissociation constant for the triprotonated cation. None of the previous authors have considered the effect of the hydration reaction on their values.

To compare the strength of anhydrous rhodizonic acid with that of the other oxocarbons, it is necessary to estimate its simple dissociation constants. The rate constant for the system to approach equilibrium (assuming that the protonation equilibrium is more rapid than the hydration–dehydration reaction) is

$$\frac{k_3 + k_4\frac{K_1'}{[H^+]} + k_5\frac{K_1'K_2'}{[H^+]^2}}{1 + \frac{K_1'}{[H^+]} + \frac{K_1'K_2'}{[H^+]^2}} + \frac{k_{-3} + k_{-4}\frac{K_1''}{[H^+]} + k_{-5}\frac{K_1'K_2''}{[H^+]^2}}{1 + \frac{K_1''}{[H^+]} + \frac{K_1''K_2''}{[H^+]^2}} \quad (22)$$

(This expression is derived in Appendix B.) In very acidic solutions, this reduces to $k_3 + k_{-3}$, but since $k_{-3} \ll k_3$, the rate constant is k_3. This corresponds to the reaction sequence

$$H^+ + HC_6O_6^- \underset{}{\overset{K_1'}{\rightleftharpoons}} H_2C_6O_6$$

$$H_2C_6O_6 \underset{k_{-3}}{\overset{k_3}{\rightleftharpoons}} H_2C_6O_4(OH)_4 \qquad \text{(fast)}$$

becoming predominant over the slow hydration of the monoanion. This fast reaction will take place when the hydrogen ion concentration is high enough that some $H_2C_6O_6$ is formed from $HC_6O_6^-$. (That this pathway exists can be demonstrated by adding concentrated acid to a solution of rhodizonate anion. The solution turns deep red, a color characteristic of anhydrous acid, and then becomes colorless immediately.) The constant k_3 is very large, as would be expected from the rate at which the acid adds water in air, and so the reaction in a solution of pH <3 is instantaneous. The fact that at pH 3 it is still measurably slow indicates that not much $H_2C_6O_6$ is in equilibrium with $HC_6O_6^-$. This shows that pK_1' must be much less than 3. An upper limit for pK_1' of 2 seems indicated.

Taking the log of eq 21 and substituting the value found for pK_2(measured), the relationship

$$pK_2' = 4.72 + \log \frac{1}{1 + K_4}$$

is found. It is not possible to estimate K_4, but log $1/(1 + K_4)$ must be less than or equal to 1, so 4.72 is an upper limit for pK_2'.

Thus, although the actual dissociation constants of anhydrous rhodizonic acid cannot be measured in aqueous solution, the estimated values indicate that K_1', and possibly K_2', are much more similar to the dissociation constants of the other oxocarbons than previously thought.

Appendix A

From the definitions of pK_1 and pK_2 given in eq 20 and 21, it follows that

$$pK_1 = pH - \log \frac{[HC_6O_6^-] + [HC_6O_4(OH)_4^-]}{[H_2C_6O_4(OH)_4]}$$

$$pK_2 = pH - \log \frac{[C_6O_6^{2-}]}{[HC_6O_6^-] + [HC_6O_4(OH)_4^-]}$$

Values of pH measured with a pH meter are already in terms of hydrogen ion activity rather than concentration; therefore only the activity coefficients of the remaining terms need to be calculated to find the thermodynamic dissociation constants. The Debye–Hückel equation is valid for solutions of this ionic strength

$$-\log \gamma = \frac{0.5z^2\sqrt{\mu}}{1 + 0.33\mathring{A}\sqrt{\mu}}$$

where $\mathring{A}$ is the ionic diameter in angstroms, approximately 6 for all four species, and μ is the ionic strength, 0.1 M. It is simplest to calculate the ratios of log γ so that the results are added directly to experimental values of pK_1 and pK_2

$$-\log \frac{\gamma[HC_6O_6^- + HC_6O_4(OH)_4^-]}{\gamma[H_2C_6O_4(OH)_4]} = 0.1$$

$$-\log \frac{\gamma(C_6O_6^{2-})}{\gamma[HC_6O_6^- + HC_6O_6(OH)_4^-]} = 0.3$$

Appendix B

The relaxation constants for the hydrate–anhydrous system, assuming that the protonation equilibrium is rapid compared to hydration, may be derived. A steady-state concentration of the intermediate monohydrate is assumed. Substituting A = $C_6O_6^{2-}$, and B = $C_6O_4(OH)_4^{2-}$, the reaction system becomes

$$\begin{array}{ccccc} H_2B & \overset{K_1''}{\rightleftharpoons} & HB & \overset{K_2''}{\rightleftharpoons} & B \\ {\scriptstyle k_3}\uparrow\downarrow{\scriptstyle k_{-3}} & & {\scriptstyle k_4}\uparrow\downarrow{\scriptstyle k_{-4}} & & {\scriptstyle k_5}\uparrow\downarrow{\scriptstyle k_{-5}} \\ H_2A & \overset{K_1'}{\rightleftharpoons} & HA & \overset{K_2'}{\rightleftharpoons} & A \end{array}$$

The total concentration of A species, c_A, is $c_A = [H_2A] + [HA] + [A]$.

$$c_A = [HA]\left[1 + \frac{K_1'}{[H^+]} + \frac{K_1'K_2'}{[H^+]^2}\right]\left(\frac{[H^+]}{K_1'}\right) = \frac{[HA][H^+]}{K_1'}\alpha_A \quad (23a)$$

Similarly, for B

$$c_B = [HB]\left[1 + \frac{K_1''}{[H^+]} + \frac{K_1''K_2''}{[H^+]^2}\right]\left(\frac{[H^+]}{K_1'}\right) = \frac{[HB][H^+]}{K_1''}\alpha_B \quad (23b)$$

These equations define α_A and α_B.

$$\frac{d(c_A)}{dt} = -k_3[H_2A] - k_4[HA] - k_5[A] + k_{-3}[H_2B] + k_{-4}[HB] + k_{-5}[B]$$

$$\frac{d(c_A)}{dt} = -[HA]\left[k_3 + k_4\frac{K_1'}{[H^+]} + k_5\frac{K_1'K_2'}{[H^+]^2}\right]\left(\frac{[H^+]}{K_1'}\right) + [HB]\left[k_{-3} + k_{-4}\frac{K_1''}{[H^+]} + k_{-5}\frac{K_1''K_2''}{[H^+]^2}\right]\left(\frac{[H^+]}{K_1''}\right)$$

$$\frac{d(c_A)}{dt} = -[HA]\left(\frac{[H^+]}{K_1'}\right)\beta_A + [HB]\left(\frac{[H^+]}{K_1''}\right)\beta_B \quad (24)$$

These equations define β_A and β_B. At equilibrium

$$\frac{d(c_A)}{dt} = 0 = -[HA]_e\left(\frac{[H^+]}{K_1'}\right)\beta_A + [HB]_e\left(\frac{[H^+]}{K_1'}\right)\beta_B$$

Combining eq 23 and 24

$$\frac{d(c_A)}{dt} = -\frac{c_A}{\alpha_A}\beta_A + \frac{c_B}{\alpha_B}\beta_B$$

Since $c_A + c_B$ is a constant, this is an equilibrium between the two first-order reactions, and

$$\ln \frac{(\Delta c_A)_{t_2}}{(\Delta c_A)_{t_1}} = \left[\frac{\beta_A}{\alpha_A} + \frac{\beta_B}{\alpha_B}\right](t_2 - t_1) \quad (25)$$

where $\Delta c_A = c_A - c_A$ (equilibrium). This is equivalent to eq 22.

Acknowledgments. The authors wish to acknowledge the Public Health Service–National Institutes of Health for their generous support of this work, and Thomas L. Henson and James E. Patton for many helpful discussions.

The Thermodynamics of Ion Solvation in Water and Propylene Carbonate

by Mark Salomon

NASA, Electronics Research Center, Cambridge, Massachusetts 02139 *(Received January 30, 1970)*

The energetics of single-ion solvation in water and propylene carbonate are evaluated on the basis of an electrostatic model. Single-ion free energies of solvation are obtained by extrapolation (to infinite ionic radius) of a plot of the differences of cation and anion conventional energies *vs.* $1/r$. The enthalpy of solvation of individual ions is a more complicated function of $1/r$ and several methods are used in evaluating these quantities.

Introduction

The free energies and enthalpies of solvation of individual ions are of fundamental importance since they constitute the basis of theories on ion–solvent interactions.[1] For the most part, the Born equation

$$\Delta G_{solv} = -\frac{(ze)^2}{2r_i}\left\{1 - \frac{1}{\epsilon}\right\} \quad (1)$$

and the Born–Bjerrum equation

$$\Delta H_{solv} = -\frac{(ze)^2}{2r_i}\left\{1 - \frac{1}{\epsilon} - \frac{T}{\epsilon}\frac{\partial \ln \epsilon}{\partial T}\right\}_p \quad (2)$$

have dominated the many attempts to calculate these quantities.[1] The usual approach is to empirically adjust the crystal radii, r_i, of cations and anions until the plot of ΔH or ΔG *vs.* $1/(r_i + \delta)$ is linear with all the ions falling on a single line.[2,3] Another method introduced by Bernal and Fowler[4] involves the assumption that ions of equal radii have equal (coulombic) energies of solvation. In order to improve on calculations based on eq 1 and 2, Laidler and Pegis,[5] and Conway and Desnoyers[6] have considered the effect of dielectric saturation. Laidler and Pegis have also shown that for the free energy, the leading term in the Born equation is the gas phase (crystal) radii and that large corrections to this radius are unjustified. Buckingham[7] showed that in addition to the Born charging enthalpy, ion–multipole and polarization energies constitute major contributions to the overall solvation enthalpy. In Buckingham's model, ions of equal crystal radii have equal enthalpy values from all contributing factors with the exception of the ion–quadrupole enthalpy. At this suggestion Halliwell and Nyberg[8] proposed a significantly different method for the calculation of the absolute solvation enthalpy of the proton, $\Delta H_{solv}(H^+)$, which involves the differences in conventional enthalpies between cations and anions. For monovalent cations and anions the conventional enthalpies are defined, respectively, as

$$\Delta H_{conv}(M^+) = \Delta H_{solv}(M^+) - \Delta H_{solv}(H^+) \quad (3)$$

$$\Delta H_{conv}(X^-) = \Delta H_{solv}(X^-) + \Delta H_{solv}(H^+) \quad (4)$$

The difference in conventional enthalpies is therefore

$$\Delta H_{conv}(M^+) - \Delta H_{conv}(X^-) = \left\{\Delta H_{solv}(M^+) - \Delta H_{solv}(X^-)\right\} - 2\Delta H_{solv}(H^+) \quad (5)$$

Since the term on the left-hand side of eq 5 is known from experiment, Halliwell and Nyberg proposed that $\Delta H_{solv}(H^+)$ could be evaluated by extrapolation of the plot of $\Delta H_{conv}(M^+) - \Delta H_{conv}(X^-)$ for ions of equal radii *vs.* $1/(r_i + \delta)^3$. On this basis a value of -260.7 kcal/mol was obtained for $\Delta H_{solv}(H^+)$. Morris[9] used more recent thermodynamic data along with a revised set of crystal radii[10] and obtained a value of -263.7 kcal/mol for this quantity.

Recently, Conway and Salomon[11,12] have pointed out that the results of this method may be too high since

(1) B. E. Conway and J. O'M. Bockris, "Modern Aspects of Electrochemistry," Vol. 1, Butterworth and Co., Ltd., London, 1954, Chapter 2.

(2) W. M. Latimer, K. S. Pitzer, and C. M. Slansky, *J. Chem. Phys.*, **7**, 108 (1939).

(3) E. J. W. Verwey, *Rec. Trav. Chim. Pays-Bas*, **61**, 127 (1942).

(4) J. D. Bernal and R. H. Fowler, *J. Chem. Phys.*, **1**, 515 (1933).

(5) K. J. Laidler and C. Pegis, *Proc. Roy. Soc., Ser. A*, **241**, 80 (1957).

(6) B. E. Conway and J. E. Desnoyers, *Phil. Trans. Roy. Soc., London*, **256A**, 389 (1964).

(7) A. D. Buckingham, *Discuss. Faraday Soc.*, **24**, 151 (1957).

(8) H. F. Halliwell and N. C. Nyberg, *Trans. Faraday Soc.*, **59**, 1126 (1963).

(9) D. F. C. Morris, *Struct. Bonding*, **4**, 63 (1968).

(10) B. S. Gourary and F. J. Adrian, *Sol. State Phys.*, **10**, 128 (1960).

(11) B. E. Conway, "Modern Aspects of Electrochemistry," J. O'M. Bockris and B. E. Conway, Ed., Vol. 3, Butterworth and Co., Ltd., London, 1964, Chapter 2.

(12) B. E. Conway and M. Salomon, "Chemical Physics of Ionic Solutions," B. E. Conway and R. G. Barradas, Ed., John Wiley and Sons, New York, N. Y., 1966.

the assumption regarding the cancellation of the ion–dipole term for $r_+ = r_-$ is only valid if the orientations of the solvent at the cation and anion are mirror images. However, if the model of Verwey[3] is considered, then the orientation of a water molecule at a cation is at 52° to the radial direction while that at anions is along this direction. For this condition the ion–dipole energy does not cancel but differs by a factor of $(1 - \cos 52°)$ for anions and cations of equal radii. The plots of conventional enthalpies should therefore involve a term in $1/r^2$ as well as one in $1/r^3$.

In order to resolve this problem, two methods, similar to that of Halliwell and Nyberg, are employed in this paper. The method is applied to ionic solvation in water and in anhydrous propylene carbonate (PC).

Conventional Free Energies

One can define a set of relations similar to (3)–(5) for the free energy, *i.e.* by

$$\Delta G_{conv}(M^+) = \Delta G_{solv}(M^+) - \Delta G_{solv}(H^+) \quad (6)$$

$$\Delta G_{conv}(X^-) = \Delta G_{solv}(X^-) + \Delta G_{solv}(H^+) \quad (7)$$

$$d\Delta G_{conv} = \Delta G_{conv}(M^+) - \Delta G_{conv}(X^-) = \{\Delta G_{solv}(M^+) - \Delta G_{solv}(X^-)\} - 2\Delta G_{solv}(H^+) \quad (8)$$

In order to evaluate $\Delta G^\circ_{solv}(H^+)$, a suitable function in r must be obtained for $\Delta G_{solv}(M^+) - \Delta G_{solv}(X^-)$. In this paper it is proposed that the function is simply $1/r$ so that eq 8 can be written as

$$d\Delta G_{conv} = \frac{\text{constant}}{r_i} - 2\Delta G_{solv}(H^+) \quad (9)$$

where r_i is the gas phase radius of Gourary and Adrian.[10] The basis of this assumption is attributed to the compensation effect between the enthalpy and entropy of solvation.[1,13] It is now generally accepted that the enthalpy of hydration is a complex function (*e.g.* a power series) of $1/r$ (7) and the corresponding entropy effects should also involve the same factors since those factors which lead to an increase in the enthalpy of interaction between the ions and water also tend to restrict the degree of freedom of the water molecule in the primary hydration shell, thereby decreasing the entropy.[13] Since these effects oppose each other, it is reasonable to assume that the free energy contributions from terms higher than r^{-1} are small and that they tend to cancel for large ions when differences in energies are considered. Having obtained $\Delta G_{solv}^\circ(H^+)$ from eq 9, the corresponding enthalpy term can be evaluated by taking $\Delta S_{solv}^\circ(H^+) = -31.3$ eu.[1,11]

Conventional Enthalpies

To evaluate the enthalpy of solvation of the proton, the conventional enthalpies were fit to the least-squares relation

$$\Delta H_{conv}(\text{ion}) = Z_i + \frac{A_i}{(r_i + \delta)^2} + \frac{B_i}{(r_i + \delta)^3} \quad (10a)$$

For cations and anions of the same radii, the absolute enthalpy of solvation of the proton is therefore obtained from

$$d\Delta H_{conv} = (Z_+ - Z_-) + \frac{(A_+ - A_-)}{(r_i + \delta)^2} + \frac{(B_+ - B_-)}{(r_i + \delta)^2} \quad (10b)$$

where $d\Delta H_{conv} = \Delta H_{conv}(M^+) - \Delta H_{conv}(X^-)$ and $Z_+ - Z_- = -2\Delta H_{solv}(H^+)$. In eq 10, δ is the radius of the solvent molecule equal to 1.38 for water and 2.62 for PC (estimated from density measurements).[14]

Results

For aqueous solutions the conventional energies are referred to the solvated proton and for PC the solvated lithium ion is taken as the standard of comparison. All data correspond to the standard states at 298.15°K and 1 atm pressure. The free energies of solvation are obtained mainly from emf data. For example, consider the electrode reaction

$$Li_s + AgCl_s = Li_h^+ + Cl_h^- + Ag_s \quad (11)$$

where the subscripts s and h refer to the solid and hydrated species, respectively. The standard free energy of solution of LiCl is given by

$$\Delta G_{soln}^\circ = \Delta G_{II}^\circ + \Delta G_f^\circ(AgCl_s) - \Delta G_f^\circ(LiCl_s) \quad (12)$$

where ΔG_f° is the free energy of formation and ΔG_{II}° is obtained from emf data. The free energy of solvation is obtained from ΔG_{soln}° by

$$\Delta G_{solv}^\circ = \Delta G_{soln}^\circ + \Delta G_{lat}^\circ \quad (13)$$

The lattice free energy is obtained from

$$\Delta G_{lat}^\circ(LiCl) = \Delta G_f^\circ(Li_g) + \Delta G_f^\circ(Cl_g) - \Delta G_f^\circ(LiCl_s) + I - A \quad (14)$$

where I and A are, respectively, the ionization potential of the metal and electron affinity of the halide. Values of ΔG_{II}° in water and other combinations of metal–halide systems were obtained from deBethune's tables[15] with the exception of the Li–H_2 couple.[16] For the alkali halides in PC our previous results are used.[17,18] In the absence of emf data free energies of solution in PC were estimated[18] from

$$\Delta G_{soln}^\circ = -2RT \ln (m_{sat}\gamma_\pm) \quad (15)$$

where m_{sat} is the solubility of the salt and $\gamma_\pm$ is the mean molal activity coefficient which is evaluated from the Davies equation as discussed previously.[18]

(13) D. D. Eley and M. G. Evans, *Trans. Faraday Soc.*, **34**, 1093 (1938).

(14) M. Salomon, *J. Phys. Chem.*, **73**, 3299 (1969).

(15) A. J. deBethune, T. S. Licht, N. Swendeman, *J. Electrochem. Soc.*, **106**, 616 (1959).

(16) D. R. Cogley and J. N. Butler, *J. Phys. Chem.*, **72**, 1017 (1968).

(17) M. Salomon, *J. Electroanalyt. Chem.*, March, 1970.

(18) M. Salomon, *ibid.*, submitted for publication.

. $\Delta G_f°$ values were taken from several recent compilations[19,20] with the exception of Rb and Cs salts which were taken from Latimer's tables.[21] Ionization potentials were obtained from a recent monograph[22] and the electron affinities of the halides are those measured by Berry and Reimann.[23] Data for the OH^- ion are based on the reaction

$$H_2O_{liq} = H_h^+ + OH_h^- \qquad (16)$$

for which we can write

$$\Delta G_{conv}°(OH^-) = \Delta G_{16}° + \Delta G_f°(H_2O_l) - \Delta G_f°(H_g^+) - \Delta G_f°(OH_g^-)$$

Values of $\Delta G_{16}°$ and $\Delta H_{16}°$ are, respectively, 19.095 and 13.526 kcal/mol.[24]

Crystal radii for the alkali metals and the halogens are those based on Gourary and Adrian's data.[10] For the OH^- ion the crystal radius as determined by X-ray crystallography is 1.03 Å (*cf.* ref 21 of the paper by Khomutov[25]). Values as high as 1.47 Å have been reported.[8] The value of 1.12 Å chosen here is slightly larger than the experimental one and is justified on the basis that some increase accompanies the solvation process due to hydrogen bonding.[25] The crystal radii for Ag^+ and Tl^+ were taken from ref 22 while the remaining values are from ref 8.

Lattice enthalpies at 298.15°K when not available from the literature were calculated from

$$-\Delta H_{lat}° = \frac{600}{r_+ + r_-}\left\{1 - \frac{0.4}{r_+ + r_-}\right\} \qquad (17)$$

This relation is claimed to be accurate to within 1–2 kcal/mol.[26] This accuracy may, however, diminish significantly due to errors in estimating crystal radii. Hence for the alkali halide salts, eq 17 does in fact predict values close to the thermodynamic ones, but the errors in $\Delta H_{lat}°$ for perchlorate, tetraphenyl arsonium ($AsPh_4^+$), and tetraphenyl borate (BPh_4^-) are unknown due to the unknown uncertainties in their radii. Finally, the entropies, enthalpies, and free energies for the $(CH_3)_4N^+$ ion were obtained from Boyd's work.[27] Table I[28] lists the values of lattice energies and solvation energies for the various 1:1 salts. All values are based on the molal scale. Table II lists the conventional free energies and enthalpies of the individual ions. Figures 1 and 2 show the plots of conventional free energies *vs.* $1/r$ for the aqueous and PC systems, respectively. There are no existing data to allow one to calculate $\Delta G_{solv}°$ for the cesium ion in PC. While some data exist on the solubility of LiF in PC, they are conflicting and give anomalous values for the free energies of transfer (*cf.* 18). The conventional energy for F^- in PC must therefore be estimated. In Figure 1 it is seen that all the anion points lie on a single straight line as do the points for Cl^-, Br^-, and I^- in PC (Figure 2). It was therefore assumed that F^- in PC also lies on this line and a simple extrapolation to the $1/r$ value for F^- gives

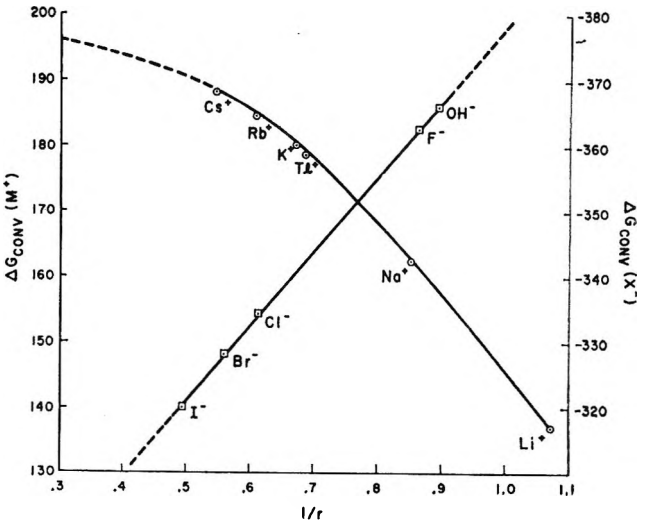

Figure 1. Conventional free energies as a function of r_i^{-1} in water.

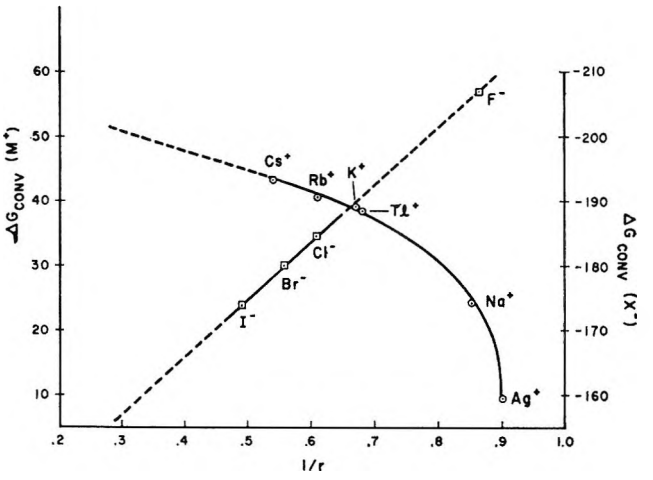

Figure 2. Conventional free energies as a function of r_i^{-1} in PC.

$\Delta G_{conv}°(F^-$ in PC) = 207.0 kcal/mol. This value was used[18] to evaluate the conventional free energies for all the alkali metal fluorides. The plots of differences in conventional energies for ions of equal radii are shown in Figures 3 and 4 for the aqueous and PC systems, re-

(19) D. D. Wagman, W. H. Evans, V. B. Parker, I. Halow, S. M. Bailey, and R. H. Schumm, "Selected Values of Thermodynamic Properties," N.B.S. Technical Note No. 270, 1968.

(20) "JANAF Thermochemical Tables," The Dow Chemical Co., Midland, Mich., Aug, 1965, and addenda.

(21) W. M. Latimer, "The Oxidation States of the Elements and Their Potentials in Aqueous Solutions," Prentice-Hall, Englewood Cliffs, N. J., 1952.

(22) J. P. Jesson and E. L. Muetterties, "Basic Chemical and Physical Data," Marcel Dekker, Inc., New York, N. Y., 1969.

(23) R. S. Berry and C. W. Riemann, *J. Chem. Phys.*, **38**, 1540 (1963).

(24) A. K. Covington, R. A. Robinson, and R. G. Bates, *J. Phys. Chem.*, **70**, 3820 (1966).

(25) N. E. Khomutov, *Russ. J. Phys. Chem.*, **39**, 336 (1965).

(26) H. F. Halliwell and S. C. Nyberg, *J. Chem. Soc.*, 4603 (1960).

(27) R. H. Boyd, *J. Chem. Phys.*, **51**, 1470 (1969).

(28) Y. Wu and H. L. Friedman, *J. Phys. Chem.*, **70**, 501 (1966).

Table I: Lattice and Solvation Enthalpies and Solvation Free Energies (25°)

Salt	$-\Delta H_{lat}°$	$-\Delta G_{lat}°$	$\Delta H_{solv}°$		$\Delta G_{solv}°$ [b]	
			H_2O	PC	H_2O	PC
HF	...	...	383.7	...	363.7	...
HCl	...	...	350.3	...	335.3	...
HBr	...	...	345.9	...	328.9	...
HI	...	...	333.1	...	320.7	...
LiF	248.6	230.0	247.5	...	226.6	207.0[a]
LiCl	205.9	188.5	214.8	207.6	198.2	183.2
LiBr	195.8	178.7	207.5	202.6	192.0	179.0
LiI	182.1	165.5	197.2	197.4	183.5	173.0
NaF	220.7	202.1	220.5	...	201.1	183.9
NaCl	188.1	170.6	187.2	182.0	172.7	(160.1)
NaBr	179.8	162.6	180.0	177.0	166.5	(155.8)
NaI	167.9	151.1	169.7	171.7	158.0	150.1
KF	196.4	178.4	200.6	...	183.6	168.5
KCl	171.4	154.1	167.3	165.8	155.2	(144.7)
KBr	164.7	147.6	160.0	160.8	149.0	(140.5)
KI	154.5	138.2	149.7	155.6	140.5	134.9
RbF	186.6	170.2	198.2	...	179.4	166.5
RbCl	164.4	149.0	160.3	159.6	151.0	142.7
RbBr	158.1	142.9	152.9	154.6	144.8	138.5
RbI	149.2	134.4	143.2	144.4	136.4	132.5
CsF	174.7	161.4	186.0	...	175.4	164.7
CsCl	157.6	144.9	153.3	153.0	147.0	140.9
CsBr	152.0	140.2	145.8	148.0	140.9	136.7
CsI	143.8	132.3	135.8	142.8	132.4	130.7
AgCl[f]	218.7	201.5	202.9	197.7	188.2	174.2
AgBr	215.9	198.7	195.8	192.7	182.0	(170.0)
AgI	212.3	195.4	185.6	187.5	173.4	(164.0)
TlCl	179.0	162.2	168.8	...	157.2	145.3
TlBr	175.2	158.4	162.2	...	150.9	141.1
TlI	169.0	152.3	151.5	...	142.4	135.7
$LiBPh_4$	107.8[c]	...	135.8	139.8	...	...
$NaBPh_4$	103.4[c]	...	108.2	114.1	...	...
$LiClO_4$	156.5[c]	...	163.8	166.0	...	...
$NaClO_4$	147.4[c]	...	144.1	150.5	...	...
$(CH_3)_4NCl$	132.1[d]	...	132.2	129.6[e]	118.0	...
$AsPh_4I$	90.0[c]	...	81.7	84.3	...	...

[a] See text for derivation of this quantity. [b] Values in parentheses are obtained from the additivity relationship for $\Delta G_{solv}°$ and/or $\Delta H_{solv}°$. The remainder of the data were obtained from emf work,[16-18] solubility[18] and heats of solution and transfer from references 28–30. Additional details can be found in ref 18 (in press). [c] $\Delta H_{lat}°$ calculated from eq 17. Heats of solution in PC and H_2O are from ref 28–30. [d] Reference 27. [e] From the heats of transfer in ref 28–30. [f] (1) J. N. Butler, D. R. Cogley, and W. Zurosky, *J. Electrochem. Soc.*, **115**, 445 (1968), free energy of solution. (2) J. N. Butler, private communication on heats of solution.

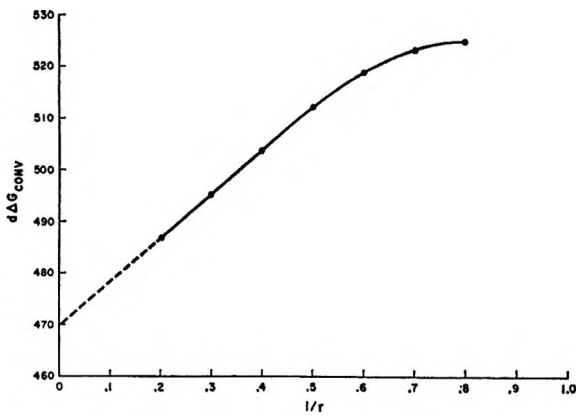

Figure 3. Conventional free energy differences between cations and anions of equal radii as a function of r_i^{-1} in water.

spectively. From the intercepts at $1/r = 0$ it is found that $\Delta G_{solv}(H^+ \text{ in } H_2O) = -235.0$ kcal/mol and $\Delta G_{solv}°(Li^+ \text{ in PC}) = -95.0$ kcal/mol. Using the value of -31.3 eu for the absolute entropy of solvation of the proton in water, the corresponding enthalpy term is -244.3 kcal/mol. The results for the various monovalent ions are listed in Table III. Also shown in this table are the heats of transfer for the individual ions based on the present work and on the assumption that for large cations and anions (such as $AsPh_4^+$ and BPh_4^-) the heats of transfer are equal.[29,30]

(29) G. Choux and R. L. Benoit, *J. Amer. Chem. Soc.*, **91**, 6221 (1969).

(30) C. V. Krishnan and H. L. Friedman, *J. Phys. Chem.*, **73**, 3934 (1969).

Table II: Conventional Energies and Enthalpies at 25°[a]

Ion	$\Delta H_{conv}°$		$\Delta G_{conv}°$	
	H_2O	PG	H_2O	PC
Li^+	136.7	...	137.2	...
Na^+	164.1	25.7	162.6	23.1
K^+	184.1	41.8	180.1	38.5
Rb^+	191.1	48.1	184.3	40.5
Cs^+	198.2	54.4	188.3	42.3
Ag^+	148.3	9.9	147.1	9.6
Tl^+	182.3	...	178.1	38.3
$(CH_3)_4N^+$	218.1	75.4	217.3	...
$AsPh_4^+$	251.4	113.1	...	...
OH^-	−386.1	...	−366.1	...
F^-	−384.6	...	−363.7	−207.0
Cl^-	−350.3	−207.6	−335.3	−183.2
Br^-	−345.9	−206.6	−329.2	−179.0
I^-	−333.1	−197.4	−320.7	−173.0
ClO_4^-	−300.5	−166.0	...	...
BPh_4^-	−272.4	−140.0	...	...

[a] Aqueous values are referred to the solvated proton; PC values are referred to the solvated Li^+ ion.

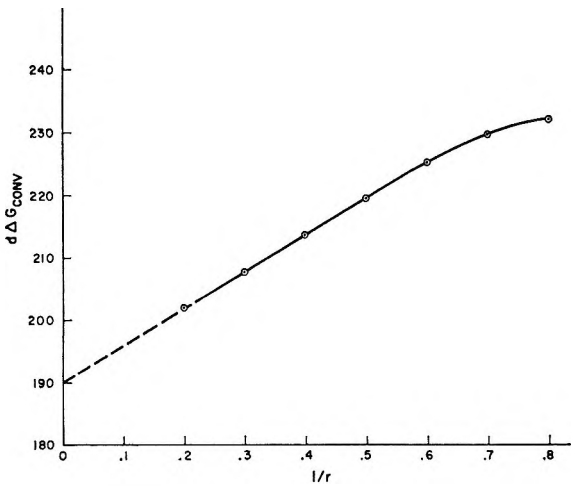

Figure 4. Conventional free energy differences between cations and anions of equal radii as a function of r_i^{-1} in PC.

A second set of calculations was carried out according to eq 10 and for the aqueous system the results are

$$\Delta H_{conv}°(M^+) = 271.09 - \frac{838.52}{(r_i + 1.38)^2} + \frac{307.65}{(r_i + 1.38)^3} \quad (\pm 8.6)$$

$$\Delta H_{conv}°(X^-) = -223.47 - \frac{1945.8}{(r_i + 1.38)^2} + \frac{2304.9}{(r_i + 1.38)^3} \quad (\pm 0.3)$$

The data are given in kcal/mol and the quantities in parentheses are the standard deviations of the intercepts. The value of $\Delta H_{solv}°(H^+)$ found by this method is −247.3 kcal/mol. The value obtained above (−244.3) has been used in evaluating the single-ion values for $\Delta H_{solv}°$ as shown in Table III. A similar treatment for solvation in PC gives the following results

$$\Delta H_{conv}°(M^+) = 171.06 - \frac{3474.1}{(r_i + 2.62)^2} + \frac{5263.0}{(r_i + 2.62)^3} \quad (\pm 0.3)$$

$$\Delta H_{conv}°(X^-) = -41.40 - \frac{7326.0}{(r_i + 2.62)^2} + \frac{18205.6}{(r_i + 2.62)^3} \quad (\pm 1.4)$$

The value of $\Delta H_{solv}°(Li^+)$ in PC is −106.2 kcal/mol.

Conclusions

The present results suggest a revision in the presently accepted values for the energy and enthalpy of solvation of the proton as well as for the other ions. The difference amounts to 16 kcal/mol, which is somewhat larger than our previous estimate of 8 kcal/mol.[11,12] In regard to other related quantities such as the proton affinity, P, no significant changes are indicated. For the process

$$H_g^+ + H_2O_g \xrightarrow{P} H_3O_g^+ \xrightarrow{\Delta H_{solv}°} H_3O_h^+$$

the solvation enthalpy of H_3O^+ can be estimated by taking its radius as 1.4 Å and from the least-squares fit it is found that $\Delta H_{solv}°(H_3O^+)$ is −67.4 kcal/mol and that P = −176.9 kcal/mol. This is consistent with the presently accepted value of ≈ −180,[31] and values as low as −150 to −160 kcal/mol[32,33] must be ruled out.

Ionic radii still appear to present some problems. For the OH^- ion in solution a value of 1.12 Å is indicated by the linear anion plot of Figure 1. A value of 1.47 Å must be considered to be in error since it is a "thermochemical" value which is based upon incorrect values for the lattice enthalpies of the alkali metal hydroxides. Waddington's[34] values of these lattice energies are obtained from a Mayer–Born–Madelung treatment from which he finds that $\Delta H_{lat}°$ for NaOH and KOH, respectively, are −197 and −175 kcal/mol. This leads to a value of −371 kcal/mol for the conventional enthalpy of OH^- which is smaller than the fluoride ion, therefore requiring a larger ionic radius. Using the thermodynamic data found in references 20 and 21, values of −244.1, −212.1, and −188.5 kcal/mol are obtained for $\Delta H_{lat}°$ of LiOH, NaOH, and KOH, respectively. These lattice energies when combined with the heats of solution[35] and conventional enthalpies of

(31) M. DePaz, J. J. Leventhal, and L. Friedman, *J. Chem. Phys.*, 51, 3748 (1969).

(32) J. L. Beauchamp and S. E. Butrill, *ibid.*, 48, 1783 (1968).

(33) D. Van Raalte and A. G. Harrison, *Can. J. Chem.*, 41, 3118 (1963).

(34) T. C. Waddington, *Adv. Inorg. Chem. Radiochem.*, 1, 158 (1959).

(35) V. B. Parker, "Thermal Properties of Aqueous Uni-univalent Electrolytes," NBS Reference Data Series NSRDS-NBS2, April 1965.

Table III: Energetics of Single-Ion Solvation at 25°[a]

Ion	$-\Delta G_{solv}°$		$-\Delta H_{solv}°$			$\Delta H_{transfer}°$		
	H_2O	PC	H_2O[b]	H_2O[c]	PC[c]	c	d	e
H^+	235.0	...	263.7	244.3	...	...	...	...
Li^+	97.8	95.0	127.5	107.6	106.2	1.4	0.73	−0.05
Na^+	72.4	71.9	99.7	80.2	80.5	−0.3	−2.44	−3.3
K^+	54.9	56.6	79.6	60.2	64.4	−4.2	−5.24	−6.0
Rb^+	50.7	54.5	73.3	53.1	58.1	−5.0	−5.87	−6.7
Cs^+	46.7	52.7	69.1	46.1	51.8	−5.7	−6.40	−7.4
Ag^+	87.9	85.4	115.4	96.0	96.3	−0.3	...	...
Tl^+	56.9	56.7	81.4	62.0	...	...	...	...
$(CH_3)_4N^+$	17.7	...	45.6	26.2	30.8	−4.6	−3.89	−4.8
$AsPh_4^+$	...	...	15.0	−7.1	−6.9	−0.2	−3.49	−2.6
OH^-	131.1	...	123.9	143.3	...	...	...	...
F^-	128.7	112.0	120.0	140.3	...	...	...	...
Cl^-	100.3	88.2	87.5	106.0	101.4	4.6	6.31	7.45
Br^-	94.2	84.0	80.0	101.6	96.4	5.2	3.24	4.35
I^-	85.7	78.0	70.2	88.8	91.2	−2.4	−0.78	0.1
ClO_4^-	...	...	36.8	56.2	59.8	−3.6	−3.93	−3.05
BPh_4^-	...	...	12.2	31.7	33.3	−1.6	−3.49	−2.6

[a] Units are all in kcal/mol. [b] Reference 9. [c] Present results. [d] Reference 10. [e] Reference 29.

Li^+, Na^+, and K^+ (Table II) give an average value of -386.5 ± 0.2 kcal/mol for $\Delta H_{conv}°(OH^-)$ which is in excellent agreement with the value calculated from the thermodynamic data for reaction 16.

The present values for $\Delta G_{solv}°$ and $\Delta H_{solv}°$ of the individual ions show that for ions of equal radii, the anion usually displays more negative values. This has been explained by Noyes[36] on the grounds that for oriented water molecules, the center of the positive charge is closer to the edge of the water molecule and therefore interacts more strongly with the anion. Blandamer and Symons[37] have objected to this on the grounds that the ability of the "lone-pair" electrons to stabilize cations should be as great as the corresponding anion contributions. This concept would not be strictly correct if Verwey's model of cation solvation is correct since the cation is at an angle of 52° to the line of centers between the ion and the water dipole. This model has recently been confirmed by Vaslow.[38]

Finally, it should be pointed out that the accuracies of the absolute ΔG and ΔH values are unknown. This is especially true for any procedure that involves an extrapolation of some reciprocal function in r to infinite radius. On the other hand, the precision of the results may be quite acceptable as in the case for the present results which is demonstrated by the fact that the use of Pauling radii in eq 9 give identical results to those based on the radii of Gourary and Adrian. The use of Pauling radii does not lead to any curvature in the plots of $\Delta G_{conv}(ion)$ or $d\Delta G_{conv}(M^+-X^-)$ *vs.* $1/r$ whereas the radii of Gourary and Adrian do (see Figure 1–4). The Gourary and Adrian crystal radii reproduce the interatomic distances to within about 1% for all the alkali halides with the exception of LiF, in which case the electron density maps[39] do not show a position of zero electron density but only a minimum (*cf.* Discussion in ref 38).

Acknowledgment. The author would like to thank Professor B. E. Conway for making several valuable comments.

(36) R. M. Noyes, *J. Amer. Chem. Soc.*, **84**, 513 (1962).

(37) M. J. Blandamer and M. C. R. Symons, *J. Phys. Chem.*, **67**, 1304 (1963).

(38) F. Vaslow, *ibid.*, **67**, 2777 (1963).

(39) J. Krug, H. Witte, and E. Wölfel, *Z. Phys. Chem.* (Frankfurt), **4**, 36 (1955).

Substituted Malononitrile Anion Radicals[1]

by F. J. Smentowski and Gerald R. Stevenson

Chemistry Department, Texas A and M University, College Station, Texas 77843 *(Received October 14, 1969)*

Monitoring by electron spin resonance the successive additions of sodium–potassium alloy to benzylidene malononitrile in 1,2-dimethoxyethane, two different anion radicals have been observed. At intermediate stages of the reduction of benzylidene malononitrile, line width variation spectra are noted. An electron spin resonance study of the reduction of substituted malononitriles reveals equilibria 1 to 6 adequately explain the data.

Introduction

Extensive kinetic and equilibrium studies have been made of monomers which undergo anionic polymerization.[2,3] Electron spin resonance (esr) has verified the presence of a paramagnetic species during the anionic polymerization of monomers such as 9-vinylanthracene[4a] and acenaphthylene,[4b] but to our knowledge definite identification of several different anion radicals during the anionic polymerization of a monomer has not been accomplished because of instability of the system and/or overlapping lines[4,5] or unfavorable rates. This report communicates the successful identification of two different anion radicals observed during different stages of the reduction of benzylidene malononitrile (I) preceding its polymerization. It is worthwhile noting that dimer *cation* radicals of aromatic derivatives such as naphthalene,[6] anthracene,[6] aryl ethers,[7] coronene,[8] and pyrene[9] have been observed by esr.

Experimental Section

X-Band esr spectra were recorded using a Varian V 4502-15 esr spectrometer with a 12-in. magnet. Temperature was controlled within $\pm 1°$ by a Varian V-4557 variable temperature controller. A copper–constantan thermocouple was used to calibrate the variable-temperature controller. Coupling constants and line widths were taken directly from the calibrated chart paper.

Benzylidene malononitrile was prepared by the condensation of benzaldehyde with malononitrile using piperidine as a catalyst. Benzylidene malononitrile was found to be greater than 99.9% pure as determined by glc analysis.

α-Methylbenzylidene malononitrile was prepared by the condensation of acetophenone with malononitrile using piperidine as a catalyst. 1,1-Dicyano-2-(*o*-chlorophenyl)ethylene was prepared by the condensation of *o*-chlorobenzaldehyde with malononitrile using piperidine as a catalyst. α-Phenylbenzylidene malononitrile was obtained from Aldrich Chemical Co., Inc., and recrystallized to constant melting point. 1,1-Diphenylethylene was obtained from K and K Laboratories, Inc.

Results

Benzylidene Malononitrile (I). Addition of a small amount of sodium–potassium alloy to a 0.01 *M* solution of I in 1,2-dimethoxyethane(DME) at $-90°$ led to a red anion radical R_1. Addition of sodium–potassium alloy to 0.001 *M* solutions of I in DME leads to R_1 concentrations barely detectable by electron spin resonance. Further addition of metal alloy to R_1 gave a blue monomer anion radical, R_2 (Figure 1). If the sample is carefully reduced, other spectra are seen after that of R_1 and before that of R_2. As with R_1, addition of sodium–potassium alloy to 0.001 *M* solutions of I in DME lead to R_2 concentrations barely detectable by esr. Both the spectra of R_1 and R_2 are almost first order. R_1 has four equivalent nitrogens, leading to nine main lines, each of which is split into a quintet by four equivalent hydrogens. The nitrogen splittings in R_1 and R_2 are easily differentiated from proton splittings by their intensity ratios. The assigned

(1) Temperature Dependent Electron Spin Resonance Studies. IV. Part III, F. J. Smentowski, R. M. Owens, and B. D. Faubion, Jr., *J. Amer. Chem. Soc.*, **90**, 1537 (1968).

(2) M. Szwarc, "Carbanions, Living Polymers, and Electron-Transfer Processes," John Wiley and Sons, New York, N. Y., 1968.

(3) (a) R. Lipman, J. Jagur-Grodzinski, and M. Szwarc, *J. Amer. Chem. Soc.*, **87**, 3005 (1965); (b) A. Eisenberg and A. Rembaum, *Polym. Lett.*, **2**, 157 (1964); (c) F. Bahstetter, J. Smid, and M. Szwarc, *J. Amer. Chem. Soc.*, **85**, 3909 (1963); (d) D. N. Bhattacharyya, C. L. Lee, J. Smid, and M. Szwarc, *ibid.*, **85**, 533 (1963); (e) C. L. Lee, J. Smid, and M. Szwarc, *ibid.*, **85**, 912 (1963); (f) G. Spach, H. Monteiro, M. Levy, and M. Szwarc, *Trans. Faraday Soc.*, **58**, 1809 (1962); (g) J. Jagur, M. Levy, M. Feld, and M. Szwarc, *ibid.*, **58**, 2168 (1962); (h) D. Gill, J. Jagur-Grodzinski, and M. Szwarc, *ibid.*, **60**, 1424 (1964); (i) M. Matsuda, J. Jagur-Grodzinski, and M. Szwarc, *Proc. Roy. Soc.*, **A288**, 212 (1965); (j) J. Jagur-Grodzinski and M. Szwarc, *ibid.*, **A288**, 244 (1965); (k) M. Shima, D. N. Bhattacharyya, J. Smid, and M. Szwarc, *J. Amer. Chem. Soc.*, **85**, 1306 (1963).

(4) (a) A. Eisenberg and A. Rembaum, *Polym. Lett.*, **2**, 157 (1964); (b) J. Moacanin and A. Rembaum, *ibid.*, **2**, 979 (1964).

(5) (a) K. Hirota, *J. Polymer Sci.*, **60**, 552 (1962); (b) K. Kuwata, H. Kawazura, and K. Hirota, *Chem. Abstr.*, **56**, 4928 (1962); (c) H. P. Leftin and W. K. Hall, *J. Phys. Chem.*, **64**, 382 (1960).

(6) (a) I. C. Lewis and L. S. Singer, *J. Chem. Phys.*, **43**, 2712 (1965); (b) O. W. Haworth and G. K. Fraenkel, *J. Amer. Chem. Soc.*, **88**, 4514 (1966).

(7) W. F. Forbes and P. D. Sullivan, *Can. J. Chem.*, **46**, 325 (1968).

(8) H. van Willigan, E. de Boer, J. T. Cooper, and W. F. Forbes, *J. Chem. Phys.*, **49**, 1190 (1968).

(9) J. T. Cooper and W. F. Forbes, *Can. J. Chem.*, **46**, 1158 (1968).

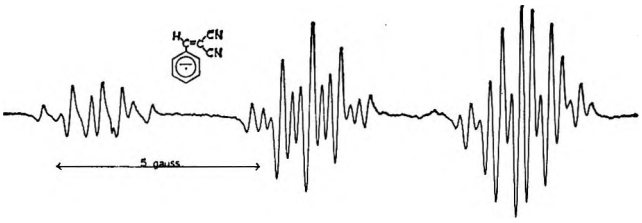

Figure 1. First-derivative esr spectrum of the anion radical of benzylidene malononitrile reduced by NaK_2 in DME; recorded at −90°. The first three of the five main groups of lines are shown.

coupling constants of both anion radicals are given in Table I. The calculated and experimental peak positions agree within ±1%. The structures of R_1 and R_2 are the dimer anion radical (·M–M⁻) and monomer anion radical (M·⁻), respectively. No temperature dependence of the esr spectral parameters is observed for the anion radical ·M–M⁻ between −90° and −10°, as indicated by the invariance of coupling constants and line intensities over this range. Below are the structures for vinylidene monomers and R_2.

Table I: Hyperfine Coupling Constants for Anion Radicals R_1 and R_2 Formed by Sodium–Potassium Alloy Reduction of I in DME at −80°

Anion radical	Position assignment	No. of protons or nitrogens	a_i, G
M·⁻[a,b]	Nitrogens	2	5.21 ± 0.01
	Ortho protons	2	0.601 ± 0.01
	Meta protons	2	0.601 ± 0.01
	Para protons	1	0.224 ± 0.01
	Vinyl protons	1	0.224 ± 0.01
·M–M⁻	Nitrogens	4	2.61 ± 0.05
	Protons	4	0.40 ± 0.01

[a] Benzylidene malononitrile anion radical. [b] HMO calculations confirm the relative order of the coupling constants, and show the equivalence of the *ortho* and the *meta* positions and the equivalence of the vinyl and *para* positions.

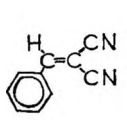

I

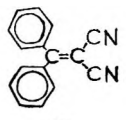

II

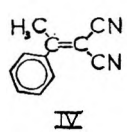

IV

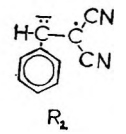

R_2

Both ·M–M⁻ and M·⁻ are not stable at higher temperatures. Above −10°, ·M-M⁻ undergoes a rapid irreversible polymerization. M·⁻ was not as stable as ·M–M⁻ and depending upon the concentration of I, the anion radical rapidly polymerized irreversibly between −60 to −40°. The esr spectra of both ·M–M⁻ and M·⁻ disappeared too rapidly at these higher temperatures, so a kinetic determination of the polymerization by esr was not possible.

Reduction of I in liquid ammonia with potassium using techniques previously described,[10] gives a diamagnetic solution, which subsequently polymerized, even at −78°.

α-Phenylbenzylidene Malononitrile (II). The anion radical of II (III) was prepared by alkali metal reduction (Li, Na, K) of II in DME. III could also be formed by electrolytic reduction using tetra-*n*-butylammonium perchlorate in DME. The coupling constants of III are given in Table II. Addition of the alkali metal to a 0.01 *M* solution of II in DME at −90° leads to a green anion radical characterized as III (Figure 2). At the beginning of the reduction, the concentration of III is low, and the hfs line width is broad. As more metal is added, the concentration of III increases, and its esr hfs sharpens (150 mG). As more metal is added, the spin concentration of III is reduced, and the hfs become broad again. As more metal is added, the solution becomes blue and diamagnetic. Throughout the reduction, only one anion radical, III, is observed. This contrasts with the reduction of I which gives two anion radicals, ·M–M⁻ and M·⁻.

Table II: Hyperfine Coupling Constants for the Anion Radical of α-Phenylbenzylidene Malononitrile Reduced by the Indicated Methods at −60°

Metal	Solvent	A_N	$A_{H(o,m)}$	$A_{H(p)}$
K	DME	2.47 ± 0.03	1.47 ± 0.03	0.17 ± 0.03
Na	DME	2.46 ± 0.03	1.49 ± 0.03	0.17 ± 0.03
Li	DME	2.46 ± 0.03	1.47 ± 0.03	0.17 ± 0.03
Electrolytic	DME	2.50 ± 0.03	1.44 ± 0.03	0.17 ± 0.03

α-Methylbenzylidene Malononitrile (IV). A 0.001 *M* solution of IV in DME upon contact with alkali metal even at −90° polymerized irreversibly. No esr spectrum was observed.

1,1-Dicyano-2-(o-chlorophenyl)ethylene and 1,1-Diphenylethylene. Addition of sodium–potassium alloy to 0.01 *M* solution of 1,1-dicyano-2(*o*-chlorophenyl)-ethylene in DME at −90° gave a pink anion radical characterized by one line (line width 10 G). Further addition of metal gave a blue monomer anion radical,

(10) F. J. Smentowski and G. R. Stevenson, *J. Amer. Chem. Soc.*, **90**, 4661 (1968).

Figure 2. First-derivative esr spectrum of $M_x \cdot^-$ formed by NaK_2 in DME; recorded at $-60°$.

with a_N = 5.2 G (with intensity ratios for two nitrogens). Also, addition of potassium to a 0.01 *M* solution of 1,1-diphenylethylene in DME at $-90°$ led to a blue anion radical characterized by one line (line width 10 G). Repeated attempts to further resolve the possible dimer anion radicals of 1,1-dicyano-2-(*o*-chlorophenyl)ethylene and 1,1-diphenylethylene were unsuccessful.

Discussion

For these vinylidene systems, the esr results indicate we are observing (1) through (6), with the relative importance of the various equilibria dependent upon the particular monomer. Thus, at temperatures below $-60°$, the system I–NaK_2–DME favors equilibria 1 through 4, with 5 also present at higher temperatures. Similar equilibria have been noted for related anions formed by metal reduction of other vinylidene monomers.[11] Thus, esr studies indicate the equilibrium concentration of anion radicals derived from vinylidene monomers is very small, with the equilibrium favoring the dimer dianion $^-$M–M$^-$.[3k] The concentration of 1,1-diphenylethylene anion radical in equilibrium with dimer dianion is less than 10^{-7} *M* when the dianion concentration is 0.1 *M*. Related results were obtained for the dimer dianions derived from the reduction of α-methylstyrene. In this work, the high concentrations of I necessary to observe M$\cdot^-$ and $\cdot$M–M$^-$ by esr indicate the formation of diamagnetic products such as M^{2-} or $^-$M–M$^-$ or a higher homolog. The formation of $^-$M–M$^-$ through equilibria 2 and 4 is more likely than (6), since (6) alone cannot explain

$$M + e = M\cdot^- \quad (1)$$

$$2M\cdot^- = {}^-M\text{–}M^- \quad (2)$$

$$M\cdot^- + M = \cdot M\text{–}M^- \quad (3)$$

$$\cdot M\text{–}M^- + e = {}^-M\text{–}M^- \quad (4)$$

$$^-M_{x-1}{}^- \text{ or } \cdot M_{x-1}{}^- + M = \text{Polymer} \quad (5)$$

$$M + M^{2-} = 2M\cdot^- \quad (6)$$

the formation of M$\cdot^-$ and $\cdot$M–M$^-$. Likewise, the direction of disproportionation (6) is usually temperature dependent.[12] Another indication that the dimer anion radical $\cdot$M–M$^-$ has been formed in the I–NaK_2–DME systems is the fact that its nitrogen hyperfine coupling constant is one half that of the monomer anion radical, M$\cdot^-$ (*vide infra*).

Possible explanations for the line width alternation spectra observed for the I–NaK_2–DME system are equilibria 7, 8, 9, or 10.

$$\cdot M\text{–}M^- = M + M\cdot^- \quad (7)$$

$$\cdot M\text{–}M^- + {}^-M\text{–}M^- = {}^-M\text{–}M^- + \cdot M\text{–}M^- \quad (8)$$

$$^-M\text{–}M^- + M = \cdot M\text{–}M^- + M\cdot^- \quad (9)$$

$$\cdot M\text{–}M^- + M = M + \cdot M\text{–}M^- \quad (10)$$

Let A, B, and C represent I–NaK_2–DME systems corresponding to successive additions of sodium–potassium alloy to I in DME. For system A (*i.e.*, low sodium–potassium alloy concentrations and high monomer concentrations) the rate of disappearance of $\cdot$M–M$^-$ is slow enough that a detailed esr spectrum can be observed. This is not the case for the *o*-chloro derivatives of I and 1,1-diphenylethylene, where conditions approaching fast exchange prevail, and only one line is observed. For system B (*i.e.*, intermediate monomer and sodium–potassium alloy concentrations) line-width alternation spectra of $\cdot$M–M$^-$ are observed, with a shorter lifetime of $\cdot$M–M$^-$ for this system than system A. For system C (*i.e.*, high sodium–potassium alloy concentrations and low monomer concentrations) only M$\cdot^-$ is observed as dictated by equilibria 1 through 4.

There is some analogy for dimer anion radical formation from the literature. Dimer anion radicals are possible intermediates during the reduction of nitrosobenzene.[13] Also the dimerization of ketyls is related to the dimerization of vinylidene monomer anion radicals (eq 2). Recently, the reverse reaction of eq 2 for many semidiones and related derivatives has been noted by Russell and coworkers.[14]

A better analogy to the dimerization of our vinylidene monomers is a related dimerization (eq 11) of cation radicals, where pi = naphthalene, anthracene, aryl

$$\text{pi}\cdot^+ + \text{pi} = \text{pi} - \text{pi}\cdot^+ \quad (11)$$

ethers, coronene, and pyrene.[6-9] The esr spectrum of a dimer cation radical, an oxidation product of naphthalene[6b] with antimony pentachloride in methylene chloride, gave two sets of eight equivalent protons, with coupling constants approximately one-half the hfs of the naphthalene anion radical. Similarly, we find that for the dimer anion radical of I, the nitrogen coupling is approximately one-half that of the nitrogen coupling of monomer anion radical R_2. For the dimer

(11) Reference 2, p 367.

(12) F. J. Smentowski and G. R. Stevenson, *J. Amer. Chem. Soc.*, **89**, 5120 (1967).

(13) G. A. Russell, E. J. Geels, F. J. Smentowski, K. Y. Chang, J. Reynolds, and G. Kaupp, *ibid.*, **89**, 3821 (1967).

(14) G. A. Russell, "Radical Ions," E. T. Kaiser and L. Kevan, Ed., Interscience Publishers, New York, N. Y., 1967, p 87.

cation radicals of naphthalene and anthracene,[6b] there appears to be no major distortion or redistribution of π electrons occurring on dimerization, with the possibility that the two hydrocarbon fragments lie in parallel planes. The dianion radical of I can assume two probable conformations in which the vinylidene parts of the molecules are in parallel planes. The one conformation in which the entire π electron system is overlapped is not the only conformer, since all of the coupling constants of the dimer anion radical are not approximately one-half those of the corresponding coupling constants of the monomer anion radical.

In contrast to the behavior of the other monomers, the systems II–DME–M (M = Li, Na, K) do not dimerize or polymerize, but undergo preferential disproportionation (eq 6). The stability of $M\cdot^-$ and/or its steric hindrance towards dimerization would explain these results. Both the change in spin concentration and the hfs line width upon addition of metal to II indicate the hfs lines of $M\cdot^-$ are broadened by M and M^{2-}.

In summary, the reduction of substituted benzylidene malononitrile monomers can be represented by eq 1 to 6, with the relative importance and direction of these reactions varying as a function of metal, solvent, and particular malonitrile derivative.

Acknowledgment. Gerald Stevenson is grateful for a NASA fellowship. We are indebted to Professor M. Szwarc and Dr. R. A. Rembaum for helpful discussion. Acknowledgment is made to the donors of The Petroleum Research Fund, administered by the American Chemical Society, for partial support of this research. We acknowledge partial support of this work by the Research Council of Texas A and M University. The esr spectrometer was made available by the National Science Foundation Grant GP-3767.

Heat Capacities and Thermodynamic Properties of Globular Molecules.

XV. The Binary System Tetramethylmethane–Tetrachloromethane[1]

by Elfreda T. Chang and Edgar F. Westrum, Jr.[2]

Department of Chemistry, University of Michigan, Ann Arbor, Michigan *(Received December 16, 1969)*

Heat capacities and derived thermal properties on five compositions of the system tetramethylmethane–tetrachloromethane (mole fraction CCl_4 = 0.200, 0.334, 0.501, 0.666, and 0.826) were determined by adiabatic calorimetry from 5 to 300°K. The temperature, enthalpy, and entropy increments of each of the transitions, including fusion, in each composition were determined. The results indicated the effects on the reorientational-rotation transitions of the pure components due to the change of molecular environment and provided a tentative partial phase diagram for this system below room temperature.

Introduction

The study of mixtures provides insight into the physical forces acting between molecules of different species, as well as phenomenological information concerning various types of phase equilibria resulting from variation of the proportions of the components. Moreover, examination of heat capacity, dielectric constant, and nuclear magnetic resonance of mixed crystals yields valuable information about the nature of the transitions occurring in their pure components.

Since one of the objectives of this investigation was to experimentally test some theories of solution thermodynamics in the solid phase, a binary system satisfying certain criteria was sought. It was (1) to be a system for which impeccable mixing enthalpies were available for the liquid phase, (2) to have molecules of sufficient similarity in shape and size to permit the existence of a continuous range of solid solutions, yet have sufficient difference between the molecules to occasion deviation from ideal behavior, and (3) be a system forming a plastically crystalline phase so that thermal equilibration might be rapid enough to make measurements practicable.

(1) Based upon a dissertation submitted to the Horace H. Rackham School of Graduate Studies of the University of Michigan by E.T.C. in partial fulfillment of the requirements for the degree of Doctor of Philosophy. This investigation was supported in part by the Division of Research of the U. S. Atomic Energy Commission.

(2) To whom correspondence concerning this work should be submitted.

The system tetramethylmethane–tetrachloromethane [$C(CH_3)_4$–CCl_4] seemed to most satisfactorily meet the chosen criteria. Moreover, the nearly isostructural, isotropic lattices of the components in the region just below the melting point made it seem probable that these two substances would form a continuous series of solid solutions. Since both components form plastic crystals,[3] their molecules have the ability to reorient themselves in the solid state and hence assume apparent spherical symmetry so that the intermolecular forces may be considered central. In addition, heat capacities of the pure tetramethylmethane[4] and tetrachloromethane[5] have been reported. Moreover, enthalpy of mixing data in the liquid phase[6] are also available for this system.

In order to ascertain the temperature dependence of the enthalpy of mixing and to acquire data on the transitions and thermodynamics of globular molecules, the heat capacities from 5 to 300°K for five compositions of the system tetramethylmethane–tetrachloromethane were measured using low-temperature adiabatic calorimetry.[7] Furthermore, the results of this investigation provided quantitative phase equilibrium data. The changes in temperature, magnitude, and shape of the anomalies in the heat capacity *vs.* temperature curves occasioned by composition variation indicated that for this system changes in molecular environment exert considerable effects on the reorientational-rotation transitions of the pure components. The melting point measurements are consistent with the existence of a continuous series of solid solutions immediately below the fusion temperature but require further investigation for definitive elucidation of the details. The expected lowering of the "rotational" transition of tetrachloromethane upon addition of tetramethylmethane is observed. The constancy at all the compositions studied of the tetramethylmethane transition temperature, 142.5°K, indicated phase separation at this temperature. Eutectoid formation appears likely judging from the occurrence of an intermediate transition at 191.6°K. The overall results further indicate that the phase diagram for a binary system of simple globular molecules can be complex.

Results of Heat Capacity Measurements

Heat Capacity. The experimental heat capacity data for the five compositions (*i.e.*, N_{CCl_4} = 0.200, 0.334, 0.501, 0.666, and 0.826) in the system tetramethylmethane–tetrachloromethane are presented in Tables I and II. In Table I the heat capacity values for each mixture are listed in chronological order so that the approximate temperature increments employed in the measurements can usually be inferred from the adjacent mean temperatures. The values given are based on the defined thermochemical calorie, 4.1840 J, and the ice point, 273.15°K. The gram molecular masses used for the calculations are 72.151 for tetramethylmethane and 153.839 for tetrachloromethane. In addition to the adjustment for curvature and for the small differences in the amounts of helium, grease, and solder, corrections were applied to some of the runs in the transition regions and are indicated by appropriate superscripts in the tabulations. Heat capacity values in the transition region are shown in detail for each mixture in Table II. Transitions are numbered in sequence with increasing temperature. The temperature increment of each run in transition peak regions is given as well as the mean temperature.

The heat capacity *vs.* temperature curves for the mixtures studied are shown in Figure 1. In addition, a detailed table of enthalpy-type measurements over heat capacity, transition, and fusion regions has been made available in a separate document.[8] These determinations provide an independent check of the enthalpy increment which is especially pertinent in regions where the thermal equilibration time is very long.

Thermodynamic Functions. Molal values of heat capacities and entropy and enthalpy increments are presented in Table III for selected temperatures for each of the five compositions studied. The values reported for nontransition regions (*i.e.*, typically from 5 to 135°K and from 245 to 300°K) were obtained by integrating the curve generated by a digital computer fit of a least-squares polynomial through all the data points in the region. Below 5°K the heat capacity of each mixture was extrapolated using the Debye T^3 limiting law. Contributions from nuclear spin, isotope mixing, and the zero point entropy and enthalpy of mixing are not included in the values reported.

Table IV summarizes the thermal data for the transition regions of the five compositions plus that reported for the two pure components.[4,5] The enthalpy increments of Transition I based on one mole of tetramethylmethane in the mixture and the enthalpies of fusion based on the ideal (additive) enthalpies of fusion of the components are also included. The total of the entropy increments of the transitions plus that of fusion is

(3) J. Timmermans, *J. Phys. Chem. Solids*, **18**, 1 (1961).

(4) J. G. Aston and G. H. Messerly, *J. Amer. Chem. Soc.*, **58**, 2354 (1936); H. Enokido, T. Shinoda, and Y. Mashiko, *Bull. Chem. Soc. Jap.*, **42**, 84 (1969).

(5) J. F. G. Hicks, J. G. Hooley, and C. C. Stephenson, *J. Amer. Chem. Soc.*, **66**, 1064 (1944).

(6) A. Englert-Chwoles, "Contribution à la Thermodynamique Statistique des Solutions," Doctoral Thesis, Free University of Brussels, Brussels, 1955.

(7) Elfreda Chang, Doctoral Dissertation, University of Michigan, 1962.

(8) Extensive supplementary tables of experimental data and results including thermodynamic functions at selected temperatures and details and figures delineating the behavior in the transition region have been deposited as a 46-page document, Number 8458, with the ADI Auxiliary Publications Project, Photoduplication Service, Library of Congress, Washington, D. C. A copy may be secured by citing the document number and remitting $6.25 for photoprints or $2.50 for 35-mm microfilm in advance by check or money order made payable to: Chief, Photoduplication Service, Library of Congress.

Table I: Heat Capacities of the System Tetramethylmethane–Tetrachloromethane (Units: cal/(g mol of solution, °K)

T	C_p
N_{CCl_4} = 0.200	
Series I	
7.38	0.359
8.15	0.514
9.00	0.726
9.93	0.953
11.00	1.237
12.30	1.604
13.85	2.110
15.68	2.723
17.75	3.440
19.83	4.152
22.01	4.842
24.30	5.550
27.12	6.303
30.62	7.165
35.53	8.185
40.28	8.996
41.98	9.260
46.83	9.970
51.99	10.672
56.68	11.288
61.99	11.989
64.30	12.300
71.11	13.175
78.76	14.251
86.28	15.40
94.92	16.66
102.33	17.81
110.23	19.13
118.93	20.76
127.87	22.70
Trans. (I) Runs A	
Trans. (II) Runs B	
195.60	27.74
202.24	28.06
208.79	28.53
215.23	28.69
221.53	28.64
230.98	29.79
236.29	30.28
242.26	37.11
Series II	
ΔHt (I) Run C	
Series III	
ΔHt (I) Run D	
Series IV	
Trans. (I) Run E	
Series V	
ΔHt (I) Runs F	
ΔHt (II) Run G	
Trans. (II) Runs H	
Enthalpy Run I	
Fusion Run J	
253.59	35.16
257.71	35.44
Series VI	
ΔHm Run K	
260.75	35.70
267.02	36.09
273.75	36.52
281.12	36.95
289.27	37.41
298.63	37.95
Series VII	
ΔHm Run L	
Series VIII	
ΔHt (I) Run M	
ΔHt (II) Run N	
Enthalpy Run O	
ΔHm Run P	
N_{CCl_4} = 0.334	
Series I	
78.15	14.12
84.79	15.07
91.52	16.00
98.62	16.99
105.84	18.07
112.50	19.11
119.74	20.38
127.24	21.81
134.97	23.78
ΔHt (I) Runs A[a,b]	
151.89	24.65[b]
156.31	26.01[b]
164.10	30.05[b]
171.51	32.92[b]
178.75	37.99[b]
183.52	43.07[b]
Trans. (II) Runs B[b]	
199.35	28.39
203.53	28.50
207.68	28.62
211.83	28.51
215.98	28.60
220.10	28.86
224.21	29.07
228.28	29.31
Fusion Runs C	
250.83	34.27
Series II	
9.36	0.839
9.96	1.018
10.93	1.281
12.09	1.608
13.25	2.008
14.44	2.439
15.79	2.921
17.37	3.485
19.22	4.128
21.32	4.824
23.56	5.523
25.83	6.172
28.26	6.799
30.90	7.411
33.70	8.010
36.89	8.598
40.41	9.198
44.08	9.731
47.87	10.25
Series III	
46.34	10.05
51.03	10.67
55.98	11.28
61.04	11.93
66.34	12.60
72.02	13.31
78.53	14.17
Series IV[a]	
Trans. (I) Runs D	
Series V[a,c]	
Trans. (I) Runs E	
Series VI[c]	
ΔHt (I) Run F	
Series VII	
134.72	23.49
ΔHt (I) Run G[b]	
Enthalpy Run H[b]	
ΔHt (II) Run I	
Enthalpy Run J	
Fusion Run K	
Series VIII	
ΔHm Run L	
248.59	34.19
255.53	34.55
263.61	34.97
271.91	35.45
279.91	35.85
287.83	36.25
295.85	36.66
N_{CCl_4} = 0.501	
Series I	
130.96	21.54
134.91	22.41
138.71	23.64
ΔHt (I) Runs A[a]	
Series II	
124.77	20.52
128.89	21.27
132.88	22.07
136.72	23.01
Trans. (I) Runs B[a]	
148.83	23.56[b]
152.41	24.97[b]
155.83	26.30[b]
160.98	27.12[b]
167.32	27.89[b]
173.82	31.60[b]
179.78	34.66[b]
Trans. (II) Runs C[a,b]	
Series III	
180.29	33.02[b,c]
183.08	36.23[b,c]
Trans. (II) Runs D[b]	
Trans. (III) Runs E[b]	
230.69	29.69
ΔHm Run F	
Series IV	
70.41	13.08
73.79	13.48
Series V	
63.51	12.29
69.23	12.95
75.05	13.64
81.48	14.48
88.51	15.42
96.17	16.38
104.30	17.45
112.45	18.60
120.89	19.89
129.29	21.33
Series VI	
71.21	13.17
78.32	14.05
85.43	15.01
92.55	15.91
99.98	16.86
Series VII	
8.94	0.746
9.66	0.966
10.58	1.206
11.68	1.528
12.95	1.990
14.35	2.515
15.90	3.100
17.75	3.790
Series VIII	
4.88	0.078
5.74	0.149
6.80	0.277
7.77	0.455
8.78	0.698
9.73	0.985
10.63	1.227
11.70	1.540
13.14	2.054
14.87	2.698
16.63	3.383
18.46	4.044
20.47	4.741
22.62	5.419
25.11	6.200
N_{CCl_4} = 0.666	
Series I	
10.37	1.313
10.99	1.450
11.96	1.767
13.03	2.177
14.17	2.628
15.42	3.121
16.87	3.690
18.66	4.365
ΔHt (I) Runs A[a,b]	
20.67	5.076
22.76	5.762
25.03	6.441
27.68	7.138
30.81	7.844
34.24	8.523
37.86	9.159
73.61	13.57
79.52	14.21
85.60	14.94
92.19	15.68
99.66	16.53
107.63	17.47
115.37	18.45
123.05	19.47
130.92	20.61
155.33	23.28[b]
159.81	24.54[b]
164.15	26.15[b]
168.29	26.22[b]
172.44	28.07[b]
176.38	28.96[b]
180.22	31.20[b]
Series IX	
Enthalpy Run G	
25.77	6.407
28.62	7.120
32.06	7.872
35.91	8.624
39.72	9.264
43.84	9.847
48.98	10.53
54.81	11.22
61.00	11.97
Series X	
59.40	11.78
65.85	12.56
Enthalpy Run H	
135.76	22.74
ΔHt (I) Run I	
Series XI	
Enthalpy Run J	
ΔHt (II) Run K	
Enthalpy Run L	
Trans. (III) Runs M[b]	
227.26	29.73[b]
229.81	29.74[b]
ΔHm Runs N	
Series XII	
Fusion Runs O	
247.12	33.26
255.28	33.62
263.77	33.91
272.60	34.33
281.63	34.74
290.86	35.03
300.15	35.57
133.61	21.10
Trans. (I) Runs D[b]	
Series V	
134.70	21.16
ΔHt (I) Run E[b]	
Enthalpy Run F[b]	
ΔHt (II, III) Run G[b]	
204.07	30.57
Series VI	
ΔHt (II) Run H[b]	
ΔHt (III) Run I[b]	
Enthalpy Run J	
ΔHm Run K	

Table I (*Continued*)

T	C_p
Series II	
39.08	9.341
43.16	9.902
47.48	10.45
52.17	11.00
57.40	11.59
63.37	12.29
69.88	13.00
Series III	
Series I	
6.13	0.187
7.48	0.444
8.33	0.662
9.13	0.918

T	C_p
183.86	33.27[b]
Trans. (II, III)	
Runs B[b]	
208.01	28.74
211.87	28.80
215.74	29.14
219.37	29.49
222.78	29.86
Fusion Runs C	
242.65	32.34
Series IV	
N_{CCl_4} = 0.826	
62.18	12.19
68.32	12.83
75.28	13.57
82.07	14.34
90.51	15.28
99.52	16.20

T	C_p
Series VII	
ΔHm Run L	
243.99	32.36
250.86	32.58
259.12	32.82
267.44	33.07
275.68	33.31
283.87	33.51
291.99	33.80
300.12	33.40
Fusion Runs D	
245.88	31.65
249.37	31.74
Series IV	
129.31	19.30

T	C_p
9.95	1.219
10.86	1.493
11.92	1.857
13.18	2.373
14.65	2.983
16.22	3.621
17.87	4.284
19.73	4.970
21.99	5.749
24.67	6.572
27.92	7.418
31.55	8.205
Series II	
30.85	8.055
34.57	8.769
38.29	9.390
42.49	9.930
47.23	10.53
52.30	11.09
57.98	11.71
Series III	

T	C_p
108.26	17.13
116.42	18.03
124.51	18.94
130.35	19.61
136.56	20.48
ΔHt (I) Runs A[b]	
147.20	21.55[b]
151.57	21.43[b]
156.77	22.12[b]
162.64	23.40[b]
168.27	24.46[b]
173.15	25.41[b]
177.37	26.17[b]
181.45	27.62[b]
185.33	29.09[b]
189.03	30.92[b]
ΔHt (II) Run B[b]	
Trans. (III)	
Runs C[b]	
227.05	29.22
231.25	29.60
234.87	30.14

T	C_p
136.62	20.44
Trans. (I) Runs E[b]	
Series V	
ΔHt (I) Run F	
Enthalpy Run G[b]	
168.80	24.96[b]
171.19	26.83[b]
173.51	25.07[b]
175.86	26.28[b]
178.15	26.92[b]
180.40	27.29[b]
Enthalpy Run H	
Trans. (II) Runs I[b]	
ΔHt (III) Run J[b]	
Enthalpy Run K	
ΔHm Run L	
250.18	31.78
257.78	31.98
266.61	32.16
276.10	32.36
285.38	32.54
294.63	32.74

[a] Run made under nonequilibrium drift condition. [b] T_2 of run has been corrected from apparent equilibrium condition by extrapolation to estimated equilibrium state. [c] Run made on undercooled phase.

nearly identical for the five mixtures and close to the values reported for the pure components.[4,5]

Two sets of reliable heat capacity data have become available for tetramethylmethane.[4] As will be seen in the comparison below, there is agreement on the integrated $S°$ at the melting point and slight differences partly in interpretation and resolution of transition values. We have selected the more recent values of Enokido[4] for use in comparison with the values for the systems (in units of cal, mol, °K) primarily because they are on a purer sample. (See Table V.)

Since the completion of the analysis of the data in this paper, a previously unreported rhombohedral crystalline modification of tetrachloromethane was discovered.[9] On freezing, tetrachloromethane initially forms face-centered cubic crystals which transform spontaneously to the more stable rhombohedral form. When crystals of either form are cooled below the −47.7° transition temperature, the monoclinic phase is formed. On rewarming through this temperature, the rhombohedral phase forms. The relationship of this finding to Bridgman's[10] high-pressure work has been questioned, but supplementary crystallographic data have been provided. Kotake, *et al.*,[11] using differential thermal analysis found that upon cooling liquid tetrachloromethane an abrupt exotherm directly follows the freezing peak. This was identified with the transition from the face-centered cubic to the rhombohedral form. The melting point of the former was found to be 3.86 ± 0.15°K lower than that of the rhombohedral phase. The high-temperature crystalline phase in all of the equilibrium measurements on tetrachloromethane in the work cited[5] was, therefore, rhombohedral and no further reinterpretation is involved. This contention is further supported by recent Japanese heat capacity data on pure tetrachloromethane from 2 to 250°K.[12] Data on C_v for the liquid phase have also recently become available.[13]

Discussion

Phase Diagram of the System Tetramethylmethane–Tetrachloromethane. Two substances will crystallize as a partial or complete series of solid solutions provided the intermolecular potentials of the two components are similar, they have comparable molal volumes and nearly isostructural crystal lattices, and special forces are absent.[14] Among binary organic systems, the formation of a complete series of solid solutions is apparently relatively rare. This is so even when the intermolecular potentials are equal, for significant strain energy or distortion introduced by dissimilarity in size or shape of the molecules tends to produce phase sep-

(9) R. Rudman and B. Post, *Science*, **154**, 1009 (1966).

(10) P. W. Bridgman, *Phys. Rev.*, **3**, 153 (1914); *Proc. Amer. Acad. Arts Sci.*, **66**, 185 (1931).

(11) K. Kotake, N. Nakamura, and H. Chihara, *Bull. Chem. Soc. Jap.*, **40**, 1018 (1967).

(12) H. Chihara, Osaka University, personal communication.

(13) N. Dass and S. K. Mitra, *J. Phys. Soc. Jap.*, **27**, 254 (1969).

(14) J. H. Hildebrand and R. Scott, "Solubility of Non-Electrolytes," Reinhold, New York, N. Y., 1950.

Table II: Heat Capacities for the System Tetramethylmethane–Tetrachloromethane in Transition and Fusion Regions[a]
[Units: cal/(g mol of solution, °K)]

T	ΔT	C_p
$N_{CCl_4} = 0.200$		
Transition I		
Series I, runs A (5 runs)		
135.87	8.51	25.19
141.03	1.81	135.5
142.39	0.91	254.3
144.48	3.65	40.27
148.85	5.10	24.42
Series IV, runs E (17 runs)		
135.48	2.05	24.42
137.50	1.98	25.27
138.97	0.96	26.16
139.71	0.52	26.33
140.23	0.52	26.60
140.75	0.51	26.62
141.26	0.51	27.18
141.68	0.25	65
141.82	0.02	2000
141.78	0.01	7820
141.82	0.06	1290
141.92	0.13	797
142.03	0.09	271
142.09	0.03	696
142.26	0.30	149
142.51	0.20	231
142.81	0.40	111
Transition II		
Series I, runs B (8 runs)		
148.85	5.11	26.22
153.84	4.91	27.27
159.58	6.80	29.32
165.95	6.26	31.85
171.90	5.89	34.65
177.44	5.35	38.18
182.90	5.64	35.19
188.97	6.57	30.03
Series V, runs H (13 runs)		
173.80	0.98	36.49
174.77	0.97	36.77
175.72	0.92	39.58
176.69	0.94	38.03
177.62	0.93	38.83
178.55	0.92	39.11
179.46	0.90	40.58
180.36	0.91	39.92
181.27	0.91	39.97
182.21	0.97	36.40
183.68	1.98	33.31
185.72	2.09	30.86
187.85	2.17	29.32
Fusion		
Series V, runs J (8 runs)		
237.64	5.97	30.72
242.47	3.69	37.31
245.24	1.86	69.21
246.64	0.94	150.5
247.37	0.52	283.3
247.85	0.44	339.3
248.49	0.85	167.0
250.47	3.12	34.98
$N_{CCl_4} = 0.334$		
Transition I		
Series IV, runs D (3 runs)[a]		
138.00	4.37	24.76
141.17	1.97	116
143.71	3.11	88.91
Series V, runs E (4 runs)[a,c]		
140.46	3.27	35.68
142.39	0.60	287
143.82	2.26	54.97[b]
147.14	4.16	24.77[b]
Transition II		
Series I, runs B (5 runs)[b]		
185.83	2.24	46.52
188.01	2.11	50.08
190.04	2.01	53.23
192.34	2.56	53.95
195.44	3.62	34.79
Fusion		
Series I, runs C (7 runs)		
232.31	4.01	29.78
236.20	3.77	32.43
239.30	2.42	56.90
241.06	1.14	134
241.96	0.74	214
242.60	0.61	262
245.41	5.08	40.70
Series VII, runs K (8 runs)		
232.10	3.48	29.55
235.50	3.36	30.97
238.44	2.58	43.75
240.40	1.38	92.42
241.44	0.81	165
242.15	0.66	205
242.84	0.78	171
244.32	2.24	52.23
$N_{CCl_4} = 0.501$		
Transition I		
Series II, runs B (4 runs)[a]		
140.15	3.08	31.10
142.07	1.08	146
143.26	1.71	72.66
145.54	3.27	27.07
Transition II		
Series II, runs C (2 runs)[a,b]		
185.24	5.18	39.42
189.38	3.10	72.84
$N_{CCl_4} = 0.501$		
Series III, runs D (7 runs)[b]		
185.76	2.51	38.65
188.16	2.28	43.50
190.41	2.21	45.00
191.55	0.59	405
193.13	2.56	37.16
195.96	3.08	29.38
199.02	3.05	29.56
Transition III		
Series III, runs E (10 runs)[b]		
201.95	3.02	29.91
204.80	2.66	35.26
207.45	2.59	36.53
209.99	2.61	36.12
212.53	2.66	35.22
215.15	2.55	37.06
217.75	2.60	36.16
220.40	2.65	35.31
222.53	2.84	32.15
225.09	2.96	30.33
Series XI, runs M (7 runs)[b]		
209.58	2.54	36.76
212.06	2.56	36.98
214.60	2.48	38.34
217.15	2.57	36.61
219.80	2.69	34.36
222.53	2.87	30.00
225.09	2.15	30.14
Fusion		
Series XII, runs O (8 runs)		
232.07	2.94	29.92
234.63	2.21	43.42
236.06	0.73	154
236.64	0.44	267
237.09	0.46	250
237.71	0.77	145
239.20	2.29	41.30
241.71	2.75	33.04
$N_{CCl_4} = 0.666$		
Transition I		
Series IV, runs D (5 runs)[b,c]		
138.12	4.39	21.91
141.32	2.04	70.86
143.46	2.52	50.40
146.63	4.11	24.47
150.86	4.34	22.52
Transitions II and III		
Series III, runs B (9 runs)[b]		
187.30	3.36	35.64
190.04	2.12	62.06
191.60	0.97	147
193.28	2.36	54.55
195.56	2.21	58.91
197.67	2.00	65.91
199.54	1.82	73.59
201.38	1.76	76.27
204.17	3.79	30.03
Fusion		
Series III, runs C (9 runs)[c]		
226.18	3.39	30.40
229.30	2.86	38.06
231.76	2.29	49.77
233.88	1.98	59.37
235.11	0.48	280
235.39	0.09	1556
235.53	0.22	624
236.73	2.19	52.70
239.44	3.22	32.31
$N_{CCl_4} = 0.826$		
Transition I		
Series IV, runs E (5 runs)[b]		
140.83	1.96	24.84
142.23	0.79	77.90
143.25	1.19	46.35
144.72	1.74	29.05
146.63	2.06	22.99
Transition II		
Series V, runs I (4 runs)[b]		
190.91	1.28	33.97
191.69	0.26	204
191.93	0.78	61.7
192.88	1.25	38.52
Transition III		
Series III, runs C (13 runs)[b]		
193.80	2.96	39.92
196.64	2.73	44.08
199.25	2.51	48.59
201.64	2.26	54.85
203.80	2.05	61.58
205.75	1.84	69.82
207.48	1.61	81.00
209.05	1.52	86.99
210.49	1.35	98.41
212.08	1.82	70.46
214.65	3.26	34.93
218.05	3.54	31.37
222.24	4.82	29.08
Fusion		
Series III, runs D (6 runs)		
238.17	3.00	38.25
240.12	0.94	145
240.83	0.56	252
241.33	0.50	280
241.81	0.51	277
243.09	2.08	60.5

[a] For interpretation of superscripts *cf.* footnotes in Table I.

Table III: Thermodynamic Properties for the System Tetramethylmethane–Tetrachloromethane at Selected Temperatures (Units: cal, g mol of solution, °K)

T	C_p	$S° - S°_0$	$H° - H°_0$
	$N_{CCl_4} = 0.200$		
10	0.958	0.337	2.48
25	5.739	3.069	52.78
50	10.426	8.690	262.2
100	17.47	17.986	952.8
200	27.95	39.21	4108
300	38.02	54.93	8003
273.15	36.48	51.44	7002
298.15	37.92	54.70	7929
	$N_{CCl_4} = 0.334$		
10	0.987	0.293	2.29
25	5.940	3.145	54.74
50	10.55	8.890	268.53
100	17.22	18.172	957.0
200	28.36	39.636	4213.5
300	36.88	54.840	7990.4
273.15	35.47	51.45	7019
298.15	36.78	54.61	7922
	$N_{CCl_4} = 0.501$		
10	1.008	0.306	2.37
25	6.164	3.276	57.03
50	10.66	9.155	275.46
100	16.90	18.407	960.6
200	29.67	38.924	4106.1
300	35.56	54.412	7914.7
273.15	34.32	51.14	6977
298.15	35.46	54.19	7849
	$N_{CCl_4} = 0.666$		
10	1.103	0.348	2.66
25	6.427	3.504	60.57
50	10.74	9.518	283.62
100	16.58	18.756	966.8
200	...	...	...
300	34.01	54.098	7848.4
273.15	33.24	50.95	6946
298.15	33.95	53.89	7786
	$N_{CCl_4} = 0.826$		
10	1.166	0.330	2.61
25	6.662	3.642	63.29
50	10.86	9.779	290.60
100	16.28	18.967	969.0
200	...	...	...
300	32.86	53.344	7765.2
273.15	32.26	50.29	6891
298.15	32.82	53.14	7704

aration. Both tetramethylmethane and tetrachloromethane are reported to have face-centered cubic structures in the phases stable just below their respective melting points. At 223 ± 5°K tetramethylmethane[15] has a unit cell with a_0 of 8.78 Å, and at 238°K, tetrachloromethane[16] has an a_0 of 8.34 Å. Both have four molecules per cell. Since both tetrahedrally symmetric molecules exhibit reorientational rotation in their plastically crystalline phases, this system might be expected to form a continuous series of solid solutions. Moreover, tetramethylmethane is so spherical that it is known to rotate even at very low temperatures.[17]

The tentative partial phase diagram for the system is depicted in Figure 2 on the basis of pertinent calorimetric data. Although such temperature–composition diagrams usually are obtained from thermal analysis studies, this method was inapplicable because the large undercooling effects and the long periods of time required for this system to attain thermal equilibrium in the transition region obscured the appearance of transitions and caused irreproducibility in cooling curve determinations. By the equilibrium method using heat capacity measurements not only the transition temperature but also the enthalpy increment of each of the solid–solid transitions and fusion were accurately determined. In each of the compositions studied Transition I appeared at the apparently constant temperature of 142.5°K and Transition II for the four tetrachloromethane-rich compositions appeared at 191.6°K. For the 142.5°K transitions the heat capacity *vs.* temperature curves had the same shape and each sample required about the same time to attain thermal equilibrium.[8] The constancy of the Transition I temperature and the fact that its magnitude is directly proportional to the amount of tetramethylmethane in the sample (*cf.* Table IV and Figure 3) indicate that phase separation takes place above this temperature. The increase in the transition temperature from that of 140.5°K reported for pure tetramethylmethane to 142.5°K in the binary mixtures may be due partly to the presence of a small concentration of tetrachloromethane in the tetramethylmethane-rich phase, α_1, and partly to the differences in the temperature scale in this region. Above 142.5°K cooperative reorientational rotation is presumed to occur in the α_1 phase transforming it to the phase designated β_1. Between Transitions I and II the phase diagram of this system is divided into three regions: on the tetramethylmethane side is phase β_1, on the tetrachloromethane side is α_2, and between is a two-phase region of $\beta_1 + \alpha_2$. The "shoulder-like" heat capacity anomaly that appears in the temperature range of 170 ± 5°K may be due to an increase in reorientational rotation in the β_1 phase.

Isothermal Transition II at 191.6°K is so closely followed by Transition III in three of the tetrachloromethane-rich mixtures studied that it is difficult to apportion enthalpy effects unambiguously between them. However, the enthalpy increment of this transition reaches a maximum between the compositions with N_{CCl_4} of 0.5 and 0.6. This observation, together with

(15) A. H. Mones and B. Post, *J. Chem. Phys.*, 20, 755 (1952), cited in A. J. C. Wilson, Ed., "Structure Reports," Vol. 16, N.V.A. Oosthoek's Uitgevers Maatschapij, Utrecht, The Netherlands, 1952, p 412.

(16) B. Post, *Acta Crystallogr.*, 12, 349 (1959).

(17) J. G. Powles and H. S. Gutowsky, *J. Chem. Phys.*, 21, 1695 (1953).

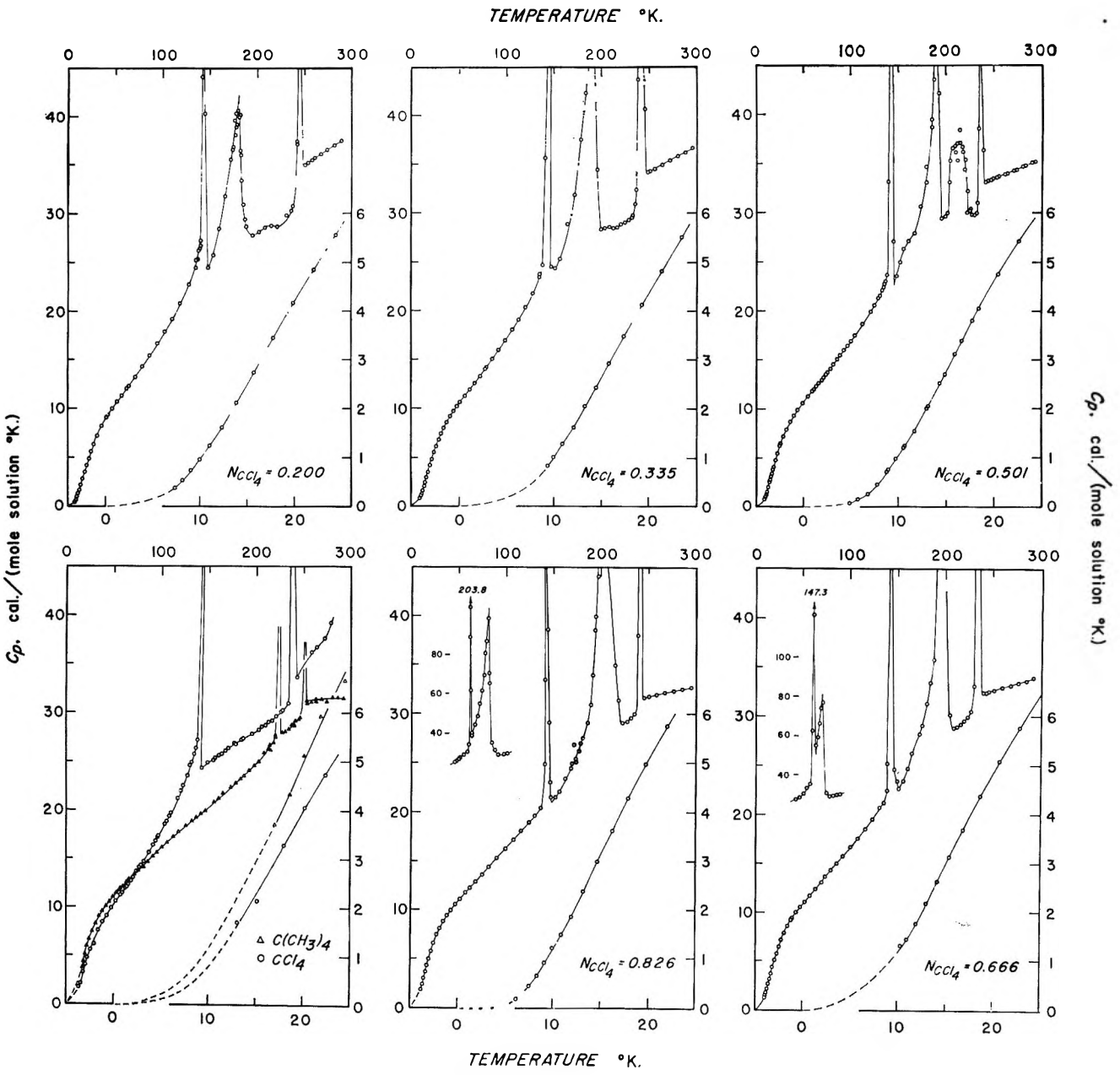

Figure 1. Heat capacities of five compositions and of the components in the system tetramethylmethane–tetrachloromethane.

the fact that Transition II appears at an essentially constant temperature, indicates that a eutectoid (a certain favored combination of β_1 and α_2) is probably formed between the compositions N_{CCl_4} of 0.5 and 0.6, and that 191.6°K is the eutectoid transformation temperature (probably involving only the α_2 phase in the eutectoid composition). On the tetrachloromethane side of the eutectoid composition the region between Transitions II and III may be a two-phase region of the phases β_2 and α_2, where α_2 is, as indicated above, a solid solution of essentially pure tetrachloromethane, and β_2 is a reorientating solid solution of the eutectoid composition. On the tetramethylmethane side of the eutectoid composition the region between Transitions II and III is another two-phase region consisting of β_1 and β_2, probably similar to the miscibility gap found in liquid solutions.

The data on compositions with N_{CCl_4} equal to 0.666 and 0.826 reveal the expected lowering of Transition III (the reorientational transition of tetrachloromethane) occasioned by the presence of tetramethylmethane. This transition may be interpreted as involving the onset of cooperative reorientational rotation in the α_2 phase to form a homogeneous solid solution with β_2. Moreover, the heat capacity *vs.* temperature curve for Transition III is very similar in shape to that obtained by Jura, *et al.*,[18] in going from a two-phase region to a

(18) G. Jura, D. Fraga, G. Maki, and J. H. Hildebrand *Proc. Nat. Acad. Sci. U. S.*, **39**, 19 (1953).

Table IV: Summary of the Transition Regions of Mixtures of the System Tetramethylmethane–Tetrachloromethane (Units: cal, g mol of solution, °K; unless Otherwise Noted)

	Mole fraction CCl_4						
	0.000	0.200	0.334	0.501	0.666	0.826	1.000
Transition I							
Temp, °K	140.5	142.4	142.5	142.5	142.5	142.5	...
ΔHt	628.7	469.1	416.9	303.6	205.9	105.9	...
$\Delta Ht'$, cal/[mol of $C(CH_3)_4$]	628.7	620.1	626.0	608.4	616.5	608.6	...
ΔSt	4.47	3.52	2.92	2.13	1.45	0.74	...
ΔSt, cal/[mol of $C(CH_3)_4$, °K]	4.47	4.39	4.38	4.27	4.34	4.25	...
Anomaly between Transitions I and II							
Temp, °K	...	179.7	...	...	...	171	...
ΔHt	...	270.8	...	...	...	18.9	...
ΔSt	...	1.56	...	...	...	0.10	...
Transition II							
Temp, °K	...	...	191.6	191.6	191.6	191.6	...
ΔHt	...	...	481.3	531.3	369.4	161.9	...
ΔSt	...	...	2.59	2.82	1.98	0.85	...
Transition III							
Transition temp							
Peak	...	...	...	215.0	200.5	210.0	225.35
Completion	...	...	...	219.0	202.0	214.0	...
ΔHt	...	...	...	148.8	352.9	739.2	1095
ΔSt	...	...	...	0.70	1.77	3.59	4.86
Fusion							
Liquidus temp	256.76	249.20	243.25	237.69	235.62	242.31	250.3
Solidus temp	256.76	246.21	240.69	235.95	235.34	240.09	250.3
ΔHm	740.0	578.8	505.1	433.7	553.4	571.6	601
ΔHm, cal/(g mol of ideal soln)	740.0	743[a]	719[a]	689[a]	659[a]	631[a]	601
ΔSm	2.88	2.51	2.08	1.83	2.36	2.37	2.40
Total Effect							
$\sum_i \Delta St_i + \Delta Sm$	7.35	7.59	7.59	7.48	7.57	7.66	7.26

[a] Note: based on the ideal additive enthalpy of fusion of the components.

Table V: Thermal Properties of Tetramethylmethane

Property	Aston, *et al.*[4]	Enokido, *et al.*[4]
$S°$ (l, 282.61°K)	51.79	51.82
ΔSm	3.03	2.88 ± 0.3
T_m	256.53°K	256.76°K
ΔSt	4.39	4.47
T_t	140.0	140.498 ± 0.05

homogeneous solution of the system perfluoro-*n*-heptane and 2,2,4-trimethylpentane. The enthalpy increment associated with this transition is nearly linearly dependent on composition as shown in Figure 3. In the vicinity of the equimolal composition, the Transition III curve may be interpreted as the critical solution temperature for solid solutions β_1 and β_2. The associated thermal anomaly is consequently the enthalpy of mixing the two phases to form a solid solution. Transition III was not detected for the $N_{CCl_4} = 0.334$ composition, possibly because at this composition the thermal anomaly may have been inherently of small magnitude, spread out by the steepness of the curve, or obscured by its proximity to Transition II. Both the comparatively large enthalpy increment and the broadness of Transition II for this sample tend to support this view. The occurrence of Transition III here probably represents the same phenomenon as it did in the equimolal mixture. The dashed curve enclosing the two-phase region of $\beta_1 + \beta_2$ was arbitrarily drawn. Above the curve designating Transition III and below

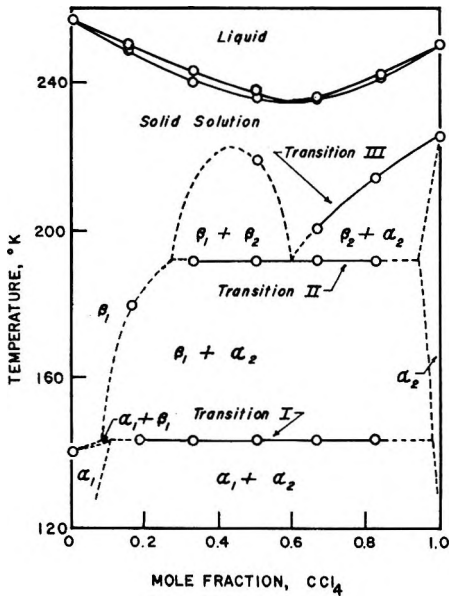

Figure 2. A tentative phase diagram of the system tetramethylmethane–tetrachloromethane.

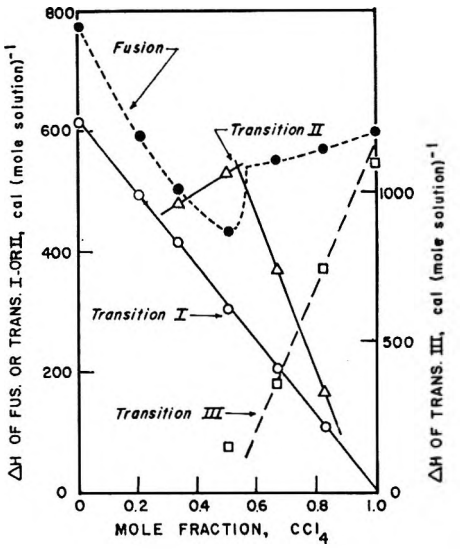

Figure 3. Enthalpy increments of Transitions I, II, III, and fusion *vs.* composition in the system tetramethylmethane–tetrachloromethane.

the melting curve a continuous series of solid solutions may exist.

The present data on the system tetramethylmethane–tetrachloromethane indicate that the melting point curve of this system is a Roozeboom[19] Type III melting diagram, *i.e.*, a melting point curve exhibiting a minimum. The considerable melting point depression (about 20°K) of this system indicates that the deviation from ideality is much greater in the solid than in the liquid and that the distortion energy in the solid is comparatively large. The enthalpy of fusion *vs.* composition curve (*cf.* Figure 3) also shows a minimum or a discontinuity between the compositions of $N_{CCl_4} = 0.5$ and 0.6. This behavior is analogous to that of the oxygen–nitrogen system[14] which has a Roozeboom eutectic Type V melting diagram. If this situation also exists in the tetramethylmethane–tetrachloromethane system, the phase diagram depicted in Figure 2 may require modification from the Type III transition diagram to one of Type V with a miscibility gap in the solid just touching the minimum in the melting point curve, or to a diagram of Type V with a narrow two-phase ($\beta_1 + \beta_2$) region, extending to the minimum in the fusion curve. However, the interpretation of the transitions and the phase behavior would be essentially unchanged. There is insufficient evidence to select between these alternative melting diagrams. Although the enthalpy of mixing is large on the tetramethylmethane-rich side of this system, it is not sufficient (*i.e.*, 124 cal mol^{-1} which is less than $RT/2$) to cause phase separation at 230°K at the equimolal composition, nor is the 12% difference in molal volumes large enough to be critical.[7] The temperature *vs.* composition curves for Transition III and fusion (*cf.* Figure 2), and the ΔHf, ΔHt_I, and ΔHt_{II} *vs.* composition curves (*cf.* Figure 3) all seem to indicate anomalous behavior in the composition range between $N_{CCl_4} = 0.5$ and 0.6. It is apparent that further thermal studies of this system are desiderata for elucidation of the details. Dielectric constant measurements (*e.g.*, such as those on the system tetrachloromethane–trimethylchloromethane[20]), nuclear magnetic resonance measurements (*e.g.*, as on the systems cyclopentane–2,2-dimethylbutane[21] and 2,2-dimethylbutane–2,3-dimethylbutane[22]), and possibly other techniques would also be desirable for a better understanding of this system. Thyrion[23] has recently examined the electron spin resonance of this system and finds no definite spectral changes occurring above 77°K. The persistence of the broad band of CCl_4 with increasing temperature suggests that positive charge transfer between CCl_4^+ and tetramethylmethane should be less efficient than for other systems studied. The feasibility of studying the thermodynamics of solid solutions by the adiabatic calorimetric technique has been established—at least for plastically crystalline systems—by the present investigation.

Experimental Section

Calorimetric Samples. Research grade tetramethylmethane with a probable impurity of *n*-butane and a reported purity of 99.92 mol % (determined by melting point measurements on a representative sample of lot No. 674) obtained from Phillips Petroleum Co., Special

(19) H. W. B. Roozeboom, *Z. Phys. Chem.*, **30**, 385, 413 (1899).

(20) W. P. Conner and C. P. Smyth, *J. Amer. Chem. Soc.*, **63**, 3424 (1941).

(21) J. G. Aston, B. Bolger, R. Trambarulo, and H. Segall, *J. Chem. Phys.*, **22**, 460 (1954).

(22) J. G. Aston, H. Segall, and N. Fuschillo, *ibid.*, **24**, 1061 (1956).

(23) F. C. Thyrion, *Can. J. Chem.*, **47**, 273 (1969).

Products Division, Bartlesville, Okla., was used. Merck reagent grade tetrachloromethane dried 24 hr over calcium chloride was twice distilled and the middle 50% retained. An all-metal high-vacuum line was used to transfer and load samples. Both samples were further purified by the process of repeatedly freezing, evacuating, and melting. The purity of the tetrachloromethane sample was determined to be 99.99 mol % by the calorimetric fractional fusion method in a separate experiment. The enthalpy of fusion determined in this experiment, 604.3 ± 1 cal/mol, is in good accord with the value 601 ± 2 reported by Hicks, *et al.*[5] The calorimetric samples were compounded by massing the components in glass bulbs provided with stainless steel valves.

Calorimetric Equipment. Most of the heat capacity measurements of this investigation (*i.e.*, those on four different compositions of mixtures of the system tetramethylmethane–tetrachloromethane, pure tetrachloromethane, and on the calorimeter W-23 plus A-5 heater–thermometer assembly) were carried out in the Mark II cryostat, described elsewhere.[24] Those on the N_{CCl_4} = 0.200 composition using calorimeter W-24 plus A-3 heater–thermometer assembly were carried out in a similar cryostat designated Mark III.

Calorimeters W-23 and W-24 are of the same basic design as calorimeter W-9, which has been described previously.[25] They are cylindrical with diameters of 3.8 cm and lengths of 7.6 cm. The central portion is machined from solid copper rod and includes the calorimeter bottom, the thermometer–heater well, and eight thin (0.4 mm), circular vanes perpendicular to the cylindrical axis equally spaced along the well. On each vane there are six 4.7-mm diameter holes, 60° apart to aid in circulation of liquids. Soldered to the top portion of the calorimeter are a cone for hanging the calorimeter and for making thermal contact with the helium refrigerant tank and a demountable gold-gasketed valve for loading. Calorimeter W-23 has a mass of 82.293 g *in vacuo* and a calculated internal volume of 79.31 cm^3. Calorimeter W-24 used for the sample for which N_{CCl_4} = 0.200 was similar in all essential details.

Calorimetric Procedures. The calorimeter was loaded by distillation under vacuum. The amount of each component in a calorimetric sample was determined directly by massing in the calorimeter. After loading, mixing was effected by freezing and melting the mixture several times. Before each freezing the calorimeter was shaken with a rotatory motion. The heat capacities of the calorimeter–heater–thermometer assemblies were determined in separate series of measurements. The same quantities of Apiezon-T grease were used for thermal contact between the heater–thermometer assembly and the calorimeter in these determinations as were employed in the measurements on the respective loaded calorimeters. About 130 Torr of helium gas at 300°K was used to facilitate thermal equilibration in the sample space. The heat capacity of the sample represented more than 68% of the total heat capacity over the entire temperature range.

In general, heat capacity measurements were made by observing the temperature rise (ΔT) of the calorimeter plus sample produced by a measured amount of energy input. The rise in temperature is determined by the increment in the equilibrium temperatures before and after the energy input. These temperatures are corrected for the slight quasiadiabaticity of the system by extrapolation of the equilibrium drifts to the midpoint of the energy input. Temperatures were determined with capsule-type, strain-free, platinum resistance thermometers contained within an entrant well in the calorimeter. Temperatures are considered to accord with the thermodynamic temperature scale to within 0.03° from 10 to 90°K and within 0.04° from 90 to 300°K. The temperature increments may be determined with more precision and are probably correct to a few tenths of a millidegree after correction for quasiadiabatic drift. The calorimeter is surrounded by a cylindrical adiabatic shield, the three portions of which are individually controlled by separate channels of automatically regulated ac power to the heaters. This recording electronic circuitry provided with proportional, rate, and reset control action is used in preference to manual shield control above 50°K and follows the temperature of the calorimeter to within approximately a millidegree, thereby reducing the energy exchange between the calorimeter and surroundings so that it is negligible compared with other sources of error. Copper–constantan thermocouples monitor the temperature difference between calorimeter and shield and between shield and the ring used to temper the gradient in the bundle of leads. All measurements of mass, resistance, potential, temperature, and time are referred to calibrations made by the National Bureau of Standards.

The degree of undercooling has a significant effect on the reproducibility of the heat capacity measurements in the transition region (135–230°K) of this system. A high degree of undercooling tends to prevent the occurrence of the transition to the low-temperature form. Therefore, since mixtures of tetramethylmethane and tetrachloromethane are easily undercooled, the loaded calorimeter has to be cooled from room temperature to below Transition I (*i.e.*, below 135°K) at a very slow rate (usually over a period of 6 to 7 days). Below this temperature the cooling rate has no effect on the reproducibility of the heat capacity measurements.

Further details on the procedure, treatment of data, adjustment for vaporization, etc., are given in a supplementary document.[8]

(24) E. F. Westrum, Jr., *J. Chem. Educ.*, **39**, 443 (1962).

(25) E. Greenberg and E. F. Westrum, Jr., *J. Amer. Chem. Soc.*, **78**, 4525 (1956).

Acknowledgment. The authors wish to express their sincere appreciation to Carolyn Barber and James Huntzicker for their assistance in the experimental measurements of the $N_{CCl_4} = 0.200$ composition of mixture; to Dr. H. G. Carlson, Dr. S.-S. Chang, Dr. J. C. Trowbridge, R. Radebaugh, and M. L. Hougen for assistance in the experimental measurements of the other four compositions of mixture; and to Dr. L. O. Case for the helpful discussion on the phase diagram of this system. The partial financial support of the United States Atomic Energy Commission is gratefully acknowledged.

Thermodynamics of Polynuclear Aromatic Molecules. III. Heat Capacities and Enthalpies of Fusion of Anthracene[1]

by P. Goursot, H. L. Girdhar, and Edgar F. Westrum, Jr.[2]

Department of Chemistry, University of Michigan, Ann Arbor, Michigan 48104 *(Received November 26, 1969)*

The heat capacity of anthracene was determined from 5 to 520°K by adiabatic calorimetry and the thermodynamic functions calculated at selected temperatures from these data. No thermal anomaly has been found in the crystalline phase. The values of C_p, $S°$, $(H° - H°_0)/T$ and $(G° - H°_0)/T$ for the crystal at 298.15°K are 50.31, 49.51, 25.04, and −24.46 cal/mol °K, respectively. The enthalpy and entropy values of melting are 7020 ± 12 cal/mol and 14.35 ± 0.02 cal/mol °K at the melting temperature of 488.97°K. A plot of S_{298} *vs.* Kitaigorodskii's coefficient shows that a linear relationship exists for condensed polynuclear aromatic molecules.

Introduction

During a series of investigations of the thermal and thermochemical aspects of the condensed phases of polynuclear aromatic hydrocarbons,[3-6] it was noted that previous measurements of the heat capacity of anthracene[7] over the rather limited range from 90 to 305°K deviated considerably from the average of data on naphthalene[8] and naphthacene.[4] This study covers the above region and extends the range of temperature over which measurements were made to 5°K and into the liquid phase (to 520°K). The resultant data not only provide definitive thermodynamic functions but also enhance the fund of data available for correlations of the thermal properties of the solid state and the melting transition with other physicochemical properties of these molecules.

Experimental Section

Cryostat and Experimental Calorimeter for Measurements from 5 to 350°K. Measurements were made in the Mark III vacuum cryostat[9] by the quasiadiabatic technique described previously.[10] The gold-plated calorimeter (laboratory designation W-42) used has a capacity of 93 cm³, horizontal vanes, a gold-gasketed closure, and is generally similar to one described previously.[11,12] A capsule-type strain-free platinum resistance thermometer (laboratory designation A-5) located within the entrant well of the calorimeter was used to determine temperatures which above the oxygen point are believed to accord with the thermodynamic scale to within 0.03°K. The heat capacity of the calorimeter–heater–thermometer assembly was deter-

(1) This research was supported in part by the U. S. Atomic Energy Commission.

(2) To whom correspondence concerning this work should be addressed.

(3) W.-K. Wong and E. F. Westrum, Jr., *J. Phys. Chem.*, **74**, 1303 (1970).

(4) W.-K. Wong and E. F. Westrum, Jr., unpublished data.

(5) S.-w. Wong and E. F. Westrum, Jr., *J. Amer. Chem. Soc.*, in press.

(6) D. Rodgers and E. F. Westrum, Jr., unpublished data.

(7) H. M. Huffman, G. S. Parks, and J. M. Barmore, *J. Amer. Chem. Soc.*, **53**, 3876 (1931).

(8) J. P. McCullough, H. L. Finke, J. F. Messerly, S. S. Todd, T. C. Kincheloe, and G. Waddington, *J. Phys. Chem.*, **61**, 1105 (1957).

(9) E. F. Westrum, Jr., *J. Chem. Educ.*, **34**, 443 (1962).

(10) E. F. Westrum, Jr., J. B. Hatcher, and D. W. Osborne, *J. Chem. Phys.*, **21**, 419 (1953).

(11) D. W. Osborne and E. F. Westrum, Jr., *ibid.*, **21**, 1884 (1953).

(12) E. F. Westrum, Jr., and E. Chang, *Colloq. Int. Cent. Nat. Rech. Sci.*, **156**, 163 (1967).

Table I: Experimental Heat Capacity of Anthracene[a]

$\bar{T}$	C_s	$\bar{T}$	C_s	$\bar{T}$	C_s
		Mark III Cryostat			
Series I		229.15	37.74	23.76	4.242
		238.38	39.35	26.68	5.029
204.43	33.45	247.30	40.94	29.98	5.870
208.61	33.21	257.64	42.76	33.25	6.670
212.74	34.93	267.87	44.65	36.92	7.519
216.79	35.64	277.29	46.34	41.32	8.448
220.75	36.37	286.39	48.04	45.99	9.361
		296.53	49.81		
Series II		306.36	51.65	Series V	
88.80	16.06	315.91	53.38	47.52	9.650
100.01	17.54	327.59	55.49	52.05	10.469
109.76	18.86	336.60	57.14	56.92	11.302
119.33	20.21	345.37	58.76	62.16	12.153
128.52	21.56	350.05	59.55		
138.03	22.96	Series IV		Series VI	
147.67	24.41	6.31	0.129	58.40	11.151
154.44	25.41	7.86	0.287	63.64	12.374
162.98	26.74	8.89	0.443	69.34	13.226
165.80	27.20	9.89	0.614	75.50	14.130
174.15	28.46	10.81	0.792	81.98	15.084
182.64	29.83	11.88	1.131	89.31	16.122
192.14	31.46	12.99	1.293		
201.85	33.12	13.39	1.534	Series VII	
210.88	34.16	15.01	1.803	80.71	14.90
219.59	36.15	16.22	2.140	88.40	16.02
Series III		17.64	2.548	96.39	17.06
		19.39	3.026	104.73	18.17
219.13	35.96	21.38	3.579		
		Mark IV Thermostat			
Series VIII		447.34	77.59	Series XI	
		457.51	79.74		
304.80	51.77	468.00	82.06	ΔH Detn D	
313.63	53.34	477.32	84.62	ΔHm Detn E	
323.42	55.07				
333.59	56.69	Series IX		Series XII	
343.51	58.72				
353.58	60.51	465.75	81.54	ΔH Detn F	
363.80	62.38	475.97	84.21	Melting Detns G	
373.78	64.12	484.94	125.9	496.74	87.50
384.04	65.99	Melting Detns A		501.63	88.02
394.58	67.84	497.01	88.96	506.50	88.56
396.78	68.26			511.34	89.13
406.76	70.05	Series X			
417.22	71.99			Series XIII	
427.47	73.77	ΔH Detn B			
437.51	75.63	ΔHm Detn C		ΔH Detn H	
				Melting Detns J	

$\bar{T}$	ΔT	C_s	$\bar{T}$	ΔT	C_s
Melting Detns A			488.92	0.012	81600
			488.93	0.008	129000
488.89	0.055	21400	488.93	0.002	430000
488.92	0.018	65000	491.62	5.365	224
488.93	0.014	82000			
488.93	0.013	89000	Melting Detns J		
488.94	0.019	70400			
491.80	5.722	204.4	488.91	0.019	58000
			488.92	0.007	150000
Melting Detns G			488.93	0.009	126000
			500.30	22.737	107
488.90	0.023	44200			

[a] Units: cal, mol, °K.

mined in a separate series of measurements. Minor adjustments were applied for the difference (between these determinations and those on the loaded calorimeter) in the amount of solder for sealing the calorimeter, Apiezon T grease for thermal contact with the heater–thermometer assembly, and helium gas for thermal conductivity in the sample space. The mass of the calorimetric sample was 68.125 g *in vacuo* and its heat capacity ranges from 68 to 81% of the total. Buoyancy corrections were made using the reported[13] density of 1.25 g/cm³. A helium pressure of 117 Torr at 300°K was used to facilitate thermal equilibration in the sample space. All measurements of mass, temperature, resistance, voltage, and time are referred to calibrations or standardizations made by the U. S. National Bureau of Standards.

Thermostat and Calorimeter for Measurements from 300 to 520°K. The previously described Mark IV intermediate range thermostat,[14] a silver calorimeter (laboratory designation W-22), and a capsule-type platinum thermometer (laboratory designation A-8) were used. The mass of the calorimetric sample was 57.197 g *in vacuo*, and its heat capacity range from 70 to 78% of the total. A helium pressure of 198 Torr at 300°K was used to facilitate thermal equilibration in the sample space.

Anthracene Sample. Dr. James Hinton of Newport News, Va. purified the anthracene sample by zone melting and independently established the purity as better than 99.99%. Fractional melting studies subsequently described in this paper further attest to the purity.

Results and Discussion

Heat Capacity and Thermodynamic Functions. The saturation pressure heat capacity values, C_s, at the mean temperature of each determination are listed in chronological order in Table I and are depicted in Figure 1 together with literature data.[7] These data have been adjusted for curvature and are given in terms of the defined thermochemical calorie of 4.1840 J, an ice point of 273.15°K, and a gram formula mass of 178.236. The smoothed heat capacity and the thermodynamic functions derived from these data are given in Table II at selected temperatures. The probable error of the heat capacity is 0.1% above 25°K, 1% at 12°K, and approximately 5% at 5°K. The thermodynamic functions are considered to have a precision characterized by a probable error of less than 0.1% above 100°K.

Fractional Melting Studies. The amount of liquid-soluble, solid-insoluble impurity had been estimated from a plot of the apparent melting temperature, T, against the fraction melted, $1/F$. The data are summarized in Table III. The best values of the triple

(13) H. Inokuchi and M. Nakagaki, *Bull. Chem. Soc. Jap.*, **32**, 65 (1959).

(14) J. C. Trowbridge and E. F. Westrum, Jr., *J. Phys. Chem.*, **67**, 2381 (1963).

Table II: Thermodynamic Properties of Anthracene[a]

T	C_s	$S°$	$H° - H°_0$	$-(G° - H°_0)/T$
		Crystal		
5	0.065	0.003	0.011	0.001
10	0.644	0.176	1.423	0.034
15	1.806	0.644	7.394	0.151
20	3.192	1.351	19.85	0.359
25	4.581	2.214	39.31	0.642
30	5.878	3.166	65.51	0.982
35	7.078	4.163	97.94	1.365
40	8.181	5.182	136.1	1.778
45	9.176	6.204	179.6	2.213
50	10.10	7.218	227.8	2.663
60	11.80	9.213	337.4	3.589
70	13.33	11.148	463.17	4.532
80	14.78	13.024	603.8	5.477
90	16.17	14.845	758.5	6.417
100	17.55	16.620	927.1	7.349
110	18.92	18.357	1109.5	8.271
120	20.31	20.063	1305.6	9.182
130	21.74	21.74	1515.8	10.08
140	23.20	23.41	1740.5	10.98
150	24.70	25.06	1979.9	11.86
160	26.24	26.70	2235	12.74
170	27.80	28.34	2505	13.61
180	29.40	29.97	2791	14.47
190	31.03	31.61	3093	15.33
200	32.69	33.24	3412	16.18
210	34.39	34.88	3747	17.04
220	36.12	36.52	4099	17.88
230	37.87	38.16	4469	18.73
240	39.64	39.81	4857	19.57
250	41.42	41.46	5262	20.42
260	43.19	43.12	5685	21.26
270	45.01	44.79	6126	22.10
273.15	45.59	45.31	6269	22.36
280	46.87	46.46	6585	22.94
290	48.76	48.14	7064	23.78
298.15	50.31	49.51	7467	24.46
300	50.66	49.82	7561	24.62
310	52.56	51.51	8077	25.46
320	54.44	53.21	8612	26.30
330	56.29	54.91	9166	27.14
340	58.11	56.62	9738	27.98
350	59.91	58.33	10327	28.83
400	68.82	66.91	13546	33.05
450	78.12	75.55	17215	37.29
488.93[b]	(86.35)	93.55	25885	40.61
		Liquid		
488.93[b]	(86.61)	96.72	27435	40.61
500	87.85	98.67	28400	41.87

[a] Units: cal, mol, °K. [b] Assuming melting to be completely isothermal.

point temperatures, T' (calorimetric sample), T'' (pure substance), and mole fraction of impurity are 488.967°K, 488.956°K, and 0.00009_9. Literature values for the melting temperature are 489.33[15] and 489.55°K.[16] Despite the endeavor to remove all traces of oxygen on loading, each successive fractional melting determination increased N_2. After melting determinations G, N_2 reached 0.0003_0, and after those of Series J it went to 0.0004_4. Since the bulk of the heat capacity studies was completed prior even to melting determinations A, they were obviously made on a sample of purity in excess of 99.997%.

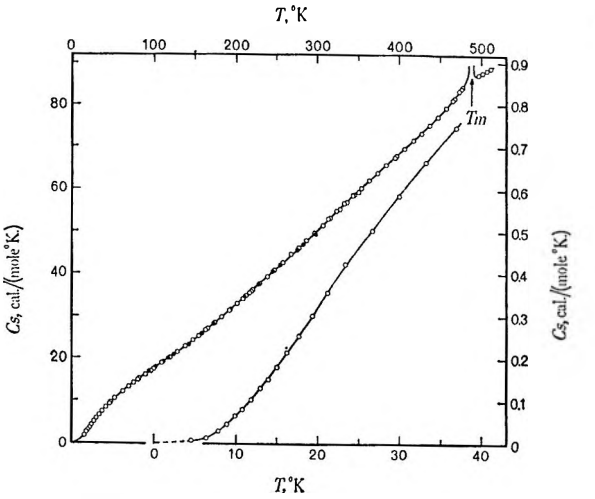

Figure 1. The heat capacity of anthracene. Circles represent the present data, squares those of Huffman, Parks, and Barmore.[7]

Table III: Fractional Melting Data for Anthracene[a]

T	$\Sigma\Delta H$	T_{final}	$1/F$
488.90	1450	488.918	2.141
488.92	2679	488.928	2.621
488.93	3857	488.934	1.820
488.93	5036	488.938	1.394
488.94	6344	488.947	1.106

[a] Units: cal, mol, °K. Based on data from melting determinations A, Series IX.

Enthalpy and Entropy of Melting. In the course of the heat capacity measurements, five series of determinations made through the melting region are summarized in Table IV. An average enthalpy of melting, calcu-

Table IV: Enthalpy of Melting of Anthracene[a]

Detn designation	No. of detns	T_1	T_2	$H_{T2} - H_{T1}$	$H_{500} - H_{460}$
A (Series IX)	10	460.57	499.38	10300	10401
C (Series X)	2	460.97	500.44	10356	10395
E (Series XI)	2	460.95	500.19	10335	10395
G (Series XII)	7	460.72	499.19	10263	10392
J (Series XIII)	5	460.20	511.67	11408	10392
				Av	10395 ± 6
				Lattice contrib	3375

[a] Units: cal, mol, °K. $\Delta H_m = 7020$; $T_m = 488.97$; $\Delta S_m = 14.36$.

(15) F. Burriel Marti, *Bull. Soc. Chim. Belges*, **39**, 590, 626 (1930).
(16) J. Hildebrand, *J. Amer. Chem. Soc.*, **39**, 2293 (1917).

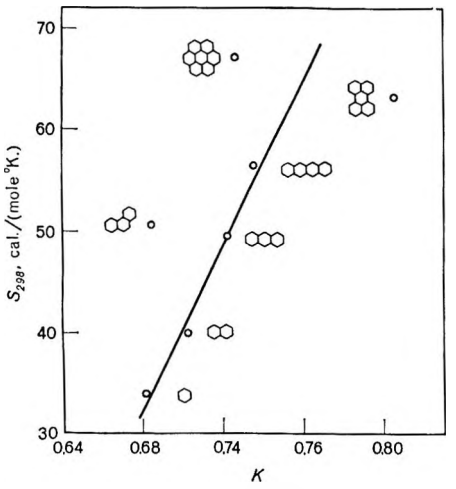

Figure 2. The entropy at 298.15°K of polynuclear aromatic hydrocarbons *vs.* the Kitaigorodskii coefficient K.

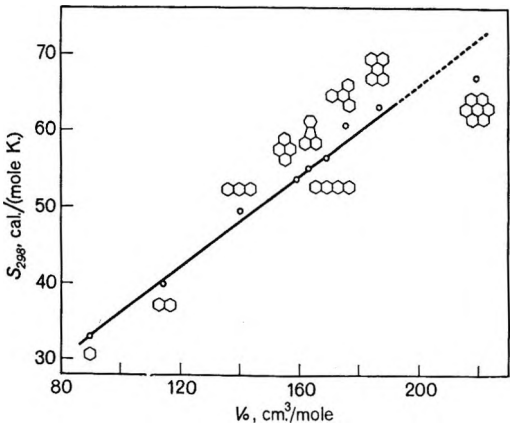

Figure 3. The entropy, S_{298}, of polynuclear aromatic hydrocarbons, *vs.* the molal volume of the crystalline phase.

lated from the excess enthalpy above smooth curves drawn to represent the crystalline and liquid heat capacities, is 7020 ± 12 cal/mol. The corresponding entropy increment obtained by numerical quadrature is 14.35 ± 0.02 cal/mol °K for a melting temperature of 488.941°K.

Discussion

As shown in Figure 1, good agreement was found with the data of Huffman, *et al.*,[7] over the common range of measurement. Although a linear relationship was found by Inokuchi, *et al.*,[17] between the enthalpies of sublimation per carbon and the number of carbons of molecules in this series, no correlations have been reported on the thermodynamics of melting. However, Andrews and Ubbelohde[18] have computed the volume required for free rotation about principal axes and concluded that most of the molecules in this series do not have sufficient room to rotate freely. Frank[19] pointed out that even when the volume per molecule in the liquid phase does not give room for individual rotation independent of the neighboring molecules, two molecules may rotate "in gear" with each other. In such a case more than half of the rotational entropy survives because the effective combined rotor had twice the moment of inertia. Although these molecules have relatively high molal entropies of fusion they decrease rapidly (on a per atom of carbon basis) near the beginning of the series and then more gradually.

The molal entropy of the crystalline state at 298°K also shows some regularity. The molal entropy divided by the number of carbon atoms per molecule plotted *vs.* the number of carbon atoms shows that the points (except that for naphthalene) define a smooth curve. Molecular packing in the crystalline state may be characterized by Kitaigorodskii's coefficient (or packing fraction),[20] which is defined as $K = Z(V_0/V)$. Here V is the cell volume, Z the number of molecules in the cell, and V_0 the molecular volume. A plot of S_{298} *vs.* K shows that a linear relationship exists for condensed chain molecules but not for disk-shaped molecules (Figure 2). A plot of S_{298} *vs.* molal volume, V_0, of the crystalline phase at the same temperature (Figure 3) shows a surprisingly linear relationship for all members of both series (except for coronene). Neither Raman[21] and infrared[22] spectral data nor 298°K elastic constant data[23] are adequate to solve model lattice dynamic calculations[24] in the absence of acoustical frequencies.

Acknowledgment. The authors appreciate the support of the U. S. Atomic Energy Commission in this research endeavor and that of Le Centre National de la Récherche Scientifique in providing a fellowship for Dr. Goursot. The cooperation of Luciana Dy and Soung-Sik Kim with the calculations is also acknowledged with gratitude.

(17) H. Inokuchi, S. Shiba, and H. Akamatu, *J. Chem. Soc. Jap.*, **25**, 298 (1952).

(18) J. N. Andrews and A. R. Ubbelohde, *Proc. Roy. Soc., Ser. A*, **228**, 435 (1955).

(19) F. C. Frank, *Trans. Faraday Soc.*, **52**, 884 (1956).

(20) A. T. Kitaigorodskii, "Organic Chemical Crystallography," Press of the Academy of Sciences of the U.S.S.R., Moscow, 1955. (English translation from the Russian by Consultants Bureau, New York, N. Y., 1961, p 106.)

(21) M. Suzuki, T. Yokoyama, and M. Ito, "Polarized Raman Spectra of Naphthalene and Anthracene," Technical Report of ISSP, Ser. A, No. 284, The Institute for Solid State Physics, Tokyo, Japan, 1967.

(22) A. Bree and R. A. Kydd, *J. Chem. Phys.*, **48**, 5319 (1968).

(23) G. K. Afanaseva, K. S. Aleksandrov, and A. I. Kitaigorodskii, *Phys. Status Solidi*, **24**, K61 (1967); H. B. Huntington, S. G. Gangoli, and J. L. Mills, *J. Chem. Phys.*, **50**, 3844 (1969).

(24) G. S. Pawley, *Phys. Status Solidi*, **20**, 347 (1967).

Thermodynamics of Globular Molecules. XVIII. Heat Capacities and Transitional Behavior of 1-Azabicyclo[2.2.2]octane and 3-Oxabicyclo[3.2.2]nonane. Sublimation Behavior of Five Globular Molecules[1]

by Edgar F. Westrum, Jr.,[2] Wen-Kuei Wong[3]

Department of Chemistry, University of Michigan, Ann Arbor, Michigan 48104

and Ernst Morawetz

Thermochemistry, Chemical Center, University of Lund, Lund, Sweden *(Received December 15, 1969)*

The thermal properties of two globular molecules, 1-azabicyclo[2.2.2]octane (quinuclidine) and 3-oxabicyclo[3.2.2]nonane, have been determined from 5°K to well within their liquid regions (438 and 480°K, respectively). Azabicyclooctane undergoes a solid–solid phase transition at 196.00°K and melts at 430°K. The entropy increments corresponding to these first-order transformations are 6.34 and 3.2 cal/(mol °K). The oxabicyclononane undergoes a broad solid–solid transition with maximum heat capacity at 208.50°K and melts at 448.43°K with associated entropy increments of 8.22 and 3.61 cal/(mol °K). The Crystal I phases of both substances are plastic (or embefic) crystals. Mechanisms are developed to account for the magnitudes of the entropy increments. The standard molal thermodynamic functions, heat capacities, entropies, Gibbs energy functions, and Gibbs energies of formation for crystalline azabicyclooctane and the oxabicyclononane are: 40.48, 44.23; 49.47, 56.47; −23.83, −27.04 cal/(mol °K); and 42.23, −7.04 kcal/mol at 298.15°K. Sublimation pressures and enthalpies of sublimation of the Crystal I phases of the above compounds plus that of bicyclo[2.2.2]octane and octene, and 3-azabicyclo[3.2.2]nonane, were determined directly. The gas phase thermodynamic functions are presented.

Introduction

As a continuation of the study of the thermodynamic characteristics of globular molecules[4] in the bicyclooctane family, measurements were obtained for 1-azabicyclo[2.2.2]octane, (quinuclidine, hereafter **1**) and for 3-oxabicyclo[3.2.2]nonane (hereafter **2**). **1** possesses a symmetry differing from that of bicyclooctane in its loss of the possible mirror plane perpendicular to the threefold axis and is similarly related to 1,4-diazabicyclo[2.2.2]octane (DABCO), the subject of a previous paper.[5] **2** is closely related to 3-azabicyclo[3.2.2]nonane, which has been the subject of two previous calorimetric determinations of thermal properties.[6]

Experimental Section

A commercial sample of **1** was subjected to fractional sublimation, gradient sublimation, and zone melting refining. *Anal.* Calcd for **1**: C, 75.62; H, 11.79; N, 12.59. Found: C, 75.80; H, 11.81; N, 12.34. A sample (25.3588 g (vacuum mass)) of this material was sublimed into calorimeter W-37 for the cryogenic thermal measurements. Calorimeter W-22 with a 35.9492 g (vacuum mass) loading was used over the intermediate temperature range that included the fusion point of the material.

Compound **2** was obtained from Eastman Chemical Products, Inc. and was subjected to the same purification process. *Anal.* Calcd for **2**: C, 76.14; H, 11.18; O, 12.68. Found: C, 76.15; H, 11.14; O, 12.80. The same calorimeters were used; W-37 was charged with 24.2942 g (vacuum mass) for the cryogenic region and W-22 with 28.4942 g (vacuum mass) for the intermediate region which included fusion.

The Mark III[7] and Mark IV[8] thermostats for the cryogenic and intermediate-temperature region have been described previously as have the methods of adiabatic shield control and computational conversion of data to molal thermodynamic properties. Automatic adiabatic shield control was used above 50°K

(1) This work was supported in part by the Division of Research, United States Atomic Energy Commission.

(2) To whom correspondence concerning this paper should be addressed.

(3) Abstracted in part from a dissertation submitted in partial fulfillment of the requirements for the Ph.D. degree from the Horace H. Rackham School of Graduate Studies at the University of Michigan, *Diss. Abstr.*, B28(3), 874 (1967).

(4) W.-K. Wong and E. F. Westrum, Jr., *J. Phys. Chem.*, **74**, 1303 (1970).

(5) J. C. Trowbridge and E. F. Westrum, Jr., *ibid.*, **67**, 2381 (1963).

(6) C. A. Wulff and E. F. Westrum, Jr., *ibid.*, **68**, 430 (1964); C. M. Barber and E. F. Westrum, Jr., *ibid.*, **67**, 2373 (1963).

(7) E. F. Westrum, Jr., G. T. Furukawa, and J. P. McCullough, in "Experimental Thermodynamics," J. P. McCullough and D. W. Scott, Ed., Butterworth and Co., Ltd., London, 1968.

(8) E. D. West and E. F. Westrum, Jr., in "Experimental Thermodynamics," J. P. McCullough and D. W. Scott, Ed., Butterworth and Co., Ltd., London, 1968.

and all measurements were referred to calibrations and standardizations by the National Bureau of Standards. The heat capacity of the sample in the cryostat ranges from 85% of the total at 10°K to a minimum of 55% at 105°K; above this temperature (except in the transition regions) it steadily increases to 70% in the solid and drops to 65% for the liquid phase. All calorimetric measurements on the condensed phases were made at the University of Michigan. Directly measured enthalpies of sublimation for five globular molecules were obtained at the University of Lund on the same samples used to obtain the thermal data. The measurement techniques employed for these measurements have been described elsewhere.[9] Sublimation pressures can be calculated from the flow rates obtained from the measurements of the enthalpies of sublimation. Since, however, the vapor flow from the calorimeter (Knudsen cell) is adiabatic and not molecular (*i.e.*, the flow Knudsen number $Kn \ll 1$) the usually applied Knudsen formula cannot be used without taking proper account of the compressibility of the outflowing vapor. For those cases when the vapor leaves the orifice with local sonic speed the following expression was derived by Nutt, *et al.*,[10] for the calculation of vapor pressure, P_s

$$P_s = 7.501 \times 10^{-4} \frac{G_{ad}}{KcAt} \left(\frac{M}{2\pi R_0 T}\right)^{-1/2} \times \left[2\pi\kappa\left(\frac{2}{\kappa+1}\right)^{\kappa+1(/\kappa-1)}\right]^{-1/2}$$

in which K is the Clausing factor ($\leqslant 1$), G_{ad} is the measured adiabatic flow rate in g sec^{-1}, c is the discharge coefficient for compressible flow through an orifice ($\sim 0.7 > c \leqslant 1$), A is the orifice area in cm^2, t is flow time in seconds, κ is the ratio of the heat capacity at constant pressure to the heat capacity at constant volume. In fact, the expression is the well known Knudsen formula except for the factor c and the term in square brackets which corrects for compressibility effects.

It was found that the magnitude of the square root of this term is rather insensitive to small variations of κ. For octane through hexadecane ($1.046 < \kappa < 1.020$) the average value was calculated to be 1.51 ± 0.005 (maximum deviation).[9] From flow rate measurements on octane (P_s = 14.3 Torr), 3,4-xylenol (P_s = 0.01 Torr) and water (P_s = 22.3 Torr) an approximate value of Kc = 0.90 ± 0.08 (maximum deviation) was obtained for a number of orifices. Using this value, sublimation pressures were calculated from flow rate measurements.

Results

The experimental heat capacities are listed in Table I and shown in Figures 1 and 2. The entries in Table I include the mean temperatures from which temperature increments within a series may be estimated. It is believed that probable errors in these data decrease from 5% at 5°K to 1% at 10°K and fall below 0.1% above 25°K. The data are stated in terms of the thermochemical calorie defined as 4.1840 J and an ice point of 273.15°K.

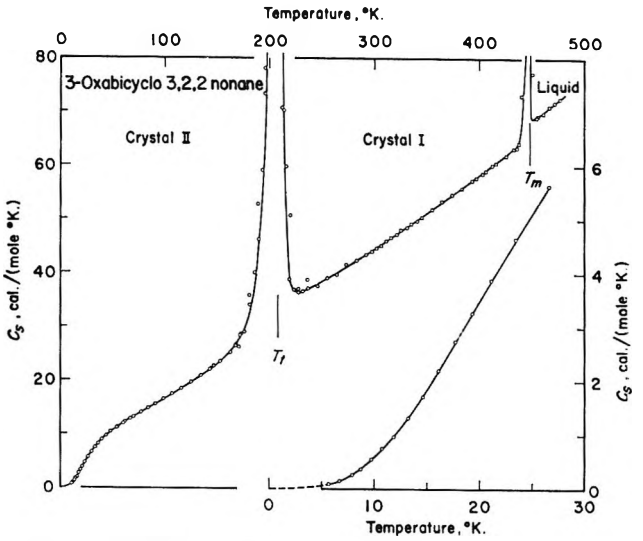

Figure 1. The heat capacity of 1-azabicyclo[2.2.2]octane.

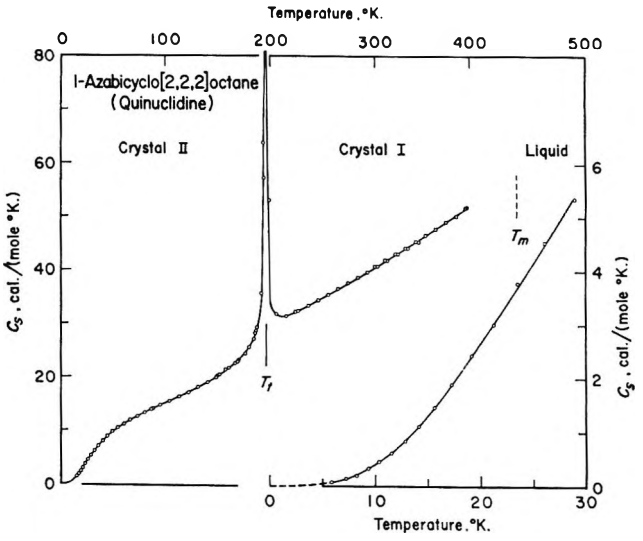

Figure 2. The heat capacity of 3-oxabicyclo[3.2.2]nonane.

Molal thermodynamic functions are presented, at selected temperatures, in Table II. Increments over regions devoid of thermal anomalies were obtained by suitable integrations of polynomials fitted to the heat capacity by high-speed computer. For regions of transition and fusion, the numerical investigations were obtained from large-scale plots of the data. It is believed that the probable errors in the derived functions are comparable to those of the heat capacities themselves. Evidence for this supposition is obtained by comparison

(9) (a) E. Morawetz and S. Sunner, *Acta Chem. Scand.*, **17**, 473 (1963); (b) E. Morawetz, "Thermodynamik Symposium," Klaus Schäfer, Ed., Heidelberg, 1967, and *Acta Chem. Scand.*, **22**, 1509 (1968).

(10) C. W. Nutt, G. W. Penmore, and H. J. Biddlestone, *Trans. Faraday Soc.*, **55**, 1516 (1959).

Table I: Experimental Heat Capacity Determinations on 1-Azabicyclo[2.2.2]octane and 3-Oxabicyclo[3.2.2]nonane[a]

1-Azabicyclo[2.2.2]octane

Data Taken in Mark III Calorimetric Cryostat

$\bar{T}$	C_s
Series I	
148.76	19.93
157.73	21.51
166.85	22.70
176.66	24.69
186.29	28.75
193.61	63.87
197.22	233.9
199.71	106.6
206.01	31.96
215.09	31.49
224.05	32.40
Series II	
ΔH Run (I)	
185.54	28.24
ΔHt Run A	
226.73	32.56
236.48	33.51
245.99	34.53
255.40	35.57
264.88	36.63
274.32	37.68
283.67	38.75
292.92	39.74
302.15	40.80
311.72	41.92
321.56	43.02
331.37	44.11
341.11	45.29
Series III	
86.71	14.01
95.38	14.77
104.30	15.54
113.39	16.40
122.51	17.28
131.48	18.19
140.65	19.18
150.03	20.28
ΔH Run (II)	
186.98	29.45
ΔHt Run B	
Series IV	
5.89	0.0603
7.26	0.1346
8.26	0.1835
9.33	0.3119
10.39	0.4416
11.56	0.5989
12.82	0.8230
14.14	1.098
15.60	1.455
17.26	1.887
19.14	2.425
21.26	3.055
23.59	3.772
26.12	4.537
28.94	5.348
32.08	6.211
35.66	7.112
40.06	8.075
44.67	8.945
49.25	9.713
54.71	10.50
60.66	11.28
66.65	11.97
73.23	12.62
80.45	13.36
88.07	14.12
Series V	
176.31	24.59
180.06	25.65
184.37	27.21
188.20	29.73
191.37	35.88
193.91	57.28
195.40	155.2
195.96	691.4
196.17	752.1
196.39	599.6
196.77	279.9
197.30	264.0
198.09	132.0
199.58	121.2
203.13	35.82
208.55	30.86
Series VI	
151.68	20.54
160.71	21.77
169.33	23.20
ΔHt Run C	
Series VII	
168.56	23.06
ΔHt Run D	

Data Taken in Mark IV Calorimetric Thermostat

$\bar{T}$	C_s
Series VIII	
299.48	40.80
309.49	41.97
319.29	43.11
328.91	44.21
338.43	45.41
347.98	46.59
357.61	47.78
367.28	49.05
377.02	50.29
386.69	51.72
396.26	53.48
Series IX	
404.84	55.93
408.72	57.01
412.51	59.20
416.18	62.27
419.66	68.08
422.87	78.33
425.68	96.66
428.02	128.3
429.94	173.3
431.43	267.7
432.49	364.5
433.34	428.5

3-Oxabicyclo[3.2.2]nonane

Data Taken in Mark III Calorimetric Cryostat

$\bar{T}$	C_s
Series I	
5.70	0.0916
6.73	0.1510
7.94	0.2617
8.74	0.3762
9.72	0.5566
10.74	0.7532
11.90	0.9798
13.23	1.329
14.61	1.729
16.12	2.202
17.76	2.751
19.37	3.283
21.14	3.881
23.45	4.678
26.61	5.648
30.02	6.622
33.18	7.441
36.50	8.209
40.06	8.934
44.13	9.651
48.94	10.42
54.36	11.18
60.59	12.01
67.18	12.81
Series II	
54.08	11.15
62.39	12.24
70.54	13.18
77.89	14.04
84.66	14.87
91.61	15.66
99.41	16.52
107.73	17.48
116.49	18.54
125.73	19.70
135.23	20.93
144.68	22.21
153.93	23.63
163.19	25.33
172.54	28.47
181.75	35.92
189.75	52.91
196.06	78.13
200.79	108.93
204.46	142.66
207.96	127.28
212.51	70.65
219.78	38.84
228.75	36.47
237.56	37.26
246.43	37.65
255.73	39.13
264.44	39.79
273.70	41.63
283.13	42.45
292.63	43.56
302.23	44.75
311.89	46.01
321.58	47.25
331.28	48.50
340.86	49.72
Series III	
ΔH Run (I)	
168.14	26.58
173.40	28.69
ΔHt Run A	
Series IV	
ΔH Run (II)	
168.28	26.72
ΔHt Run B	
Series V	
171.65	26.29
176.92	29.09
181.77	34.19
186.14	40.10
190.09	46.26
193.49	59.19
196.33	73.32
198.77	86.35
200.92	98.64
202.93	102.1
204.86	109.1
206.67	117.1
208.31	137.8
209.89	126.9
211.71	99.03
214.05	70.36
216.88	59.88
220.13	50.81
224.06	36.91
228.40	37.17
232.73	36.74
236.99	38.75

Data Taken in Mark IV Calorimetric Thermostat

$\bar{T}$	C_s
Series VI	
298.15	44.07
309.86	45.18
316.05	46.66
325.69	48.06
335.43	49.23
345.22	50.44
335.03	51.87
364.67	53.41
374.18	54.67
383.72	55.92
393.38	57.32
403.02	58.64
412.65	60.21
Series VII	
397.40	57.89
406.41	59.13
415.93	60.56
425.65	62.02
432.91	63.31
437.67	64.28
441.98	83.61
444.81	214.1
446.16	364.0
447.15	412.5
447.96	425.6
450.16	77.26
454.48	69.02
Series VIII	
435.84	63.51
440.36	73.22
443.73	184.8
445.46	311.2
446.24	409.6
446.88	462.8
447.44	565.9
448.29	301.1
Series IX	
ΔHm Run A	
Series X	
ΔHm Run B	
455.71	69.37
461.09	69.88
466.43	71.20
471.72	71.88
476.99	72.55

[a] Units: cal, mol, °K.

Table II: Thermodynamic Properties of 1-Azabicyclo[2.2.2]octane and 3-Oxabicyclo[3.2.2]nonane[a]

$\bar{T}$	C_s	$S°$	$H° - H°_0$	$-(G° - H°_0)/T$
	1-Azabicyclo[2.2.2]octane			
Crystal II Phase				
5	0.029	0.020	0.076	0.005
10	0.380	0.121	0.899	0.031
15	1.303	0.430	4.862	0.106
20	2.677	0.986	14.68	0.252
25	4.199	1.746	31.87	0.472
30	5.648	2.642	56.54	0.757
35	6.938	3.612	88.09	1.095
40	8.053	4.613	125.6	1.472
45	9.011	5.618	168.4	1.877
50	9.836	6.612	215.5	2.301
60	11.19	8.530	320.9	3.181
70	12.31	10.34	438.6	4.076
80	13.32	12.05	566.8	4.967
90	14.28	13.68	704.8	5.845
100	15.20	15.23	852.2	6.706
110	16.11	16.72	1009	7.549
120	17.03	18.16	1174	8.374
130	18.01	19.56	13.50	9.181
140	19.09	20.94	1535	9.971
150	20.30	22.29	1732	10.75
160	21.67	23.65	1942	11.51
170	23.29	25.01	2166	12.27
180	25.50	26.40	2410	13.01
Transition Region				
190	(32)	27.90	2688	13.75
196.00	(955)	30.19	3133	14.21
200	(83)	35.19	4119	14.60
Crystal I Phase				
210	31.01	37.12	4512	15.63
220	31.96	38.58	4827	16.64
230	32.90	40.02	5151	17.63
240	33.89	41.44	5485	18.59
250	34.94	42.85	5829	19.53
260	36.06	44.24	6184	20.45
270	37.22	45.62	6551	21.36
273.15	37.58	46.06	6669	21.64
280	38.38	47.00	6929	22.25
290	39.54	48.36	7318	23.13
298.15	40.48	49.47	7645	23.83
300	40.69	49.72	7720	23.99
310	41.84	51.08	8132	24.84
320	43.01	52.42	8556	25.69
330	44.20	53.77	8992	26.52
340	45.43	55.10	9441	27.34
350	46.71	56.44	9901	28.15
360	48.04	57.77	10375	28.95
370	49.41	59.11	10862	29.75
380	50.76	60.44	11363	30.54
	3-Oxabicyclo[2.2.2]nonane			
Crystal II				
5	0.065	0.021	0.080	0.005
10	0.591	0.180	1.372	0.043
15	1.849	0.637	7.220	0.156
20	3.499	1.391	20.52	0.365
25	5.137	2.351	42.18	0.664
30	6.603	3.420	71.61	1.033
35	7.865	4.535	107.9	1.453
40	8.929	5.657	149.9	1.909
45	9.826	6.762	196.9	2.387
50	10.60	7.838	248.0	2.878
60	11.92	9.890	360.7	3.878
70	13.12	11.82	485.9	4.876
80	14.31	13.65	623.06	5.859
90	15.48	15.40	772.0	6.822
100	16.62	17.09	932.5	7.765
110	17.76	18.73	1104	8.687
120	18.95	20.32	1288	9.591
130	20.22	21.89	1484	10.48
140	21.58	23.44	1693	11.35
150	23.02	24.98	1916	12.20
Transition Region				
160	24.6	26.51	2153	13.05
170	27.3	28.08	2412	13.89
180	33.6	29.79	2711	14.72
190	46.6	31.91	3106	15.57
200	89.4	35.23	3753	16.46
208.50	(147)	40.05	4740	17.32
210	127.3	41.03	4945	17.48
220	41.5	44.38	5661	18.65
Crystal I				
230	36.60	46.06	6040	19.80
240	37.27	47.63	6409	20.92
250	38.20	49.19	6786	22.04
260	39.50	50.78	7175	23.19
270	40.85	52.38	7576	24.31
273.15	41.26	52.84	7706	24.63
280	42.10	53.88	7991	25.34
290	43.27	55.41	8418	26.38
298.15	44.23	56.47	8775	27.04
300	44.45	56.81	8857	27.29
310	45.71	58.16	9307	28.13
320	47.05	59.69	9771	29.15
330	48.43	61.16	10249	30.10
340	49.81	62.72	10740	31.13
350	51.18	64.16	11245	32.03
360	52.57	65.69	11763	33.01
370	54.00	67.16	12296	33.92
380	55.46	68.56	12844	34.76
390	56.89	70.03	13405	35.66
400	58.27	71.44	13981	36.48
410	59.65	72.81	14571	37.27
420	61.19	74.25	15175	38.12
430	62.86	75.91	15795	39.17
440	64.40	77.37	16431	40.03
448.82[b]	(65.70)	78.47	16919	40.78
Liquid				
448.82[b]	(67.96)	82.08	18533	40.78
450	68.35	82.46	18703	40.90
460	70.01	83.98	19394	41.82
470	71.58	85.50	20103	42.73
480	72.91	87.02	20825	43.64

[a] Units: cal, mol, °K. [b] Assuming melting to be truly isothermal.

of long enthalpy-type runs with integrated heat capacities over the same temperature region (*cf.* Table III).

Table III: Enthalpy Increments of Transition for 1-Azabicyclo[2.2.2]octane and of Transition and Fusion for 3-Oxabicyclo[3.2.2]nonane[a]

1-Azabicyclo[2.2.2]octane Transition[c]

Source of data	No. of runs	T_1	T_2	$H_{T_2} - H_{T_1}$	$H_{215} - H_{190}$
Series I	6	190.87	219.63	2154	2004
Series II	1	188.11	221.81	2240	2002
Series III	1	191.82	214.02	1882	2007
Series VI	1	173.54	224.87	2724	2008
Series VII	1	172.76	221.09	2359	2005
				Av	2005 ± 1
				Graphical integ	2007
				Lattice contrib	756
				ΔHt	1249

3-Oxabicyclo[3.2.2]nonane Transition[d]

					$H_{230} - H_{155}$
Series II	12	149.33	233.32	4255	4011[b]
Series III	3	165.74	246.71	4356	4010
Series IV	2	164.09	244.96	4332	4010
Series V	20	168.93	230.56	3652	4009[b]
				Av	4010 ± 1
				Graphical integ	4009
				Lattice contrib	2333
				ΔHt	1677

3-Oxabicyclo[3.2.2]nonane Melting[e]

					$H_{465} - H_{430}$
Series VIII	8	430.53	456.73		3949[b]
Series IX	1	432.82	451.49	2828	3947
Series X	3	435.68	463.79	3509	3954
				Av	3950 ± 2
				Graphical integ	3951
				Lattice contrib	2336

[a] Units: cal, mol, °K. [b] A correction has been made for quasi-adiabatic conditions. [c] ΔSt = 6.34 cal mol °K; Tt = 196°K. [d] ΔSt = 8.22 cal/(mol °K); Tt = 208.50°K. [e] ΔHm = 1614 ± 2; ΔSm = 3.61 cal/(mol °K); Tm = 448.43°K.

Compound **1** was observed to undergo transition at 196.00°K. Five series of thermal measurements through the region centered on this temperature are listed in Table III. Heat capacities approaching 900 cal/(mol °K) were observed and are indicative that the solid–solid transition is first order. The intermediate-range calorimetric data covering the fusion region are tentative. Partial reaction of the sample with the silver calorimeter at elevated temperatures (noted by abnormal, progressively increasing positive drifts as the melting point was approached) prohibited more than a single evaluation of the thermodynamics of the fusion process. A white powdery residue (0.200 g) insoluble in organic solvents and liquid ammonia was found in the silver calorimeter with an elementary analysis. *Anal.* Calcd for **1**: C, 72.12; H, 11.24; N, 11.14, and 5.50% residue. The single result indicated that fusion occurred at 430°K with an enthalpy increment of 1.4 kcal/mol corresponding to ΔSm = 3.2 cal/(mol °K). The melting temperature is higher than a literature value of 156°.[11] While the uncertainty to be assigned to the entropy of fusion is certainly larger than normally obtainable by this method, it is still believed to be less than 0.3 cal/(mol °K). No purity determination by fractional fusion was obtained from the calorimetric sample.

Table III also contains the data for the transition and melting regions of **2**. For the broad solid–solid transition, spanning the region 165–230°K four series of measurements, listed in Table III, average a ΔSt = 8.22 cal/(mol °K). Fusion data contained in Tables III and IV indicate an amount of liquid-soluble, solid-insoluble impurity in the sample of 0.34 mol % and a triple-point temperature of 448.43°K for the pure substance. The relatively low purity may be a contributing factor in the breadth of the solid–solid transition region. Recent enthalpy of combustion data[12] have been used together with tabulated values for the entropies of the elements[13] to evaluate the standard enthalpies and Gibbs energies of formation of **1** and **2** as $\Delta Hf°$ (**1**) = −13.17 ± 0.14, $\Delta Hf°$ (**2**) = −65.89 ± 0.10 kcal/mol and $\Delta Gf°$ (**1**) = 42.23 ± 0.18, $\Delta Gf°$ (**2**) = −7.04 ± 0.14 kcal/mol for the Crystal I phases at 298.15°K.

Table IV: Fractional Melting Data for 3-Oxabicyclo[3.2.2]nonane[a,b]

T	C_s	ΔT	$\Sigma \Delta H$	T_{final}	$1/F$
445.46	311	0.872	527	445.90	3.063
446.24	410	0.680	757	446.58	2.132
446.88	463	0.608	1096	447.19	1.473
447.44	900	0.304	1346	447.46	1.199

[a] Units: cal, mol, °K. Data from Melting Runs Series VIII. [b] Triple point of sample, 447.59; triple point of pure compound, 448.43; mole fraction impurity, 0.0034.

The sublimation pressures and enthalpy of sublimation results are presented in Table V together with the pertinent standard deviations. Using these data, the thermal functions for (ideal) gaseous phase, *i.e.*, the

(11) S. Wawzonek, M. F. Nelson, Jr., and P. J. Thelen, *J. Amer. Chem. Soc.*, 73, 2806 (1951).

(12) S.-w. Wong, Ph.D. Thesis, University of Michigan, 1966. *Diss. Abstr.*, B28(6), 2383 (1967).

(13) D. D. Wagman, W. H. Evans, I. Halow, V. B. Parker, S. M. Bailey, and R. H. Schumm, U. S. National Bureau of Standards Technical Note 270-1, U. S. Government Printing Office, Washington, D. C., 1965.

Table V: Enthalpy of Vaporization (Sublimation) and Vapor Pressure of Globular Molecules at 298.15°K

Substance	Series	ΔH_v, kcal/mol Exptl[a]	ΔH_v, kcal/mol Cor	Mean $\Delta\overline{H_v}$,[b] kcal/mol	P_{sat},[c] Torr
Bicyclo[2.2.2]octane	I	11.450 ± 0.014	11.464	11.48 ± 0.05	2.7 ± 0.6
	II	11.485 ± 0.023	11.499		
Bicyclo[2.2.2]octene	I	10.468 (± 0.016)[d]	10.482	10.48 ± 0.03	6.6 ± 1.4
	II	10.474 ± 0.017	10.488		
1-Azabicyclo[2.2.2]octane	I	11.918 ± 0.016	12.132	12.14 ± 0.04	0.93 ± 0.19
	II	12.137 (± 0.024)[d]	12.151		
3-Azabicyclo[3.2.2]nonane	I	13.791 ± 0.012	13.805	13.81 ± 0.03	0.27 ± 0.06
	II	13.598 ± 0.005	13.812		
3-Oxabicyclo[3.2.2]nonane	I	12.745 ± 0.016			0.45 ± 0.09

[a] Precision indices are standard deviations. [b] Precision indices are "absolute" errors. [c] Precision indices are estimated standard deviations. [d] Precision indices are average deviations, three determinations per series.

standard enthalpies and Gibbs energies of formation (in kcal/mol) at 298.15°K, are

$\Delta Hf°$ (1) = −1.03 ± 0.18; $\Delta Hf°$ (2) = −53.19 ± 0.14

$\Delta Gf°$ (1) = 46.20 ± 0.22; $\Delta Gf°$ (2) = −2.63 ± 0.18

Discussion

The existence of solid–solid phase transitions with entropy increments considerably larger than those for the subsequent fusions are evidence that both **1** and **2** are embefic crystals. Guthrie and McCullough[14] have suggested a model (based on a superposition of molecular symmetry elements with subgroups of the lattice site symmetry) to account for transitional entropy increments in these systems. Crystal-structural data have not been obtained for **1** but it is reasonable to assume that the molecules occupy O_h lattice sites as they do for other globular molecular crystals. Only the C_{3v} subgroup provides a natural set of symmetry elements for the **1** cage. Using the four threefold lattice axes and the head-for-tail distinguishability of **1**, sixteen possible orientations are apparent for the disordered Crystal I phase. If one assumes that Crystal II is ordered (to be considered in detail subsequently)[15] the model predicts an entropy increment of R ln 16 = 5.54 cal/(mol°K); the observed value, 6.34 cal/(mol°K) is attributable to increased libration of the molecule above the transition temperature. The difference between the transitional entropies for bicyclooctane and **1**, 6.66 − 6.34 = 0.32 cal/(mol°K) is in accord with the models adopted for bicyclo[2.2.2]octane[16] and **1** which predict R ln (20/16) = 0.44 cal/(mol °K).

Compound **2** (Figure 2) differs in symmetry from bicyclooctane in the same way as does bicyclooctene.[16] One would therefore expect that the same model would be applicable and that the entropies of transition of **2** and bicyclooctene would be similar. The 8.22 value for **2** is indeed comparable to the 8.54 cal/(mol °K) sum for the two transitions of bicyclooctene. The difference is well within the range of values that have been associated with increased librational entropy.[14] The transitional entropy increment for **2** differs considerably, however, from that observed for the corresponding amine, 3-azabicyclo[2.2.2]octane.[6] The possibility of a disordered state for **2** persisting to 0°K cannot be excluded at this point, nor can the existence of a unique transition mechanism for the azabicyclononane. Such a mechanism may be necessary to account for the larger molecular envelope needed to include the hydrogen bonded to nitrogen and/or the possibility of hydrogen-bonded clusters in the azabicyclononane Crystal II.

The assumed number of quasiisoenergetic configurations available to the systems in the Crystal I phases are consistent with the melting theories of Amzel and Becka.[17] The latter authors also discuss the implications contained in the ideas of Darmon and Brot[18] as they can be applied to these cage-like systems.

Acknowledgment. The authors appreciate the enabling financial support of the Division of Research of the U. S. Atomic Energy Commission and the experimental assistance of W. G. Lyon and Carolyn Barber. We thank Mr. Craig Garren of the Eastman Chemical Products, Inc. for their kind provision of the sample of oxabicyclononane.

(14) G. B. Guthrie and J. P. McCullough, *J. Phys. Chem. Solids*, **18**, 53 (1961).

(15) C. A. Wulff and E. F. Westrum, Jr., *J. Chem. Therm.*, in press.

(16) O. Ermer and J. D. Dunitz, *Chem. Commun.*, **10**, 567 (1968).

(17) L. M. Amzel and L. N. Becka, *J. Phys. Chem. Solids*, **30**, 521 (1969).

(18) I. Darmon and C. Brot, *Mol. Crystallogr.*, **2**, 301 (1967).

Nonelectrolyte Liquid Mixture Studies by Medium Pressure Gas–Liquid Chromatography. Infinite Dilution Activity Coefficients of C_5–C_8 Hydrocarbons in 1-*n*-Alkylbenzenes

by Brian W. Gainey and Robert L. Pecsok

Department of Chemistry, University of California, Los Angeles, California 90024 *(Received October 16, 1969)*

The infinite dilution activity coefficients are reported for a number of hydrocarbons in a series of *n*-alkylbenzenes that have been measured by medium pressure gas–liquid chromatography. Nitrogen + hydrocarbon mixed second virial coefficients simultaneously obtained by the technique are shown to agree satisfactorily with previous measurements and with theoretical predictions. The activity coefficients can be correlated within experimental error in most cases by a simple extension of the quasi-lattice theory in terms of segment interchange energies. The temperature dependence of the benzene results is sufficient for an evaluation of the infinite dilution partial molal heats.

Introduction

Gas liquid chromatography (glc) has become widely used for analytical and preparative purposes and it is perhaps surprising to discover that until recently the development of glc as a method of obtaining physicochemical information has been relatively slow.

This is linked to the absence, in the past, of an adequate understanding and theory connecting experimental measurements with the particular physicochemical property under consideration. Probably it was also due to the fact that early workers did not realize that the criteria governing the accurate determination of thermodynamic properties from glc depended upon quite different experimental considerations than did analytical or preparative glc.

It is now generally recognized that the most accurate physicochemical data are obtained with specially designed equipment and experiments where the experimental conditions are all precisely controlled.

The gas–liquid chromatographic technique is a dynamic one involving carrier gas, volatile solute, and stationary phase that allows access to many physicochemical situations which are difficult to study by other methods. Provided that a well-proven theory is available that characterizes the required experimental conditions and an apparatus capable of the necessary precision, then it should be possible to measure many physicochemical properties by glc. Several excellent reviews have appeared on this subject.[1-4]

This work utilizes medium pressure glc to study simultaneously liquid–liquid and gas–vapor mixtures. The now well-established theory predicts that by measuring the pressure dependence of the solute retention volume it is possible to study concurrently liquid–liquid interactions characterized by the infinite dilution activity coefficient (γ_1^∞) and gas–vapor interactions characterized by the mixed second virial coefficient (B_{12}).

Basic Theory

The previously developed theory of gas chromatographic elution of a highly dilute solute[5,6] has recently been extended[7] to include second-order gas phase imperfection terms, yielding a precise expression for the ideal retention volume in terms of the thermodynamic parameters of the system.

The assumptions underlying the development of the theory were as follows. (1) An elution process corresponded to ideal (zero resistance to mass transfer) chromatography. This condition is likely to be violated whenever highly polar, viscous solvents (*e.g.*, glycerol)[7] are used because of the slow diffusion of solute into the stationary phase (hereafter called the solvent). (2) No solute adsorption occurred at any of the three interfaces: solvent–gas, solid–gas, or solid–solvent. Martin[8] first pointed out that solute adsorption at the gas–liquid interface (on the surface of the bulk liquid) could drastically increase the solute retention volumes in certain glc systems. Also, the order of elution of so-

(1) J. H. Purnell, *Endeavour*, **23**, 142 (1964).

(2) R. Kobayashi, P. S. Chappelear, and H. A. Deans, *Ind. Eng. Chem.*, **10**, 63 (1967).

(3) C. L. Young, *Chrom. Rev.*, **14**, 1 (1968).

(4) J. R. Conder, *Advan. Anal. Chem. Instrum.*, **6**, 209 (1968).

(5) A. J. B. Cruickshank, M. L. Windsor, and C. L. Young, *Proc. Roy. Soc., Ser. A*, **295**, 1271 (1966).

(6) A. J. B. Cruickshank, B. W. Gainey, and C. L. Young, "Gas Chromatography 1968," C. L. A. Harbourn, Ed., Inst. of Petroleum, Butterworths, 1969, p 76.

(7) A. J. B. Cruickshank, B. W. Gainey, C. P. Hicks, T. M. Letcher, R. W. Moody, and C. L. Young, *Trans. Faraday Soc.*, **65**, 1014 (1969).

(8) R. L. Martin, *Anal. Chem.*, **33**, 347 (1961); **35**, 116 (1963).

lutes could vary depending upon the polar solvent support ratio. Martire[9] has shown that these effects are also present in polar–polar systems, while Pecsok and Gump[10] have shown that polar solutes on nonpolar solvents can apparently also exhibit this phenomenon. A review of the subject has been written by Martire.[11] Studies by Urone and Parcher[12] have indicated that adsorption of solute may take place not only at the uncoated solid surface, presumably in competition with the carrier gas at low temperatures, but also at the liquid–solid interface in competition with the solvent. Purnell, *et al.*,[13] have examined in detail the effects of solute adsorption at the solid–gas interface and at the gas–liquid interface. They propose experiments that produce only the partition process contribution and then report studies on the normal alcohols with squalane as solvent.[14]

Since the theory used in this work assumes only partitioning of the solute between the gas and liquid phases, it is obviously necessary by preliminary experiments to ensure that other factors such as the three mentioned above are either absent or negligible.

Asymmetric elution peaks often indicate that such processes may be occurring together with the solute peak maximum retention volumes that vary with carrier gas flow rate, with coverage ratio of solvent to inert support, and with solute sample size even where the conditions of "effective infinite dilution" are satisfied (0.2 to 2 μmol sample size).[7]

Preliminary measurements on these systems showed that all these effects were of negligible importance when columns with about 20% solvent coverage were used. (3) Spreading the involatile stationary phase on the inert gas permeable solid support had not affected the properties of the former. (4) The solute concentration in the solvent was at all times effectively zero. A full discussion of these two approximations and their significance has been given previously.[3,6,15]

The gas chromatographic data were analyzed in a manner described previously[7] and summarized by the following equations

$$\ln V_N = \ln V_N^0 + \beta' p_o J_3^4 + \text{(ignoring higher terms in } (p_o J_3^4)^n) \quad (1)$$

$$\ln V_N^0 = \ln \frac{n^1 RT}{p_1^0 \gamma_{13}^\infty} - \frac{(B_{11} - v_1^0)p_1^0}{RT} \quad (2)$$

$$\beta' = \frac{2B_{12} - v_{13}^\infty}{RT} + \lambda\left(1 - \left(\frac{\partial \ln \gamma_1^\infty}{\partial x_2}\right)_0\right) \quad (3)$$

where p_i = column inlet pressure, p_o = column outlet pressure, J_3^4 = a mean column pressure,[16] V_N = the net retention volume, V_N^0 = zero pressure net retention volume. n^1 = number of moles of stationary phase on the column: B_{11}, v_1^0, and p_1^0 are pure solute properties, second virial coefficient, molar volume, and vapor pressure, respectively. λ is the carrier gas solubility and x_2 its mole fraction in the solvent. γ_1^∞ is now the activity coefficient of solute 1 in the "mixed solvent" consisting of solvent 3 plus dissolved carrier gas 2.

Experimental Section

Apparatus. The apparatus requirements necessary to achieve the optimum experimental precision have been outlined and reviewed in three papers;[3,6,15] therefore, only those aspects of the present apparatus that differ from those published previously will be mentioned.

The carrier gas inlet pressure was measured by a Heise Bourdon tube gauge (Newtown, Conn.) which measured 0–15 atm to ± 0.01 atm. Control of carrier gas inlet pressure, measurement of flow rate, column pressure drop, column outlet pressure, and sample vapor injection were identical with the methods previously described for a former apparatus used by one of us (B. W. G.) elsewhere.[6]

A Gow-Mac (Madison, N. J.) flame ionization detector was used in conjunction with a Loenco electrometer (Altadena, Calif.) and a Sargent recorder (Model SR). The apparatus was constructed with 1/4-in. copper tubing and Swagelok couplings.

Columns and Materials. The experimental packed chromatographic columns were usually around 20% liquid loading on Johns-Manville, nonacid washed, 60–80 mesh Chromosorb W inert support, packed by the method proposed by Purnell.[17] Column specifications are given in Table I. The *n*-alkylbenzenes with one exception were obtained from Eastman Organic

Table I: Columns and Materials

Stationary phase	Wt of stationary phase, g	% Liquid loading
1-Phenyldecane	2.959	18.5
1-Phenyldodecane	2.906	19.5
1-Phenyltetradecane	2.973	19.9
1-Phenylpentadecane	3.034	20.0
1-Phenylnonadecane	3.009	19.2

(9) D. E. Martire, *Anal. Chem.*, **38**, 244 (1966).

(10) B. H. Gump and R. L. Pecsok, *J. Phys. Chem.*, **71**, 2202 (1967).

(11) D. E. Martire, *Advan. Anal. Chem. Instrum.*, **6**, 93 (1968).

(12) P. Urone and J. F. Parcher, *Anal. Chem.*, **38**, 270 (1966).

(13) J. R. Conder, D. C. Locke, and J. H. Purnell, *J. Phys. Chem.*, **73**, 700 (1969).

(14) D. F. Cadogan, J. R. Conder, D. C. Locke, and J. H. Purnell, *ibid.*, **73**, 708 (1969).

(15) A. J. B. Cruickshank, M. L. Windsor, and C. L. Young, *Proc. Roy. Soc., Ser. A*, **295**, 259 (1966).

(16) D. H. Everett, *Trans. Faraday Soc.*, **61**, 1637 (1965).

(17) J. H. Purnell, "Gas Chromatography," John Wiley and Sons, New York, N. Y., 1962, p 235.

Chemicals, Rochester, N. Y., with a stated purity of better than 99%. *n*-Nonadecylbenzene was obtained from Research Organic/Inorganic Chemical Co., Sun Valley, Calif. (also 99.0%). The manufacturer's purity claims were substantiated by glc analyses. The main impurities were the neighboring even carbon number *n*-alkylbenzenes, except for *n*-pentadecylbenzene and *n*-nonyldecylbenzene, which had neighboring odd number impurities.

Most of the hydrocarbon solutes were obtained from Phillips Petroleum Co., Bartlesville, Okla. (research grade). 3,3-Dimethylpentane was purchased from K and K Laboratories, Hollywood, Calif. 2-Methylhexane, 3-methylhexane, 2,3-dimethylpentane, 2,2-dimethylpentane, 2,2-dimethylhexane, 2,2,3,3-tetramethylbutane, and 2,2,3-trimethylbutane were obtained from Aldrich Chemical Co., Milwaukee, Wis. All were repurified by preparative glc. All solutes were at least 99.9% pure. The hexafluorobenzene sample was a gift from Imperial Smelting Corp., Avonmouth, England (99.9% purity). These purities were confirmed by glc analysis. The nitrogen carrier gas was oxygen free from the Matheson Gas Co.

Results

A series of measurements was made of the change in the net retention volume of a single pure solute in a specific stationary phase as a function of mean column pressure. Computer least-squared fitting of the data in accordance with eq 1 gave values for B_{12} and γ_1^∞ as indicated by eq 1 through 3. The mixed second virial coefficients are given in Table II. They were computed assuming that nitrogen was ideally soluble in the *n*-alkylbenzenes.[18]

A comparison with previous results and with an empirical equation for predicting B_{12} values in conjunction with two different combining rules is given in Table III. A full discussion of the use of these equations has been given previously. As in previous work, the McGlashan and Potter[19] equation in conjunction with the Hudson and McCoubrey[20] combining rule gives the best available representation of the data. The infinite dilution activity coefficients are given in Tables IV and V.

Table II: Mixed Second Virial Coefficients. Nitrogen + Hydrocarbon Mixtures at 40°, $-B_{12}$ in cm³ mol⁻¹

	Solvent				
Solute	1-Phenyldecane	1-Phenyldodecane	1-Phenyltetradecane	1-Phenylpentadecane	1-Phenylnonadecane
n-Pentane	81	85	95	84	86
n-Hexane	104	110	111	106	109
n-Heptane	110	109	111	114	113
n-Octane	128	133	139	...	132
2-Methylbutane	...	92	...	91	...
2-Methylpentane	...	107	...	105	...
3-Methylpentane	...	96	...	96	...
2,3-Dimethylbutane	...	102	...	96	...
2,2-Dimethylbutane	...	83	...	...	...
2,2-Dimethylpentane	...	...	...	117	...
2,2-Dimethylhexane	...	...	...	150	...
2-Methylhexane	...	116	...	113	...
3-Methylhexane	...	104	...	104	...
2,3-Dimethylpentane	...	108	...	108	...
2,4-Dimethylpentane	...	111	...	118	...
3,3-Dimethylpentane	...	116	...	117	...
2,2,3-Trimethylbutane	...	100	...	103	...
2,2,3,3-Tetramethylbutane	...	...	...	128	...
Cyclohexane	...	118	...	114	...
Benzene	95	98	99	108	101
Hexafluorobenzene	...	124	130	122	...

Table III: Comparison of Mixed Second Virial Coefficients with Previous Work and with Theoretical Predictions at 40°, $-B_{12}$ cm³ mol⁻¹

Solute	Av from Table II[f]	Previous[e] work	Theoretical a	Theoretical b
n-Pentane	86	85	125	88
n-Hexane	110	107	153	98
n-Heptane	110	111	182	107
n-Octane	134	143[c]	219	119
2-Methylbutane	92	...	122	86
2-Methylpentane	106	93[c]	150	96
3-Methylpentane	96	...	152	97
2,3-Dimethylbutane	99	...	148	96
2,2-Dimethylbutane	83	...	145	93
2,2-Dimethylpentane	117	...	...	...
2,2-Dimethylhexane	150	...	...	...
2-Methylhexane	115	...	...	...
3-Methylhexane	105	...	...	...
2,3-Dimethylpentane	108	...	...	...
2,4-Dimethylpentane	115	109[c]	179	106
3,3-Dimethylpentane	117	...	...	...
2,2,3-Trimethylbutane	100	...	...	...
2,2,3,3-Tetramethylbutane	128	...	...	...
Cyclohexane	116	122[d]	155	110
Benzene	100	104[d]	143	107
Hexafluorobenzene	126	128	...	...

[a] McGlashan and Potter equation + geometric mean combining rule. [b] McGlashan and Potter equation + Hudson and McCoubrey combining rule. [c] Previous work at 30°, ref 42, C. L. Young, Thesis, University of Bristol, 1967. [d] Previous work at 35°, ref 26. [e] Previous work other than that separately referenced (ref 42 and 43), B. W. Gainey, Thesis, University of Bristol, 1967. [f] The uncertainty on these measurements is ±6 cm³ mol⁻¹.

(18) D. H. Everett, B. W. Gainey and C. L. Young, *Trans. Faraday Soc.*, **64**, 2667 (1968).

(19) M. L. McGlashan and D. B. Potter, *Proc. Roy. Soc., Ser. A*, **267**, 478 (1962).

(20) G. M. Hudson and J. C. McCoubrey, *Trans. Faraday Soc.*, **56**, 761 (1960).

Table IV: Infinite Dilution Activity Coefficients. Hydrocarbons in *n*-Alkylbenzenes at 40° (log γ_f^∞)[a]

Solute	Solvent: 1-Phenyldecane	1-Phenyldodecane	1-Phenyltetradecane	1-Phenylpentadecane	1-Phenylnonadecane
n-Pentane	0.060	0.028	0.016	−0.006	−0.051
n-Hexane	0.062	0.038	0.017	0.003	−0.037
n-Heptane	0.066	0.046	0.025	0.013	−0.024
n-Octane	0.071	0.051	0.032	...	−0.014
2-Methylbutane	...	0.048	...	0.013	...
2-Methylpentane	...	0.055	...	0.022	...
3-Methylpentane	...	0.039	...	0.004	...
2,3-Dimethylbutane	...	0.042	...	0.008	...
2,2-Dimethylbutane	...	0.074	...	...	...
2,2-Dimethylpentane	...	...	...	0.050	...
2,2-Dimethylhexane	...	...	...	0.042	...
2-Methylhexane	...	0.063	...	0.025	...
3-Methylhexane	...	0.055	...	0.020	...
2,3-Dimethylpentane	...	0.037	...	0.004	...
2,4-Dimethylpentane	...	0 085	...	0.052	...
3,3-Dimethylpentane	...	0.037	...	0.000	...
2,2,3-Trimethylbutane	...	0.051	...	0.017	...
2,2,3,3-Tetramethylbutane	...	...	...	0.198	...
Cyclohexane	...	−0.066	...	−0.101	...

[a] The uncertainty on these measurements is between ±0.001 and ±0.002 on log γ_f^∞.

Table V: Infinite Dilution Activity Coefficients for Benzene and Hexafluorobenzene in *n*-Alkylbenzenes, log γ_f^∞ [a]

Solvent	Temp, °C	Benzene	Hexafluorobenzene
1-Phenyldecane	32	−0.059	...
	40	−0.064	...
	50	...	...
1-Phenyldodecane	32	−0.073	0.129
	40	−0.082	0.126
	50	−0.092	0.124
1-Phenyltetradecane	32	−0.088	0.126
	40	−0.095	0.125
	50	−0.102	0.124
1-Phenylpentadecane	32	−0.102	0.122
	40	−0.107	0.122
	50	−0.115	0.118
1-Phenylnonadecane	32	−0.139	...
	40	−0.151	...
	50	−0.161	...

[a] The estimated experimental error on the activity coefficients is slightly less than ±0.002 on log γ_f^∞.

Discussion

The purpose of this work has been to extend the currently available thermodynamic data on well defined nonelectrolyte systems. Most methods of obtaining activity coefficients of binary mixtures precise enough to test statistical theories of liquid mixtures utilize data from equilibrium stills,[21,22] static vapor pressure measurements,[23,24] or less precisely for a volatile–nonvolatile mixture by means of a sensitive microbalance or quartz-spiral balance.[25] The static vapor pressure technique, as well as the spiral balance method, are least accurate in the low-concentration region of the volatile component, just where infinite dilution glc operates.

Comparison with Solution Theories. A previous publication[26] has shown that the Hildebrand and Scatchard "solubility parameter" theory is incapable of accurately explaining the χ values obtained from hydrocarbon + *n*-alkane mixtures. In general the predicted values for *n*-alkanes, cyclohexane, benzene, and the alk-1-enes were lower than the experimental χ values while for branched chain molecules the predictions were too high. A similar trend was apparent in this work with poor agreement of theory and experiment. The point to be made here is that the solubility parameter approach is only a "rule of thumb" theory and should not be expected to accurately predict solution thermodynamic behavior, but at the same time neither should it produce an absurd result.

These current results will be now used to show how a simple extention of the quasilattice theory can be util-

(21) I. Brown, *Aust. J. Res.*, **A5**, 1 (1952).

(22) D. F. Othmer, R. Gilmont, and J. J. Conti, *Ind. Eng. Chem.*, **52**, 625 (1960).

(23) D. H. Everett and M. F. Penney, *Proc. Roy. Soc., Ser. A*, **212**, 164 (1952).

(24) M. L. McGlashan and A. G. Williamson, *Trans. Faraday Soc.*, **57**, 588 (1961).

(25) A. J. Ashworth and D. H. Everett, *ibid.*, **56**, 1609 (1960).

(26) A. J. B. Cruickshank, B. W. Gainey, and C. L. Young, *ibid.*, **64**, 337 (1968).

ized to correlate and accurately predict the observed activity coefficients.

The basic central assumption of the theory is that the logarithm of the activity coefficient may be expressed as the sum of two completely independent contributions; a configurational contribution due to the different sizes of the molecules (an entropic effect); and an interactional contribution due to the interaction of the molecules with each other.[23,27,28]

$$\ln \gamma_1 = \ln \gamma_1^{\text{config}} + \ln \gamma_1^{\text{interaction}} \quad (4)$$

The interaction contribution, $\ln \gamma_1^{\text{interaction}}$, is, of course, a free energy of interaction and thus also contains an entropy contribution.

Configurational Contribution. Several treatments exist for calculating the configuration contribution. The Flory[28] treatment (*i.e.*, formally equivalent to the Miller–Guggenheim[29] relation when z, the number of nearest lattice neighbors approaches infinity) is preferred in this work with r the size ratio of the molecules taken as the ratio of the molar volumes of solvent to solute. This is based upon Everett and Munn's analysis[30] of the *n*-hexane + *n*-hexadecane data of McGlashan and Williamson.[24] At solute infinite dilution, Flory's equation becomes

$$\ln \gamma_1^{\text{config}} = \ln \left(\frac{1}{r}\right) + \left(1 - \frac{1}{r}\right) \quad (5)$$

Using eq 4 and 5 it is possible to calculate values of $\ln \gamma_1^{\text{interaction}}$.

Interactional Contribution. The interaction contribution is given by

$$\ln \gamma_1^{\text{interaction}} = \chi \varphi_2^2 \quad (6)$$

where φ_2 is the volume fraction of the larger component, while χ is the so-called interaction parameter, which by definition is equal to ω_{12}/kT, where ω_{12} is the energy of interchange of a molecule of component 1 from pure component 1 when interchanged with an equivalent number of molecules of component 2 from pure component 2. The problem is now to discover a means of predicting χ values for various solute–solvent combinations.

Recent publications[31-34] have indicated that the χ values for *n*-alkane mixtures can be satisfactorily predicted in terms of both a segment[35] and a contact point treatment.[36] The approaches are formally equivalent and differ only in the mathematical evaluation of the requisite "surface fractions." While intuitively the segment approach is preferred because it appears to be a more realistic proposition, both approaches will be investigated. The basic segment concept is that the interaction of chain-like molecules can, to a first approximation, be treated as the sum of the various interactions of very simple segments of which the molecule is composed. The treatment therefore assumes a degree of segment autonomy. The total interaction energy, ω, is then made up of the component segment interchange energies for each type of segment with all unlike segments. The contact point treatment differs from this only in that to each segment is then allotted a certain number of contact points.

(*a*) *n-Alkane + n-Alkylbenzene Mixtures.* For binary liquid mixtures containing three different types of segments it has been shown that[34]

$$-\frac{\chi T}{r_1} = (a_1 - a_2)(b_1 - b_2)\frac{\omega_{AB}}{k} + (b_1 - b_2)(c_1 - c_2)\frac{\omega_{BC}}{k} + (a_1 - a_2)(c_1 - c_2)\frac{\omega_{AC}}{k} \quad (7)$$

where r_1 is the number of segments in the solute molecule. a, b, and c are fractions of the three types of segment A, B, and C in either solute 1 or solvent 2 as indexed. For example, a_1 is the fraction of segments of type A in the solute 1. ω_{AB}/k, ω_{AC}/k, and ω_{BC}/k are interchange energies for, respectively, A with B, A with C, and B with C segments. T is the absolute temperature. Putting $c_1 = c_2 = 0$ reduces the formula to the two types of segment formalism used earlier containing only one interchange energy.[32] Analogous equations exist for the contact point treatment.

By studying a series of solutes in a series of stationary phases in the same family of compounds it is possible to evaluate the various segment interchange energies. If the theory is valid these segment interchange energies at a fixed temperature should be constant for all the combinations of solute and solvent to within the combined uncertainty on the experimental measurements. Earlier work with C_1–C_8 *n*-alkanes with C_{16}–C_{32} *n*-alkanes has established that a two-segment model (CH_3–CH_2CH_2) correlates a wide range of *n*-alkane binary mixtures with a single interchange energy, ω/k (CH_3/CH_2).[31-33]

If the central assumption used in calculating the interactional contribution is valid (*i.e.*, that the segments of the components act independently of one another),

(27) M. L. Huggins, *J. Chem. Phys.*, **9**, 440 (1941); *Ann. N. Y. Acad. Sci.*, **1**, 43 (1942).

(28) P. J. Flory, *J. Chem. Phys.*, **10**, 51 (1942).

(29) K. Miller, *Proc. Cambridge Phil. Soc.*, **38**, 109 (1942); **39**, 154 (1943).

(30) D. H. Everett and R. J. Munn, *Trans. Faraday Soc.*, **60**, 1951 (1964).

(31) B. W. Gainey and C. L. Young, *ibid.*, **64**, 349 (1968).

(32) C. L. Young, *ibid*, **64**, 1537 (1968).

(33) C. L. Young and C. P. Hicks, *ibid.*, **64**, 2675 (1968).

(34) A. J. B. Cruickshank, B. W. Gainey, C. P. Hicks, T. M. Letcher, and C. L. Young, *ibid.*, **65**, 2356 (1969).

(35) E. A. Guggenheim, "Mixtures" (Oxford U. Press), 1952, Chapters X, XI. [See also H. Tompa, "Polymer Solutions," Butterworths, England, 1956, Chapter 4, and M. L. McGlashan, A. G. Williamson, and K. W. Morcum, *Trans. Faraday Soc.*, **57**, 601 (1961).]

(36) J. A. Barker, *J. Chem. Phys.*, **20**, 1526 (1952).

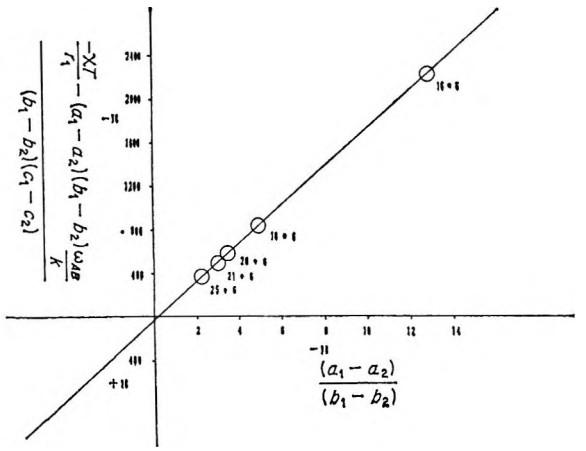

Figure 1. Graph of the *n*-hexane + *n*-alkylbenzene data at 40°: quasilattice segment approach; ordinate, $[-(\chi T/r_1) - (a_1 - a_2)(b_1 - b_2)(\omega_{AB}/k)]/(b_1 - b_2)(c_1 - c_2)$; abscissa, $(a_1 - a_2)/(b_1 - b_2)$; gradient = $\omega_{CH_3/phenyl\ group}/k$ (from alkyl benzene); intercept = $\omega_{CH_2CH_2/phenyl\ group}/k$ (from alkyl benzene). The number graph points refer to the number of carbon atoms in the respective solvent + solute mixture (*e.g.*, 16 + 6 refers to 1-phenyldecane with *n*-hexane).

then it should be possible to use the previously derived CH_3–CH_2CH_2 interchange energy in an analysis of the current *n*-alkane + *n*-alkylbenzene data. This reduces the unknown quantities in eq 7 to two, once a choice has been made of segments. From roughly equal segment molar volume considerations the segments chosen were CH_3 and CH_2CH_2 as with the *n*-alkane work, and $(^1/_3)$ (C_6H_5). The two unknown segment interchange energies are then evaluated by rearranging eq 7 and employing a graphical procedure. The *n*-hexane + *n*-alkylbenzene results were computer least-squared to give a gradient and intercept related, respectively, to ω/k(end/benzene) and ω/k(middle/benzene). The results are shown plotted in Figure 1. The uncertainty on these segment interchange energies is about ±4°K.

The three segment interchange energies are then used to calculate ln $\gamma_1^{interaction}$ for other solute + *n*-alkylbenzene binary mixtures. This is then combined with the configurational contribution to produce a predicted activity coefficient.

Table VI gives a comparison of predicted and experimental activity coefficients for *n*-alkanes in *n*-alkylbenzenes. Included are results obtained from the contact point treatment assigning six contact points to the phenyl grouping, differentiating between end and middle groups, and allotting contact points equal to the number of hydrogen atoms on the alkyl chain. A similar approach was adopted by one of us (B. W. G.) in a previous publication.[31] Both approaches give satisfactory argeement with theory. The contact point interchange energies obtained from plotting the *n*-hexane + *n*-alkylbenzene data (as with the segment model) that correlate all the experimental results with the above mentioned allotted contact points are as

Table VI: Infinite Dilution Activity Coefficients. *n*-Alkanes with *n*-Alkylbenzenes at 40°[a]

System	Experimental, log γ_f^∞	Segment approach	Contact point approach
	Solutes in 1-Phenyldecane		
n-Pentane	0.060	0.064	0.074
n-Hexane	0.062	0.062	0.064
n-Heptane	0.066	0.065	0.066
n-Octane	0.071	0.069	0.069
	Solutes in 1-Phenyldodecane		
n-Pentane	0.028	0.036	0.038
n-Hexane	0.036	0.039	0.040
n-Heptane	0.046	0.044	0.045
n-Octane	0.051	0.050	0.050
	Solutes in 1-Phenyltetradecane		
n-Pentane	0.016	0.012	0.015
n-Hexane	0.017	0.017	0.017
n-Heptane	0.025	0.024	0.023
n-Octane	0.032	0.031	0.030
	Solutes in 1-Phenylpentadecane		
n-Pentane	0.001	0.003	0.001
n-Hexane	0.003	0.005	0.006
n-Heptane	0.013	0.013	0.013
n-Octane	...	0.020	0.021
	Solutes in 1-Phenylnonadecane		
n-Pentane	−0.051	−0.044	−0.044
n-Hexane	−0.037	−0.037	−0.037
n-Heptane	−0.024	−0.030	−0.027
n-Octane	−0.014	−0.019	−0.017

[a] The estimated experimental error on the activity coefficients is slightly less than 0.002 on log γ_f^∞.

follows: ω/k(end/middle) = 54°K; ω/k(end/benzene) = 86°K; ω/k(middle/benzene) = 23°K. Using twelve contact points, instead of six, for the phenyl grouping gives an equally good correlation to the experimental results. In this case the contact point interchange energies are as follows: ω/k(end/benzene) = 54°K, ω/k(middle/benzene) = 15°K, ω/k(end/middle) = 54°K. The relationship is shown graphically in Figure 2.

(*b*) *The Branched Hydrocarbons + n-Alkylbenzene Mixtures.* The straight chain alkanes and those with various degrees of chain branching in two of the *n*-alkylbenzenes are compared with an equivalent set of data recently published in *n*-octadecane.[26] The same general trends are found in each set of data. Those solutes that show the smallest negative deviations from Raoult's law in *n*-octadecane have the largest positive deviations in 1-phenyldodecane or 1-phenylpentadecane (See Table VII). Those solutes exhibiting the largest

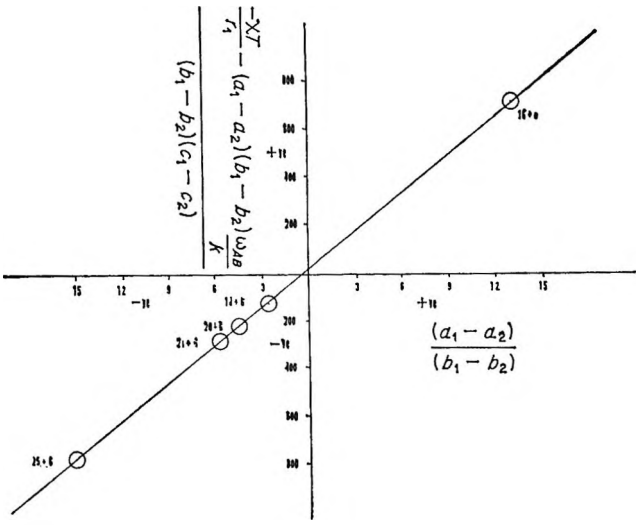

Figure 2. Graph of the n-hexane + n-alkylbenzene data at 40°: quasilattice contact point approach (allowing twelve contact points for the phenyl group); ordinate, $[-(\chi T/r_1) - (a_1 - a_2)(b_1 - b_2)\omega_{AB}/k]/(b_1 - b_2)(c_1 - c_2)$; abscissa, $(a_1 - a_2)/(b_1 - b_2)$; gradient = $\omega_{CH_3/\text{phenyl group}}/k$ (from alkylbenzene); intercept = $\omega_{CH_2CH_2/\text{phenyl group}}/k$ (from alkylbenzene); the numbered graph points refer to the number of carbon atoms in the respective solvent + solute mixture (*e.g.*, 16 + 6 refers to 1-phenyldecane with n-hexane).

Table VII: Comparison of Activity Coefficients. n-Alkanes in 1-n-Alkylbenzenes at 40° with Those for n-Alkanes in n-Octadecane at 35°

	Solvent		
Solute	n-Octadecane[a]	1-Phenyldodecane	1-Phenylpentadecane
n-Pentane	−0.060	0.028	−0.006
n-Hexane	−0.057	0.036	0.003
n-Heptane	−0.049	0.046	0.013
n-Octane	−0.039	0.051	...
2-Methylbutane	−0.047	0.048	0.013
2-Methylpentane	−0.041	0.055	0.022
3-Methylpentane	−0.057	0.039	0.004
2,3-Dimethylbutane	−0.057	0.042	0.008
2,2-Dimethylbutane	−0.025	0.074	...
2,4-Dimethylpentane	−0.013	0.085	0.052
Cyclohexane	−0.117	−0.066	−0.101
Benzene	−0.006	−0.082	−0.107
Hexafluorobenzene	0.320	0.126	0.122

[a] n-Octadecane results from Cruickshank, Gainey, and Young, *Trans. Faraday Soc.*, **64**, 337 (1968).

negative deviations in n-octadecane show the smallest positive deviation in either 1-phenyldodecane or 1-phenylpentadecane. The phenyl grouping on the solvent thus gives an *approximately* constant contribution to each activity coefficient. The results are shown graphically in Figure 3. Cyclohexane and benzene show similar trends in passing from 1-phenyldodecane to 1-phenylpentadecane but the trends are reversed as might be expected when comparing the activity coefficients in n-octadecane with either 1-phenyldodecane or 1-phenylpentadecane.

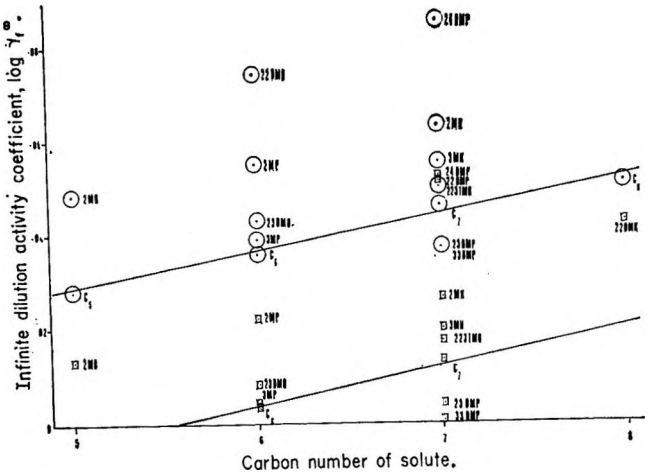

Figure 3. Graph of the log of the solute activity coefficients at infinite dilution *vs.* carbon number; ordinate, log γ_f^∞; abscissa, carbon number of solute; ⊙, solutes in 1-phenyldodecane; ⊡, solutes in 1-phenylpentadecane.

Close examination of the results shows a larger positive activity coefficient for branched chain isomers over the equivalent straight chain species when one or both of the n-alkane terminal groups contain methyl radicals. This suggests that molecules containing the groupings

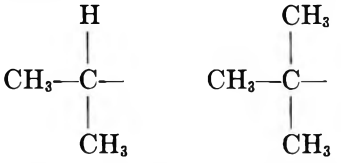

give rise to larger interactions with the respective n-alkylbenzenes than do the equivalent straight chain n-alkanes. It has previously been suggested that terminal groupings play a major part in determining nonelectrolyte interactions.[34] However, apparently, substitution in the middle of a molecule (*e.g.*, 3,3-dimethylpentane) actually reduces the interaction. 2,3-Substituted molecules also give a smaller interaction provided that it does not fall into the first category (*e.g.*, 2,3-dimethylbutane). Within a particular group of branched chain isomers a regular pattern exists. Likewise structurally similar solutes having characteristic groupings (*e.g.*, 2-methyl-substituted compounds) give activity coefficients that vary systematically with increase in chain length.

2,2,3,3-Tetramethylbutane is a particularly interesting hydrocarbon. It has a melting point of 101° and boils at 106.5°.[37] Because the solid has a high vapor pressure it was possible to inject a sample of the vapor which is in equilibrium with the solid. The activity coefficient of 2,2,3,3-tetramethylbutane in 1-phenyl-

(37) Selected Values of Physical and Thermodynamic Properties of Hydrocarbons and Related Compounds, API Project 44, Carnegie Press, 1953.

Table VIII: Interaction Parameters Obtained from Infinite Dilution Activity Coefficients. Hydrocarbons in 1-Alkylbenzenes at 40°

Solute	Solvent: 1-Phenyldodecane, $-\log \gamma_1^{config}$	1-Phenyldodecane, χ	1-Phenylpentadecane, $-\log \gamma_1^{config}$	1-Phenylpentadecane, χ	T_1^c
n-Pentane	0.132	0.369	0.175	0.389	469.8
n-Hexane	0.103	0.325	0.142	0.320	507.9
n-Heptane	0.078	0.286	0.114	0.292	540.2
n-Octane	0.058	0.250	0.090	...	569.4
2-Methylbutane	0.134	0.420	0.177	0.438	461.0
2-Methylpentane	0.100	0.358	0.140	0.373	498.1
3-Methylpentane	0.105	0.331	0.144	0.341	504.4
2,3-Dimethylbutane	0.104	0.335	0.143	0.348	500.3
2,2-Dimethylbutane	0.099	0.398	0.138	...	489.4
2-Methylhexane	0.079	0.327	0.111	0.371	531.1
3-Methylhexane	0.076	0.302	0.088	0.299	535.6
2,3-Dimethylpentane	0.082	0.273	0.115	0.322	537.8
2,4-Dimethylpentane	0.074	0.367	0.112	0.304	520.3
3,3-Dimethylpentane	0.081	0.272	0.118	0.281	536.0
2,2,3-Trimethylbutane	0.080	0.302	0.110	0.373	531.5
2,2,3,3-Tetramethylbutane	0.065	...	0.117	0.269	544.0

pentadecane is considerably different from that of 2,2,3-trimethylbutane in the same solvent. Any future attempt at the accurate prediction of these activity coefficients by a quasilattice approach is likely to be unsuccessful but must first await the accurate prediction of branched chain–straight chain hydrocarbon mixture activity coefficients. Work of this nature is currently being undertaken.

Recently, Luckhurst and Martire[38] have proposed that the interactional contribution to the solute activity coefficient can be obtained by a perturbation treatment based upon an earlier statistical approach by Longuet-Higgins.[39] Their final conclusion is that the interactional contribution for a series of solutes in a given solvent at the same temperature should bear a linear relationship to the solute critical temperature. This idea is supported by literature experimental data and it is concluded that all solute isomers (both straight and branched) can be simultaneously correlated in this manner. If this proposition were finally substantiated, it would provide a simple but powerful approach to nonelectrolyte solution studies and so the present data were subjected to a similar analysis.

The relevant data are given in Table VIII. The data are plotted in Figure 4 which also includes data for solutes in *n*-octadecane.[26]

The correlation is adequate for the *n*-alkanes (although not strictly linear) while the branched chain isomers deviate from a linear least-squares plot of the *n*-alkane data, the deviation depending upon the particular isomer. These data suggest the correlation to be only fair, and indeed plotting the data against several other solute parameters (carbon number for example) gives similar results. Some of the data chosen by Luckhurst and Martire with which to test their data is of unknown quality. The data given by Pease and Thorburn[40] were obtained using multiple sample liquid

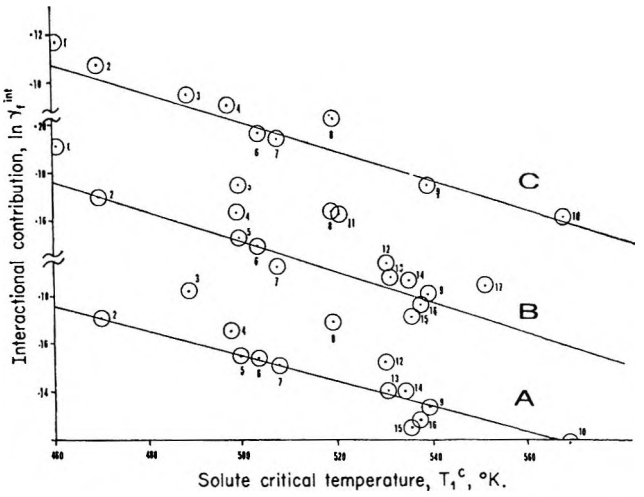

Figure 4. Graph of the interactional contribution to the total activity coefficient, ln γ^{int}, *vs.* the critical temperature of the solute molecule, T_1^c. A, solutes in 1-phenyldodecane at 40°; B, solutes in 1-phenylpentadecane at 40°; C, solutes in *n*-octadecane at 35°; ordinate, ln γ^{int} (*ie.*, χ); abscissa, solute critical temperature (T_1^c°K). The numbers on the points refer to the following solutes: (1) 2-methylbutane, (2) *n*-pentane, (3) 2,2-dimethylbutane, (4) 2-methylpentane, (5) 2,3-dimethylbutane, (6) 3-methylpentane, (7) *n*-hexane, (8) 2,4-dimethylpentane, (9) *n*-heptane, (10) *n*-octane, (11) 2,2-dimethylpentane, (12) 2-methylhexane, (13) 2,2,3-trimethylbutane, (14) 3-methylhexane, (15) 3,3-dimethylpentane, (16) 2,3-dimethylpentane.

injections (which might have invalidated the infinite dilution condition). The data were analyzed in terms of specific retention volume which ignores the pressure dependence of the net retention volume, the fugacity

(38) G. R. Luckhurst and D. E. Martire, *Trans. Faraday Soc.*, **65**, 1248 (1969).

(39) H. C. Longuet-Higgins, *Discussions Faraday Soc.*, **15**, 73 (1953).

(40) E. C. Pease and S. Thorburn, *J. Chromatogr.*, **30**, 344 (1967).

effect (dominated by the solute + carrier gas mixed second virial coefficient), and the direct effect of carrier gas dissolution in the solvent.[3,7] An analysis was made of the Pease and Thorburn data, incorporating all of these corrections. After a consideration of their experimental apparatus a mean column pressure of 1.5 atm was assumed. After subtracting the configurational contribution from the total activity coefficient, the obtained interactional contributions for the higher solutes on hexatriacontane at 120° were negative. In order to explain this behavior it is necessary to use a negative segment interchange energy. Since dispersion forces dictate the type of behavior in these particular mixtures, it must be concluded that the experimental results are slightly in error. Unpublished work from this laboratory suggests the latter to be true. Further, the *n*-heptane + *n*-dotriacontane result at 80° differs from the van der Waals and Herman's[41] static value by over five times the combined experimental error.[42]

It is concluded that the ln γ^{th} *vs.* solute critical temperature relationship is useful in chemical engineering and applied thermodynamical calculations. It is perhaps too restricted in its range of applicability for serious consideration in connection with solution theory, but is not, however, without merit.

(*c*) *Benzene + n-Alkylbenzene Mixtures.* The explanation of the benzene + *n*-alkylbenzene activity coefficients requires a knowledge of four different types of segment interactions. Extending eq 7 gives

$$\frac{-\chi T}{r_1} = (a_1 - a_2)(b_1 - b_2)\frac{\omega_{AB}}{k} + (a_1 - a_2)(c_1 - c_2)\frac{\omega_{AC}}{k} + (a_1 - a_2)(d_1 - d_2)\frac{\omega_{AD}}{k} + (b_1 - b_2)(c_1 - c_2)\frac{\omega_{BC}}{k} + (b_1 - b_2)(d_1 - d_2)\frac{\omega_{BD}}{k} + (c_1 - c_2)(d_1 - d_2)\frac{\omega_{CD}}{k} \quad (8)$$

where d_1 and d_2 are the fractions of components 1 and 2, respectively, of segment type D, while ω_{BD}/k, ω_{CD}/k, and ω_{AD}/k are the segment interchange energies for B, C, and A segments with D segments, respectively. Therefore, once the segments in each molecule have been chosen then the six unknown segment interchange energies must be determined to evaluate χ, the interaction parameter.

In particular binary mixtures studied in this work it is possible to distinguish $-CH_3$, $-CH_2CH_2$, benzene and benzene (from the *n*-alkylbenzene) groupings. The interchange energies between each and all of these groupings are now required.

The position is not quite as hopeless as might at first be imagined if it is possible to utilize the segment interchange energies determined in previous studies.

The *n*-alkane + *n*-alkane studies by Cruickshank, Gainey, and Young[26] established that these binary mixtures could be correlated with a single segment interchange energy. This previous use of $-CH_2CH_2$ and CH_3 segments on the basis of roughly equal segment volume and the segment interchange energy for $-CH_2-CH_2$ with $-CH_3$ segments will be employed in this work.

The benzene + *n*-alkane studies of Gainey and Young[31] established the magnitude of the benzene–end and benzene–middle segment interchange energies again splitting up the molecules into segments on the basis of roughly equal molar volumes.

The *n*-alkane + *n*-alkylbenzene studies of this work have established the interchange energies for benzene (in the *n*-alkylbenzene) with $-CH_3$ groups and with $-CH_2CH_2$ groups.

Therefore, if it is indeed a reasonable approximation to use these previously determined segment interchange energies in this work, then the only unknown segment interchange energy is that for benzene (in the *n*-alkylbenzene) with benzene. The actual numerical values of the segment interchange energies depend entirely upon the choice of segments. Since a consistent method has been chosen for their selection and bearing in mind the four approximations given earlier upon which the theory is based, it would appear that an analysis of the current data in this way is a valid procedure. The unknown interchange energy can reasonably be expected to be very small. There is no restriction on the sign of any particular segment interchange energy but in these mixtures where disperison forces play a dominant part in determining solution behavior it seems reasonable to set the unknown interchange energy to a small nominal positive value (1°K is used here). However, equally well the interchange energy could have been put equal to zero.

The hexafluorobenzene results (Table V) show little change with temperature or with the chain length of the *n*-alkylbenzene. This is contrary to a similar set of results for hexafluorobenzene on long-chain *n*-alkanes.[42,43] However, they all become less positive with increase in temperature and increase in chain length. Identical trends are observed in the benzene results and here the temperature variation is sufficient to evaluate the infinite dilution excess partial molal heats. These results are given in Table IX. They increase linearly from 1-phenyldecane up to 1-phenylnonadecane.

(41) J. H. van der Waals and J. J. Hermans, *Rec. Trav. Chim.*, **69**, 971 (1950).

(42) C. L. Young, Thesis, University of Bristol, 1967.

(43) B. W. Gainey, Thesis, University of Bristol, 1967.

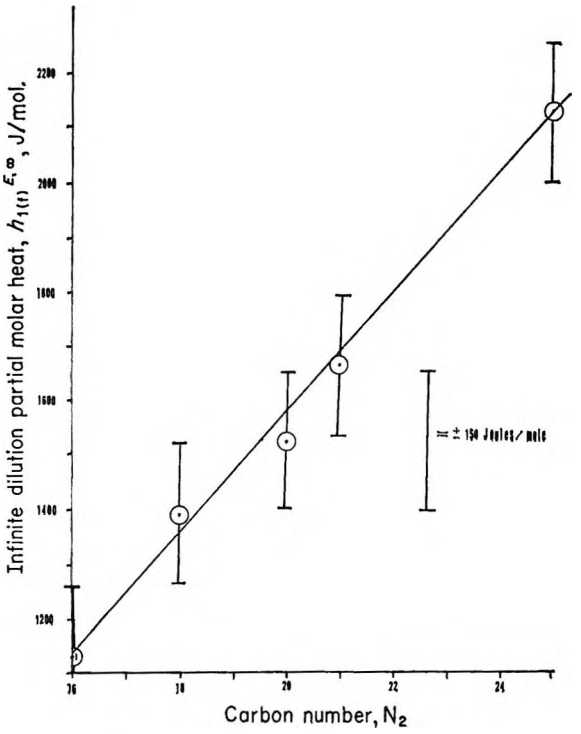

Figure 5. A plot of the infinite dilution partial molar heat of benzene in *n*-alkylbenzenes as a function of the size of the *n*-alkylbenzene; ordinate, $h_{1(t)}^{E,\infty}$, the infinite dilution partial molar heat of benzene in *n*-alkylbenzenes (J/mol); abscissa, carbon number of the *n*-alkylbenzene.

Table IX: Infinite Dilution Excess Partial Molar Enthalpies (J/mol) for Benzene + *n*-Alkylbenzenes

1-Phenyldecane	1130 ± 150
1-Phenyldodecane	1390 ± 150
1-Phenyltetradecane	1520 ± 150
1-Phenylpentadecane	1660 ± 150
1-Phenylnonadecane	2130 ± 150

Figure 5 gives the change in partial molar heat as a function of *n*-alkylbenzene carbon number. The results are not over a wide enough temperature range to say anything about the temperature dependence of the partial molar heat.

The predicted activity coefficients are given in Table X. It is seen that the segment interchange energies evaluated at 40° correlate the work at this temperature quite satisfactorily. However, to obtain equally good correlations at other temperatures it is necessary to invoke a temperature dependence of the segment interchange energies. No results are given since the significance of temperature dependent segment interchange energies is perhaps questionable.

It may be noted that because of the large liquid range of the *n*-alkylbenzenes it is possible to measure the solute activity coefficients for all the solvents over the same temperature range. This was not practically possible in previous work with *n*-alkane solvents where

Table X: Interaction Parameters and Infinite Dilution Activity Coefficients for Benzene with *n*-Alkylbenzenes at 40°

n-Alkylbenzene, total carbon no.	Exptl $\log \gamma_1^{\infty}$	χT (exptl)	χT (theor)	Predicted, $(a)^a$
16	−0.064	78.18	77.63	−0.065
17	...	...	84.05	−0.074
18	−0.082	90.51	89.91	−0.083
19	...	...	95.29	−0.092
20	−0.095	104.94	100.24	−0.102
21	−0.107	107.67	104.81	−0.111
22	...	...	109.04	−0.120
23	...	...	112.95	−0.130
24	...	...	116.62	−0.139
25	−0.151	117.99	120.03	−0.148

[a] Segment interchange energies used were as follows: ω/k°K. CH_3–CH_2CH_2, 157; benzene–CH_3, 107; benzene–CH_2CH_2, 72; benzene (from *n*-alkylbenzene)–CH_3, 174; benzene (from *n*-alkylbenzene)–CH_2CH_2, 40; benzene (from *n*-alkylbenzene)–benzene, 1.

the lower homologs had a relatively high vapor pressure at temperatures above the higher *n*-alkane melting points. The advantage of this eventuality was that the (isochoric) partial molar intrinsic energy at infinite dilution, $u_1^{E,\infty}$ may be calculated from the $h_1^{E,\infty}$ (isobaric) value. The thermodynamic arguments that lead to this conversion have been documented in several papers[44,45] and require a knowledge of the partial molar excess volume at infinite dilution of benzene in the *n*-alkylbenzenes as well as the thermal pressure coefficients κ and $(\partial P/\partial T)_v$. It should then be possible to identify $u_1^{E,\infty}$ with $RT\chi$, the molar solution interchange energy obtained directly from the activity coefficients. Since the required ancillary data are at present unavailable, no such correlation has yet been attempted.

The significance of this work is that it clearly shows that nonelectrolyte mixtures, where specific interactions are absent, do possess a certain degree of segment autonomy and that end interactions do apparently dominate these solution interactions. It would also appear that the four main assumptions upon which the treatment is based are probably valid or indeed a good approximation. This work does not imply that the interchange energies and the chosen segments are necessarily the most appropriate when a wider range of similar mixtures are considered. Since the magnitude of the segment interchange energies depends entirely on the size of segment chosen, these could be treated as two independent variables as has been successfully attempted previously.[34] This more complete analysis of these data is underway whereby it is possible to discover

(44) R. L. Scott, *J. Phys. Chem.*, **62**, 1241 (1960).

(45) R. J. Knight, I. R. McKinnon, I. D. Watson, and A. G. Williamson, *Trans. Faraday Soc.*, **64**, 1769 (1968).

underlying relationships between the various solution theory parameters used in this treatment. The success of this work is that the choice of segments based on equal segment molar volume considerations has at least been consistent. The possibility of being able to predict very accurately the activity coefficient of a particular solute in a multicomponent stationary phase is now very real. Experimental work on this problem is in progress.

Finally, the success of the quasilattice theory equations does not necessarily vindicate the model but rather serves to pinpoint the type of factors that should be considered when a more sophisticated, possibly more realistic, solution model is proposed.

Acknowledgment. B. W. G. acknowledges gratefully the award of a postdoctoral fellowship from the University of California at Los Angeles.

Fluorescence and Photochemistry of the Charge-Transfer Band in Aqueous Europium(III) Solutions

by Yehuda Haas, Gabriel Stein, and Micha Tomkiewicz

Department of Physical Chemistry, The Hebrew University, Jerusalem, Israel *(Received March 10, 1970)*

Aqueous solutions of Eu^{3+} show fluorescence upon excitation at the charge-transfer band. This emission appears to consist of two distinct bands. Evidence is given to support the following assignments: one band is due to charge-transfer emission, the other to emission from an excited state of Eu^{2+}. These assignments, as well as the formation of Eu^{2+} in the system, are further supported by photochemical experiments.

Introduction

The broad absorption band found in aqueous solutions of Eu^{3+} salts has been assigned by Jørgensen[1] to a charge-transfer transition. This assignment has been substantiated by Jørgensen[1] and by Barnes and Day[2] by observing the influence of different ligands on the wavelength of maximum absorption. We have recently reported[3] the observation of new fluorescence bands in aqueous and acetonitrile solutions appearing on excitation in this absorption band. In this paper we report further details and give possible assignment to the band appearing in aqueous solutions. We also report some experiments on photochemical processes which occur on light absorption in the CT band.

Experimental Section

Solutions of $Eu(ClO_4)_3$ were prepared by dissolving Eu_2O_3 99.97% (Fluka) in perchloric acid (Analar grade). $Eu(ClO_4)_2$ solutions were prepared from $EuCO_3$ (kindly supplied to us by Dr. Mayer of the Department of Inorganic Chemistry) by dissolving it in oxygen free perchloric acid. Absorption spectra were obtained with a Cary Model 14 recording spectrophotometer and fluorescence spectra with a spectrofluorimeter described by Feitelson.[4] A xenon arc served as a light source, thus limiting the excitation wavelength to ≥ 250 mμ. Flash technique was used to follow the decay of Eu^{2+}. The flash-photolysis setup was described by Ottolenghi and Rabani.[5]

Photochemical Experiments. These were performed with a special apparatus, designed to measure products gas chromatographically. A quartz vessel was connected to the gas chromatograph; the solution in it was flushed with argon and then illuminated with the appropriate lamp. After illumination, argon was again passed through the solution and into the gas chromatograph.

We used a Varian Aerograph Model 90-P with active carbon column, enabling separation of hydrogen from air. Calibration was performed using aqueous solutions saturated with purified hydrogen (Matheson). Actinometry was done with uranyl oxalate–oxalic acid solution.

Results

Absorption spectra in the region 250–330 mμ were found to follow Beer's law when the concentration was

(1) C. K. Jørgensen, *Mol. Phys.*, 5, 271 (1963).
(2) J. C. Barnes and P. Day, *J. Chem. Soc.*, 3886 (1964).
(3) Y. Haas and G. Stein, *Chem. Phys. Lett.*, 3, 313 (1969).
(4) J. Feitelson, *J. Phys. Chem.*, 68, 391 (1964).
(5) M. Ottolenghi and J. Rabani, *ibid.*, 72, 593 (1968).

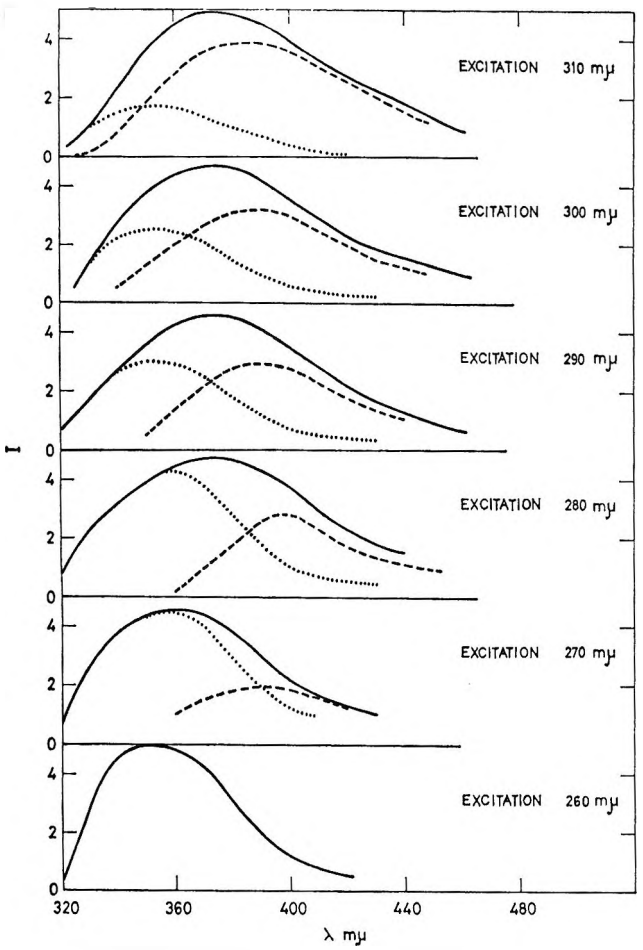

Figure 1. CT emission spectra of aqueous europium perchlorate solutions upon excitation at various wavelengths: ——, total luminescence normalized to same arbitrary scale; . . . . . , band I, excited at 260 mμ, normalized as above; - - - - - -, band II, obtained by subtracting band I from total luminescence.

≥ 0.1 *M*. There is some increase of the molar absorption with increasing pH; however, in the pH range 0–2 no effect on fluorescence was observed. At lower concentrations (<0.1 *M*) optical density was too low for accurate measurements. Such samples were prepared for use by dilution from more concentrated solutions.

Two distinct fluorescence spectra could be distinguished. Excitation with wavelengths up to 260 mμ gave a symmetric emission band with a maximum at 350 mμ. Excitation at longer wavelengths led to a broad, unsymmetrical emission band with a maximum varying between 360 and 380 mμ, explained by increasing admixture of a component peaking ~390 mμ.

Figure 1 shows the changes in total luminescence of the solution upon excitation at different wavelengths. As stated above, excitation at $\lambda < 260$ mμ gave only the symmetrical band centered about 350 mμ, hereafter called band I. The unsymmetric bands appearing upon excitation at higher wavelengths were resolved, as shown in Figure 1, into two more symmetrical bands: band I and another band, which we name band II, centered about 390 mμ. It is seen that as the excitation wavelength is increased, band II becomes stronger than band I. We could not obtain band II without band I. Nevertheless, the evidence presented shows conclusively that the total luminescence at longer wavelengths is not a distorted image of band I, but the superposition of two distinct bands.

Figure 2 shows the absorption band together with the two emission bands. It is evident from the figure that neither band is a mirror image of the absorption band. Excitation spectra, corrected for lamp and monochromator spectral response for the two bands, are given in Figure 3. The excitation spectrum of band I seems to coincide with the absorption spectrum.

It was found that the normalized intensity of band I was dependent upon the concentration. As shown in Figure 4, the intensity decreased with increasing concentration in the 0.2–1 *M* range. At lower concentrations the intensity is constant within experimental error. The concentration quenching does not follow a simple Stern–Volmer law. Oxygen did not quench either fluorescence to a measurable degree. For concentrations where no concentration quenching was observed, the quantum yield was 0.06 and 0.001 for bands I and II, respectively, as measured against aqueous solutions of sodium salicylate as a standard.[6]

An oxygen-free solution of $Eu(ClO_4)_2$ was prepared. Its spectrum did not change markedly when kept in the dark.

This solution did not show any fluorescence upon excitation at 260, 280, or 310 mμ, *i.e.*, at the well-known absorption bands of Eu^{2+} aqueous solutions. No emission was observed even upon working with the most sensitive setups of the instrument. We can thus safely conclude that the quantum yield of fluorescence from Eu(II) aqueous solutions is less than 10^{-5}. This result is in agreement with previous work.[7]

Discussion

The charge-transfer band which is responsible for the absorption is due to a transfer of an electron from an orbital centered mainly on the water molecule to an orbital centered mainly on the Eu(III) ion.[1] Thus the transition may be represented by the formula

$$Eu^{3+}\text{–}H_2O \xrightarrow{h\nu} [Eu^{2+}\text{–}H_2O^{+}]^* \qquad (1)$$

assuming a one-electron transition and neglecting the influence of other water molecules of the solvation shell. The excited species may lose its extra energy by one of the following processes: (1) radiative coupling to ground state; (2) nonradiative coupling to ground state either by intra- or by intermolecular processes; (3) transition to a new chemical species which we suggest, for reasons to become soon apparent, to be an excited europous ion.

(6) (a) G. Weber and F. W. J. Teale, *Trans. Faraday Soc.*, **53**, 646 (1957); (b) G. Stein and M. Tomkiewicz, in press.

(7) F. D. S. Butement, *Trans. Faraday Soc.*, **44**, 617 (1948).

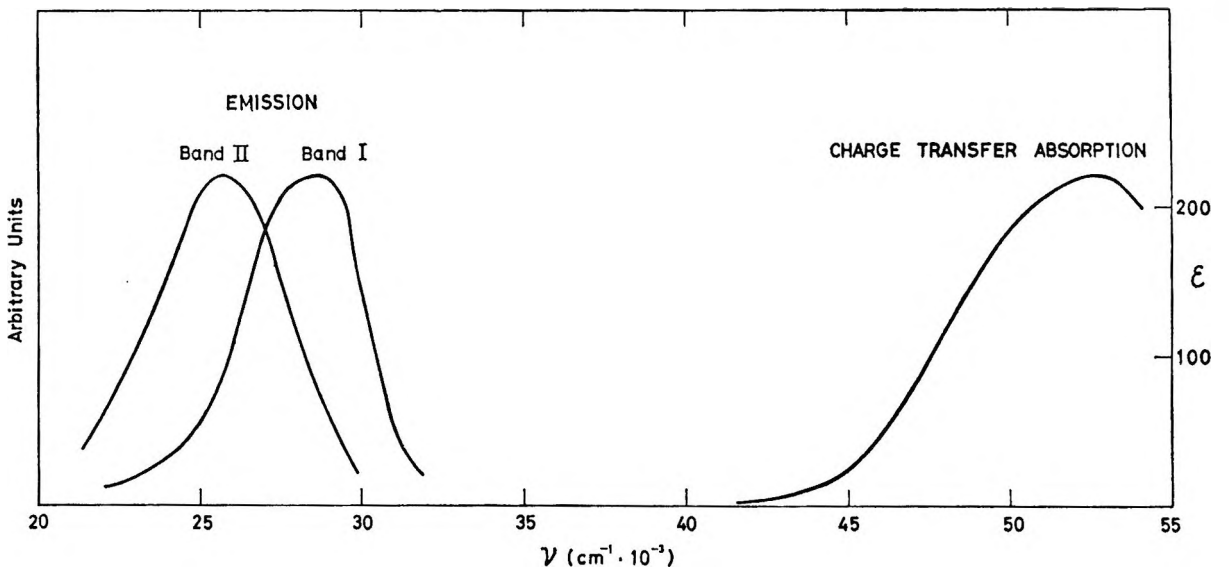

Figure 2. Absorption and emission CT spectra of aqueous europium perchlorate solutions. The spectra are normalized to unit height.

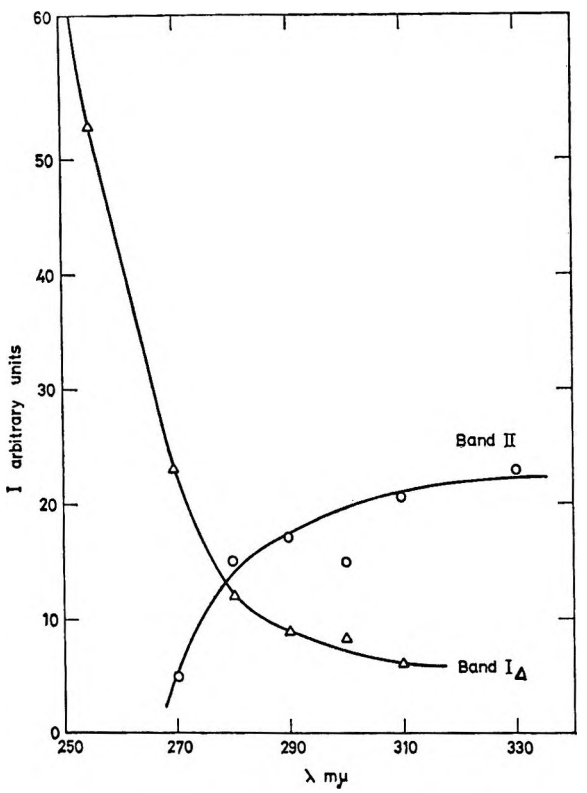

Figure 3. Excitation spectra of band I and II, derived from Figure 1. Data corrected for spectral dependence of exciting light intensity: Δ-Δ-Δ, band I; O-O-O, band II.

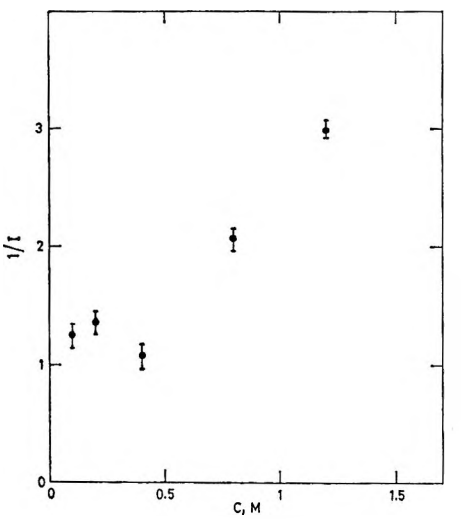

Figure 4. Influence of concentration on the intensity of band I. Excitation at 260 mμ. Reciprocal intensity is given in arbitrary units for emission at 350 mμ.

Our results may be fully accounted for by considering these three processes. The assumption of an excited europous ion is crucial to this discussion, and a large part of the work was devoted to its verification.

The following possibilities exist for the fate of this, as yet unspecified, excited europous ion. (1) The formation of the europous ion must be accompanied by oxidation of a water molecule to H_2O^+, equivalent to a hydroxyl radical

$$H_2O^+ \longrightarrow OH + H_{aq}^+ \qquad (2)$$

These two species are formed close to each other, so that reoxidation of the ion to the +3 state by geminate recombination with the hydroxyl radical is possible

$$(Eu^{2+})^* \cdots OH \longrightarrow Eu^{3+}OH^- \qquad (3)$$

(2) Oxidation by other oxidizing agents present in the solution, *e.g.*, water, may take place by the process

$$(Eu^{2+})^* + H_3O^+ \longrightarrow Eu^{3+} + H + H_2O \qquad (4)$$

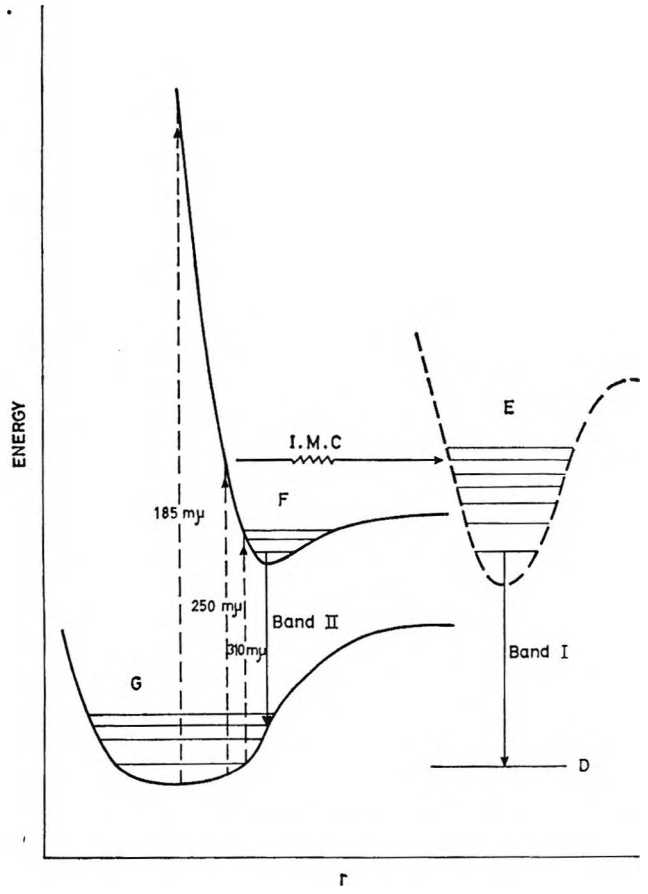

Figure 5. Energy level diagram for the system Eu^{3+}–H_2O. r is internuclear distance along the critical coordinate responsible for the transitions observed. G is the ground-state level of the charge-transfer complex [Eu^{3+}–H_2O]. F is an excited state of the same charge-transfer complex. D is the ground-state level of Eu^{2+} hydrate. F is an excited state of the same charge-transfer complex. D is the ground-state level of Eu^{2+} hydrate. E is an excited state of Eu^{2+} hydrate. I.M.C. denotes intermolecular crossing of the excited state of the charge-transfer complex into the excited state of Eu^{2+} hydrate. The transitions observed in the spectrum are denoted by arrows.

yielding atomic H. This process may result in the formation of molecular hydrogen. (3) There may be emission of a light quantum and transition to ground state. (4) Nonradiative coupling to ground state may also occur.

By considering the processes enumerated above, we can adequately account for our results with the aid of the following energy level diagram (Figure 5).

This figure, given in the "critical vibration" approximation shows the charge-transfer absorption band as a transition from ground state G to an excited state F with a shallow minimum as is common with this type of transition.[8] Absorption at wavelengths shorter than about 270 mμ leads to dissociation within few vibrations, leading to an excited state of Eu^{2+}, E, which may or may not fluoresce. Absorption at wavelengths longer than 270 mμ leads to relaxation to the lowest vibrational level of the excited state. This process may lead finally to fluorescence from this level to ground state.

Thus the fluorescence from the yet undefined $(Eu^{2+})^*$ ion is our band I, and the emission from the CT excited state band II. This energy level diagram is further supported by the excitation spectra. Band I seems to have an excitation spectrum coinciding with the absorption spectrum. Band II has an excitation spectrum beginning at 270 mμ. The fact that neither band is a mirror image of the absorption spectrum is also readily accounted for by this model.

The deviation from Stern–Volmer kinetics is further evidence that band I does not result from the energy level excited directly by the absorbed light. If the assignment of band I emission is correct, it must be due to an energy level inaccessible by direct absorption of light from the ground state of Eu^{2+}. That this is so is demonstrated by the absence of emission on exciting the accessible levels in Eu^{2+} solutions. This situation is reminiscent of the triplet phosphorescence in aromatic compounds, though no simple assignment of the state concerned suggests itself. Laser measurements[3] indicate very short lifetimes, of the order of less than 10 nsec for one component and about 20–30 nsec of the second. These values, combined wiith the quantum yield, lead to a natural lifetime of about 10^{-6} sec, another evidence for a forbidden transition.

The transition observed in *emission* may be an allowed one to a state with energy slightly higher than ground state. The pertinent energy diagram is shown in Figure 6.

The ground state g of Eu^{2+} can be radiatively coupled to an excited state f, which does not fluoresce but loses its energy to solvent, in the case of water most probably by interacting chemically with the formation of H atoms. The transition f → e is thus highly improbable. If e, this other excited state of Eu^{2+}, is somehow populated (*e.g.*, by the mechanism suggested above for the CT complex) it can return to ground state g *via* state d. The existence of bivalent europium in the solution exciting the charge transfer of Eu^{2+} cannot be proved by fluorescence measurements alone. As mentioned before, it is highly probable that an excited species of Eu^{2+} would react rapidly with water. It is well known that aqueous solutions of Eu^{2+} are stable in the dark, but decompose rapidly upon illumination. There is no reason to suppose that excited states reached by means other than direct light absorption should be less reactive. They lead primarily to formation of hydrogen atoms as in reaction 4 and then to hydrogen molecules.

Thus, evolution of hydrogen upon illuminating the solution in the charge-transfer band should be a proof of the mechanism suggested.

(8) S. P. McGlynn, *Chem. Rev.*, **58**, 1113 (1958).

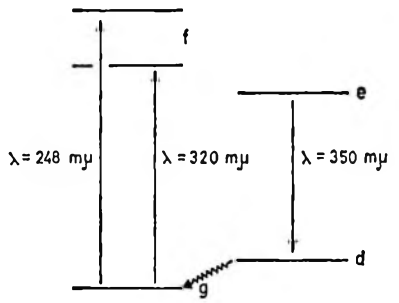

Figure 6. Possible energy level diagram for Eu^{2+} ion in aqueous solution.

Another possibility of proving the existence of Eu^{2+} is direct observation of its characteristic absorption spectrum.

These considerations led to photochemical experiments, in which we tried to obtain hydrogen upon irradiating the solution in the charge-transfer absorption band.

Hydrogen Formation

Experiments in which solutions with different Eu^{3+} (0.5–0.05 *M*) concentration were illuminated in the absence of O_2 with the 2537 Å ($\epsilon = 0.3$) line gave negative results, and no evolution of molecular hydrogen was detected. It was concluded that without added H atom scavengers the inevitable impurities in the solution scavenged any H atoms produced at the primary stage. In order to overcome this difficulty, ethanol was used as a scavenger for H atoms[9]

$$CH_3CH_2OH + H \longrightarrow H_2 + CH_3CHOH \quad (5)$$

Ethanol also scavenges OH radicals, according to

$$CH_3CH_2OH + OH \longrightarrow H_2O + CH_3CHOH \quad (6)$$

yielding the same organic radical.

Changing the concentrations of ethanol had little effect on either absorption or fluorescence spectra. Illumination of a reference solution, identical with the test solutions but not containing Eu^{3+} ions, did not produce hydrogen.

The results are given in Table I, and prove the formation of hydrogen. The quantum yield was calculated by taking into account only the absorption of the charge transfer band and cannot be clearly related to a definite mechanism. Its high value makes it probable that in some stage of the reaction sequence (Eu^{2+}) is produced, which absorbs significantly at 254 mμ ($\epsilon \simeq 2000$). In addition to the formation of Eu^{2+} by light emission from the excited state, a process that is likely to occur is the reduction of Eu^{3+} by the radical formed in reactions 5 and 6

Table I

Sample	Concn, *M* Eu^{3+}	Concn, *M* EtOH	Concn, *M* $HClO_4$	Quantum yield for hydrogen formation
1	0.048	0.07	2.38	6
2	0.048	0.007	2.38	3
3	0.048	0.007	0.2	6.5

$$CH_3CHOH + Eu^{3+} \longrightarrow CH_3CHO + Eu^{2+} + H^+ \quad (7)$$

A similar reaction has been observed[10] in the photochemistry of Fe^{3+} in aqueous solution.

(9) C. Lifshitz and G. Stein, *J. Chem. Soc.*, 3706 (1962).
(10) B. Behar and G. Stein, to be published.

Temperature-Dependent Splitting Constants in the Electron Spin Resonance Spectra of Cation Radicals. II.[1] The Methoxyl Group

by Paul D. Sullivan

Department of Chemistry, Ohio University, Athens, Ohio 45701 *(Received January 20, 1970)*

The temperature dependence of the proton splitting constants of the cation radicals of 1,4-dimethoxybenzene (DMB), 1,4-dimethoxynaphthalene (DMN), 9,10-dimethoxyanthracene (DMA), and dimethoxydurene (DMD) have been measured. From the temperature dependencies of the methoxyl proton splitting constants potential barriers to rotation have been estimated from approximate methods to be 4.9 ± 0.4 kcal for DMN, 0.6–0.9 kcal for DMA, 1.75 ± 0.15 kcal for DMD, and >16 kcal for DMB. Semiempirical molecular orbital calculations have also enabled us to obtain a qualitative fit to the signs and magnitudes of the temperature dependencies of all the other proton splitting constants.

Introduction

The esr spectra of compounds containing methoxyl groups often show hyperfine interactions attributed to the protons of this group. The interaction is believed to occur *via* a hyperconjugative coupling between the protons and the unpaired spin located on the oxygen atom, and as such, is expected to have a positive sign for positive spin density on the oxygen atom. In the case of substituted aromatic compounds the spin density on oxygen arises from overlap with the $p\pi$ orbitals of the aromatic ring and will be at a maximum when the methoxyl group is coplanar with the aromatic plane. Working against this tendency for coplanarity will be steric interactions between the methoxyl group and adjacent groups on the ring. The methoxyl group may, therefore, be treated as in a potential well with a minimum either in or close to the aromatic plane. Torsional oscillations about this potential minimum may then lead to a temperature dependence of the splitting constant of the methoxyl group protons,[2] which will be a function of the depth of the potential minimum.

Studies of the temperature dependence of the splitting constants of β-alkyl protons[3,4] have led to estimates of their potential barrier to rotation. One of the objects of this paper was to apply the theories developed for β-alkyl protons to the protons of the methoxyl group and obtain estimates for their barriers to rotation in a series of compounds. In this regard, some preliminary results of this study have already appeared.[1]

Experimental Section

Of the compounds studied, 1,4-dimethoxynaphthalene and 9,10-dimethoxyanthracene were prepared from the corresponding quinones by methods described in the literature.[5] A similar attempt to form 1,4-dimethoxy 2,3-dimethylnaphthalene was unsuccessful. 1,4-Dimethoxybenzene and dimethoxydurene (1,4-dimethoxy-2,3,5,6-tetramethylbenzene) were obtained as previously described.[6,7] The cation radicals were prepared with the aluminum chloride–nitromethane system.[8] Attempts to form the cation radicals in the sulfuric acid–nitromethane system[9] were unsuccessful, the spectrum observed being that of the corresponding hydroxyl compound. The esr spectra were measured on a modified Varian V-4560 spectrometer equipped with a TE_{104} dual cavity operating at modulation frequencies of 100 and 10 kHz. The sample under investigation was placed in the front cavity, the temperature of which could be controlled in the usual way. The rear cavity contained the Wurster's Blue cation radical (for which the splitting constants have been accurately determined against a proton resonance probe[10]) as a means of calibrating the field for each spectrum taken. The splitting constants of the sample under investigation were obtained by a least-squares analysis,[11] having first identified the lines in the spectrum with their appropriate spectral index numbers, $\bar{M}_i$. In order to calculate the temperature dependence, the spectra were completely analyzed in the above manner at a minimum of four temperatures. At each temperature at least two, and more normally four, spectra were analyzed.

(1) Part I: P. D. Sullivan, *J. Phys. Chem.*, **73**, 2790 (1969).

(2) W. F. Forbes and P. D. Sullivan, *J. Chem. Phys.*, **48**, 1411 (1968).

(3) E. W. Stone and A. H. Maki, *ibid.*, **37**, 1326 (1962).

(4) M. D. Sevilla and G. Vincow, *J. Phys. Chem.*, **72**, 3647 (1968).

(5) J. S. Meek, P. A. Monroe, and C. J. Bouboulis, *J. Org. Chem.*, **28**, 2572 (1963).

(6) W. F. Forbes and P. D. Sullivan, *Can. J. Chem.*, **44**, 1501 (1966).

(7) P. D. Sullivan, *J. Amer. Chem. Soc.*, **89**, 4294 (1967).

(8) W. F. Forbes and P. D. Sullivan, *ibid.*, **88**, 2862 (1966).

(9) P. D. Sullivan and J. R. Bolton, *J. Magn. Resonance*, **1**, 356 (1969).

(10) W. Knolle and J. R. Bolton, private communication.

(11) J. R. Bolton and G. K. Fraenkel, *J. Chem. Phys.*, **40**, 3307 (1964).

Table I: Summary of Splitting Constants and Temperature Coefficients for the Compounds Studied

Cation radical	Splitting const	Temp coeff of splitting const, mG/deg	*g* factor
1,4-Dimethoxybenzene	$a^{H}_{CH} = 2.26^{a} \pm 0.01$	*b*	2.00368 ±
	$a^{H}_{OCH_3} = 3.36^{a} \pm 0.01$	±0.09[c]	0.00002
Dimethoxydurene[d]	$a^{H}_{CH_3} = 2.119 \pm 0.010$	0.28 ± 0.05	2.00330 ±
	$a^{H}_{OCH_3} = 2.955 \pm 0.010$	−1.51 ± 0.09	0.00002
1,4-Dimethoxynaphthalene[e]	$a^{H}_{CH}(2,3) = 3.354 \pm 0.006$	*b*	
	$a^{H}_{CH}(5,8) = 1.456 \pm 0.006$	0.32 ± 0.04	2.00321 ±
	$a^{H}_{CH}(6,7) = 0.699 \pm 0.006$	*b*	0.00002
	$a^{H}_{OCH_3} = 2.194 \pm 0.004$	−0.41 ± 0.003	
9,10-Dimethoxyanthracene[f]	$a^{H}_{CH}(1,4,5,8) = 1.752 \pm 0.002$	0.44 ± 0.05	2.00312 ±
	$a^{H}_{CH}(2,3,6,7) = 1.084 \pm 0.002$	*b*	0.00002
	$a^{H}_{OCH_3} = 1.186 \pm 0.001$	−1.15 ± 0.10	

[a] Averaged values. [b] No significant temperature dependence within the experimental error. [c] Upper limit. [d] Splitting constants measured at −80°. [e] Splitting constants measured at −73°. [f] Splitting constants measured at −55°.

Results

1,4-Dimethoxybenzene (*DMB*). The cation radical of DMB has been studied in detail in previous papers.[6,12] The spectrum was analyzed in terms of *cis* and *trans* isomers[6] at temperatures below room temperature. The isomers were attributed to the constraint of the methoxyl groups in the aromatic plane. The methoxyl group splitting constants showed no significant trends when the temperature was varied. From the errors involved in the measurement of the splitting constants it was possible to place an upper limit (0.09 mG/deg) on the temperature dependence of the methoxyl group splitting constant.

Dimethoxydurene (*DMD*). Previous studies[7] have shown that the cation radical of DMD exists as only one species over the temperature range −80 to −30°. The methoxyl proton splitting constant was found to be significantly temperature dependent, a linear least-squares analysis yielding a temperature coefficient of −1.51 ± 0.09 mG/deg.

1,4-Dimethoxynaphthalene (*DMN*). The esr spectrum of the cation radical of DMN was examined over the temperature range −75 to −10° and was found to consist of only one species throughout this range. The spectrum has not been reported previously but was easily analyzed in terms of splittings from one group of six equivalent protons, and three groups, each of two equivalent protons. The splitting constants and assignments are shown in Table I at a temperature of −73°. The assignments were made on the basis of molecular orbital calculations and by analogy with the results for 1,4-dihydroxynaphthalene.[13,14] A study of the temperature dependence of the splitting constants showed that the methoxyl group had a temperature coefficient of −0.41 ± 0.03 mG/deg. The splitting constants of the protons at positions 2,3 and 6,7 gave no significant temperature dependence within the experimental error, while the protons at positions 5,8 gave a temperature coefficient of 0.32 ± 0.04 mG/deg.

9,10-Dimethoxyanthracene (*DMA*). The esr spectrum of the cation radical of DMA is shown in Figure 1 at three temperatures. The overall features of the spectrum immediately indicate that some of the splitting constants are temperature dependent. It was only possible to obtain well resolved spectra suitable for analysis in the temperature range −55 to −24°. The spectra are easily analyzed in terms of one species with splittings due to a group of six and two groups of four equivalent protons. Table I shows the splitting constants at −55° and their assignments, which were made on the basis of molecular orbital calculations. The analysis of the temperature dependence of the splitting constants showed that the methoxyl group has a temperature coefficient of −1.15 ± 0.10 mG/deg, while protons at positions 1,4,5,8 have a temperature coefficient of 0.44 ± 0.05 mG/deg and protons at positions 2,3,6,7 have no temperature dependence within the experimental error.

Other Methoxyl Containing Cation Radicals. During the course of our studies several other cation radicals containing methoxyl groups have been examined.[2] These include the cation radicals of 2,5-dimethyl-, 2,5-di-*t*-butyl, and 2,5-dihydroxy-1,4-dimethoxybenzene, 2,3-dimethyl-1,4-dimethoxybenzene, and 1,2,4,5-tetramethoxybenzene. Although these compounds were not studied as accurately as the other compounds it was apparent that only one of these compounds showed a significantly large temperature dependence of the methoxyl group splitting constant. This occurred in the radical derived from 2,5-di-*t*-butyl-1,4-di-

(12) W. F. Forbes, P. D. Sullivan, and H. M. Wang, *J. Amer. Chem. Soc.*, 89, 2705 (1967).

(13) J. R. Bolton, A. Carrington, and J. dos Santos Veiga, *Mol. Phys.*, 5, 465 (1962).

(14) P. D. Sullivan, unpublished results.

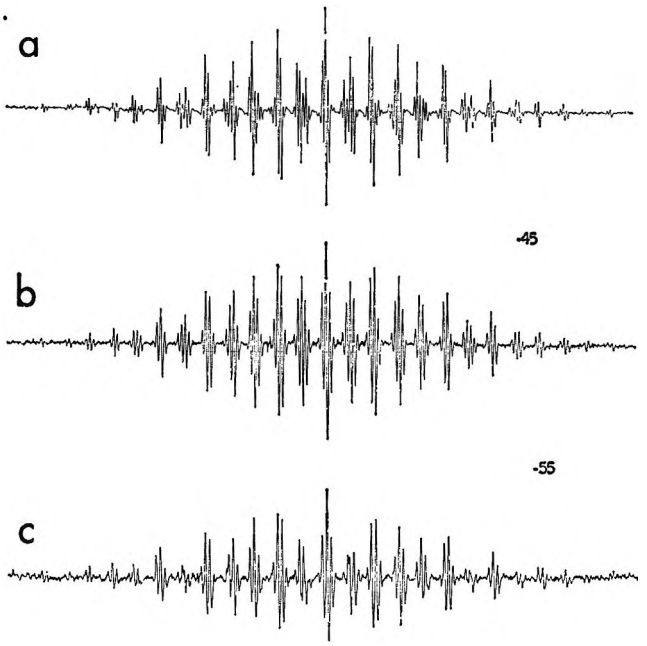

Figure 1. The esr spectrum of the cation radical of 9,10-dimethoxyanthracene at (a) −24°, (b) −45°, and (c) 55°.

methoxybenzene and gave a temperature coefficient of −0.72 mG/deg. All the other compounds showed little or no temperature dependence of the methoxyl group splitting constant.

Discussion

The Methoxyl Group. In the limit that the methoxyl group is constrained in the aromatic plane with no torsional oscillations, the splitting constant of the protons of the methoxyl group should be given by eq

$$a^{H}_{OCH_3} = Q^{H}_{OCH_3}\rho_O^{\pi} \quad (1)$$

1.[15] $Q^{H}_{OCH_3}$ should be positive, reflecting the hyperconjugative mechanism of the coupling, and ρ_O^{π} is the unpaired spin density in the pπ orbital of the oxygen atom for the planar methoxyl group. In reality, the methoxyl group is located in a potential minimum centered around the aromatic plane ($\theta = 0°$), and torsional oscillations will occur around this minimum. The effect of an out of plane movement ($\theta > 0°$) by the methoxyl group will be to decrease the overlap between the ring carbon and the oxygen atom (*i.e.*, k_{OC}, the overlap integral parameter in the HMO theory is expected to decrease by the factor cos θ). To a first approximation the spin density on the oxygen atom should, therefore, decrease by $\cos^2\theta$. For an angle of twist, θ, out of the plane, eq 1 should be modified to

$$a^{H}_{OCH_3} = Q^{H}_{OCH_3}\rho_O^{\pi}\cos^2\theta \quad (2)$$

eq 2. In practice, however, a time-averaged value of θ is required, thus giving eq 3. Since the time-aver-

$$a^{H}_{OCH_3} = Q^{H}_{OCH_3}\rho_O^{\pi}\langle\cos^2\theta\rangle \quad (3)$$

aged value ($\langle\cos^2\theta\rangle$) will change with temperature, the experimental results can be discussed qualitatively in terms of eq 3 as follows. The observation of *cis* and *trans* isomers for DMB together with the insensitivity of the methoxyl group splitting constant to changes in temperature indicates that the methoxyl group is constrained close to the aromatic plane ($\theta = 0°$) in a fairly deep potential well which allows only very small torsional oscillations. This large potential barrier slows down the rate of rotation (jumping) of the methoxyl group to such an extent that on the time scale of the esr experiment the isomers exist long enough to give a characteristic spectrum.

DMD, on the other hand, shows the presence of only one species and has a relatively large temperature dependence of the methoxyl group splitting constant, although the absolute value of the splitting constant is only 12–18% smaller than that of DMB. These results indicate that because of the increased steric interactions the methoxyl group is constrained in a much shallower potential well, with considerable torsional oscillation out of the aromatic plane ($\theta > 0°$). The smaller potential barrier allows the methoxyl group to rotate (or jump) much faster than in DMB, so that on the esr time scale only a time-averaged spectrum of one species is observed.

DMA is qualitatively similar to DMD, the methoxyl group torsionally oscillating in a shallow potential minimum leading to a relatively large temperature dependence of the methoxyl group splitting constant. DMN, however, might be expected to exist preferentially in a *cis* configuration leading to a smaller temperature dependence than DMD or DMA.

Qualitatively, the potential barrier to rotation about the >C–O bond might be predicted to increase in the order DMB > DMN > DMA $\cong$ DMD.

Quantitatively, the value of $\langle\cos^2\theta\rangle$ may be evaluated using a model similar to that proposed for a torsionally oscillating alkyl group.[3,4] If it is assumed that the methoxyl group oscillates harmonically in a sinusoidal twofold potential of maximum barrier height V_0, with the potential minimum occurring at $\theta = 0°$, then the time-averaged value of $\cos^2\theta$ can be evaluated assuming a Boltzmann distribution over the energy states. For values of the energy $E_i < V_0$, the limiting harmonic oscillator functions are used while for $E_i > V_0$ the limiting free rotator functions are used. The calculations were performed with a slightly modified version of a program written by Carter.[16] Input parameters required are the maximum barrier height V_0 and the reduced moment of inertia I_r. The values of I_r were 0.47, 0.565, 0.579, and 0.567 × 10^{-38} g cm^2 for DMB, DMN, DMA, and DMD, respectively. Since the value of $\langle\cos^2\theta\rangle$ is not very sensitive to changes in I_r, only two

(15) Contributions from a spin polarization mechanism have been neglected since they are expected to be small.

(16) M. K. Carter, Dissertation, University of Washington, 1966.

Table II: Calculated Temperature Coefficients for Different Barrier Heights for DMN, DMD, and DMA

				1,4-Dimethoxynaphthalene[a]					
V_0, kcal	2.0	3.0	4.0	4.6	4.7	4.8	4.9	5.0	6.0
Calcd temp coeff,[b] mG/deg	−1.01	−0.68	−0.52	−0.44	−0.43	−0.42	−0.41	−0.40	−0.33
				Dimethoxydurene[c]					
V_0, kcal	0.7	1.0	1.2	1.4	1.6	1.7	1.8	1.9	2.0
Calcd temp coeff,[d] mG/deg	−2.02	−1.97	−1.87	−1.71	−1.68	−1.49	−1.50	−1.34	−1.34
				9,10-Dimethoxyanthracene[e]					
V_0, kcal	0.3	0.5	0.6	0.7	0.8	0.9	1.0	1.1	1.2
Calcd temp coeff,[f] mG/deg	−0.90	−1.02	−1.05	−1.06	−1.05	−1.06	−1.01	−1.01	−0.95

[a] Temperature range 200–265°K. [b] Experimental −0.41 ± 0.03. [c] Temperature range 193–303°K. [d] Experimental −1.51 ± 0.09. [e] Temperature range 218–249°K. [f] Experimental −1.15 ± 0.10.

values of I_r were used, namely 0.47 and 0.573 × 10^{-38} g cm². Values of $\langle\cos^2\theta\rangle$ were then calculated for various barrier heights (1–20 kcal) and for a range of temperatures (200–300°K). The calculated data were treated on the assumption that eq 3 is valid. A temperature coefficient was then calculated over the experimental temperature range. The calculated temperature dependence is not truly linear with temperature but the curvature is only slight and no serious errors will be introduced by treating it as a linear function. The calculated temperature coefficients in mG/deg are shown in Table II for DMN, DMD, and DMA for various barrier heights. A comparison of the calculated and experimental temperature coefficients enables us to estimate the barrier height for DMN to be 4.9 ± 0.4 kcal, and for DMD to be 1.75 ± 0.15 kcal. For DMA the maximum calculated temperature coefficient is −1.06 mG/deg, occurring at a potential barrier of between 0.6 and 0.9 kcal as compared to an experimental value of −1.15 ± 0.10 mG/deg. For DMB it is possible to calculate a minimum value of V_0 corresponding to a temperature coefficient of −0.09 mG/deg; this occurs at a barrier height of 16 kcal.

The relative magnitudes of these results are in agreement with the qualitative conclusions. The significance of the actual barrier heights should, however, be considered carefully in the light of the assumptions inherent in the calculations. Two assumptions of obvious concern are first, the $\cos^2\theta$ dependence of the oxygen spin density and second, the shape of the potential barrier. The former assumption is discussed in more detail in the next section. The latter assumption is almost certainly an oversimplification especially in the case of DMA where a double potential minimum at $\pm\theta°$ seems more likely than the single potential minimum at $\theta = 0°$. This would have the result of including contributions for larger angles of torsion which could lead to larger temperature dependencies. In addition at barrier heights of less than 5 kcal it is possible that errors may be introduced through the use of the limiting harmonic oscillator and rigid rotator approximations. At these low barrier heights it would be more reliable to use solutions of the Mathieu equation.[17,18]

Molecular Orbital Calculations. These calculations were carried out using the McLachlan perturbation corrections[19] to the Hückel LCAO–MO method (λ = 1.20). The object of the calculations was twofold. First a set of coulomb and resonance integral parameters for oxygen (h_O, k_{OC}) were needed which would reproduce the spin density distributions at the positions of known spin density (*i.e.*, from the proton splitting constants $a^H_{CH} = Q^H_{CH}\rho_C^\pi$, where $Q^H_{CH} = -27$G). Second, by small changes in the k_{OC} and/or h_O parameters it was hoped to reproduce the spin density changes with temperature.

(*a*) *Reproduction of the Experimental Spin Densities.* The first problem was how to treat the methoxyl group. Several methods exist for approximately including methyl groups in simple HMO calculations. The method chosen was the hyperconjugative model of Coulson and Crawford[20] with the following parameters[21] for the methoxyl group (O–C′–X): $h_{C'} = -0.1$, $h_X = -0.50$, $k_{OC'} = 0.70$, $k_{CX} = 2.50$.

The amount of available information from the experimental proton splitting constants is unfortunately insufficient to evaluate the complete spin-density distribution for the compounds studied. Therefore, after consideration of several possibilities the following ap-

(17) N. L. Bauld, J. D. McDermed, C. E. Hudson, Y. S. Rim, J. Zoellar, R. D. Gordon, and J. S. Hyde, *J. Amer. Chem. Soc.*, **91**, 6666 (1969).

(18) We are presently undertaking to make a comparison between the two methods.

(19) A. D. McLachlan, *Mol. Phys.*, **3**, 233 (1960).

(20) C. A. Coulson and V. A. Crawford, *J. Chem. Soc.*, 2052 (1953).

(21) D. Lazdins and M. Karplus, *J. Amer. Chem. Soc.*, **87**, 920 (1965).

proach was taken. DMN was considered first, since for this molecule there are three proton splitting constants which together with McConnell's equation give the spin densities at three carbon atoms. The assignment of the spin densities or splitting constants to their appropriate position on the naphthalene ring was made in accordance with a preliminary calculation with approximate values for the h_O and k_{OC} parameters. By analogy with previous calculations[22,23] on hydroxyl-substituted compounds it was expected that h_O should be in the range 1.0–2.0 and k_{OC} in the range 0.8–1.4. Within these ranges the MO calculations were consistent with an assignment as shown in Table I. To obtain accurate agreement with the experimental spin densities, calculations were carried out over the whole range of suggested parameter values. From the calculations it was possible to construct plots of the values of h_O and k_{OC} which give the experimental spin densities ("iso ρ" lines). Three "iso ρ" lines result, one for each of the three positions. For exact agreement of all three positions these " iso ρ" lines should intersect at a point. For the indicated parameters this did not occur. In order to bring about exact agreement for all three positions it was found necessary to use some auxiliary parameters. As stated earlier, one might expect the methoxyl groups in DMN to exist in a preferred *cis* configuration. If this is indeed the case it should be recalled that in order to reproduce the spin density distribution in the *cis* and *trans* isomers of DMB[6] it was necessary to use auxiliary parameters for the carbon atoms. By analogy, this means that for DMN the coulomb integrals of carbon atoms 2 and 3 should increase by a small amount. Calculations showed that a value of $h_C(2) = h_C(3) = 0.17$ resulted in the intersection of the three "iso ρ" lines. This value of the auxiliary parameter is hearteningly close to that employed for the *cis* isomer of DMB. Using these additional parameters almost exact agreement with the experimental spin densities at $-73°$ was found when $h_O = 1.57$, $k_{OC} = 1.03$, and $Q^H_{CH} = -27$ G. The results are shown in Table III and if it is assumed that the $\rho'_O{}^\pi$ obtained in these calculations is equal to $\rho_O{}^\pi \langle \cos^2 \theta \rangle$ (where $\rho_O{}^\pi$ is the spin density on oxygen in the planar configuration and $\rho'_O{}^\pi$ is the spin density on oxygen in the time-averaged nonplanar configuration) then $Q^H_{OCH_3}$ for DMN is equal to 19.66 G.

When the DMA results are considered, several difficulties arise. Rough calculations indicate that the larger proton splitting constant should be associated with the protons at positions 1,4,5,8 and the smaller splittings with positions 2,3,6,7. However, if as with DMN, Q^H_{CH} is taken to be -27 G then under no conditions can agreement be obtained between the experimental and calculated spin densities at positions 2,3,6,7 because of the fact that the calculated spin density at this position increases asymptotically with h_O to a value less than the experimental value.[24] The only way around this problem is to increase the value of Q^H_{CH}; however, by how much should it be increased? Our way out of this problem was to assume that the value of $Q^H_{OCH_3}$ derived for DMN should also hold for DMA, enabling $\rho'_O{}^\pi$ to be obtained. While this step may be criticized, it was apparently the best way to treat the results with the limited amount of experimental data which are available. The quantitative results should therefore be treated with caution until perhaps, at some future date, sufficient carbon-13 and/or oxygen-17 data become available to either support or modify our conclusions.

Table III: Summary of Molecular Orbital Calculations

Position	ρ_i calcd	a^H_i Calcd	a^H_i Exptl
	1,4-Dimethoxynaphthalene		
1	0.17795		
2	0.12372	−3.340[a]	3.354
5	0.05546	−1.497[a]	1.496
6	0.02581	−0.697[a]	0.699
9	−0.00195		
11(0)	0.11153		2.193[b]
	9,10-Dimethoxyanthracene		
1	0.05628	−1.759[c]	1.752
2	0.03454	−1.079[c]	1.084
9	0.23012		
11	0.01221		
15(0)	0.06007	1.181[d]	1.186
	1,4-Dimethoxybenzene		
1	0.15102		
2	0.08368	−2.26[a]	2.26
7(0)	0.17055	3.36[d]	3.36

[a] Calculated from $a^H_{CH} = Q^H_{CH}\rho_C{}^\pi$, where $Q^H_{CH} = -27$ G. [b] If $a^H_{OCH_3} = Q^H_{OCH_3}\rho_O{}^\pi$, then $Q^H_{OCH_3}$ is calculated to be 19.66 G. [c] Calculated from $a^H_{CH} = Q^H_{CH}\rho_C{}^\pi$, where $Q^H_{CH} = -31.25$. [d] Calculated from $a^H_{OCH_3} = Q^H_{OCH_3}\rho_O{}^\pi$, where $Q^H_{OCH_3} = 19.66$ G.

Our criteria for agreement with the MO calculations were, therefore, based on the value of $\rho'_O{}^\pi = 0.06032$ and the ratio a_C (1,4,5,8)/a_C (2,3,6,7) = 1.622. These two criteria were satisfied when $h_O = 1.72$ and $k_{OC} = 0.92$, with the results as shown in Table III. Under these conditions $Q^H_{CH} = -31.25$, a not unreasonable increase in value.

For DMB only one averaged proton splitting constant is available, and the required spin density can be reproduced by many combinations of h_O and k_{OC}. Again, to be consistent, the value of $Q^H_{OCH_3} = 19.66$ G derived from DMN was used to obtain a value of $\rho'_O{}^\pi$ (0.1706) from the experimental methoxyl group split-

(22) P. D. Sullivan and J. R. Bolton, *J. Amer. Chem. Soc.*, **90**, 5366 (1968).

(23) P. D. Sullivan, J. R. Bolton, and W. E. Geiger, Jr., *ibid.*, in press.

(24) This problem is not new; Snyder and Amos[25] have shown that for a series of polyacenes the calculated spin density at the 2 position is always low.

(25) L. C. Snyder and A. T. Amos, *J. Chem. Phys.*, **42**, 3670 (1965).

Table IV: Calculated and Experimental Changes in Spin Density with Temperature

Position	Temp, °K	Splitting const, G	Exptl ρ	Exptl $\Delta\rho$	Calcd $\Delta\rho^a$	Calcd $\Delta\rho^b$
			1,4-Dimethoxynaphthalene			
$a^H_{CH}(2,3)$	200	3.356	0.12372	−0.00015	−0.00043	−0.00042
	265	3.352	0.12357			
$a^H_{CH}(5,8)$	200	1.497	0.05546	+0.00078	+0.00065	+0.00099
	265	1.518	0.05624			
$a^H_{CH}(6,7)$	200	0.701	0.02581	−0.00005	+0.00008	+0.00016
	265	0.699	0.02576			
$a^H_{OCH_3}$	200	2.193	0.11153	−0.00137	−0.00061	−0.00137
	265	2.166	0.11016			
			9,10-Dimethoxyanthracene			
$a^H_{CH}(1,4,5,8)$	218	1.751	0.05628	+0.00042	+0.00077	+0.0102
	249	1.764	0.05670			
$a^H_{CH}(2,3,6,7)$	218	1.082	0.03454	0.00	0.00	+0.00004
	249	1.082	0.03454			
$a^H_{OCH_3}$	218	1.184	0.06007	−0.00183	−0.00115	−0.00183
	249	1.148	0.05824			

[a] Calculated assuming a constant h_O value, for DMN $k_{OC} = 1.0238$, $h_O = 1.57$; for DMA $k_{OC} = 0.909$, $h_O = 1.72$. [b] Calculated for a variable h_O value, for DMN $k_{OC} = 1.0238$, $h_O = 1.5795$; for DMA $k_{OC} = 0.909$, $h_O = 1.7292$.

ting constant. For $Q^H_{CH} = -27$ G, the spin densities were reproduced for $h_O = 1.51$ and $k_{OC} = 1.22$ as shown in Table III.

MO calculations for DMD were not attempted due to difficulties regarding the proportionality constant $Q^H_{CH_3}$.

The results for the series DMB, DMN, DMA indicate that h_O increases along the series from 1.51 to 1.57 to 1.72 while k_{OC} decreases from 1.22 to 1.03 to 0.92. The decreasing value of k_{OC} suggests a decrease in bond order and hence an increase in bond length along the series. The concurrent increase in h_O is also consistent with previous observations in the *p*-benzosemiquinone–hydroquinone series.[23]

(*b*) *Qualitative Fit of the Temperature Dependence of the Spin Densities.* One of our assumptions with regard to the methoxyl group was that for an out-of-plane movement of $\theta°$, that k_{OC} the overlap integral should decrease by cos θ with a resultant change in spin density on oxygen of $\cos^2\theta$. This assumption may be examined with the MO calculations by comparing the calculated and experimental changes in spin density with temperature at the ring carbon atoms. Thus for DMN the spin densities have been fitted as shown above to the splitting constants at 200°K with $h_O = 1.57$ and $k_{OC} = 1.03$. In addition, the values of $\langle\cos^2\theta\rangle$ have been evaluated over the temperature range in our calculations of the potential barrier. At 200°, $\langle\cos^2\theta\rangle = 0.9604$ and at 265° (the highest experimental temperature) $\langle\cos^2\theta\rangle = 0.9486$. The appropriate value of k_{OC} at 265° is therefore $1.03(\sqrt{0.9486/0.9604}) = 1.0238$. Calculations with this value of k_{OC} combined with a constant value of $h_O = 1.57$ gave the changes in spin density as shown in Table IV. The calculated values are compared to the experimental changes in spin density, obtained assuming constant values of Q^H_{CH} and $Q^H_{OCH_3}$ over the temperature range. The results show that the calculated decrease in ρ_O^π is less than the experimental value. This result may be improved if h_O is allowed to vary. From the previous section and from earlier work,[23] changes in k_{OC} have always been accompanied by opposite changes in h_O. Therefore, if in this case h_O is allowed to increase (since k_{OC} decreases) from its value of 1.57, good agreement between the experimental and calculated changes in ρ_O^π is obtained when $h_O = 1.5795$ (see Table IV). Good agreement is also obtained for the proton splitting constants. The protons at positions 5,8 are predicted to have the largest temperature dependence with a positive temperature coefficient (calculated +0.41 mG/deg, experimental +0.32 mG/deg), the protons at positions 2,3 are predicted to have a small negative temperature coefficient, and the protons at positions 6,7 are predicted to have a negligible temperature dependence. These results are all in good qualitative and quantitative agreement with experiment.

Similar considerations for DMA indicate that on changing the temperature from 218 to 249°, k_{OC} should be reduced from 0.92 to 0.909. The calculated changes in spin density for this change (assuming h_O to remain constant) are again too small for ρ_O^π (Table IV). Agreement for $\Delta\rho_O^\pi$ may be obtained if h_O is allowed to increase from 1.72 to 1.7292 (Table IV). Good qualitative agreement is then obtained for the proton splitting constants. The protons at positions 2,3,6,7 are predicted to have a negligible temperature dependence as

observed experimentally and the protons at positions 1,4,5,8 are predicted to have a significant positive temperature coefficient. The magnitude is, however, predicted to be +1.06 mG/deg against an experimental value of +0.44 mG/deg.

The above calculations indicate that our initial assumption regarding the $\cos^2\theta$ dependence of ρ_0^π is at least substantiated for the DMN system where good agreement can be obtained for the temperature dependence of the proton splitting constants. The agreement for DMA is not as good and together with the low value of the calculated temperature coefficient for the methoxyl group suggests that further modifications may be necessary for this molecule.

Acknowledgments. I would like to express my appreciation to Dr. J. R. Bolton, in whose laboratory the experimental measurements were carried out, for all his help and encouragement during the course of this work. Acknowledgment is made to the donors of the Petroleum Research Fund, administered by the American Chemical Society, for partial support of this research. The research was also supported in part under Grant No. NSF-GP-8416 from the National Science Foundation.

NOTES

Analysis of Sound Velocities in Aqueous Mixtures in Terms of Excess Isentropic Compressibilities

by M. J. Blandamer and D. Waddington

Department of Chemistry, The University, Leicester, LE1 7RH, England *(Received October 9, 1969)*

Many studies of sound velocities as a function of mixture composition have established that at constant temperature and pressure, the velocity, c, generally increases when alcohol is added to water.[1] (A similar trend is observed when methyl cyanide,[2] *t*-butyl alcohol,[3,4] and *n*-propyl alcohol,[5] are added.) When more alcohol is added the velocity goes through a maximum and then decreases. Measurements of sound absorption have been less extensive.[6] First indications were that the absorption (α/f^2—where α is the amplitude absorption coefficient and, f, the frequency) also passed through a maximum, the PSAC[7] (peak sound absorption concentration). However, it is now known that over the composition range where c rapidly increases, α/f^2 remains relatively constant. We wish to examine these two trends.

The analysis described here was used in an examination of the properties of methyl cyanide + water mixtures,[2] but it may have a wider application. Certainly this analysis shows how the link between the absorption and the velocity can be made more readily than by a direct comparison of the plots of c and α/f^2 against composition.

The key to our approach is in an analysis of velocity data in terms of an excess isentropic compressibility, κ_s^E. This quantity is defined in eq 3 and 4 below. If κ_s represents a complex isentropic compressibility

$$\kappa_s^* = \kappa_s' - j\kappa_s'' \qquad (1)$$

where κ_s' is the real part and κ_s'' is the imaginary part; these two quantities are the two axes of an Argand diagram where j is the root of -1.

The quantity κ_s'' can be linked with sound absorption[8] (out of phase component), while κ_s' can be related to the phase velocity, the in-phase component with respect to the pressure variation of the travelling sound wave. Since the frequency dependence of the velocity is generally small compared with that of the absorption, κ_s' can be calculated from the measured sound velocity at low frequencies by the equation of Newton and Laplace

$$\kappa_s' = (\partial \ln V/\partial P)_s = 1/\rho c^2 \qquad (2)$$

where ρ is the density.

(1) F. Franks and D. J. G. Ives, *Quart. Rev.*, **20**, 1 (1966).

(2) M. J. Blandamer and D. Waddington, *Trans. Faraday Soc.*, in press.

(3) J. Kenttamaa, E. Tommila, and M. Martti, *Ann. Acad. Sci. Fenn., Ser. A2*, **93**, 3 (1959).

(4) C. J. Burton, *J. Acoust. Soc. Amer.*, **20**, 186 (1948).

(5) B. Jacobson, *Ark. Kemi*, 2 (11), 177 (1951); data are from J. Timmermans, "Physico-chemical Constants of Binary Systems in Concentrated Solutions," Vol. 4, Interscience, New York, N. Y., 1960.

(6) See for example, G. W. Willard, *J. Acoust. Soc. Amer.*, 12, 1941 (1941).

(7) M. J. Blandamer and D. Waddington in *Advan. Mol. Relaxation Processes*, in press.

(8) See for example, K. Herzfeld and T. A. Litovitz, "Absorption and Dispersion of Ultrasonic Waves," Academic Press, Inc., Ltd., London, 1959.

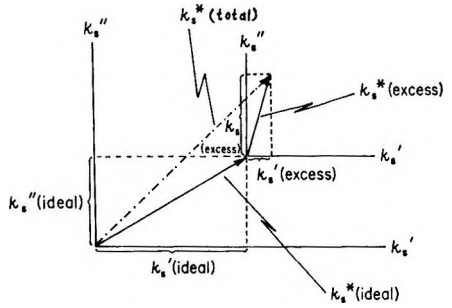

Figure 1. Relationships between the various isentropic compressibilities.

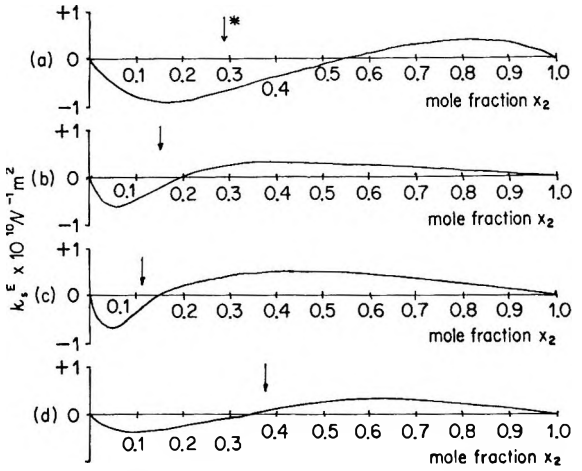

Figure 2. Variation of excess isentropic compressibility $(\kappa_s')^E$ with mixture composition for: (a) ethanol + water; (b) *n*-propyl alcohol + water; (c) *t*-butyl alcohol + water; (d) methyl cyanide + water, all at 298° K. The asterisk indicates the position of the maximum in the ultrasonic absorption (the PSAC, see text).

The real (in-phase) component of the isentropic compressibility of an ideal binary mixture, $(\kappa_s')_{id}$, can be calculated from the mole fraction of water, x_1, and of the cosolvent, x_2, by

$$(\kappa_s')_{id} = x_1(\kappa_s')_1^\circ + x_2(\kappa_s')_2^\circ \quad (3)$$

where $(\kappa_s')_1^\circ$ and $(\kappa_s')_2^\circ$ are the isentropic compressibilities of the two pure liquids. The excess isentropic compressibility is given by

$$(\kappa_s')^E = \kappa_s' - (\kappa_s')_{id} \quad (4)$$

The relationship between the various isentropic compressibilities is summarized in Figure 1.

Plots of $(\kappa_s')^E$, as a function of liquid composition, are given in Figure 2 for a number of binary aqueous mixtures. For each system there is a given composition where $(\kappa_s')^E$ is zero; in this context these are ideal mixtures, however, on other grounds they are not ideal. Thus they correspond to systems having excess absorptions. A striking feature, and one which we wish to draw attention to, is that for those mixtures with large excess absorptions, *e.g.*, *t*-butyl alcohol + water,[9] methyl cyanide + water,[2] the maximum in α/f^2 occurs quite close to the composition where $(\kappa_s')^E$ is zero. In terms of the Argand diagram approach outlined above, this means that where the velocity changes rapidly and α/f^2 remains unaffected, the vector κ_s^* is directed along the κ_s' axis. At the maximum in α/f^2, the projection on the κ_s'' axis has correspondingly reached it maximum value. Here all the nonideal properties of the binary liquid mixture contribute towards the imaginary (out-of-phase component) isentropic compressibility.

Acknowledgments. We thank Professor M. C. R. Symons and Dr. N. J. Hidden for valuable discussion. We acknowledge the award of a maintenance grant to D. W. from S. R. C.

(9) M. J. Blandamer, D. E. Clarke, N. J. Hidden, and M. C. R. Symons, *Trans. Faraday Soc.*, **64**, 2691 (1968).

The Reaction of Silica Surfaces with Hydrogen Sequestering Agents

by J. A. Hockey

Chemistry Department, University of Manchester Institute of Science and Technology, Manchester, England
(Received December 8, 1969)

It is possible to obtain information on the concentration and coordination of the surface hydroxyls present on silicas by studying the reactions of these surface groups with hydrogen sequestering agents.[1-4] In a recently published study,[1] the reactions of alkyl chlorosilanes with the surface hydroxyls of a Cabosil silica have been followed in an elegant manner by a combination of analytical and spectroscopic techniques. The infrared spectrum shown in this paper[1] illustrates that with high spectral resolution the absorption band at about 3750 cm^{-1}, which previous authors[5] have assigned as corresponding to isolated or single surface hydroxyls, may be resolved into three adjacent sharp peaks at 3751, 3747, and 3743 cm^{-1}. Similar results to this have been obtained in the author's own laboratory. However, it has always been felt that this splitting is artefactual rather than real. The spectra in Figure 1 illustrate this point.

Spectrum a corresponds to the absorption spectrum of the residual water vapor in the optical path of a "dry air" flushed PE 125 spectrophotometer on "single

(1) M. L. Hair and W. Hertl, *J. Phys. Chem.*, **73**, 2372 (1969).

(2) C. G. Armistead, A. J. Tyler, F. H. Hambleton, S. A. Mitchell, and J. A. Hockey, *ibid.*, **73**, 3947 (1969).

(3) J. B. Peri, *ibid.*, **70**, 3168 (1966).

(4) H. P. Boehm, M. Schneider, and F. Arendt, *Z. Anorg. Chem.*, **66**, 800 (1962).

(5) L. H. Little, "Infrared Spectra of Adsorbed Species," Academic Press, Inc., New York, N. Y., 1966.

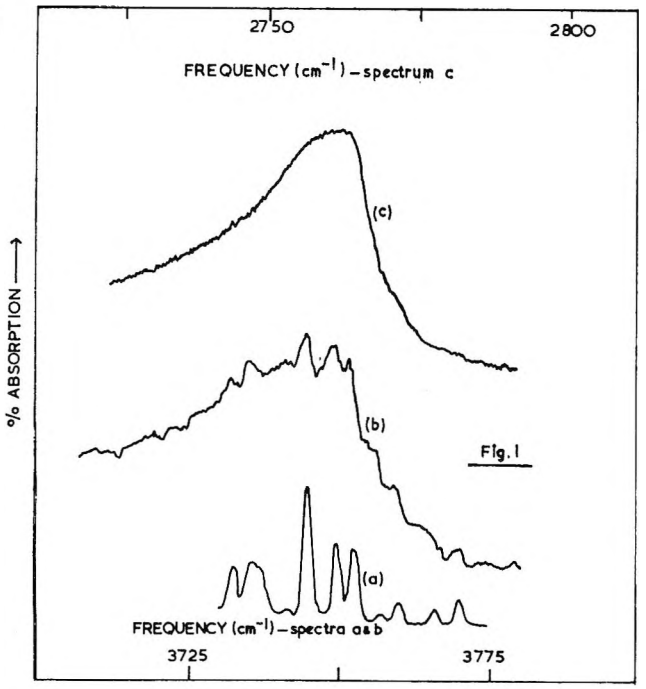

Figure 1. Absorption spectra.

beam" operation with a spectral slit width of 0.4 cm^{-1}. It can be seen that the water vapor spectrum exhibits three strong absorption bands at 3752, 3749, and 3744 cm^{-1}. The intensity of these bands is of course dependent on the efficiency of the system used to dry the flushing air. Spectrum b corresponds to the absorption spectrum, recorded under double-beam conditions with identical resolution, of an Aerosil silica pressed disk after evacuation at 700° and subsequent cooling *in vacuo* to room temperature. Three absorption bands similar to those recorded by the authors of ref 1 are clearly apparent. Spectrum c is the absorption spectrum—again recorded under identical spectroscopic conditions to spectrum b—of a similarly treated disk but one in which the surface hydroxyls have been converted by isotopic exchange to their deuterium analogs.[2] In this last spectrum the fine structure is no longer apparent. It has therefore been always concluded that the fine structure which is observed in spectrum b is the result of the combined absorption spectra of the surface hydroxyls and any residual water vapor within the spectrophotometer. The point that the fine structure in spectrum b is due to the water vapor in the instrument is further reinforced by the fact that the intensities of the three bands at 3751, 3747, and 3744 cm^{-1} in spectrum b may be enhanced by reducing the efficiency of the flushing system used for drying the air within the spectrometer.

One other general point: when analyzing the results obtained from studies of the reactions of hydroxylated silicas and compounds such as alkyl chlorosilanes, infrared spectroscopic data are extremely useful in following the reaction of the surface hydroxyls with the organic reagent. The spectroscopic technique is, however, in this case perhaps too useful, since it leads one to analyze the data in a manner which assumes that the organic reagent reacts solely with the surface hydroxyl groups. As our own recent studies of such systems have shown,[6] this is not always the case. The reaction at room temperature of "fully" hydroxylated silicas with reagents such as BCl_3 and $TiCl_4$ may almost certainly be analyzed correctly on this basis. However, with reagents such as the alkyl chlorosilanes in which the reaction between the solid and the vapor phase silane is carried out at temperatures of 300–400°, this assumption is not necessarily valid. In particular, it may be expected to be most incorrect for those silicas which have been evacuated at temperatures $\geq 500°$ prior to reaction with the organic reagent vapor at 300–400°. Such high-temperature evacuation removes the hydrogen-bonded hydroxyls from the surface and leaves a corresponding number of strained-surface siloxane bridges.

It follows that, since the hydrogen sequestering agents used in such work are of necessity susceptible to nucleophilic attack at the metal or metalloid atom (*e.g.*, Ti, Al, Si, B) [in those reactions involving the surface hydroxyls the nucleophile is the oxygen atom of the hydroxyl group], it is unjustified to implicitly exclude the possibility that the oxygen atoms of the surface siloxane bridges do not themselves act as nucleophilic centers of sufficient strength to react directly with the organic reagent under the high-temperature conditions used. In this context, an example of this latter siloxane reactivity has recently been reported by Yates and his coworkers[7] in their account of the reaction of $AlMe_3$ with silica surfaces.

(6) R. J. Peglar, F. H. Hambleton, and J. A. Hockey, to be published.
(7) D. J. C. Yates, G. W. Demblinski, W. R. Kroll, and J. J. Elliot, *J. Phys. Chem.*, **73**, 911 (1969).

The Absorption Spectra of Triarylborons

by D. S. Miller and J. E. Leffler

Department of Chemistry, Florida State University, Tallahassee, Florida 32306 *(Received December 17, 1969)*

The spectra of triarylborons and triarylcarbonium ions are similar in their response to temperature changes as well as in other respects. Tris(*p*-N,N-dimethylaminophenyl)boron has a long wavelength absorption band at 357 nm with a shoulder at 340 nm in methylcyclohexane–isopentane at room temperature. On cooling to 77°K the shoulder decreases in relative intensity. The temperature effect resembles that reported for crystal violet and a similar explanation is suggested. Spectroscopic data are also given for

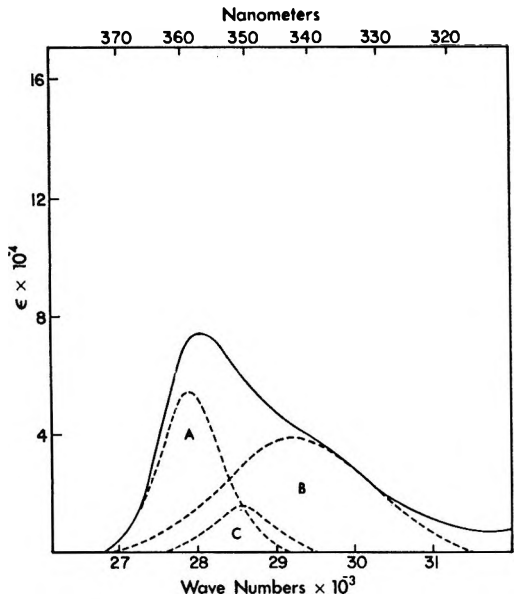

Figure 1. Ultraviolet spectrum of tris(*p*-dimethylaminophenyl)borane at 298°K.

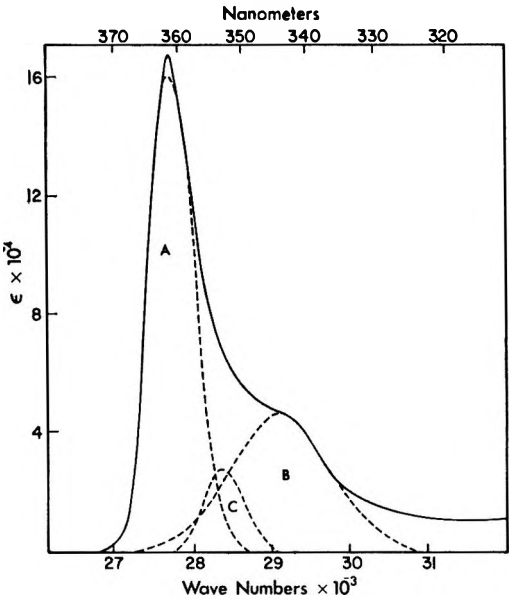

Figure 2. Ultraviolet spectrum of tris(*p*-dimethylaminophenyl)borane at 77°K.

tris(*p*-methoxyphenyl)boron, tris(*p*-chlorophenyl) boron, triphenylboron, and trimesitylboron.

Triarylborons[1] have long wavelength overlapping optical transitions in the near-ultraviolet similar to those of triarylcarbonium ions[2] in the visible. In both series these absorption bands vanish when the central atom is complexed with a nucleophile, and the simplest model for the transition is an intramolecular n,π charge transfer between the substituent aryl groups as donors and the central atom as acceptor. As is required by the charge-transfer model, the Ar_3C^+ or Ar_3B transition energies are correlated with the corresponding ArH ionization potentials.

For a hypothetical ϕ_3C^+ of D_{3h} symmetry it can be shown that the acceptor is a single nonbonding molecular orbital with an important contribution from the central 2p atomic orbital, while the donor orbitals are degenerate. In a real molecule, which will certainly have less than D_{3h} symmetry, this degeneracy will be reduced and the charge-transfer band should consist of more than one transition. In fact, the long wavelength absorption of both Ar_3B and Ar_3C^+ usually consists of two partially overlapping bands or a main band with a prominent shoulder.

In the case of crystal violet (tris(*p*-dimethylaminophenyl)carbonium ion) (CV) the shoulder on the high-energy side of the long wavelength band almost disappears on cooling to 114°K while the main band becomes more intense.[3] The boron analog of crystal violet (tris(*p*-dimethylaminophenyl)boron) (CVB) behaves similarly, as can be seen from its spectra at 298°K (Figure 1) and 77°K (Figure 2).

Lewis[3] showed that the temperature dependence of the CV absorption spectrum can be accommodated by a two-isomer model, each isomer responsible for one of the two transitions.[4] The existence of stabilized unsymmetrical propeller forms or of propeller isomerism for triarylcarbonium ions and related species is supported by physical evidence in several cases[5] although the average conformation of triarylcarbonium ions on the nmr time scale is symmetrical.[6] The temperature effects on the spectrum of CVB can also be accommodated by a two-isomer model like that used by Lewis. In order to make a semiquantitative comparison of the two systems we have analyzed the CVB spectra in terms of assumed gaussian components:[7] the apparent heat of isomerization is about 250 cal mol^{-1}. Like the 580 cal mol^{-1} for CV, this number seems reasonable for the type of isomerism suggested by Lewis. We would like to point out, however, that it is not necessary for the two isomers each to have just one absorption band. The system would behave in much the same way if *both* isomers have both transitions but with greatly different

(1) (a) B. G. Ramsey and J. E. Leffler, *J. Phys. Chem.*, **67**, 2242 (1963); (b) B. G. Ramsey, *ibid.*, **70**, 611 (1966).

(2) W. B. Smith and P. S. Rao, *J. Org. Chem.*, **26**, 254 (1961).

(3) G. N. Lewis, T. T. Magel, and D. Lipkin, *J. Amer. Chem. Soc.*, **64**, 1774 (1942).

(4) The apparent $\Delta H°$ for the interconversion of the two isomers was 580 cal mol^{-1}.

(5) (a) M. S. deGroot, I. A. M. Hesselmann, and J. H. van der Waals, *Mol. Phys.*, **10**, 241 (1966); (b) J. S. Hyde, R. Breslow, and C. DeBoer, *J. Amer. Chem. Soc.*, **88**, 4763 (1966); (c) T. J. Weismann and J. C. Schug, *J. Chem. Phys.*, **40**, 956 (1964).

(6) (a) D. G. Farnum, *J. Amer. Chem. Soc.*, **89**, 2970 (1967); (b) R. Dehl, W. R. Vaughan, and R. S. Berry, *J. Org. Chem.*, **24**, 1616 (1959); (c) R. B. Moodie, T. M. Connor, and R. Stewart, *Can. J. Chem.*, **37**, 1402 (1959); (d) R. S. Berry, R. Dehl, and W. R. Vaughan, *J. Chem. Phys.*, **34**, 1460 (1961); (e) I. I. Schuster, A. K. Colter, and R. J. Kurland, *J. Amer. Chem. Soc.*, **90**, 4679 (1968).

(7) See Figures 1 and 2. Curve C, whose area remains at a constant 9% of the total at all four temperatures may represent the error introduced by assuming gaussian line shapes. As a further constraint on the analysis the positions of the maxima of A, B, and C were kept the same at all four temperatures.

Table I: Absorption Spectra of Ar_3B in 4:1 Methylcyclohexane–Isopentane at 298°K

Aryl Group	λ_{max}, nm and ($\epsilon \times 10^{-4}$)			
p-N,N-Dimethylaminophenyl	356.5 (7.5)	340 (sh) (3.4)	304.0 (.95)	245.0 (2.4)
	362.0[a] (4.5)	345 (sh) (2.1)[a]	308.0 (1.1)[a]	249.0 (2.2)
p-Methoxyphenyl	311.0 (5.2)	297 (sh) (2.2)	262.5 (.31)	233.5 (sh) (1.1)
p-Chlorophenyl[b]	300.5 (2.9)	287 (sh) (1.5)	255.0 (.28)	231.0 (1.0)
Phenyl[b]	287.0 (3.7)	276 (sh) (3.3)	236.0 (2.0)	
Mesityl	331.0 (1.6)	283 (.39)	245 (.80)	

[a] In absolute ethanol. [b] With 10^{-3} *M* tri-*n*-propylboron added. This compound is transparent, is a stronger Lewis acid, and acts as a scavenger for oxygen and Lewis bases (see the Experimental Section).

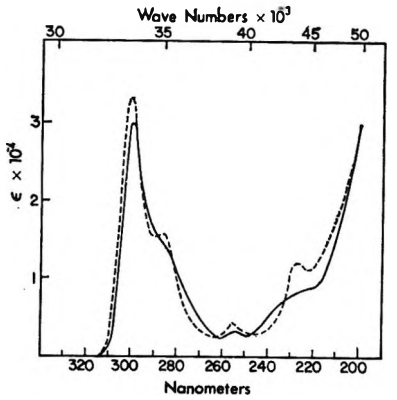

Figure 3. Ultraviolet spectrum of tris(*p*-methoxyphenyl)-borane at 298° and 77°K: 298°K, —; 77°K, - - -.

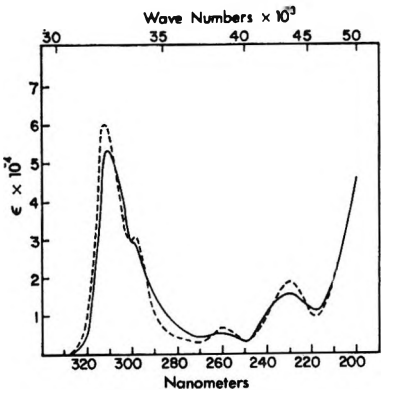

Figure 4. Ultraviolet spectrum of tris(*p*-chlorophenyl)borane at 298° and 77°K, in methylcyclohexane–isopentane with 10^{-3} *M* tri-*n*-propylboron: 298°K, —; 77°K, - - -.

transition probabilities, as might be expected on theoretical grounds. The triarylboron spectra are summarized in Table I.

Experimental Section

Tris(p-dimethylaminophenyl)boron (CVB). This compound was prepared by the method of Wittig and Herwig.[8] After crystallization from acetone under N_2, yellow-green needles, mp 209–211° (vac), were obtained. *Anal.* Calcd for B: B, 2.91. Found: B, 2.92%. The long wavelength band at 356.5 nm and its shoulder are suppressed only in the presence of a large excess of triethylamine under conditions in which the corresponding band of triphenylboron requires only one equivalent of the amine. Although degassed methylcyclohexane solutions of CVB are stable in the dark, continuous exposure to the ordinary laboratory illumination caused a 50% decrease in the intensity of the 357-nm band and the appearance of a maximum near 275 nm. Short exposure of a methylcyclohexane solution of CVB to air causes only a slight decrease in the 357-nm intensity, but the band disappears on prolonged exposure.

Tris(p-methoxyphenyl)boron.[9] This compound melted at 124–126° (lit. 128°) after recrystallization from ether under N_2. *Anal.* Calcd for B: B, 3.33%. Found: B, 3.29. (See Figure 3.)

Tris(p-chlorophenyl)boron. This compound melted at 197–202° after recrystallization from benzene. Its preparation will be described elsewhere.

Ultraviolet Spectra. All measurements were made on a Cary 14 recording spectrophotometer. Solutions were made up in an oxygen-free atmosphere in a glove box. Solvents were spectroscopic grade and were dried over $LiAlH_4$, distilled, and degassed four times at less than 10^{-6} mm. Constant temperatures were obtained by using baths of liquid N_2 (77°K), CF_4 (145°K), and $ClCF_3$ (192°K). Corrections were made for contraction of the solvent. No dependence of the shape of the spectrum on concentration was observed.

Triphenylboron (PB) and tris(*p*-chlorophenyl)-boron (CLB) (Figure 4) required a special technique in addition to the precautions described above. In contrast to CVB and tris(*p*-methoxyphenyl)boron, these compounds are more readily autoxidized and, being stronger Lewis acids, also form reversible complexes with unknown impurities that we were unable to remove. The complex formation was suppressed, however, by adding 10^{-3} *M* tri-*n*-propylboron as a scavenger. Without the scavenger, a good triphenylboron spectrum is obtained at room temperature, but on cooling, the intensity of the long wavelength band

(8) G. Wittig and W. Herwig, *Ber.*, **88**, 962 (1955).
(9) E. Krause and P. Nobbe, *ibid.*, **63**, 934 (1930).

first increases due to contraction of the solvent and then decreases markedly until at 77°K there remains only a weak absorption at 270 nm with an end absorption at 235 nm and beyond. These changes in the spectrum are a reversible function of the temperature and they are completely suppressed at all temperatures by the tri-*n*-propylboron scavenger even in dilute solution.

Acknowledgment. The authors wish to acknowledge support of this project under the National Defense Education Act and also the use of the facilities of the Florida State University computing center.

The Bending Frequency of Gaseous Aluminum Oxide

by A. Snelson

IIT Research Institute, Chicago, Illinois 60616
(Received January 23, 1970)

The infrared spectrum of Al_2O in inert gas matrices has been reported by Linevsky, *et al.*[1] The asymmetric and symmetric stretching frequencies were observed at 994 and 715 cm^{-1}, respectively, in an argon matrix. From isotopic studies the molecule was assigned C_{2v} symmetry with an Al–O–Al bond angle of 145 ± 5°. The bending frequency was not observed and was assumed to lie below 250 cm^{-1}, the long wavelength limit of the investigation. A frequency of 240 cm^{-1} was deduced for this mode from some rather old electronic spectra attributed to Al_2O, but with the reservation that this might apply to an excited state rather than the ground state of the molecule. More recently, Innes, *et al.*,[2] have demonstrated that this electronic transition corresponds to $^2\Delta_i \rightarrow A^2\pi_i$ of AlO. In an attempt to locate the bending mode of Al_2O, the spectrum has been reexamined in neon and argon matrices, at liquid helium temperature in the spectral range 2000–190 cm^{-1}.

The matrix isolation equipment and spectrometer used in this study have been described elsewhere.[3] The species Al_2O was produced by heating aluminum metal and aluminum oxide[1] in either rhenium or alumina Knudsen cells at temperatures of 1400 ± 50°. As in the earlier investigation, only two absorption bands were observed under conditions of good isolation, two very strong features at 994 and 993 cm^{-1} in argon and neon matrices, respectively, and a much weaker one at 715 cm^{-1} in both argon and neon matrices. This spectrum is in excellent accord with that reported by Linevsky, *et al.*[1] No frequency corresponding to the bending mode at about 240 cm^{-1} was observed in either matrix in the previously unexplored spectral region between 190 and 250 cm^{-1}. It is possible that the non-appearance of an absorption band in this spectral region corresponding to the bending mode of Al_2O could be due to this mode having a very low extinction coefficient. Based on the most intense spectra recorded in the present study the bending mode extinction coefficient would have to be less than one-fiftieth of that of the asymmetric stretching mode to not be detected. From the data available for triatomic species such a large difference in extinction coefficients does not seem too likely. It is possible that matrix effects might result in the bending frequency suffering a large frequency shift to the red, resulting in the matrix frequency lying beyond the long wavelength limit of the investigation. However, the very close similarity between the frequencies observed in the argon and neon matrices for ν_1 and ν_3 suggests that large matrix-induced frequency shifts for this molecule are unlikely. It is thus concluded that the bending mode of Al_2O lies below 190 cm^{-1}, and that the previously deduced value for ν_2 at 240 cm^{-1} is in error.

When the earlier investigation on Al_2O was made, a comparison of the then derived force constants with those of other similar molecules was not possible since data were unavailable. Recently the infrared spectrum of Li_2O[4] had been examined and the force constants derived. Büchler, *et al.*,[5] have presented arguments which suggest that the metal–oxygen bonds in Al_2O and Li_2O are probably largely ionic. Although the former molecule has a bent configuration, and the latter is almost certainly linear, the proposed similarity in the ionic character of the bonds suggests that a transference of the ratio of the bond stretching to bond bending force constants in Li_2O to Al_2O is not unreasonable. The spectrum of Li_2O[4] was analyzed in terms of a three

Table I: Force Constants for Al_2O

Apex angle, deg	f_r	f_{rr}	f_α	ν_2, cm^{-1} $Al_2{}^{16}O$
150	5.70	1.92	0.038	143[a]
145	5.00	1.14	0.033	118[a]
140	4.82	0.89	0.032	113[a]
145	5.00	1.14	0.042	133[b]
145	5.01	1.15	0.028[d]	108[c]

[a] $f_r/f_\alpha = 150$. [b] $f_r/f_\alpha = 120$. [c] $f_r/f_\alpha = 180$. [d] Force constants are in mdyn/Å.

(1) M. J. Linevsky, D. White, and D. E. Mann, *J. Chem. Phys.*, **41**, 542 (1966).

(2) J. K. McDonald and K. K. Innes, *J. Mol. Spectrosc.*, **32**, 501 (1969).

(3) A. Snelson, *J. Phys. Chem.*, **73**, 1919 (1969).

(4) D. E. Mann, K. S. Seshadri, and D. White, "Department of Navy Report No. TR-5," Office of Naval Research Contract Nonr-495(12), Sept 1966.

(5) A. Büchler, J. L. Stauffer, W. Klemperer, and L. Wharton, *J. Chem. Phys.*, **34**, 587 (1961).

term quadratic potential function, the ratio f_r/f_α being about 153. If a similar ratio is applied to Al_2O, using the matrix frequencies $\nu_2 = 994$ and $\nu_1 = 715$, $\nu_3 = 951$ and $\nu_1 = 700$ cm^{-1}, respectively, for the ^{16}O and ^{15}O substituted molecules, the results shown in Table I are obtained.

Using these force constants, the observed frequencies of the ^{16}O and ^{18}O substituted species can be reproduced to within less than 1% when the apex angle is 145° and to within slightly greater than 1% when the apex angle is 140 or 150°.

In conclusion, the infrared spectrum of Al_2O observed in this study demonstrates that the ν_2 bending mode of this molecule lies below 190 cm^{-1}. Comparison of Al_2O with Li_2O suggests that the bending frequency of Al_2O probably lies at about 120 ± 30 cm^{-1}.

Acknowledgment. The author wishes to thank the Air Force Rocket Propulsion Laboratory, Edwards, Calif., for supporting this study under Contract No. FO4611-69-C-0093.

Vibrational Energy Transfer in High-Energy Hydrogen–Argon Collisions[1]

by Hyung Kyu Shin

Department of Chemistry, University of Nevada, Reno, Nevada
(Received January 26, 1970)

In calculating vibrational transition probabilities in molecular collisions, potential energies of the Lennard-Jones (LJ) type are often assumed mainly for mathematical convenience.[2a,b] Sometimes use of the exponential potentials is preferred, but such use requires either the introduction of an adjustable parameter on which the probabilities depend sensitively or the fitting of the exponential potential to the LJ function, commonly to the LJ(12–6) function.[2a,2b] However, the quantitative knowledge that is available on such potentials has been derived from a knowledge of macroscopic properties of the gas, which depends on the behavior of a gas in near equilibrium.[3] In studying inelastic collision processes, on the other hand, we need to know the characteristics of the interaction potentials when the molecules are in close proximity. In recent years, knowledge of short-range interaction potentials between atoms, between molecules, and between an atom and a molecule has become available from measurements for the scattering of high-velocity beams;[4,5] such studies show that most experimental data can best be fit to the inverse-power form $U(r) = K/r^s$. In this note we report a calculation of vibrational transition probabilities for H_2–Ar based on such a potential in the high collision energy region. We assume a collinear collision model and H_2 a harmonic oscillator, which is initially in the ground state.

The probability P_{on} that at $t = +\infty$ the oscillator will be in the nth excited state due to the interaction with the incident atom, may be obtained by solving

$$i\hbar \frac{\partial \psi(t)}{\partial t} = \left[\frac{p^2}{2M} + \frac{M\omega^2}{2} q^2 + V'(t,q)\right]\psi(t) \equiv H\psi(t) \tag{1}$$

where M and ω are the reduced mass and vibrational frequency of the oscillator, respectively, and $V'(t,q)$ is the perturbation due to the potential of interaction between the colliding pair, q being the vibrational coordinate. The transition probability can be expressed by

$$P_{on} = \lim_{t\to\infty} \left| \int_{-\infty}^{\infty} \psi_n^* \psi(t) \mathrm{d}q \right|^2 \tag{2}$$

For the collinear collision, the interaction between the nearest atoms dominates the overall energy, the distance between the atoms being $z = r - {}^1/_2 q$. On approximating the interaction potential as $U(z) = K/z^s$ and expanding in powers of q, we obtain

$$U(z) = \frac{K}{r^s} + \frac{sK}{2r^{s+1}} q + \frac{s(s+1)K}{8r^{s+2}} q^2 + \ldots \equiv U(r) - F(r)q + G(r)q^2 + \ldots \tag{3}$$

The scattering measurements give[5] $U(r) = 159/r^{6.28}$ eV for H_2–Ar, so that in this equation, $K = 159$ eV·Å$^{6.28}$ and $s = 6.28$. We take expansion terms up to quadratic in q for $V'(t,q)$. The perturbing potential is an implicit function of time through the intermolecular separation $r(t)$. The dependence of r on t is given by the trajectory of the colliding pair

$$t = \sqrt{\frac{\mu}{2}} \int_{r^*}^{r} \frac{\mathrm{d}r}{\sqrt{E - U}} = i\sqrt{\frac{\mu}{2}} \left[\int_0^{r^*} \frac{\mathrm{d}r}{\sqrt{U - E}} - \int_0^{r} \frac{\mathrm{d}r}{\sqrt{U - E}} \right] \equiv it_c - i\sqrt{\frac{\mu}{2}} \int_0^{r} \frac{\mathrm{d}r}{\sqrt{U - E}} \tag{4}$$

where μ and E are the reduced mass and initial relative energy of the collision system, respectively, $U(r^*) = E$, and the last relation defines the collision time t_c. The perturbation term $V'(t,q)$ is then $-F(t)q + G(t)q^2$

(1) This work was carried out under Grant AFOSR-68-1354 from the U. S. Air Force Office of Scientific Research.

(2) (a) D. Rapp and T. Kassal, *Chem. Rev.*, **69**, 61 (1969), present a critical discussion of the recent methods and results; (b) K. F. Herzfeld and T. A. Litovitz, "Absorption and Dispersion of Ultrasonic Waves," Academic Press, New York, N. Y., 1959, pp 278–285.

(3) J. O. Hirschfelder, C. F. Curtiss, and R. B. Bird, "Molecular Theory of Gases and Liquids," John Wiley and Sons, New York, N. Y., 1964, Chapter 13.

(4) E. A. Mason and J. T. Vanderslice in "Atomic and Molecular Processes," D. R. Bates, Ed., Academic Press, New York, N. Y., 1962, pp 663–695.

(5) S. O. Colgate, J. E. Jordan, I. Amdur, and E. A. Mason, *J. Chem. Phys.*, **51**, 968 (1969); also see references therein.

so that we can write $H = p^2/2M + M\omega'^2q^2/2 - F(t)q$, where $\omega'^2 = \omega^2 + 2G(t)/M$. In the region of strong interaction we find $t = it_c - (i/4.14)\sqrt{\mu/2K}r^{4.14}$.

In the linear approximation of $U(z)$, $V'(t,q)$ is simply $-F(t)q$, and for such a case it has already been shown[6-9] that

$$P_{on} = \frac{\epsilon_0{}^n \exp(-\epsilon_0)}{n!}; \quad \epsilon_0 = \Delta E_{(1)}/\hbar\omega \tag{5}$$

where $\Delta E_{(1)}$ is the amount of the vibrational energy transferred to the oscillator in the linear approximation. In the present case the same form results for P_{on}, but the amount of energy transfer is now given by

$$\Delta E_{(2)} = \frac{1}{2M}\left|\int_{-\infty}^{\infty} F(t)\exp\left[i\omega t + \frac{i}{M\omega}\int_{-\infty}^{t} G(t')\mathrm{d}t'\right]\mathrm{d}t\right|^2 \tag{6}$$

With the result of eq 4, the value of $\Delta E_{(2)}$ found by contour integration[8,10] is

$$\Delta E_{(2)} = \frac{1}{2M}\left[\frac{6.28\pi K}{\omega\Gamma(1.758)}\right]^2\left(0.170\omega\sqrt{\frac{\mu}{K}}\right)^{3.517}\left[1 - \frac{\gamma'}{(\beta E^{-0.659} + t_c)^2}\right]^2 \exp\left(-2\omega t_c - \frac{\gamma}{\beta E^{-0.659} + t_c}\right) \tag{6a}$$

with $\gamma = \mu/3M\omega$, $\gamma' = \gamma/2\omega$, $\beta = 0.170\sqrt{\mu}K^{0.159}$, and

$$t_c = 0.112\,\frac{\Gamma(0.659)}{\Gamma(1.159)}\sqrt{\frac{\pi\mu}{E}}\left(\frac{K}{E}\right)^{0.159}$$

The calculated values of $\Delta E_{(2)}$ are plotted in Figure 1. The second term of the exponent is in general small for H_2–Ar; thus $\Delta E_{(2)}$ increases with E as $\sim\exp(-\text{constant}/E^{0.659})$. Beyond $E = 5$ eV, $\Delta E_{(2)}$ increases nearly linearly with E toward the dissociation limit D_0. For $E > 4.5$ eV, $\Delta E_{(2)}$ exceeds the vibrational quantum $\hbar\omega$ and multilevel transitions become important. The probabilities P_{01} and P_{02} calculated by use of eq 5 and 6a are also shown in Figure 1; other multilevel transition probabilities can be calculated similarly. For $E < 2$ eV, $\Delta E_{(2)}$ is small ($\ll\hbar\omega$) and $P_{on} \simeq [\Delta E_{(2)}/\hbar\omega]^n/n!$; *e.g.*, $P_{01} \simeq \Delta E_{(2)}/\hbar\omega$, which is the usual perturbation result.[2a] The excitation $0 \rightarrow 1$ is very efficient in the energy region from 2 to 8 eV, while $0 \rightarrow 2$ is efficient in 3 to 9 eV. The maximum values of P_{01} and P_{02} are 0.367 and 0.270 for $E \simeq 4.5$ and $\simeq 5.5$ eV, respectively. For $0 \rightarrow n$, the maximum value $P_{on}{}^{\max} = n^n\exp(-n)/n!$ occurs at $\Delta E_{(2)} = n\hbar\omega$. The collision time decreases slowly as E increases; *e.g.*, $t_c = 1.46 \times 10^{-14}$, 5.88×10^{-15}, and 3.72×10^{-15} sec for $E = 0.5$, 2, and 4 eV, respectively.

We can define the thermal average of the energy transfer as $\langle\Delta E_{(2)}\rangle = (kT)^{-1}\int_0^\infty \Delta E_{(2)}\exp(-E/kT)\mathrm{d}E$. By writing $\Delta E_{(2)} = \phi\exp[-\alpha/E^{0.659} - \gamma/(\beta E^{-0.659} + t_c)]$ and by using the Laplace integration method,[11] we obtain

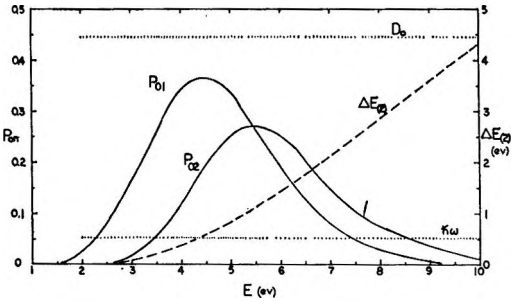

Figure 1. The vibrational energy transferred to H_2, $\Delta E_{(2)}$, and vibrational transition probabilities P_{01}, P_{02} as functions of the collision energy E. The dissociation limit D_0 and vibrational quantum $\hbar\omega$ are indicated.

$$\langle\Delta E_{(2)}\rangle = \sqrt{\frac{2\pi}{1.093\alpha}}\frac{\phi^*}{kT}\epsilon^{0.801} \times \exp\left(-2.517\,\frac{\epsilon^{0.602}}{kT} - \frac{\gamma}{\beta\epsilon^{-0.397} + t_c{}^*} + \frac{\hbar\omega}{2kT}\right) \tag{7}$$

where $\epsilon = 0.659\alpha kT$ and ϕ^*, $t_c{}^*$ are ϕ, t_c evaluated at $E = \epsilon^{0.602}$. The third term $\hbar\omega/2kT$ in the exponent is independent of the exact form of the interaction potential because symmetrization yielding this term affects only the leading term.[12] When $\langle\Delta E_{(2)}\rangle$ is introduced in eq 5, the resulting expression may be defined as thermal average transition probability; we shall denote this by $\langle P_{on}\rangle$. Note that the usual definition of the average probability is[2a] $\langle P_{on}\rangle = (kT)^{-1}\int_0^\infty P_{on}\cdot\exp(-E/kT)\mathrm{d}E$; this integral is impossible to solve explicitly for eq 5 and 6a unless we assume $\Delta E_{(2)} \ll \hbar\omega$.

For numerical illustration we write the relaxation time as $\tau = \{Z\langle P_{01}[1 - \exp(-\hbar\omega/kT)]\}^{-1}$, where Z is the number of collisions per second, $4N\sigma^2\sqrt{\pi kT/\mu}$, N being the number of molecules per cm^3 and σ a collision diameter to be defined. By taking $\sigma = 3$ Å, we obtain the relaxation times at 1 atm $P\tau = 96$, 24, 8.1, and 3.5 μsec-atm at 1600, 2000, 2400, and 2800°K, respectively. When these values are compared with experiment,[13] we find the ratio $\tau/\tau_{\text{expl}} = 9.6$, 4.7, 2.7, and 1.8, respectively, at the four temperatures. It is seen that

(6) I. I. Gol'dman and V. D. Krivchenkov, "Problems in Quantum Mechanics" (English ed, Addison-Wesley Publishing Co., Reading, Mass., 1961, pp 103–106.

(7) C. E. Treanor, *J. Chem. Phys.*, **43**, 532 (1965); **44**, 2220 (1966).

(8) H. Shin, *Chem. Phys. Lett.*, **5**, 137 (1970).

(9) For other approaches, see (a) M. S. Bartlett and J. E. Moyal, *Proc. Cambridge Phil. Soc.*, **45**, 545 (1949); (b) H. Shin, *Chem. Phys. Lett.*, **3**, 125 (1969).

(10) H. Shin, *J. Phys. Chem.*, **73**, 4321 (1969).

(11) N. G. de Bruijn, "Asymptotic Methods in Analysis," 2nd ed, North-Holland Publishing Co., Amsterdam, 1961, Chapter 4.

(12) H. Shin, *J. Chem. Phys.*, **42**, 59 (1965).

(13) J. H. Kiefer and R. W. Lutz, *ibid.*, **44**, 668 (1966); see Figure 6.

the calculated values of P_T decrease as temperature increases at a greater rate than do the experimental data. In spite of the collinear collision model and uncertainty in the expression for Z, the calculation gives reasonable values at higher temperatures. (The so-called steric factor is not introduced in the calculation.) If we used the LJ(12–6) or Morse potential, the same procedure would give P_T values which are too small compared to these values. In ref 13, we may note that complicated calculations for such potentials result in P_T almost two orders of magnitude too short.

At present, a full three-dimensional analysis including the problem of rotational transitions is not possible because we do not know enough of the details of the interaction potential as a function of the various angles and distances involved in such an analysis; see ref 2a for a review of approximate studies. As scattering measurements become available and theories develop, however, we will ultimately be able to find complete solutions of such problems.

Mass Spectrometric Determination of the Heat of Atomization of the Molecule SiCN

by D. W. Muenow and J. L. Margrave

Department of Chemistry, Rice University, Houston, Texas 77001
(Received March 5, 1970)

A gaseous molecule containing one atom each of silicon, carbon, and nitrogen has been mass spectrometrically observed and its heat of formation and atomization energy obtained. A molecule containing an additional oxygen atom, OSiCN, has been identified as well.

The species, SiCN or SiNC, is isoelectronic with the gaseous molecules C_2N and Si_2N reported previously.[1,2] From optical spectra both the CCN and CNC isomers of C_2N are known. Spectra attributable to the free radicals NCN, PCN, and AsCN have also been observed;[3] the structure M–CN is suggested. A previous mass spectrometric study[4] revealed the gaseous species NaCN, and more recently,[5] similar molecules with stoichiometries AlCN, OAlCN, BCN, and OBCN.

Measurements were performed with a Bendix Model 14-206A time-of-flight mass spectrometer equipped with a high-temperature Knudsen-effusion cell.[6] Two reaction equilibria were studied

$$\mathrm{SiC(hex)} + {}^1/_2\mathrm{N_2(g)} = \mathrm{SiCN(g)} \quad \text{(I)}$$

$$\mathrm{Si(g)} + \mathrm{C(graph)} + {}^1/_2\mathrm{N_2(g)} = \mathrm{SiCN(g)} \quad \text{(II)}$$

The previously unobserved ions $SiCN^+$ and $OSiCN^+$ were identified by their isotopic intensity distribution and shutterability. Their appearance potentials, 8.7 ± 0.5 and 7.4 ± 0.5 eV, respectively, suggest that both ions are formed by direct ionization of the corresponding neutral molecules, SiCN and OSiCN, and not by fragmentation.

A tantalum Knudsen cell was used for both systems. For equilibrium I several single hexagonal crystals of SiC were mixed with small chips of previously outgassed, high-purity boron nitride. The mixture was heated by radiation and electron bombardment of the cell, and the resultant molecular beam examined with 15-V ionizing electrons. Cell temperatures were measured with a Pt—Pt 10%–Rh thermocouple peened into the base of the cell. In order to obtain a third-law as well as a second-law heat for reaction I, an instrument-sensitivity constant was determined by the silver calibration technique.[7] Before temperature-dependent ion-intensity data could be collected, however, extensive outgassing of the BN chips was required to remove small amounts of boron oxide found to be present. This is necessary since the most abundant isotopic species of the $B_2O_2^+$ ion has the same m/e value as $SiCN^+$. When an oxygen-rich sample was purposely examined, the ion $OSiCN^+$ was observed as well, and was differentiated from the parent $B_2O_3^+$ ion by its isotopic-intensity distribution. For the oxygen-free sample the only parent ions observed in the temperature range studied (1656–1752°K) are N_2^+ and $SiCN^+$. Comparison of measured appearance potentials for the other observed ions, Si^+ and SiC^+, with published values[8] indicate these to be ion fragments, rather than parent ions produced from the ionization of gaseous decomposition products of SiC.

Loading the cell with small chips of spectroscopic grade graphite and silicon nitride permitted reaction II to be studied. Mass peaks for the ions Si^+, N_2^+, Si_2N^+, SiN^+, SiO^+, SiC^+, $SiCN^+$, and very small intensities for Si_2^+ and Si_3^+ were observed. Comparing measured appearance potentials with literature values[2,8,9] indicates Si^+, N_2^+, SiO^+, Si_2N^+ ions to be parents. The low value obtained for $SiCN^+$ agrees with that measured in equilibrium I and suggests a parent ion as well. The few per cent oxygen contained within the chips of silicon nitride are undoubtedly responsible for the small amount of SiO(g). The pres-

(1) (a) A. J. Merer and D. N. Travis, *Can. J. Phys.*, **43**, 1795 (1965); (b) *ibid.*, **44**, 353 (1966).

(2) K. F. Zmbov and J. L. Margrave, *J. Amer. Chem. Soc.*, **89**, 2492 (1967).

(3) (a) N. Basco and K. K. Yee, *Chem. Commun.*, **3**, 150 (1968); (b) *ibid.*, **3**, 152 (1968); (c) *ibid.*, **3**, 153 (1968).

(4) R. F. Porter, *J. Chem. Phys.*, **35**, 318 (1961).

(5) (a) K. A. Gingerich, *Naturwiss.*, **54**, 646 (1967); (b) *J. Amer. Chem. Soc.*, **91**, 4302 (1969); (c) *Chem. Commun.*, **13**, 764 (1969).

(6) A. Kant, *J. Chem. Phys.*, **41**, 1872 (1964).

(7) J. L. Margrave, Ed., "The Characterization of High Temperature Vapors," John Wiley and Sons, 1967, pp 222–227.

(8) J. Drowart, G. DeMaria, and M. G. Inghram, *J. Chem. Phys.*, **29**, 1015 (1958).

(9) D. L. Hildenbrand and E. Murad, *ibid.*, **51**, 807 (1969).

ence of oxygen in the system also suggests small quantities of the species OSiCN, but since the m/e values for the more abundant Si_2N^+-ion overlap, this is not certain. (This uncertainty also explains the absence of measurements for the obvious equilibrium, $Si_2N(g) + 2C(graph) + {}^1/_2N_2(g) = 2SiCN(g)$).

The ion intensities corresponding to Si^+, N_2^+, and $SiCN^+$ were measured as a function of temperature and were used to calculate the equilibrium constants for reactions I and II. From JANAF[10] free energy functions for Si(g) and N_2(g), estimated values for SiCN(g) (71 cal deg^{-1} mol^{-1} at 1700°K, ref 298°) and the equilibrium constants one derives the corresponding heats of reaction by the third-law method. These results are given in Table I. From a second-law treatment for reaction I one also obtains the value $\Delta H°_{298} = 113 \pm 3$ kcal mol^{-1}.

Table I: Equilibrium Data for SiCN(g) Formation

Reaction	Temp, °K	$-\log K_p$	$-\Delta[(G_T° - H°_{298})]/T$, cal deg^{-1} mol^{-1}	$\Delta H°_{298}$, kcal mol^{-1}
$SiC(hex) + {}^1/_2N_2(g) = SiCN(g)$	1656	7.4	(32)	109
	1680	7.1	(32)	108
	1701	7.0	(32)	109
	1721	6.5	(32)	106
	1752	6.6	(32)	109
			Av	108
$Si(g) + {}^1/_2N_2(g) + C(graph) = SiCN(g)$	1780	1.2	(5.5)	−20
	1792	1.0	(5.5)	−18
	1803	0.9	(5.5)	−17
	1820	0.9	(5.5)	−18
	1853	0.8	(5.5)	−17
			Av	−18

Using the average of the second- and third-law heats for reaction I, $\Delta H°_{298} = 110.5 \pm 4$ kcal mol^{-1} and the heat of formation of hexagonal silicon carbide, $\Delta H°_{298} = -18 \pm 4$ kcal mol^{-1},[11] one calculates $\Delta H_f°$[SiCN(g)] = 92.0 ± 7 kcal mol^{-1}. Similar treatment for reaction II and the heat of sublimation of silicon, $\Delta H_s°_{298} = 108.4 \pm 3$ kcal mol^{-1},[12] gives $\Delta H_f°$[SiCN(g)] = 90.3 ± 4 kcal mol^{-1}, in good agreement with that obtained using the data for reaction I. Values for the heat of atomization of SiCN(g), as calculated from the heats of equilibria I and II, the dissociation energy of N_2(g), $D_0° = 226 \pm 2$ kcal mol^{-1},[10] the heat of sublimation of carbon, $\Delta H_s°_{298} = 170.9 \pm 0.5$ kcal mol^{-1},[10] and the heat for the reaction, Si(g) + C(graph) = SiC(hex), $\Delta H°_{298} = -125 \pm 3$ kcal mol^{-1},[11] are ΔH_{atoms}[SiCN(g)] = 296 ± 8 and 300 ± 4 kcal mol^{-1}, respectively. Since fewer auxiliary thermodynamic data are required for computation using reaction II, the latter value with smaller error limits is favored, and one finally chooses for the heat of atomization, the average weighted-value, $\Delta H°_{atoms}$[SiCN(g)] = 298 ± 6 kcal mol^{-1}. This value is comparable to atomization energies given for similar molecules BC_2 (294 ± 6),[13] SiC_2 (303 ± 6),[13] BCN (301 ± 5),[5c] and AlCN (297 ± 5) kcal mol^{-1}.[5b]

Infrared matrix isolation studies are being conducted to obtain structural information on the species SiCN as well as AlCN and BCN.

Acknowledgment. This work was supported by the United States Atomic Energy Commission.

(10) "JANAF Thermochemical Tables," Dow Chemical Co., Midland, Mich., 1967.

(11) J. Drowart and G. DeMaria, *Silicon Carbide; High Temp. Semicond. Proc. Conf.*, 16 (1960).

(12) H. L. Shick, "Thermodynamics of Certain Refractory Compounds," Vol. 1, Academic Press, Inc , New York, N. Y., 1966, p 158.

(13) G. Verhaegen, F. E. Stafford, and J. Drowart, *J. Chem. Phys.*, **40**, 1622 (1964).

COMMUNICATIONS TO THE EDITOR

Ion Exchange between Solids

Sir: Ion exchange normally occurs through the medium of a liquid phase. The exchanging ions may be dissolved in water, various nonaqueous solvents, mixtures of solvents, or they may be present in fused salts. It has now been found that certain types of ion exchangers, such as the various zirconium phosphates, have the ability to exchange ions directly with solids or gases. The exchanger, in the hydrogen form, is heated with an anhydrous metal salt which on exchange forms a volatile acid. The exchange reaction proceeds by continuous removal of the volatile acid. The details are given in the text which follows.

Zirconium phosphate crystals and gels were prepared as described previously.[1] For the qualitative ion-exchange experiments weighed amounts of dried zirconium phosphate and the anhydrous metal salt were ground together in an agate mortar. The mixtures were then transferred to a platinum dish and heated in a furnace at several temperatures. Temperature control was good to ±2%. X-Ray diffraction patterns of the cooled products were then obtained with a recording Norelco wide angle diffractometer. For the quantitative weight loss experiments, weighed amounts of finely divided zirconium phosphate and metal salt were dispersed in dry benzene and then quantitatively transferred to a crucible. The solvent was then removed at reduced pressure. The dry solid mixture and crucible were weighed and the weight losses at various temperatures determined.

The reactions described below may be represented by the equation

$$Zr(HPO_4)_2 \cdot H_2O + {}^2/_x MCl_x \rightleftharpoons Zr(M)_{2/x}(PO_4)_2 + 2HCl + H_2O \quad (1)$$

The results of reaction of a number of salts with α-zirconium phosphate crystals[2] are summarized in Table I. The lithium and sodium exchanged phases were identified by comparison with the X-ray patterns of phases formed by the uptake of these ions from aqueous solution followed by dehydration.[2-4] The 7.41-Å phase has not previously been reported. That it represents a partially exchanged phase was shown in the following way. If copper(II) chloride reacts as in eq 1, the total weight loss for complete exchange should be 20.8%.

Table I: Results of Heating α-Zirconium Phosphate with Several Metal Halides

Salt	Reactant mole ratio, M/α-ZrP	Temp, °C	Time, hr	Product(s)[a]
LiCl	2	130	1	$Zr(LiPO_4)_2 \cdot H_2O$, phase H
NaCl	2	125	1	Mixture of 3 partially exchanged phases
NaCl	2	375	4	$Zr(NaPO_4)_2$, phase G
$ZnCl_2$	1	115	24	7.41 Å phase
$ZnCl_2$	1	370	20	7.87 + 7.41 Å phases
$MnCl_2$	1	160	12	7.41 phase
$CoCl_2$	1	160	48	7.41 Å phase
$AlCl_3$	${}^2/_3$	125	1	8.04 + 7.41 Å phases
$AlCl_3$	${}^2/_3$	130	24	7.41 phase
$HfCl_4$	${}^1/_2$	200	24	7.41 phase

[a] Numbers in angstrom units refer to the first interplanar spacing observed in the X-ray powder patterns. X-Ray patterns for phase H and G are given in ref 2.

Weight loss *vs.* temperature data for a 1:1 mol ratio of copper(II) chloride and α-zirconium phosphate are shown in Table II. Traces of a second phase (7.87 Å) were evident at a total weight loss of only 6.53%. When zinc chloride or hafnium chloride were exchanged instead of Cu(II) chloride, the 7.41-Å phase persisted up to about ${}^2/_3$ of the total capacity of the cation.

Table II: Reaction of $CuCl_2$ with α-Zirconium Phosphate

Temp °C	Total time at temp, hr	% wt loss	Color	X-Ray results
125	3	4.91	Brown	σ-Zirconium phosphate + $CuCl_2$
125	21	5.41	Brown	7.41 phase + $CuCl_2$
200	48	6.53	Brownish green	7.41 Å phase + trace of 7.87 phase + $CuCl_2$
260	24	15.66	Blue	7.87 Å phase
260	48	17.15	Blue	7.87 Å phase
330	12	20.8	Blue	7.87 Å phase
360	4	21.1	Blue	7.87 Å phase
400	8	21.1	Blue	7.87 Å phase

These wide ranges of metal content forming the same structure indicate that solid solutions of cation within the crystal lattice are forming. At cation loadings of from 30 to 100% the 7.87-Å phase was obtained. This phase must also represent a range of solid solution compositions. The fact that a variety of cation types give the same phases (almost identical interplanar spacings but different intensities) is indicative that the crystal lattice remains rigid with the cations occupying similar exchange sites. This is unlike the behavior of α-zirconium phosphate exchanging ions in aqueous electrolyte solutions where the lattice expands by movement of the α-zirconium phosphate layers to accommodate hydrated cations.[2] It would rather be expected that the phase changes might resemble those observed with fused salts.[5]

That the phenomena we are observing is indeed ion exchange is shown by the fact that the cations may be eluted with dilute acid solutions. The cations may also be removed by contacting the exchanged phases with gaseous hydrogen chloride. In some cases the original α-zirconium phosphate, minus its mole of water, was obtained. In other cases the structure was altered as in yet undetermined ways.

Ion-exchange separations may also be affected by the dry method. A solution containing equal parts of lith-

(1) A. Clearfield and J. A. Stynes, *J. Inorg. Nucl. Chem.*, **26**, 117 (1964).

(2) A. Clearfield, W. L. Duax, A. S. Medina, G. D. Smith, and J. R. Thomas, *J. Phys. Chem.*, **73**, 3424 (1969).

(3) A. Clearfield and J. M. Troup, *ibid.*, **74**, 314 (1970).

(4) E. Torracca, *J. Inorg. Nucl. Chem.*, **31**, 1189 (1969).

(5) G. Alberti, S. Allulli, and G. Cardini, *J. Chromatogr.*, **45**, 298 (1969).

ium and cesium chlorides was evaporated to dryness and the dry salt mixture ground together with α-zirconium phosphate crystals. On heating the mixture at 125° for several hours the lithium ion exchanged leaving the cesium chloride behind. This behavior is in accord with the known sieving properties of α-ZrP crystals and the idea of a rigid lattice proposed above. The crystals contain cavities which are quite large but the entranceways into the cavity are only large enough to permit a cation of about 2.6 Å diameter to enter.[2,6] Thus, cesium ion should be excluded as was in fact observed.

The phenomena described here seem to be a general property of ion exchangers in the hydrogen form. We have observed exchange in the dry state to occur with titanium, thorium, and cerium phosphate (both crystals and gels), zeolites, and Dowex-50. In the latter case exchange was determined from the amount of HCl evolved. Work aimed toward establishing selectivity series for different exchangers in the dry state and the exploration of the fuller implications of these phenomena is underway.

(6) A. Clearfield and G. D. Smith, *Inorg. Chem.*, **8**, 341 (1969).

DEPARTMENT OF CHEMISTRY
CLIPPINGER GRADUATE RESEARCH LABORATORIES
OHIO UNIVERSITY
ATHENS, OHIO

A. CLEARFIELD
J. M. TROUP

RECEIVED JANUARY 23, 1970

Contact Angles and Diffraction by a Plateau Border

Sir: A vertical soap film, pulled up from a bulk solution, lifts a "plateau border,"[1] each surface of which has the shape of a meniscus against a plane wetted wall (Figure 1). These two surfaces meet at a cusp above which the film rises. For the present purpose the film will be regarded as having negligible thickness. The angle, θ, at which each surface meets the plane of the film is the "contact angle" and is a sensitive indicator of certain film properties.[2] Light directed normal to the plane of the film and traversing the uppermost part of the border is refracted downward by the liquid of the border acting as a prism of wedge angle 2θ and refractive index n. Since the surfaces of this prism are not planar but concave outward (with curvature proportional to height above the flat horizontal surface), the lower the light passes through the border, the more it is deflected so that the light emerging from the border forms a "fan." On the basis of geometrical optics, the contact angle can be determined from the angle of deflection, α, of the top of this fan.[3] Unfortunately, diffraction effects cause a disturbance of this simple picture, and lead to fringes which complicate the

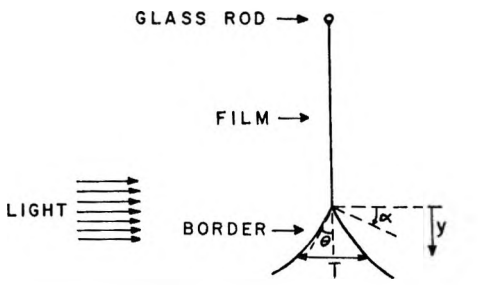

Figure 1. Cross section of vertical soap film joining a plateau border rising from the bulk liquid.

determination of the contact angle, as shown in Figure 3 of ref 3.

The angular position of the maxima and minima of the diffraction fringes can be observed with good accuracy. These features can be used to estimate the contact angle by the following quantitative, though simplified, argument. The thickness of the border increases with y, the vertical coordinate measured downward from the cusp, as

$$T = 2\theta y + \kappa y^2 \qquad y \geq 0 \tag{1}$$

where κ is the curvature of the surface immediately below the cusp. Higher powers of θ and y are neglected. The major effect on the light of traversing the border is to delay it in phase by the angle $(n - 1)kT$ where $k = 2\pi/\lambda$. Thus its amplitude after that traversal is proportional to $A(y) = \exp[(n - 1)kT]$. The wave front of this distribution may be resolved by Fourier analysis into components of various angles of deflection. The component of (downward) deflection α (higher powers of which are neglected) is proportional to

$$B(\alpha) = \int_{-\infty}^{+\infty} A(y)e^{-ik\alpha y}\,dy \simeq \int_0^{\infty} e^{ik(by^2-\beta y)}\,dy \tag{2}$$

where $\beta = \alpha - 2(n - 1)\theta$ and $b = (n - 1)\kappa$. The contribution to $B(\alpha)$ from negative y, representing light passing above the cusp, is small except for very small α and has been discarded. After making the substitution $kb(y - \beta/2b)^2 = \pi t^2/2$, one obtains

$$B(\alpha) = (\lambda/4b)^{1/2}e^{-i\pi\beta^2/2\lambda b}\int_{-\infty}^{\beta/\sqrt{\lambda b}} e^{i\pi t^2/2}\,dt \tag{3}$$

The magnitude of this expression, hence of the intensity of the deflected light, has maxima and minima for values of $\beta/\sqrt{\lambda b}$ that are very close to

$$\frac{\beta}{\sqrt{\lambda b}} = \frac{\alpha - 2(n-1)\theta}{\sqrt{\lambda b}} = \left(\frac{4m-1}{2}\right)^{1/2}$$
$$m = 1, 2, 3, \ldots \tag{4}$$

(1) K. J. Mysels, K. Shinoda, and S. Frankel, "Soap Films," Pergamon Press, New York, N. Y., 1959.

(2) F. Huisman and K. J. Mysels, *J. Phys. Chem.*, **73**, 489 (1969); A. Scheludko, B. Radoev, and T. Kolarov, *Trans. Faraday Soc.*, **64**, 2213 (1968); T. Kolarov, A. Scheludko, and D. Exerowa, *ibid.*, **64**, 2864 (1968).

(3) H. M. Princen, *J. Phys. Chem.*, **72**, 3342 (1968).

where m is odd for the maxima and even for the minima. (This approximation is in error by <1% for $m = 1$, <0.1% thereafter.) Thus, by plotting the observed values of α at the maxima and minima *vs.* these discrete numbers, $2(n - 1)\theta$ is obtained as the intercept. The slope of the straight line is given by $\sqrt{\lambda b}$, which permits the calculation of the curvature κ at the top of the border, if the conditions of observation do not permit its determination in other ways.

The diffraction fringes of a number of observations reported in ref 3 are in good agreement with eq 4. In one fringe nine successive maxima and minima of intensity could be recognized. Their deflection angles, α, were in the range 0.1585 (first maximum) to 0.211 radian (fifth maximum). These angles were consistent with eq 4 within the accuracy of estimation (approximately ± 0.0002).

A more detailed and refined analysis of the use of the diffraction pattern for the estimation of θ will be presented shortly.[4]

Acknowledgment. One of us (H. M. P.) thanks the Lever Brothers Co. for permission to publish this paper.

(4) H. M. Princen and S. Frankel, forthcoming publication.

411 N. MARTEL AVENUE STANLEY FRANKEL
LOS ANGELES, CALIFORNIA 90036

LEVER BROTHERS RESEARCH CENTER H. M. PRINCEN
EDGEWATER, NEW JERSEY 07020

RECEIVED MARCH 2, 1970

Comments on "Kinetics of the Addition of Ethyl, Isopropyl, *n*-Butyl, and Isopentyl Radicals to Ethylene"

Sir: In a recent article under the above title, Watkins and O'Deen[1] reported the kinetics of the addition of ethyl, isopropyl, *n*-butyl, and isopentyl radicals to ethylene. The nature of the method employed in their study requires a detailed quantitative analysis of the products, and also involves difficulties because of the necessity for an essentially complete reaction mechanism. In such a system, the reported cross disproportionation-to-combination rate-constant ratios may not be very accurate because of the difficulty of disentangling the disproportionation, and sometimes combination products. The rate constant ratios, on the other hand, could be checked in a simple way.

The total rate of formation of 1-C_4H_8 in the ethyl–ethylene system has been used in the calculation of the cross disproportionation-to-combination ratio of ethyl and *n*-butyl radicals $\Delta(\mathrm{Et}, \mathrm{Bu}^n)$, k_6/k_5, by Watkins and O'Deen. $R_{1\text{-}C_4H_8}$ by reaction 9a is about 9% at 75° and 17% at 142° taking $\Delta(\mathrm{Bu}^n, \mathrm{Bu}^n)$ to be 0.14 and considering the total rate of formation of n-C_8H_{18}.

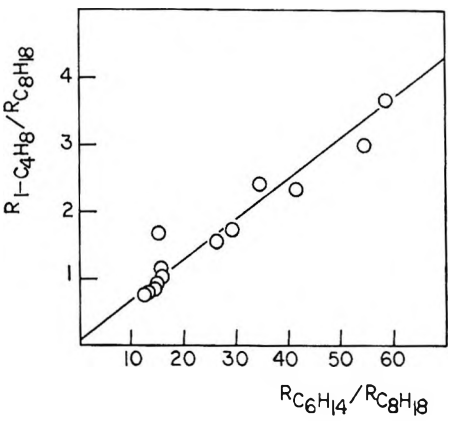

Figure 1. The evaluation of $\Delta(\mathrm{Et}, \mathrm{Bu}^n)$ and $\Delta(\mathrm{Bu}^n, \mathrm{Bu}^n)$ from eq IV.

Now, the total rate of formation of 1-C_4H_8 can be written as

$$R_{1\text{-}C_4H_8\,(\mathrm{tot})} = R_{1\text{-}C_4H_8\,(6)} + R_{1\text{-}C_4H_8\,(9a)} \qquad (\mathrm{I})$$

where

$$R_{1\text{-}C_4H_8\,(6)} = \frac{k_6}{k_5} R_{C_6H_{14}\,(5)} \qquad (\mathrm{II})$$

$$R_{1\text{-}C_4H_8\,(9a)} = \frac{k_{9a}}{k_9} R_{n\text{-}C_8H_{18}\,(9)} \qquad (\mathrm{III})$$

Inserting eq II and III into the eq I and dividing both sides by $R_{n\text{-}C_8H_{18}\,(9)}$ we have

$$\frac{R_{1\text{-}C_4H_8\,(\mathrm{tot})}}{R_{n\text{-}C_8H_{18}\,(9)}} = \frac{k_6}{k_5}\frac{R_{C_6H_{14}\,(5)}}{R_{n\text{-}C_8H_{18}\,(9)}} + \frac{k_{9a}}{k_9} \qquad (\mathrm{IV})$$

If the contribution of the hexane and octane produced from other reactions are negligible, R_5 and R_9 can be substituted by their total rate of formation [$R_{C_6H_{14}\,(\mathrm{tot})}$ and $R_{n\text{-}C_8H_{18}\,(\mathrm{tot})}$]. Thus by plotting the ratio of the total rate of formation of 1-butene over the rate of formation of *n*-octane against the ratio of the rate of formation of *n*-hexane over the *n*-octane, k_6/k_5, $\Delta(\mathrm{Et}, \mathrm{Bu}^n)$, may be obtained from the slope and k_{9a}/k_9, $\Delta(\mathrm{Bu}^n, \mathrm{Bu}^n)$, from the intercept. The evaluation of the data in this way is shown in Figure 1. A least-square treatment of the results gave $k_6/k_5 = \Delta(\mathrm{Et}, \mathrm{Bu}^n) = 0.059 \pm 0.005$ and $k_{9a}/k_9 = \Delta(\mathrm{Bu}^n, \mathrm{Bu}^n) = 0.12 \pm 0.07$ (runs 1–7 and 20 of the Table I are not included because of the uncertainty on the product analysis).

$\Delta(\mathrm{Bu}^n, \mathrm{Bu}^n)$ has been shown to be 0.14 independent of temperature, from a careful study of the photolysis of azo-*n*-butane.[2] The agreement between these two values of $\Delta(\mathrm{Bu}^n, \mathrm{Bu}^n)$ can be considered to be satisfactory.

(1) K. W. Watkins and L. A. O'Deen, *J. Phys. Chem.*, **73**, 4094 (1969).

(2) W. E. Morganroth and J. G. Calvert, *J. Amer. Chem. Soc.*, **88**, 5387 (1966).

The previously reported values[3,4] for $\Delta(Bu^n, Bu^n)$ would now appear to be in error. The above result also obeys the Δ relation with the entropy differences of the products.

Most of the available information[5] on the total set of reactions between two different radicals, $R(a)$ and $R(b)$, indicate a simple relation.[6]

$$\frac{1 + \Delta_{ab}(\text{cross}) + \Delta_{ba}(\text{cross})}{\{[1 + \Delta_{aa}(\text{auto})][1 + \Delta_{bb}(\text{auto})]\}^{1/2}} \Phi = 2 \quad (V)$$

where

$$\Phi = k_{ab}/(k_{aa}k_{bb})^{1/2}$$

In this way taking $\Delta(Et, Et) = 0.13$, $k_7/k_5 = \Delta(Bu^n, Et)$ can be found to be 0.066.

The autodisproportionation-to-combination reactions of isopentyl radicals in the isopropyl–ethylene system have not been taken into account in the reaction scheme (reactions 17–27). They can be written as

$$2i\text{-}C_5H_{11} \longrightarrow C_{10}H_{22} \text{ (2,7-dimethyloctane)} \quad (28)$$

$$2i\text{-}C_5H_{11} \longrightarrow i\text{-}C_5H_{12} + C_5H_{10} \text{ (3-methyl-1-butene)} \quad (29)$$

Now, $k_{23}/k_{21} = \Delta(Pe^i, Pr^i)$ can be evaluated as

$$R_{i\text{-}C_5H_{12}\,(\text{tot})} = R_{i\text{-}C_5H_{12}\,(23)} + R_{i\text{-}C_5H_{12}\,(29)} \quad (VI)$$

where

$$R_{i\text{-}C_5H_{12}\,(23)} = \frac{k_{23}}{k_{21}} R_{C_8H_{18}} \quad (VII)$$

$$R_{i\text{-}C_5H_{12}\,(29)} = \frac{k_{29}}{k_{28}} R_{C_{10}H_{22}\,(28)} \quad (VIII)$$

The Φ relation requires that

$$R_{C_{10}H_{22}\,(28)} = \frac{R^2_{C_8H_{18}}}{4R_{C_6H_{14}}} \quad (IX)$$

Therefore

$$R_{i\text{-}C_5H_{12}\,(29)} = \frac{k_{29}}{k_{28}} \frac{R^2_{C_8H_{18}}}{4R_{C_6H_{14}}} \quad (X)$$

Inserting eq VII and X into eq VI and dividing both sides by $R_{C_8H_{18}}$ we have

$$\frac{R_{i\text{-}C_5H_{12}\,(\text{tot})}}{R_{C_8H_{18}}} = \left[\frac{1}{4}\frac{k_{29}}{k_{28}}\right]\left[\frac{R_{C_8H_{18}}}{R_{C_6H_{14}}}\right] + \frac{k_{23}}{k_{21}} \quad (XI)$$

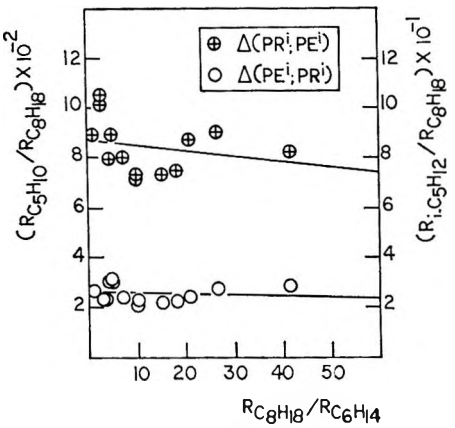

Figure 2. The evaluation of $\Delta(Pr^i, Pe^i)$, $\Delta(Pe^i, Pr^i)$ from eq XI and XII.

and similarly for $\Delta(Pr^i, Pe^i)$

$$\frac{R_{C_5H_{10}\,(\text{tot})}}{R_{C_8H_{18}}} = \left[\frac{1}{4}\frac{k_{29}}{k_{28}}\right]\left[\frac{R_{C_8H_{18}}}{R_{C_6H_{14}}}\right] + \frac{k_{22}}{k_{21}} \quad (XII)$$

When $R_{i\text{-}C_5H_{12}\,(\text{tot})}/R_{C_8H_{18}}$ and $R_{C_5H_{10}\,(\text{tot})}/R_{C_8H_{18}}$ are plotted against $R_{C_8H_{18}}/R_{C_6H_{14}}$, k_{23}/k_{21} and k_{22}/k_{21} can be obtained from intercepts and k_{29}/k_{28} from the slopes of the resulting straight lines as shown in Figure 2. A least-square treatment of the results gave $k_{23}/k_{21} = \Delta(Pe^i, Pr^i) = 0.265 \pm 0.003$ and $k_{22}/k_{21} = \Delta(Pr^i, Pe^i) = 0.087 \pm 0.003$. Unfortunately, $k_{29}/k_{28} = \Delta(Pe^i, Pe^i)$ could not be obtained from the resulting slopes since in both cases, negative slope was found. However, it can be found from eq V, taking $k_{20}/k_{19} = \Delta(Pr^i, Pr^i) = 0.60$, $k_{29}/k_{28} = \Delta(Pe^i, Pe^i) = 0.13$.

Acknowledgments. The author wishes to thank Dr. G. G. Meisels for his helpful comments and also the United States Atomic Energy Commission which supported this work under Contract No. AT-(40-1)-3606.

(3) J. A. Kerr and A. F. Trotman-Dickenson, *J. Chem. Soc.*, 1602 (1960).

(4) J. C. J. Thynne, *Trans. Faraday Soc.*, **58**, 1533 (1962).

(5) J. O. Terry and J. H. Futrell, *Can. J. Chem.*, **45**, 2327 (1967).

(6) A. R. Blake, J. F. Henderson, and K. O. Kutschke, *ibid.*, **39**, 1920 (1961).

DEPARTMENT OF CHEMISTRY
UNIVERSITY OF HOUSTON
HOUSTON, TEXAS 77004

YUKSEL INEL

RECEIVED MARCH 17, 1970